Synthesis and characterization of new hybrid polyoxometalates for photocatalytic and biological applications

Zeinab El Hajj

THÈSE DE DOCTORAT

NNT : 2023UPASF078

Synthesis and characterization of new hybrid polyoxometalates for photocatalytic and biological applications

Synthèse et caractérisation de nouveaux polyoxométallates hybrides pour applications photocatalytiques et biologiques

Thèse de doctorat de l'Université Paris-Saclay et de l'Université Libanaise

École doctorale n°571 : Sciences chimiques : Molécules, Matériaux, Instrumentation et Biosystèmes (2MIB)
Spécialité de doctorat : Chimie
Graduate School: Chimie. Référent: Université de Versailles Saint-Quentin-en-Yvelines

Thèse préparée dans les unités de recherche **Institut Lavoisier de Versailles** (Université Paris-Saclay, UVSQ, CNRS) et **Laboratoire de Chimie de Coordination Inorganique et Organométallique** (Université Libanaise, EDST), sous la direction de **Sébastien FLOQUET**, Professeur des universités, et la co-direction de **Daoud NAOUFAL**, Professeur des universités.

Thèse soutenue à Beyrouth, le 19 Décembre 2023, par

Zeinab EL HAJJ

Composition du Jury

Membres du jury avec voix délibérative

Laure CATALA Professeure des universités, Université Paris Saclay	Présidente
Bassem BASSIL Professeur des universités, Université Jacobs de Brême	Rapporteur & Examinateur
Richard VILLANNEAU Maître de conférences-HDR, Sorbonne Université	Rapporteur & Examinateur
Sébastien BLANCHARD Maître de conférences-HDR, Sorbonne Université	Examinateur
Ahmad MEHDI Professeur des universités, Université de Montpellier	Examinateur
Mourtada SROUR Professeur des universités, Université Libanaise	Examinateur

université PARIS-SACLAY
ÉCOLE DOCTORALE
Sciences Chimiques : Molécules, Matériaux, Instrumentation et Biosystèmes (2MIB)

Title : Synthesis and characterization of new hybrid polyoxometalates for photocatalytic and biological applications.

Keywords : Polyoxometalates, SiW_{10}-monoB_{10} adduct, Cyclodextrins, Closo-decaborate anions, $B_{20}H_{18}$ clusters, Imido hexamolybdates.

Abstract : The development of a novel class of multifunctional POM hybrids, denoted as **"SiW_{10}-B_{10}-Organic ligand"** starting from the POM-Borate precursor "SiW_{10}-monoB_{10}",has been investigated for biological applications. The latter resulted from the reaction of the carbonyl group of closo-decahydrodecaborate anion $[B_{10}H_9CO]^-$ with one of the two pendant amine groups of the organic linker 3-(Aminopropyl)triethoxysilane (APTES), which is covalently attached to the POM Keggin-type polyoxometalate $[SiW_{10}O_{36}]^{2-}$.Herein,we aimed to go further by functionalizing the second amine function of SiW_{10}-monoB_{10}.The mono-adduct "SiW_{10}-monoB_{10}" compound was firstly synthesized with good purity and in sufficient quantities, then characterized by atypical ^1H-^{15}N HMQC NMR, which allowed the examination of the nature of the free amine function and showed the presence of non-zero amine fraction that would not be involved in the H-H interaction with the decaborate cluster. Consequently, the possibility of new functional groups on this free amino arm of SiW_{10}-monoB_{10} adduct was tested and followed through ^1H and ^{11}B NMR. Despite our best efforts and the various strategies, we have investigated, the studies carried out show that interactions with the POM part and with B-H groups are preferential to the formation of the covalent bonds we had hoped for.

In the following section, we turned our attention to other hybrid POMs used as photoinitiators. Anthracene-, benzophenone- and anthraquinone-based derivatives were respectively covalently grafted onto the polyoxometalate (POM) platform $[Mo_6O_{19}]^{2-}$, giving rise to highly colored organo-imido Lindqvist complexes: POM-imidoanthraquinone **(POM-AQ)**, POM-imidoanthracene **(POM-AC)**, and POM-imidobenzophenone **(POM-AB)**. It has been evidenced that photosystems combining N-methyldiethanolamine (MDEA) as electron donor and these hybrid POMs promote free-radical photopolymerization of acrylate monomer derivatives under irradiation in the visible range, while in similar conditions, no polymerization was observed considering when adding each of the hexamolybdate cluster or the organic entity alone with the MDEA as electron donor and these hybrid POMs promote free-radical photopolymerization of acrylate monomer derivatives under irradiation in the visible range, while in similar conditions, no polymerization was observed considering when adding each of the hexamolybdate cluster or the organic entity alone with the MDEA and acrylate monomers. Such organo-imido Lindqvist species can represent new, easy-to-synthesize, efficient visible-light photoinitiators. Moreover, due to the presence of the POM, coatings prepared using the **POM-AQ**/MDEA/Soybean oil epoxidized acrylate photosystem exhibit excellent mechanical properties, with very good flexibility, resistance to brittle fracture, and adherence to the steel.

In the last chapter, the preparation of new closo-borate/CD inclusion complexes has been studied to elaborate systems strong enough to be considered for biological application. Playing on the volume and charge of $[B_{10}H_{10}]^{2-}$ was set out to increase their chaotropic character and thus enhance their binding affinity to cyclodextrins. The encapsulation of $[B_{10}H_9NCCH_3]^-$ and $[B_{20}H_{18}]^{2-}$ anions within cyclodextrins has been investigated in two different parts. ESI-MS and NMR evidenced the formation of inclusion complexes between the borate compounds and β- and γ-CDs, while weaker interactions are evidenced with α-CD, for which the binding constants were determined by NMR and ITC. These constants values are much higher than those obtained in previous work with $[B_{10}H_{10}]^{2-}$ thus validating the approach followed in this thesis work.

A new approach in $[B_{20}H_{18}]^{2-}$ chemistry has also been studied at the end of the work related to the Hydrogen-Deuterium exchange process in $[B_{20}H_{18}]^{2-}$ aqueous solution.$^1H\{^{11}B\}$ and $^{11}B\{^1H\}$ NMR evidenced selective deuterium-proton exchange processes with the protons of equatorial Boron atoms over a period of time with the presence of degradation. Interestingly, it has been shown through NMR of $[B_{20}H_{18}]^{2-}$/CD solutions in D_2O that β- and γ-CDs would protect the anion from degradation after 4-5 months, opening the route for designing Boron-based drugs with enhanced stability suitable for medical use.

université PARIS-SACLAY
ÉCOLE DOCTORALE
Sciences Chimiques : Molécules, Matériaux, Instrumentation et Biosystèmes (2MIB)

Titre : Synthèse et caractérisation de nouveaux polyoxométallates hybrides pour applications photocatalytiques et biologiques.

Mots clés : Polyoxométallates, SiW_{10}-monoB_{10} adduct, Cyclodextrines, Closo-decaborate anions, $B_{20}H_{18}$ anion, Imidohexamolybdates.

Résumé : Le développement d'une nouvelle classe de POM hybrides multifonctionnels, désignés sous le nom de **"SiW_{10}-B_{10}-Ligand organique"**, à partir du précurseur POM-Borate "SiW_{10}-monoB_{10}", a été étudié pour des applications biologiques. Ce dernier résulte de la réaction du groupe carbonyle de l'anion closo-décahydrodécaborate $[B_{10}H_9CO]^-$ avec l'un des deux groupes amine pendants du lien organique 3-(aminopropyl)triéthoxysilane, qui est attaché de manière covalente au polyoxométalate de type Keggin POM $[SiW_{10}O_{36}]^{2-}$.L'objectif initiale de cette étude était d'aller plus loin en fonctionnalisant la deuxième fonction amine de SiW_{10}-monoB_{10}.Le composé mono-adduct "SiW_{10}-monoB_{10}" a d'abord été synthétisé avec une bonne pureté et en quantité suffisante, puis caractérisé par une spectrométrie RMN ^1H-^{15}N HMQC, ce qui a permis d'examiner la nature de la fonction amine libre et de montrer la présence d'une fraction d'amine non nulle qui ne serait pas impliquée dans l'interaction H-H avec le cluster de déca-borate. Malgré tous nos efforts et différentes stratégies étudiées, les études réalisées montrent que les interactions avec la partie POM et avec les groupements B-H sont préférentielles à la formation des liaisons covalentes espérées. Dans la partie suivante, nous nous sommes intéressés à d'autres POMs hybrides utilisés comme photo-amorceurs. Des dérivés à base d'anthracène, de benzophénone et d'anthraquinone ont été respectivement greffés de manière covalente sur la plateforme de polyoxométalate (POM) $[Mo_6O_{19}]^{2-}$,donnant naissance à des complexes Lindqvist organo-imido: POM-imidoanthraquinone **(POM-AQ)**,POM-imidoanthracène **(POM-AC)** et POM-imidobenzophénone **(POM-AB)**.Il a été démontré que les photosystèmes combinant la N-méthyldiéthanolamine (MDEA) en tant que donneur d'électrons et ces hybrides POM favorisent la photopolymérisation radicalaire libre de dérivés de monomères acrylates sous irradiation dans le domaine visible, tandis que dans des conditions similaires, aucune polymérisation n'a été observée lorsque l'on ajoutait chacun des clusters d'hexamolybdate ou de l'entité organique seule avec la MDEA et les monomères acrylates. Grâce à la présence du POM, les revêtements préparés à l'aide du photosystème **POM-AQ**/MDEA/acrylate d'huile de soja époxydée présentent d'excellentes propriétés mécaniques, avec une très bonne flexibilité, et une résistance à la rupture fragile.

Dans le dernier chapitre, la préparation de nouveaux complexes d'inclusion closo-borate/CD a été étudiée pour élaborer des systèmes suffisamment forts pour être envisagés pour des applications biologiques. Jouant sur le volume et la charge de $[B_{10}H_{10}]^{2-}$,on a cherché à augmenter leur caractère chaotrope des clusters de bore et ainsi à augmenter leur affinité de liaison avec les CDs. L'encapsulation des anions $[B_{10}H_9NCCH_3]^-$ et $[B_{20}H_{18}]^{2-}$ dans les CDs a été étudiée en deux parties distinctes. La spectrométrie de RMN ont montré la formation de complexes d'inclusion entre $[B_{10}H_9NCCH_3]^-$ et $[B_{20}H_{18}]^{2-}$ et les β- et γ-CDs, tandis que des interactions plus faibles ont été observées avec la α-CD, pour laquelle les constantes de liaison ont été déterminées par RMN et ITC. Ces valeurs sont bien supérieures à celles obtenues lors de travaux antérieurs avec $[B_{10}H_{10}]^{2-}$ validant ainsi l'approche suivie dans ce travail de thèse.

Une nouvelle approche en chimie du $[B_{20}H_{18}]^{2-}$ a également été étudiée à la fin du travail lié au processus d'échange hydrogène-deutérium en solution aqueuse de $[B_{20}H_{18}]^{2-}$.La RMN $^1H\{^{11}B\}$ et $^{11}B\{^1H\}$ a mis en évidence des processus d'échange de deutérium-proton avec les protons des atomes de bore sur une période de temps en présence de dégradation. Il est intéressant de noter que, par le biais de la RMN de solutions $[B_{20}H_{18}]^{2-}$/CD dans D_2O,il a été démontré que les cyclodextrines β et γ protégeraient l'anion de la dégradation après 4 à 5 mois, ouvrant la voie à la conception de médicaments à base de bore offrant une stabilité accrue adaptée à une utilisation médicale.

Acknowledgments

I wanted to take a moment to express my heartfelt gratitude and appreciation to everyone who contributed in one way or another to my PhD journey. First and foremost, I would like to thank the jury members for their acceptance to evaluate this work: **Prof. Laure Catala, Prof. Bassem Bassil, Dr. Richard Villanneau, Prof. Ahmad Mehdi, Prof. Mourtada Srour, and Dr. Sébastien Blanchard.**

I consider this research a significant milestone in my academic and personal life. It has been a remarkable and rewarding experience, and I couldn't have accomplished it without the invaluable contributions of my co-directors and mentors. **Prof. Sébastien Floquet**, my supervisor in Versailles, your mentorship has been at the heart of my research growth. Your willingness to share insights, patience in guiding me through challenges, and unwavering support have influenced my success. I am grateful for your countless hours of advising and mentoring me, which undoubtedly made a significant difference in my research. I am also grateful for your support in securing funding for my research, and your belief in my abilities has enabled me to pursue projects I once only dreamed of.

I would also like to thank **Dr. Olivier Oms**; you have played a pivotal role in my academic journey. Your ability to challenge my ideas, encourage critical thinking, and provide constructive feedback has been invaluable in refining my research and improving my skills. Working in the same lab with you and **Prof. Pierre Mialane** and watching your passion for doing experiments, your dedication to making it work, and your incredible skills and way of scientific thinking had reflected on me immensely by giving me determination and encouragement to pursue my goals in the research. Your open-door policy and approachability have made it easy for me to seek advice and clarification when needed.

To my supervisor in Beirut, **Prof. Daoud Naoufal**, I am deeply thankful for your mentorship, encouragement, and enthusiasm toward this research. Your dedication to excellence, willingness to share your knowledge, and commitment to helping me succeed have profoundly given me the confidence to take on challenges and strive for excellence in my work.

I also want to express my gratitude towards **Dr. Mohamed Haouas** for sharing your expertise on NMR spectroscopy experiments essential for my research. Your efforts in maintaining critical equipment and ensuring the smooth functioning of the machine and your dedication to guiding me through challenges have consistently exceeded my expectations. I will carry the knowledge and experiences gained during our work together throughout my future career. I am also thankful to **Dr. Manal Diab** for your moral and scientific support, with valuable and constructive suggestions during my research that helped develop this work.

I am grateful to everyone at Institut Lavoisier de Versailles ILV, with whom I have the opportunity to work, for providing a stimulating and conducive academic and personal development environment. Your camaraderie and collaborative spirit have made my time at the lab even more enriching and enjoyable, even during difficult times. **Prof. Emmanuel Cadot**, thank you for consistently demonstrating a deep commitment to fostering an environment of learning, collaboration, and innovation. **Dr. Catherine Roch**, thank you for providing me with a smooth basis to understand polyoxometalate chemistry. Your friendly personality makes me feel welcome, breaking language and culture barriers. **Dr. Nathalie Leclerc**, thanks for the morning smile and for constantly ensuring lab security. It makes me feel safe and less stressed. **Dr. Marc Lepeltier**, thank you for letting me use your place whenever I need to; seeing how focused and organized you are doing experiments encourages me to be the same.

I also owe many thanks to **Prof. Davy-Louis Versace** (Université Paris-Est Créteil, Paris) for his collaboration on the photochemistry study on the new monosubstituted organoimido POM derivatives. Thanks go also to **Prof. David Landy** (Littoral Côte d'Opale in Dunkerque) for ITC studies on Borate/CD systems, **Dr. Jérôme Marrot** for crystallography, **M. Flavien Bordeaux** for helping me perfect NMR recordings, and **Mme. Aurelie Damond** for the ESI-MS (ILV, Versailles).

I would also like to extend my appreciation to my colleagues and friends. Our discussions, debates, and shared experiences have expanded my horizons, deepened my understanding of our field, and encouraged me to push the boundaries of my research. The collaborative environment we fostered allowed us to learn from one another and grow both personally and academically. **Cédric**, thank you for always being willing to help me with the paperwork and telephone calls needed in French, whether inside or outside academic life. Thank you for always checking on us foreigners if we need any help and ensuring we are socially integrated inside and outside the lab. **Sergiu**, I treasure your kindness and how you care about others; it is truly heartwarming. You were always by my side, discussing science and sharing funny talks and encouragement when I was down. **Sa** and **Diana**, thank you for your beautiful spirit. I hope you reach what you are aiming for. **Nour**, with whom I shared long times arguing and discussing ideas, shared lunch and coffee breaks daily, countless evenings, and memorable trips. Thank you for your encouragement and support, and I wish you the best in your life. To my lab mates in Lebanon, **Nadine**, **Walaa**, and **Ali**, who have supported me since the Master's, your insights and diverse perspectives enriched my research. I am grateful for the countless hours we spent learning from one another.

To my best friends **Ola, Rewa, Fatima A., Fatima T., Shaimaa,** and **Amanda** for comforting me during challenging times; your unwavering support has been my pillar of strength. Our adventures and countless inside jokes have filled my life with laughter and unforgettable memories. You've stood by my side through thick and thin, and I couldn't be more grateful.

Special thanks to my father, brothers, and sisters for your love, support, and guidance; it has been my compass in navigating life's twists and turns. To my mother, thank you for being the extraordinary person you are. I love you more than words can express; your encouragement and support in my pursuits, dreams, and aspirations have given me the courage to chase after them relentlessly. Your love has made me who I am today, and I am eternally grateful for that. I would also like to thank my beloved husband, **Ali**; your willingness to take on added responsibilities and your ability to provide a loving and stable environment have allowed me to pursue my studies with peace of mind. Every time I faced a daunting challenge, you reminded me of my capabilities and encouraged me to push forward. I am blessed to have a partner as loving and supportive as you.

List of Publications

The following publications were published as a result of work undertaken over the course of this thesis.

1) "Recent Achievements on Functionalization within Closo-Decahydrodecaborate $[B_{10}H_{10}]^{2-}$ Clusters". Mahfouz, N.; Ghaida, F. A.; **El Hajj, Z.**; Diab, M.; Floquet, S.; Mehdi, A.; Naoufal, D. ChemistrySelect, **2022**, 7 (21), e202200770.

2) "Grafting of Anionic Decahydro-Closo-Decaborate Clusters on Keggin and Dawson-Type Polyoxometalates: Syntheses, Studies in Solution, DFT Calculations and Electrochemical Properties". Diab, M.; Mateo, A.; El Cheikh, J.; **El Hajj, Z.**; Haouas, M.; Ranjbari, A.; Guérineau, V.; Touboul, D.; Leclerc, N.; Cadot, E.; Naoufal, D.; Bo, C.; Floquet, SMolecules , **2022**, 27 (22), 7663.

3) "Shifting from UV to Visible-Light the Activity of Organic Photoinitiators via the Covalent Grafting of Polyoxometalates". **El Hajj, Z.**; Pierau, L.; Malval, J.-P.; Marrot, J.; Mazeran, P.-E.; Naoufal, D.; Ha-Thi, M.-H.; Steenkeste, K.; Dolbecq, A.; Floquet, S.; Oms, O.; Versace, D.-L.; Mialane, P. Macromolecules, **2023**, 56 (15), 6105–6116.

4) Playing with the Chaotropic Effect to Improve the Encapsulation of Decaborate Clusters within Cyclodextrins". **El Hajj, Z.**; Calancea, S.; Haouas, M.; Landy, D.; Naoufal, D.; Floquet, S. J Clust Sci, **2023**.

Résumé : Le développement d'une nouvelle classe de POM hybrides multifonctionnels, désignés sous le nom de "SiW_{10}-B_{10}- ligand organique", à partir du précurseur POM-Borate "SiW_{10}-monoB_{10}", a été étudié pour des applications biologiques. Ce dernier résulte de la réaction du groupe carbonyle de l'anion closo-décahydrodécaborate $[B_{10}H_9CO]^-$ avec l'un des deux groupes amine pendants du lien organique 3-(aminopropyl)triéthoxysilane (APTES), qui est attaché de manière covalente au polyoxométalate de type Keggin POM $[SiW_{10}O_{36}]^{2-}$. L'objectif initiale de cette étude était d'aller plus loin en fonctionnalisant la deuxième fonction amine de SiW_{10}-monoB_{10}. Le composé mono-adduit "SiW_{10}-monoB_{10}" a d'abord été synthétisé avec une bonne pureté et en quantité suffisante, puis caractérisé par une spectrométrie RMN ^1H-^{15}N HMQC, ce qui a permis d'examiner la nature de la fonction amine libre et de montrer la présence d'une fraction d'amine non nulle qui ne serait pas impliquée dans l'interaction H-H avec le cluster de déca-borate. Par conséquent, la possibilité de nouveaux groupes fonctionnels sur ce bras amino libre du complexe adduit SiW_{10}-monoB_{10} a été testée et suivie par RMN ^1H et ^{11}B en utilisant différents mélanges de SiW_{10}-monoB_{10}/ligand organique/DIPEA dans des solutions de CD_3CN. Malgré tous nos efforts et différentes stratégies étudiées, les études réalisées montrent que les interactions avec la partie POM et avec les groupements B-H sont préférentielles à la formation des liaisons covalentes espérées.

Dans la partie suivante, nous nous sommes intéressés à d'autres POMs hybrides utilisés comme photo-amorceurs UV. Des dérivés à base d'anthracène, de benzophénone et d'anthraquinone ont été respectivement greffés de manière covalente sur la plateforme de polyoxométalate (POM) $[Mo_6O_{19}]^{2-}$, donnant naissance à des complexes Lindqvist organo-imido hautement colorés : POM-imidoanthraquinone (POM-AQ), POM-imidoanthracène (POM-AC) et POM-imidobenzophénone (POM-AB). Il a été démontré que les photosystèmes combinant la N-méthyldiéthanolamine (MDEA) en tant que donneur d'électrons et ces hybrides POM favorisent la photopolymérisation radicalaire libre de dérivés de monomères acrylates sous irradiation dans le domaine visible, tandis que dans des conditions similaires, aucune polymérisation n'a été observée lorsque l'on ajoutait chacun des clusters d'hexamolybdate ou de l'entité organique seule avec la MDEA et les monomères acrylates. Après 800 secondes, des rendements de conversion de l'acrylate allant jusqu'à 90 % sous irradiation LED à 405 nm et 50 % sous irradiation LED à 470 nm ont été obtenus avec le système POM-imidoanthraquinone (POM-AQ)/MDEA. Cela montre que de telles espèces Lindqvist organo-imido peuvent représenter de nouveaux photoamorceurs de lumière visible faciles à synthétiser et efficaces. De plus, grâce à la présence du POM, les revêtemen

préparés à l'aide du photosystème POM-AQ/MDEA/acrylate d'huile de soja époxydée présentent d'excellentes propriétés mécaniques, avec une très bonne flexibilité, une résistance à la rupture fragile et une adhérence à l'acier.

Dans le dernier chapitre, la préparation de nouveaux complexes d'inclusion closo-borate/CD a été étudiée pour élaborer des systèmes suffisamment forts pour être envisagés pour des applications biologiques. Jouant sur le volume et la charge de $[B_{10}H_{10}]^{2-}$, on a cherché à augmenter leur caractère chaotrope des clusters de bore et ainsi à augmenter leur affinité de liaison avec les cyclodextrines. L'encapsulation des anions $[B_{10}H_9NCCH_3]^-$ et $[B_{20}H_{18}]^{2-}$ dans les cyclodextrines α, β et γ a été étudiée en deux parties distinctes. La spectrométrie de masse ESI et la RMN ont montré la formation de complexes d'inclusion 1:1 entre $[B_{10}H_9NCCH_3]^-$ et les cyclodextrines β et γ, tandis que des interactions plus faibles ont été observées avec la cyclodextrine α, pour laquelle les constantes de liaison ont été déterminées par RMN et ITC. Les paramètres thermodynamiques mesurés par ITC confirment que l'insertion du $[B_{10}H_9NCCH_3]^-$ dans la cavité de la CD est associée à un effet chaotrope. Comme prévu, l'amélioration drastique du processus d'encapsulation du $[B_{10}H_9NCCH_3]^-$ par rapport au $[B_{10}H_{10}]^{2-}$, tandis que le système hôte-invité le plus stable est obtenu avec la γ-CD.

De plus, la RMN du $[B_{20}H_{18}]^{2-}$ avec les trois cyclodextrines a montré la formation de complexes d'inclusion 1:1 entre le $[B_{20}H_{18}]^{2-}$ et les cyclodextrines α, β et γ, et a permis de déterminer de fortes constantes d'association avec une constante optimale obtenue avec la β-CD. Les mesures ITC ont confirmé les constantes d'association du $[B_{20}H_{18}]^{2-}$ et des complexes α et β, associées à un effet chaotrope avec des valeurs très supérieures à celles obtenues dans de précédents travaux avec $[B_{10}H_{10}]^{2-}$ validant ainsi l'approche suivie dans ce travail de thèse.

Une nouvelle approche en chimie du $[B_{20}H_{18}]^{2-}$ a également été étudiée à la fin du travail lié au processus d'échange hydrogène-deutérium en solution aqueuse de $[B_{20}H_{18}]^{2-}$. La RMN $^1H\{^{11}B\}$ et $^{11}B\{^1H\}$ a mis en évidence des processus d'échange sélectif de deutérium-proton avec les protons des atomes de bore équatoriaux sur une période de temps en présence de dégradation. Il est intéressant de noter que, par le biais de la RMN de solutions $[B_{20}H_{18}]^{2-}$/CD dans D_2O, il a été démontré que les cyclodextrines β et γ protégeraient l'anion de la dégradation après 4 à 5 mois, ouvrant la voie à la conception de médicaments à base de bore offrant une stabilité accrue adaptée à une utilisation médicale.

Table of Contents

General Introduction

General Introduction

Boron is the neighbor of carbon element in the periodic table. It exists as traces of boric acid and minerals in soil, rocks, oceans, and the earth's crust. Boron isn't the core of life as carbon; however, it is an essential nutrient for green plants and important in many industries such as glass manufacturing, laundry, crucibles, nanotubes, and cosmetics [1]. Interestingly, boron compounds would be used in the treatment of brain tumors and tiny cancerous clusters since the boron-10 isotope has a large cross-sectional area for neutrons, so it can efficiently absorb low-energy thermal neutrons and undergoes fission into lethal particles capable of destructing tumor cells.

Boron and carbon exhibit an important similarity: their ability to bond to themselves, resulting in large families of discrete structures. However, boron chemical bonding with hydrogen in boron hydride compounds (hydroborates) differs in hydrocarbons. Since the boron element is electron deficient, it can hypercoordinate into a large scope of three-dimensional polyhedral clusters, which have extraordinary properties that provide a wide variety of applications. Polyhedral boron hydrides of the general formula $B_nH_n^{2-}$ (n=6-12) have outstanding thermal, oxidative, and hydrolytic stability, especially the highly symmetric $[B_{10}H_{10}]^{2-}$ and $[B_{12}H_{12}]^{2-}$ cages. Therefore, they have attracted attention for a long time in many applications, such as extraction of heavy metals, materials sciences, nuclear waste treatment, and medical applications [2,3].

The exceptional reactivity of closo-decahydrodecaborate anion $[B_{10}H_{10}]^{2-}$ provokes extensive investigations throughout the past fifty years of the substitution of their exo-polyhedral (terminal) hydrogen atoms with carbon, nitrogen, oxygen, sulfur, and halogens [4]. Many B_{10} derivatives have been evident to have unique biological activities efficient for diagnosing and treating certain types of cancer. For instance, the $[B_{10}H_9CO]^-$ cluster features a highly reactive carbonyl function sensitive to all kinds of nucleophiles. It can lead to a closo-decaborate-triethoxysilane compound $[2\text{-}B_{10}H_9CONH(CH_2)_3Si(OC_2H_5)_3]^{2-}$ whose silane functions can be linked to silica nanoparticles doped with a luminescent dye, thus facilitating the tracing of the closo-decaborated drug pathway in cancer treatments [5].

On the other hand, polyoxometalates (POMs) are a discrete inorganic class of soluble multinuclear anionic metal oxides with the general formula $[M_mO_y]^{p-}$ for isopolyoxometalates or $[X_xM_mO_y]^{q-}$ for heteropolyoxometalates, where X is the central heteroatom and can be a non-metal atom such as P, Si, As, Sb while M is the main transition metal in their highest oxidation state (usually Mo^{VI} or W^{VI}). There is a large number of polyoxometalates that are known in the literature with diverse structures, sizes, compositions, and properties. This diversity makes the chemistry of POMs attractive in plenty of applications due to their high charge density, thermal and hydrolytic stability, resistance to oxidative degradation, and ability to electron storage.

POMs can be functionalized with organic or inorganic moieties to obtain novel tailor-made hybrid functional POM-based molecules with synergetic properties. This allows control over tuning their solubility, charge, electronic, and electrochemical properties. Grafting alkoxy tripodal ligands such as tris(hydroxymethyl)aminomethane (TRIS) on Anderson POMs of the general formula $[X^{n+}(OH)_6M_6O_{18}]^{(6-n)-}$ (n = 2–8, M = addenda atom, X = heteroatom) or aminopropyl-tri(ethoxy)silane (APTES) ligand on the nucleophilic surface of the lacunary Keggin POM $[SiW_{10}O_{38}]^{8-}$ and the Dawson POM $[P_2W_{17}O_{61}]^{10-}$ or by replacing the nucleophilic oxo group at the surface Lindqvist isopolyoxometalates $[M_6O_{19}]^{2-}$ with nitrogen-based ligands (isocyanate, phosphoimine, and aromatic amines), can enrich their chemistry, enhance their properties and open the route for designing new compounds through post-functionalization [6].

In this context, preparing new hybrid compounds combining boron clusters and polyoxometalates would open up numerous prospects both from a fundamental and an application point of view. In fact, Manal Diab, during her PhD thesis between 2014-2017, succeeded to couple the carbonyl decaborate derivative $[B_{10}H_9CO]^-$ with one or two amine groups of the TRIS-functionalized Anderson-Evans POMs and the APTES-functionalized Keggin and Dawson POMs [7,8].

Building on this, the initial objectives of this PhD work were to develop new hybrids POMs by combining POM-Borate adducts synthesized by Manal with organic ligands. However, research work in chemistry often presents unforeseen reactions, and as we'll see in the manuscript, we had to adapt our objectives according to the results obtained. Therefore, the manuscript will be organized as follows.

Chapter I is divided into two parts. The first part presents generalities about POM chemistry, with special attention paid to the hybrids POMs, while the second part presents the chemistry of borate and its interest in biomedical applications. It also highlights the interest in combining POMs and Borates. Finally, in the last part, we presented the initial goal of the thesis.

Chapter II focuses on the initial objective of this PhD work, which aims to isolate and optimize the synthesis of new adducts through post-functionalization of free amine groups in the POM-Borate adducts with organic ligands, that would bring new advantages, including improved stability and new synergetic properties. Since the initial objective to isolate novel POM-borate adducts was hard to achieve, we decided to focus on the organic functionalization of polyoxometalates in the following chapter, while decaborate clusters were investigated for their encapsulation properties within cyclodextrins in Chapter IV.

Chapter III presents the synthesis of three novel imido POM derivatives obtained from coupling the aromatic amine ligands (2-aminoanthracene, 2-aminobenzophenone, and 2-aminoanthraquinone) with the Lindqvist POM $[Mo_6O_{19}]^{2-}$. The three isolated hybrid materials have been fully characterized in the solid-state and solution. UV-Vis studies showed that the optical performance of the organoimido derivatives is enhanced enormously in comparison

with precursors entities. Photochemistry and photopolymerization studies have evidenced that photosystems combining N-methyldiethanolamine (MDEA) as electron donor and these hybrid POMs promote free-radical photopolymerization of acrylate monomer derivatives under irradiation in the visible range.

Chapter IV investigates for the first time the encapsulation of $(Et_3NH)[B_{10}H_9NCCH_3]$ and $Li_2[B_{20}H_{18}]$ compounds within CD cavities to get strong association constants enough to envision biological applications. Solution studies performed by NMR and ITC demonstrated the formation of stable inclusion complexes driven by the chaotropic effect. The last part of this chapter discusses the hydrogen-deuterium (H/D) exchange process and its effect on the stability of $Li_2[B_{20}H_{18}]$ compound in D_2O solutions through $^{1}H\{^{11}B\}$ and $^{11}B\{^{1}H\}$ NMR recordings over time. It also proves that encapsulating $[B_{20}H_{18}]^{2-}$ cluster within CD's cavities would protect the former from H/D exchange and reduce its degradation in an aqueous solution.

References

(1) Woods, W. G. An Introduction to Boron: History, Sources, Uses, and Chemistry. *Environ Health Perspect* **1994**, *102* (Suppl 7), 5–11.

(2) Zhu, Y.; Cai, J.; Hosmane, N.; Zhang, Y. Introduction: Basic Concept of Boron and Its Physical and Chemical Properties; **2022**; pp 1–57. https://doi.org/10.1016/B978-0-12-822127-3.00003-X.

(3) *50th Anniversary of Electron Counting Paradigms for Polyhedral Molecules: Historical and Recent Developments*; Mingos, D. M. P., Ed.; Structure and Bonding; Springer International Publishing: Cham, **2021**; Vol. 187. https://doi.org/10.1007/978-3-030-84863-7.

(4) Sivaev, I. B.; Prikaznov, A. V.; Naoufal, D. Fifty Years of the *Closo*-Decaborate Anion Chemistry. *Collect. Czech. Chem. Commun.* **2010**, *75* (11), 1149–1199. https://doi.org/10.1135/cccc2010054.

(5) Abi-Ghaida, F.; Clément, S.; Safa, A.; Naoufal, D.; Mehdi, A. Multifunctional Silica Nanoparticles Modified via Silylated-Decaborate Precursors. *Journal of Nanomaterials* **2015**, *2015*, e608432. https://doi.org/10.1155/2015/608432.

(6) Anyushin, A. V.; Kondinski, A.; Parac-Vogt, T. N. Hybrid Polyoxometalates as Post-Functionalization Platforms: From Fundamentals to Emerging Applications. *Chem. Soc. Rev.* **2020**, *49* (2), 382–432. https://doi.org/10.1039/C8CS00854J.

(7) Diab, M.; Mateo, A.; Cheikh, J. A.; Haouas, M.; Ranjbari, A.; Bourdreux, F.; Naoufal, D.; Cadot, E.; Bo, C.; Floquet, S. Unprecedented Coupling Reaction between Two Anionic Species of a Closo-Decahydrodecaborate Cluster and an Anderson-Type Polyoxometalate. *Dalton Trans.* **2020**, *49* (15), 4685–4689. https://doi.org/10.1039/C9DT04676C.

(8) Diab, M.; Mateo, A.; El Cheikh, J.; El Hajj, Z.; Haouas, M.; Ranjbari, A.; Guérineau, V.; Touboul, D.; Leclerc, N.; Cadot, E.; Naoufal, D.; Bo, C.; Floquet, S. Grafting of Anionic Decahydro-Closo-Decaborate Clusters on Keggin and Dawson-Type Polyoxometalates: Syntheses, Studies in Solution, DFT Calculations and Electrochemical Properties. *Molecules* **2022**, *27* (22), 7663. https://doi.org/10.3390/molecules27227663.

Chapter One

Chapter 1: Generalities on POMs and Boron Chemistries

Polyoxometalates Chemistry

I. The development of POM chemistry

Polyoxometalates (POMs) are a discrete inorganic class of multinuclear anionic metal oxide clusters. They are basically composed of $\{MO_x\}$ building blocks linked by bridging oxygen atoms, where M stands for early transition metals in their highest oxidation state (d^0, d^1, e.g., Mo^{VI}, W^{VI}, V^V, Nb^V, Ta^V) [1].

Polyoxometalates chemistry emerged at the end of the 19th century, specifically in 1826, when *Berzelius* reported the formation of the first POM in his publication. Berzelius noted the formation of a yellow precipitate of ammonium dodecamolybdatophosphate complex $[NH_4]_3[PMo_{12}O_{40}]$ (heteropolyanion) resulting from mixing ammonium molybdate and phosphoric acid [2]. However, it was not until 1933 that *Keggin* initiated the crystallographic studies on POMs and determined the crystal structure of hexahydrated phosphotungstic acid $H_3[PW_{12}O_{40}].6H_2O$ through X-ray diffraction [3].

The subsequent burgeoning of spectroscopic and electrochemical methods allows the synthesis and characterization of novel polyoxometalates with multitudinous structures, sizes, reactivity, and applications [4–6]. Polyoxometalate's charm is attributed to its high charge density, thermal and hydrolytic stability, resistance to oxidative degradation, and ability to accept and release electrons reversibly without significant alterations in their structure, making them great electron reservoirs [7]. These spectacular properties reflect on a plethora of applications ranging from medicine, catalysis, optics, and bio-nano-technology to magnetism [8–17].

A tremendous number of publications and surveys are released each year related to different aspects of POMs chemistry [1,13,18–21]. So, it will be complicated to demonstrate full-scale information about polyoxometalate properties, derivatives, and applications. Nevertheless, in this chapter, we will focus on the generalities of POM's main classes, spotlight organically functionalized POMs, and mention some interesting applications.

II. Classification of polyoxometalates

There is a mounting number of known polyoxometalates in the literature with unmatched physical and chemical properties, a wide range of sizes varying from a few Ångström to tens of nanometers, and a fruitful number of architectures and derivatives. Therefore, it isn't easy to distinguish between different POMs types and subtypes. However, the classification of

polyoxometalates based on their composition can be generally presented into two broad classes: Isopolyoxometalates and Heteropolyoxometalates.

II.1 Isopolyoxometalates $[M_xO_y]^{p-}$

Isopolyoxometalates have only one kind of transition metal center. It consists of metal oxide fragments adapting an octahedral geometry $\{MO_6\}$ (M designates the metal center).

The production of polyoxometalate clusters is often simple and requires few steps or even one step (one pot syntheses). It depends on variable parameters such as type of countercations, acid, metal ions, temperature, solvent, and ionic strength. However, the pH of the solution is considered one of the primary factors that play a critical role in architecting the polyoxometalates [18].

Lowering the pH, for example, of a sodium molybdate solution will cause the protonation of the tetrahedral mononuclear $\{MO_4\}^{2-}$ ion followed by condensation, yielding highly negative iso-polynuclear anion of the general formula $[M_xO_y]^{p-}$ (reaction 1) [22] and structures varying from the smallest $[Mo_6O_{19}]^{2-}$ to polyanions with several hundred metal centers as to the nanosized $[H_xMo_{368}O_{1032}(H_2O)_{240}(SO_4)_{48})]^{48-}$ $\{Mo_{368}\}$.

$$x\ MO_4^{n-} + z\ H^+ \rightarrow [M_xO_y]^{p-} + 1/2\ z\ H_2O \quad (1)$$

During the condensation process, the coordination number of the metal centers changes from four $\{MO_4\}$ to six $\{MO_6\}$, and the building block units of the polyhedral entity become octahedra sharing corners, edges, and rarely faces (Figure 1). There are oxygen atoms occupying the octahedra vertices, linking between central metals (M-O-M) known as μ-oxo bridges and others at terminal non-bridging positions (M-O).

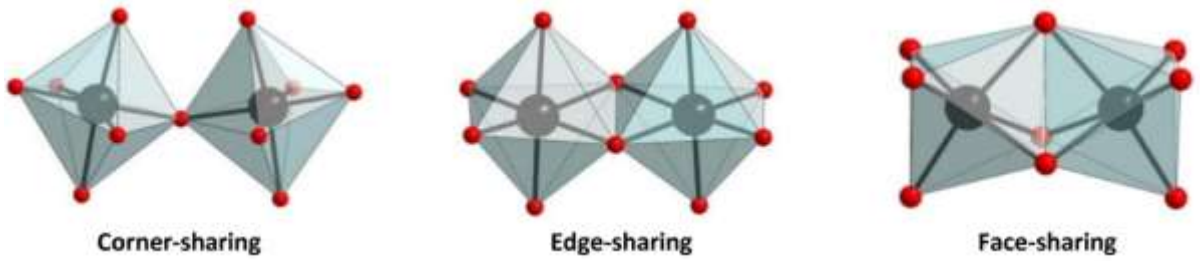

Figure 1. Possible connectivity modes between octahedra present in POMs.[23] (Grey octahedra: $\{MO_6\}$; black spheres: M;red spheres: O)

The most common examples of isopolyoxometalates are those with the Lindqvist structure, heptamolybdate, and giant polyoxometalates.

Lindqvist POMs have the general molecular formula $[M_6O_{19}]^{2-}$ ($M=Mo^{VI}$, W^{VI}, V^{V}, Nb^{V}) and overall O_h symmetry. It comprises six MO_6 octahedra, each with one terminal oxygen, and shares four edges with neighboring octahedra, meaning there is a total of 12 μ_2-O bridges.

Also, all octahedrons share one vertex at the central oxygen atom (μ_6-O) in the middle of POM (Figure 2) [24].

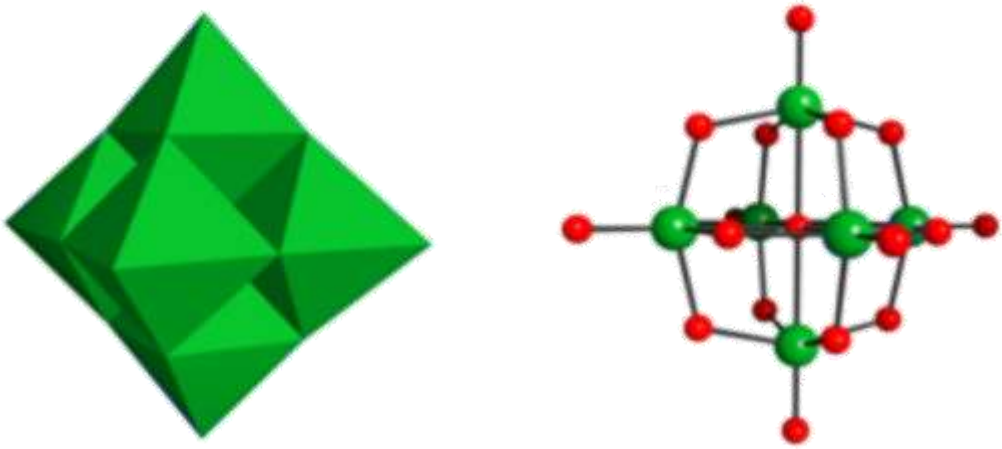

*Figure 2. Polyhedral **(left)** and ball-and-stick **(right)** representations of the {M_6} Lindqvist isopolyoxometalate. (Green octahedra: {MO_6}; green spheres: Mo; red spheres: O)*

Lindqvist ions have recently attracted attention because of their high symmetry, negative charge, and strongly basic surface oxygens. These make them unambiguously serve as building blocks for designing new materials [25–29].

Heptamolybdate has the general formula $[Mo_7O_{24}]^{6-}$. Their geometry can be visualized as two units: a front unit of four MoO_6 octahedrons and a back unit of three octahedrons. The front unit is placed above the back unit, resulting in seven edge-sharing octahedrons (Figures 3-4) [30].

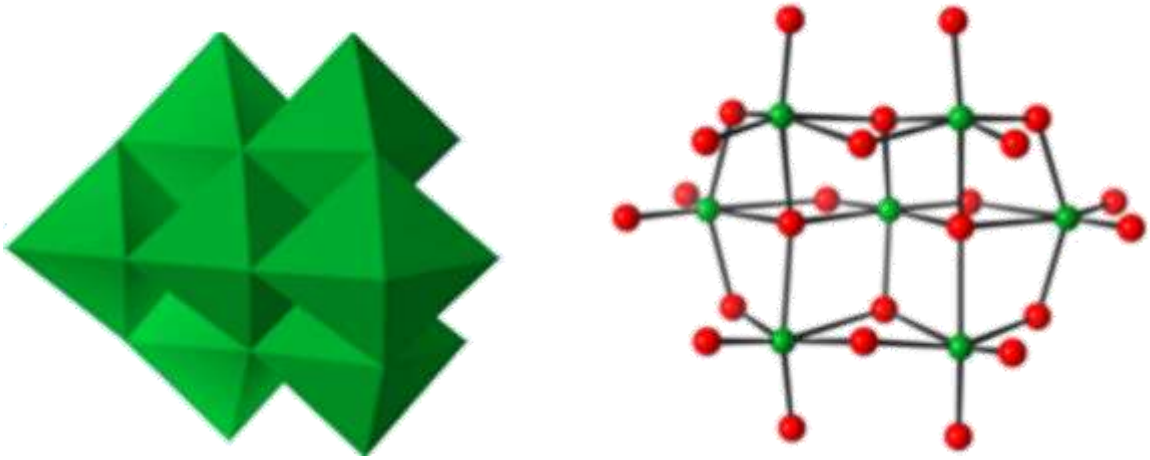

*Figure 3. Polyhedral **(left)** and ball-and-stick **(right)** representations of the {Mo_7} heptamolybdate iso-polyoxometalate. (Green octahedra: {MO_6}, green spheres: Mo; red spheres: O)*

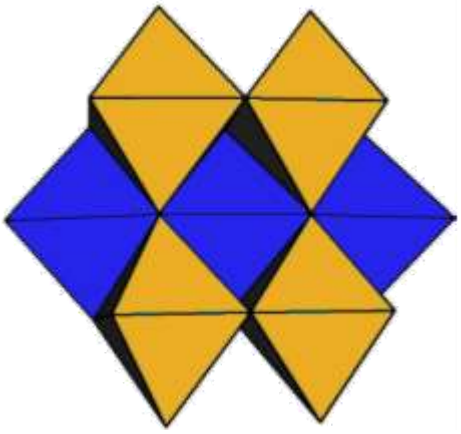

Figure 4. The front unit (orange) and back unit (blue) combine to produce the overall structure of heptamolybdate. (Orange and blue octahedra: {MoO_6})

The interest in heptamolybdate relies on its commercial availability as the precursor (Mo source) for synthesizing new materials among different disciplines, such as fabricating electrical material with high capacity for rechargeable batteries [31].

In the last few years, heptamolybdates have received immense attention in the biological field, driven by their multi-electron redox stability and solubility in water. In fact, Yamase and his coworkers were the first to report anti-tumor activity of $[NH_3Pri]_6[Mo_7O_{24}]$ (PM-8, NH_3PRi: isopropylammonium cation) in suppressing the growth of human cancer-nude mice systems. Investigations were done to confirm the specificity of the heptamolybdate anion to anti-tumor activity. Thus, the first experiment replaced the cation $[NH_3Pri]^+$ with $[NH_4]^+$ and K^+, while the second replaced $[Mo_7O_{24}]^{6-}$ with Cl^-. Interestingly, $[NH_3Pri]Cl$ shows to be ineffective; on the contrary, both $[NH_4]_6[Mo_7O_{24}]$ and $K_6[Mo_7O_{24}]$ activities were comparable to $[NH_3Pri]_6[Mo_7O_{24}]$. This means that the antitumor activity is associated with the polyoxometalate, while the cation presumably enhances the solubility of the POM, hence its bioavailability [32].

In the late 90s, Muller and his coworkers discovered a series of giant polyoxometalates with nuclearity as high as 368 [33]. {Mo_{132}} "Keplerate" anion is one of the fascinating ultra-large clusters because of its eye-catching hollow spherical structure (Figure 5), which can serve as nanoflasks for catalysis and various chemical transformations [34,35].

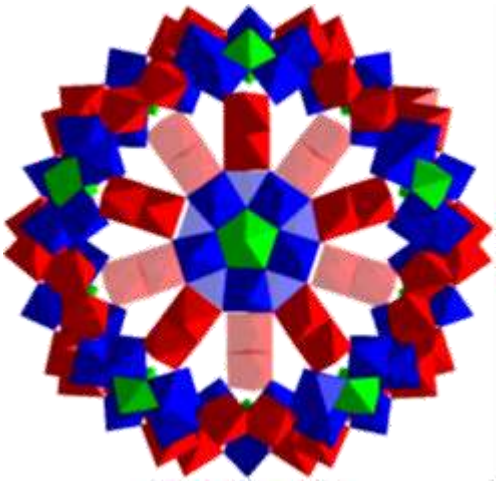

Figure 5. Polyhedral representation of {Mo_{132}}.[34] (Green trigonal bipyramids: {$Mo^{VI}O_7$}; blue octahedra: {$Mo^{VI}O_6$}; red octahedra: {$Mo^{V}O_6$})

Dissolving the readily available ammonium heptamolybdate in an aqueous solution under appropriate pH and in the presence of a reducing agent causes partial reduction of Mo(VI) into Mo(V) and spontaneous assembly of molybdenum building blocks [36]. In this sense, the Mo^{VI} (total 72 Mo^{VI} atoms) assemble into twelve pentagons, which can be described as a central trigonal bipyramidal MoO_7 surrounded by five MoO_6 octahedra {(Mo^{VI} (Mo^{VI}_5)}, linked by binuclear 30 Mo^{V}_2 spacers (total 60 Mo^{V}) which are stabilized by bidentate ligands (Figure 6). Therefore, the general formula of {Mo_{132}} can be simply illustrated as [(pentagon)$_{12}$(Linker)$_{30}$(Ligand)$_{30}$] ≡ [(Mo{Mo_5})$_{12}$(Mo_2O_4)$_{30}$(Ligand)$_{30}$] (ligand can be CH_3COO^-, $HCOO^-$, $H_2PO_4^-$, SO_4^{2-}, PO_4^{3-}) [37,38].

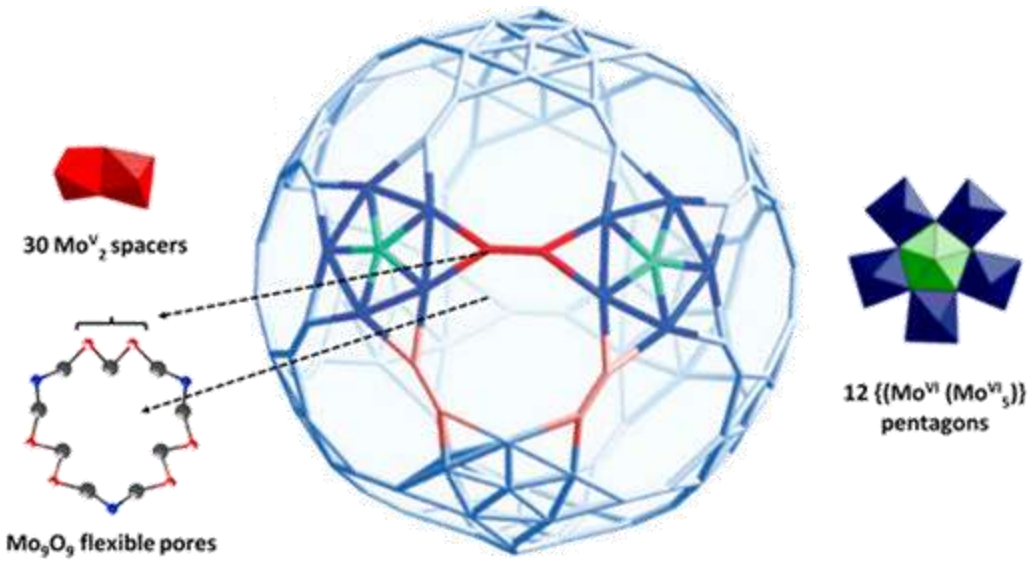

Figure 6. Diagram of the structural building blocks of {Mo_{132}}.[33] (Green trigonal bipyramids: {$Mo^{VI}O_7$}; blue octahedra: {$Mo^{VI}O_6$}; red octahedra: {$Mo^{V}O_6$}; red spheres: Mo(V); blue spheres: Mo(VI); grey spheres: O belonging to the bidentate ligand)

{Mo_{132}} capsule comprises twenty Mo_9O_9 flexible pores of 3nm diameter, giving access to a 700 $Å^3$ internal central cavity. These unique features and properties allow the Keplerate anion to encapsulate many guest molecules (inorganic host-guest complex) and selectively exchange water and small cations with the surrounding environment (modeling cell membranes) in addition to many promising applications in catalysis [39–42], electric conductivity [43], non-linear optics [44,45], liquid crystals [46–48], vesicles [49], and "blackberry" aggregates [15].

Many other nicely shaped giant POMs are well-documented in the literature known by molybdenum blue such as {Mo_{154}} $[Mo_{154}O_{462}H_{14}(H_2O)_{70}]^{14-}$ and {Mo_{176}} $[Mo_{176}O_{528}H_{16}(H_2O)_{80}]^{16-}$ (Figure 7) [50,51] which are constructed from the same pentagonal building blocks {$MoMo_5$} as the molybdenum brown {Mo_{132}}, however, they have a wheel-like shape of 3.4 and 4.1 nm diameter, respectively. Interestingly, specific sites of the ring structure possess nucleophilic character and thus act like receptors for some cations and sites for chemical transformations.

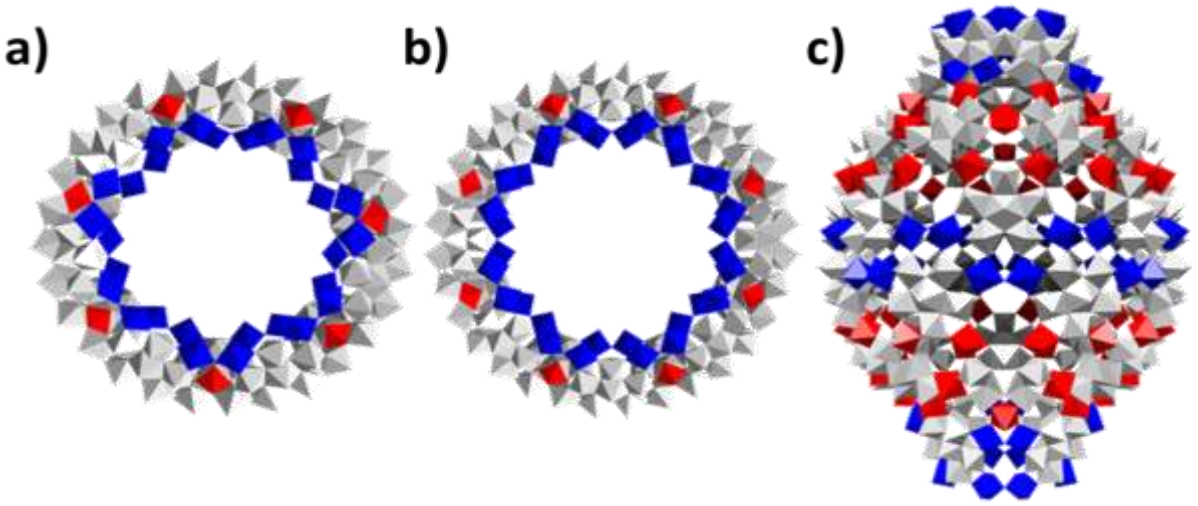

Figure 7. Polyhedral representation of structures of the "big wheels" ***a)*** *{Mo_{154}}, **b)** {Mo_{176}}, and the "blue lemon"* ***c)*** *{Mo_{368}}.[33] (Grey & red polyhedra: {Mo^{VI}} units ; blue polyhedra: {Mo^{V}} units)*

II.2 Heteropolyoxometalates $[X_mM_xO_y]^{p-}$

Heteropolyoxometalates $[X_mM_xO_y]^{p-}$ comprises two types of atoms, the addenda transition metal M (usually Mo or W) and the heteroatom X, which may be non-metal p block elements (P, Si, As, Sb, etc.) or other transition metal (Co, Fe, Mn, etc.). They are synthesized by condensing simple monomeric oxo anions of the heteroatom X and the addenda element in an acidic medium (reaction 2) [22]. The addenda atom condenses into octahedron units $\{MO_6\}_x$ sharing edges and corners, creating central cavities occupied by heteroatoms whose coordination mode varies between tetrahedron, trigonal, or octahedron.

$$m\ XO_4^{z-} + x\ MO_4^{n-} + z\ H^+ \rightarrow [X_mM_xO_y]^{p-} + 1/2\ z\ H_2O \quad (2)$$

Despite the structural variety of heteropolyoxometalates, three classical types: **Anderson-Evans** [52] ($[XM_6O_{24}]^{p-}$, noted $\{XM_6\}$), **Keggin** ($[XM_{12}O_{40}]^{p-}$ [3], noted $\{XM_{12}\}$), and **Well-Dawson** [53] ($[X_2M_{18}O_{62}]^{p-}$ noted $\{X_2M_{18}\}$) POMs have been dominantly studied throughout history, and named after the researcher who discovered them. Details about these structures will be discussed below.

II.2.1 Anderson structure $[H_y(XO)_6M_6O_{18}]^{p-}$

Anderson structure was proposed by J.S. Anderson in 1937 [52] and later confirmed by E.T. Evans [54] through X-ray diffraction of $[TeMo_6O_{24}]^{6-}$. This polyoxometalate has a flat circular structure with a central heteroatom octahedron $\{XO_6\}$ (X = d or p block elements) sharing edges with six surrounding octahedra $\{MO_6\}$ (M=Mo, W) (Figures 8a, c). There are three distinguished coordination modes of oxygen atoms: twelve terminal oxygen atoms (O_t) attached to the metal centers and twelve bridged-oxygen atoms (μ-O): six double-bridged oxygen atoms (μ_2-O) are shared between addenda metal atoms, while another six triple-bridged oxygen atoms (μ_3-O) are shared between two addenda metal atoms and the central heteroatom (Figure 8b) [55].

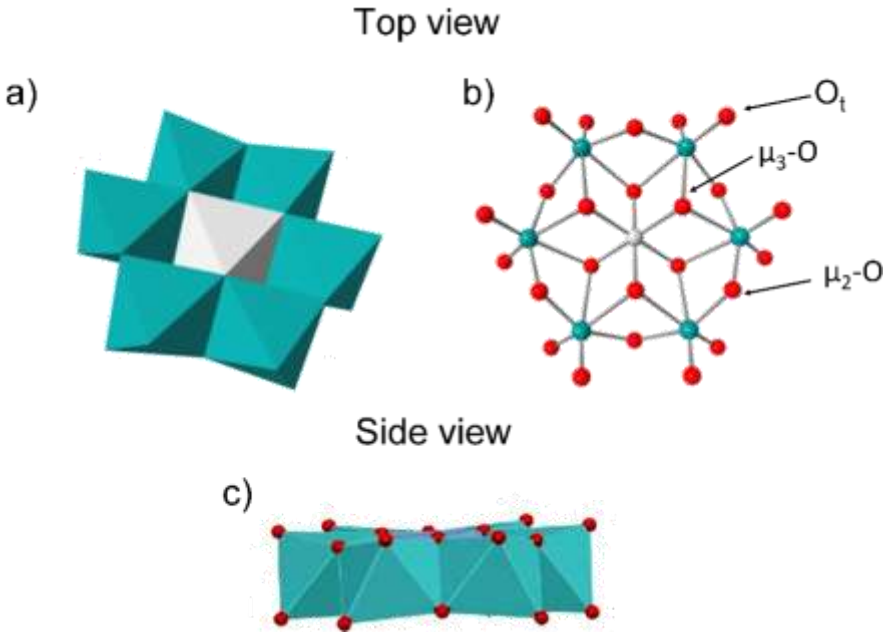

*Figure 8. Representations of the top view of Anderson structure in **a)** polyhedra, **b)** ball-and-stick, and **c)** the polyhedral side view.[55,56] (Turquoise octahedra: {MO_6}; grey octahedra: XO_6; turquoise spheres: M ddenda atom; grey sphere: X heteroatom; red spheres: O)*

According to the state of the six μ_3-O, whether protonated or not, two types of Anderson structures are described (Figure 9).The non-protonated A-type of the general formula $[(X^{n+}O_6)M_6O_{18}]^{(12-n)-}$ with the central heteroatom X^{n+} in high oxidation state (e.g., Te^{VI}, I^{VII}) [57] and the protonated B-type of the general formula $[X^{n+}(OH)_6M_6O_{18}]^{(6-n)-}$ with the central heteroatom in lower oxidation state (e.g., Cr^{III}, Fe^{III}, Al^{III}, Mn^{III}) [58,59].

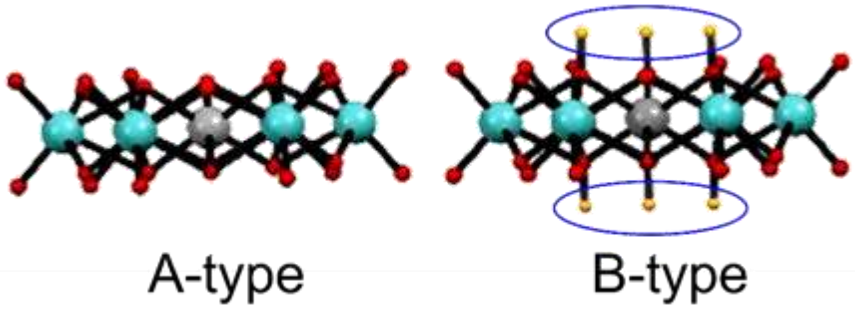

Figure 9. Representation of side view of the A-type and B-type (three protons at each side) of Anderson structure.[56] (Grey sphere: X; red spheres: O; turquoise spheres: M; yellow spheres: H)

Anderson-type POM is a highly flexible structure since it can undergo various modifications: (1) varying the central heteroatom, which impacts the stability and solubility of the POM; (2) incorporating inorganic and/or organic cations to design supramolecular architectures, and (3) replacing the surface protons in B-type Anderson POM with organic moieties which tunes the physical and chemical properties of the inorganic and organic parts [60–63].

Modifying the central heteroatoms in the Anderson structure has a unique role in constructing catalytic systems that bio-mimic the enzymatic oxidation systems in the human body. In this sense, systems such as $Na_3[Cr(OH)_6Mo_6O_{18}]$ and $(NH_4)_3[Co(OH)_6Mo_6O_{18}]$ show an extraordinary performance in aerobic oxidation desulfurization of sulfur oxides (SO_x) under mild conditions. These POMs can substitute the expensive, non-safe traditional techniques to reduce sulfur oxides emissions from fuel compositions causing acid rain and air pollution [60,61,64].

Another important role of Anderson-type POM is demonstrated as an efficient, recyclable, easy-to-make catalyst in organic transformations, like Cu-based Anderson POM $[Cu(OH)_6Mo_6O_{18}]^{3-}$ used as an oxidation catalyst to the aldehyde in water, or the Fe based one $[Fe(OH)_6Mo_6O_{18}]^{3-}$ used in aerobic oxidation of aldehydes/ketones and amine, and last but not least $[IMo_6O_{24}]^{5-}$ in the oxidation of alcohols [65,66].

In biology, Tellurium-centered Anderson−Evans Polyoxotungstate $[TeW_6O_{24}]^{6-}$ is used extensively in protein crystallography since it fulfills the crystallization requirements: high solubility in water, stability under crystallization conditions at pH range 4-9, ability to interact with the protein while maintaining its integrity [67–69].

II.2.2 Keggin structure $[XM_{12}O_{40}]^{p-}$

It comprises twelve $\{MO_6\}$ (M= Mo, W) octahedra surrounding a central heteroatom of tetrahedron configuration $\{XO_4\}$. Every three octahedra aggregate by edge-sharing into one trimeric unit $\{M_3O_{13}\}$, so there is a total of four units interconnected to each other and the central heteroatom by corner-sharing through bridging oxygen atoms. The overall view of the

Keggin structure has three regions: the top and bottom with three octahedra each, and six octahedra in the middle (Figure 10) [22].

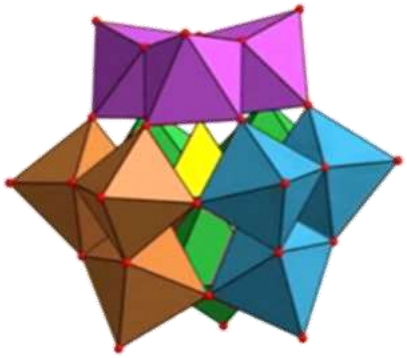

Figure 10. Representation of the {α-XM_{12}} Keggin structure highlighting the four distinct {M_3O_{13}} triads and the central tetrahedron {XO_4} . (The four {M_3O_{13}} units are differentiated by the colors: brown, blue, green, and purple; yellow tetrahedron: {XO_4}; red spheres: O)

Figgis and Baker predicted that this parent Keggin structure, designated as α-structure, could isomerize into four geometrical isomers of lower symmetry through rotation of the triads by 60°C around a three-fold axis of rotation (Figure 11). Rotation of one, two, three, or four triads results in β, γ, δ ,and Ɛ isomers, respectively [70], the α and β isomers being the most stable. However, the rare Ɛ-Keggin structure can be stabilized by transition metals capping groups; for example, Mialane et al. reported the first $[(Ɛ\text{-}PMo_{12}O_{36})(OH)_4\text{-}\{La(H_2O)_4\}_4]^{5+}$ rare Ɛ-Keggin structure stabilized by four capping $\{La(H_2O)_4\}^{3+}$ groups giving its net positive charge [71].

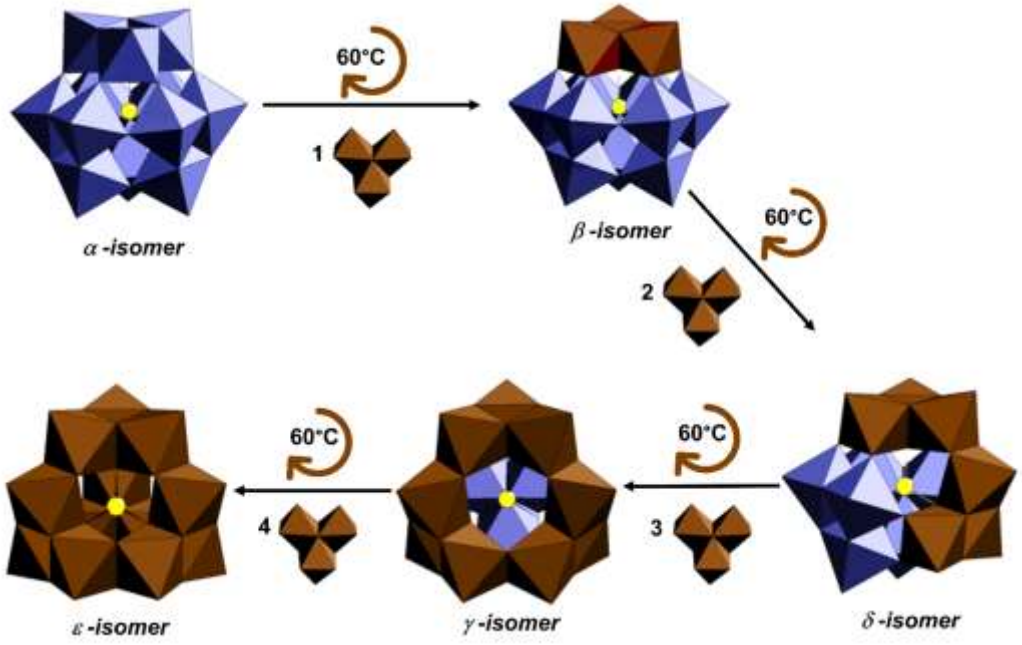

Figure 11. Polyhedral representation of the different isomers of Keggin POM.[72] (The brown octahedra show the {M_3O_{13}} units, which have been rotated 60°C with respect to the α-isomer, and the yellow sphere is the heteroatom X)

II.2.2.1 Lacunary POMs derived from Keggin structure

Lacunary or vacant polyoxometalates result from alkaline hydrolysis of single {MO} to multiple metal fragments $\{M_xO_{2x}\}$ in the saturated (plenary) polyoxometalates, forming vacant sites. The unsaturation degree in lacunary polyoxometalates, whether monovacant $\mathbf{[XM_{11}O_{39}]^{p-}}$ $\{XM_{11}\}$, divacant $\mathbf{[XM_{10}O_{36}]^{p-}}$ $\{XM_{10}\}$, or trivacant $\mathbf{[XM_9O_{34}]^{p-}}$ $\{XM_9\}$, is amazingly defined by strict pH values of the solution: the more basic the solution, the more lacunary the resulting POMs. Therefore, fine-managing of synthetic parameters, temperature, heteroatom nature, ionic strength, and buffer capacity is critical in defining the lacunary POM's formation, stability, and equilibrium [73].

This is magnificently illustrated with Keggin POMs synthesis, particularly the tungstosilicate anions $[SiW_xO_y]^{p-}$, representing the most spectacular example of many stable plenary and lacunary POM species that can be selectively isolated starting either from alkaline hydrolysis of the isomers of the plenary $[SiW_{12}O_{40}]^{8-}$ or acidic condensation of simple WO_4^{2-}oxoanions and metasilicate SiO_3^{2-}, as shown in figure 12 [70].

$[\alpha\text{-}SiW_{12}O_{40}]^{4-}$ and $[\beta\text{-}SiW_{12}O_{40}]^{4-}$ are only stable at very low pH (pH<2). Increasing the pH strictly to pH=6-8 will cause their partial decomposition into the monolacunary $[\alpha\text{-}SiW_{11}O_{39}]^{8-}$ and the $[\beta_2\text{-}SiW_{11}O_{39}]^{8-}$, respectively. The latter isn't stable; thus, it will isomerize from $\beta_2 \rightarrow \beta_3$ to the most stable α isomer [74]. In all β-isomers, one triad is rotated by 60°C with respect to the α isomer; however, the location of the removed octahedron varies among them. In β_1, the octahedron is removed from the triad adjacent to the rotated one. In β_2, the vacant site is on the belt (middle), while in β_3, it is part of the rotated triad. Dilacunary $[\gamma\text{-}SiW_{10}O_{36}H]^{7-}$ is prepared at pH=9 from the hydrolysis of monolacunary $[\beta_2\text{-}SiW_{11}O_{39}]^{8-}$. Trilacunary Keggin, whether it is α or β isomers, is known as A-type when derived from the loss of three shared octahedra from three different triads. $[A\text{-}\alpha\text{-}SiW_9O_{34}]^{10-}$ is prepared by hydrolysis of the monolacunary POMs $[\alpha\text{-}SiW_{11}O_{39}]^{8-}$ at pH=9, whereas $[A\text{-}\beta\text{-}SiW_9O_{34}H]^{9-}$ more easily from the condensation of $WO_4^{2-}$and SiO_3^{2-} at pH=9.

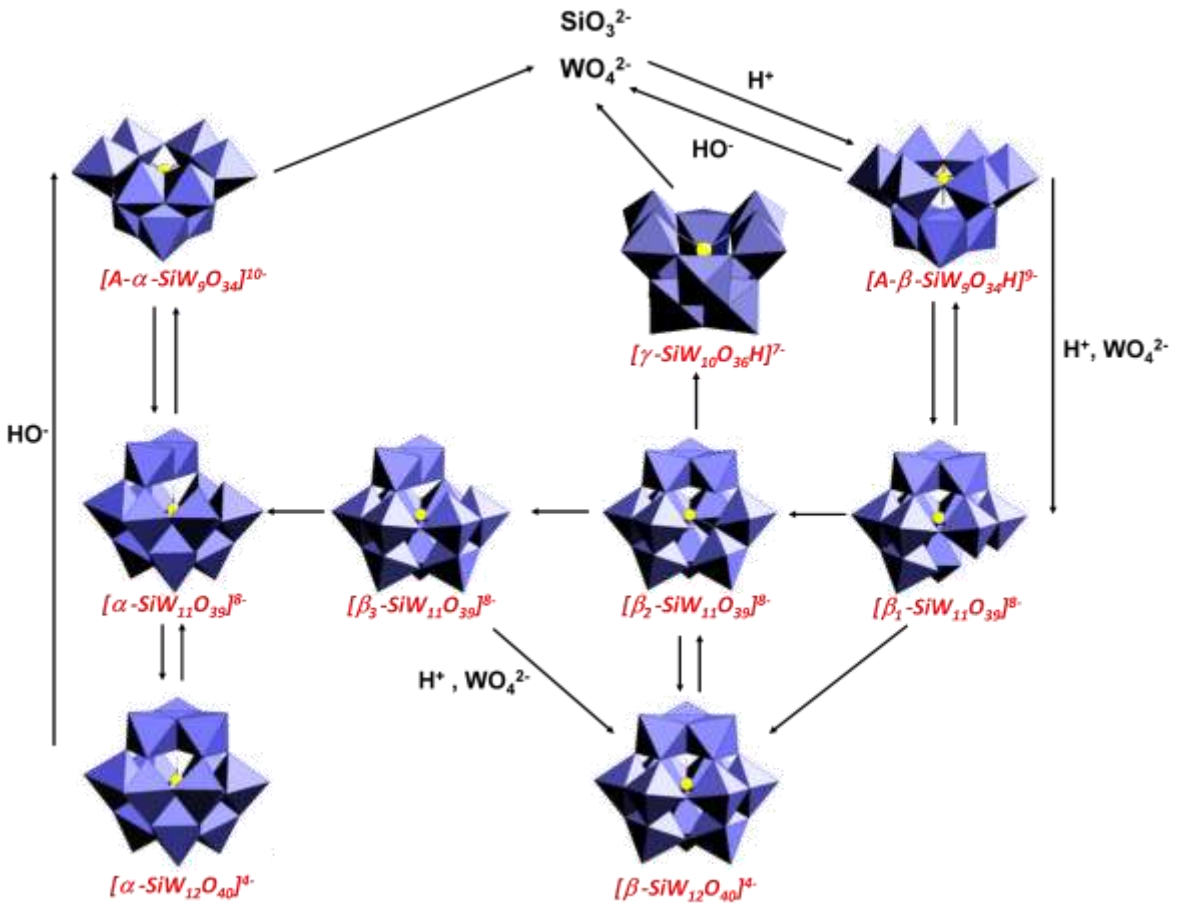

Figure 12. Chemical equilibria between the various silicotungstate isomers derived from the Keggin structure.[70] (Violet octahedra: {WO_6}; yellow sphere: heteroatom Si)

In plenary POMs the external oxo ligands inert. In contrast, removing one, two, or three metal centers leads to lacunary POMs with electrons localized on the terminal oxo ligands of the lacunas. As a result, they exhibit nucleophilic character. The monolacunary **$[SiW_{11}O_{38}]^{8-}$** (noted {SiW_{11}}) and dilacunary **$[\gamma\text{-}SiW_{10}O_{36}H]^{7-}$** (noted {$SiW_{10}$}) POMs have four terminal nucleophilic oxygen atoms, while there are six in the trilacunary **$[SiW_9O_{34}]^{10-}$** (noted {SiW_9}) (Figure 13).

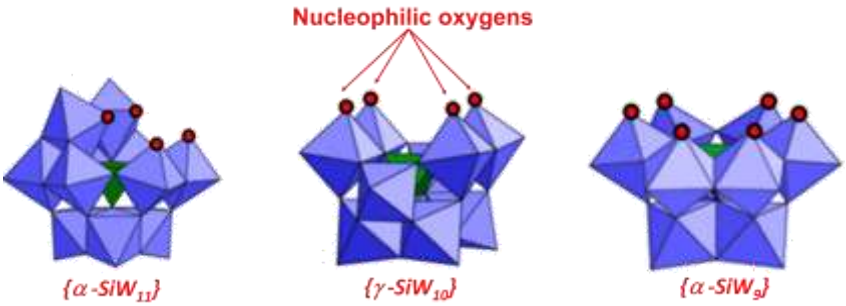

Figure 13. Polyhedral representations showing the nucleophilic oxygens of lacunary Keggin structures {α-SiW_{11}}, {γ-SiW_{10}}, and {α-SiW_9}.[21] (Violet octahedra: {WO_6}; green tetrahedron: {SiO_4}, red spheres: O)

It is worth mentioning that the coordination of di-lacunary Keggin heteropolyanion with various transition metals, including manganese, iron, cobalt, chromium, nickel, and noble atoms, has been exploited intensely as a catalyst in the field of organic chemical industries [75].

Lacunary POMs thus behave as multidentate ligands that couple to electrophiles as transition metals (Cu, V, Mn, Fe, Pd) or p-block elements (Si, P, Sn). Indeed, thousands of transition-metal-substituted POMs (TMSP) have been published to possess highly efficient catalytic activity. Mizuno group, for instance, elaborated several examples of catalysts based on γ-SiW_{10} (Figure 14a), such as dipalladium-substituted γ-Keggin silicotungstate [γ-$SiW_{10}O_{36}Pd_2(OAc)_2]^{6-}$ (Figure 14b). Many pharmaceutical, agricultural, plastic, detergent, and lubricant industries use the latter as a catalyst for producing amide from nitrile hydration [76]. Also, divanadium-substituted γ-Keggin silicotungstate $[\gamma\text{-}SiW_{10}O_{38}V_2(OH)_2]^{4-}$ shows impressive selectivity and efficiency for epoxidation of alkenes with hydrogen peroxide (Figure 14c) [77,78].

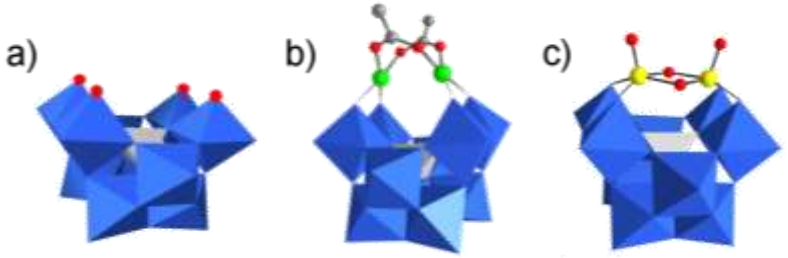

Figure 14. Representations of plenary Keggin ***a)*** *γ-SiW_{10},* ***b)*** *Dipalladium (II) substituted γ-SiW_{10},[76] and* ***c)*** *Divanadium (V) substituted γ-SiW_{10} .[78] (Blue octahedra: {WO_6}; grey tetrahedron: {SiO_4}; green spheres: Pd (II); grey spheres: C; yellow spheres: V(V); Red spheres: O)*

II.2.3 Wells-Dawson structure $[X_2M_{18}O_{62}]^{p-}$

It can be visualized as the fusion of two half units of the trivacant Keggin POM $\{A\text{-}XM_9O_{34}\}^{p-}$ linked through nearly linear M-O-M (162°) corner shared junctions (Figure 15) [79].

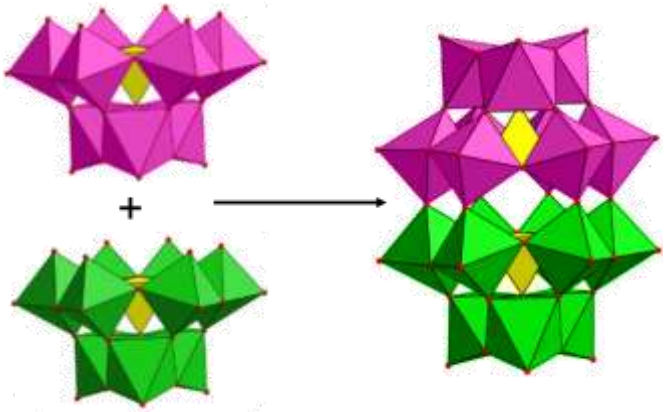

Figure 15. Structural combination of two Keggin type POMs $\{A\text{-}XM_9O_{34}\}^{p-}$ ***(left)*** *forming Wells-Dawson POM* ***(right)****.[79] (The two half units $\{A\text{-}XM_9O_{34}\}^{p-}$ are differentiated by the colors pink and green. (Pink and green octahedra: {MO_6}; yellow tetrahedra: {XO_4}; red spheres: O)*

Hence, it consists of three parts: two caps, each composed of three $\{MO_6\}$ octahedra, and two central belts, each composed of six octahedra, whereas the two heteroatoms (X) are in the vacancies of the half units. Wells-Dawson, or simply Dawson structure, as Keggin POM, has many possible isomers since the two triad groups at the extremities could successively rotate by 60°C. However, the α isomer, which has two identical half-units shown in Figure 15 exhibits D_{3h} symmetry, is the most stable (Figure 16) [80].

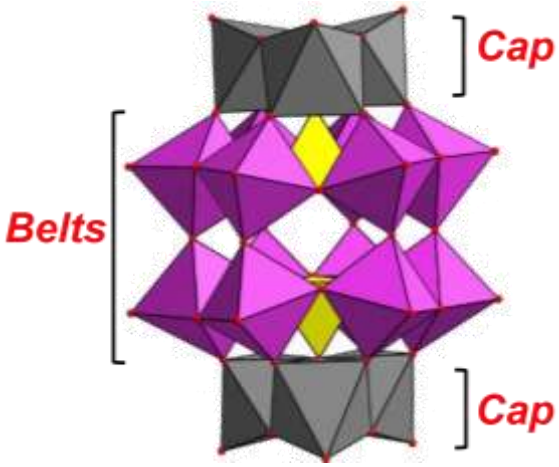

Figure 16. Polyhedral presentation of Well-Dawson structure $[X_2M_{18}O_{62}]^{p-}$. (Grey and purple octahedra: $\{MO_6\}$; yellow tetrahedra: $\{XO_4\}$; red spheres: O)

II.2.3.1 Lacunary POMs derived from Dawson structure

Like many heteropolyoxo-anions, the Well-Dawson structure $[X_2M_{18}O_{62}]^{p-}$ can lose MO units under controlled alkaline hydrolysis. Contrary to the Keggin structure, their direct synthesis through acidic condensation of the oxides of the addenda atom M and the simple heteroatom anions is not reported.

For $[\alpha\text{-}X_2M_{18}O_{62}]^{p-}$ Dawson isomers, mono-, tri-, and hexalacunary species have been isolated (Figure 17). There are two monolacunary isomers, $\mathbf{[\alpha_1\text{-}X_2M_{17}O_{61}]^{p-}}$ and $\mathbf{[\alpha_2\text{-}X_2M_{17}O_{61}]^{p-}}$ $\{X_2M_{17}\}$, resulting from the loss of a single octahedron from the belt or the cap, respectively, thus there are four nucleophilic oxygen sites exposed at the surface on the lacuna. Trilacunary structures $\mathbf{[\alpha\text{-}X_2M_{15}O_{56}]^{p-}}$ $\{X_2M_{15}\}$ are obtained by removing a full cap triad (three octahedra), while hexalacunary structures $\mathbf{[\alpha\text{-}X_2M_{12}O_{48}]^{p-}}$ $\{X_2M_{12}\}$ result from removing one face (six octahedra) from the $\{X_2M_{18}\}$ structure, one octahedron from each of the triads and four from the double belts, meaning there are eight nucleophilic sites [81,82].

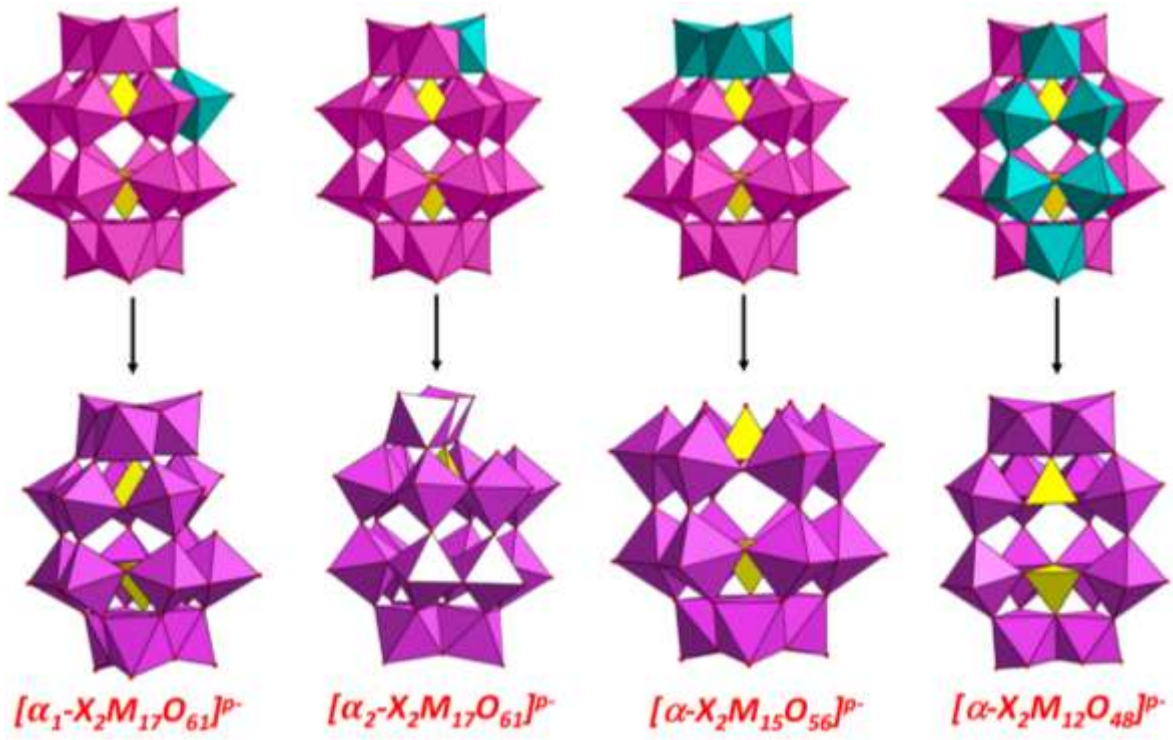

*Figure 17. Polyhedral representation of **mono-**, **tri-**, and **hexalacunary** Wells-Dawson derivatives derived from the plenary structure. (The turquoise octahedra show the {MO_6} units which have been lost, resulting in lacunary POM, and the yellow tetrahedron is {XO_4})*

As lacunary Keggin POMs, the oxygen atoms at the vacant site of lacunary Dawson structures also exhibit nucleophilic character; hence, they anchor to transition metals and organometallic moieties. Incorporation with metals of high oxidation state and multiple coordination sites results in incredibly sophisticated structures comprising multiple lacunary POM clusters linked at their vacant sites through organometallic multidentate ligands. Monolacunary POM {P_2W_{17}} can form triangular trimeric species as the [{α_2-$P_2W_{17}O_{61}(Si_2O)$}$_3$(μ-O)$_3$]$^{18-}$ complex (Figure 18a) [83], made up of three POM clusters connected through Si-O-Si bridges. Moreover, trilacunary {P_2W_{15}} can dimerize into sandwich-like configuration [(α_2-$P_2W_{15}O_{56}$)$_2$$Cu_4(H_2O)_2$]$^{16-}$ having tetrameric $Cu_4(H_2O)_2$ cluster in between (Figure 18b) [84].

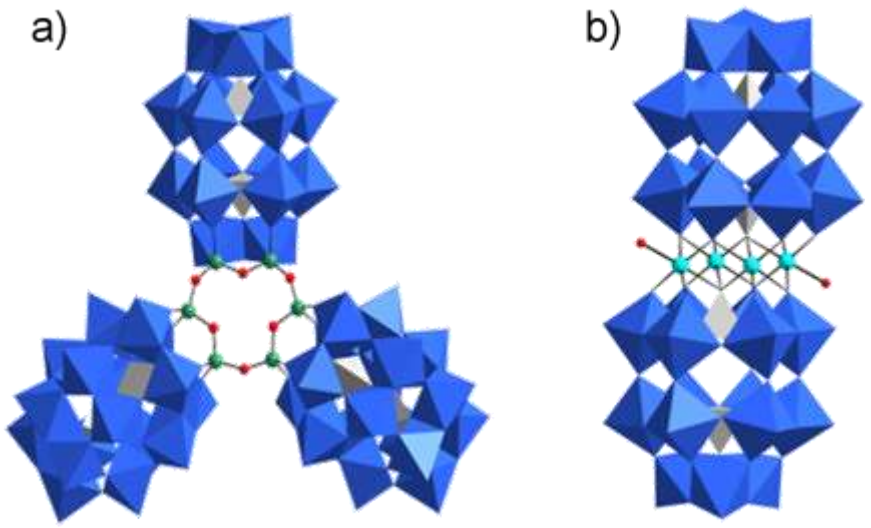

Figure 18. Mixed representation of ***a)*** *[{α_2-$P_2W_{17}O_{61}(Si_2O)$}$_3$(μ-O)$_3$]$^{18-}$ [83] and* ***b)*** *[(α_2-$P_2W_{15}O_{56}$)$_2$$Cu_4(H_2O)_2$]$^{16-}$.[84] (Blue octahedra: {$WO_6$}; grey tetrahedra: {$PO_4$}; green spheres: Si; light blue spheres: Cu; red spheres: O)*

In addition, Wells-Dawson polyoxometalates functionalized with Hf (IV), Zr (IV), and Ln (La, Sm, Eu, and Yb) present an emergent class as catalysts in lewis acid-mediated organic reactions. Combining both entities results in a synergy of their properties; POMs are electron acceptors, and early transition metals and lanthanides are oxophilic. Thus, Lanthanide and Hafnium complexes of the monovacant Dawson polyoxometalates $(TBA)_5H_2[\alpha_1\text{-}Ln(H_2O)_4\text{-}P_2W_{17}O_{61}]$ and $(TBA)_5K[\alpha_1\text{-}Hf(H_2O)_4\text{-}P_2W_{17}O_{61}]$ (Figure 19a) act as recoverable and selective catalysts in aldol reactions [85]. In the proteomics (the study of proteins in organisms) and biotechnology field, $Zr(P_2W_{17}O_{61})_2$ (Figure 19b) was found to be an efficient Lewis acid catalyst for peptide bond hydrolysis [86].

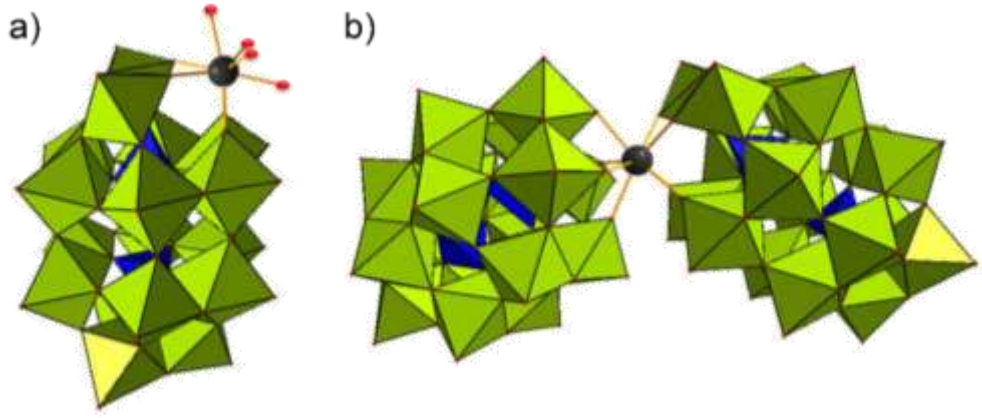

Figure 19. Mixed polyhedral representation of ***a)*** *[α_1-$X(H_2O)_4$-$P_2W_{17}O_{61}$]$^{p-}$,(X=Ln,Hf) [85] and* ***b)*** *$X(P_2W_{17}O_{61})_2$ (X=Zr).[86] (Green octahedra: {WO_6}; blue tetrahedra: {PO_4}; black sphere: (X=Ln, Hf, or Zr); red spheres: O)*

III. Covalent Functionalization: "hybrid POMs"

Hybrid POM can be categorized based on the type of interaction between the organic and inorganic moieties. Non-covalent interactions between the two moieties (i.e., Hydrogen bonds, electrostatic interactions, and van der Waals interactions) fall under ***class I***. On the other hand, in ***class II***, covalent bonds connect the organic and inorganic moieties [21]. Organic ligands can be joined directly to the metallic core by replacing the nucleophilic oxo group at the surface of POM. In the case of Lindqvist isopolyoxometalates $[Mo_6O_{19}]^{2-}$, the $Mo\text{-}O_{terminal}$ is replaced with an Mo≡N bond in the reactions with nitrogen-based ligands (isocyanate, phosphoimine, and aromatic amines) [87].

In the Anderson-type POMs, organic covalent interaction is only reported with tris alkoxy ligands $RC(CH_2OH)_3$, described in detail in this chapter. While in lacunary Keggin and Well-Dawson POMs, the oxygen atoms that are concentrated on their surface have a nucleophilic nature, making them good derivatization precursors with electrophilic organic groups via p-elements (Si, P, Sn, Ge, etc.) [88].

Several advantages are thus available when applying this approach, including control of the interaction between the different domains, improved assembly stability, and combining the properties of both parts. This strategy was thus used to synthesize a large library of new hybrid species with interesting architectures and properties. The tremendous potentialities of heteropolyoxometalates: **Anderson**, **Keggin**, and **Dawson** in terms of functionalization by organic groups will be discussed in this part. In particular, alkoxylation of Anderson POM and organosilylation of Keggin and Well-Dawson POM.

III.1 Organoalkoxy Anderson-type derivatives

Organoalkoxylation of Anderson polyoxometalates presents one of the most prominent branches in the covalent hybrid POM family. This is because multidentate alkoxy ligands will favorably replace through a dehydrative condensation reactions, the H^+ protons of six triple bridged oxygen atoms (μ_3-OH) on the planar surface of B-type Anderson POM $[X^{n+}(OH)_6M_6O_{18}]^{(6-n)-}$. Consequently, the resulting strong metal-oxygen-carbon bond improves the stability of the POM-hybrid in organic media and, at the same time, enhances their compatibility with water [56,65,88].

Since the six μ_3-O atoms are symmetrically distributed on both sides of the planar D_{3h} Anderson POM, meaning three on each side of the plane, their reactivity is identical so that both sides would be simultaneously functionalized with the same alkoxy tripodal ligand such as tris(hydroxymethyl) methane derivatives $RC(CH_2OH)_3$ ($R=NO_2$, CH_3, CH_2OH) resulting naturally in symmetrical double-sided functionalized Anderson derivative $[\{RC(CH_2O)_3\}]_2XM_6O_{18}]^{3-}$ ($X=Mn^{III}$, Fe^{III}) as was initially reported by Hasenknopf *et al.* in 2002 [89,90].

Their traditional route for preparing $[XMo_6O_{18}\{(OCH_2)_3\text{-}CR\}_2]^{3-}$ ($X=Mn^{III}$, Fe^{III}, $R=NO_2$, CH_3, CH_2OH, CH_2NH_3) was refluxing 1 equiv. of tetrabutylammonium octamolybdate $TBA_4[Mo_8O_{26}]$ with 1.5 equiv. of acetylacetonate or acetate salts of the templating heteroatoms ($X=Mn^{III}$, Fe^{III}) and 3 equiv. of tris-(alkoxo) ligand in an organic solvent, usually acetonitrile (Figure 20). However, there were a few drawbacks related to the low solubility of heteroatom salts in organic solvents besides the multistep synthesis needed to successfully isolate the desired derivative, starting from preparing the octamolybdate precursor through condensation of dimolybdate anion under acidic conditions and ending with isolating and purification of the derivative [91].

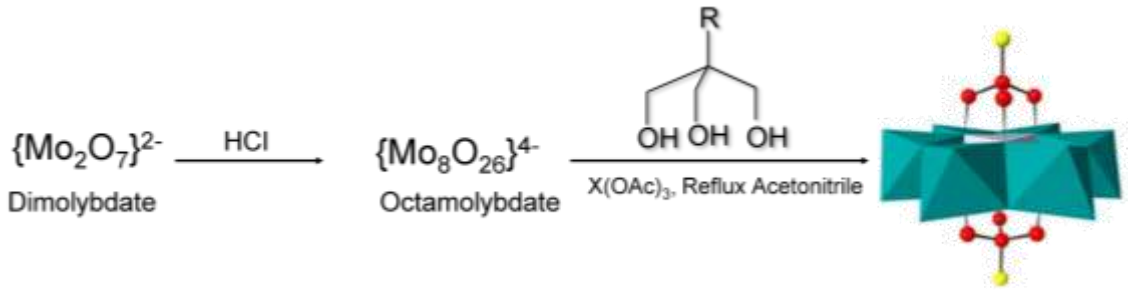

Figure 20. The traditional way of synthesis of symmetrical double-sided tris-alkoxo functionalized Anderson derivatives.[92] (Turquoise octahedra: {MoO_6}; grey octahedra: {XO_4}; red spheres: C; yellow spheres: R)

Alternatively, a more recent, highly efficient, and eco-friendly procedure was reported for synthesizing double-sided tris-alkoxo functionalized Anderson derivatives consisting of reacting heteroatom salt and Tris ligand directly from heptamolybdate anion in an aqueous medium inside one pot (hydrothermal procedure) (Figure 21) [91].

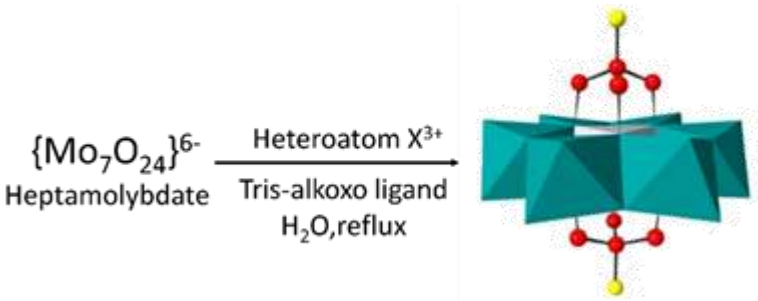

Figure 21. Hydrothermal process for the synthesis of symmetrical double-sided functionalized Anderson POM.[91] (Turquoise octahedra: {MoO_6}; grey octahedra: {XO_4}; red spheres: C; yellow spheres: R)

Double amine functionalized Anderson type POM $[MnMo_6O_{18}\{(OCH_2)_3\text{-}CNH_2\}_2]^{3-}$, denoted as $MnMo_6$-(Tris-NH_2)$_2$, is the most popular stable and easy-to-prepare platform in double-sided organoalkoxy functionalized Anderson POMs. They can undergo further condensation reactions, forming new bonds such as amide, ester, and imine [90]. For instance, Dai's group

successfully prepared $MnMo_6$-(Tris-bisDOPA)$_2$ (Figure 22a) as a flame retardant compound for epoxy resin (EP), a polymer used in electronic packaging, coatings, and adhesives [93].

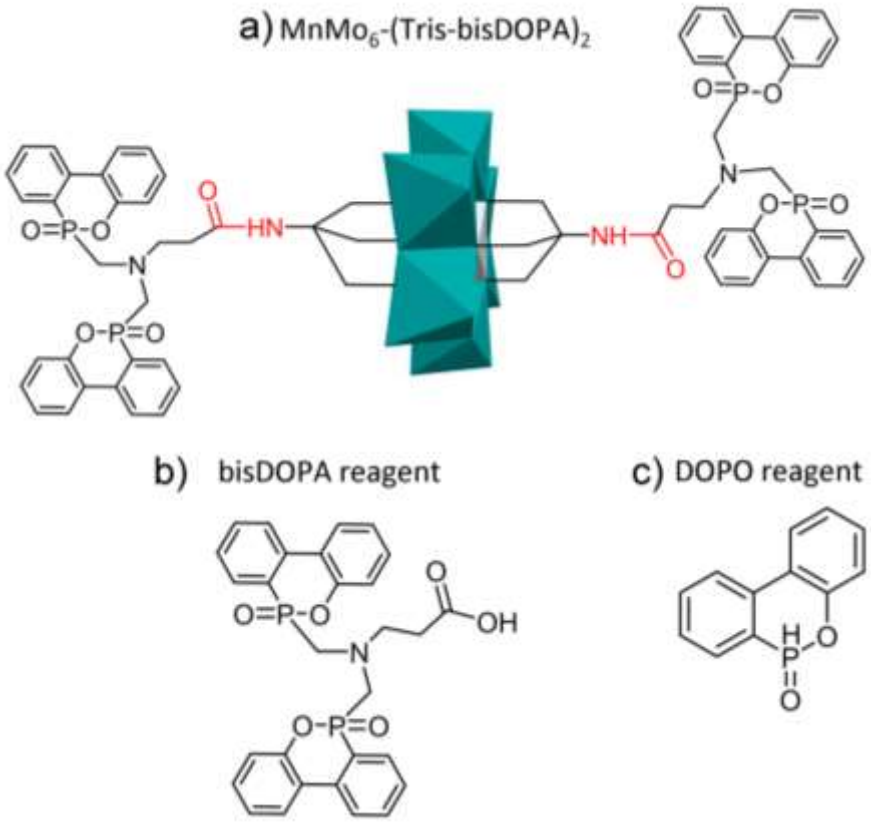

*Figure 22. Structures of **a)** $MnMo_6$-(Tris-bisDOPA)$_2$, **b)** bisDOPA, and **c)** DOPO reagent.[93] (Turquoise octahedra: {MoO_6}; grey octahedra: {XO_4})*

Since DOPO (9,10-dihydro-9-oxa-10-phosphaphenanthrene-10-oxide) (Figure 22c) reagent has a high affinity to polymers and flame retardance [94], while on the other hand, molybdenum and manganese precursors, MoO_3 and MnO_2, are also effective flame retardants and smoke suppression agents [95]. Therefore, combining NH_2-$MnMo_6$-NH_2 with the bisDOPA reagent (Figure 22b) would tune their properties. The $MnMo_6$-(Tris-bisDOPA)$_2$ hybrid enhances the mechanical properties of epoxy resin, as it would be loaded into the polymer without damaging it. Moreover, it enhances the resin's thermal stability, preventing harmful smoke release.

Another example of double-sided organoalkoxy functionalized Anderson is the Mn-Anderson type POM covalently linked to two SPtris entities, denoted as $(TBA)_3[MnMo_6O_{18}\{(OCH_2)_3CNHC_{21}H_{19}N_2O_4\}_2]$ (Figure 23), which constitute a unique photochromic and multi-electrochromic materials, combining for the first time in a single molecule the optical properties of such organic and inorganic components [96].

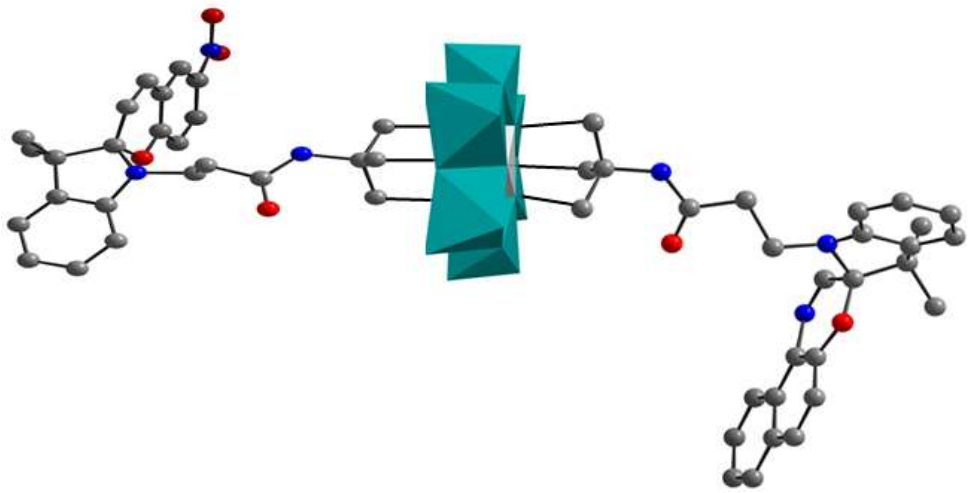

Figure 23. Mixed polyhedral and ball-and-stick representation of di-SPtris functionalized $MnMo_6$.[96] (Turquoise octahedra: {MoO_6}; grey octahedra: {XO_4}; grey spheres: C; blue spheres: N; red spheres: O)

It was until 2011 that the Wei group announced the synthesis of the first single-sided functionalized Anderson polyoxometalate $\{RC(CH_2OH)_3X(OH)_3M_6O_{18}\}^{3-}$ (R=$HOCH_2$, X=Cr^{III}) in the aqueous medium rather than organic medium (Figure 24) because the degree of protonation is influential in selective functionalization of Anderson POM with two (double-sided) or one triol ligand (single sides) since excess protonation will cause temporary passivation of μ_3-OH toward further alkoxylation [97].

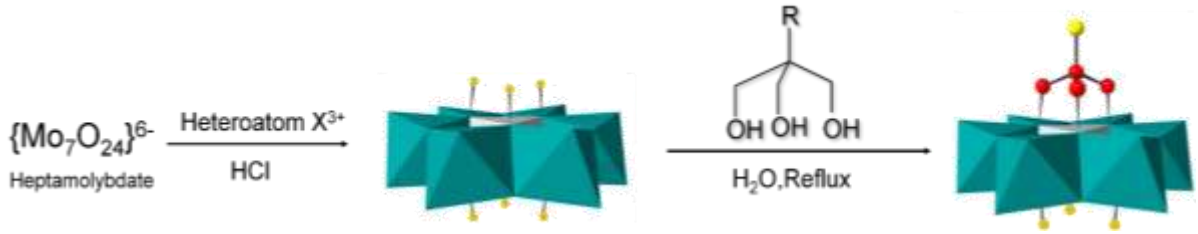

Figure 24. Hydrothermal process for the synthesis of asymmetrical single-sided functionalized Anderson POM.[92] (Turquoise octahedra: {MoO_6}; grey octahedra: {XO_4}; red spheres: C; light yellow spheres: R; dark yellow spheres: H)

An interesting example of single-sided functionalized Anderson-type POM that exhibits importance in the medical sector is $(TBA)_3[Al(OH)_3Mo_6O_{18}\text{-}\{(OCH_2)_3CNHCOC_{11}H_{23}\}]$, denoted as {$AlMo_6$-LA} (Figure 25) which consists of hexamolybdoaluminate POM linked, via amide bond to a long fatty acid chain called lauric acid (LA, $C_{12}H_{12}O_2$). {$AlMo_6$-LA} POM hybrid has an affinity to binding sites of human serum albumin (HAS), the main protein in blood plasma that transports various biomolecules through the bloodstream as fatty acids so that it can act as a vehicle for bioactive POMs [98].

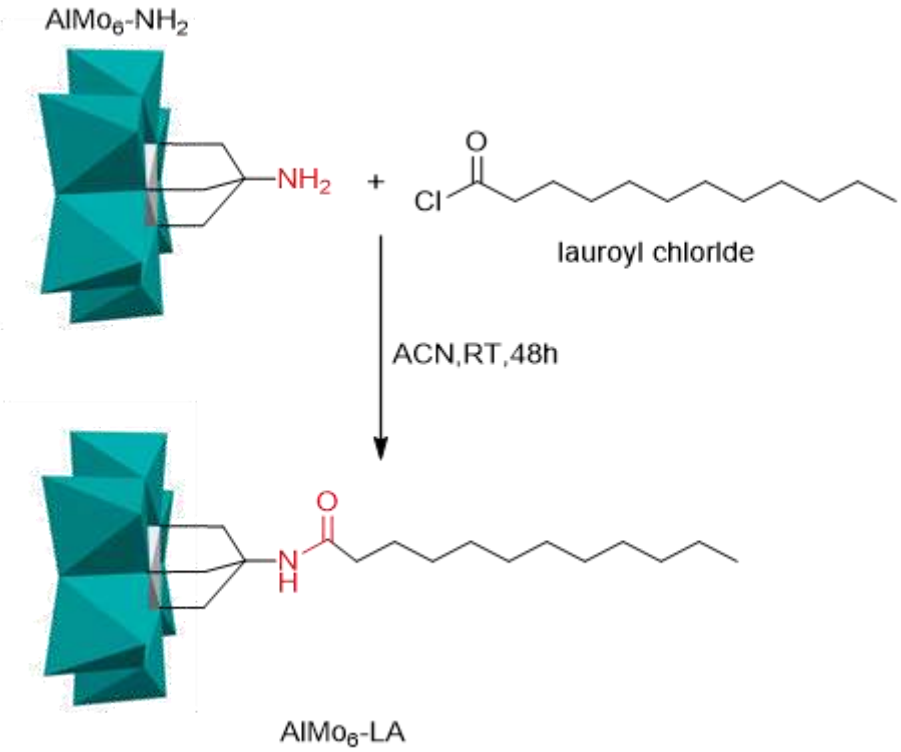

Figure 25. Synthesis of $AlMo_6$-LA.[98] (Turquoise octahedra: {MoO_6}; grey octahedra: {AlO_4})

III.2 Organosilyl Keggin-type POM Derivatives

Organosilylation of the di-lacunary Keggin-type polyoxotungstate $[\gamma\text{-}SiW_{10}O_{36}]^{8-}$ consists of anchoring dimeric $[(RSi)_2O]^{4+}$ or cyclotetrasiloxane $[(RSiO)_4]^{4+}$ groups (R: organic part) into the terminal tetra nucleophilic oxygen atoms of the POM cluster, resulting in bis-and tetrakis(organosilyl) decatungstosilicate anions, $[\gamma\text{-}SiW_{10}O_{36}(RSi)_2O]^{4-}$ (1) and $[\gamma\text{-}SiW_{10}O_{36}(RSiO)_4]^{4-}$ (2), respectively (Figure 26).

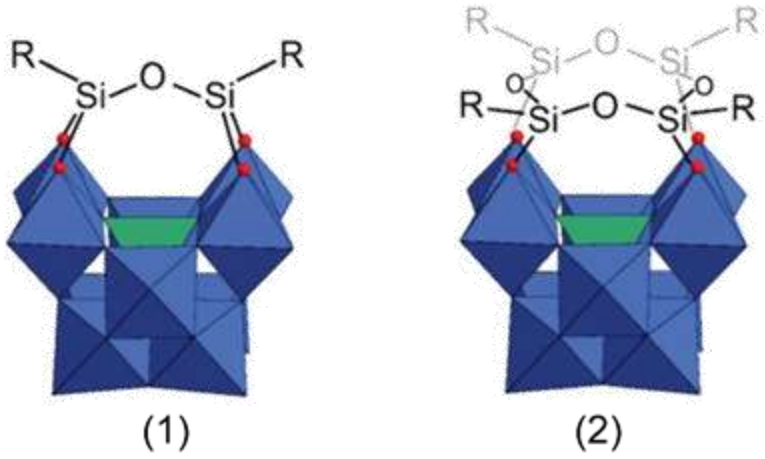

*Figure 26. Proposed structures for $[\gamma\text{-}SiW_{10}O_{36}(RSi)_2O]^{4-}$ **(1)** and $[\gamma\text{-}SiW_{10}O_{36}(RSiO)_4]^{4-}$ **(2)**.[99] (blue octahedra: {WO_6}; green tetrahedron: {$SiWO_4$})*

Mayer and his coworkers confirmed the formation of these POM-hybrids with NMR studies (^{183}W and ^{29}Si) in association with MALDI-TOF spectrometry. They mentioned that organosiloxane ligands are connected to the POM core through covalent μ-oxo bridges (W-O-Si) between tungsten atoms at the heteropolyanion surface and silicon atoms of the organosiloxane moieties. In both topologies, there is retention in the (C_{2v}) symmetry of [γ-$SiW_{10}O_{36}]^{8-}$ framework. More precisely, two and four organic pendant arms are connected to the POM cluster in [γ-$SiW_{10}O_{36}(RSiO)_4]^{4-}$ and [γ-$SiW_{10}O_{36}(RSi)_2O]^{4-}$ (R=H, vinyl, -$C_3H_6OC(O)C$-(Me)=CH_2, phenyl), respectively (Figure 27) [99].

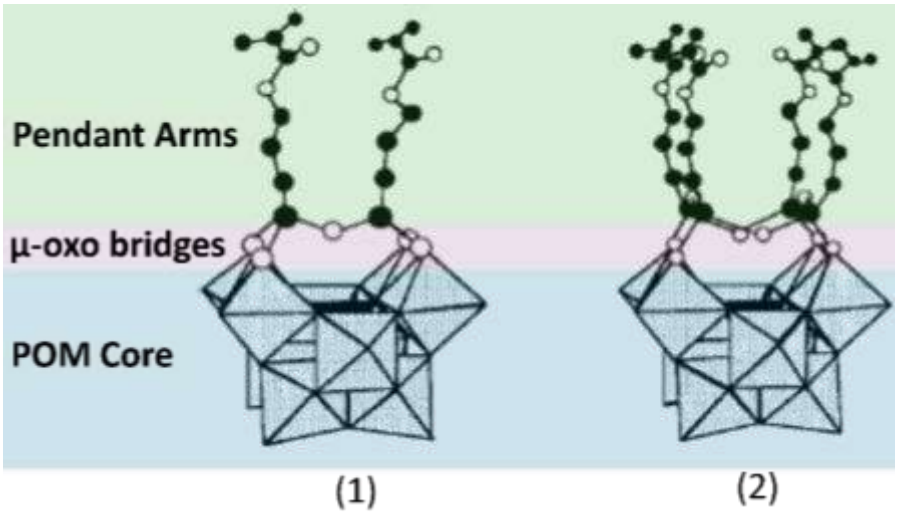

Figure 27. Representation of the components of [γ-$SiW_{10}O_{36}(RSi)_2O]^{4-}$ ***(1)*** *and [γ- $SiW_{10}O_{36}(RSiO)_4]^{4-}$* ***(2)****.*[99] *(R=H, vinyl, -$C_3H_6OC(O)C$- (Me)=CH_2, phenyl; White spheres: O; black spheres: C)*

In general, synthesis of organosilyl derivatives of [γ-$SiW_{10}O_{36}]^{8-}$ results from mixing the latter with trialkoxysilane ($RSi(OR')_3$ (R' = alkyl group), in the presence of hydrochloric acid in acetonitrile/water mixture. Selective formation of either (1) or (2) is dependent on the stoichiometric ratio of the precursors [γ-$SiW_{10}O_{36}]^{8-}$/$RSi(OR')_3$ during the synthetic procedure, whether SiW_{10}/RSi =1/2 or 1/4, respectively [99]. Scheme 4 gives a better understanding of the mechanistic details of the functionalization process.

$$RSi(OR')_3 + 3H_2O \longrightarrow RSi(OH)_3 + 3R'OH$$

$$[\gamma\text{-}SiW_{10}O_{36}]^{8-} + 2RSi(OH)_3 + 4H^+ \longrightarrow [\gamma\text{ -}SiW_{10}O_{36}(RSi)_2O]^{4-} + 5H_2O$$

$$[\gamma\text{ -}SiW_{10}O_{36}]^{8-} + 4RSi(OH)_3 + 4H^+ \longrightarrow [\gamma\text{ -}SiW_{10}O_{36}(RSiO)_4]^{4-} + 8H_2O$$

Scheme 4: *Synthesis of [γ-$SiW_{10}O_{36}(RSi)_2O]^{4-}$ and [γ -$SiW_{10}O_{36}(RSiO)_4]^{4-}$.*[99]

Double ligation of bis-lacunary Keggin POMs with two aminopropyl trialkoxysilane spacers ([$NH_2(CH_2)_3Si(OR')$]) in the presence of acid provides two terminal free amino groups in the POM-derivative [γ-$SiW_{10}O_{36}(NH_2(CH_2)_3Si)_2O]^{4-}$ (Figure 28), which are accessible for different post-functionalization routes such as condensation reactions with various nucleophiles

bringing out new functional groups like amide, imine, and sulfonamide alluring in a broad scope of applications.

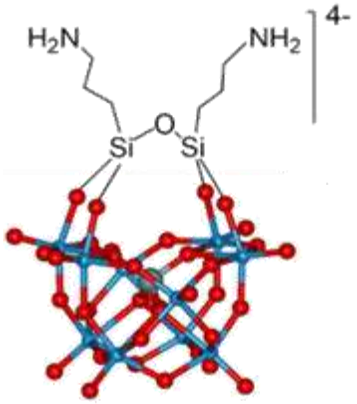

Figure 28. Structure of [γ-$SiW_{10}O_{36}(NH_2(CH_2)_3Si)_2O]^{4-}$.[99] (Blue spheres: W; red spheres: O; grey sphere: Si)

Post-functionalization is a valuable tool for installing bis-pyrene units into [γ-$SiW_{10}O_{36}(NH_2(CH_2)_3Si)_2O]^{4-}$ via covalent sulfonamide bonds formed due to reaction between pendant bis-amino groups anchored to 3-aminopropylsilane and pyrene sulfonyl chloride, in the presence of triethylamine base in acetonitrile solution [100,101]. Engineering of [γ-$SiW_{10}O_{36}\{(C_{16}H_9)SO_2NH(CH_2)_3Si\}_2O]^{4-}$ with terminal aromatic groups arranged in a tweezer-like shape (Figure 29) directs supramolecular hydrophobic and electrostatic interactions (π-π stacking) between POM-bis pyrene tweezer and carbon nanostructures (CNS) as C_{60}, C_{70}, and Carbon nanotubes (CNTs) [101].

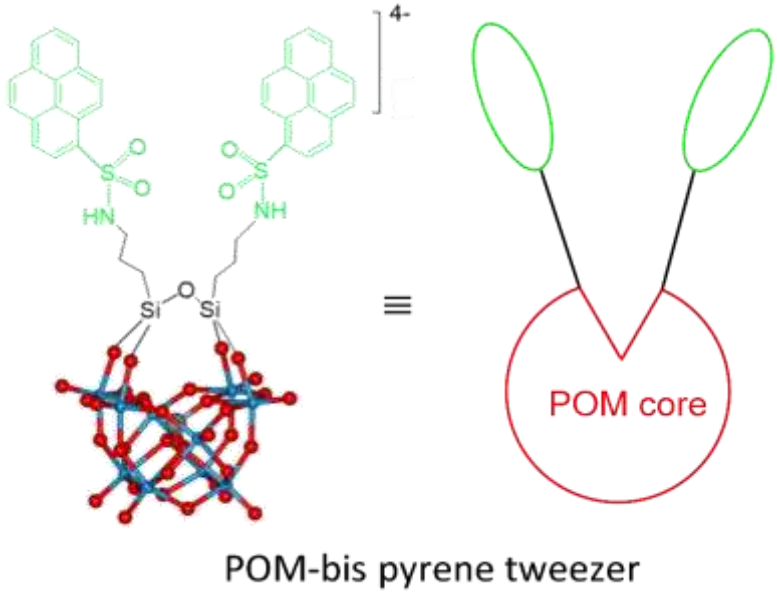

Figure 29. Structure of [γ-$SiW_{10}O_{36}\{(C_{16}H_9)SO_2NH(CH_2)_3Si\}_2O]^{4-}$ that has a tweezer-like shape.[101] (Blue spheres: W; red spheres: O; grey sphere: Si)

Self-assembled Keggin POM hybrids/carbon nanotubes have a unique fingerprint in dealing with worldwide challenges concerning the urgent need for sustainable and durable energy. This is obvious in their current applications in energy storage (electrodes for rechargeable lithium batteries and supercapacitors), electrocatalysis for water splitting in hydrogen fuel production, and, last but not least, sensor devices for environmental pollutants.

Another example of covalently derivatized $[\gamma\text{-}SiW_{10}O_{36}]^{8-}$ are those with two appendant alkyl thiols functions, which have been proven to offer robust stabilization for POM-based nanoparticle hybrids used as highly efficient and selective performance binary catalyst system for organic reactions (e.g., Carbon-carbon coupling reactions, aerobic oxidation of methane...).

Grafting $[\gamma\text{-}SiW_{10}O_{36}\{O(Si(CH_2)_3\text{-}SH_2)_2\}]^{4-}$ sulfide derivative, designated as $[POM\text{-}(SH)_2]^{4-}$, into gold nanoparticles, leads to the generation of POM-Au nanoscale hybrid systems of promising applications in catalysis [102]. Notably, the dilacunary Keggin $[\gamma\text{-}SiW_{10}O_{36}]^{8-}$ was firstly functionalized with dimeric (sulfanylpropyl)-silyl ligand (RSi-O-SiR where R is $-C_3H_6SH$), and secondly adsorbed into the surface of Au nanoparticles (Figure 30).Notably, mixing noncoupled Keggin POM and Au nanoparticles solutions will cause a reduction of the POM. Hence, prefunctionalization of the POM is essential to protect it from reduction. Moreover, the organosilyl ligand $\{(Si(CH_2)_3\text{-}SH_2)_2\}$ acts as a spacer and linker between the gold particles and the parent Keggin POM since it is covalently attached to the Au nanoparticle through the thiol groups while covalently attached to the POM through silyl groups. Remarkably, the thiol groups stabilize the connection between the nanoparticles by preventing them from desorption from the nanoparticle's surface. On the other hand, tetrabutylammonium (TBA^+) counteraction associated with $[POM\text{-}(SH)_2]^{4-}$ renders it soluble in acetonitrile/water mixtures.

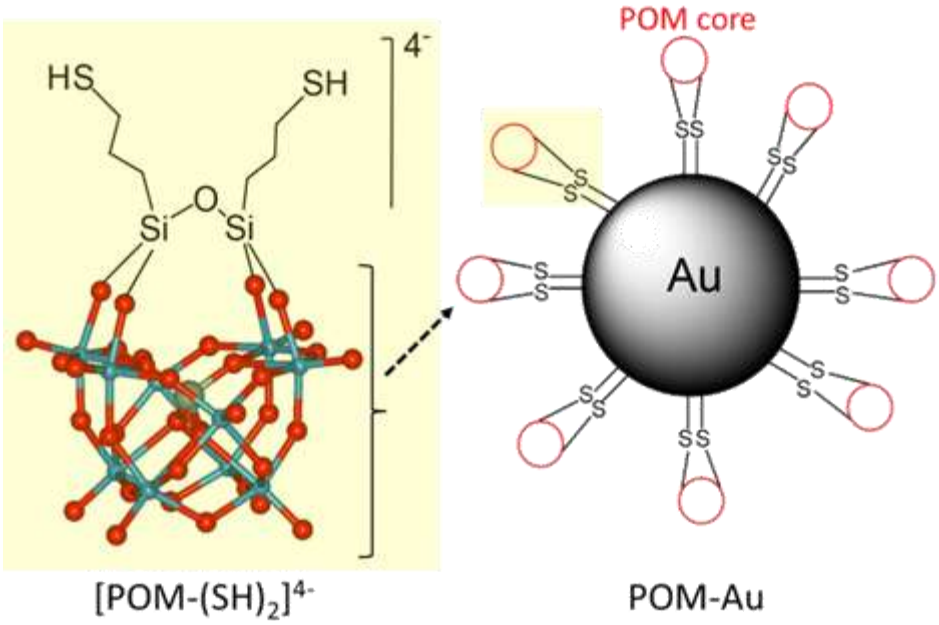

Figure 30. *Grafting* $[\gamma\text{-}SiW_{10}O_{36}\{O(Si(CH_2)_3\text{-}SH_2)_2\}]^{4-}$ *into the surface of Au-nanoparticles through R-S-Au bridges.*[102] *(Blue spheres: W; red spheres: O; grey sphere: Si)*

III.3 Organosilyl Well-Dawson-type POM derivatives

Similarly, Well-Dawson POMs containing thiol groups are employed to manufacture nanocomposite hybrid materials by covalent grafting of bis(silyl) mercaptopropyl monovacant Dawson anion $[\alpha_2\text{-}P_2W_{17}O_{61}(HSC_3H_6Si)_2O]^{6-}$ into the shell of chlorobenzyl functionalized nanopolymer core, dispersed in an aqueous medium. Well-Dawson POMs shell acts as a protective coat, contributing to the colloidal stability of the shell-core hybrid system (Figure 31) [103].

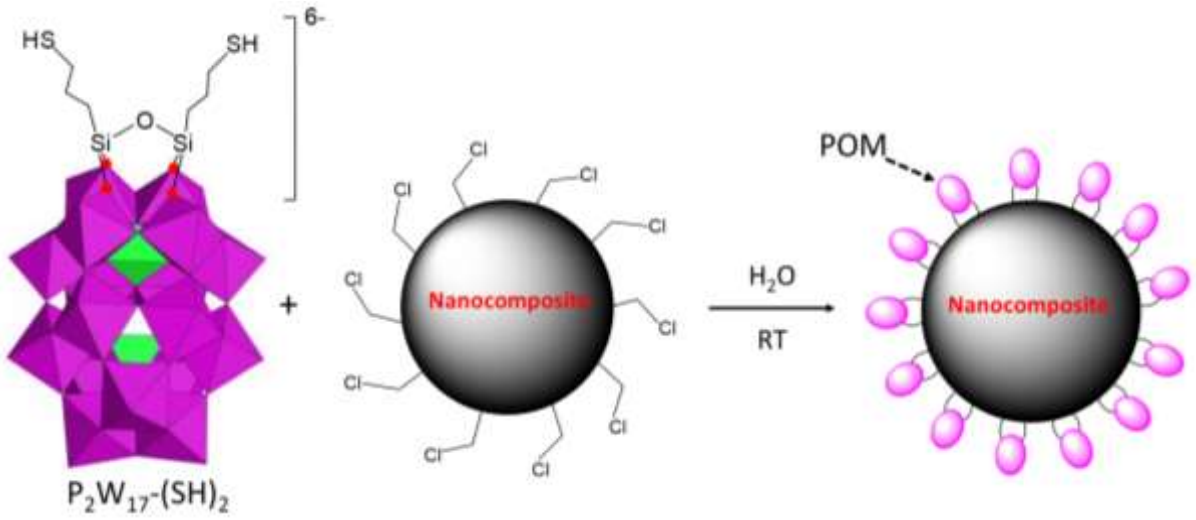

Figure 31. Grafting of $[\alpha_2\text{-}P_2W_{17}O_{61}(HSC_3H_6Si)_2O]^{6-}$ into the shell of chlorobenzyl functionalized nanopolymer.[103] (Purple octahedra: {WO_6}; green tetrahedra: {PO_4}; red spheres: O)

Well-Dawson organosilyl derivatives having two appendant azide groups $[\alpha_2\text{-}P_2W_{17}O_{61}\{O(SiAr\text{-}N_3)_2\}]^{6-}$ [104] are excellent starting materials for synthesizing POM-Photosensitizer hybrids (POM-PS) by reacting via copper-catalyzed azide alkynes cycloaddition (CuAAC) mechanism with organometallic photosensitizers (metalloporphyrin compounds, Metals (M) $=Ir^{III}$, Zn^{II}, Ru^{III}) bearing terminal alkyne group (Figure 32). These systems have spectacular photophysical and optical properties useful in artificial photosynthesis. The high electron affinity of the POM cluster combined with the visible absorption range of the organometallic photosensitizers are ideal for harvesting solar energy into chemical energy by mimicking the mechanism of green plants [105].

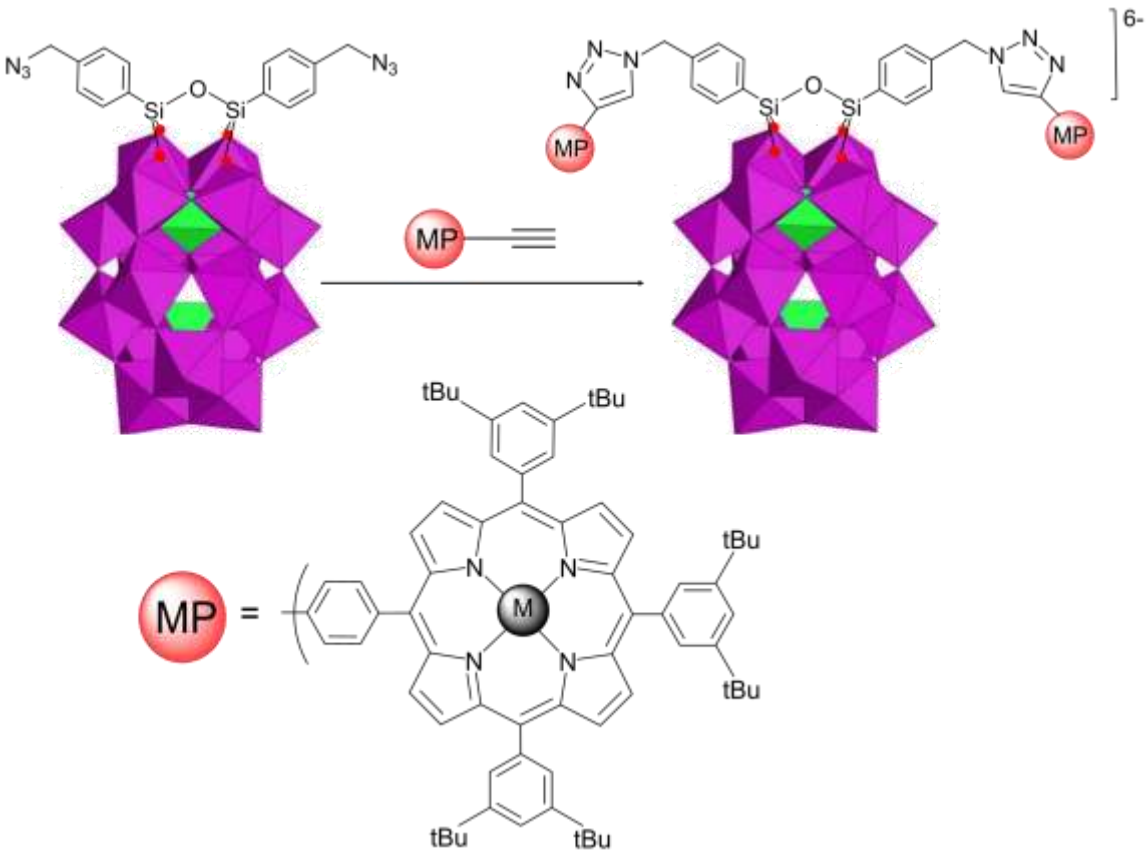

Figure 32. Synthesis of photosensitized POM-based hybrids from $[\alpha_2\text{-}P_2W_{17}O_{61}\{O(SiAr\text{-}N_3)_2\}]^{6-}$.[105,106] *(Metals (M)= Ir^{III}, Zn^{II}, Ru^{III}; purple octahedra: $\{WO_6\}$; green tetrahedra: $\{PO_4\}$; red spheres: O)*

IV. Conclusion

The chemistry of POMs is so rich that we could mention just a small number of multifunctional POM systems out of the other many examples in the literature. Also, the importance of functionalized POMs by organic groups leads to versatile platforms for creating novel functional hybrids with synergetic properties, displaying different properties and applications.

Borate Chemistry

I. Generalities

The chemistry of boron hydrides or boranes emerged many years ago by Alfred Stock and coworkers in 1912. Stock named them ”boranes” after their analog hydrocarbons, ”alkanes”, hydrides of carbon element (C) adjacent to boron in the periodic table [107]. Both boron [108,109] and carbon share the same property known as catenation, defined as the ability of the element to be covalently bound to itself many times; however, modes of chemical bonding in the two elements are different [110,111].

Carbon bonding with hydrogen or with itself is simple. It consists of 2c-2e bonds (two centers-two electrons) where the two atoms share a pair of electrons, forming chains and cyclic structures in one or two-dimensional planes. In contrast, boron chemical bonding is strikingly unusual and has been problematic for many years since boron element is electron deficient, which means there are fewer bonding electrons than boron atoms [112]; hence, 2e-2c can’t be the only bonding type in boron hydride compounds.

William N. Lipscomb tackled this dilemma in his Noble prize awarded work of 1976, titled ”Studies on the structure of boranes illuminating problems of chemical bonding". He addressed unfamiliar bonds B-B-B and B-H-B, known as 3c-2e bonds (three centers-two electrons), involving three atoms sharing two electrons. These are crucially formed due to the deficiency in bonding electrons. Boron hydride atoms hypercoordinate into three-dimensional polyhedral clusters, or, more specifically, cages, since boron atoms only occupy the outer vertices of the polyhedra while the interior is empty [112,113].

Boron hydrides are classified based on structure into three main classes: *closo*, *nido*, and *arachno* boranes (Figure 33). *Closo*-boranes are closed deltahedra with triangular faces of boron vertices (BBB) and general formula $B_nH_n^{2-}$ (n=6-12) (Figure 34). Their name c*loso*- comes from the Greek word ”*clovos*” which means cage, because B-H groups occupy the vertices of the triangulated polyhedron while its interior is empty. On the other hand, *nido*-(B_nH_{n+4}) and *arachno*-(B_nH_{n+6}) boranes are opened deltahedra derived by removing one or two boron vertices from the parent *closo*-boranes, respectively. The prefixes *nido*- and *arachno*- describes the structures of these open boranes, coming from the Latin word ”*nidus=nest*” and the Greek word ”*arachne=spider*”, respectively [114].

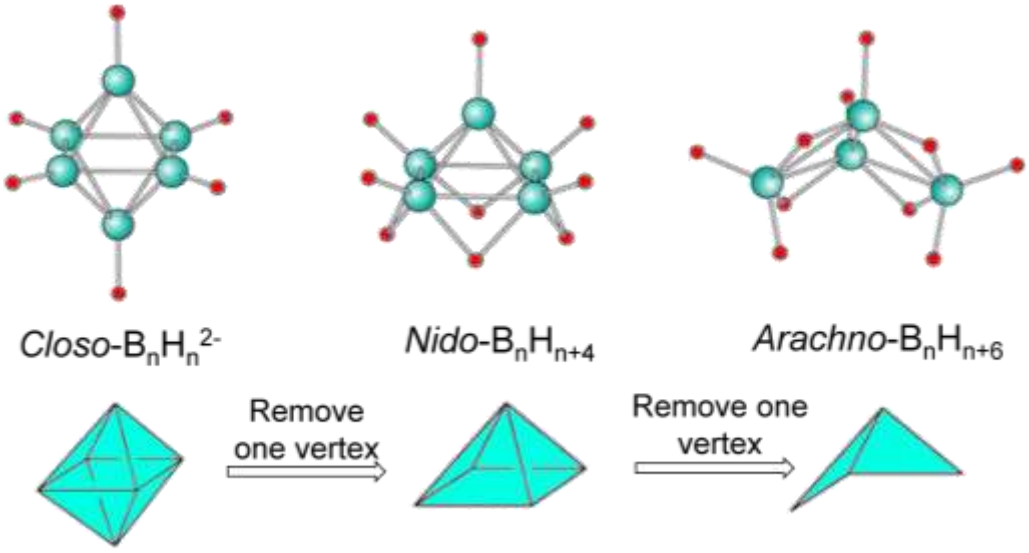

Figure 33. Polyhedron structures of closo-, nido-, and arachno-boranes.[114] (Turquoise spheres: B; red spheres: H)

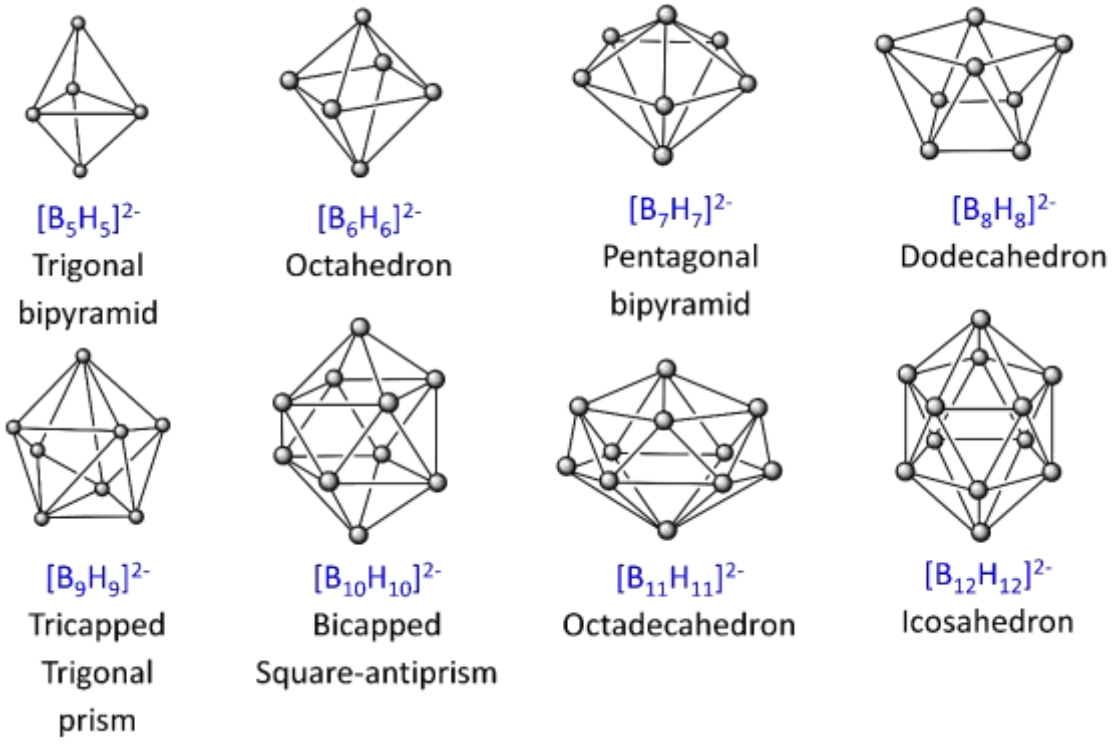

Figure 34. Structures of closo-boranes with five to twelve vertices. (H's are omitted for clarity; grey spheres: BH groups)

Concerning stability, neutral boranes (*arachno*- and *nido*-) are generally toxic, flammable, and highly sensitive to air and water, unlike *closo*-boranes (Figure 34), particularly the highly symmetric ones $[B_{10}H_{10}]^{2-}$and $[B_{12}H_{12}]^{2-}$, which are outstandingly stable to air, water, and moisture [115,116]. As a matter of fact, Cs^+, Na^+, and Li^+ salts of $[B_{12}H_{12}]^{2-}$ icosahedron show

extraordinary stability up to 800°C [117]. Despite *closo*-boranes being distinct in chemical bonding from hydrocarbons, they surprisingly display positive resonance energies like aromatic hydrocarbons, as reported by theoretical studies of the Aihara et al. group in 1978 [118]. While hydrocarbon aromatic systems involve the delocalization of electrons between unhybridized orbitals in planar rings, *closo*-borane presents non-classical aromaticity expressed by strong delocalization of electrons in a 3D hypercoordinate σ bonds system.

Due to cost issues, *closo*-dodecaborate anion $[B_{12}H_{12}]^{2-}$ has been in the spotlight for a long period over *closo*-decaborate anion $[B_{10}H_{10}]^{2-}$. However, the latter wins in terms of reactivity; therefore, studies in the literature focus on elucidating the activation of their exo-polyhedral B-H with various functional groups [119]. In this regard, we will briefly discuss the chemistry of the decahydro-*closo*-decaborate cluster.

II. Chemistry of *closo*-decahydrodecaborate

II.1 Structure and properties of $[B_{10}H_{10}]^{2-}$

Closo-decahydrodecaborate salts were prepared for the first time in 1961 by Hawthorne and Pitochelli [120]. One year later, Lipscomb identified their structure through X-ray diffraction as a bicapped square antiprism archetype (D_{4d}) where two boron atoms (B_{apical} =B1, B10) of lower connectivity CN=5 occupy apical positions, whereas the remaining eight boron atoms ($B_{equatorial}$ =B3-B9) with higher connectivity CN=6 are at the equatorial positions (Figure 35). There are two types of covalent bonds, the B-B-B (3c-2e) and B-H (2c-2e). Also, each boron atom is covalently connected to a terminal hydrogen atom radiating outwardly from the polyhedron center.

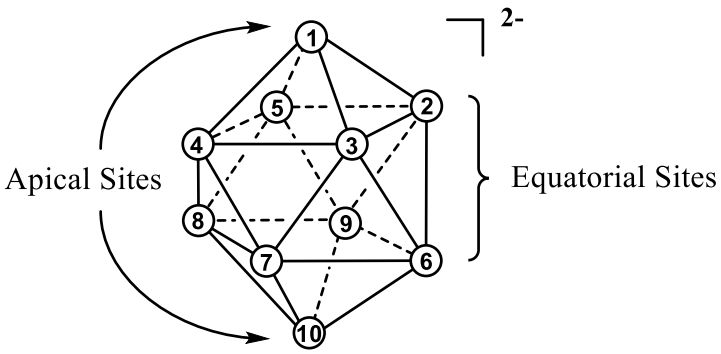

Figure 35. Structure of ***$[B_{10}H_{10}]^{2-}$*** *.(spheres are BH groups)*

At the same time, ^{11}B NMR of $[B_{10}H_{10}]^{2-}$ [120] was useful for distinguishing between apical and equatorial boron atoms (Figure 36). Indeed, two doublets are detected at ~ -25 ppm and ~ -1 ppm, displaying an intensity of eight and two boron atoms, respectively. This confirms the non-equivalent delocalization of bonding electrons throughout the cluster.

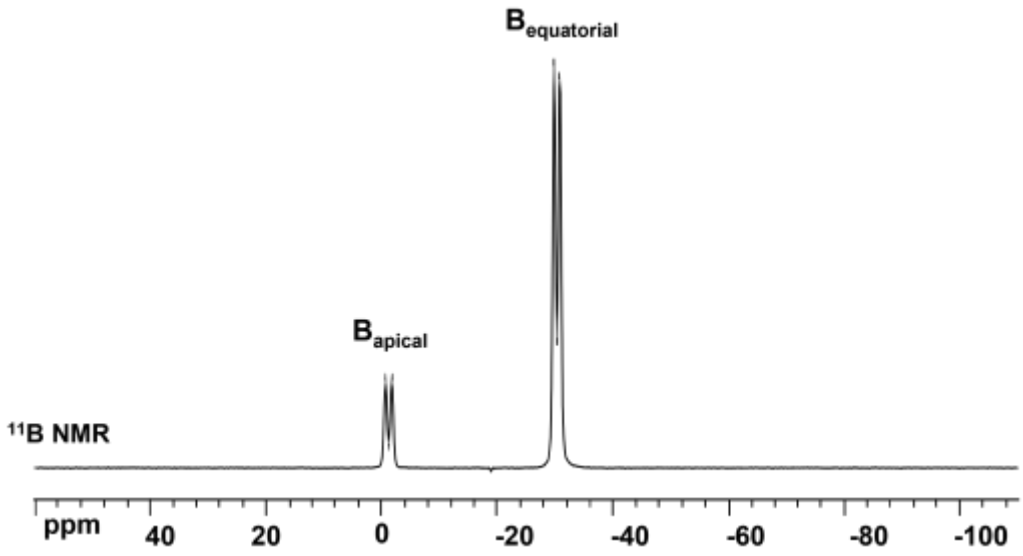

Figure 36. ^{11}B NMR of ***$(NH_4)_2B_{10}H_{10}$*** *in D_2O.*

II.2 Synthesis of $[B_{10}H_{10}]^{2-}$

The first route for synthesizing the *closo*-decahydrodecaborate anion is based on the closure of *nido*-decaborane compound $B_{10}H_{14}$ through the following reactions pathway (Figure 37): reaction of *nido*-$B_{10}H_{14}$ with ligand L (MeCN or Me_2S) gives the bis-ligand adduct $B_{10}H_{12}L_2$, which when treated with triethylamine Et_3N or ammonium NH_3 bases, will rearrange itself into $[B_{10}H_{10}]^{2-}$ associated with Et_3NH^+ or NH_4^+ cations, respectively [116,121].

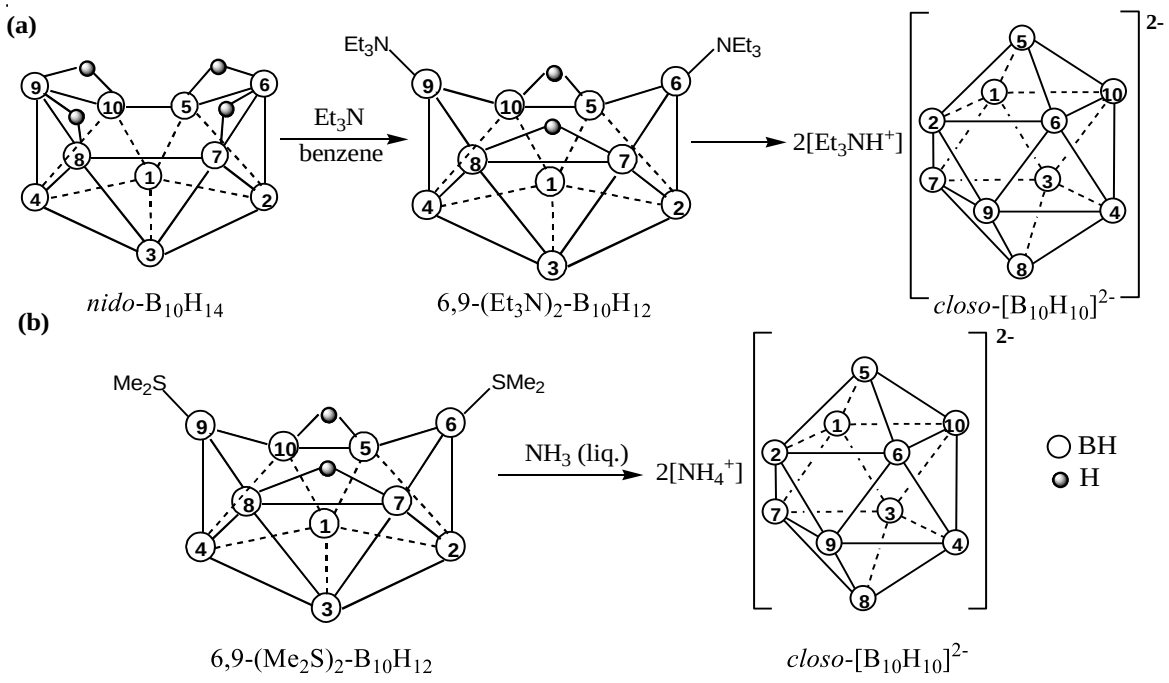

Figure 37. Synthesis of ***$[B_{10}H_{10}]^{2-}$*** *.[116,119]*

This approach has hazardous problems related to $B_{10}H_{14}$ synthesis from expensive diborane B_2H_6 under harsh synthetic and purification temperatures (210-250°C). Moreover, $B_{10}H_{14}$ is an extremely toxic and volatile solid and would form explosive intermediates under the air [122, 123].

A more appropriate approach is undoubtedly mandatory, resting on solid-state pyrolysis of cheaper, non-toxic precursor $(Et_4N)[BH_4]$ at 185°C under an inert atmosphere, giving $(Et_4N)_2[B_{10}H_{10}]$ in high yield [124,125].

II.3 Applications of $[B_{10}H_{10}]^{2-}$

Owing to their advantageous characteristics, the 10-vertex *closo*-borane cluster $[B_{10}H_{10}]^{2-}$ is embedded in many fields as liquid crystals, polymers, non-linear optics (NLO), luminescent materials, and medical applications [126–130]. In this work, the focus will be on medical applications.

To date, tens of millions of people worldwide are diagnosed with cancer annually. Half of them eventually die despite all the medical practices (surgery, chemotherapy, radiotherapy) used nowadays for treating cancer patients [131]. Doctors can successfully remove surgically cancerous tumors in their early stages; however, there is a considerable risk of removing normal cells around. It becomes harder to selectively remove only cancerous cells in the case of too small or too big tumors. Moreover, surgery is not even an option in case of metastatic cancers that spread all over the body, such as lung, prostate, and breast cancers. Unfortunately, targeting cancerous cells with chemotherapy drugs, administered orally or intravenously, can't distinguish cancerous from naturally fast-growing cells like hair cells; that's why it provokes unpleasant side effects in patients, such as hair loss, nausea, appetite loss, and skin problems. The same applies to radiotherapy; external gamma radiation beams targeting the tumors will contact normal cells.

Therefore, scientists have dedicated efforts to designing new therapeutic methods with specificity to tumor cells and fewer side effects, such as Boron Neutron Capture Therapy (BNCT) and Targeted Radionuclide Treatment (TRT).

Targeted Radionuclide Treatment (TRT) involves coupling α-emitting radioactive drugs (radionuclides) with cancer cells-targeting molecules that guarantee their selective delivery into cancerous cells where they emit highly energetic lethal α-particles with short path lengths, allowing them to penetrate single or small clumps of cancerous cells without affecting neighboring normal cells (Figure 38) [132,133]. Combining radionuclides with cancer cells-targeting molecules is also crucial to bypass their cytotoxicity during their stay in the body and ensure their fast delivery to the tumor since they have a short lifetime (e.g., 45.6 mins for ^{213}Bi and 7.21 hrs. for ^{211}At), so they may lose their effectiveness before reaching the tumor [134].

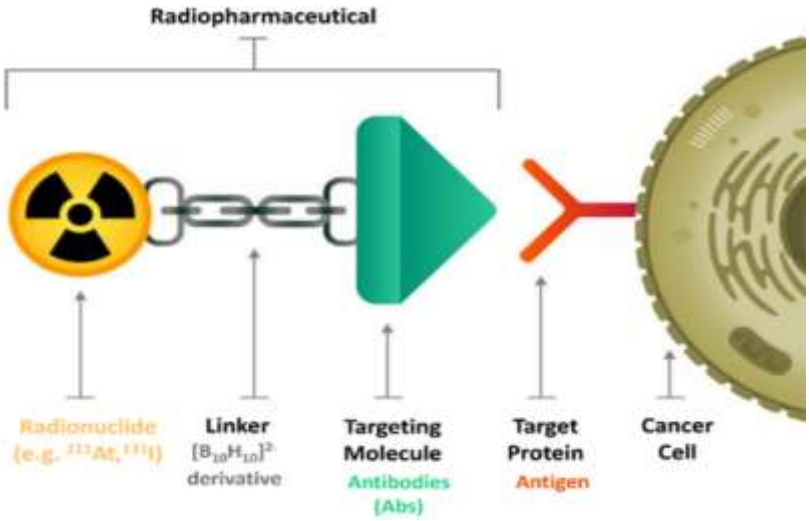

Figure 38. Principle of Targeted Radionuclide Treatment (TRT) of cancer cells.[135]

Examples of cells-targeting molecules are antibodies (Abs) or fragments of antibodies (Fabs) that bind to unique antigen receptors at the surface of unwanted cancerous cells, in addition to protein molecules specific to peptide receptors overexpressed in the tumor cell surface or inhibit enzyme activities vital for cancerous cell's life.

It has been reviewed that direct coupling of radionuclides such as [^{211}At] to cancer cells-targeting molecules results in rapid deastatenation (dissociation of ^{211}At) in vivo [136]. Accordingly, researchers find another approach to overcome the stability problems established by conjugating [^{211}At] indirectly to the target proteins via organic aromatic linker molecules as benzoate derivatives. Nonetheless, [^{211}At]-labeled benzoates are unstable when conjugated with small, rapidly metabolized molecules like Fab.

Lately, [^{211}At]-labeled conjugates containing boron cage moieties: *nido*-carborane ($\{CB_{11}H_{12}\}^-$, $\{C_2B_{10}H_{12}\}$), and *closo*-decaborate (2-) derivatives were proven stable towards deastatenation in vivo with minimal effect on the properties of the conjugated protein because the [^{211}At]-boron bond is stronger than [^{211}At]-Carbon, hence stable against enzymatic degradations and oxidative cleavage [137].

It is worth mentioning that *closo*-decaborate derivatives are useful in nuclear imaging since they can conjugate cancer-targeting agents and be labeled with radioactive halogens (^{76}Br,^{132}I), which emit gamma radiations detectable by special nuclear imaging techniques, thus efficiently locating cancerous cells accurately [134,137,138].

Boron Neutron Capture Therapy (BNCT) is also a promising targeted chemo-radiotherapeutic technique for killing cancer cells selectively without damaging the healthy nearby cells. In 1936, three years after the discovery of neutrons, Taylor, Fermi, and others found that boron-10 isotope (^{10}B) has a large neutron surface cross-section ≈ of 400 barns, so it could absorb slow neutrons to emit lethal lithium-7, α-particles, and gamma rays; this was known as the

boron neutron capture reaction (BNC). One year later, Locher proposed applying this reaction to kill cancer cells by the fatal energy released, especially since ^{10}B has a larger affinity to slow neutrons than endogenous elements (C, H, N) [139–141].

The concept of BNCT is based on accumulating concentrated dosages of ^{10}B isotope inside cancerous cells through B10-delivery agents that seek these cells selectively, then irradiating them with thermal (E ≈ 0.025 eV, penetration range ≈2.5 cm) or epithermal neutron (1eV < E < 10keV, penetration range ≈2-10 cm) for treating superficial tumors as melanoma skin cancer or deep malignant brain tumors, respectively [140]. Consequently, the accumulated ^{10}B isotopes inside the tumor will capture the neutrons and get excited to non-stable ^{11}B isotopes, which will simultaneously undergo fission reactions into Helium-4 nuclei (α-particles), lithium-7 nuclei and gamma-rays (Figure 39).^{4}He and ^{7}Li nuclei energy paths, ~ 9 µm, and 5 µm respectively, fortunately, don't exceed one cell diameter, thus all their intense energy deposit within tumor cells, leaving the normal outside cells harmless.

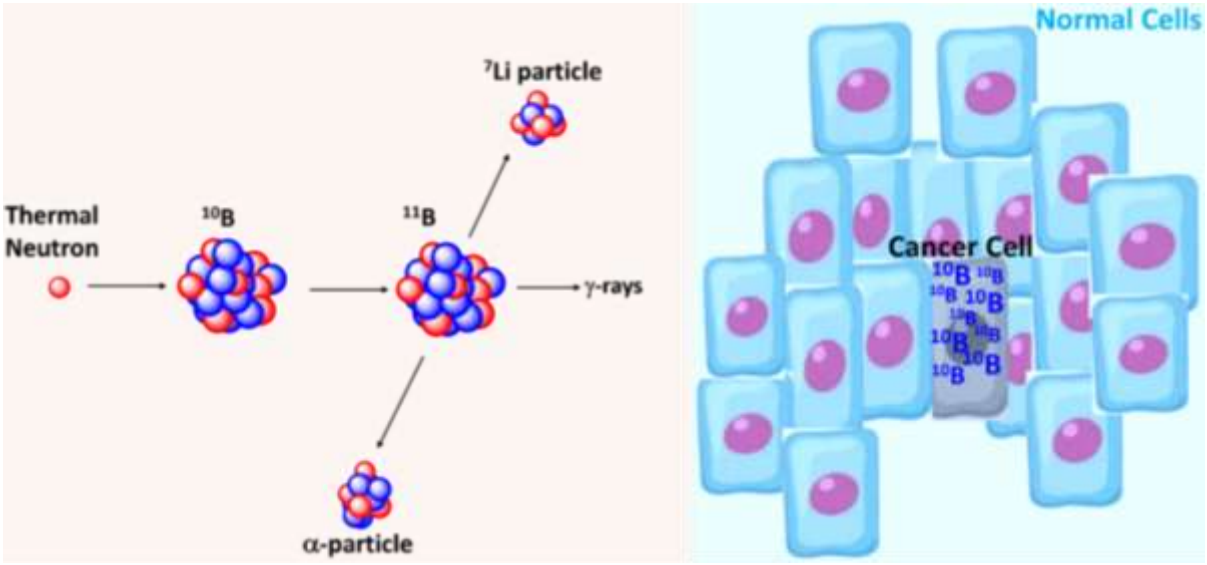

Figure 39. Principle of Boron Neutron Capture Therapy (BNCT) in a tumor cell.[142]

Polyhedral boranes derivatives of $[B_{10}H_{10}]^{2-}$ and $[B_{12}H_{12}]^{2-}$ are one of the ideal B10-containing compounds that respect the crucial factors necessary for successful BNCT: water solubility, chemical stability, high boron content, and non-toxicity. Sulfhydryl borane $Na_2[B_{12}H_{11}SH]$ (BSH) is applied in clinical trials in Europe, Japan, and the USA for head, neck, and recurrent glioma cancers [143]. The functionalization of *closo*-$[B_{10}H_{10}]^{2-}$ with amide, sulfuryl, isocyanate, and other functional groups provides plenty of compounds that can be covalently bonded to biomolecules such as antibodies, nucleosides, and carbohydrates which act as vehicles for boron cage moieties toward tumor cells.

II.4 Substitution in the $[B_{10}H_{10}]^{2-}$ anion

Substitution of exo-polyhedral hydrogen atoms (terminal hydrogen atoms) of the *closo*-decahydrodecaborate anion with carbon, nitrogen, oxygen, sulfur, and halogen compounds has been well established in the literature [119,144,145].

Various isomers of *closo*-borate derivatives can exist due to different boron environments, apical and equatorial. Such as, for monosubstituted derivatives $[B_{10}H_9L]^{2-}$ (L^-: Ligand), there are two possible isomers: apically and equatorially substituted *closo*-borates, $[1\text{-}B_{10}H_9L]^{2-}$ and $[2\text{-}B_{10}H_9L]^{2-}$, respectively (Figure 40).

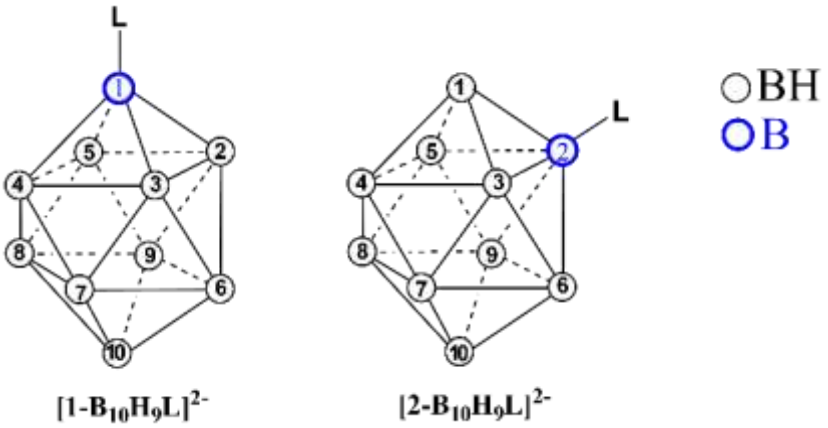

Figure 40. Mono-substituted products of ***$[B_{10}H_{10}]^{2-}$***.

The same may happen with disubstituted derivatives $[B_{10}H_8L_2]^{2-}$, there are seven possible isomers 1,2-, 1,6-[ae-$B_{10}H_8L_2]^{2-}$ (a=apical, e=equatorial),1,10-[a^2-$B_{10}H_8L_2]^{2-}$, 2,3-, 2,4-, 2,6(9)-, and 2,7(8)-[e^2-$B_{10}H_8L_2]^{2-}$ (Figure 41). However, no reports were recorded for the isolation and characterization of all seven positional isomers, possibly due to steric hindrance and electron distribution. The ligand's degree of substitution and position depends on the reagent's nature and synthetic conditions. Yet, substitution at the equatorial position is the most documented derivative of $[B_{10}H_{10}]^{2-}$.

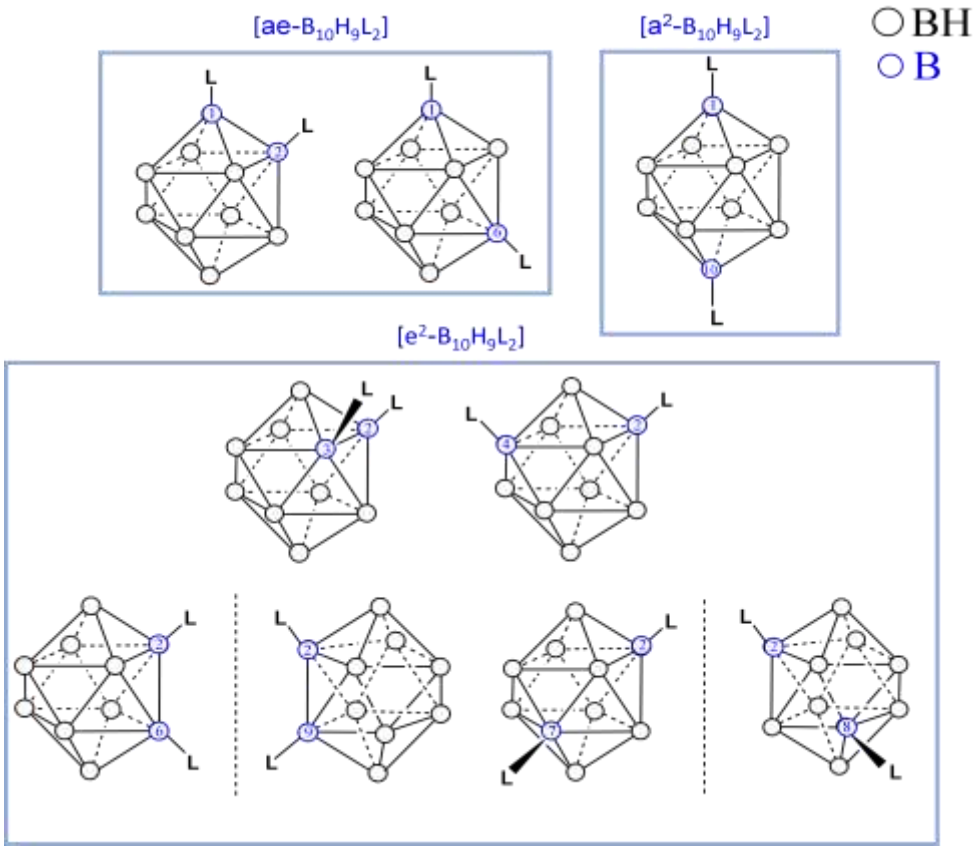

Figure 41. Structures of di-substituted derivative isomers of $[B_{10}H_{10}]^{2-}$. (Top: 1,2-, 1,6-, 1,10-; Middle: 2,3-, 2,4-; Bottom: 2,6(9)-, 2,7(8)- $[B_{10}H_8L_2]^{2-}$)

II.5 Nucleophilic substitution in the $[B_{10}H_{10}]^{2-}$ Anion

Many monosubstituted derivatives have been reported through an electrophilic-induced nucleophilic substitution mechanism (EINS) regioselective to the equatorial position [144,146]. Markedly, the (-2) charge of $[B_{10}H_{10}]^{2-}$ delocalizes on the terminal hydrogens, so they possess hydride character [147]; therefore, an acidic electrophile such as Bronsted or lewis acids (BF_3, CF_3COOH, CF_3SO_3H, etc.) are essential to promote nucleophilic substitution.

The mechanism of EINS was suggested as following (Figure 42): first $[B_{10}H_{10}]^{2-}$ is protonated by the acid, resulting in a highly reactive undecahydrodecborate anion $[B_{10}H_{11}]^-$, where the 11th proton caps the upper apical triangular face through μ_3-bridge with one B_{apical} and two $B_{equatorial}$ atoms [148,149]. Next, the proton will migrate to the equatorial Boron atom at position (2), forming $[B_{10}H_9(H_2)]^-$. After hydrogen migration, the dihydrogen molecule is eliminated, giving $[B_{10}H_9]^-$ which will interact with the ligand L^-, resulting in monosubstituted derivatives $[B_{10}H_9L]^{2-}$. The same steps happen forward resulting in the disubstituted derivatives $[B_{10}H_8L_2]^{2-}$

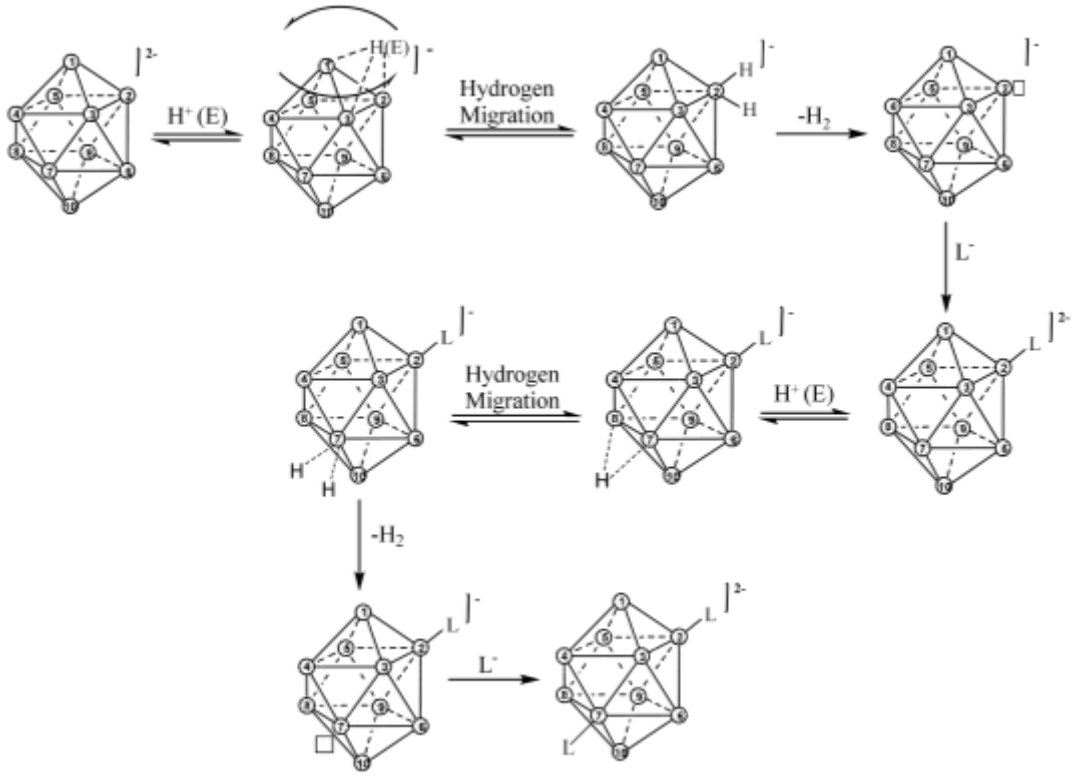

Figure 42. Mechanism of nucleophilic substitution in ***[B$_{10}$H$_{10}$]$^{2-}$***.[144,150]

This subsequent segment will briefly discuss the synthetic strategies and applications of *closo*-decahydrodecaborate derivatives of boron-carbon, boron-nitrogen, and boron-oxygen bonds.

II.5.1 Closo-decaborate derivatives with boron-carbon bonds

The mono-carbonyl derivative of *closo*-decaborate anion has always been popular in boron chemistry first due to its easy preparation under mild conditions by reacting [Ph$_3$PMe$_2$]$_2$[*closo*-B$_{10}$H$_{10}$] with oxalyl chloride (COCl)$_2$ in anhydrous dichloromethane resulting in high yield [Ph$_3$PMe$_2$][2-B$_{10}$H$_9$CO], where the carbonyl group is positioned at the equatorial boron atom {B2} (Figure 43). In addition, Cs$^+$, Me$_4$N$^+$, and Et$_3$NH$^+$ salts can be obtained in acetonitrile and THF solvents. Salts of the carbonyl derivatives exhibit oxidative stability in the air, moisture resistance, solubility in water, and thermal stability, as they won't lose the CO group at ambient temperature [146,151].

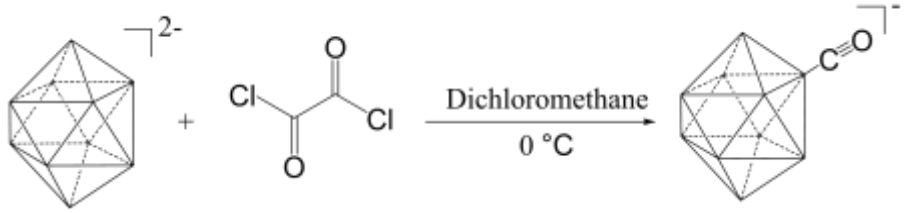

Figure 43. Synthesis of ***[2-B$_{10}$H$_9$CO]$^-$***.[151]

As a result, $[2\text{-}B_{10}H_9CO]^-$ can undergo further reactions with different nucleophiles, summarized in Figure 44, through the highly reactive carbonyl group, which exhibits the most electrophilicity at the carbon site, as proven by theoretical studies [116].

For instance, reacting $[2\text{-}B_{10}H_9CO]^-$ with water in refluxing acetone will give the carboxylic acid derivative $[2\text{-}B_{10}H_9COOH]^{2-}$, while reacting with sodium azide in neutral pH=7 will generate the isocyanate derivative $[2\text{-}B_{10}H_9NCO]^{2-}$.Also, adding a primary amine or alcohol will give the amide $[2\text{-}B_{10}H_9C(O)NHR]^{2-}$ or the ester derivatives $[2\text{-}B_{10}H_9CO_2R]^{2-}$,respectively [151]. Very recently, Mahfouz *et al.* reported the synthesis of mono-substituted *closo*-decaborate derivatives $[2\text{-}B_{10}H_9COR]^{2-}$ through a nucleophilic addition reaction between the carbonyl derivative of *closo*-decaborate $[2\text{-}B_{10}H_9CO]^-$ and the corresponding Grignard reagent RMgX, where R is the ethyl, iso-propyl, pentyl, allyl, vinyl, and propynyl groups. This approach is accomplished under green, fast, and mild conditions with 70-80% yields. The significance of these derivatives is their ability to constitute building blocks for polymeric integration via the allyl, vinyl, and propynyl substituents [152].

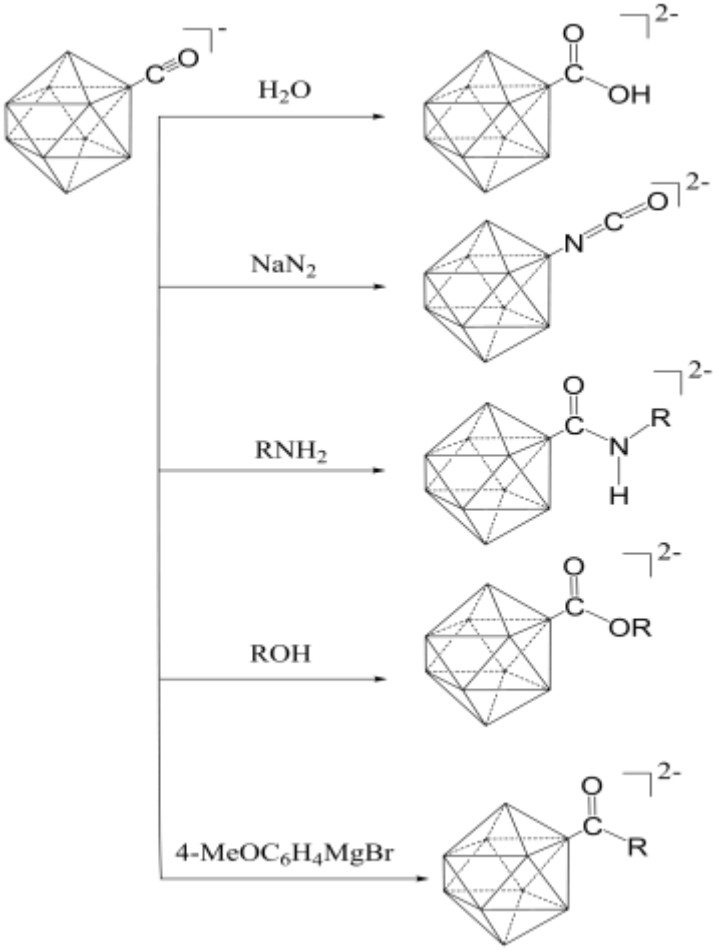

Figure 44. Reactivity of ***[2-B₁₀H₉CO]⁻***.[151,152]

In this sense, mono-carbonyl derivative $[2\text{-}B_{10}H_9CO]^-$ is deployed intensively as a precursor for manufacturing *closo*-decaborate drug agents, such as amide *closo*-decaborate derivatives,

which are efficient in the realm of diagnostic and therapeutic cancer treatment methods as BNCT.

For example, reacting $[2\text{-}B_{10}H_9CO]^-$ with 3-aminopropyltriethoxysilane (APTES) in refluxing dichloromethane, and the presence of the diisopropylethylamine base will result in the drug agent triethoxysilylated *closo*-decaborate $[2\text{-}B_{10}H_9CONH(CH_2)_3Si(OC_2H_5)_3]^{2-}$ (Figure 45).This derivative contains an amide group formed from reacting the -CO group of the *closo*-decaborate anion with the amino group of the APTES, and a terminal silane group available to covalently anchor into biocompatible drug carriers, such as mesoporous silica nanoparticles (MSN) suitable for medical applications (Figure 46) [153].

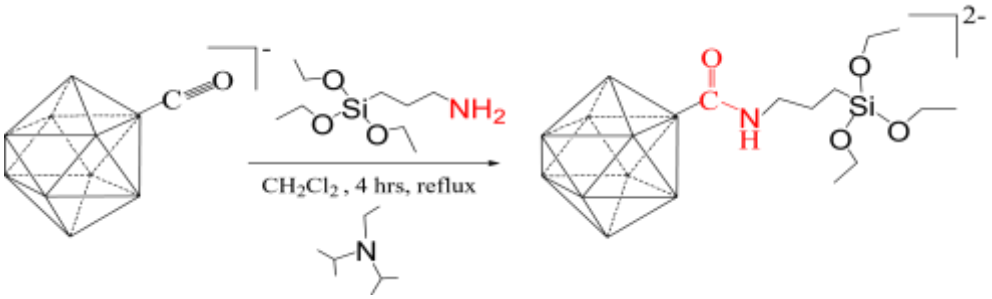

Figure 45. Preparation of 3-aminopropyltriethoxysilane derivative from $[2\text{-}B_{10}H_9CO]^-$.[153]

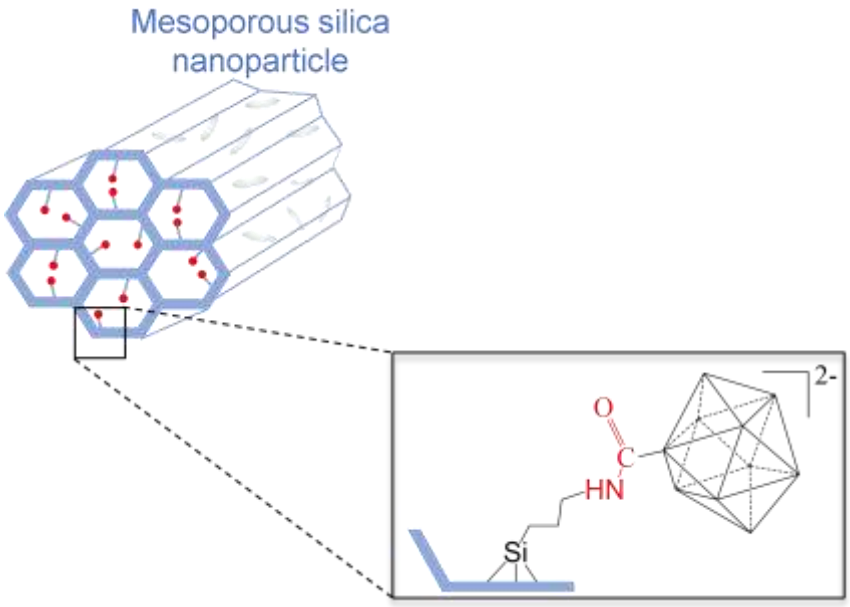

Figure 46. Schematic illustration of closo-decaborate functionalized mesoporous silica nanoparticles.[153]

Moreover, $[2\text{-}B_{10}H_9CO]^-$ is a precursor for the synthesis of diverse *closo*-decaborate derivatives containing pendant groups that can couple with ^{211}At-labeled proteins conjugates and provide them in vivo stability against deastatenation as well minimize the retention of their catabolites in the liver and kidney. For example, the *closo*-decaborate (-2) derivative

with terminal maleimidopropionate group is an optimal drug for TRT cancer treatment because it can conjugate covalently with thiol groups of cancer cells targeting agents (monoclonal antibodies and its fragments), then astatinated with ^{211}At radionuclide (Figure 47) [138].

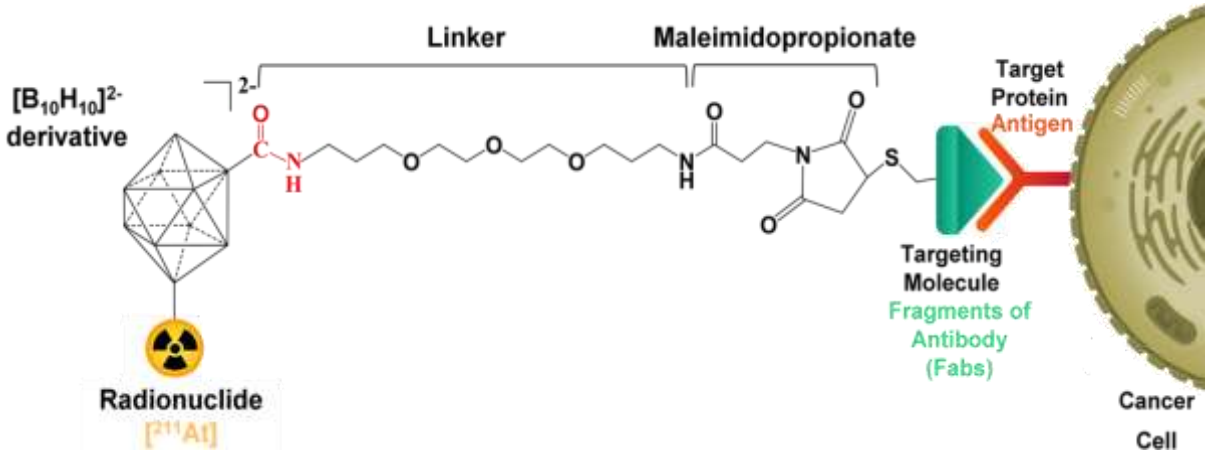

Figure 47. The maleimide-closo-decaborate (2-) reagent conjugated with antibodies labeled with ^{211}At.[138]

On the other hand, reacting triethylammonium salt of the *closo*-decaborate anion with benzoyl chloride in anhydrous acetonitrile at room temperature results in the benzoyl derivative $[2\text{-}B_{10}H_9C(O)C_6H_5]^{2-}$ having a carbonyl group resembling organic ketones. This means that the benzoyl derivative can perform more chemical reactions: nucleophilic addition reaction, reduction reaction, oxidation reaction, halogenations, and reaction with alkalis [154].

In addition, the hydrazone derivative $[2\text{-}B_{10}H_9\text{-}C(Ph)=N\text{-}NHPhCO_2H]^{2-}$ resulting from reacting the benzoyl derivative $[2\text{-}B_{10}H_9C(O)C_6H_5]^{2-}$ with 4-hydrazinobenzoic acid ($H_2N\text{-}NHPhCO_2H$) appears good to minimize the retention of radiohalogen-labeled proteins conjugates in the liver and kidney [155].

II.5.2 Closo-decaborate derivatives with boron-nitrogen bonds

Nitrilium derivatives $[2\text{-}B_{10}H_9N{\equiv}CR]^-$ (R=CH_3, C_2H_5, C_3H_7, C_6H_5,1-$C_{10}H_7$) are synthesized in high yield by refluxing of $[closo\text{-}B_{10}H_{10}]^{2-}$ and trifluoracetic acid in distilled nitrile solvent (RCN, R=CH_3, C_2H_5, C_3H_7, C_6H_5,1-$C_{10}H_7$) for 3 hours at 60°C (Figure 48) [156]. Herein, the trifluoroacetic acid protonates $[closo\text{-}B_{10}H_{10}]^{2-}$ to give $[closo\text{-}B_{10}H_{11}]^-$, then the equatorial hydride is replaced by nucleophilic substitution with nitrile group (-NCR) where the solvent plays the role of the ligand (L=-NCR).

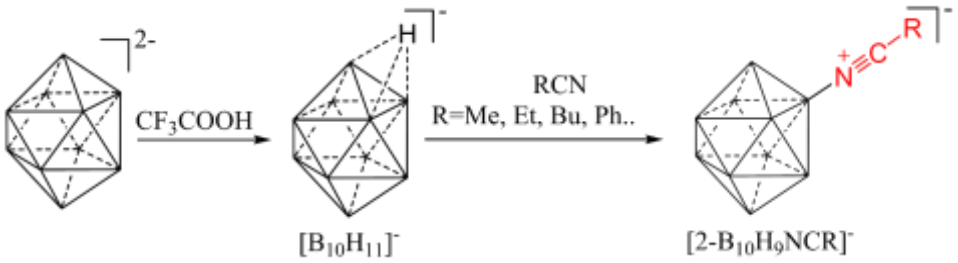

Figure 48. Synthesis of nitrile derivatives of closo-decaborate.[156]

The nitrile functional group in $[2\text{-}B_{10}H_9N{\equiv}CR]^-$ can be transformed into an amine group $[2\text{-}B_{10}H_9NH_3]^-$ by undergoing two-step reactions in the following sequence: (1) hydrolysis with water yields the acetamide derivative $[2\text{-}B_{10}H_9NH_2C(O)R]^-$, then (2) alkaline hydrolysis gives the amine derivative $[2\text{-}B_{10}H_9NH_3]^-$ (Figure 49, top) [157]. Luckily, the derivative is a precursor for preparing compounds convenient for BNCT, as Sivaev suggested, namely, *closo*-decaborate functionalized with the benzylamine group. The reaction of $[2\text{-}B_{10}H_9NH_3]^-$ with aromatic aldehydes ArC(O)H (R=C_6H_5, C_6H_4-2-OMe, C_6H_4-4-NHCOMe) results in the corresponding Schiff bases $[2\text{-}B_{10}H_9NH{=}CHAr]^-$ that are reduced with sodium tetrahydroborate into benzylamine derivatives $[2\text{-}B_{10}H_9NH_2CH_2Ar]^-$ (Figure 49, bottom).

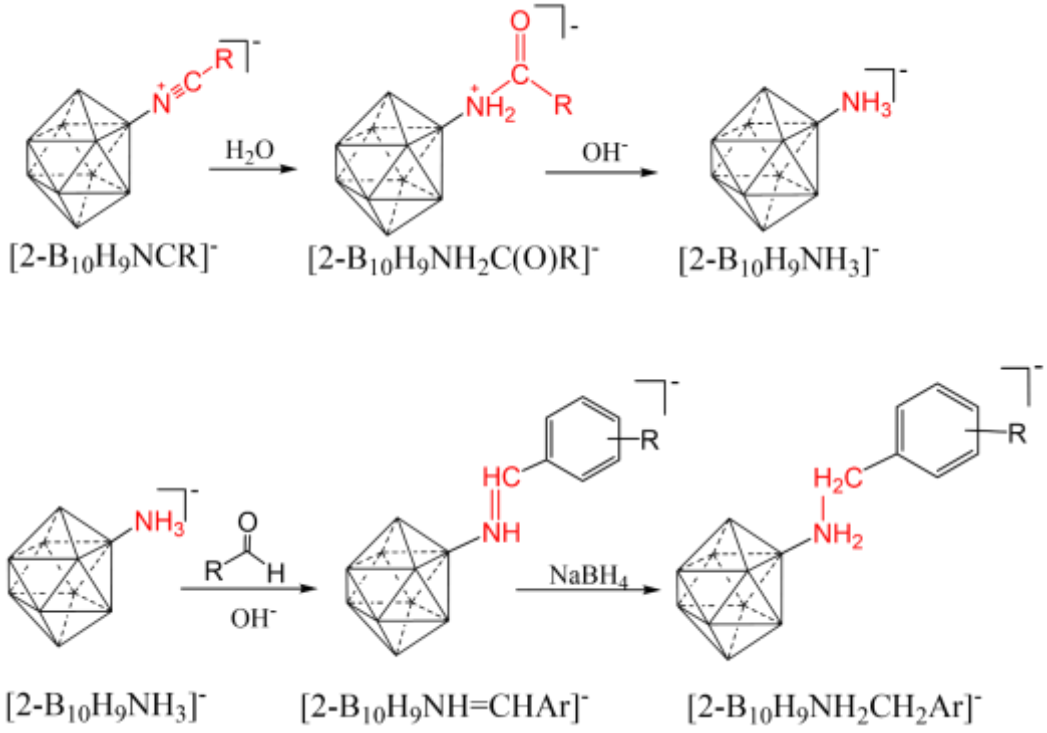

Figure 49. Synthesis of the amine derivative $[2\text{-}B_{10}H_9NH_3]^-$ ***(top)*** *and benzylamine derivatives $[2\text{-}B_{10}H_9NH_2CH_2Ar]^-$* ***(bottom)*** *for BNCT application.*[157]

Functionalization of a *closo*-decaborate cluster with the diazonium groups $-N_2^+$ through electrophilic substitution is selective to the apical positions {B1, B10}. It is envisioned as an

adequate framework for synthesizing diverse 10-vertex *closo*-borane derivatives suitable for medical application and material science [115,119,158]. The synthesis of monosubstituted dinitrogen derivative $[1\text{-}B_{10}H_9N_2]^-$ proceeds through a diazo-transfer reaction where $[B_{10}H_{10}]^{2-}$ reacts with $C_6H_5Br_3N_2^+$, BF_3^- in anhydrous acetonitrile, at -35°C followed by addition of sodium propionate base in acetonitrile at room temperature (Figure 50) [158].

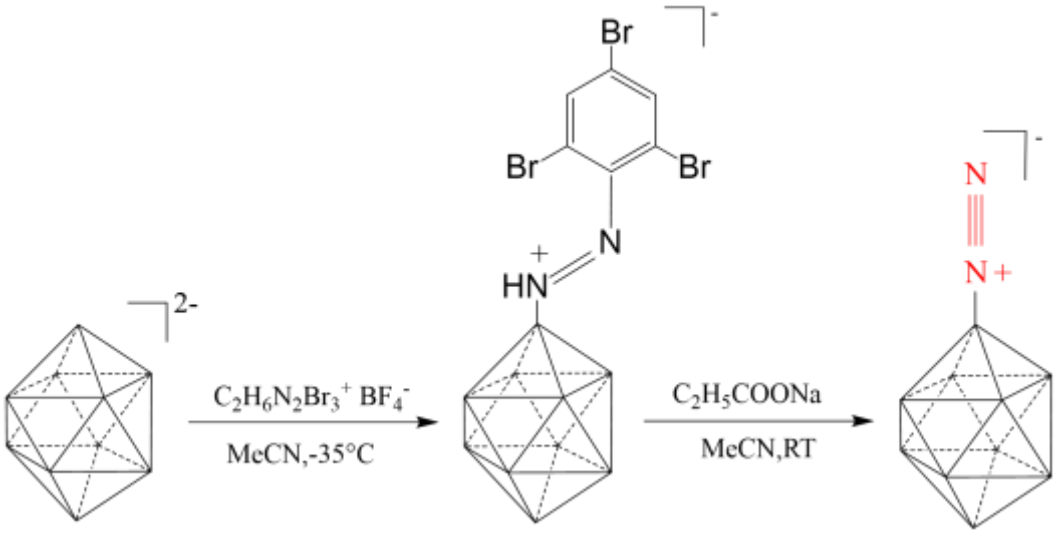

Figure 50. Synthesis of $[1\text{-}B_{10}H_9N_2]^-$.[158]

Silylated derivatives of $[1\text{-}B_{10}H_9N_2]^-$ are integrated into mesoporous silica nanoparticles for medical purposes. This derivative is synthesized in two steps reactions: (1) reaction of the diazo derivative with ethylenediamine $H_2N(CH_2)_2NH_2$ to produce $[1\text{-}B_{10}H_9NH_2(CH_2)_2NH_2]^-$, then (2) reaction of the peripheral amine in the cluster with -N=C=O group in 3-isocyanateopropyltriethoxysilane giving $[1\text{-}B_{10}H_9NH_2(CH_2)_2NHCONH(CH_2)_3Si(OC_2H_5)_3]^-$ in high yield (81%) (Figure 51) [153].

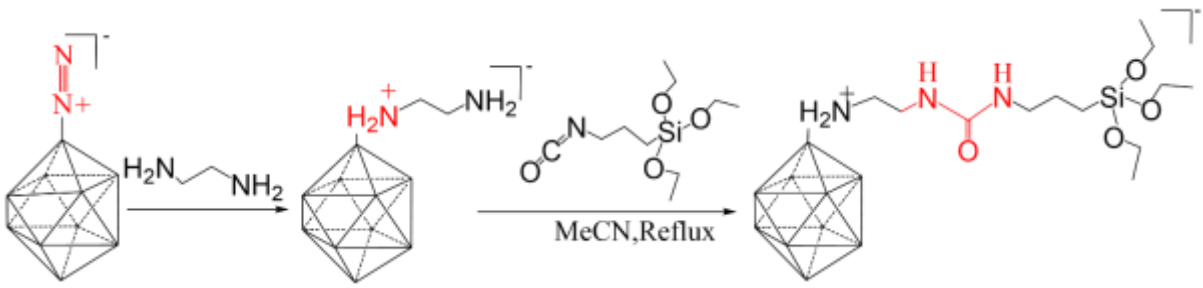

Figure 51. Synthesis of $[1\text{-}B_{10}H_9NH_2(CH_2)_2NHCONH(CH_2)_3Si(OC_2H_5)_3]^-$.[153]

Another use of diazo *closo*-decaborate anion $[1\text{-}B_{10}H_9N_2]^-$ is the preparation of hydrophobic monoanionic derivatives having a secondary or tertiary amino group in the axial position $[1\text{-}R_1R_2R_3N\text{-}B_{10}H_9]^-$ (R=C_6H_5, $C_6H_5CH_2$, H). While the direct reaction of $[1\text{-}B_{10}H_9N_2]^-$ with secondary amine R_2NH proceeds smoothly at 120°C, it fails with bulky tertiary amines R_3N.Hence, tertiary amine derivatives are synthesized by two steps: (1) synthesis of appropriate primary

or secondary amine derivative and (2) reaction of this intermediate with alkyl halides in an alkaline aqueous solution (Figure 52) [159].

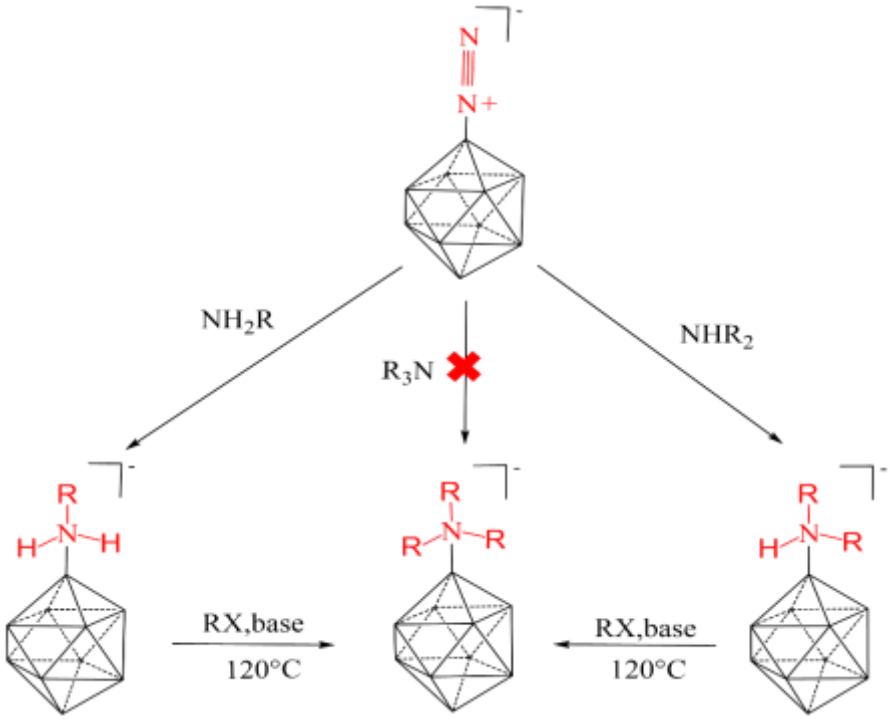

Figure 52. Synthesis of [1-$R_1R_2R_3$N-$B_{10}H_9$]$^-$ (R=C_6H_5, $C_6H_5CH_2$, H) from [1-$B_{10}H_9N_2$]$^-$.[159]

Notably, attaching bulky aromatic groups to the amino nitrogen in [1-$R_1R_2R_3$-$NB_{10}H_9$]$^-$ with lowering the electrostatic charge of the *closo*-decaborate cage from (-2) in [1-$B_{10}H_{10}$]$^{2-}$ to (-1) [159], together would bring in hydrophobic character to the cluster making it useful in liquid-liquid extraction for treating radioactive heavy metal wastes, particularly Cs^+, generated from converting nuclear energy to electrical energy. The extraction technique is based on the complexation between anionic hydroborates as [1-(C_6H_5)$_2$($C_6H_5CH_2$)-$NB_{10}H_9$]$^-$ and metal cation Cs^+ (M^{n+}) in an acidic aqueous medium forming a neutral compound extracted by organic solvent [160].

Additionally, mono-dinitrogen *closo*-decaborate derivatives can be further rationally functionalized by multistep reactions with hetero-(1,10)-diapical π onium substituents as thanium and alkoxy pyridinium groups with linear σ- onium fragments as alkyl chains exhibiting liquid crystalline behavior and non-linear optical properties (Figure 53) [161].

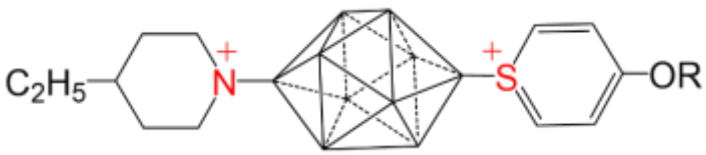

Figure 53. Hetero-(1,10)-disubstituted sulfonium and pyridinium derivative of closo-decaborate anion for liquid crystals.

II.5.3 Closo-decaborate derivatives with boron-oxygen bonds

There are many species of the *closo*-decaborate anion attached to nucleophiles through oxygen atoms such as hydroxyl $[B_{10}H_9OH]^{2-}$, acyloxy $[B_{10}H_{10-n}(OAc)_n]^{2-}$, carboxylate $[B_{10}H_{10-n}(OCOR)_n]^{2-}$, and alkoxy $[B_{10}H_9OR]^{2-}$ derivatives [162–164].

Among all, cyclic oxonium derivatives are the most interesting in medical applications since its ring opening through nucleophilic reagents leads to new derivatives with an oxygen atom anchored to the equatorial boron atom, alkoxy spacer, and pendant functional groups (Figure 54) capable of anchoring to biological molecules (protein, nucleotides, liposomes, etc.), thus providing drug carrier agents for BNCT.

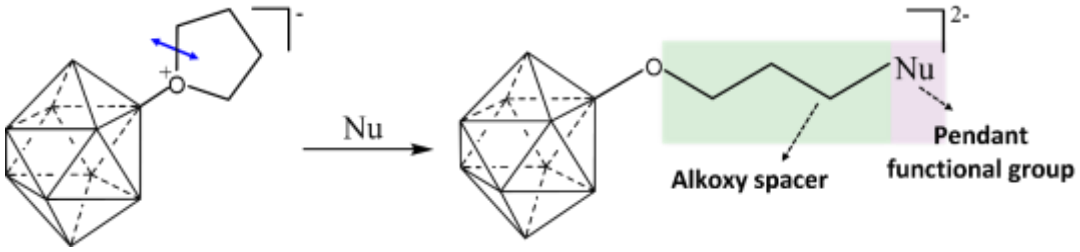

Figure 54. Ring-opening of cyclic oxonium derivatives of the closo-decaborate anion.

Zhizhin and Matveev group elucidated the preparation of cyclic oxonium derivatives through the reaction of $[B_{10}H_{10}]^{2-}$ with tetrahydrofuran (THF),1,4-dioxane, or tetrahydropyrane (THP) in the presence of CF_3COOH resulting in $[2\text{-}B_{10}H_9(OC_4H_8)]^-$, $[2\text{-}B_{10}H_9(O_2C_4H_8)]^-$, and $[2\text{-}B_{10}H_9(OC_5H_{10})]^-$, respectively; with cyclic oxonium attached to the B_{10} cluster (Figure 55). Moreover, they reported enormous interactions between cyclic oxonium closo-borate compounds with negatively charged N-nucleophiles (amine, azide, isocyanate, etc.), O-nucleophiles (HOC_6H_4COOMe), ROH), and S-nucleophiles (thiols, thiocyanate, thiosulfate) [165].

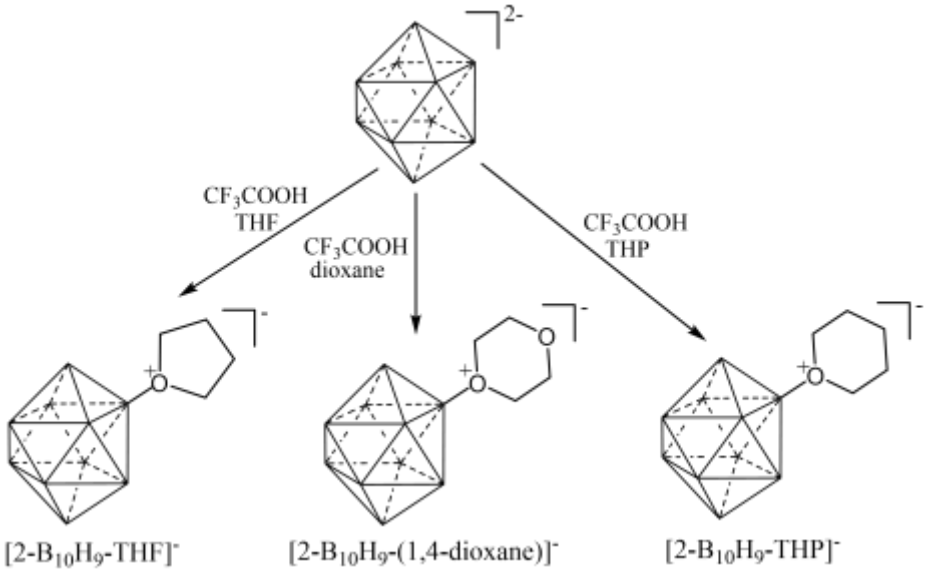

Figure 55. Synthesis of $[2\text{-}B_{10}H_9(OC_4H_8)]^-$, $[2\text{-}B_{10}H_9(O_2C_4H_8)]^-$,and $[2\text{-}B_{10}H_9(OC_5H_{10})]^-$.

Avdeeva et al. proposed an approach for synthesizing *closo*-borate derivative with alkoxy spacer and pendant carboxylic group, which, when coupled to peptide functional group, the histidine methyl ester (H-His-OMe) (Figure 56), shows antiviral activity in vitro against the modern strain of A/H1N1 influenza virus at 10 and 5µg/ml [166].

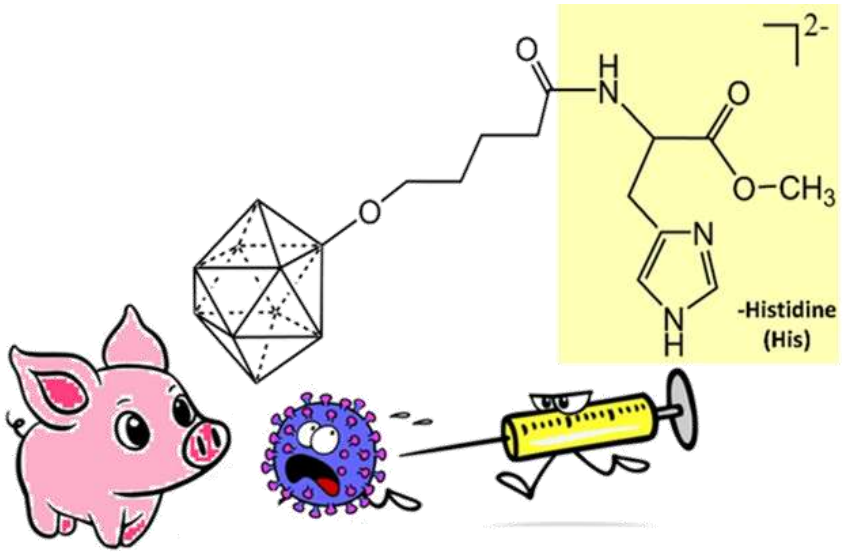

Figure 56. Closo-decaborate anion containing -C(O)-His-OMe pendant group possesses antiviral activity against the H1N1 influenza virus.

III. Coupling of Polyoxometalates and Closo-decahydrodecaborate

The coordination of lacunary Anderson, Keggin, and Dawson POMs with organic ligands offers multiple properties by combining or synergizing those of the POM and the organic ligands, as shown previously. Building on these examples and with a viewpoint to generate new bio-active systems that act as anti-tumor inhibitors with therapeutic efficacy and low toxicity, Manal Diab had developed in her PhD work (2014-2017), a new class of hybrid compounds by chemically associating boron clusters with POMs.She succeeded in conquering all the challenges encountered related to both species being anionic compounds with two complementary redox characters, oxidative for the boron cluster and reductive for polyoxometalates.

The synthetic strategy involved preparing Anderson POMs functionalized with tris(hydroxymethyl)aminomethane (TRIS), $[AlMo_6O_{18}(OH)_3(TRIS)]^{3-}$ (noted as $AlMo_6$-Tris) and $[Mn^{III}Mo_6O_{18}(TRIS)_2]^{3-}$ (noted as $MnMo_6$-$(TRIS)_2$), and the Keggin and Dawson-type POMs functionalized with aminopropyl-tri(ethoxy)silane (APTES) ligand, noted as SiW_{10}-APTES and P_2W_{17}-APTES (Figure 57).

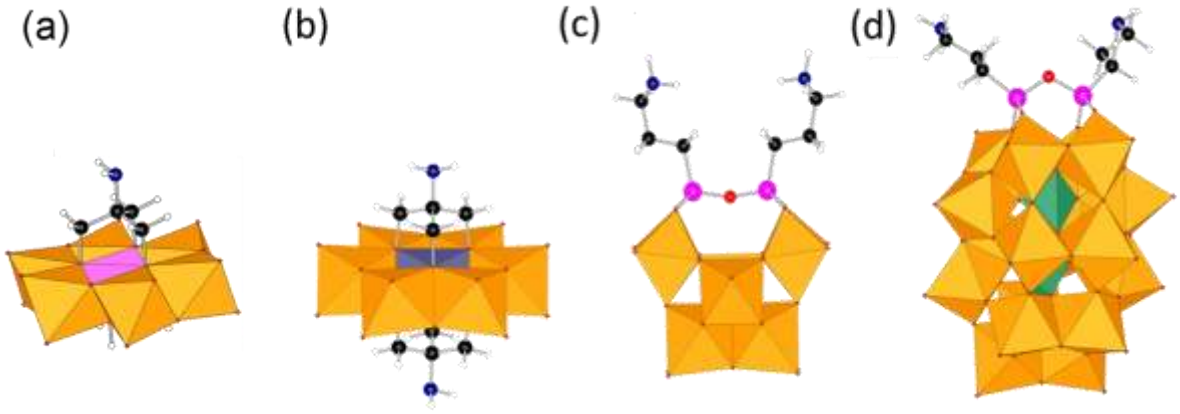

Figure 57. Views of the molecular structures of precursors (a) ***AlMo$_6$-TRIS*** *[167], b)* ***MnMo$_6$-(TRIS)$_2$*** *[90], (c)* ***SiW$_{10}$-APTES*** *and (d)* ***P$_2$W$_{17}$-APTES****.[99] (Orange octahedra: {MoO$_6$}; pink octahedron: {AlO$_6$}; blue octahedron: {MnO$_6$}; green tetrahedra: {PO$_4$}; dark blue spheres: N; white spheres: H; black spheres: C; pink spheres: Si; red spheres: O)*

Each of these precursors possesses 1 or 2 amine functions, which in a second step enabled the covalent grafting of decaborate clusters $[B_{10}H_9CO]^-$ cluster in the presence of a hindered base such as DIPEA. Five original and innovative compounds combining POMs and decaborates were obtained in total as shown in Figure 58. These compounds have been extensively characterized in the solid state and solution by mass spectrometry and a wide range of NMR techniques (^{1}H, ^{13}C, ^{11}B, ^{29}Si, ^{31}P, ^{183}W, DOSY, ROESY...) [168,169].

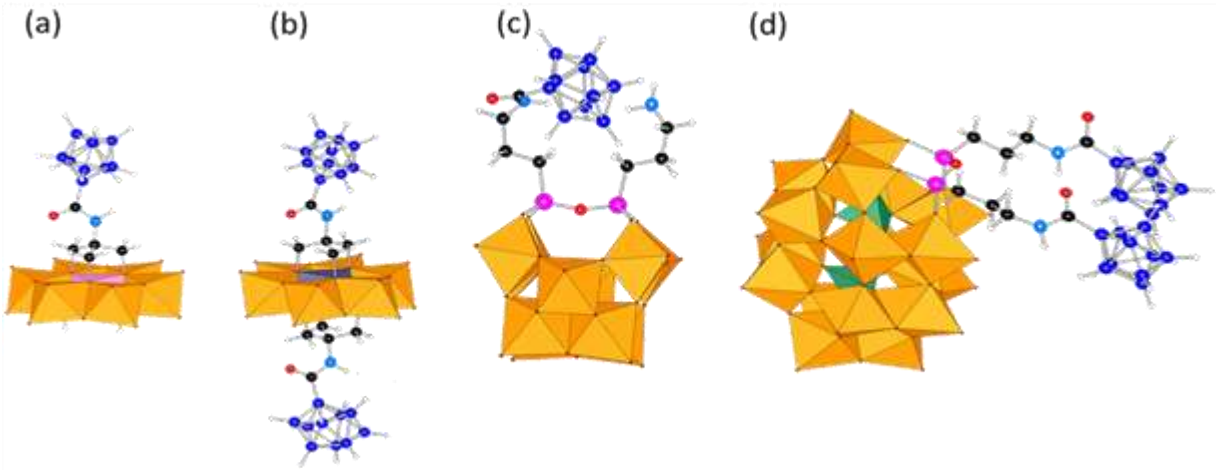

Figure 58. Molecular structures for the compounds (a) ***AlMo$_6$(TRIS-B$_{10}$)*** *, (b)* ***MnMo$_6$(TRIS-B$_{10}$)$_2$,*** *[168] (c)* ***SiW$_{10}$-monoB$_{10}$,*** *and (d)* ***P$_2$W$_{17}$-diB$_{10}$****.[169] (Orange octahedra: {MoO$_6$};pink octahedron: {AlO$_6$}; blue octahedron: {MnO$_6$}; green tetrahedra: {PO$_4$}; blue: B; light blue spheres: N ; white spheres: H; black spheres: C; pink spheres: Si; red spheres: O)*

Among these, the most interesting hybrid system is the mono-adducted compound **SiW$_{10}$-monoB$_{10}$** (Figure 58c), which has one $[B_{10}H_9CO]^-$ derivative coupled via an amide bond with one of the amine functions of the APTES linker on SiW$_{10}$-APTES-type POM. Indeed, in the field of POM-hybrids, this result is exceptional as no other system is known in the literature

featuring a single functionalization, therefore offering a possible dissymmetric functionalization on the POM. As Figure 59 suggests, this compound was obtained thanks to the intramolecular dihydrogen contact between the free amine function and the B-H groups of the grafted boron cluster stabilizing this adduct.

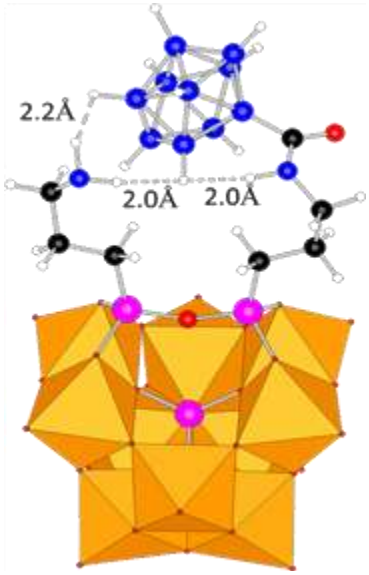

Figure 59. Optimized molecular structure for the compound ***SiW$_{10}$-monoB$_{10}$***.[169] *(Orange octahedra: {WO$_6$}; pink spheres: Si; blue spheres: B; light blue spheres: N; white spheres: H; black spheres: C; red spheres: O)*

In solution, we can envision an amine function available for a second distinct functionalization. This will be a landmark in the field of hybrid POMs since the synthesis of a multifunctional hybrid of dilacunary Keggin POM has never been reported and is inevitably not an easy task.

Therefore, in the second chapter of this PhD work, we discussed the possibility to functionalize the remaining amine function in the monoadduct **SiW$_{10}$-monoB$_{10}$** to obtain the first asymmetrical bi-functionalized POM hybrid of the organosilyl derivative of $[SiW_{10}O_{38}]^{8-}$ divacant Keggin POM, with a Boron cluster and a second function of a variable.

IV. References

(1) Pope, M. T.; Müller, A. Polyoxometalate Chemistry: An Old Field with New Dimensions in Several Disciplines. *Angewandte Chemie International Edition in English* **1991**, *30* (1), 34–48. https://doi.org/10.1002/anie.199100341.

(2) Berzelius, J. The Preparation of the Phosphomolybdate Ion $[PMo_{12}O_{40}]^{3-}$. *Pogg. Ann* **1826**, *6*, 369–371.

(3) Keggin, J. F.; Bragg, W. L. The Structure and Formula of 12-Phosphotungstic Acid. *Proceedings of the Royal Society of London. Series A, Containing Papers of a Mathematical and Physical Character* **1997**, *144* (851), 75–100. https://doi.org/10.1098/rspa.1934.0035.

(4) Kortz, U.; Müller, A.; van Slageren, J.; Schnack, J.; Dalal, N. S.; Dressel, M. Polyoxometalates: Fascinating Structures, Unique Magnetic Properties. *Coordination Chemistry Reviews* **2009**, *253* (19), 2315–2327. https://doi.org/10.1016/j.ccr.2009.01.014.

(5) *Polyoxometalate Chemistry From Topology via Self-Assembly to Applications*; Pope, M. T., Müller, A., Eds.; Kluwer Academic Publishers: Dordrecht, **2002**. https://doi.org/10.1007/0-306-47625-8.

(6) Rathee, B.; Wati, M.; Sindhu, R.; Sindhu, S. Applications of Polyoxometalates (A Review). *Oriental Journal Of Chemistry* **2022**, *38*, 327–335. https://doi.org/10.13005/ojc/380213.

(7) Sadakane, M.; Steckhan, E. Electrochemical Properties of Polyoxometalates as Electrocatalysts. *Chem. Rev.* **1998**, *98* (1), 219–238. https://doi.org/10.1021/cr960403a.

(8) *Polyoxometalate Molecular Science*, Softcover reprint of the original 1st ed. **2003** edition.; Borrás-Almenar, J. J., Coronado, E., Müller, A., Pope, M. T., Eds.; Springer: Dordrecht, 2003.

(9) Du, D.-Y.; Yan, L.-K.; Su, Z.-M.; Li, S.-L.; Lan, Y.-Q.; Wang, E.-B. Chiral Polyoxometalate-Based Materials: From Design Syntheses to Functional Applications. *Coordination Chemistry Reviews* **2013**, *257* (3), 702–717. https://doi.org/10.1016/j.ccr.2012.10.004.

(10) Lv, H.; Geletii, Y. V.; Zhao, C.; Vickers, J. W.; Zhu, G.; Luo, Z.; Song, J.; Lian, T.; Musaev, D. G.; Hill, C. L. Polyoxometalate Water Oxidation Catalysts and the Production of Green Fuel. *Chem. Soc. Rev.* **2012**, *41* (22), 7572–7589. https://doi.org/10.1039/C2CS35292C.

(11) Miras, H. N.; Yan, J.; Long, D.-L.; Cronin, L. Engineering Polyoxometalates with Emergent Properties. *Chem. Soc. Rev.* **2012**, *41* (22), 7403–7430. https://doi.org/10.1039/C2CS35190K.

(12) Okuhara, T.; Mizuno, N.; Misono, M. Catalytic Chemistry of Heteropoly Compounds. In *Advances in Catalysis*; Eley, D. D., Haag, W. O., Gates, B., Eds.; Academic Press, **1996**; Vol. 41, pp 113–252. https://doi.org/10.1016/S0360-0564(08)60041-3.

(13) Proust, A.; Matt, B.; Villanneau, R.; Guillemot, G.; Gouzerh, P.; Izzet, G. Functionalization and Post-Functionalization: A Step towards Polyoxometalate-Based Materials. *Chem. Soc. Rev.* **2012**, *41* (22), 7605–7622. https://doi.org/10.1039/C2CS35119F.

(14) Wang, Y.; Weinstock, I. A. Polyoxometalate-Decorated Nanoparticles. *Chem. Soc. Rev.* **2012**, *41* (22), 7479–7496. https://doi.org/10.1039/C2CS35126A.

(15) Yin, P.; Li, D.; Liu, T. Solution Behaviors and Self-Assembly of Polyoxometalates as Models of Macroions and Amphiphilic Polyoxometalate–Organic Hybrids as Novel Surfactants. *Chem. Soc. Rev.* **2012**, *41* (22), 7368–7383. https://doi.org/10.1039/C2CS35176E.

(16) Yu, R.; Kuang, X.-F.; Wu, X.-Y.; Lu, C.-Z.; Donahue, J. P. Stabilization and Immobilization of Polyoxometalates in Porous Coordination Polymers through Host–Guest Interactions. *Coordination Chemistry Reviews* **2009**, *253* (23), 2872–2890. https://doi.org/10.1016/j.ccr.2009.07.003.

(17) Zheng, S.-T.; Yang, G.-Y. Recent Advances in Paramagnetic-TM-Substituted Polyoxometalates (TM = Mn, Fe, Co, Ni, Cu). *Chem. Soc. Rev.* **2012**, *41* (22), 7623–7646. https://doi.org/10.1039/C2CS35133A.
(18) Hutin, M.; Rosnes, M. H.; Long, D.-L.; Cronin, L. 2.10 - Polyoxometalates: Synthesis and Structure – From Building Blocks to Emergent Materials. In *Comprehensive Inorganic Chemistry II (Second Edition)*; Reedijk, J., Poeppelmeier, K., Eds.; Elsevier: Amsterdam, **2013**; pp 241–269. https://doi.org/10.1016/B978-0-08-097774-4.00210-2.
(19) Long, D.-L.; Tsunashima, R.; Cronin, L. Polyoxometalates: Building Blocks for Functional Nanoscale Systems. *Angew Chem Int Ed Engl* **2010**, *49* (10), 1736–1758. https://doi.org/10.1002/anie.200902483.
(20) Long, D.-L.; Burkholder, E.; Cronin, L. Polyoxometalate Clusters, Nanostructures and Materials: From Self Assembly to Designer Materials and Devices. *Chem. Soc. Rev.* **2006**, *36* (1), 105–121. https://doi.org/10.1039/B502666K.
(21) Dolbecq, A.; Dumas, E.; Mayer, C. R.; Mialane, P. Hybrid Organic−Inorganic Polyoxometalate Compounds: From Structural Diversity to Applications. *Chem. Rev.* **2010**, *110* (10), 6009–6048. https://doi.org/10.1021/cr1000578.
(22) Mattes, R. Heteropoly and Isopoly Oxometalates. Von M. T. Pope. Springer-Verlag, Berlin 1983. XIII, 180 S., Geb. DM 124.00. *Angewandte Chemie* **1984**, *96* (9), 730–730. https://doi.org/10.1002/ange.19840960939.
(23) Kondinski, A. On the Isomer Problem of Mixed−Addenda and Heterogroup−Substituted Polyoxometalates, Jacobs University Bremen, **2016**. http://nbn-resolving.org/urn:nbn:de:gbv:579-opus-1004465 (accessed 2023-10-02).
(24) Ghammami, S. The Crystal and Molecular Structure of Bis(Tetramethylammonium) Hexamolybdate(VI). *Crystal Research and Technology - CRYST RES TECH* **2003**, *38*, 913–917. https://doi.org/10.1002/crat.200310112.
(25) Cindrić, M.; Veksli, Z.; Kamenar, B. Polyoxomolybdates and Polyoxomolybdovanadates – from Structure to Functions: Recent Results. *Croatica Chemica Acta* **2009**, *82* (2), 345–362.
(26) Al-Yasari, A.; Van Steerteghem, N.; Kearns, H.; El Moll, H.; Faulds, K.; Wright, J. A.; Brunschwig, B. S.; Clays, K.; Fielden, J. Organoimido-Polyoxometalate Nonlinear Optical Chromophores: A Structural, Spectroscopic, and Computational Study. *Inorg. Chem.* **2017**, *56* (17), 10181–10194. https://doi.org/10.1021/acs.inorgchem.7b00708.
(27) Bakker, T. M. A.; Mathew, S.; Reek, J. N. H. Lindqvist Polyoxometalates as Electrolytes in P-Type Dye Sensitized Solar Cells. *Sustainable Energy Fuels* **2018**, *3* (1), 96–100. https://doi.org/10.1039/C8SE00495A.
(28) Li, Y.; Shetye, K.; Baral, K.; Jin, L.; Oster, J. D.; Zhu, D.-M.; Peng, Z. Main-Chain Polyoxometalate-Containing Donor–Acceptor Conjugated Copolymers: Synthesis, Characterization, Morphological Studies and Applications in Single-Component Photovoltaic Cells. *RSC Adv.* **2016**, *6* (36), 29909–29919. https://doi.org/10.1039/C6RA03251F.
(29) Yu, H.; Le, S.; Zeng, X.; Zhang, J.; Xie, J. Facile Synthesis of a Novel Mono-Organoimido Functionalized Polyoxometalate Cluster $[(n\text{-}C_4H_9)_4N]_2[Mo_6O_{18}(NAr)]$ ($Ar=p\text{-}C_2H_5C_6H_4$): Crystal Structure, Spectral Characterization and Initial Antitumor Activity. *Inorganic Chemistry Communications* **2014**, *39*, 135–139. https://doi.org/10.1016/j.inoche.2013.11.001.
(30) Lindqvist, I. Structure of the Paramolybdate Ion. *Acta Cryst* **1950**, *3* (2), 159–160. https://doi.org/10.1107/S0365110X50000355.

(31) Huang, B.; Yang, D.-H.; Han, B.-H. Application of Polyoxometalate Derivatives in Rechargeable Batteries. *J. Mater. Chem. A* **2020**, *8* (9), 4593–4628. https://doi.org/10.1039/C9TA12679A.
(32) Hasenknopf, B. Polyoxometalates: Introduction to a Class of Inorganic Compounds and Their Biomedical Applications. *Front Biosci* **2005**, *10*, 275–287. https://doi.org/10.2741/1527.
(33) Müller, A.; Gouzerh, P. From Linking of Metal-Oxide Building Blocks in a Dynamic Library to Giant Clusters with Unique Properties and towards Adaptive Chemistry. *Chem. Soc. Rev.* **2012**, *41* (22), 7431–7463. https://doi.org/10.1039/C2CS35169B.
(34) Gouzerh, P.; Che, M. From Scheele and Berzelius to Müller: Polyoxometalates (POMs) Revisited and the "Missing Link" between the Bottom up and Top down Approaches. *Actualite Chimique* **2006**, 9–22.
(35) Müller, A.; Beckmann, E.; Bögge, H.; Schmidtmann, M.; Dress, A. Inorganic Chemistry Goes Protein Size: A Mo368 Nano-Hedgehog Initiating Nanochemistry by Symmetry Breaking. *Angew Chem Int Ed Engl* **2002**, *41* (7), 1162–1167. https://doi.org/10.1002/1521-3773(20020402)41:7<1162::aid-anie1162>3.0.co;2-8.
(36) Ziv, A.; Grego, A.; Kopilevich, S.; Zeiri, L.; Miro, P.; Bo, C.; Müller, A.; Weinstock, I. A. Flexible Pores of a Metal Oxide-Based Capsule Permit Entry of Comparatively Larger Organic Guests. *J. Am. Chem. Soc.* **2009**, *131* (18), 6380–6382. https://doi.org/10.1021/ja900452d.
(37) Petina, O.; Rehder, D.; Haupt, E. T. K.; Grego, A.; Weinstock, I. A.; Merca, A.; Bögge, H.; Szakacs, J.; Müller, A. Guests on Different Internal Capsule Sites Exchange with Each Other and with the Outside. *Angewandte Chemie. International Edition* **2011**, *50* (2).
(38) Schäffer, C.; Bögge, H.; Merca, A.; Weinstock, I. A.; Rehder, D.; Haupt, E. T. K.; Müller, A. A Spherical 24 Butyrate Aggregate with a Hydrophobic Cavity in a Capsule with Flexible Pores: Confinement Effects and Uptake-Release Equilibria at Elevated Temperatures. *Angew Chem Int Ed Engl* **2009**, *48* (43), 8051–8056. https://doi.org/10.1002/anie.200903910.
(39) Kopilevich, S.; Müller, A.; Weinstock, I. A. Amplified Rate Acceleration by Simultaneous Up-Regulation of Multiple Active Sites in an Endo-Functionalized Porous Capsule. *J. Am. Chem. Soc.* **2015**, *137* (40), 12740–12743. https://doi.org/10.1021/jacs.5b06211.
(40) Kopilevich, S.; Gil, A.; Garcia-Ratés, M.; Bonet-Ávalos, J.; Bo, C.; Müller, A.; Weinstock, I. A. Catalysis in a Porous Molecular Capsule: Activation by Regulated Access to Sixty Metal Centers Spanning a Truncated Icosahedron. *J. Am. Chem. Soc.* **2012**, *134* (31), 13082–13088. https://doi.org/10.1021/ja304513t.
(41) Rezaeifard, A.; Haddad, R.; Jafarpour, M.; Hakimi, M. Catalytic Epoxidation Activity of Keplerate Polyoxomolybdate Nanoball toward Aqueous Suspension of Olefins under Mild Aerobic Conditions. *J. Am. Chem. Soc.* **2013**, *135* (27), 10036–10039. https://doi.org/10.1021/ja405852s.
(42) Rezaeifard, A.; Haddad, R.; Jafarpour, M.; Hakimi, M. $\{Mo_{132}\}$ Nanoball as an Efficient and Cost-Effective Catalyst for Sustainable Oxidation of Sulfides and Olefins with Hydrogen Peroxide. *ACS sustainable chemistry* **2014**.
(43) Ostroushko, A. A.; Grzhegorzhevskii, K. V. Electric Conductivity of Nanocluster Polyoxomolybdates in the Solid State and Solutions. *Russ. J. Phys. Chem.* **2014**, *88* (6), 1008–1011. https://doi.org/10.1134/S0036024414060211.
(44) Zhou, Y.; Shi, Z.; Zhang, L.; ul Hassan, S.; Qu, N. Notable Third-Order Optical Nonlinearities of a Keplerate-Type Polyoxometalate in Solution and in Thin Films of PMMA. *Applied Physics A: Materials Science & Processing* **2013**, *113*, 563–568. https://doi.org/10.1007/s00339-013-7997-4.

(45) Zhang, L.; Shi, Z.; Zhang, L.; Zhou, Y.; Hassan, S. Fabrication and Optical Nonlinearities of Ultrathin Composite Films Incorporating a Keplerate Type Polyoxometalate. *Materials Letters* **2012**, *86*, 62–64. https://doi.org/10.1016/j.matlet.2012.07.028.

(46) Floquet, S.; Terazzi, E.; Hijazi, A.; Guénée, L.; Piguet, C.; Cadot, E. Evidence of Ionic Liquid Crystal Properties for a $DODA^+$ Salt of the Keplerate $[Mo_{132}O_{372}(CH_3COO)_{30}(H_2O)_{72}]^{42-}$. *New J. Chem.* **2012**, *36* (4), 865–868. https://doi.org/10.1039/C2NJ20923C.

(47) Floquet, S.; Terazzi, E.; Korenev, V. S.; Hijazi, A.; Guénée, L.; Cadot, E. Layered Ionic Liquid-Crystalline Organisations Built from Nano-Capsules $[Mo_{132}O_{312}S_{60}(SO_4)_x(H_2O)_{132-2x}]^{(12+2x)-}$ and $DODA^+$ Cations. *Liquid Crystals* **2014**, *41* (7), 1000–1007. https://doi.org/10.1080/02678292.2014.896054.

(48) Watfa, N.; Floquet, S.; Terazzi, E.; Salomon, W.; Guénée, L.; Buchwalder, K. L.; Hijazi, A.; Naoufal, D.; Piguet, C.; Cadot, E. Synthesis, Characterization and Study of Liquid Crystals Based on the Ionic Association of the Keplerate Anion $[Mo_{132}O_{372}(CH_3COO)_{30}(H_2O)_{72}]^{42-}$ and Imidazolium Cations. *Inorganics* **2015**, *3* (2), 246–266. https://doi.org/10.3390/inorganics3020246.

(49) Li, H.; Yang, Y.; Wang, Y.; Wang, C.; Li, W.; Wu, L. Self-Assembly and Ion-Trapping Properties of Inorganic Nanocapsule-Surfactant Hybrid Spheres. *Soft Matter* **2011**, *7* (6), 2668–2673. https://doi.org/10.1039/C0SM01044H.

(50) Müller, A.; Krickemeyer, E.; Meyer, J.; Bögge, H.; Peters, F.; Plass, W.; Diemann, E.; Dillinger, S.; Nonnenbruch, F.; Randerath, M.; Menke, C. $[Mo_{154}(NO)_{14}O_{420}(OH)_{28}(H_2O)_{70}]^{(25\pm5)-}$: A Water-Soluble Big Wheel with More than 700 Atoms and a Relative Molecular Mass of About 24000. *Angewandte Chemie International Edition in English* **1995**, *34* (19), 2122–2124. https://doi.org/10.1002/anie.199521221.

(51) Müller, A.; Peters, F.; Pope, M. T.; Gatteschi, D. Polyoxometalates: Very Large Clusters-Nanoscale Magnets. *Chem Rev* **1998**, *98* (1), 239–272. https://doi.org/10.1021/cr9603946.

(52) Anderson, J. S. Constitution of the Poly-Acids. *Nature* **1937**, *140* (3550), 850–850. https://doi.org/10.1038/140850a0.

(53) d'Amour, H. Vergleich der heteropolyanionen $[PMo_9O_{31}(H_2O)_3]^{3-}$, $[P_2Mo_{18}O_{62}]^{6-}$ und $[P_2W_{18}O_{62}]^{6-}$. *Acta Cryst B* **1976**, *32* (3), 729–740. https://doi.org/10.1107/S0567740876003890.

(54) Evans, H. T. Jr. THE CRYSTAL STRUCTURES OF AMMONIUM AND POTASSIUM MOLYBDOTELLURATES. *J. Am. Chem. Soc.* **1948**, *70* (3), 1291–1292. https://doi.org/10.1021/ja01183a521.

(55) Blazevic, A.; Rompel, A. The Anderson–Evans Polyoxometalate: From Inorganic Building Blocks via Hybrid Organic–Inorganic Structures to Tomorrows "Bio-POM." *Coordination Chemistry Reviews* **2016**, *307*, 42–64. https://doi.org/10.1016/j.ccr.2015.07.001.

(56) Wu, P.; Wang, Y.; Huang, B.; Xiao, Z. Anderson-Type Polyoxometalates: From Structures to Functions. *Nanoscale* **2021**, *13* (15), 7119–7133. https://doi.org/10.1039/D1NR00397F.

(57) Kondo, H.; Kobayashi, A.; Sasaki, Y. The Structure of the Hexamolybdoperiodate Anion in Its Potassium Salt. *Acta Cryst B* **1980**, *36* (3), 661–664. https://doi.org/10.1107/S0567740880004037.

(58) Perloff, A. Crystal Structure of Sodium Hexamolybdochromate(III) Octahydrate, $Na_3(CrMo_6O_{24}H_6).8H_2O$. *Inorg. Chem.* **1970**, *9* (10), 2228–2239. https://doi.org/10.1021/ic50092a006.

(59) Wu, C.; Lin, X.; Yu, R.; Yang, W.; Lu, C.; Zhuang, H. $[Na_4(H_2O)_7][Fe(OH)_6Mo_6O_{18}]$: A New [12] Metallacrown-6 Structure with an Octahedrally Coordinated Iron at the Center. *Sc. China Ser. B-Chem.* **2001**, *44* (1), 49–54. https://doi.org/10.1007/BF02879735.

(60) Sun, L.; Su, T.; Xu, J.; Hao, D.; Liao, W.; Zhao, Y.; Ren, W.; Deng, C.; Lü, H. Aerobic Oxidative Desulfurization Coupling of Co Polyanion Catalysts and P-TsOH-Based Deep Eutectic Solvents through

a Biomimetic Approach. *Green Chem.* **2019**, *21* (10), 2629–2634. https://doi.org/10.1039/C8GC03941K.

(61) Chi, M.; Zhu, Z.; Sun, L.; Su, T.; Liao, W.; Deng, C.; Zhao, Y.; Ren, W.; Lü, H. Construction of Biomimetic Catalysis System Coupling Polyoxometalates with Deep Eutectic Solvents for Selective Aerobic Oxidation Desulfurization. *Applied Catalysis B: Environmental* **2019**, *259*, 118089. https://doi.org/10.1016/j.apcatb.2019.118089.

(62) Mukhacheva, A. A.; Volchek, V. V.; Yanshole, V. V.; Kompankov, N. B.; Gushchin, A. L.; Benassi, E.; Abramov, P. A.; Sokolov, M. N. Is It Possible To Prepare a Heterometal Anderson-Evans Type Anion? *Inorganic Chemistry* **2020**, *59* (4), 2116–2120. https://doi.org/10.1021/acs.inorgchem.9b02898.

(63) Caudillo-Flores, U.; Ansari, F.; Bachiller-Baeza, B.; Colón, G.; Fernández-García, M.; Kubacka, A. $(NH_4)_4[NiMo_6O_{24}H_6].5H_2O$ / g-C_3N_4 Materials for Selective Photo-Oxidation of CO and CC Bonds. *Applied Catalysis B: Environmental* **2020**, *278*, 119299. https://doi.org/10.1016/j.apcatb.2020.119299.

(64) Lü, H.; Zhang, Y.; Jiang, Z.; Li, C. Aerobic Oxidative Desulfurization of Benzothiophene, Dibenzothiophene and 4,6-Dimethyldibenzothiophene Using an Anderson-Type Catalyst $[(C_{18}H_{37})_2N(CH_3)_2]_5[IMo_6O_{24}]$. *Green Chem.* **2010**, *12* (11), 1954–1958. https://doi.org/10.1039/C0GC00271B.

(65) Wei, Z.; Wang, J.; Yu, H.; Han, S.; Wei, Y. Recent Advances of Anderson-Type Polyoxometalates as Catalysts Largely for Oxidative Transformations of Organic Molecules. *Molecules* **2022**, *27* (16), 5212. https://doi.org/10.3390/molecules27165212.

(66) Zhai, Y.; Zhang, M.; Fang, H.; Ru, S.; Yu, H.; Zhao, W.; Wei, Y. An Efficient Protocol for the Preparation of Aldehydes/Ketones and Imines by an Inorganic-Ligand Supported Iron Catalyst. *Org. Chem. Front.* **2018**, *5* (23), 3454–3459. https://doi.org/10.1039/C8QO00833G.

(67) Bijelic, A.; Rompel, A. Ten Good Reasons for the Use of the Tellurium-Centered Anderson–Evans Polyoxotungstate in Protein Crystallography. *Acc. Chem. Res.* **2017**, *50* (6), 1441–1448. https://doi.org/10.1021/acs.accounts.7b00109.

(68) Molitor, C.; Bijelic, A.; Rompel, A. In Situ Formation of the First Proteinogenically Functionalized $[TeW_6O_{24}O_2(Glu)]^{7-}$ Structure Reveals Unprecedented Chemical and Geometrical Features of the Anderson-Type Cluster. *Chem. Commun.* **2016**, *52* (83), 12286–12289. https://doi.org/10.1039/C6CC07004C.

(69) Mauracher, S. G.; Molitor, C.; Al-Oweini, R.; Kortz, U.; Rompel, A. Crystallization and Preliminary X-Ray Crystallographic Analysis of Latent Isoform PPO4 Mushroom (Agaricus Bisporus) Tyrosinase. *Acta Crystallogr F Struct Biol Commun* **2014**, *70* (Pt 2), 263–266. https://doi.org/10.1107/S2053230X14000582.

(70) Canny, J.; Teze, A.; Thouvenot, R.; Herve, G. Disubstituted Tungstosilicates. 1. Synthesis, Stability, and Structure of the Lacunary Precursor Polyanion of a Tungstosilicate γ-$SiW_{10}O_{36}^{8-}$. *Inorg. Chem.* **1986**, *25* (13), 2114–2119. https://doi.org/10.1021/ic00233a003.

(71) Mialane, P.; Dolbecq, A.; Lisnard, L.; Mallard, A.; Marrot, J.; Sécheresse, F. [ε-$PMo_{12}O_{36}(OH)_4La(H_2O)_{44}]^{5+}$: The First ε-$PMo_{12}O_{40}$ Keggin Ion and Its Association with the Two-Electron-Reduced α-$PMo_{12}O_{40}$ Isomer. *Angewandte Chemie International Edition* **2002**, *41* (13), 2398–2401. https://doi.org/10.1002/1521-3773(20020703)41:13<2398::AID-ANIE2398>3.0.CO;2-A.

(72) Sartzi, H.; Miras, H. N.; Vilà-Nadal, L.; Long, D.-L.; Cronin, L. Trapping the δ Isomer of the Polyoxometalate-Based Keggin Cluster with a Tripodal Ligand. *Angewandte Chemie* **2015**, *127* (51), 15708–15712. https://doi.org/10.1002/ange.201505377.

(73) Klemperer, W. Inorganic Syntheses, Volume 27. In *Cheminform*; **2007**; Vol. 22, pp 71–85. https://doi.org/10.1002/9780470132586.ch14.

(74) Chermette, H.; Lefebvre, F. Theoretical Study of the Four Isomers of $[SiW_{11}O_{39}]^{8-}$: Structure, Stability and Physical Properties. *Comptes Rendus Chimie* **2012**, *15* (2), 143–151. https://doi.org/10.1016/j.crci.2011.09.002.

(75) Patel, A.; Narkhede, N.; Singh, S.; Pathan, S. Keggin-Type Lacunary and Transition Metal Substituted Polyoxometalates as Heterogeneous Catalysts: A Recent Progress. *Catalysis Reviews* **2016**, *58* (3), 337–370. https://doi.org/10.1080/01614940.2016.1171606.

(76) Hirano, T.; Uehara, K.; Kamata, K.; Mizuno, N. Palladium(II) Containing γ-Keggin Silicodecatungstate That Efficiently Catalyzes Hydration of Nitriles. *J. Am. Chem. Soc.* **2012**, *134* (14), 6425–6433. https://doi.org/10.1021/ja3006012.

(77) Nakagawa, Y.; Mizuno, N. Mechanism of $[\gamma\text{-}H_2SiV_2W_{10}O_{40}]^{4-}$-Catalyzed Epoxidation of Alkenes with Hydrogen Peroxide. *Inorg Chem* **2007**, *46* (5), 1727–1736. https://doi.org/10.1021/ic0623258.

(78) Kamata, K.; Yonehara, K.; Nakagawa, Y.; Uehara, K.; Mizuno, N. Efficient Stereo- and Regioselective Hydroxylation of Alkanes Catalysed by a Bulky Polyoxometalate. *Nature Chem* **2010**, *2* (6), 478–483. https://doi.org/10.1038/nchem.648.

(79) Dawson, B. The Structure of the 9(18)-Heteropoly Anion in Potassium 9(18)-Tungstophosphate, $K_6(P_2W_{18}O_{62}).14H_2O$. *Acta Cryst* **1953**, *6* (2), 113–126. https://doi.org/10.1107/S0365110X53000466.

(80) López, X.; Carbó, J. J.; Bo, C.; Poblet, J. M. Structure, Properties and Reactivity of Polyoxometalates: A Theoretical Perspective. *Chem. Soc. Rev.* **2012**, *41* (22), 7537–7571. https://doi.org/10.1039/C2CS35168D.

(81) Massart, R.; Contant, R.; Fruchart, J. M.; Ciabrini, J. P.; Fournier, M. Phosphorus-31 NMR Studies on Molybdic and Tungstic Heteropolyanions. Correlation between Structure and Chemical Shift. *Inorg. Chem.* **1977**, *16* (11), 2916–2921. https://doi.org/10.1021/ic50177a049.

(82) Baker, L. C. W.; Figgis, J. S. New Fundamental Type of Inorganic Complex: Hybrid between Heteropoly and Conventional Coordination Complexes. Possibilities for Geometrical Isomerisms in 11-, 12-, 17-, and 18-Heteropoly Derivatives. *J. Am. Chem. Soc.* **1970**, *92* (12), 3794–3797. https://doi.org/10.1021/ja00715a047.

(83) Kurashina, T.; Aoki, S.; Hirasawa, R.; Hasegawa, T.; Kasahara, Y.; Yoshida, S.; Yoza, K.; Nomiya, K. Cyclic Oligomer of Oxide Clusters through a Siloxane Bond. Synthesis and Structure of Reaction Products of α_2-Mono-Lacunary Dawson Polyoxometalate with Tetrachlorosilane and Tetraethoxysilane. *Dalton Trans.* **2009**, No. 28, 5542–5550. https://doi.org/10.1039/B902904D.

(84) Weakley, T. J. R.; Finke, R. G. Single-Crystal X-Ray Structures of the Polyoxotungstate Salts $K_{8.3}Na_{1.7}[Cu_4(H2O)_2(PW_9O_{34})_2].24H_2O$ and $Na_{14}Cu[Cu_4(H_2O)_2(P_2W_{15}O_{56})_2].53H_2O$. *Inorg. Chem.* **1990**, *29* (6), 1235–1241. https://doi.org/10.1021/ic00331a025.

(85) Wan, R.; Ma, P.; Han, M.; Zhang, D.; Zhang, C.; Niu, J.; Wang, J. Discovery and Isolation of the Trans-Isomers of Two 1 :2-Type Lanthanide-Containing Monolacunary Dawson-Type Tungstophosphates: $[LnIII(\alpha_2\text{-}P_2W_{17}O_{61})_2]^{17-}$ (Ln = La, Ce). *Dalton Trans.* **2017**, *46* (16), 5398–5405. https://doi.org/10.1039/C7DT00250E.

(86) Absillis, G.; Parac-Vogt, T. N. Peptide Bond Hydrolysis Catalyzed by the Wells–Dawson $Zr(\alpha_2\text{-}P_2W_{17}O_{61})_2$ Polyoxometalate. *Inorg. Chem.* **2012**, *51* (18), 9902–9910. https://doi.org/10.1021/ic301364n.

(87) Wei, Y.; Xu, B.; Barnes, C. L.; Peng, Z. An Efficient and Convenient Reaction Protocol to Organoimido Derivatives of Polyoxometalates. *J. Am. Chem. Soc.* **2001**, *123* (17), 4083–4084. https://doi.org/10.1021/ja004033q.

(88) Anyushin, A. V.; Kondinski, A.; Parac-Vogt, T. N. Hybrid Polyoxometalates as Post-Functionalization Platforms: From Fundamentals to Emerging Applications. *Chem. Soc. Rev.* **2020**, *49* (2), 382–432. https://doi.org/10.1039/C8CS00854J.

(89) Hasenknopf, B.; Delmont, R.; Herson, P.; Gouzerh, P. Anderson-Type Heteropolymolybdates Containing Tris(Alkoxo) Ligands: Synthesis and Structural Characterization. *European Journal of Inorganic Chemistry* **2002**, *2002*, 1081–1087. https://doi.org/10.1002/1099-0682(200205)2002:5<1081::AID-EJIC1081>3.0.CO;2-W.

(90) Marcoux, P. R.; Hasenknopf, B.; Vaissermann, J.; Gouzerh, P. Developing Remote Metal Binding Sites in Heteropolymolybdates. *European Journal of Inorganic Chemistry* **2003**, *2003* (13), 2406. https://doi.org/10.1002/ejic.200200677.

(91) Cheng, M.; Xiao, Z.; Yu, L.; Lin, X.; Wang, Y.; Wu, P. Direct Syntheses of Nanocages and Frameworks Based on Anderson-Type Polyoxometalates via One-Pot Reactions. *Inorg. Chem.* **2019**, *58* (18), 11988–11992. https://doi.org/10.1021/acs.inorgchem.9b01313.

(92) Zhang, J.; Huang, Y.; Li, G.; Wei, Y. Recent Advances in Alkoxylation Chemistry of Polyoxometalates: From Synthetic Strategies, Structural Overviews to Functional Applications. *Coordination Chemistry Reviews* **2019**, *378*, 395–414. https://doi.org/10.1016/j.ccr.2017.10.025.

(93) Peng, C.; Chen, T.; Zeng, B.; Chen, G.; Yuan, C.; Xu, Y.; Dai, L. Anderson-Type Polyoxometalate-Based Hybrid with High Flame Retardant Efficiency for the Preparation of Multifunctional Epoxy Resin Nanocomposites. *Composites Part B: Engineering* **2020**, *186*, 107780. https://doi.org/10.1016/j.compositesb.2020.107780.

(94) Liu, C.; Chen, T.; Yuan, C.; Chang, Y.; Chen, G.; Zeng, B.; Xu, Y.; Luo, W.; Dai, L. Highly Transparent and Flame-Retardant Epoxy Composites Based on a Hybrid Multi-Element Containing POSS Derivative. *RSC Adv.* **2017**, *7* (73), 46139–46147. https://doi.org/10.1039/C7RA09327F.

(95) Xu, W.; Zhang, B.; Xu, B.; Li, A. The Flame Retardancy and Smoke Suppression Effect of Heptaheptamolybdate Modified Reduced Graphene Oxide/Layered Double Hydroxide Hybrids on Polyurethane Elastomer. *Composites Part A: Applied Science and Manufacturing* **2016**, *91*, 30–40. https://doi.org/10.1016/j.compositesa.2016.09.013.

(96) Oms, O.; Hakouk, K.; Dessapt, R.; Deniard, P.; Jobic, S.; Dolbecq, A.; Palacin, T.; Nadjo, L.; Keita, B.; Marrot, J.; Mialane, P. Photo- and Electrochromic Properties of Covalently Connected Symmetrical and Unsymmetrical Spiropyran–Polyoxometalate Dyads. *Chem. Commun.* **2012**, *48* (99), 12103–12105. https://doi.org/10.1039/C2CC35376H.

(97) Zhuang, Q.; Sun, Z.; Lin, C.-G.; Qi, B.; Song, Y.-F. Latest Progress in Asymmetrically Functionalized Anderson-Type Polyoxometalates. *Inorg. Chem. Front.* **2023**, *10* (6), 1695–1711. https://doi.org/10.1039/D2QI02690B.

(98) Bijelic, A.; Dobrov, A.; Roller, A.; Rompel, A. Binding of a Fatty Acid-Functionalized Anderson-Type Polyoxometalate to Human Serum Albumin. *Inorg. Chem.* **2020**, *59* (8), 5243–5246. https://doi.org/10.1021/acs.inorgchem.9b03407.

(99) Mayer, C.; Fournier, I.; Thouvenot, R. Bis- and Tetrakis(Organosilyl) Decatungstosilicate, [γ-$SiW_{10}O_{36}(RSi)_2O]^{4-}$ and [γ-$SiW_{10}O_{36}(RSiO)_4]^{4-}$: Synthesis and Structural Determination by Multinuclear NMR Spectroscopy and Matrix-Assisted Laser Desorption/Desorption Time-of-Flight Mass Spectrometry. *Chemistry - A European Journal* **2000**, *6*, 105–110. https://doi.org/10.1002/(SICI)1521-3765(20000103)6:1<105::AID-CHEM105>3.0.CO;2-L.

(100) Carraro, M.; Modugno, G.; Fiorani, G.; Maccato, C.; Sartorel, A.; Bonchio, M. Organic-Inorganic Molecular Nano-Sensors: A Bis-Dansylated Tweezer-Like Fluoroionophore Integrating a Polyoxometalate Core. *European Journal of Organic Chemistry* **2011**, *2012* (2), 281.
(101) Modugno, G.; Syrgiannis, Z.; Bonasera, A.; Carraro, M.; Giancane, G.; Valli, L.; Bonchio, M.; Prato, M. The Supramolecular Design of Low-Dimensional Carbon Nano-Hybrids Encoding a Polyoxometalate-Bis-Pyrene Tweezer. *Chem. Commun.* **2014**, *50* (38), 4881–4883. https://doi.org/10.1039/C3CC49725A.
(102) Mayer, C. R.; Neveu, S.; Cabuil, V. A Nanoscale Hybrid System Based on Gold Nanoparticles and Heteropolyanions. *Angew Chem Int Ed Engl* **2002**, *41* (3), 501–503. https://doi.org/10.1002/1521-3773(20020201)41:3<501::aid-anie501>3.0.co;2-z.
(103) Cannizzo, C.; Mayer, C. R.; Sécheresse, F.; Larpent, C. Covalent Hybrid Materials Based on Nanolatex Particles and Dawson Polyoxometalates. *Advanced Materials* **2005**, *17*, 2888–2892. https://doi.org/10.1002/adma.200500685.
(104) Odobel, F.; Séverac, M.; Pellegrin, Y.; Blart, E.; Fosse, C.; Cannizzo, C.; Mayer, C. R.; Elliott, K. J.; Harriman, A. Coupled Sensitizer–Catalyst Dyads: Electron-Transfer Reactions in a Perylene–Polyoxometalate Conjugate. *Chemistry – A European Journal* **2009**, *15* (13), 3130–3138. https://doi.org/10.1002/chem.200801880.
(105) Elliott, K. J.; Harriman, A.; Pleux, L. L.; Pellegrin, Y.; Blart, E.; Mayer, C. R.; Odobel, F. A Porphyrin–Polyoxometallate Bio-Inspired Mimic for Artificial Photosynthesis. *Phys. Chem. Chem. Phys.* **2009**, *11* (39), 8767–8773. https://doi.org/10.1039/B905548G.
(106) Harriman, A.; Elliott, K. J.; Alamiry, M. A. H.; Pleux, L. L.; Séverac, M.; Pellegrin, Y.; Blart, E.; Fosse, C.; Cannizzo, C.; Mayer, C. R.; Odobel, F. Intramolecular Electron Transfer Reactions Observed for Dawson-Type Polyoxometalates Covalently Linked to Porphyrin Residues. *J. Phys. Chem. C* **2009**, *113* (14), 5834–5842. https://doi.org/10.1021/jp900643m.
(107) Stone, F. G. A. Chemical Reactivity of the Boron Hydrides and Related Compounds. In *Advances in Inorganic Chemistry and Radiochemistry*; Emeleus, H. J., Sharpe, A. G., Eds.; Academic Press, **1960**; Vol. 2, pp 279–313. https://doi.org/10.1016/S0065-2792(08)60192-2.
(108) *Boron: The Fifth Element*; Hnyk, D., McKee, M., Eds.; Challenges and Advances in Computational Chemistry and Physics; Springer International Publishing: Cham, **2015**; Vol. 20. https://doi.org/10.1007/978-3-319-22282-0.
(109) Zhu, Y.; Cai, J.; Hosmane, N.; Zhang, Y. Introduction: Basic Concept of Boron and Its Physical and Chemical Properties; **2022**; pp 1–57. https://doi.org/10.1016/B978-0-12-822127-3.00003-X.
(110) Jemmis, E. D.; Jayasree, E. G. Analogies between Boron and Carbon. *Acc. Chem. Res.* **2003**, *36* (11), 816–824. https://doi.org/10.1021/ar0300266.
(111) Hunter, P. Not Boring at All. *EMBO reports* **2009**, *10* (2), 125–128. https://doi.org/10.1038/embor.2009.2.
(112) *50th Anniversary of Electron Counting Paradigms for Polyhedral Molecules: Historical and Recent Developments*; Mingos, D. M. P., Ed.; Structure and Bonding; Springer International Publishing: Cham, **2021**; Vol. 187. https://doi.org/10.1007/978-3-030-84863-7.
(113) King, R. B. Three-Dimensional Aromaticity in Polyhedral Boranes and Related Molecules. *Chem. Rev.* **2001**, *101* (5), 1119–1152. https://doi.org/10.1021/cr000442t.
(114) Rudolph, R. W. Boranes and Heteroboranes: A Paradigm for the Electron Requirements of Clusters? *Acc. Chem. Res.* **1976**, *9* (12), 446–452. https://doi.org/10.1021/ar50108a004.

(115) Knoth, W. H.; Sauer, J. C.; Balthis, J. H.; Miller, H. Charles.; Muetterties, E. L. Chemistry of Boranes. XXX. Carbonyl Derivatives of $B_{10}H_{10}^{2-}$ and $B_{12}H_{12}^{2-}$. *J. Am. Chem. Soc.* **1967**, *89* (19), 4842–4850. https://doi.org/10.1021/ja00995a004.

(116) Muetterties, E. L.; Balthis, J. H.; Chia, Y. T.; Knoth, W. H.; Miller, H. C. Chemistry of Boranes. VIII. Salts and Acids of $B_{10}H_{10}^{-2}$ and $B_{12}H_{12}^{-2}$. *Inorg. Chem.* **1964**, *3* (3), 444–451. https://doi.org/10.1021/ic50013a030.

(117) Pitt, M. P.; Paskevicius, M.; Brown, D. H.; Sheppard, D. A.; Buckley, C. E. Thermal Stability of $Li_2B_{12}H_{12}$ and Its Role in the Decomposition of $LiBH_4$. *J. Am. Chem. Soc.* **2013**, *135* (18), 6930–6941. https://doi.org/10.1021/ja400131b.

(118) Aihara, J. Three-Dimensional Aromaticity of Polyhedral Boranes. *J. Am. Chem. Soc.* **1978**, *100* (11), 3339–3342. https://doi.org/10.1021/ja00479a015.

(119) Sivaev, I. B.; Prikaznov, A. V.; Naoufal, D. Fifty Years of the *Closo*-Decaborate Anion Chemistry. *Collect. Czech. Chem. Commun.* **2010**, *75* (11), 1149–1199. https://doi.org/10.1135/cccc2010054.

(120) Lipscomb, W. N.; Pitochelli, A. R.; Hawthorne, M. F. PROBABLE STRUCTURE OF THE B10H10-2 ION. *J. Am. Chem. Soc.* **1959**, *81* (21), 5833–5834. https://doi.org/10.1021/ja01530a073.

(121) Pitochelli, A. R.; Ettinger, Raymond.; Dupont, J. A.; Hawthorne, M. Frederick. Observations on The Mechanism of $B_{10}H_{10}^{-2}$ Formation. *J. Am. Chem. Soc.* **1962**, *84* (6), 1057–1058. https://doi.org/10.1021/ja00865a041.

(122) Naoufal, D.; Laila, Z.; Yazbeck, O.; Hamad, H.; Ibrahim, G.; Aoun, R.; Ali, S.; El Jamal, M.; Kanj, A. Synthesis, Characterization and Mechanism of Formation of 6-Substituted Nido-$B_{10}H_{13}$ Decaboranes by the Opening Reaction of Closo-Decahydrodecaborate $[B_{10}H_{10}]^{2-}$ Cage. *Main Group Chemistry* **2013**, *12*, 39–48. https://doi.org/10.3233/MGC-130088.

(123) Hansen, B. R. S.; Paskevicius, M.; Li, H.-W.; Akiba, E.; Jensen, T. R. Metal Boranes: Progress and Applications. *Coordination Chemistry Reviews* **2016**, *323*, 60–70. https://doi.org/10.1016/j.ccr.2015.12.003.

(124) Power, D.; Spalding, T. R. Some Comments on the Mechanism of the Preparation of $(Et_4N)_2B_{10}H_{10}$ by Thermolysis of Et_4NBH_4. *Polyhedron* **1985**, *4* (7), 1329–1331. https://doi.org/10.1016/S0277-5387(00)84128-5.

(125) Makhlouf, J. M.; Hough, W. V.; Hefferan, G. T. Practical Synthesis for Decahydrodecaborates. *Inorg. Chem.* **1967**, *6* (6), 1196–1198. https://doi.org/10.1021/ic50052a028.

(126) Rzeszotarska, E.; Novozhilova, I.; Kaszyński, P. Convenient Synthesis of [Closo-$B_{10}H_9$-1-I]$^{2-}$ and [Closo-$B_{10}H_8$-1,10-I_2]$^{2-}$ Anions. *Inorg. Chem.* **2017**, *56* (22), 14351–14356. https://doi.org/10.1021/acs.inorgchem.7b02477.

(127) Dash, B. P.; Satapathy, R.; Maguire, J. A.; Hosmane, N. S. Polyhedral Boron Clusters in Materials Science. *New J. Chem.* **2011**, *35* (10), 1955–1972. https://doi.org/10.1039/C1NJ20228F.

(128) Ali, F. Chapter 4 - Boron Materials for Energy Applications. In *Fundamentals and Applications of Boron Chemistry*; Zhu, Y., Ed.; Developments in Inorganic Chemistry; Elsevier, **2022**; Vol. 2, pp 203–289. https://doi.org/10.1016/B978-0-12-822127-3.00004-1.

(129) Gigante, A.; Duchêne, L.; Pupier, M.; Moury, R.; Remhof, A.; Hagemann, H. Direct Solution-Based Synthesis of the $Na_4(B_{12}H_{12})(B_{10}H_{10})$ Solid Electrolyte. **2019**.

(130) Li, S.; Qiu, P.; Kang, J.; Ma, Y.; Zhang, Y.; Yan, Y.; Jensen, T. R.; Guo, Y.; Zhang, J.; Chen, X. Iodine-Substituted Lithium/Sodium Closo-Decaborates: Syntheses, Characterization, and Solid-State Ionic Conductivity. *ACS Appl. Mater. Interfaces* **2021**, *13* (15), 17554–17564. https://doi.org/10.1021/acsami.1c01659.

(131) Debela, D. T.; Muzazu, S. G.; Heraro, K. D.; Ndalama, M. T.; Mesele, B. W.; Haile, D. C.; Kitui, S. K.; Manyazewal, T. New Approaches and Procedures for Cancer Treatment: Current Perspectives. *SAGE Open Medicine* **2021**, *9*. https://doi.org/10.1177/20503121211034366.

(132) Bruskin, A.; Sivaev, I.; Persson, M.; Lundqvist, H.; Carlsson, J.; Sjöberg, S.; Tolmachev, V. Radiobromination of Monoclonal Antibody Using Potassium [^{76}Br] (4 Isothiocyanatobenzyl-Ammonio)-Bromo-Decahydro-Closo-Dodecaborate (Bromo-DABI). *Nucl Med Biol* **2004**, *31* (2), 205–211. https://doi.org/10.1016/j.nucmedbio.2003.08.005.

(133) Ersahin, D.; Doddamane, I.; Cheng, D. Targeted Radionuclide Therapy. *Cancers (Basel)* **2011**, *3* (4), 3838–3855. https://doi.org/10.3390/cancers3043838.

(134) Wilbur, D. S.; Hamlin, D. K.; Chyan, M.-K.; Brechbiel, M. W. Streptavidin in Antibody Pretargeting. 5. Chemical Modification of Recombinant Streptavidin for Labeling with the α-Particle Emitting Radionuclides ^{213}Bi and ^{211}At. *Bioconjug Chem* **2008**, *19* (1), 158–170. https://doi.org/10.1021/bc7002428.

(135) Vallathol, D. H.; Digumarti, R. AN UPDATE ON TOXICITY OF THERAPEUTIC RADIONUCLIDES. *Medical Research Archives* **2021**, *9* (4). https://doi.org/10.18103/mra.v9i4.2388.

(136) Fujiki, K.; Kanayama, Y.; Yano, S.; Sato, N.; Yokokita, T.; Ahmadi, P.; Watanabe, Y.; Haba, H.; Tanaka, K. ^{211}At-Labeled Immunoconjugate via a One-Pot Three-Component Double Click Strategy: Practical Access to α-Emission Cancer Radiotherapeutics. *Chem. Sci.* **2019**, *10* (7), 1936–1944. https://doi.org/10.1039/C8SC04747B.

(137) Wilbur, D. S.; Chyan, M.-K.; Hamlin, D. K.; Vessella, R. L.; Wedge, T. J.; Hawthorne, M. F. Reagents for Astatination of Biomolecules. 2. Conjugation of Anionic Boron Cage Pendant Groups to a Protein Provides a Method for Direct Labeling That Is Stable to in Vivo Deastatination. *Bioconjug Chem* **2007**, *18* (4), 1226–1240. https://doi.org/10.1021/bc060345s.

(138) Wilbur, D. S.; Thakar, M. S.; Hamlin, D. K.; Santos, E. B.; Chyan, M.-K.; Nakamae, H.; Pagel, J. M.; Press, O. W.; Sandmaier, B. M. Reagents for Astatination of Biomolecules. 4. Comparison of Maleimido-Closo-Decaborate (2-) and Meta-[^{211}At]Astatobenzoate Conjugates for Labeling Anti-CD45 Antibodies with [^{211}At]Astatine. *Bioconjugate Chem.* **2009**, *20* (10), 1983–1991. https://doi.org/10.1021/bc9000799.

(139) Hawthorne, M. F. The Role of Chemistry in the Development of Boron Neutron Capture Therapy of Cancer. *Angewandte Chemie International Edition in English* **1993**, *32* (7), 950–984. https://doi.org/10.1002/anie.199309501.

(140) Barth, R. F.; Soloway, A. H.; Fairchild, R. G.; Brugger, R. M. Boron Neutron Capture Therapy for Cancer. Realities and Prospects. *Cancer* **1992**, *70* (12), 2995–3007. https://doi.org/10.1002/1097-0142(19921215)70:12<2995::aid-cncr2820701243>3.0.co;2-#.

(141) Barth, R. F.; Soloway, A. H.; Brugger, R. M. Boron Neutron Capture Therapy of Brain Tumors: Past History, Current Status, and Future Potential. *Cancer Investigation* **1996**, *14* (6), 534–550. https://doi.org/10.3109/07357909609076899.

(142) Kageji, T.; Nagahiro, S.; Mizobuchi, Y.; Matsuzaki, K.; Nakagawa, Y.; Kumada, H. Boron Neutron Capture Therapy (BNCT) for Newly-Diagnosed Glioblastoma: Comparison of Clinical Results Obtained with BNCT and Conventional Treatment. *J Med Invest* **2014**, *61* (3–4), 254–263. https://doi.org/10.2152/jmi.61.254.

(143) Hawthorne, M. F. New Horizons for Therapy Based on the Boron Neutron Capture Reaction. *Molecular Medicine Today* **1998**, *4* (4), 174–181. https://doi.org/10.1016/S1357-4310(98)01226-X.

(144) Zhizhin, K. Yu.; Zhdanov, A. P.; Kuznetsov, N. T. Derivatives of Closo-Decaborate Anion $[B_{10}H_{10}]^{2-}$ with Exo-Polyhedral Substituents. *Russ. J. Inorg. Chem.* **2010**, *55* (14), 2089–2127. https://doi.org/10.1134/S0036023610140019.

(145) Mahfouz, N.; Ghaida, F. A.; El Hajj, Z.; Diab, M.; Floquet, S.; Mehdi, A.; Naoufal, D. Recent Achievements on Functionalization within Closo-Decahydrodecaborate $[B_{10}H_{10}]^{2-}$ Clusters. *ChemistrySelect* **2022**, *7* (21), e202200770. https://doi.org/10.1002/slct.202200770.

(146) Klyukin, I. N.; Kolbunova, A. V.; Novikov, A. S.; Nelyubin, A. V.; Zhdanov, A. P.; Kubasov, A. S.; Selivanov, N. A.; Bykov, A. Y.; Zhizhin, K. Y.; Kuznetsov, N. T. Synthesis of Disubstituted Carboxonium Derivatives of Closo-Decaborate Anion $[2,6\text{-}B_{10}H_8O_2CC_6H_5]^-$: Theoretical and Experimental Study. *Molecules* **2023**, *28* (4), 1757. https://doi.org/10.3390/molecules28041757.

(147) Diab, M.; Floquet, S.; Haouas, M.; Abramov, P. A.; López, X.; Landy, D.; Damond, A.; Falaise, C.; Guérineau, V.; Touboul, D.; Naoufal, D.; Cadot, E. Encapsulation of Chaotropic Closo-Decahydrodecaborate Clusters Within Cyclodextrins: Synthesis, Solution Studies, and DFT Calculations. *European Journal of Inorganic Chemistry* **2019**, *2019* (29), 3373–3382. https://doi.org/10.1002/ejic.201900602.

(148) Shore, S. G.; Hamilton, E. J. M.; Bridges, A. N.; Bausch, J.; Krause-Bauer, J. A.; Dou, D.; Liu, J.; Liu, S.; Du, B.; Hall, H.; Meyers, E. A.; Vermillion, K. E. The Solid State Structure of $[B_{10}H_{11}]^-$ and Its Dynamic NMR Spectra in Solution. *Inorg. Chem.* **2003**, *42* (4), 1175–1186. https://doi.org/10.1021/ic020540s.

(149) Kochnev, V. K.; Avdeeva, V. V.; Goeva, L. V.; Malinina, E. A.; Kuznetsov, N. T. The Undecahydrodecaborate Anion $B_{10}H_{11}^-$ as the Starting Reagent in Exopolyhedral Substitution and Complexation: Theoretical and Experimental Prerequisites. *Russ. J. Inorg. Chem.* **2012**, *57* (3), 331–336. https://doi.org/10.1134/S003602361203014X.

(150) Laila, Z.; Abi-Ghaida, F.; Al Anwar, S.; Yazbeck, O.; Jahjah, R.; Aoun, R.; Tlais, S.; Mehdi, A.; Naoufal, D. Study of the Controlled Temperature Reaction between Closo-Decahydrodecaborate And Alcohols in H_2SO_4 Medium. *Main Group Chemistry* **2015**, *14* (4), 301–312. https://doi.org/10.3233/MGC-150173.

(151) Shelly, K.; Knobler, C. B.; Hawthorne, M. F. Synthesis of Monosubstituted Derivatives of Closo-Decahydrodecaborate(2-). X-Ray Crystal Structures of $[Closo\text{-}2\text{-}B_{10}H_9CO]^-$ and $[Closo\text{-}2\text{-}B_{10}H_9NCO]^{2-}$. *Inorg. Chem.* **1992**, *31* (13), 2889–2892. https://doi.org/10.1021/ic00039a041

(152) Mahfouz, N.; Abi-Ghaida, F.; Kotob, W.; Mehdi, A.; Naoufal, D. Selective Functionalization of Carbonyl Closo-Decaborate $[2\text{-}B_{10}H_9CO]^-$ with Building Block Properties via Grignard Reagents. *Molecules* **2023**, *28* (16), 6076. https://doi.org/10.3390/molecules28166076.

(153) Abi-Ghaida, F.; Laila, Z.; Ibrahim, G.; Naoufal, D.; Mehdi, A. New Triethoxysilylated 10-Vertex Closo-Decaborate Clusters. Synthesis and Controlled Immobilization into Mesoporous Silica. *Dalton Trans.* **2014**, *43* (34), 13087–13095. https://doi.org/10.1039/C4DT00772G.

(154) Wegner, P. A.; Adams, D. M.; Callabretta, F. J.; Spada, L. T.; Unger, R. G. Reaction of the Decahydrodecaborate (2-) Ion with Benzoylating Agents. Effect of Acid. *J. Am. Chem. Soc.* **1973**, *95* (22), 7513–7514. https://doi.org/10.1021/ja00803a055.

(155) Wilbur, D. S.; Chyan, M.-K.; Hamlin, D. K.; Perry, M. A. Preparation and in Vivo Evaluation of Radioiodinated Closo-Decaborate(2-) Derivatives to Identify Structural Components That Provide Low Retention in Tissues. *Nuclear Medicine and Biology* **2010**, *37* (2), 167–178. https://doi.org/10.1016/j.nucmedbio.2009.10.004.

(156) Dou, D.; Mavunkal, I. J.; Bauer, J. A. K.; Knobler, C. B.; Hawthorne, M. F.; Shore, S. G. Synthesis and Structure of Triethylammonium 2-(Acetonitrile)Nonahydro-Closo-Decaborate (1-). *Inorg. Chem.* **1994**, *33* (26), 6432–6434. https://doi.org/10.1021/ic00104a069.
(157) Sivaev, I. B.; Votinova, N. A.; Bragin, V. I.; Starikova, Z. A.; Goeva, L. V.; Bregadze, V. I.; Sjöberg, S. Synthesis and Derivatization of the 2-Amino-Closo-Decaborate Anion $[2\text{-}B_{10}H_9NH_3]^-$. *Journal of Organometallic Chemistry* **2002**, *657* (1), 163–170. https://doi.org/10.1016/S0022-328X(02)01419-5.
(158) Knoth, W. H.; Sauer, J. C.; Miller, H. C.; Muetterties, E. L. Diazonium and Carbonyl Derivatives of Polyhedral Boranes. *J. Am. Chem. Soc.* **1964**, *86* (1), 115–116. https://doi.org/10.1021/ja01055a027.
(159) Naoufal, D.; Grüner, B.; Bonnetot, B.; Mongeot, H. Replacement of the Nitrogen of $[1\text{-}N_2B_{10}H_9]^-$ by Amines or Nitriles, a Route to Hydrophobic Monoanions. *Polyhedron* **1999**, *18* (7), 931–939. https://doi.org/10.1016/S0277-5387(98)00354-4.
(160) Naoufal, D.; Selucký, P.; Grüner, B.; Bonnetot, B.; Mongeot, H. Solvent Extraction of Radioactive Cs^+ by Hydroborate Anionic Extractants of the $[1\text{-}LB_{10}H_9]^-$ Type (L = Amine or Phosphine). *J Radioanal Nucl Chem* **2005**, *266* (1), 145–148. https://doi.org/10.1007/s10967-005-0886-3.
(161) Jankowiak, A.; Baliński, A.; Harvey, J. E.; Mason, K.; Januszko, A.; Kaszyński, P.; Young, V. G.; Persoons, A. $[closo\text{-}B_{10}H_{10}]^{2-}$ as a Structural Element for Quadrupolar Liquid Crystals: A New Class of Liquid Crystalline NLO Chromophores. *J. Mater. Chem. C* **2013**, *1* (6), 1144–1159. https://doi.org/10.1039/C2TC00547F.
(162) Klyukin, I. N.; Zhdanov, A. P.; Matveev, E. Yu.; Razgonyaeva, G. A.; Grigoriev, M. S.; Zhizhin, K. Yu.; Kuznetsov, N. T. Synthesis and Reactivity of Closo-Decaborate Anion Derivatives with Multiple Carbon–Oxygen Bonds. *Inorganic Chemistry Communications* **2014**, *50*, 28–30. https://doi.org/10.1016/j.inoche.2014.10.008.
(163) Klyukin, I. N.; Voinova, V. V.; Selivanov, N. A.; Zhdanov, A. P.; Zhizhin, K. Yu.; Kuznetsov, N. T. New Methods for the Synthesis of Alkoxy Derivatives of the Closo-Decaborate Anion $[2\text{-}B_{10}H_9(OR)]^{2-}$, Where R = C_2H_5, Iso-C_3H_7, C_4H_9. *Russ. J. Inorg. Chem.* **2018**, *63* (12), 1546–1551. https://doi.org/10.1134/S0036023618120112.
(164) Semioshkin, A. A.; Sivaev, I. B.; Bregadze, V. I. Cyclic Oxonium Derivatives of Polyhedral Boron Hydrides and Their Synthetic Applications. *Dalton Trans.* **2008**, No. 8, 977–992. https://doi.org/10.1039/B715363E.
(165) Matveev, E. Yu.; Razgonyaeva, G. A.; Mustyatsa, V. N.; Votinova, N. A.; Zhizhin, K. Yu.; Kuznetsova, N. T. Oxonium Derivatives of Closo-Decaborate in Reactions with Sulfur-Containing Nucleophiles. *Russ Chem Bull* **2010**, *59* (3), 556–559. https://doi.org/10.1007/s11172-010-0125-0.
(166) Avdeeva, V. V.; Garaev, T. M.; Breslav, N. V.; Burtseva, E. I.; Grebennikova, T. V.; Zhdanov, A. P.; Zhizhin, K. Y.; Malinina, E. A.; Kuznetsov, N. T. New Type of RNA Virus Replication Inhibitor Based on Decahydro-Closo-Decaborate Anion Containing Amino Acid Ester Pendant Group. *J Biol Inorg Chem* **2022**, *27* (4–5), 421–429. https://doi.org/10.1007/s00775-022-01937-4.
(167) Ai, H.; Wang, Y.; Li, B.; Wu, L. Synthesis and Characterization of Single-Side Organically Grafted Anderson-Type Polyoxometalates. *European Journal of Inorganic Chemistry* **2014**, *2014* (17), 2766–2772. https://doi.org/10.1002/ejic.201301596.
(168) Diab, M.; Mateo, A.; Cheikh, J. A.; Haouas, M.; Ranjbari, A.; Bourdreux, F.; Naoufal, D.; Cadot, E.; Bo, C.; Floquet, S. Unprecedented Coupling Reaction between Two Anionic Species of a Closo-Decahydrodecaborate Cluster and an Anderson-Type Polyoxometalate. *Dalton Trans.* **2020**, *49* (15), 4685–4689. https://doi.org/10.1039/C9DT04676C.
(169) Diab, M.; Mateo, A.; El Cheikh, J.; El Hajj, Z.; Haouas, M.; Ranjbari, A.; Guérineau, V.; Touboul, D.; Leclerc, N.; Cadot, E.; Naoufal, D.; Bo, C.; Floquet, S. Grafting of Anionic Decahydro-Closo-

Decaborate Clusters on Keggin and Dawson-Type Polyoxometalates: Syntheses, Studies in Solution, DFT Calculations and Electrochemical Properties. *Molecules* **2022**, *27* (22), 7663. https://doi.org/10.3390/molecules27227663.

Chapter Two

Chapter 2: Coupling of Polyoxometalates and Closo-decahydrodecaborate: Synthesis, Characterization and Biological Properties.

I. Introduction

The association of closo-decaborate anions with Anderson, Keggin, or Dawson polyoxometalates appears as synergistic systems of interest for both components. Indeed, the new POM-decaborate hybrids could be effective in biology as an anti-microbial, anti-bacterial, and anti-viral reagents or in cancer treatment because of the physio-chemical and biological properties of the constituents [1–3]. The addition of boron clusters to POMs would enable the latter to penetrate cells more effectively; meanwhile, the interaction properties of POMs with proteins and their electron storage properties would enable hydroborate clusters to enhance their biological activity, in particular by keeping them close to these biological materials and making them more reactive.

Nevertheless, from a synthetic point of view, it is quite challenging to chemically couple two anionic entities directly, bearing in mind that POMs contain metals in their high oxidation states, while boron clusters can be considered as reductants. In the previous PhD work of Manal Diab (2014-2017), the repulsion issue between the two components was creatively tackled by combining them through organic spacers compatible with each POM type and well-known in the literature. For instance, the Anderson-type POMs $[MnMo_6(OH)_6O_{18}]^{3-}$ (noted as $MnMo_6$) and $[AlMo_6(OH)_6O_{18}]^{3-}$ (noted as $AlMo_6$) are functionalized with tris(hydroxymethyl)aminomethane (TRIS)[4] ligand, while divacant Keggin POM $[SiW_{10}O_{36}]^{8-}$ (noted hereafter SiW_{10}) and the monovacant Dawson POM $[P_2W_{17}O_{61}]^{10-}$ (noted hereafter P_2W_{17}) are functionalized with aminopropyl-tri(ethoxy)silane (APTES) ligand (Figure 1) [5,6] to give the very popular POM hybrid platforms known as organosilyl derivatives of the Keggin and Dawson types polyoxotungstates.

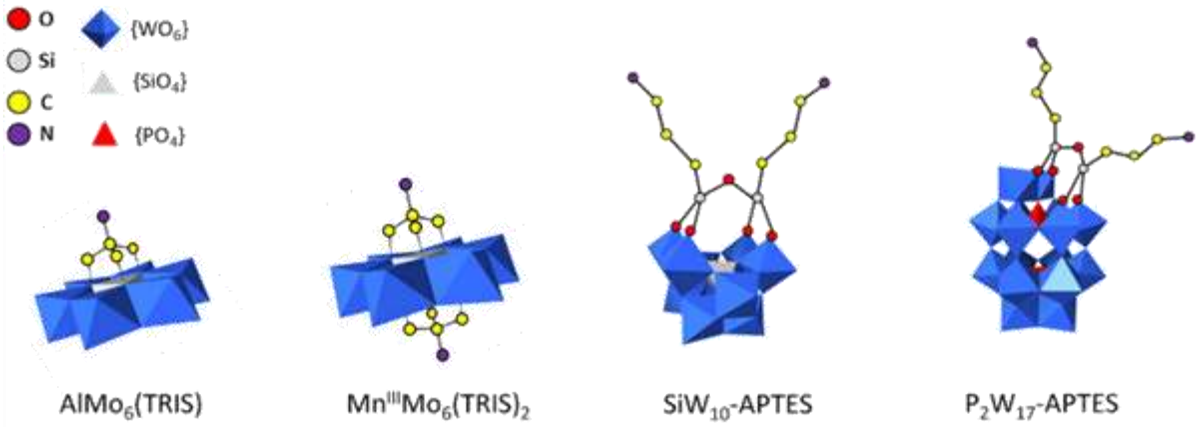

Figure 1. Views of the molecular structures of TRIS and APTES functionalized POMs.[4–6]

These organic linkers are anchored to the POM side through its silane groups while carrying two reactive amino functional groups on the other end, available for reacting with one or two of the electrophilic -CO group of $[B_{10}H_9CO]^-$ (denoted hereafter B_{10}) [7] resulting in the formation of the amide groups. These POM-Borate hybrids are, to our knowledge, the first examples associating POM and closo-B_{10} cage and were named mono-adducts and di-adducts for those carrying one or two B_{10} cages, respectively (Figure 2) [8,9].

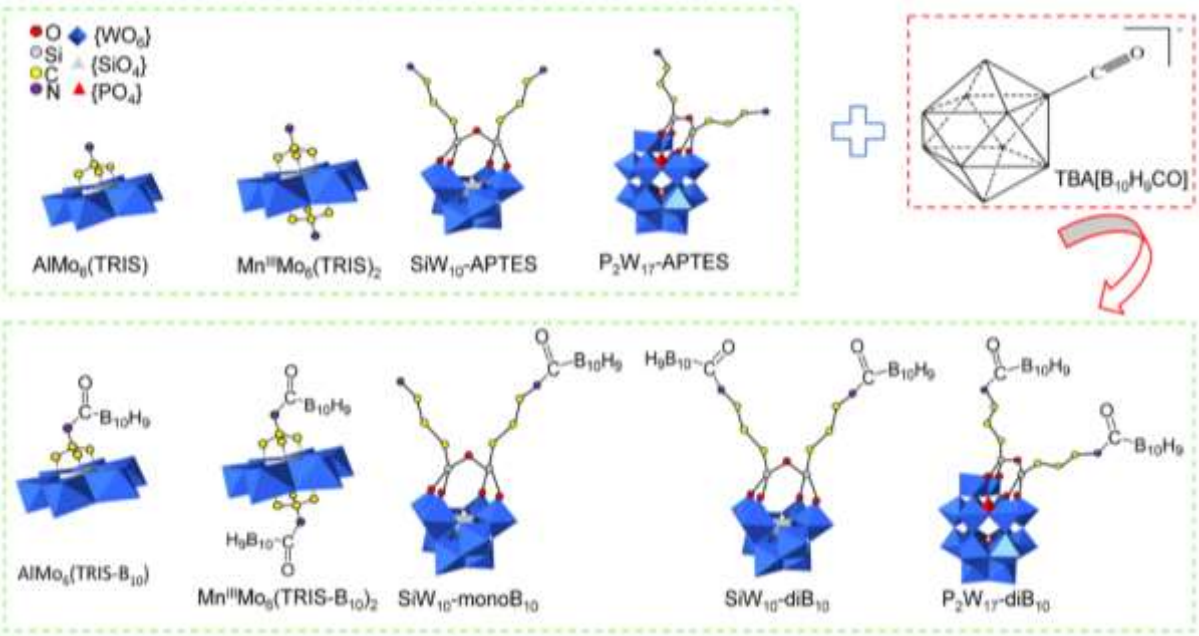

Figure 2. The synthetic approach was followed to obtain hybrid POMs-Borate adducts.[8,9]

Among all the five POM-decaborate hybrids synthesized by Manal Diab in her PhD work, the mono-functionalized compound presents the biggest appeal since we can imagine another functionalization leading to hybrid POM with two distinct functional groups noted here as «**SiW_{10}-B_{10}-Organic ligand»**. A key point for multifunctional compounds.

This compound, identified as mono-adduct, will be the starting point of this PhD work and will be used as a precursor to pursue our goal of synthesizing new POM hybrid systems constituted from the POM platform already coupled to one anionic decaborate boron cluster and then coupled to another different organic ligand.

If we take a closer look at the SiW_{10}-monoB_{10} compound, DFT calculations evidenced that the best optimized molecular structure is derived from the precursor SiW_{10}-APTES with a closed rather than open conformation. The closo-decaborate cage is kept near the two N-H groups in the neighboring organic arm, which favors strong dihydrogen H-H interactions between two B-**H** hydrides and two protons of amine groups N-**H** in the 2.0-2.2 Å range (Figure 3a). In contrast, the closo-decaborate cage is kept far from the two N-H groups in the open conformation (Figure 3b), so no intramolecular hydrogen bond was detected, and this structure is thus less stable. However, in both cases, there is dihydrogen interaction between

the hydride B-**H** of the B_{10} cluster and proton of the amide -N**H**-CO-B_{10} of distance around 2.0 Å in agreement with the B-H…H-N interactions reported in the literature (Figure 3b) [10–12].

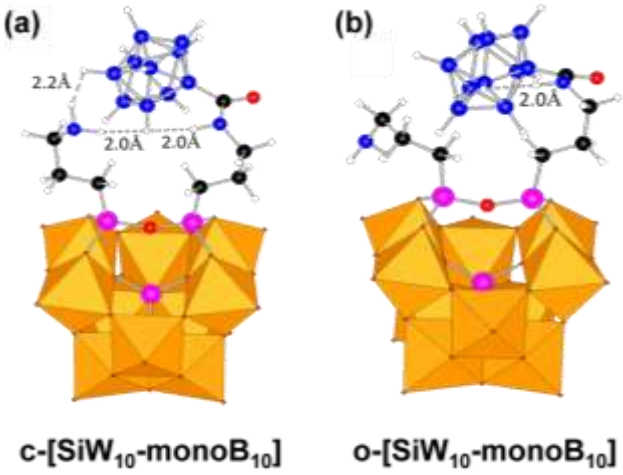

*Figure 3. DFT-optimized molecular structures of SiW_{10}-$monoB_{10}$ with **(a)** closed and **(b)** open conformations.[9] (Legends: C in black, H in white, N in dark blue, Si in pink, O in red, B in blue, WO_6 octahedra in orange, and PO_4 tetrahedra in green)*

Such strong dihydrogen contacts are impossible for di-adducts, so DFT calculations (Figure 4) show that the most stable adduct is SiW_{10}-$monoB_{10}$, which is stabilized by 22 kCal.mol^{-1} compared to the precursor SiW_{10}-APTES.

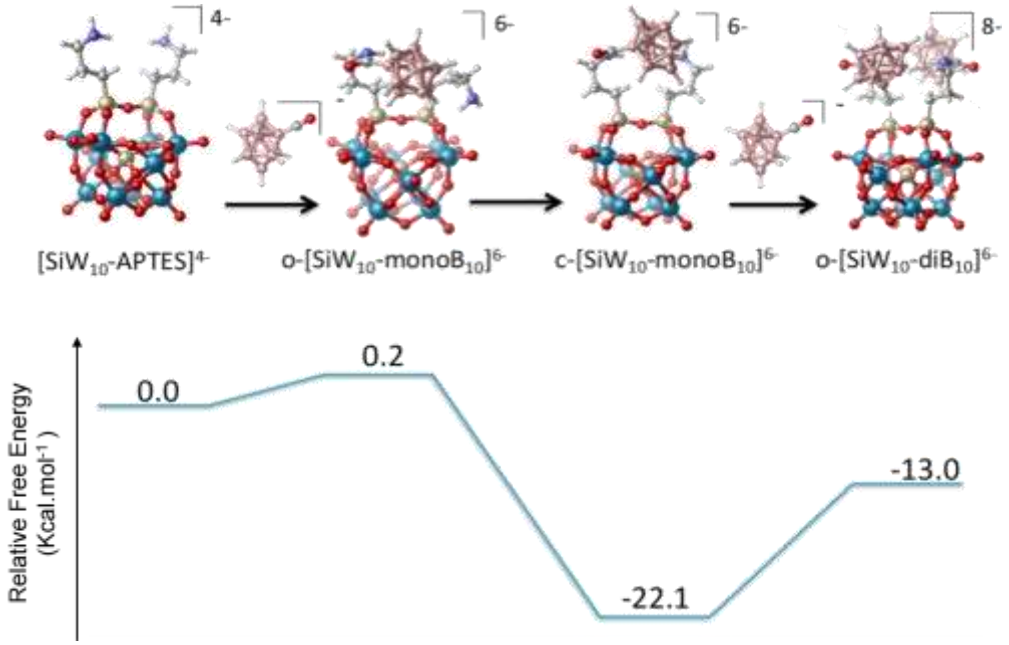

*Figure 4. Structural models obtained by geometrical optimization of **SiW_{10}-APTES**, **SiW_{10}-$monoB_{10}$, and SiW_{10}-diB_{10}** (open and closed forms) and variation of the Gibbs energy of the formation of mono-adducts from the starting precursors in CD_3CN.[9] (Legends: C in grey, H in white, N in violet, Si in light yellow, O in red, B in light pink)*

To our knowledge, such a monofunctionalized hybrid POM compound isolated directly from the synthesis is unprecedented in the literature. This work aimed to go further by functionalizing the second amine function of SiW_{10}-monoB_{10}, *a priori* difficult task given the stability of this compound and the fact that the second amine interacts strongly with the decaborate cluster through H-H contact.

The objectives of this work in this chapter were thus:

- to synthesize this mono-adducted compound with good purity and in sufficient quantities;
- to characterize it in solution by ^{1}H-^{15}N HMQC NMR to identify the nature of the free amine function, which Manal Diab had not done in her work, and to see if there was a non-zero amine fraction that would not be involved in the H-H interaction with the decaborate cluster;
- to define some strategies for functionalizing this amine function and characterize the adducts.

II. Synthesis and characterization of the mono-adduct SiW_{10}-monoB_{10}

As mentioned above, the synthesis of this compound is performed from the protocol established by Manal Diab from the precursors SiW_{10}-APTES and $[B_{10}H_9CO]^-$ (Figure 5). Using a base in the coupling reaction with the B_{10} cluster was necessary since the SiW_{10}-APTES precursor has two alkyl pendant arms, each carrying a terminal amino group that is probably protonated [13,14]. Firstly, it will deprotonate the $-NH_3^+$ ammonium arm to give a nucleophilic amino group able to attack the carbonyl -CO group in $[B_{10}H_9CO]^-$. Secondly, it will trap the proton in the amide group formed, thus stabilizing the bond.

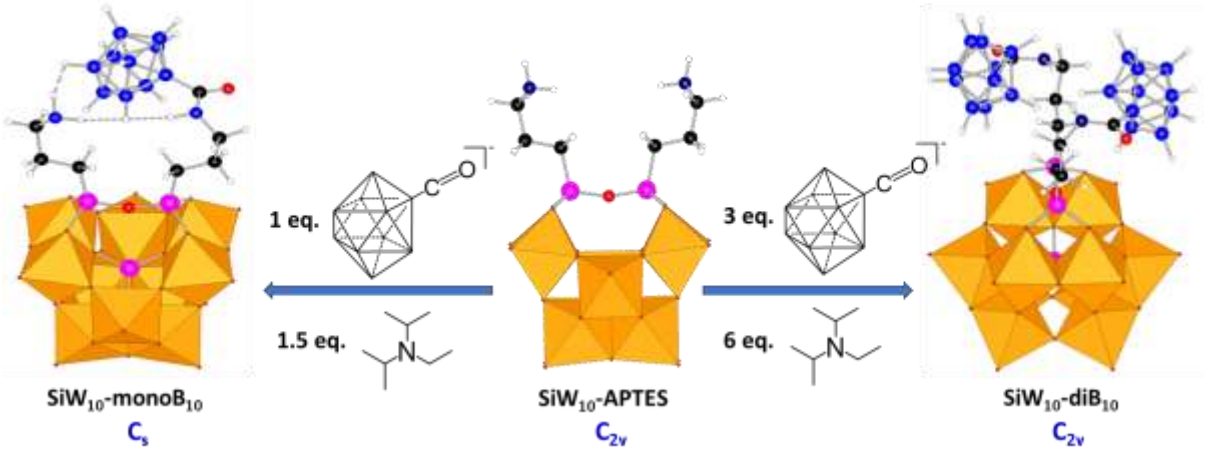

Figure 5. Scheme of the preparation of POM-Borate derivative $(TBA)_3(DIPEAH)_3[(SiW_{10}O_{36})(B_{10}H_9CONHC_3H_6Si)(NH_2C_3H_6Si)O].3H_2O$, *noted as* ***$SiW_{10}$-mono$B_{10}$***.[9] *(Legends: C in black, H in white, N in dark blue, Si in pink, O in red, B in blue, WO_6 octahedra in orange)*

Notably, the base used in the reaction should be exclusively a weak nucleophile so that it will not compete against the APTES amino group in the nucleophilic substitution reaction with the $[B_{10}H_9CO]^-$. For instance, a base like Et_3N will replace the carbonyl group of $[B_{10}H_9CO]^-$ to yield $[B_{10}H_9CONEt_3]^-$ instead of SiW_{10}-monoB_{10} adduct [15]. Accordingly, a moderate, bulky organic base, diisopropylethylamine (DIPEA), was used to synthesize adducts with two or just one decaborate cluster (Figure 5). The synthesis of di-adduct was optimized with 6 equivalents of base, while the mono-adduct was specifically isolated with 1.5 equivalents of DIPEA in dry acetonitrile under an inert atmosphere and at room temperature [9].

Ultimately, we isolated the SiW_{10}-monoB_{10} mono-adduct selectively as mixed TBA^+ and $DIPEAH^+$ salt and confirmed its formation by FT-IR (Figure S8 in the appendix), EA (Section VI.2), ^1H NMR (Figure 6 and Figure S1 in the appendix) and ^{11}B NMR (Figure S3 in the appendix).

III. NMR Studies

As part of her thesis work, Manal Diab characterized her products in solution by ^1H, ^{29}Si, ^{11}B, and ^{183}W NMR. Despite all these results, and in the absence of a structure, additional characterizations were requested by the reviewers to be able to publish them. As a first step, I therefore completed this work with a ^1H-^{15}N HMBC NMR study, an unusual method that allows us to see couplings with nitrogen atoms, reconstruct a ^{15}N NMR spectrum, and conclude the attribution of protons to amine or amide functions.

The ^1H NMR was useful in observing what happened in the APTES linker protons, specifically detecting the change in the symmetry from C_{2v} in SiW_{10}-APTES to C_s in SiW_{10}-monoB_{10} which is the key indicator of coupling one B_{10} cage into one of APTES arms. The ^1H NMR spectra of SiW_{10}-APTES and SiW_{10}-monoB_{10} are given in Figure 6, while the ^1H $\{^{11}B\}$ NMR spectrum of SiW_{10}-monoB_{10} is in Figure S1 in the appendix.

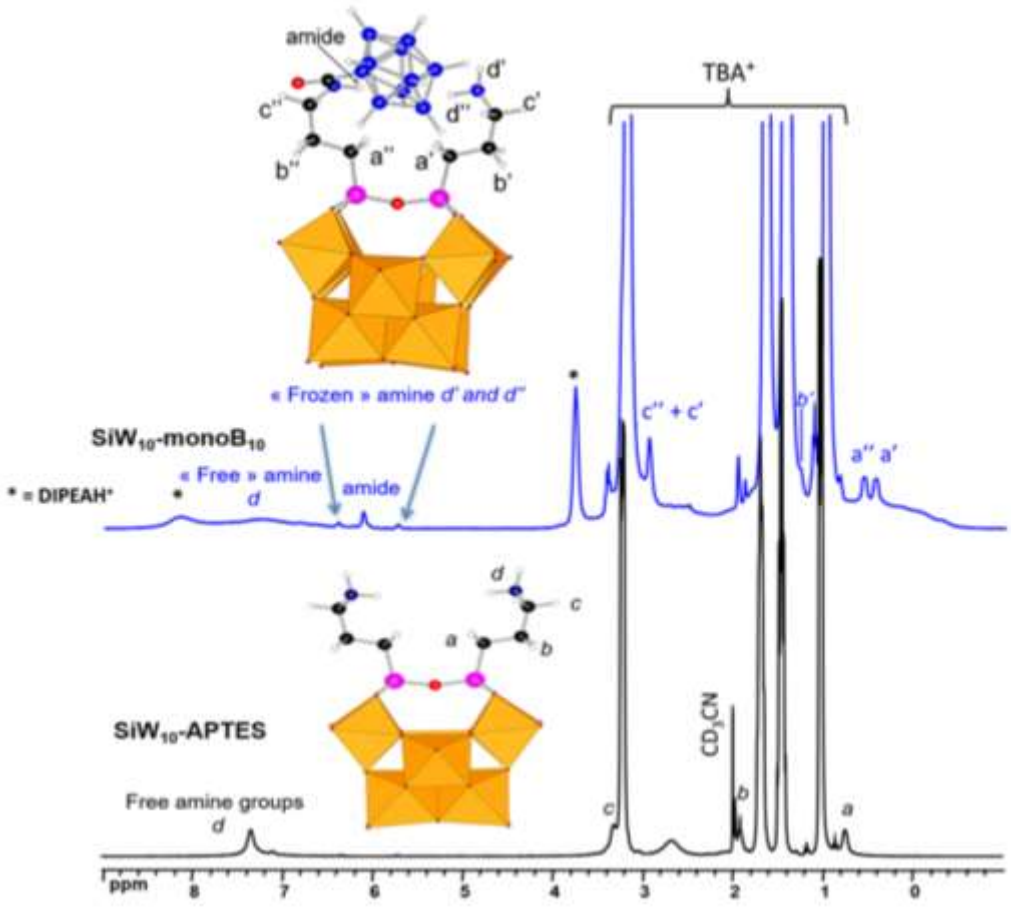

*Figure 6. ^{1}H NMR spectra of **SiW_{10}-APTES** and **SiW_{10}-monoB$_{10}$** in CD_3CN at 400MHz.*

As seen in Figure 6, the ^{1}H NMR of SiW_{10}-APTES agrees with the literature [13]. In addition to four peaks related to TBA^+ protons at 1.01, 1.45, 1.67, and 3.21 ppm, four broad peaks corresponding to APTES protons have been observed: three are related to -CH_2 methylene groups denoted as *a*, *b*, and *c* at (0.75, 1.91, and 3.30 ppm respectively), and one deshielded signal related to the terminal -NH_3^+ groups, denoted as *d* and located at 7.35 ppm. Protons «a» are the -CH_2 groups near Si atoms of APTES, while «c» protons are those in the alpha position of the terminal amine group. Due to overlapping with signals of TBA^+ cations and the solvent CHD_2CN, only the «a» and «d» signals were easily exploited.

The ^{1}H NMR of SiW_{10}-monoB$_{10}$ was shown to be more complicated compared to the SiW_{10}-APTES since it is crowded with many signals related to the protons of the countercations TBA^+ (-C**H$_2$**,-C**H$_3$**) and $DIPEAH^+$ (-C**H**, -C**H**$_3$, and i-Pr_2EtN**H**$^+$), the solvents, the APTES part, and those of the B_{10} cage which are very broad signals between -0.5 and +1.2 ppm. Despite these difficulties, it was evidenced through the comparison between SiW_{10}-APTES and SiW_{10}-monoB$_{10}$ spectra that each of the three methylenic signals of APTES (a, b, c) splits into a new set of signals. It is easier to notice it mostly with protons «a», which appear as two distinctive small signals, a' and a'', at 0.45 and 0.57 ppm, respectively. This is definitive proof that the APTES arms aren't equivalent, marking that the $[B_{10}H_9CO]^-$ cage has been grafted into SiW_{10}-

APTES along with the appearance of a new peak at 6.12 ppm is attributed to the amide function.

The ^{1}H NMR also reveals the appearance of two small peaks, d' and d'', at 5.70 and 6.33 ppm, respectively, assigned to the protons of free amine in a frozen configuration as depicted on the structure optimized by DFT. Such an attribution is confirmed by the ^{1}H-^{15}N HMBC NMR technique. Concomitantly,^{1}H-^{15}N HMBC (Heteronuclear Multiple Bond Correlation) NMR spectrum (Figure 7) confirms the presence of a signal at -272 ppm corresponding to amine nitrogen and correlated with two non-equivalent protons d' and d'', at 5.70 and 6.33 ppm, respectively. The signal of amide nitrogen is detected at -251 ppm (amide) correlated to the proton signal at 6.12 ppm. Besides, an additional broad signal is also observed at ca 7.2 ppm in the ^{1}H NMR in Figure 6, attributed to free amine groups.

Unfortunately, the correlation with the broad signal at 7.2 ppm cannot be seen in the ^{1}H-^{15}N NMR spectrum, but it corresponds well to the signal of amines in the SiW_{10}-APTES precursor, which confirms our assumption. This is a very important result for us since it shows that, in solution, we can have a part of the amine available for further functionalization.

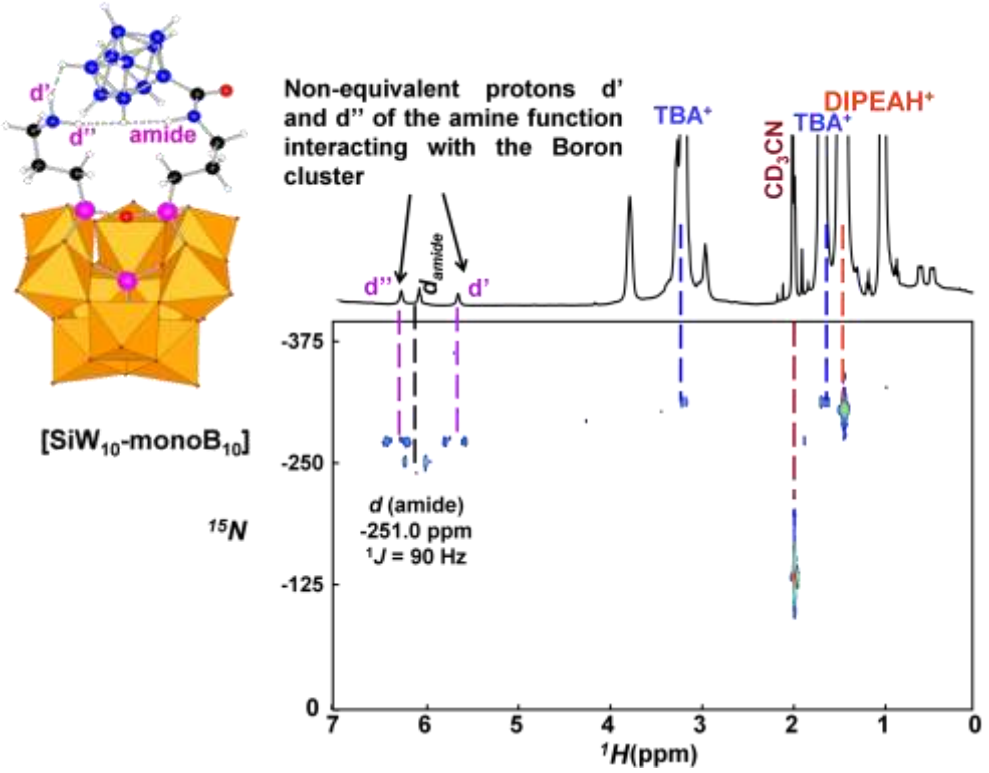

Figure 7. ^{1}H-^{15}N HMBC NMR spectra of SiW_{10}-monoB$_{10}$ in CD_3CN at 400MHz.[9]

IV. Study of the Reactivity of SiW_{10}-monoB$_{10}$ with Organic ligands in CD_3CN

We just evidenced that the mono-adduct has been successfully obtained and that at least a part of the free amine is not involved in H-H contact. Then, our first objective was to test the

possibility of grafting new functional groups on this free amino arm of SiW_{10}-monoB_{10} adduct and to follow this grafting through ^{1}H and ^{11}B NMR using different mixtures of SiW_{10}-monoB_{10}/organic ligand/DIPEA in CD_3CN solution.

The choice of the second group is clearly important to bring new functions to our hybrid system. As evidenced by Izzet, Keggin-based hybrids bearing pyridine or terpyridine functional groups and driven by metal coordination can promote the formation of supramolecular species with well-defined topology based on the orientation of their alkyl chains, parallel or perpendicular, resulting in triangular or squares assembly, respectively [16,17]. In this context, we initially focused on using organic ligands with a pyridine functional group, such as (pyridine aldehyde and alkyl pyridine...) for synthesizing the «**SiW_{10}-B_{10}-Organic ligand»** derivative.

In case of success, the idea is to exploit the pyridine coordinating function by adding a suitable metal to form supramolecular systems associating at least two hybrid POMs around this metal, which would be very interesting from a fundamental point of view. The same function could also be used to graft a Pt(terpy)-type complex onto the hybrid (Figure 8). The grafted complex could interact with nucleotides or intercalate in DNA, thus promoting antitumor action similar to that of the cis-platinum complex widely used in chemotherapy, or else by promoting the action of borate and POM [18,19].

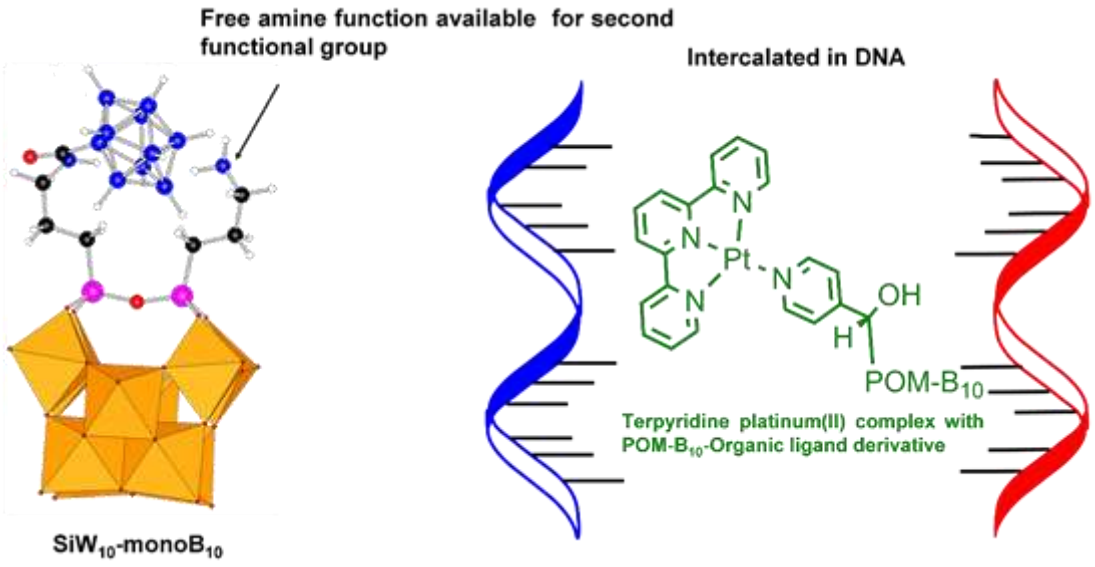

*Figure 8. Perspective application of the **«SiW_{10}-B_{10}-Organic ligand»** derivative in cancer treatment.*

A second idea was to move on to grafting peptide or polyethyleneglycol (PEG) chains instead of pyridine compounds. Preliminary studies on POM-borate adducts obtained by Manal Diab during her thesis show promising results regarding anti-inflammatory and anti-proliferative activity in colon cancer cells. These results add to the equally positive results of other POM-hybrids obtained at Versailles by the Dolbecq group on breast cancer cells [20], inspires us to study the biological properties (anti-bacterial, anti-microbial, anti-viral properties in particular) of these multifunctional hybrid systems.

Finally, the last idea for this chapter was to study the aggregation formation in solution through ^{1}H DOSY NMR, which is a very powerful NMR method for characterizing species in solution and highlighting supramolecular interactions with other molecules that may be substrates, biological material, or simple organic counteractions.

By way of example, Figure 9 shows how ^{1}H DOSY can be used to determine the diffusion coefficients of organic cations in the presence of POMs with different concentrations and how the value of this diffusion coefficient can be used to trace the association constants in solution, which are far from negligible [21]. In this case, the diffusion coefficient of NMe_4^+ was measured for different concentrations *C°* in the series $(Y)_{52}\{Mo_{132}\}$ Keplerate with Y = Li^+, Na^+, or NH_4^+ [22].

During her thesis, Manal Diab was confronted with unexpected results using this technique, which suggested the formation of aggregates between the POM-borate adducts and TBA^+ cations in a non-aqueous solution, as recently reported by Izzet in organic solvent with hybrid derivatives of P_2W_{17} [16]. This problem is of fundamental interest, and very few studies are currently being carried out in this field, even though this issue is crucial to understanding the properties of certain POM-hybrids in solution. Therefore, it will be interesting to investigate this question in our work with different organic cations in different media.

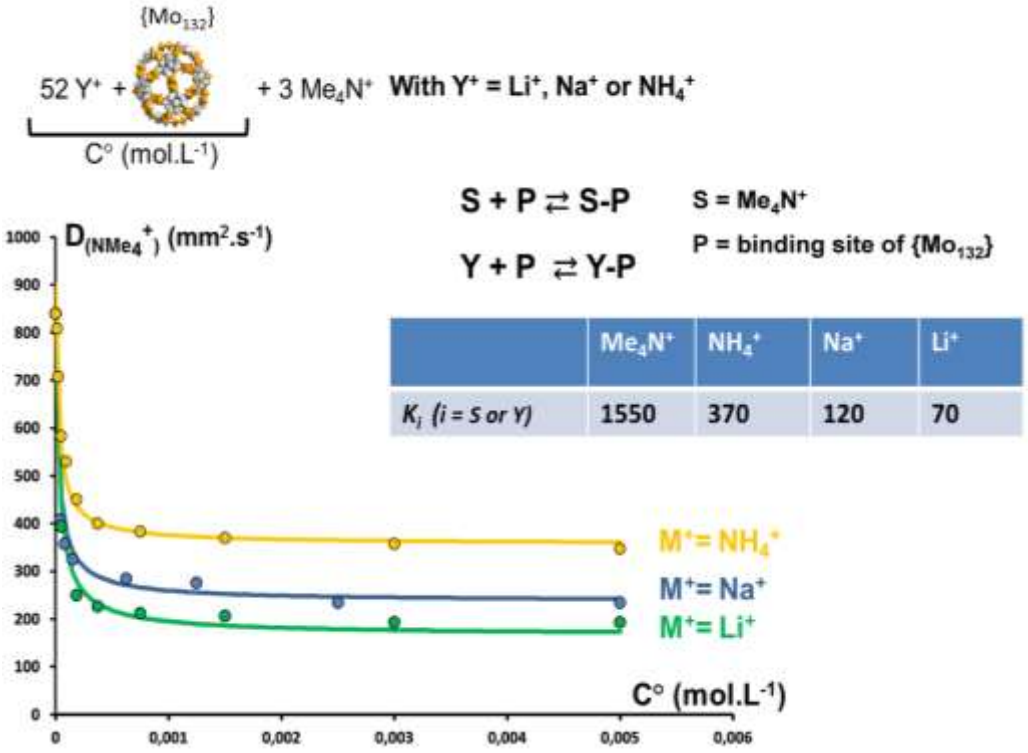

Figure 9. Demonstration of supramolecular cation/POM interactions in solution by DOSY.[22]

IV.1 Reactivity with organic ligands

1°) General Procedure

The general procedure for preparing the reaction medium of SiW_{10}-monoB_{10}/Organic ligand/DIPEA is dissolving a constant quantity of $(TBA)_3(DIPEAH)_3[(SiW_{10}O_{36})(B_{10}H_9CONHC_3H_6Si)(NH_2C_3H_6Si)O].3H_2O$, **$SiW_{10}$-mono$B_{10}$** (40mg, 0.01 mmol) in 0.5ml CD_3CN in a closed NMR tube. Then the organic ligand **(3-(Iodomethyl)pyridine-hydroiodide, pyridine-4-carboxaldehyde, or 4-chloromethyl benzonitrile)** is added in various amounts while stirring. Finally, DIPEA is added, as needed, drop by drop for 3hrs. The ^{1}H and ^{11}B NMR studies done in solution are shown in the following part and in the appendix (Figures S4-S5).

2°) Reactivity with pyridine-4-carboxaldehyde

The first tests were conducted with some **pyridine-4-carboxaldehyde** (Figure 10), whose aldehyde function is supposed to react with the amine function to form imine, a classic reaction in organic chemistry.

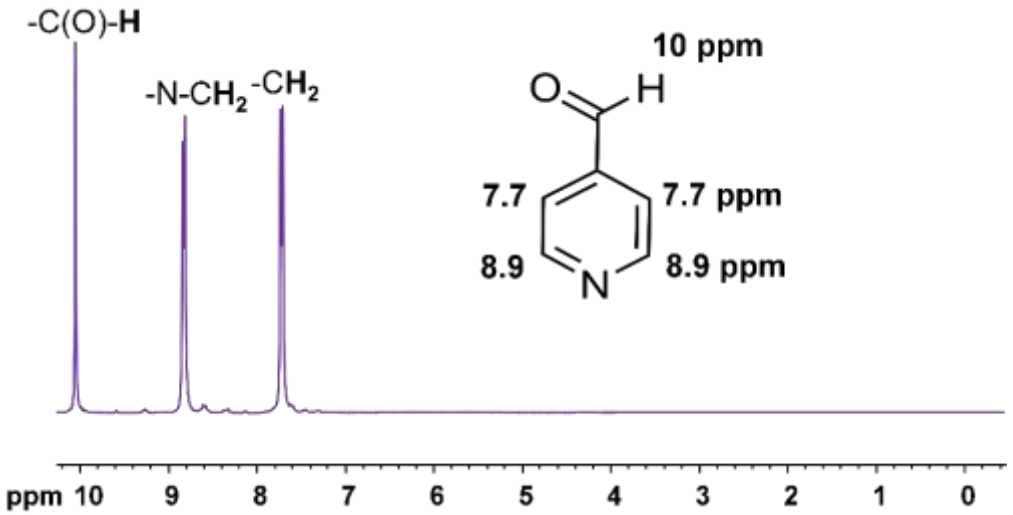

*Figure 10. ^{1}H spectra (300MHz) of **pyridine-4-carboxaldehyde** (C_6H_5NO) in CD_3CN.*

As seen in Figure 11, the addition of 1 or 2 equivalents of **pyridine-4-carboxaldehyde** (C_6H_5NO) ligand into SiW_{10}-monoB_{10} in CD_3CN seems not to affect the APTES part of the mono-adduct since two signals for protons a' and a" are still observed. Furthermore, the major part of the ligand introduced displays unchanged signals. However, small new peaks in the 7-9 ppm range are detected, while a small shift in the signals of NH protons of the POM precursor between 5.4-6.8 ppm is seen. It could indicate that a small fraction of the ligand has reacted as expected or that the **pyridine-4-carboxaldehyde**, neutral or more probably protonated, strongly interacts with the POM through H-bond and/or H-H dihydrogen contact. In all cases, reactivity between both reactants is not good and we need to change our strategy.

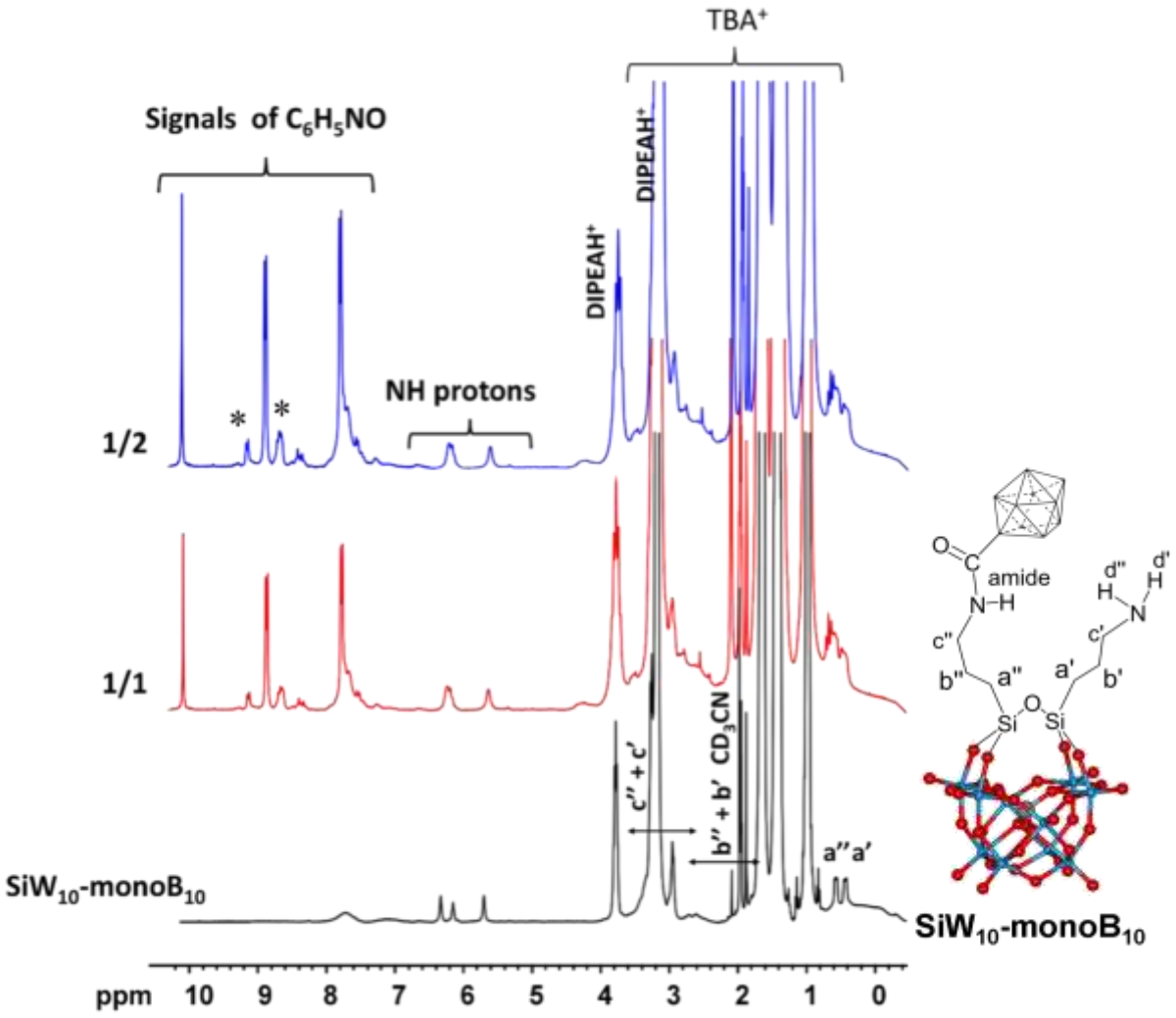

*Figure 11. ^{1}H spectra (300MHz) of **SiW_{10}-monoB$_{10}$** and **SiW_{10}-monoB$_{10}$/C_6H_5NO mixtures** of the proportions (**1/1** and **1/2**) in CD_3CN.(∗ symbols designate a small fraction of the ligand interacts with SiW_{10}-monoB$_{10}$)*

3°) Reactivity with 4-chloromethyl benzonitrile

A second test was carried out using **4-chloromethyl benzonitrile** with a chloromethyl group that was assumed to be more reactive. Here, the pyridine ring is replaced by a benzonitrile, which is easy to follow in NMR and less likely to form an H bond with the precursor.

Comparison between the ^{1}H spectrum of free C_7H_6ClN (Figure 12) and that of SiW_{10}-monoB$_{10}$ and the reaction medium SiW_{10}-monoB$_{10}$/C_7H_6CN of the proportions 0.5,1,1.5, and 2eq (Figure 13) shows no change in the NMR signals of both reactants and no new peak were obtained. Besides, the NH signals, d' and d'' of SiW_{10}-monoB$_{10}$ precursor remain intact which means it don't interact with the 4-chloromethyl benzonitrile ligand, in contrary to pyridine-4-carboxaldehyde with SiW_{10}-monoB$_{10}$.

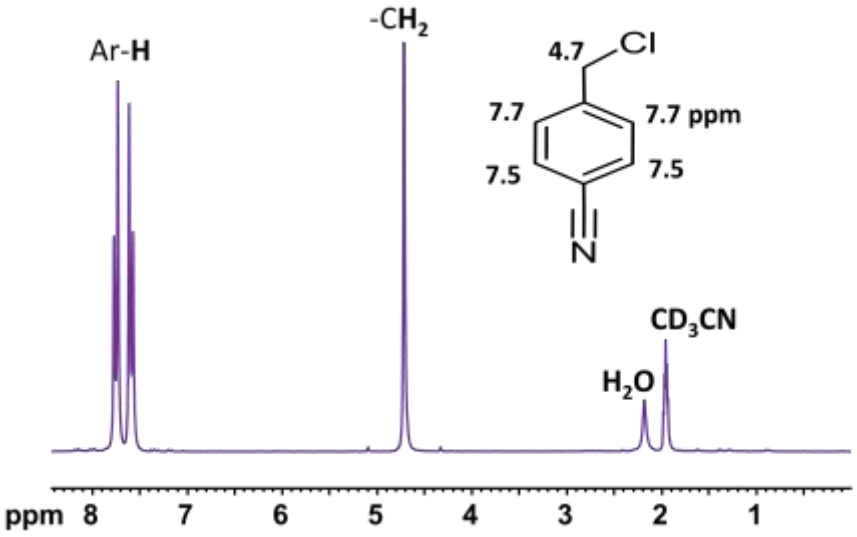

Figure 12. ^{1}H spectra (300MHz) ***of 4-chloromethyl benzonitrile*** *(C_7H_6ClN) in CD_3CN.*

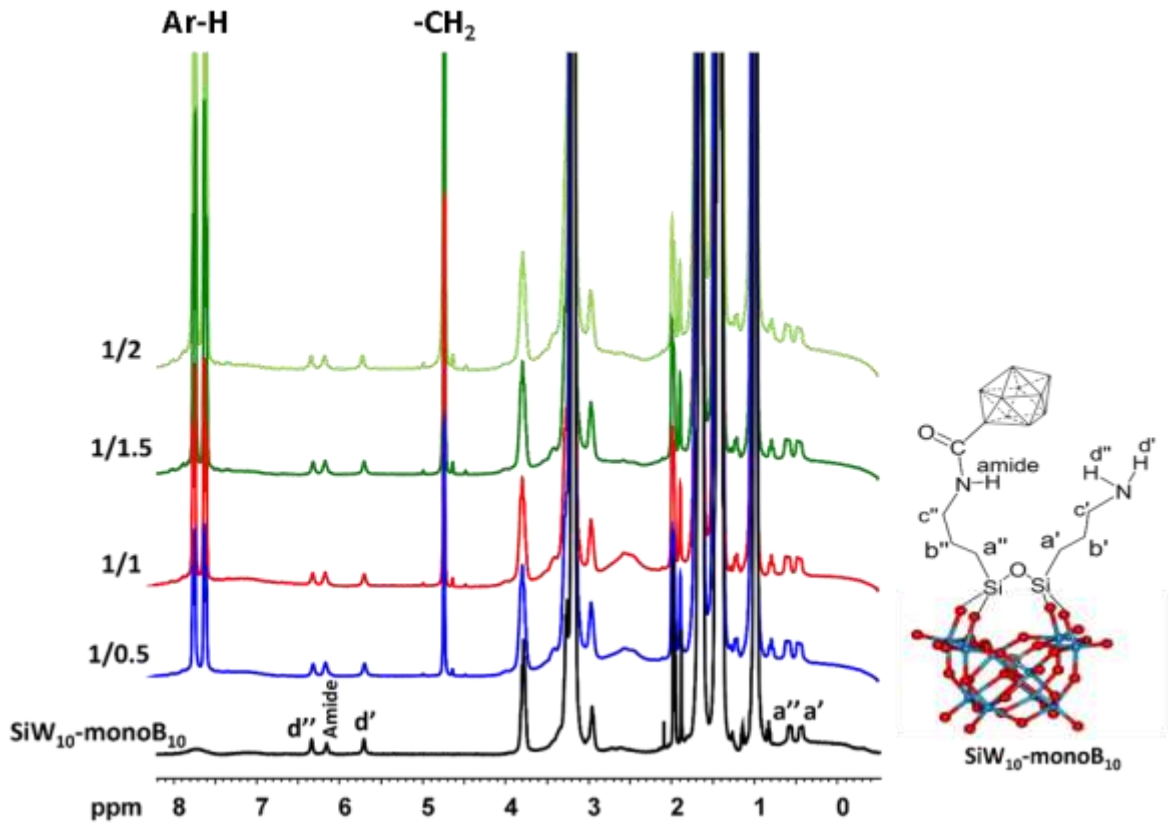

Figure 13. ^{1}H spectra (300MHz) of ***SiW_{10}-monoB$_{10}$*** *and* ***SiW_{10}-monoB$_{10}$/C_7H_6ClN mixtures*** *of different proportions in CD_3CN.*

4°) Reactivity with 3-(Iodomethyl)pyridine hydroiodide

Finally, we decided to test the reactivity of the SiW_{10}-monoB_{10} precursor with the reactant 3-(Iodomethyl)pyridine hydroiodide (Figure 14a) for different reasons: the iodide group must be replaced more easily than chloride in nucleophilic substitution and second, the position of the protonated pyridine group is adequate to give a strong H-H contact with the nearby decaborate, which we hope will favor the expected reaction (Figure 14b). In this strategy, we clearly want to exploit the formation of such interaction to our benefit.

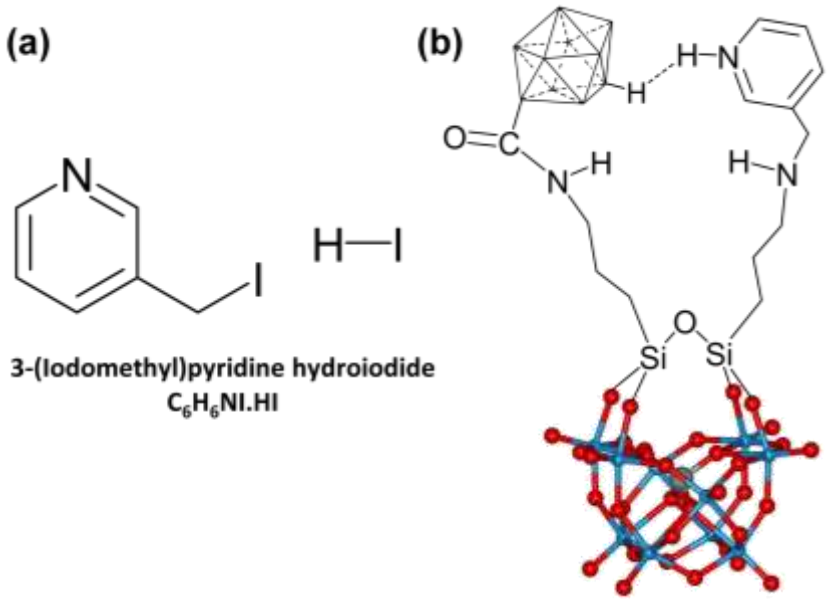

Figure 14. Structures of ***(a)*** *the organic ligand* ***3-(Iodomethyl)pyridine hydroiodide*** *and* ***(b)*** *the* ***«SiW$_{10}$-monoB$_{10}$-Organic ligand»*** *derivative that could be obtained from the association of $C_6H_6NI.HI$ with SiW_{10}-monoB_{10}.*

Mixtures SiW_{10}-monoB_{10}/3-(Iodomethyl)pyridine hydroiodide

In this way, solutions of the ratio **SiW_{10}-monoB_{10} /$C_6H_6NI.HI$ =1/x, x=0,1,2**, were first prepared in CD_3CN and stirred for 3hrs at room temperature without base in a closed vial under an inert atmosphere. Then, ^1H NMR experiments were performed for each solution mixture to detect if there was a coupling reaction between the two components.

As shown in Figure 15b, adding $C_6H_6NI.HI$ into SiW_{10}-monoB_{10} solution without adding base causes the appearance of several new peaks in the spectra. Moreover, tracking the changes in the protons «b» and «c» was difficult since their signals overlap with those of TBA^+ cations and $DIPEAH^+$, so we focused on protons between 0.3-0.75 ppm, corresponding to the methylenic groups in the vicinity of the Si atoms of APTES. Following the C_s symmetry, the ^1H spectrum of SiW_{10}-monoB_{10} precursor gives two small and broad signals (a' and a'') of the same intensity at 0.45 and 0.57 ppm, respectively.

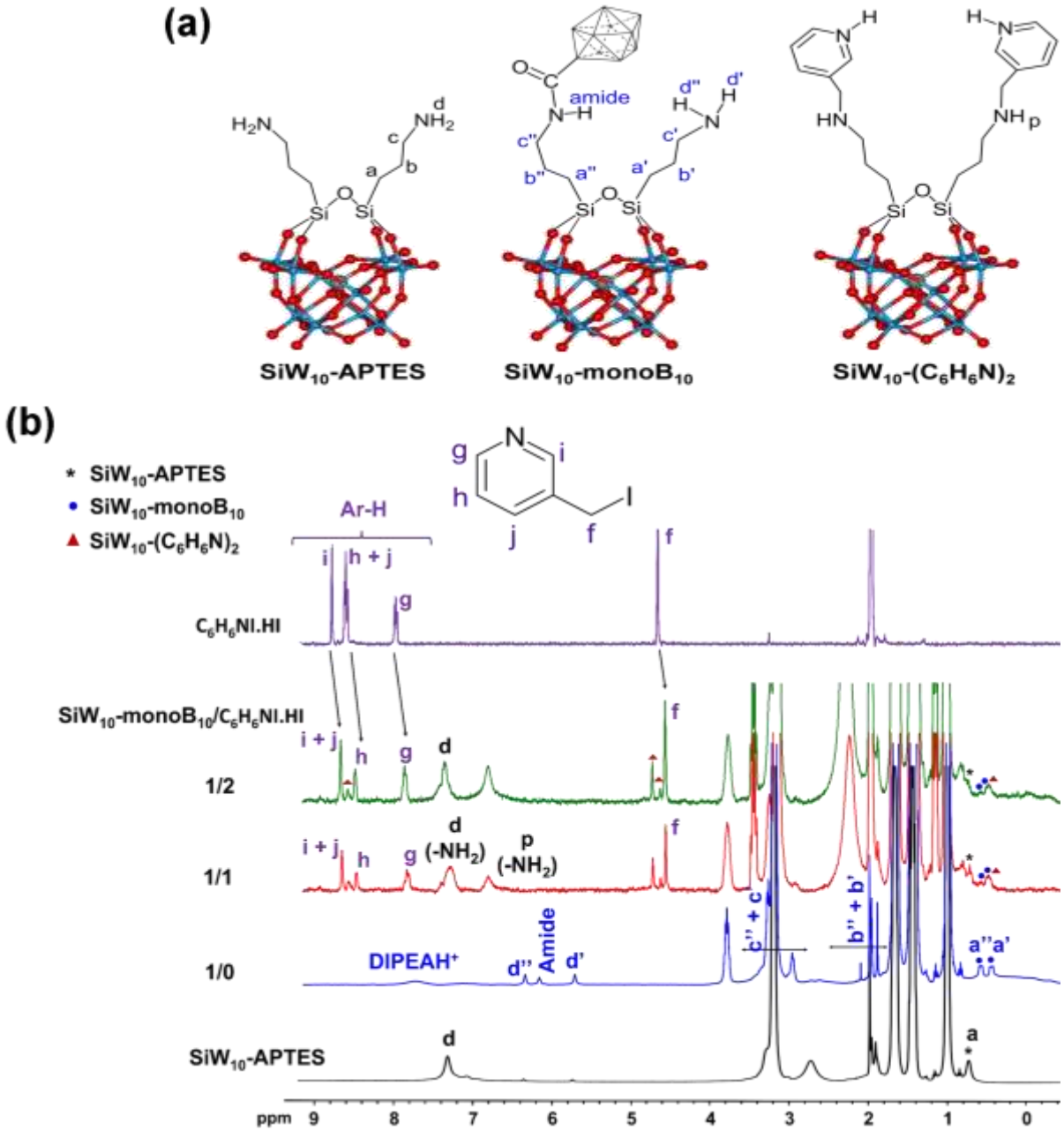

Figure 15. ***(a)*** *Structures of POM-hybrid derivatives are probably detected in* ***(b)*** *^{1}H NMR spectra (300MHz) of the reaction medium of* ***SiW_{10}-monoB$_{10}$/$C_6H_6NI.HI$*** *with different proportions in CD_3CN.*

As the amount of $C_6H_6NI.HI$ increases; new broad peaks appear at 0.75 ppm, marked as «*» in Figure 15b, related to the methylene protons «a» of SiW_{10}-APTES. Regarding the signals of methylenic protons of SiW_{10}-monoB$_{10}$, there is a huge decrease in the intensity of the signals of protons «a'» and «a''» at 0.45 and 0.57 ppm; respectively, suggesting the disappearance of this species.

The broad signal at 0.75 ppm well corresponds to the precursor SiW_{10}-APTES. At the same time, a broad peak denoted as «d» at 7.35 ppm assigned to the amine function of this precursor increases, while the amide signal at 6.12 disappears. It means that the amide

function allowing the connection of the decaborate cluster in SiW_{10}-monoB_{10} is hydrolyzed in these conditions. Furthermore, another new small peak marked as a triangle in Figure 15b appears at 0.43 ppm as the amount of $C_6H_6NI.HI$ increases. It is broad but unique in agreement with a C_{2v} structure. Such a geometry suggests the formation of a di-adduct where the two alkyl arms connected to the POM are equivalent. Therefore, it could correspond to a hybrid compound POM-APTES-$(C_6H_6N)_2$ as a minor species (Figure 15a). In this case, we expect some modification of the protons of the ligand close to the connection. Indeed, the signals at 4.63 ppm and 8.58 ppm (marked as triangles in Figure 15b) could be attributed to the protons «f» and «i» of the ligands in such POM-APTES-$(C_6H_6N)_2$ species. Finally, the major part of the ligand, compared to free C_6H_6NI, appears probably not connected to the POM, but the small chemical shift variation ($\Delta\delta$) of 0.11-0.12 ppm of protons g, h, j and i compared to free ligand suggests that the ligand interacts with the POM entity (Table 1).

Table 1. NMR data.

Compounds	Main Chemical Shifts (signals of TBA^+ and $DIPEAH^+$ are not given)
SiW_{10}-APTES	0.75 (a), 1.91 (b), 3.30 (c), 7.35 (d, amine group)
SiW_{10}-monoB_{10}	0.45 (a'), 0.57 (a''), 1.90 (b'' + b'), 2.97 (c'), 3.43 (c''), 6.15 (amid), 7.24 (d)
C_6H_6NI	4.66 (f), 7.97 (g), 8.60 (h + j), 8.78 (i)
SiW_{10}-monoB_{10}/ C_6H_6NI	0.43 (▲), 0.45 (a', •), 0.57 (a'', •), 0.75 (∗), 3.43 (c''), 6.80 (p),7.39 (d) ,4.66 (f), 7.86 (g), 8.48 (h), 8.67 (i + j), 4.63(▲), 4.71 (▲), 8.58 (▲)

In summary, in these experimental conditions, the SiW_{10}-monoB_{10} is probably hydrolyzed into the starting POM, SiW_{10}-APTES. A minority part of this precursor reacts then with the ligand to give, presumably, a di-adduct POM-APTES-$(C_6H_6N)_2$, while the majority of the ligand remains unbound but in interaction with the polyanionic species. We thus have a mixture of free ligand, POM-APTES, and POM-Ligand but no evidence of the formation of the expected hybrid POM.

Notably, the protons of the B_{10} cluster in the coupled ^1H NMR experiments are highly broadened and difficult to observe, as seen in ^1H NMR spectra of $TBA[B_{10}H_9CO]$, SiW_{10}-monoB_{10} and SiW_{10}-monoB_{10}/$C_6H_6NI.HI$ mixture of the proportion 1/1 (Figure 16). That's why doing non-coupled $^1H\{^{11}B\}$ NMR experiments helped see resolved peaks of B-H groups.

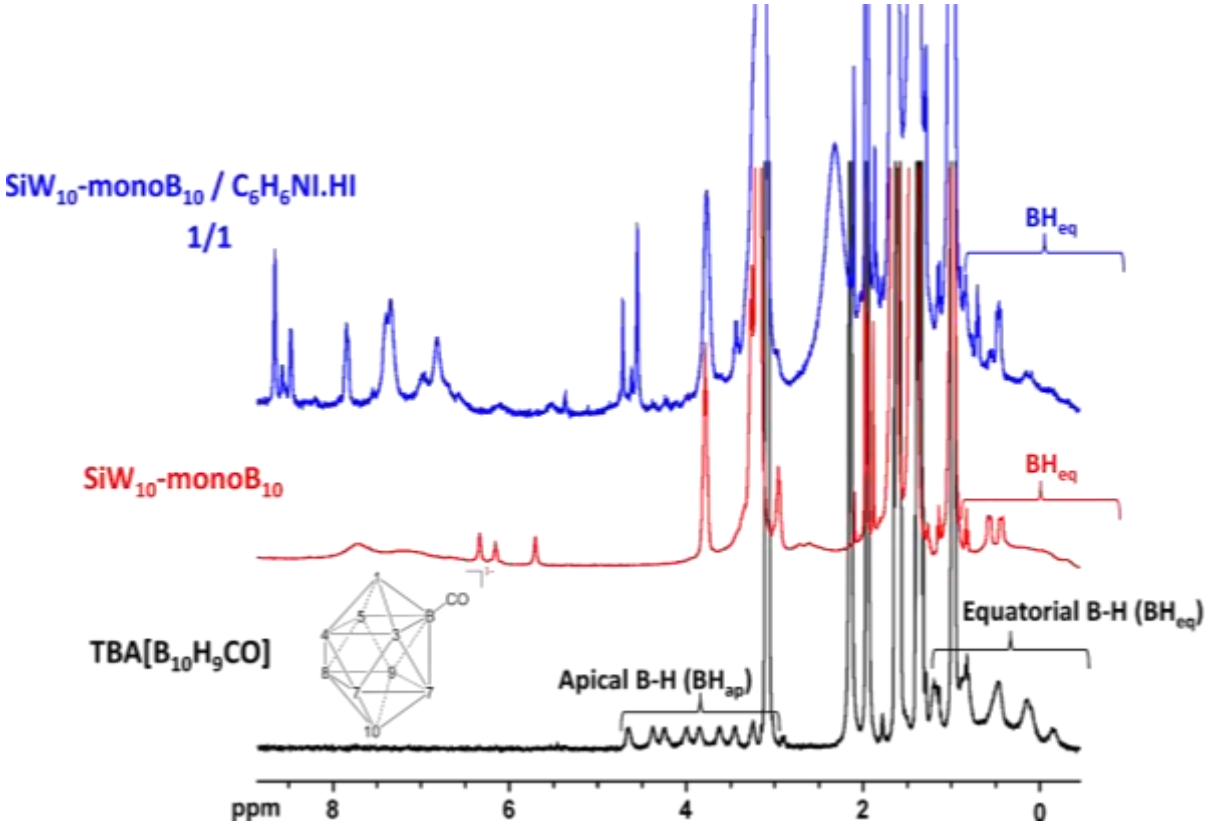

Figure 16. ^{1}H NMR spectra of ***TBA[$B_{10}H_9CO$], SiW_{10}-monoB$_{10}$*** *, and* ***SiW_{10}-monoB$_{10}$/C_6H_6NI.HI*** *mixture of the proportion* ***(1/1)*** *in CD_3CN at 400MHz.*

In the $^{1}H\{^{11}B\}$ spectra of SiW_{10}-monoB$_{10}$ (Figure 17), the equatorial B-H groups are seen in the range between -0.4 and +1.2 ppm, shifting from that of TBA[$B_{10}H_9CO$] at 0.4-0.7 ppm. However, the apical B-H groups couldn't be seen because they are probably masked with TBA^+ cations signals at 3.25 ppm. Concerning the spectra of the SiW_{10}-monoB$_{10}$/C_6H_6NI mixture, broad equatorial B-H signals were seen and correspond to the boron precursor $[B_{10}H_9CO]^-$ with a small shift, in agreement with the hydrolysis of the mono-adduct into SiW_{10}-APTES and $[B_{10}H_9CO]^-$, while the apical B-H groups, as for SiW_{10}-monoB$_{10}$ are not observed.

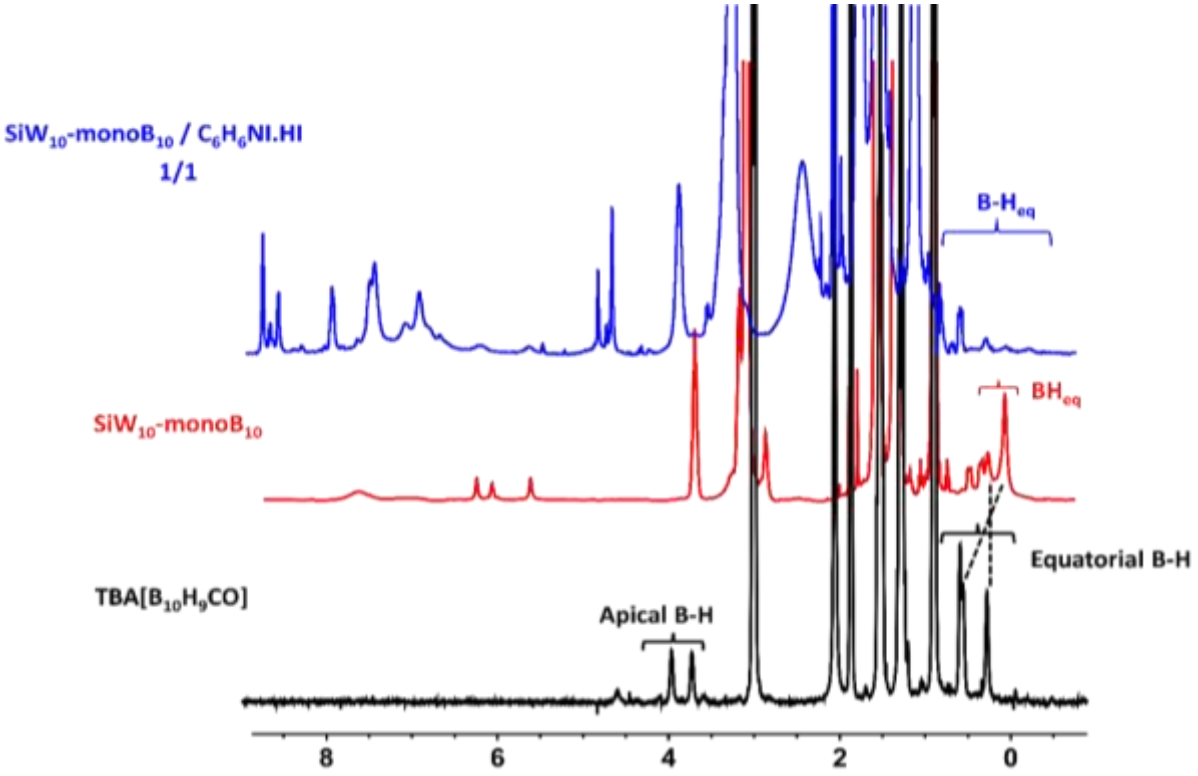

Figure 17. $^{1}H\{^{11}B\}$ NMR spectra (400MHz) of ***TBA[$B_{10}H_9CO$]****,* ***SiW_{10}-monoB_{10}*** *and* ***SiW_{10}-monoB_{10} /C_6H_6NI.HI*** *mixture of the proportion* ***1/1*** *in CD_3CN.*

The comparison between the $^{11}B\{^{1}H\}$ spectra of TBA[$B_{10}H_9CO$], SiW_{10}-monoB_{10} and the SiW_{10}-monoB_{10}/C_6H_6NI.HI mixture of the proportion 1/1 in (Figure 18) confirms this hypothesis. It reveals the presence of two sets of peaks attributed to two different types of B_{10} clusters, [**$B_{10}H_9CO$**]$^{-}$ and [($SiW_{10}O_{36}$)(**$B_{10}H_9CO$**NHC_3H_6Si)($NH_2C_3H_6Si$)O]$^{6-}$. The appearance of the singlet at -44.4 ppm characteristic of the equatorial boron at position 2 (B2) carrying the CO substituent signifies the breakage of the amide bond -NH-C(O)B_{10} resulting in free SiW_{10}-APTES and [$B_{10}H_9CO$]$^{-}$, which was not easily seen by ^{1}H NMR studies because of the broadness of the peaks [7]. On the other hand, the peak at -25.5 ppm of B(2)-C(O)NH- confirms the presence of unreacted SiW_{10}-monoB_{10}, in agreement with ^{1}H NMR studies. (See ^{11}B spectra of TBA[$B_{10}H_9CO$], SiW_{10}-monoB_{10}, and the SiW_{10}-monoB_{10}/C_6H_6NI.HI mixture of the proportion 1/1 in Figures S2, S3 and S4 in the appendix, respectively).

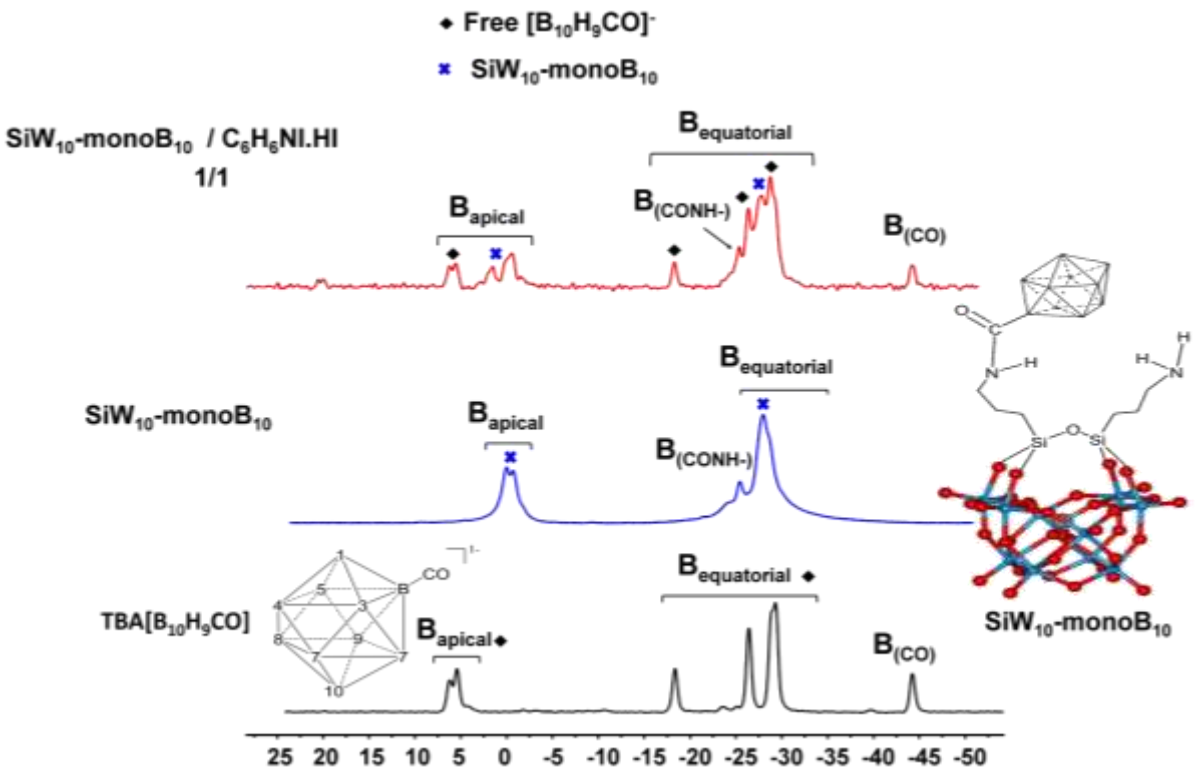

Figure 18. $^{11}B\{^1H\}$ NMR spectra (400MHz) of ***TBA[$B_{10}H_9CO$], SiW_{10}-monoB$_{10}$*** *and* ***SiW_{10}-monoB$_{10}$ /$C_6H_6NI.HI$*** *mixture of the proportion* ***1/1*** *in CD_3CN.*

In summary, the presence of pyridinium salt of iodide and the organic ligand C_6H_6NI causes hydrolysis of the amide group formed between SiW_{10}-APTES and $[B_{10}H_9CO]^-$ which conflicts with our expectations of synthesizing POM hybrid carrying the B_{10} cluster beside a different functional group. Therefore, it is evident that using N,N-Diisopropylethylamine base to neutralize the acidic medium is needed in further experiments.

Mixtures SiW_{10}-monoB$_{10}$/3-(Iodomethyl)pyridine hydroiodide/DIPEA

To evaluate the effect of DIPEA on the reaction between the free amino group of the SiW_{10}-monoB$_{10}$ and the Iodomethyl group of $C_6H_6NI.HI$, we fixed the amount of SiW_{10}-monoB$_{10}$ and $C_6H_6NI.HI$ while varied that of DIPEA. The ^1H NMR spectra of **SiW_{10}-monoB$_{10}$/ $C_6H_6NI.HI$/DIPEA** mixtures are given in Figure 19.

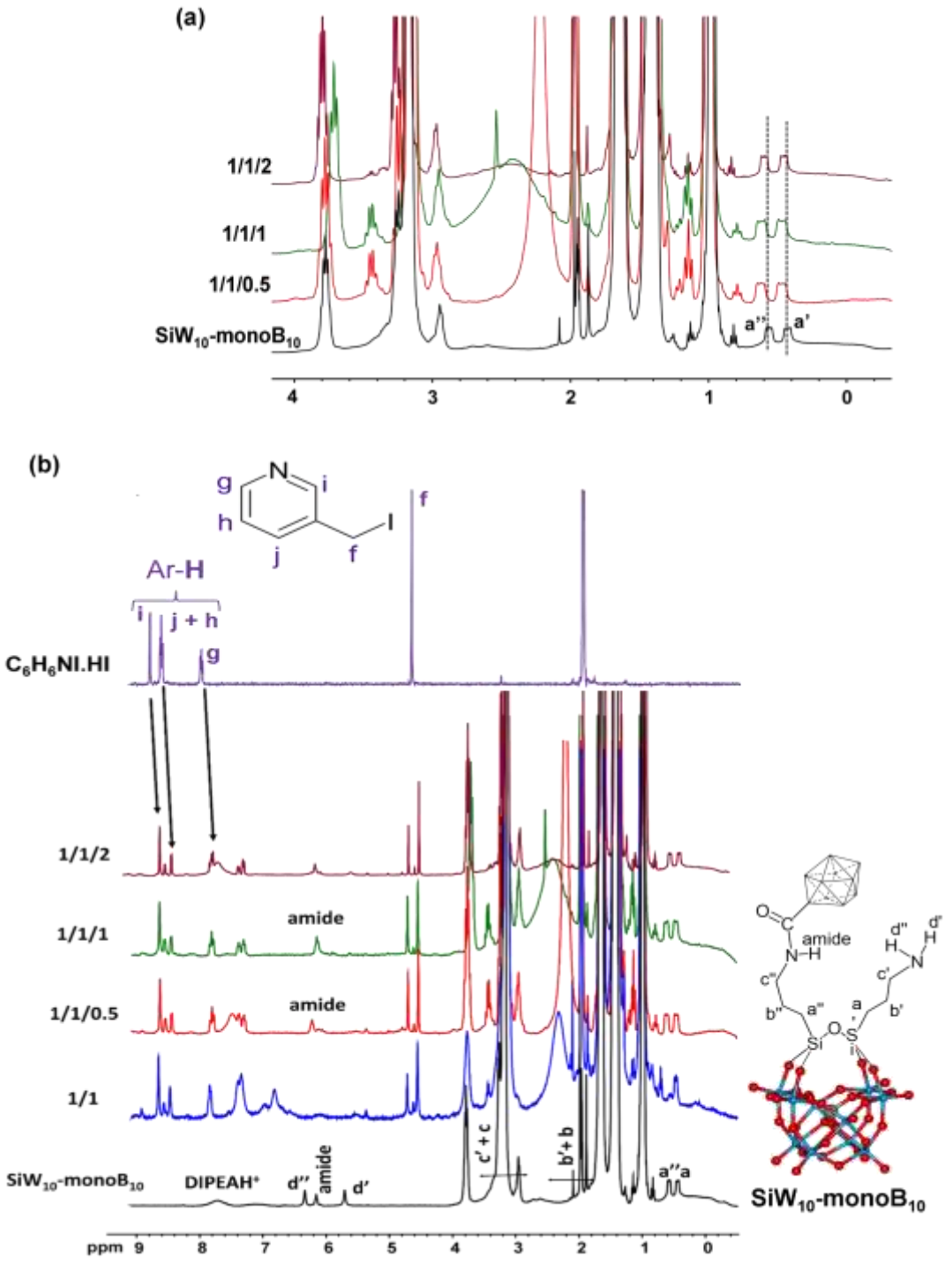

Figure 19. ^{1}H NMR spectra (300MHz) of the reaction medium of ***SiW$_{10}$-monoB$_{10}$/C$_6$H$_6$NI.HI/DIPEA*** *with different proportions in CD_3CN in the range -0.5-4.1 ppm* ***(a)*** *, and -0.5-9 ppm* ***(b)****.*

When increasing the amount of DIPEA added from 0.5 to 2eq, the «a'» and «a''» small signals of APTES methylene protons in SiW_{10}-$monoB_{10}$ slightly shift from 0.45 and 0.57 ppm to 0.47 and 0.62 ppm, respectively (Figure 19a). This could suggest that a new POM adduct is formed with a C_{2v} geometry with two non-equivalent APTES arms. One arm should contain the B(2)-

C(O)NH- amide bond formed between the B_{10} cage and the SiW_{10}-APTES, appearing as a broad peak at 6.23 ppm (Figure 19b).

The second arm could contain either the unreacted amine group in interaction with reactants or the expected group of the ligand (-CH_2-C_5H_4N) grafted to the POM. The comparison of SiW_{10}-monoB_{10}/C_6H_6NI.HI/DIPEA mixtures spectra with the spectra of free C_6H_6NI, shows a significant splitting of the methyl and aromatic protons of the ligand in the regions 4.4-4.9 ppm and 7-8.6 ppm, respectively (Figure 19b), as previously seen in the ^1H spectra of SiW_{10}-monoB_{10} /C_6H_6NI.HI mixtures of the proportions (1/1 and 1/2) without a base added (Figures 15b), but in the latter mixtures, the SiW_{10}-monoB_{10} was hydrolyzed into SiW_{10}-APTES, and the hypothesis of the formation of a hybrid POM with methylpyridine groups was supposed. In the present case, the SiW_{10}-monoB_{10} is preserved, so that this hypothesis couldn't be applied here.

The $^{11}B\{^1H\}$ and ^{11}B NMR spectra of SiW_{10}-monoB_{10} /C_6H_6NI.HI solutions with 0.5, 1 or 2eq of added DIPEA, shown in Figures 20 and S5 (in the appendix); respectively, confirm this hypothesis since the amide group B(2)-C(O)NH- amide remained intact, in agreement with the ^1H spectrum (Figure 19). We figured out that DIPEA prevents the dissociation of the B_{10} cluster from SiW_{10}-monoB_{10} by neutralizing the acids in the medium.

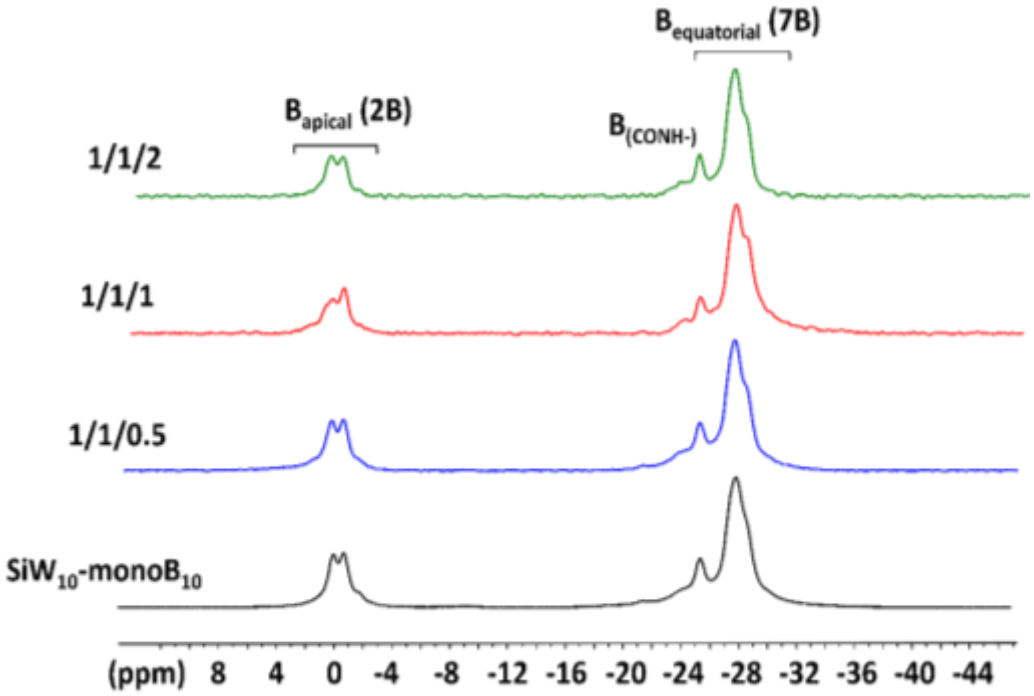

Figure 20.$^1B\{^1H\}$ NMR spectra (400MHz) of ***TBA[$B_{10}H_9CO$]***, ***SiW_{10}-monoB_{10}*** *and* ***SiW_{10}-monoB_{10} /C_6H_6NI.HI*** *mixture of the proportion* ***1/1*** *in CD_3CN.*

Figure 22 showing the modification of the ^1H NMR spectrum of free C_6H_6NI upon adding 2eq of DIPEA (see spectrum of DIPEA-HCl in Figure 21) gives another hypothesis. These spectra evidence that DIPEA base, which was chosen in this work based on its non-reactivity with our

reactants, provokes the splitting of the signals of the $C_6H_6NI.HI$, which suggests the presence of some reactivity between both the ligand and the base.

In particular, the three signals attributed to protons ”f" of the ligand in the region between 4.63 and 4.7 ppm are observed in the mixture of $C_6H_6NI.HI$ and DIPEA with or without the presence of POM but with a different ratio. This point is not in favor of the formation of the expected adduct. In these conditions, the variation of the chemical shift of the ligand and of the protons a’ and a” detected in the ^1H spectra of SiW_{10}-monoB_{10}/$C_6H_6NI.HI$/DIPEA mixtures of different proportion (Figures 19) are probably due to the reactivity of the ligand with DIPEA and only interaction by H-bond and/or H-H dihydrogen contact between the ligand and the SiW_{10}-APTES-monoB_{10} precursor.

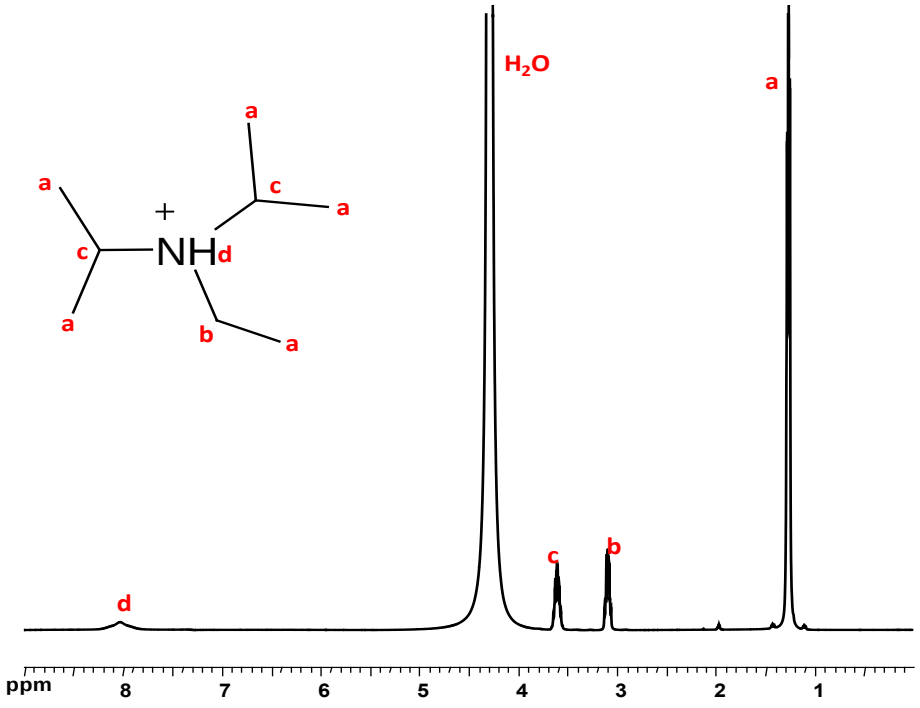

*Figure 21. ^1H NMR spectrum of **DIPEA-HCl** in CD_3CN.*

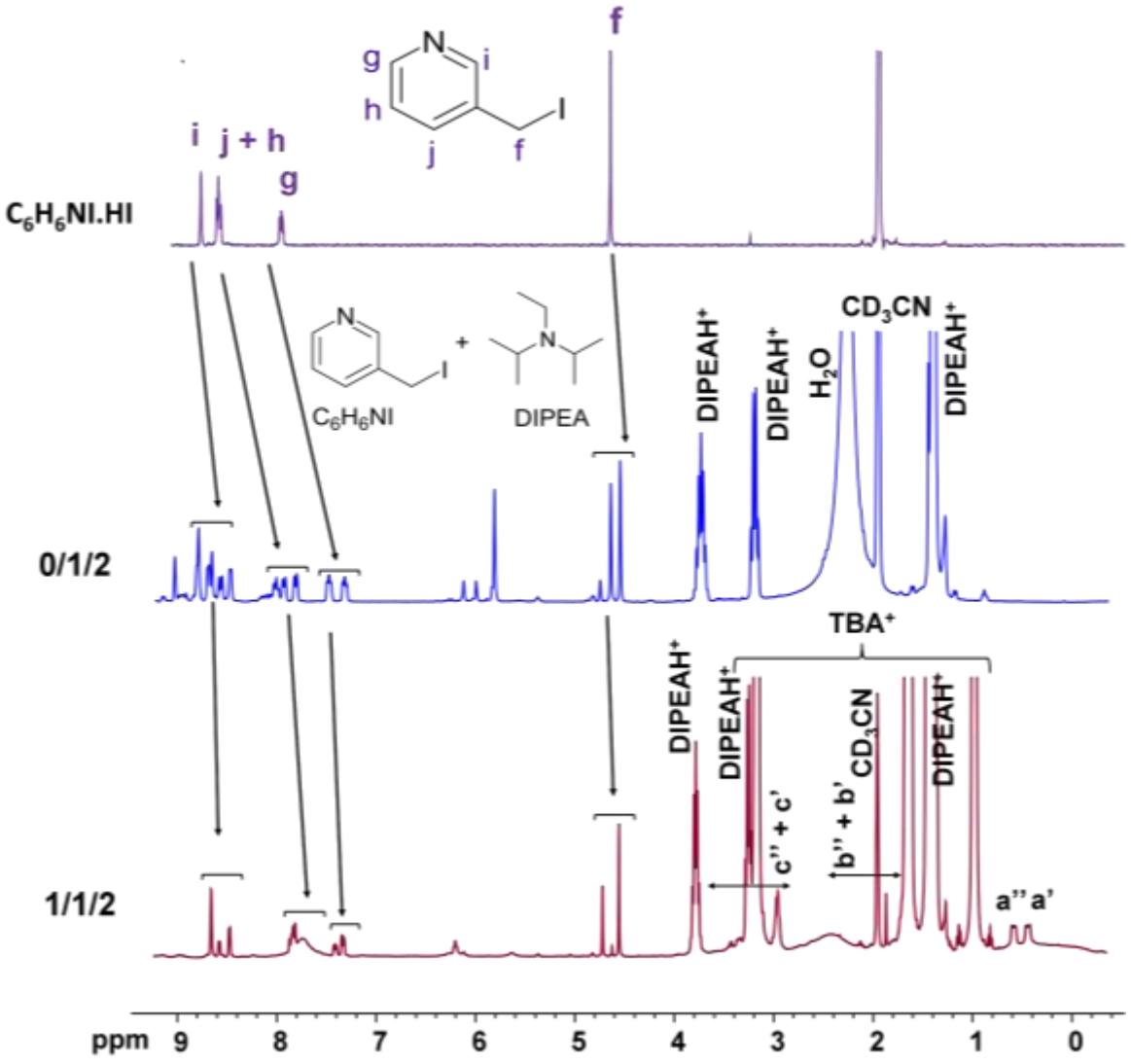

*Figure 22. ^{1}H NMR spectra (300MHz) of the reaction medium of **SiW_{10}-monoB_{10}/C_6H_6NI.HI/DIPEA** of the proportions (**1/1/2**, **0/1/2**, and **0/1/0**) in CD_3CN.*

Mixtures SiW_{10}-monoB_{10}/3-(Iodomethyl)pyridine hydroiodide/K_2CO_3

In a last attempt, we decided to replace the DIPEA base with the inorganic base K_2CO_3; perhaps the ^{1}H NMR will be less tricky, so we would understand what happened on the organic side and consequently try to optimize the conditions for synthesizing the «**SiW_{10}-B_{10}-Organic ligand»** adduct. Even so, K_2CO_3 unfortunately didn't contribute to anything different than the DIPEA base in comparing the spectra of the reaction medium SiW_{10}-monoB_{10}/ C_6H_6NI.HI with DIPEA (Figure 23a) or K_2CO_3 (Figure 23b).

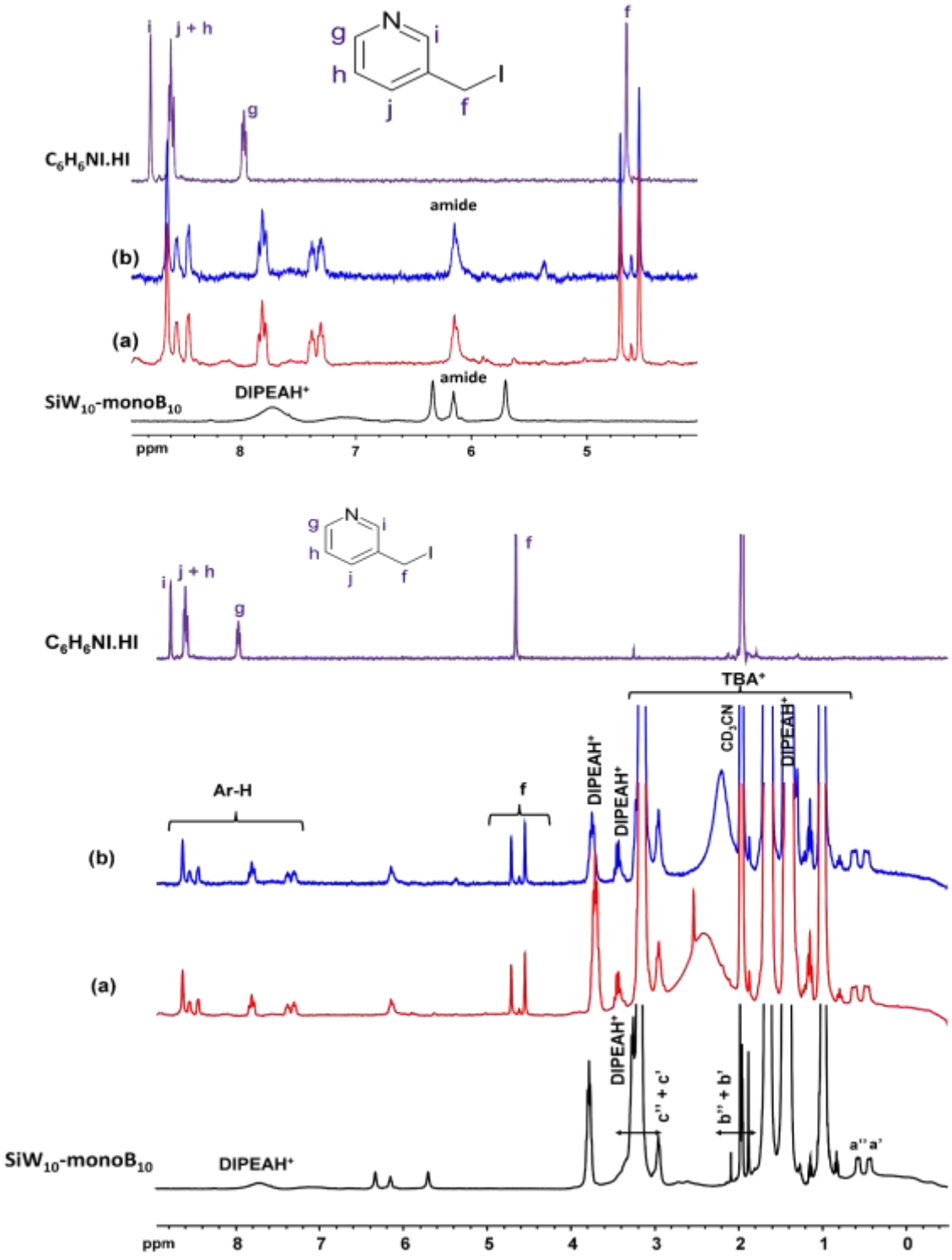

Figure 23.[1]H NMR spectra (400 MHz) of SiW_{10}-$monoB_{10}$, the reaction medius of ***(a)*** *SiW_{10}-$monoB_{10}$/$C_6H_6NI.HI$/DIPEA and* ***(b)*** *SiW_{10}-$monoB_{10}$ /$C_6H_6NI.HI$/K_2CO_3 of the proportion 1/1/1, and $C_6H_6NI.HI$ in CD_3CN in the ranges 4-9ppm* ***(top)*** *and -0.5 -9 ppm* ***(bottom)****.*

V. Conclusion

In conclusion to this chapter, the ^{1}H and ^{11}B NMR studies in solution to associate a second functional group with the free amine of SiW_{10}-monoB_{10} revealed to be very complicated and the SiW_{10}-monoB_{10} appears sensitive to hydrolysis.

No reaction was obtained with **pyridine-4-carboxaldehyde** and **4-chloromethyl benzonitrile**, probably because of the intramolecular hydrogen bonding formed between the free amine group and hydrides of the B_{10} cluster in the SiW_{10}-monoB_{10} compound, which was identified by ^{1}H NMR, ^{1}H-^{15}N HMBC NMR and DFT calculations of SiW_{10}-monoB_{10} that particularly proves it formation is energetically favorable which led to its stabilization.

By trying to form intramolecular H-H contact between SiW_{10}-monoB_{10} and **3-(Iodomethyl)pyridine**, we observed some reactivity, but the reaction is highly dependent on the experimental conditions, and the adducts possibly formed are not stable in time, which preclude further investigation.

Once again, intermolecular interactions between reactants are preferred. Such interactions are not so surprising. It seems clear to us that these interactions between POM and protonated reagents are sometimes so strong that they are preferred to the formation of covalent bonds. This is true in aqueous media, as highlighted by Nancy Watfa in her thesis with the very strong interaction of alkyl ammonium cations with keplerate-type POMs [22], but also in Mouhammad Awada's work at Versailles with keplerate and proline ligands [23]. In this case, the interaction with the protonated amine function is stronger than the coordination of the carboxylate function and it is not possible to carry out the coordination reaction.

In our case, we can assume strong interactions between the POM moiety and the protonated ligand, but also very strong H-H interactions between the boron cluster and the protonated ligand, or hydrogen interactions between the POM-amine and the non-protonated ligand. We think that maybe such interactions are particularly stronger in organic medium and discussion with other groups working on similar topics seems in agreement with that. This point would deserve a full study in organic medium but this is not the purpose of the PhD work.

Given this difficulty, we decided to discontinue our study on synthesizing a new POM-Borate hybrid and focus on the chemistry of each species alone: Hybrid POMs (see Chapter Three) and Borate-Cyclodextrins complexes (see Chapter Four).

VI. Experimental Part

VI.1 General procedures

Nuclear magnetic resonance (NMR). Solution spectra were recorded at 25 °C. ^{1}H,^{11}B, and ^{15}N NMR were measured with a Bruker Avance 400 MHz spectrometer equipped with a 5 mm BBI probe head and operated at a magnetic field strength of 9.4 T. Quartz NMR tubes are used to avoid background signals from the standard glass tubes in case of ^{11}B. CD_3CN was used as the solvent. Typically, ^{1}H spectra were recorded with one pulse sequence at a 30° flip angle (pulse duration 2.4 µs), using 1 s recycle delay, 1.6 s acquisition time, and 80 scans. In the case of samples containing boron, Waltz16 ^{11}B decoupling was applied during acquiring ^{1}H spectra. The ^{11}B spectra were recorded with Hahn echo sequence (echo delay 117 µs) under proton decoupling condition, using 0.1 s recycle delay, 21 ms acquisition time, and 1024 scans. According to conventional standards, chemical shifts are reported relative to 1% Me_4Si in $CDCl_3$ for ^{1}H NMR and 15% BF_3—Et_2O in $CDCl_3$ for ^{11}B NMR, according to conventional standards [24].

Elemental analyses. The analytical service of the CNRS at Gif sur Yvette, France, carried out elemental analyses of C, H, and N. Quantitative analyses of metals were carried out by ICP analysis, performed in CREALINS laboratory in Vernaison, France.

VI.2 Syntheses and isolation of products

All reagents were purchased from commercial sources and used without further purification**.** All synthetic reactions were performed under an Argon atmosphere using a vacuum line and Schlenk-techniques. All solvents were dried and distilled unless stated otherwise because of the sensitivity of the boron precursor used. $(NH_4)_2[B_{10}H_{10}]$ is provided by katchem company and $(TBA)_2[B_{10}H_{10}]$ was precipitated from an aqueous solution of $(NH_4)_2[B_{10}H_{10}]$ using saturated solution of TBABr. $K_8(\beta_2\text{-}SiW_{11}O_{39}).14H_2O$ and $K_8(\gamma\text{-}SiW_{10}O_{36}).12H_2O$ POMs were prepared according to the literature and checked by routine methods.

VI.2.1 Synthesis of the *closo*-decaborate carbonyl derivative $TBA[B_{10}H_9CO]$

$(TBA)_2[B_{10}H_{10}]$ (4 g, 6.6 mmol) was dissolved in 150 mL of dry CH_2Cl_2 and stirred under an inert atmosphere while the flask was placed in an ice path. Then, oxalyl chloride solution $COCl_2$ (2 mL, 22.9 mmol) was added with a syringe, and the mixture was stirred at 0 °C for 30 min. The solution was allowed to warm to room temperature and stirred for an additional 30 min. Later, the volume of the solution was reduced by 2/3 under reduced pressure. After evaporation in vacuum, 2.28 g of a yellow product corresponding to $TBA[B_{10}H_9CO]$ was obtained (yield 88.9 %). The product was analyzed by FT-IR, ESI-MS, and ^{11}B NMR in CH_3CN; all were consistent with the literature.

FT-IR spectrum is given in Figure S6 in the appendix. In addition to the vibration bands of TBA cations, the spectrum displays the characteristic bands at 2515 cm^{-1} and 2095 cm^{-1} assigned to B-H and C≡O groups, respectively.**^{11}B NMR** (δ ppm, 400 MHz, CD_3CN): 5.4 (s, 1 B), 6.2 (s, 1 B), -18.3 (s, 1 B), -26.5 (s, 2 B), -28.9 (s, 2 B), -29.4 (s, 2 B), -44.4 (s, 1 B),**^{11}B{^{1}H} NMR** (δ ppm, 400 MHz, CD_3CN): 5.4 (d, 1 B), 6.2 (d, 1 B), -18.3 (d, 1 B), -26.5 (d, 2 B), -28.9 (d, 2 B), -29.4 (d, 2 B), -44.4 (s, 1 B). **^{1}H NMR** (δ ppm, 400 MHz, CD_3CN):-0.27 to 0.64 (crown-like structure, 0.99 (t, TBA), 7 H equatorial), 1.63 (m, TBA), 1.38 (m, TBA),3.15 (t, TBA), 3.39 to 4.81 (crown-like structure, 2 H apical),**^{1}H{^{11}B} NMR** (δ ppm, 400 MHz, CD_3CN): 0.38 (d, 1 H),0.65 (d, 3 H), 0.69 (d, 4 H), 3.83 (s, 1 H),4.06 (s, 1 H), in addition to TBA^+ peaks listed above.

VI.2.2 Synthesis of $(Bu_4N)_3H[(\gamma\text{-}SiW_{10}O_{36})(Si(CH_2)_3NH_2)_2O].3H_2O$, denoted hereafter SiW_{10}-APTES.

According to Mayer's work, $k_8(\gamma\text{-}SiW_{10}O_{36}).12H_2O$ (6 g, 2 mmol) was suspended with NBu_4Br (1.94 g, six mmol) in a mixture of acetonitrile (60 mL) and water (16 mL). 3-aminopropyltriethoxysilane (0.94 mL, four mmol) and HCl (12 M, 1 mL) were successively added under vigorous stirring. The mixture was stirred for a further six hours. The white compound obtained after evaporation of the organic solution in a rotary evaporator was copiously washed with water, filtrated, and dried by ether. Purification was done by redissolving the solid in 40 mL acetonitrile, centrifugation to remove insoluble residue, then evaporation of acetonitrile in a vacuum to yield 5.6 g of the light-yellow product (82 %).

FT-IR spectrum is given in Figure S7 in the appendix. IR (v/cm^{-1}): 2962 (m), 2936 (m, sh), 2874 (m), 1625 (m, br), 1483 (m), 1380 (w), 1101 (m), 1042 (m, br), 961 (m), 901 (s), 887 (s), 819 (s), 780 (s), 736 (m, br). **Elemental analysis** for $(NBu_4)_3H[(\gamma\text{-}SiW_{10}O_{36})(Si(CH_2)_3\ NH_2)_2O].3H_2O$ ($C_{54}H_{131}N_5O_{40}Si_3W_{10}$, MW = 3413.4 $g.mol^{-1}$),**EA(Calc.):** H (3.87); C (19.00); N (2.05),**EA(Found):** H 3(3.84); C(19.41); (2.04).**^{1}H NMR** (δ ppm, 400.13 MHz, CD_3CN): 0.75 (t, -SiC**H$_2$**$CH_2CH_2NH_2$),), 1.01 (t, TBA), 1.45 (m, TBA),1.67 (m, TBA),1.91 (m, -$SiCH_2C$**H$_2$**CH_2NH_2),3.21 (t, TBA),3.30 (t, -$SiCH_2CH_2C$**H$_2$**NH_2),7.30 (s, -$SiCH_2CH_2CH_2N$**H$_2$**).

VI.2.3 Synthesis of $(TBA)_3(DIPEAH)_3[(SiW_{10}O_{36})(B_{10}H_9CONHC_3H_6Si)(NH_2C_3H_6Si)O].3H_2O$, noted as SiW_{10}-monoB_{10} .

The synthesis of **SiW_{10}-APTES** was adapted from Diab's work [9].SiW_{10}-APTES (1 g, 0.29 mmol) was dissolved in 2 mL of dry acetonitrile, then $TBA[B_{10}H_9CO]$ (113 mg, 0.29 mmol) was added with 1 mL of dry acetonitrile and stirred till total solubility. DIPEA (76 µL, 0.44 mmol) was added drop by drop with vigorous stirring. The solution was kept at room temperature for 3 hours under Nitrogen. After the reaction time, the solution was kept under the hood for evaporation of the acetonitrile phase. An oily residue was obtained and triturated by diethyl ether until a dry light-yellow solid was obtained, filtrated, washed with diethyl ether for removing the excess of DIPEA and dried under vacuum for a few hours to yield 1.1 g of $(C_{16}H_{36}N)_3(C_8H_{19}N)_3[(SiW_{10}O_{36})\ (B_{10}H_9CONHC_3H_6Si)(NH_2C_3H_6Si)O](H_2O)_3$ (96.2 %).

FT-IR spectrum is given in Figure S8 in the appendix: 2961 (m), 2933 (m, sh), 2873 (m), 2469 (m), 1664 (sh), 1626 (m, br), 1482 (m), 1380 (w), 1099 (m), 959 (m), 899 (s), 884 (s), 819 (s), 733 (m, br). **Elemental analysis** for $B_{10}C_{79}H_{195}N_8O_{41}Si_3W_{10}$ (MW = 3944.31g.mol^{-1}). **EA(Calc.):** H(4.98); C(24.06); N(2.84); B(2.74); Si (2.14), **EA(Found)**: H(4.83); C(24.18); N(2.12); B(2.39); Si(1.87).^{1}**H NMR** (δ ppm, 400.13 MHz, CD_3CN): 0.45 (t,-SiC**H$_2$**$CH_2CH_2NH_2$), 0.57 (t,-SiC**H$_2$**CH_2CH_2NHCO-), 1.01 (t,TBA(-$N^+CH_2CH_2CH_2C$**H$_3$**)),1.45 (overlapping TBA (-$N^+CH_2CH_2C$**H$_2$**CH_3) and DIPEAH$^+$ ([$(CH_3)_2CH]_2NH^+CH_2C$**H$_3$**) ,1.68 (m, TBA (-N^+CH_2C**H$_2$**CH_2CH_3)), 1.90 (m, -$SiCH_2C$**H$_2$**CH_2NH_2 and $SiCH_2C$**H$_2$**CH_2NHCO- overlapped with CH_3CN), 2.97 (t, -$SiCH_2CH_2C$**H$_2$**NH_2), 3.19 (t, TBA$^+$ (-N^+C**H$_2$**$CH_2CH_2CH_3$)), 3.26 (sh,DIPEAH$^+$ ([$(CH_3)_2CH]_2NH^+C$**H$_2$**CH_3) overlapped with TBA$^+$ peak), 3.43 (t, -$SiCH_2CH_2C$**H$_2$**NHCO-), 3.77 (m, DIPEAH$^+$ ([$(CH_3)_2C$**H**$]_2NH^+CH_2CH_3$), 6.15 (s, -$SiCH_2CH_2CH_2N$**H**CO-), 7.24 (s, -$SiCH_2CH_2CH_2N$**H$_2$**), 8.72 (s, DIPEAH$^+$ ([$(CH_3)_2CH]_2N$**H**$^+CH_2CH_3$). ^{11}**B{^{1}H} NMR** (δ ppm, 128.38 MHz, CD_3CN): -0.047 (d, 1 B), -0.8 (d, 1 B), -25.6 (s, 1 B), -28.0 (m, broad, 7 B).

VII. References

(1) Mahfouz, N.; Ghaida, F. A.; El Hajj, Z.; Diab, M.; Floquet, S.; Mehdi, A.; Naoufal, D. Recent Achievements on Functionalization within Closo-Decahydrodecaborate $[B_{10}H_{10}]^{2-}$ Clusters. *ChemistrySelect* **2022**, *7* (21), e202200770. https://doi.org/10.1002/slct.202200770.

(2) Sadakane, M.; Steckhan, E. Electrochemical Properties of Polyoxometalates as Electrocatalysts. *Chem. Rev.* **1998**, *98* (1), 219–238. https://doi.org/10.1021/cr960403a.

(3) Zamolo, V. A.; Modugno, G.; Lubian, E.; Cazzolaro, A.; Mancin, F.; Giotta, L.; Mastrogiacomo, D.; Valli, L.; Saccani, A.; Krol, S.; Bonchio, M.; Carraro, M. Selective Targeting of Proteins by Hybrid Polyoxometalates: Interaction Between a Bis-Biotinylated Hybrid Conjugate and Avidin. *Frontiers in Chemistry* **2018**, *6*.

(4) Marcoux, P. R.; Hasenknopf, B.; Vaissermann, J.; Gouzerh, P. Developing Remote Metal Binding Sites in Heteropolymolybdates. *European Journal of Inorganic Chemistry* **2003**, *2003* (13), 2406. https://doi.org/10.1002/ejic.200200677.

(5) Mayer, C.; Fournier, I.; Thouvenot, R. Bis- and Tetrakis(Organosilyl) Decatungstosilicate, $[\gamma\text{-}SiW_{10}O_{36}(RSi)_2O]^{4-}$ and $[\gamma\text{-}SiW_{10}O_{36}(RSiO)_4]^{4-}$: Synthesis and Structural Determination by Multinuclear NMR Spectroscopy and Matrix-Assisted Laser Desorption/Desorption Time-of-Flight Mass Spectrometry. *Chemistry - A European Journal* **2000**, *6*, 105–110. https://doi.org/10.1002/(SICI)1521-3765(20000103)6:1<105::AID-CHEM105>3.0.CO;2-L.

(6) Mayer, C. R.; Roch-Marchal, C.; Lavanant, H.; Thouvenot, R.; Sellier, N.; Blais, J.-C.; Sécheresse, F. New Organosilyl Derivatives of the Dawson Polyoxometalate $[\alpha_2\text{-}P_2W_{17}O_{61}(RSi)_2O]^{6-}$: Synthesis and Mass Spectrometric Investigation. *Chemistry – A European Journal* **2004**, *10* (21), 5517–5523. https://doi.org/10.1002/chem.200400217.

(7) Shelly, K.; Knobler, C. B.; Hawthorne, M. F. Synthesis of Monosubstituted Derivatives of closo-Decahydrodecaborate(2-). X-Ray Crystal Structures of $[closo\text{-}2\text{-}B_{10}H_9CO]^-$ and $[closo\text{-}2\text{-}B_{10}H_9NCO]^{2-}$. *Inorg. Chem.* **1992**, *31* (13), 2889–2892. https://doi.org/10.1021/ic00039a041.

(8) Diab, M.; Mateo, A.; Cheikh, J. A.; Haouas, M.; Ranjbari, A.; Bourdreux, F.; Naoufal, D.; Cadot, E.; Bo, C.; Floquet, S. Unprecedented Coupling Reaction between Two Anionic Species of a Closo-Decahydrodecaborate Cluster and an Anderson-Type Polyoxometalate. *Dalton Trans.* **2020**, *49* (15), 4685–4689. https://doi.org/10.1039/C9DT04676C.

(9) Diab, M.; Mateo, A.; El Cheikh, J.; El Hajj, Z.; Haouas, M.; Ranjbari, A.; Guérineau, V.; Touboul, D.; Leclerc, N.; Cadot, E.; Naoufal, D.; Bo, C.; Floquet, S. Grafting of Anionic Decahydro-Closo-Decaborate Clusters on Keggin and Dawson-Type Polyoxometalates: Syntheses, Studies in Solution, DFT Calculations and Electrochemical Properties. *Molecules* **2022**, *27* (22), 7663. https://doi.org/10.3390/molecules27227663.

(10) Yisgedu, T. B.; Chen, X.; Lingam, H. K.; Huang, Z.; Meyers, E. A.; Shore, S. G.; Zhao, J.-C. Intermolecular Dihydrogen- and Hydrogen-Bonding Interactions in Diammonium Closo-Decahydrodecaborate Sesquihydrate. *Acta Crystallogr C* **2010**, *66* (Pt 1), m1-3. https://doi.org/10.1107/S0108270109040815.

(11) Sivaev, I. B. Nitrogen Heterocyclic Salts of Polyhedral Borane Anions: From Ionic Liquids to Energetic Materials. *Chem Heterocycl Comp* **2017**, *53* (6), 638–658. https://doi.org/10.1007/s10593-017-2106-9.

(12) Avdeeva, V. V.; Polyakova, I. N.; Goeva, L. V.; Buzanov, G. A.; Malinina, E. A.; Kuznetsov, N. T. Synthesis and Structure of $[NiL_6][B_{10}H_{10}]$ (L=DMF or DMSO) as Precursors for Solid-Phase Synthesis of

Nickel(II) Coordination Compounds. *Inorganica Chimica Acta* **2016**, *451*, 129–134. https://doi.org/10.1016/j.ica.2016.07.016.
(13) Carraro, M.; Modugno, G.; Fiorani, G.; Maccato, C.; Sartorel, A.; Bonchio, M. Organic-Inorganic Molecular Nano-Sensors: A Bis-Dansylated Tweezer-Like Fluoroionophore Integrating a Polyoxometalate Core. *European Journal of Organic Chemistry* **2011**, *2012* (2), 281.
(14) Bonchio, M.; Carraro, M.; Scorrano, G.; Bagno, A. Photooxidation in Water by New Hybrid Molecular Photocatalysts Integrating an Organic Sensitizer with a Polyoxometalate Core. *Advanced Synthesis & Catalysis* **2004**, *346* (6), 648–654. https://doi.org/10.1002/adsc.200303189.
(15) Abi-Ghaida, F.; Laila, Z.; Ibrahim, G.; Naoufal, D.; Mehdi, A. New Triethoxysilylated 10-Vertex Closo-Decaborate Clusters. Synthesis and Controlled Immobilization into Mesoporous Silica. *Dalton Trans.* **2014**, *43* (34), 13087–13095. https://doi.org/10.1039/C4DT00772G.
(16) Izzet, G.; Abécassis, B.; Brouri, D.; Piot, M.; Matt, B.; Serapian, S. A.; Bo, C.; Proust, A. Hierarchical Self-Assembly of Polyoxometalate-Based Hybrids Driven by Metal Coordination and Electrostatic Interactions: From Discrete Supramolecular Species to Dense Monodisperse Nanoparticles. *J. Am. Chem. Soc.* **2016**, *138* (15), 5093–5099. https://doi.org/10.1021/jacs.6b00972.
(17) Piot, M.; Hupin, S.; Lavanant, H.; Afonso, C.; Bouteiller, L.; Proust, A.; Izzet, G. Charge Effect on the Formation of Polyoxometalate-Based Supramolecular Polygons Driven by Metal Coordination. *Inorg. Chem.* **2017**, *56* (14), 8490–8496. https://doi.org/10.1021/acs.inorgchem.7b01187.
(18) Li, C.; Xu, F.; Zhao, Y.; Zheng, W.; Zeng, W.; Luo, Q.; Wang, Z.; Wu, K.; Du, J.; Wang, F. Platinum(II) Terpyridine Anticancer Complexes Possessing Multiple Mode of DNA Interaction and EGFR Inhibiting Activity. *Front Chem* **2020**, *8*, 210. https://doi.org/10.3389/fchem.2020.00210.
(19) Martinho, N.; Santos, T. C. B.; Florindo, H. F.; Silva, L. C. Cisplatin-Membrane Interactions and Their Influence on Platinum Complexes Activity and Toxicity. *Frontiers in Physiology* **2019**, *9*.
(20) Bijelic, A.; Aureliano, M.; Rompel, A. Polyoxometalates as Potential Next-Generation Metallodrugs in the Combat Against Cancer. *Angew Chem Int Ed Engl* **2019**, *58* (10), 2980–2999. https://doi.org/10.1002/anie.201803868.
(21) Floquet, S.; Brun, S.; Lemonnier, J.-F.; Henry, M.; Delsuc, M.-A.; Prigent, Y.; Cadot, E.; Taulelle, F. Molecular Weights of Cyclic and Hollow Clusters Measured by DOSY NMR Spectroscopy. *J Am Chem Soc* **2009**, *131* (47), 17254–17259. https://doi.org/10.1021/ja9052619.
(22) Watfa, N.; Melgar, D.; Haouas, M.; Taulelle, F.; Hijazi, A.; Naoufal, D.; Avalos, J. B.; Floquet, S.; Bo, C.; Cadot, E. Hydrophobic Effect as a Driving Force for Host–Guest Chemistry of a Multi-Receptor Keplerate-Type Capsule. *J. Am. Chem. Soc.* **2015**, *137* (17), 5845–5851. https://doi.org/10.1021/jacs.5b01526.
(23) Awada, M.; Floquet, S.; Haouas, M.; Watfa, N.; Marrot, J.; Roch-Marchal, C.; Coeffard, V.; Greck, C.; Bour, C.; Gandon, V.; Taulelle, F.; Cadot, E. Functionalization of Mo_{132} Keplerate Nanocapsules by Cyclic Carboxylates: L-Proline vs Cyclopentanecarboxylate. *Current Inorganic Chemistry (Discontinued)*. **2017**, *7* (1), 39–47.
(24) Harris, R. K.; Becker, E. D.; Cabral de Menezes, S. M.; Goodfellow, R.; Granger, P. NMR Nomenclature: Nuclear Spin Properties and Conventions for Chemical Shifts: IUPAC Recommendations 2001. *Solid State Nuclear Magnetic Resonance* **2002**, *22* (4), 458–483. https://doi.org/10.1006/snmr.2002.0063.

Chapter Three

Chapter 3: Visible light photoinitiators made of covalently bonded polyaromatics and polyoxometalates units.

I. Introduction

Photopolymerization processes are thriving nowadays due to their tremendous applications in 3D printing [1–3], adhesives and coatings manufacturing [4,5], and bioactive materials elaboration [6,7]. However, even today, an important part of the reported photoinitiators (PIs) is only active under UV irradiation [8–11]. Nevertheless, various strategies have been considered to elaborate new PIs active in the near UV and visible range by appropriately functionalizing PIs active only in the UV range. For example, anthraquinone (AQ) is a PI widely used for photopolymerization processes under UV light but is only marginally effective under visible light irradiation. Thus, its rational functionalization by organic groups has allowed to obtain derivatives active under irradiation in the visible range [12–17]. The same strategy has been applied to related PIs such as benzophenone [18–21] or anthracene [22–24].

Meanwhile, the inorganic POM clusters exhibit properties that can be exploited in numerous fields [25–27], these species being, for example, relevant for photochemical [28] or biological [29] applications due in particular to their unique redox behaviors. While the classical acid or alkali salts of POMs are generally highly soluble in water, limiting their recyclability and reusability in important applications such as catalysis [30], this disadvantage can be overcome by incorporating them into matrices. For instance, the decatungstate polyanion $[W_{10}O_{32}]^{4-}$ and the seminal $[PMo_{12}O_{40}]^{3-}$ and $[SiMo_{12}O_{40}]^{4-}$ Keggin species, highly recognized for their catalytic properties, have been immobilized into polymers using photopolymerization techniques. In that way, $[W_{10}O_{32}]^{4-}$ POMs were associated with silanes (or borane derivatives) and iodonium salts to promote free-radical cationic photopolymerization of epoxides under polychromatic Hg-Xe irradiation [31]. Similar results were obtained with the three-component photo-initiating systems $[XMo_{12}O_{40}]^{n-}$ (X = P, n = 3 or X = Si, n = 4) / hydrogen donors (silane, germane) / iodonium salts for initiating the radical and cationic polymerization of acrylates and epoxides under UV irradiation, respectively [32]. The reduction of iodonium salts by $[PMo_{12}O_{40}]^{3-}$ generates phenyl radicals (Ph•), which are involved in the H-abstraction reaction process with silane (or germane), thus forming initiating silyl (or germyl) radicals for free-radical polymerization of acrylate monomers. Subsequently, the oxidation of silyl (or germyl) radicals by iodonium salt leads to initiating cationic reactive species, which can afford free-radical-promoted cationic photopolymerization.

More recently, new structures of onium salts containing polyoxomolybdates or polyoxotungstates as counter anions were elegantly proposed [33]. Interestingly, POM derivatives proved effective for sensitizing iodonium salts by intramolecular electron transfer reaction under UV irradiation, generating radical and cationic species for synthesizing

interpenetrated epoxy/acrylate materials under air conditions. Moreover, the elaborated POM-containing polymers have also proved to be highly active in the degradation of pharmaceutical compounds or the degradation of dyes [34–36]. Noticeably, all the photosystems described above consist of a mixture of anionic POMs with cationic photoinitiators (PIs), allowing photopolymerization under irradiation with $\lambda \leq 405$ nm and leading to POM-incorporating composites. However, to the best of our knowledge, a covalent association of POMs and PIs has never been investigated, although such an association could bring new optical properties to the photosystem.

The reaction between the Lindqvist POM $[Mo_6O_{19}]^{2-}$ and organic amines, leading to imido derivatives, has been widely studied over the last two decades. As early as 2001, Peng et al. reported a protocol to obtain such hybrid species in high yield [37]. We can discuss their optical properties, taking as an example the naphthalene derivative $[Mo_6O_{18}N(C_{10}H_7)]^{2-}$. The lowest energy electronic transitions are observed at 300 nm for the 2-naphtaleneamine ligand and 325 nm for the $[Mo_6O_{19}]^{2-}$ precursor. This last transition was assigned to a charge-transfer from the oxygen π-type HOMO to the molybdenum π-type LUMO. Strikingly, in the hybrid complex $[Mo_6O_{18}N(C_{10}H_7)]^{2-}$, this band becomes more intense and is bathochromically shifted by nearly 60 nm (λ_{max} = 383 nm). This originates from the charge-transfer transition of the coordinated N atom to the molybdenum atom as a result of the delocalization of the π-electrons of the naphthalene ring to the hexamolybdate unit and evidences a strong electronic interaction between the POM and the covalently bonded organic conjugated ligand [38].

Obviously, the shift amplitude strongly depends on the π-electrons delocalization characterizing the organic sub-unit. It follows that such functionalization allows the tunability of the POM and organic substrate optical properties, and while the yellow $[Mo_6O_{19}]^{2-}$ precursor only poorly absorbs in the visible domain, strongly colored hybrid species can be obtained after the grafting of such colorless aromatic amines. However, to the best of our knowledge, the potentiality of such functionalized POMs to act as photoactive species in the visible range has never been explored.

From these perspectives, in this chapter, we report the synthesis of three novel imido derivatives $[Mo_6O_{18}NR]^{2-}$ obtained from the $[Mo_6O_{19}]^{2-}$ precursor and aromatic amino derivatives R-NH_2 of the anthracene, benzophenone, and anthraquinone photoinitiators, respectively (Figure 1). While these organic PIs are only active under UV irradiation or very poorly active under visible-light stimulation for the polymerization processes targeted in our study, their performances could increase enormously once connected to the POM unit. Importantly, this represents a novel strategy for shifting the organic photoinitiator's activity from UV to visible light irradiation.

The three isolated hybrid materials have been fully characterized in the solid-state and solution. Their optical and photophysical properties have been deeply studied by UV-vis spectroscopy, cyclic voltammetry, fluorescence, and laser flash photolysis experiments. Their

use for the free-radical polymerization of trimethylolpropane triacrylate (TMPTA) and soybean oil epoxidized acrylate (SOA) has also been investigated by Real-Time Fourier Transform InfraRed Spectroscopy (RT-FTIR) and electron paramagnetic resonance-spin trapping (EPR-ST). The influence of such POM derivatives on the mechanical properties of the obtained hybrid polymers is discussed.

Notably, TMPTA is a tri-functional monomer holding three vinyl groups, enabling it to interconnect with nearby polymers. It creates a highly crosslinked polymer matrix of low toxicity and high mechanical resistance, ideal for various industrial applications [39]. Soybean oil epoxidized acrylate (SOA) is a biodegradable and low-cost monomer, readily available through the epoxidation of the natural soybean vegetable oil, made up of triglyceride molecules ,followed by the ring-opening of the epoxide groups with acrylic acid [40] (Figure 1).

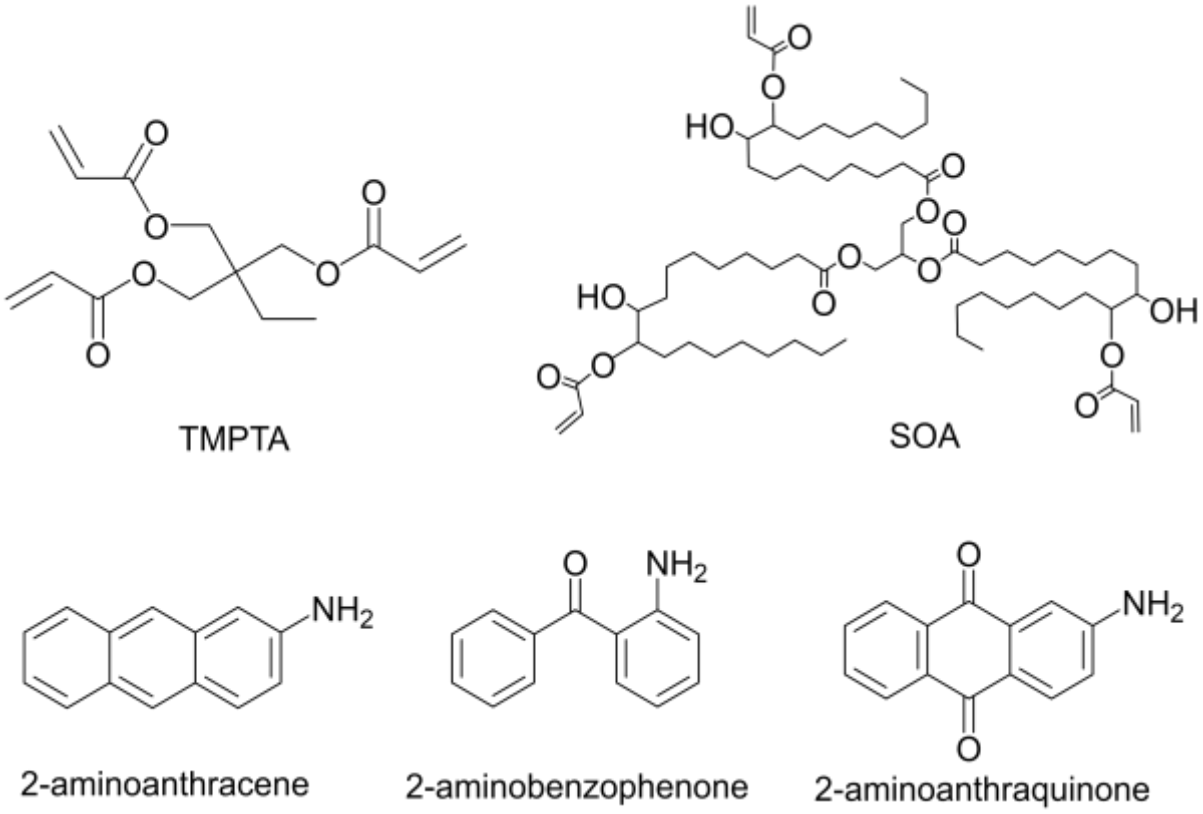

Figure 1. Chemical structures of TMPTA and SOA monomers,2-aminoanthracene, 2-aminobenzophenone, and 2-aminoanthraquinone.

II. General Strategy

Our strategy for synthesizing a new series of monosubstituted organoimido POM derivatives was mainly following the DCC (N, N'-dicylohexylcarbodiimide) dehydrating synthetic protocol established by Peng and Wei for POM-amine coupling reactions [37]. The presence of DCC was confirmed to be crucial for the reaction to proceed by two means: i) as a dehydrating agent since the $[Mo_6O_{18}(NAr)]^{2-}$ complexes are moisture sensitive and would decompose by

hydrolysis [41,42] and ii) as a catalyst because it activates the Mo-O terminal bond by increasing the electrophilicity of molybdenum atom so speeding up the reaction rate of the nucleophilic addition by amine ligands [43].

Initially, we had many attempts of reacting octamolybdate polyanion $[Mo_8O_{26}]^{4-}$ with aromatic amines (2-aminobenzophenone, 2-aminoanthracene, and 2-aminoanthraquinone) in the presence of DCC in refluxing acetonitrile. Unfortunately, the outcome wasn't satisfactory as we obtained a mixture of unidentified products. Hence, consequent trials were then performed to optimize the synthetic conditions (reactants amounts, temperature, solvent type, and reaction time...) to enhance the yield and purity of the POM derivatives. The synthetic procedure developed by Fielden et al. inspired us to prepare similar organoimido POM hybrids by replacing acetonitrile with DMSO [44–47]. It has also been found that organoimido functionalization of the Lindqvist POM $(TBA)_2[Mo_6O_{19}]$ (TBA= tetrabutylammonium) is more highly reactive and favored compared to other isopolyoxometalates or mixed-metal hexametalates since the former reaction is simple, direct, thermodynamically and kinetically favored [43,48–52].

In this manner, equivalent amounts of $(TBA)_2[Mo_6O_{19}]$ and the corresponding aromatic amines were reacted together in the presence of 1.4 equivalents of DCC in hot anhydrous DMSO (70°C) under an inert atmosphere (Figure 2), leading to the isolation of highly colored monosubstituted imidohexamolybdate derivatives $(TBA)_2[O_{18}Mo_6(NC_6H_4C(O)C_6H_5)]$ **(POM-AB),** $(TBA)_2[O_{18}Mo_6(NC_{14}H_9)]$ **(POM-AC)** and $(TBA)_2[O_{18}Mo_6(NC_{14}H_7O_2)]$ **(POM-AQ).**

Interestingly, the hybrids were optimally isolated in a very short reaction time (1 h), in contrast to previously reported POM imido derivatives, whose synthesis usually required at least 10 h. After one hour, the reaction mixture was filtered to discard the dicyclohexylcarbodiurea suspensions originating from DCC, and then the crude product was precipitated in a large quantity of diethyl ether. After purification, **POM-AB** and **POM-AC** are isolated as orange and dark red powders with 71% and 35% yields, respectively. While for **POM-AQ,** it is more complicated to estimate the yield because the sample contains traces of unreacted POM hexamolybdate.

Purification of crude POM derivatives was challenging. Nevertheless, **POM-AB** and **POM-AC** were purified through recrystallization from hot acetonitrile (50°C). On the other hand, it was difficult to completely eliminate unreacted precursors from crude **POM-AQ**, regardless of all the purification procedures tried, whether washing the crude product with different solvents (EtOAc, $CHCl_3$, THF, Acetone) or by recrystallization or diffusion of either tert-butyl methyl ether or diethyl ether into concentrated acetonitrile solutions. Nevertheless, higher purity (80%) was obtained by dissolving the crude product in a minimum volume of acetonitrile and

then filtrating the mixture after a few hours. The filtrate was evaporated and **POM-AQ** was isolated as a brown powder after trituration with diethyl ether.

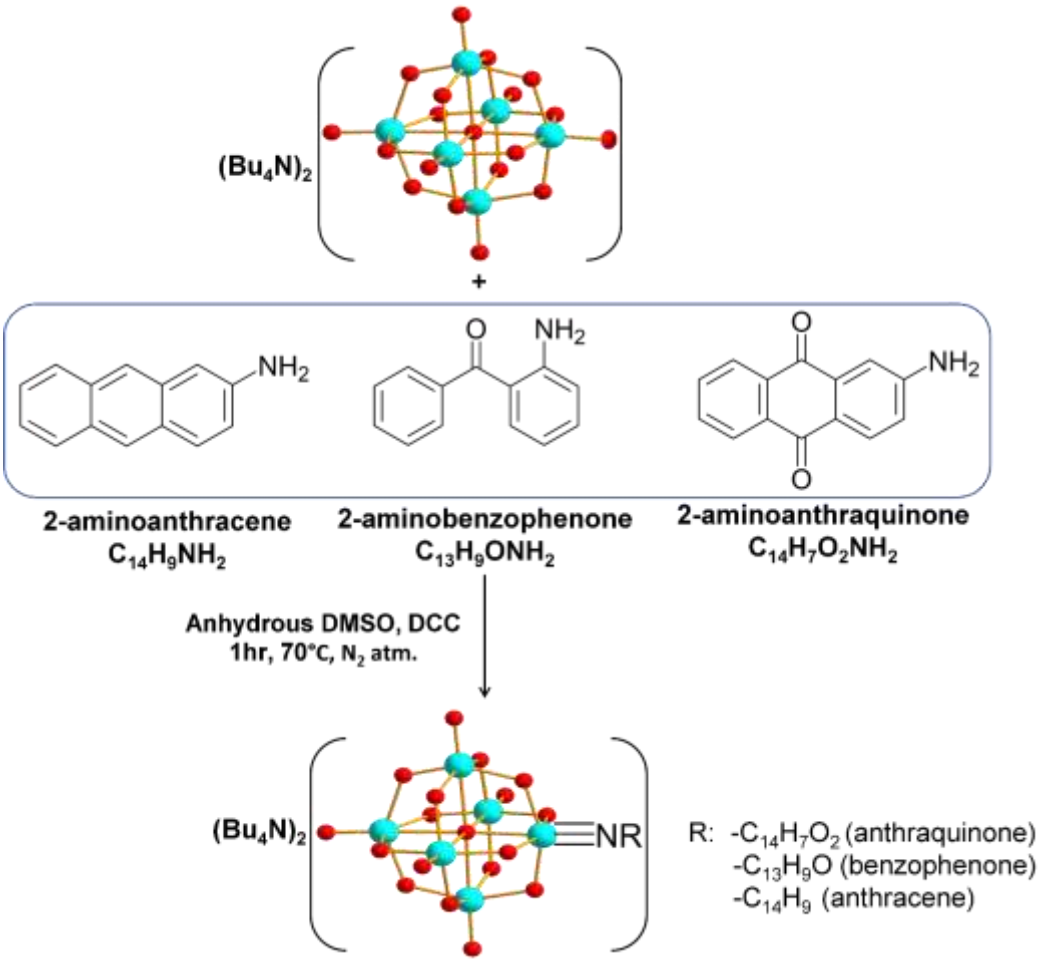

Figure 2. Synthetic pathway of the organoimido POM derivatives, ***POM-AC****,* ***POM-AB,*** *and* ***POM-AQ.****(Turquoise spheres are Mo, red spheres are O)*

III. ^{1}H NMR studies on POM derivatives

^{1}H NMR spectroscopy is a convenient tool to monitor the efficiency of POM-amine coupling reactions [45,53,54]. The NMR data acquired in CD_3CN for this study are gathered in Table 1, while ^{1}H NMR spectra are given inf Figures 3-8.

Table 1. ^{1}H NMR data in CD_3CN, 300 MHz.

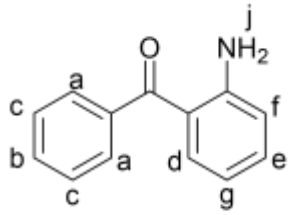

2-aminobenzophenone

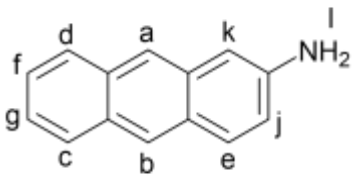

2-aminoanthracene

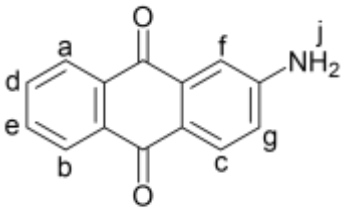

2-aminoanthraquinone

Compounds	Main chemical shifts/ppm		Integration
2-aminobenzophenone	a + b	7.57-7.62	2H +1H, m
	c	7.48-7.51	2H, m
	d + e	7.3-7.4	2H, m
	f	6.85	1H, d
	g	6.61	1H, t
	j	6.43	-NH_2, s
POM-AB	f + d	7.79-7.84	2H, m
	a + b + c + e + g	7.19-7.70	7H, m
2-aminoanthracene	a	8.30	1H, s
	b	8.19	1H, s
	c + d + e	7.83-7.95	3H, m
	f + g	7.3-7.44	2H, m
	j + k	7.01-7.09	2H, m
	l	4.52	-NH_2, s
POM-AC	a + b	8.5	2H, d
	j + k +e	8.02-8.09	3H, m
	f	7.86	1H, s
	d + c	7.47-7.59	2H, m
	g	7.38	1H, dd
2-aminoanthraquinone	a + b	8.22-8.29	2H, m
	c	8.03	1H, d
	d + e	7.82	2H,
	f	7.39	1H, s
	g	7.02	1H, q
	j	5.27	NH_2, s
POM-AQ	f + g + c	8.27	3H
	a + d + e	7.92	3H
	b	7.62	1H

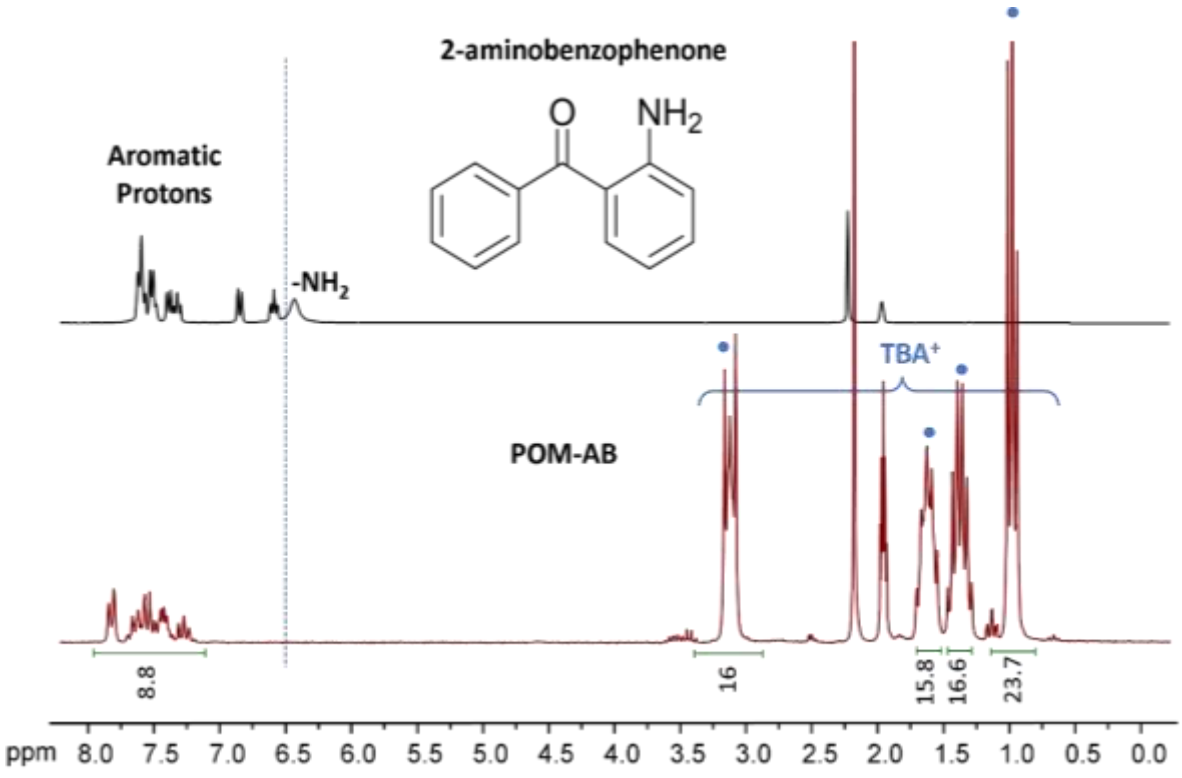

*Figure 3. ^{1}H NMR spectra of 2-aminobenzophenone and **POM-AB** in CD_3CN.*

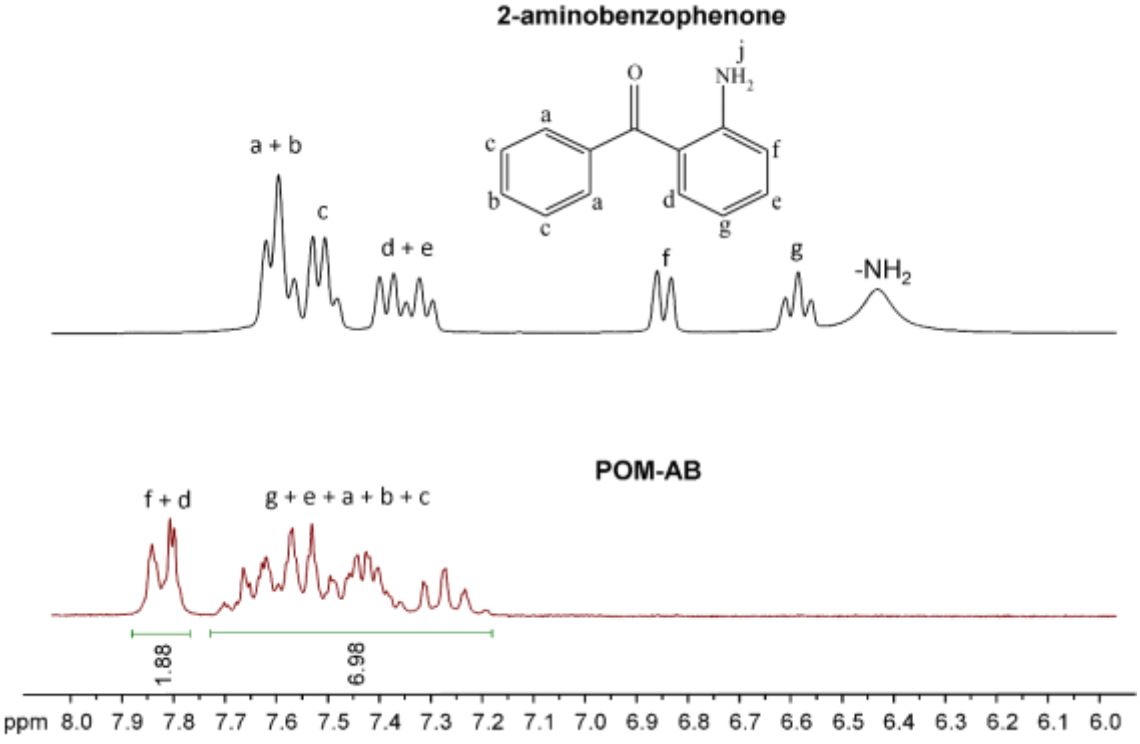

*Figure 4. ^{1}H NMR spectra of 2-aminobenzophenone and **POM-AB** in CD_3CN in the 6-8 ppm range.*

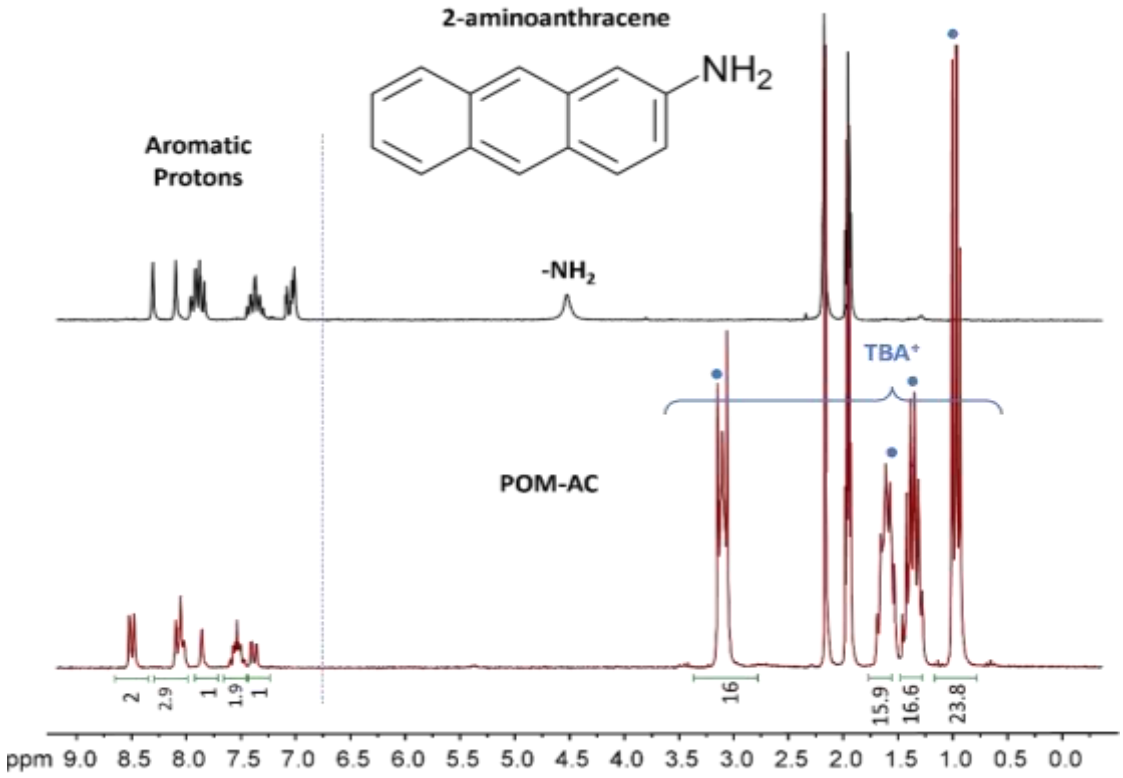

*Figure 5. ^{1}H NMR spectra of 2-aminoanthracene and **POM-AC** in CD_3CN.*

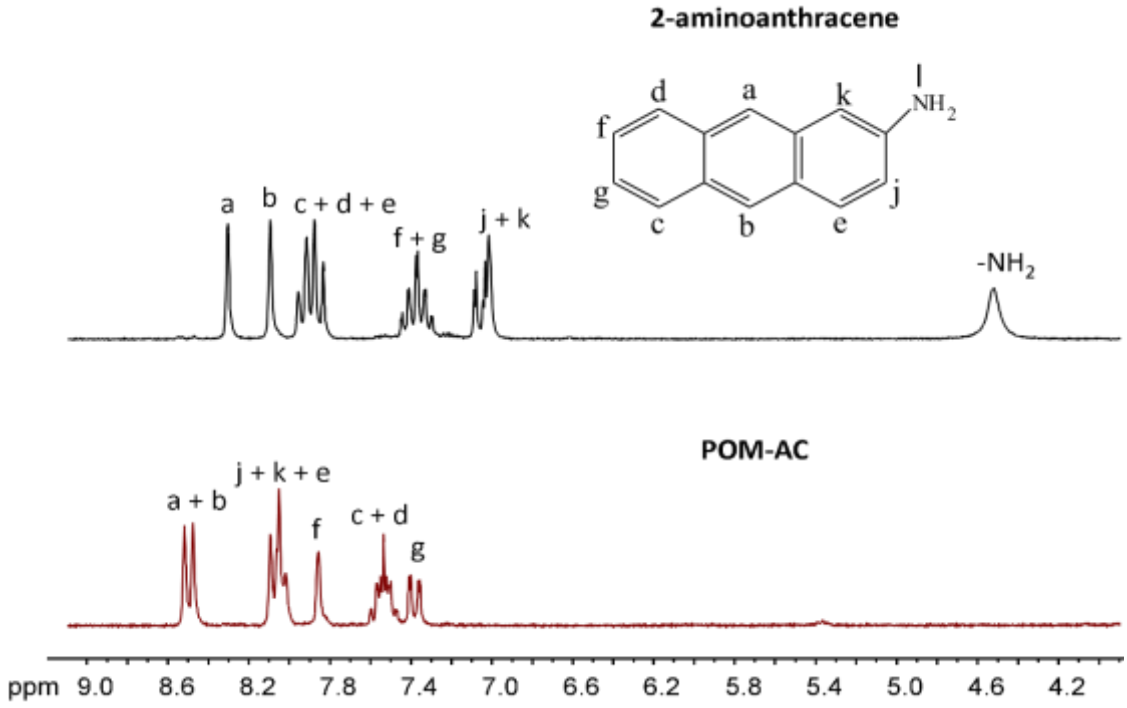

*Figure 6. ^{1}H NMR spectra of 2-aminoanthracene and **POM-AC** in CD_3CN in the 4-9 ppm range.*

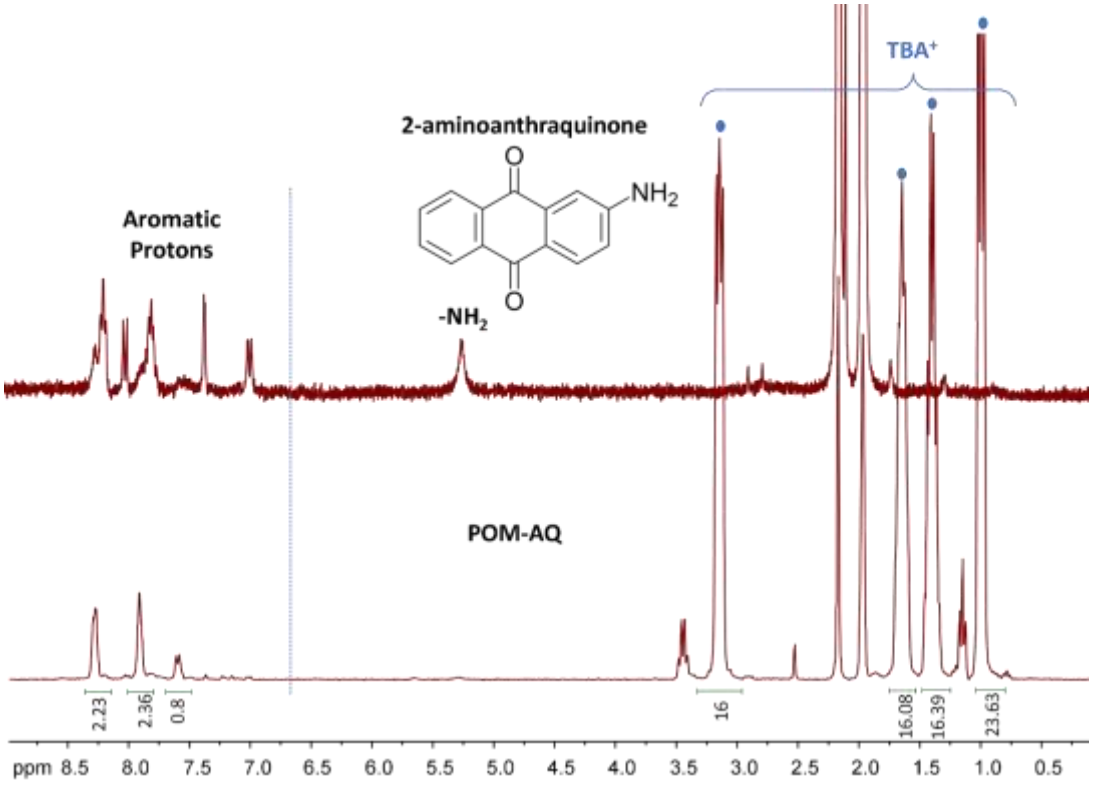

*Figure 7. ^{1}H NMR spectra of 2-aminoanthraquinone and **POM-AQ** in CD_3CN.*

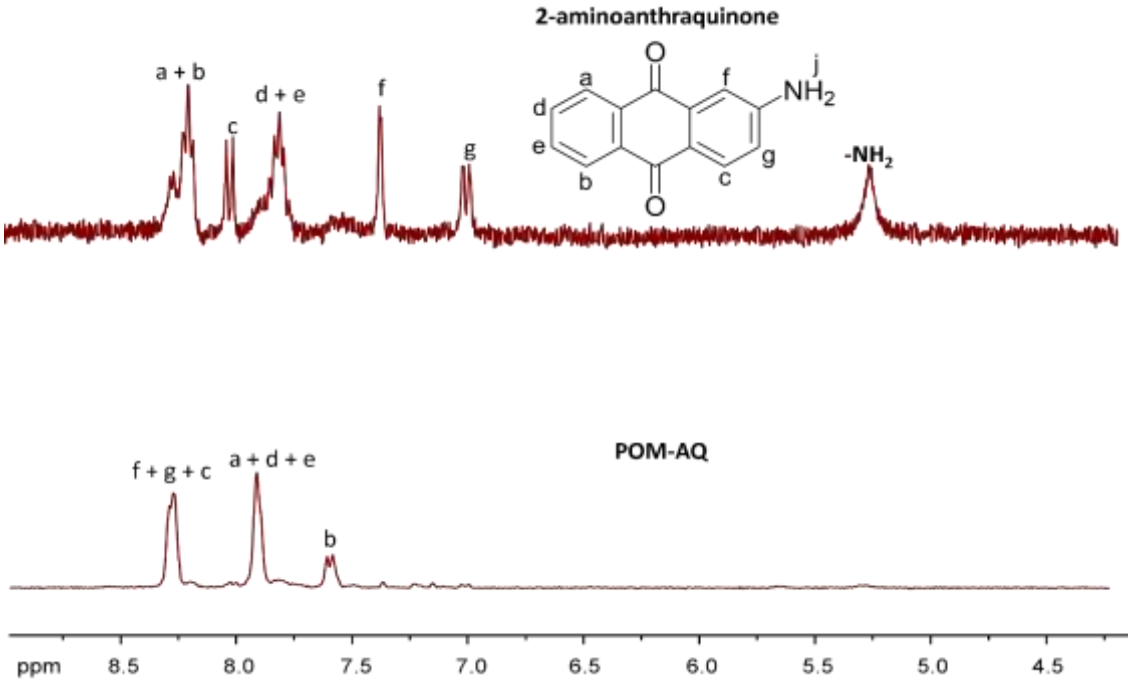

*Figure 8. ^{1}H NMR spectra of 2-aminoanthraquinone and **POM-AQ** in CD_3CN in the 5-9 ppm range.*

As shown in the spectra of the three POM hybrids (**POM-AB, POM-AC,** and **POM-AQ**) (Figures 3-8), there are aromatic organic peaks in the 5-9 ppm range related to the organoimido part

and those related to the two TBA^+ cations associated with hexamolybdate anion in the 0.9-3.5 ppm range.

The comparison between each POM hybrid spectrum and its correlated free amino-organic ligand reveals the disappearance of the broad signal of the amine function of $R\text{-}NH_2$ reactants and markable deviation in the peaks of the aromatic protons, which points to a strong interaction between the inorganic and organic moieties. The chemical shifts of the aromatic protons are downfield shifted compared to the corresponding noncoupled amines, underlining the electron-withdrawing effect of the POM platform [55,56].

The degree of substitution of the ligand on $(TBA)_2[Mo_6O_{19}]$ can be evaluated from the ratio between the integrations of the aromatic organic part and those of the counter cations TBA^+ in the hybrid POM spectra. By theory, a mono-functionalized imido-hexamolybdate $[Mo_6O_{18}(NR)_x]^{2-}$ (x=1) corresponds to an organic group/TBA integration ratio of 0.5, which perfectly matches the experimental ratio determined from **POM-AB** and **POM-AC** spectra (Figures 3 and 5). In contrast, a ratio of 0.4 is observed for **POM-AQ**, indicating a slight default of the anthraquinone ligand (Figure 7). This suggests the presence of unreacted $(TBA)_2[Mo_6O_{19}]$ in the isolated material. Despite numerous efforts, it was hard to remove this precursor impurity entirely.

IV. FT-IR Measurements

Comparison of the FT-IR spectra of **POM-AB**, **POM-AC**, and **POM-AQ** with their parent hexamolybdate $(TBA)_2[Mo_6O_{19}]$ at the region above 1000 cm^{-1} (Figures 9-11) primarily shows standard bands around 2900 cm^{-1} relative to the stretching vibrations of aliphatic C-H groups of the countercation TBA^+. However, numerous new stretching bands appear in the spectra of the hybrid POMs compared to that of $(TBA)_2[Mo_6O_{19}]$, which only contain bands belonging to the TBA cation. Particularly, in the medium-frequency region (1700–1600 cm^{-1}), there are characteristic peaks for the (C=O) bond in **POM-AB** and **POM-AQ** (Figures 9 and 11). The bands in the 1300-1550 cm^{-1} area are related to (C=C) bonds of the benzene rings, besides numerous new bands exclusively present on POM hybrids spectra correlated to the conjugated π system, which constitutes strong evidence of the grafting of organic moieties into the hexamolybdate.

Whereas, below 1000cm^{-1}, the region characteristic to the inorganic part $[Mo_6O_{19}]^{2-}$, in the POM hybrids spectra, there are two strong peaks located at 945 ± 1 cm^{-1} and 765 ± 1 cm^{-1} assigned to the stretching vibrations $\nu(Mo\text{-}O_t)$ and $\nu(Mo\text{-}O_b\text{-}Mo)$ respectively, that are red-shifted compared to stretching vibrations of free $(TBA)_2[Mo_6O_{19}]$ at 951 cm^{-1} and 783 cm^{-1}. These typical variations indicate that Mo-O bonds are weaker in the hybrid POMs due to the strong new Mo-N one. Indeed, a new sharp peak appears at 976±1 cm^{-1} corresponding to the Mo≡N stretching vibration, which is characteristic of monosubstituted organoimido substituted derivatives [49,57,58].

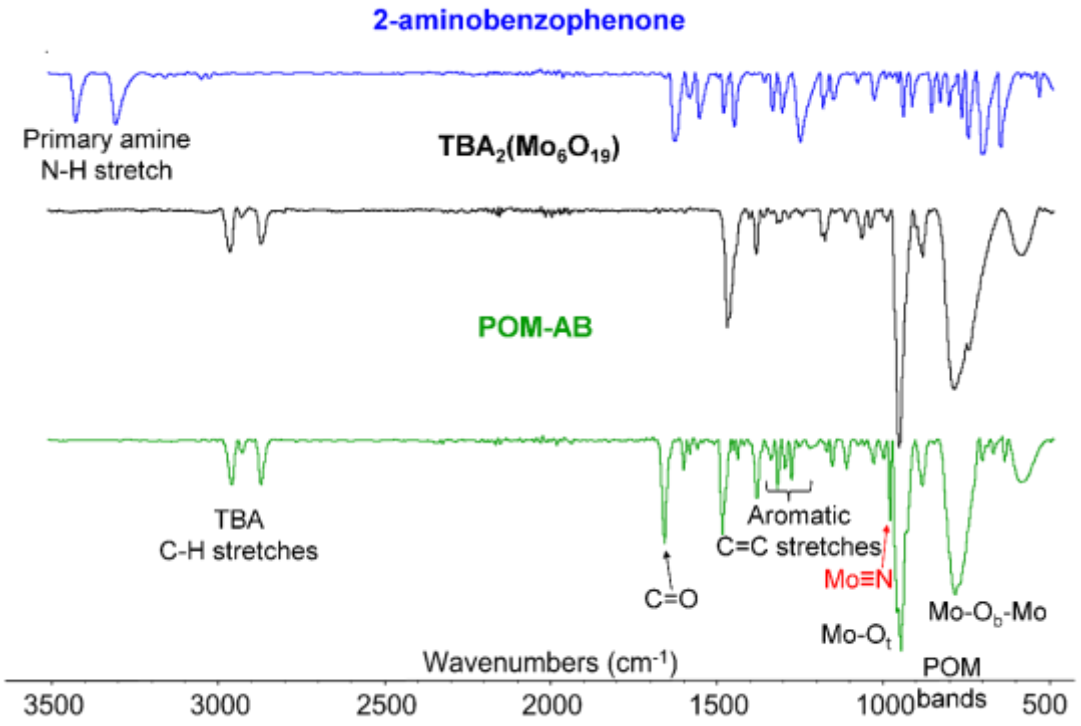

*Figure 9. Infrared spectra of 2-aminobenzophenone, $(TBA)_2[Mo_6O_{19}]$ and **POM-AB.***

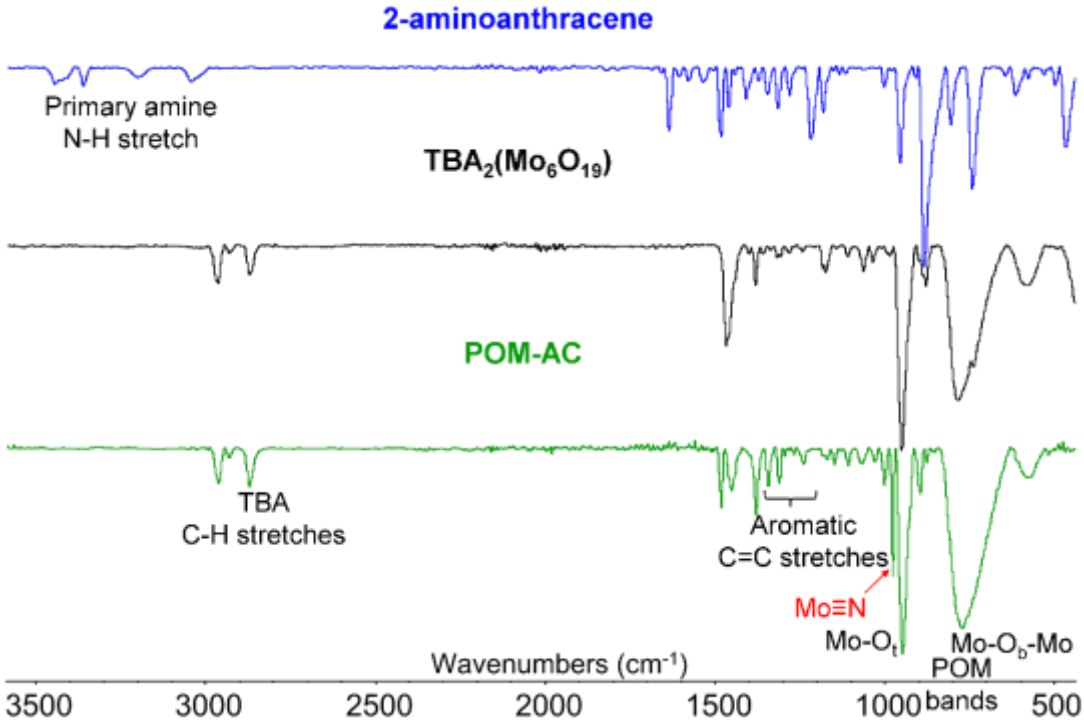

*Figure 10. Infrared spectra of 2-aminoanthracene, $(TBA)_2[Mo_6O_{19}]$ and **POM-AC**.*

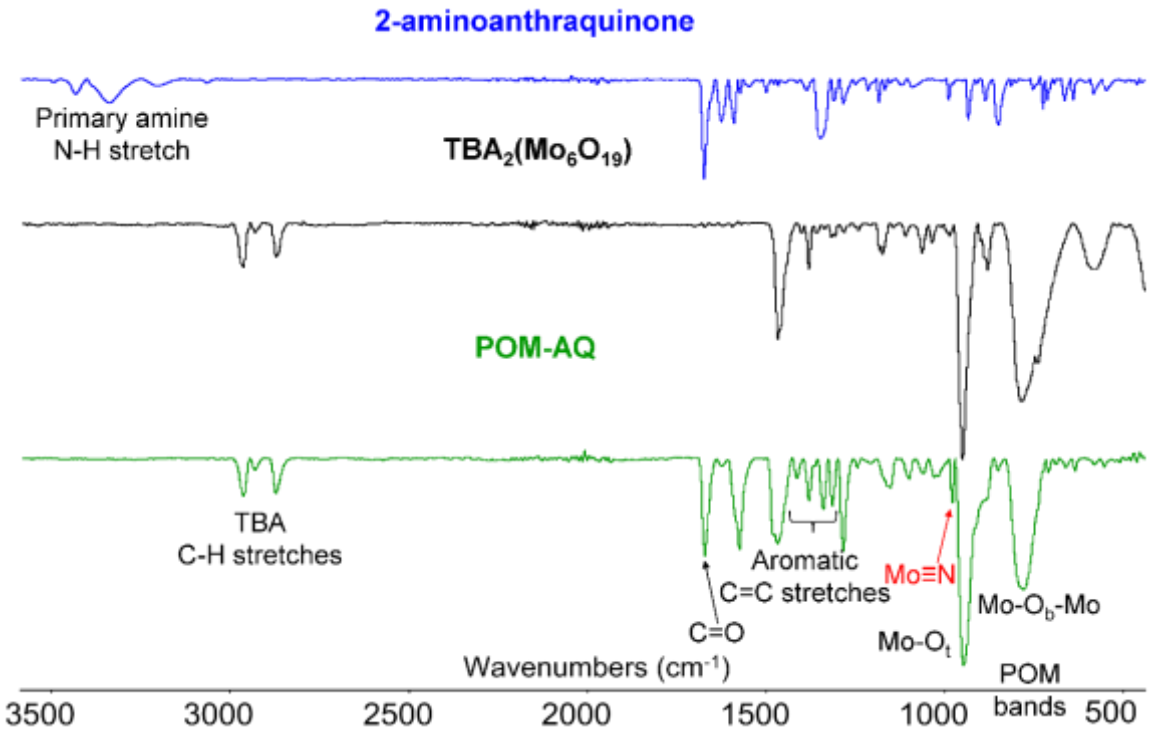

*Figure 11.Infrared spectra of 2-aminoanthracene, $(TBA)_2[Mo_6O_{19}]$ and **POM-AQ**.*

V. Characterization by ElectroSpray Ionization Mass Spectrometry (ESI-MS)

The purpose of ESI-MS spectra of the three functionalized POM derivatives is not limited to illustrating the successful synthesis of the targeted products but also confirming their stability in acetonitrile solution [59]. The ESI-MS results of the three functionalized polyoxometalates in acetonitrile solution with a concentration of 10^{-5} M are summarized in Table 2.

Actually, for **POM-AB**, the isotopic peaks centered at *m/z* 529.19 can be assigned to the dianion $\{Mo_6O_{18}(NC_6H_4\text{-}C(O)\text{-}C_6H_5)\}^{2-}$ in agreement with the calculated value (*m/z* 529.42), while the minor peak at *m/z* 1302.70 corresponds to the anionic aggregate $\{(TBA)[Mo_6O_{18}(NC_6H_4\text{-}C(O)\text{-}C_6H_5)]\}^-$ (calc. *m/z* 1301.32) (Figure 12). Analogously, for **POM-AC**, the peak related to the inorganic part $\{Mo_6O_{18}(NC_{14}H_9)\}^{2-}$ is observed at *m/z* 528.19 (calc. m/z 527.43), and the isotopic peaks centered at *m/z* 1296.67 (calc. *m/z* 1297.33) can be attributed to the $\{(TBA)[Mo_6O_{18}\ (NC_{14}H_9)]\}^-$ aggregate resulting from the association of the dianion and a TBA cation (Figure 13). Lastly, for **POM-AQ**, the isotopic peaks at *m/z* 540.17 (calc. m/z 542.42) and *m/z* 1328.68 (calc. *m/z* 1327.42) correspond to $\{Mo_6O_{18}(NC_{14}H_7O_2)\}^{2-}$ and $\{(TBA)[Mo_6O_{18}(NC_{14}H_7O_2)]\}^-$ respectively while the peak at *m/z* 1085.39 (calc. *m/z* 1085.96) can be assigned to $\{H[Mo_6O_{18}(NC_{14}H_7O_2)]\}^-$ (Figure 14).

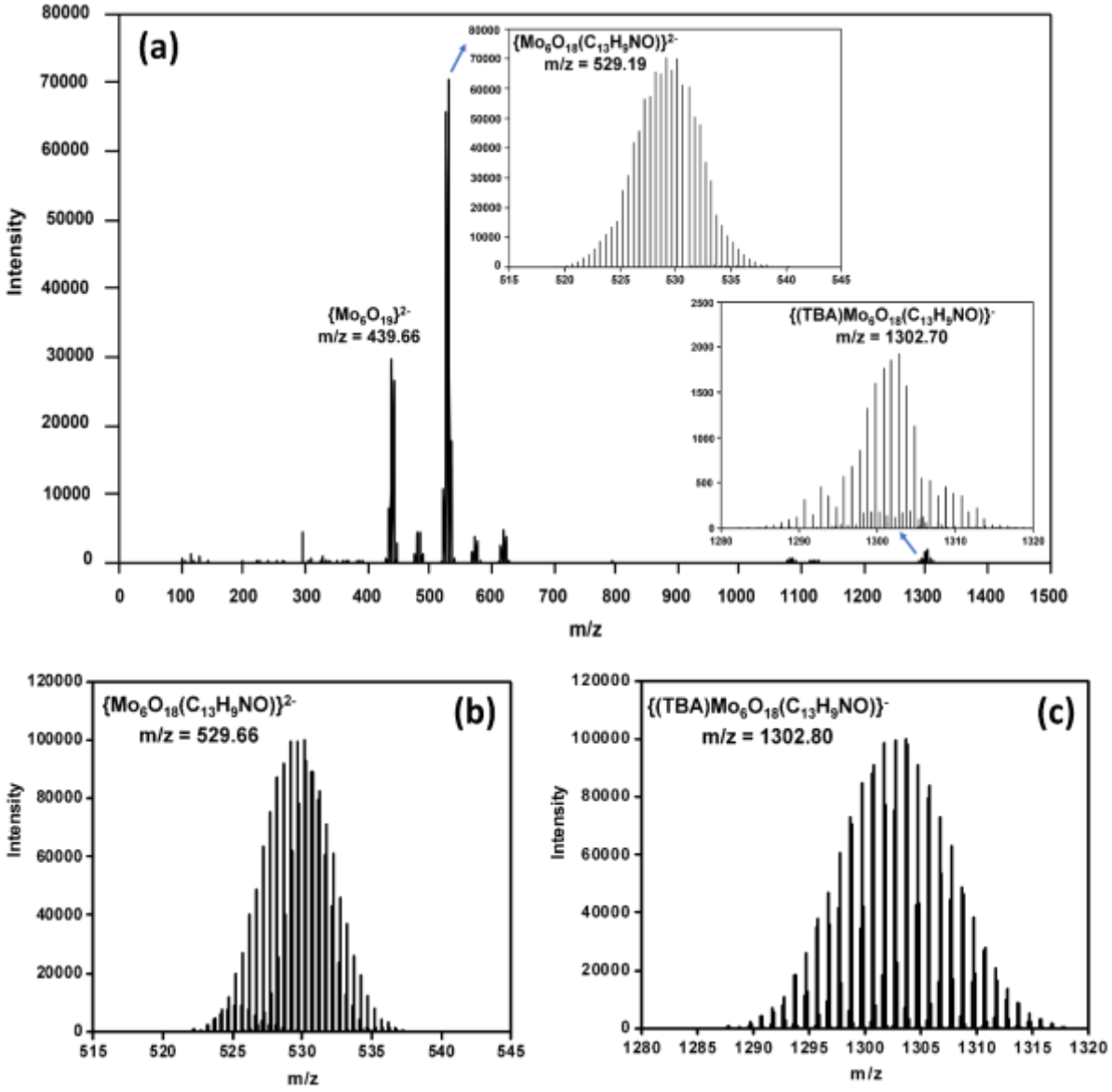

Figure 12. ESI-MS spectrum of (a) ***POM-AB*** *solution in acetonitrile (C=10^{-5}M); ESI-MS simulated signals of (b) {****POM-AB****}$^{2-}$ and (c) {TBA +* ***POM-AB****}$^{-}$.*

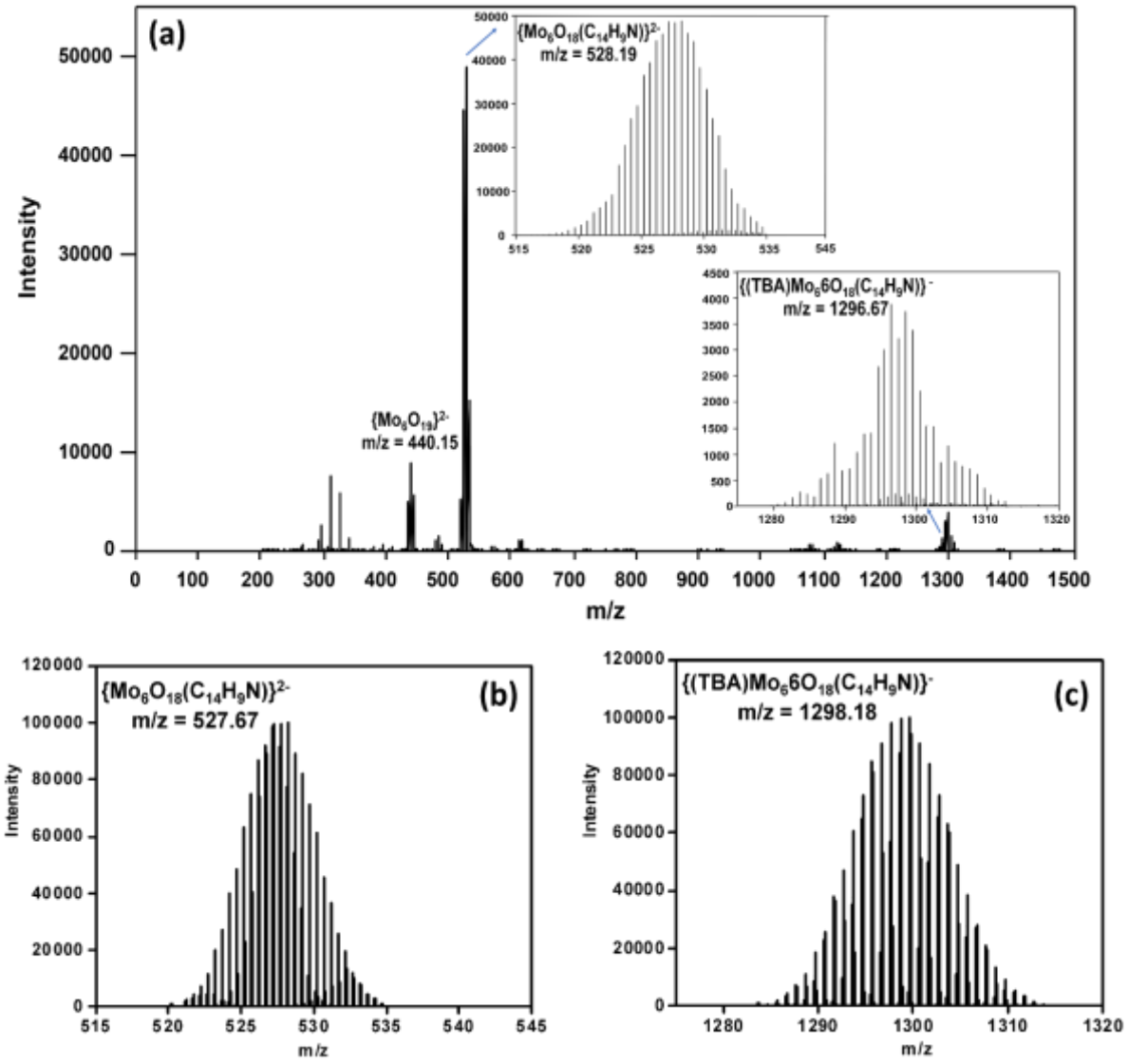

Figure 13. ESI-MS spectrum of (a) ***POM-AC*** *solution in acetonitrile (C=10^{-5}M); ESI-MS simulated signals of (b) {****POM-AC****}$^{2-}$, and (c) {TBA +* ***POM-AC****}$^{-}$.*

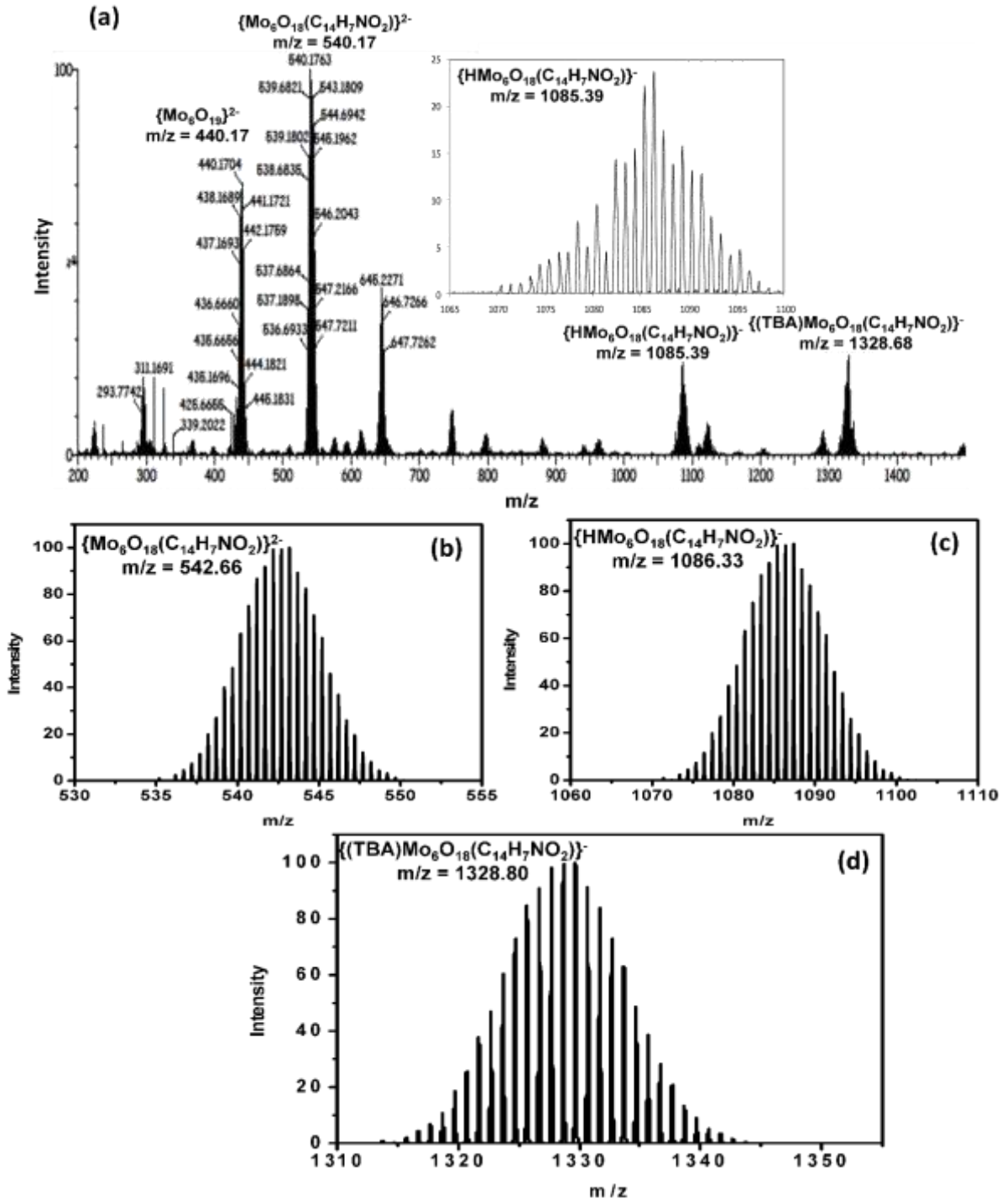

Figure 14. ESI-MS spectrum of (a) ***POM-AQ*** *solution in acetonitrile (C=10^{-5}M); ESI-MS simulated signals of (b) {****POM-AQ****}$^{2-}$,(c) {H +* ***POM-AQ****}$^{-}$, and (d) {TBA +* ***POM-AQ****}$^{-}$.*

Table 2. Summarized ESI-MS data.

Compounds	Exp. m/z	Peak's Assignments	Calc. m/z
POM-AB	439.66	$\{Mo_6O_{19}\}^{2-}$	439.81
	529.19	$\{Mo_6O_{18}(C_{13}H_9NO)\}^{2-}$	529.42
	1123.61	$\{Na[Mo_6O_{18}(C_{13}H_9NO)]\ (CH_3CN)\}^{-}$	1122.89
	1302.70	$\{(TBA)Mo_6O_{18}(C_{13}H_9NO)\}^{-}$	1301.32
POM-AC	440.15	$\{Mo_6O_{19}\}^{2-}$	439.81
	528.19	$\{Mo_6O_{18}(C_{14}H_9N)\}^{2-}$	527.43
	1296.67	$\{(TBA)Mo_6O_{18}(C_{14}H_9N)\}^{-}$	1297.33
POM-AQ	440.17	$\{Mo_6O_{19}\}^{2-}$	439.81
	540.17	$\{Mo_6O_{18}(C_{14}H_7O_2N)\}^{2-}$	542.42
	645.22	$\{Mo_6O_{18}(C_{14}H_7O_2N)_2\}^{2-}$	645.09
	880.75	$\{HMo_6O_{19}\}^{-}$	880.75
	1085.39	$\{HMo_6O_{18}(C_{14}H_7O_2N)\}^{-}$	1085.96
	1291.17	$\{HMo_6O_{18}(C_{14}H_7O_2N)_2\}^{-}$	1291.07
	1328.68	$\{(TBA)Mo_6O_{18}(C_{14}H_7O_2N)\}^{-}$	1327.42

VI. X-Ray Diffraction Studies

Orange crystals of **POM-AB** suitable for X-ray diffraction were obtained through recrystallization from a hot concentrated acetonitrile solution of the crude solid, while red crystals of **POM-AC** were obtained by diffusion of *tert*-butyl methyl ether into an acetonitrile concentrated solution. Crystallographic data are given in Table 3, while bond lengths and bond angles of **POM-AB** and **POM-AC** obtained by X-Ray Diffraction are gathered in 4.

*Table 3. Crystallographic data for **POM-AB** and **POM-AC**.*

	POM-AB	**POM-AC**
Chemical formula	$Mo_6O_{19}N_3C_{45}H_{81}$	$Mo_6O_{18}N_3C_{46}H_{81}$
M_r *(g.mol^{-1})*	1543.89	1539.91
Cell setting, space group	Monoclinic, $P2_1/n$	Orthorhombic, $Pna2_1$
Temperature (K)	210	210
a, *b*, *c* (Å)	16.0547(7), 21.3423(8), 17.4658(7)	19.5715(10), 18.4467(9),15.8310(9)
α, β, γ (°)	90, 90.063(2), 90	90, 90, 90
V (Å^3)	5984.6(4)	5715.5(5)
Z	4	4
D_x (g cm^{-3})	1.713	1.705
Radiation type	Mo *K*α	Mo *K*α
μ (mm^{-1})	1.29	1.34
Crystal form, color	Parallelepiped, orange	Parallelepiped, orange
Absorption correction	Multi-scan SADABS	Multi-scan SADABS
No. of measured and independent reflections	210376, 17433	294064, 10093
Criterion for observed reflections	$I > 2\sigma(I)$	$I > 2\sigma(I)$
R_{int}	0.029	0.090
GoF	1.100	1.136
Refinement on	F^2	F^2
R, $wR_2[F^2 > 2\sigma(F^2)]$	0.021, 0.051	0.0928, 0.2407
No. of parameters	658	596
H-atom treatment	Constrained to parent site	Constrained to parent site

$$[a]R_1 = \frac{\sum\left||F_0| - |F_c|\right|}{\sum|F_c|} \quad [b]R_2 = \sqrt{\frac{\sum w(F_o^2 - F_c^2)^2}{\sum w(F_o^2)^2}}$$

*Table 4. Bond Lengths and Bond Angles of **POM-AB** and **POM-AC** obtained by X-Ray Diffraction.*

	POM-AB	**POM-AC**
Mo1-N bond	1.7392(1) Å	1.7737(1) Å
C-N-Mo1 angle	170.361(4) °	154.597(4) °
Oc -Mo1 bond	2.2167(1) Å	2.2058(1) Å
Oc -Mo(2-6)	2.3183(1) -2.3625(1) Å	2.3078(1) -2.3775(1) Å

Single crystal X-ray diffraction studies confirm that in **POM-AC** and **POM-AB,** the organic moiety is covalently linked to the hexamolybdate core through the nitrogen atom, which replaces one terminal oxo ligand (O_t) of the Lindqvist POM. For **POM-AB**, the short-formed Mo1-N bonds (1.7392(1) Å), along with the C-N-Mo1 angle close to 180° (170.361(4)°), are illustrative of organoimido groups bound to an octahedral d^0 metal center *via* a Mo-N triple bond (Figure 15a) [37,60,61]. This is also the case for **POM-AC,** but the Mo1-N bond is slightly longer (1.7737(1) Å), while the more acute C-N-Mo1 angle (154.597(4)°) shows a distortion, probably due to the steric hindrance of the anthracene group (Figure 15b).

Also, as a typical feature for organoimido POM derivatives, the bond between the central oxygen (O_c) and the molybdenum (Mo1) bearing the organic moiety is significantly shorter (2.2167(1) Å for **POM-AB** and 2.2058(1) Å for **POM-AC**) than the bonds between O_c and the five other metal centers (Mo2-6) (in the 2.3183(1)-2.3625(1) Å range for **POM-AB** and the 2.3078(1)-2.3775(1) Å range for **POM-AC**). This is attributed to the so-called "trans influence", suggesting that the central oxygen atom is slightly shifted toward the imido-bearing molybdenum atom due to weaker electronegativity of the imido group compared to the terminal oxo group (O_t) [38,62].

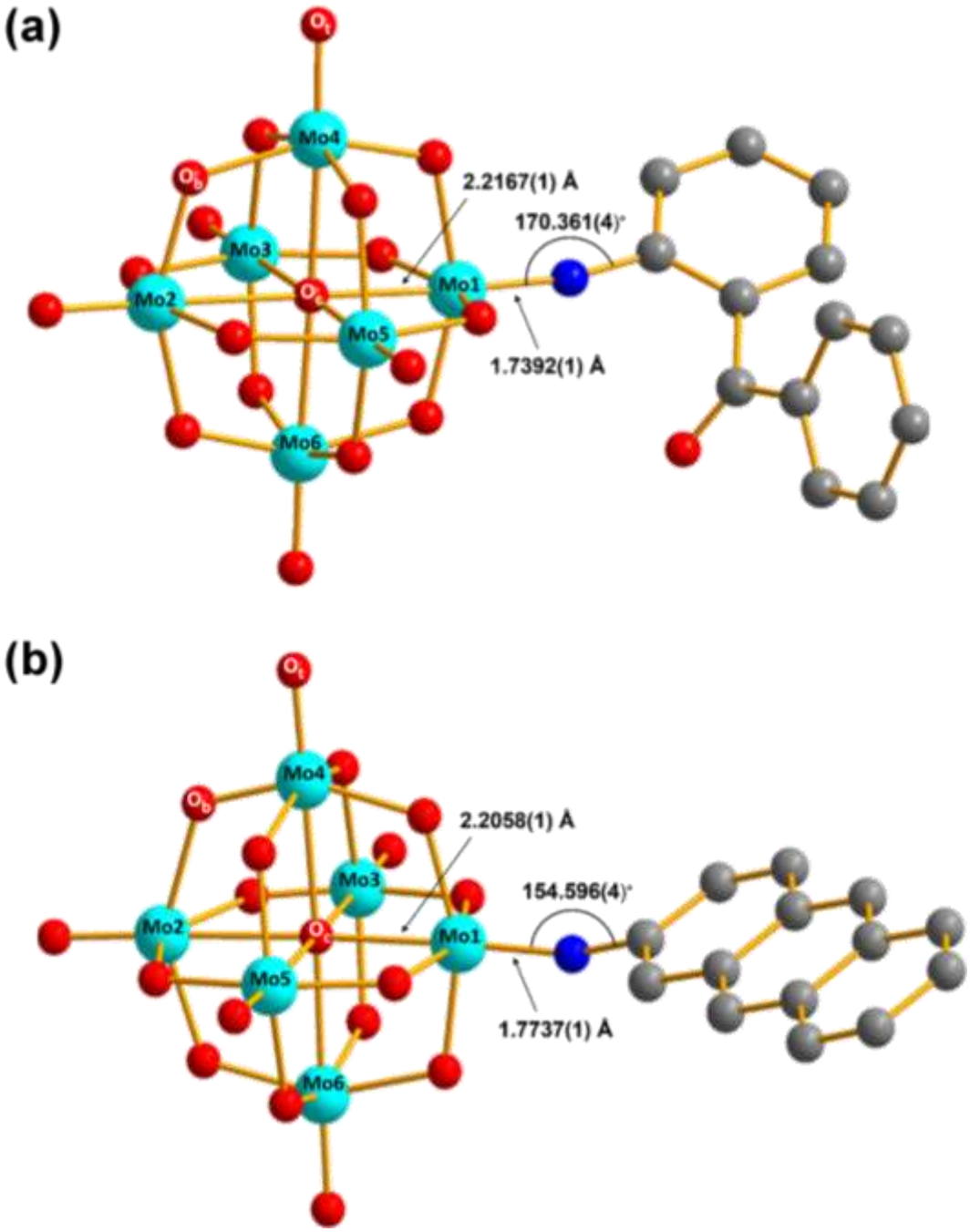

Figure 15. Molecular structures of (a) ***POM-AB*** *and (b)* ***POM-AC****. TBA cations and H atoms were omitted for clarity. Turquoise spheres: Mo, red spheres: O, blue spheres: N, grey spheres: C.*

The crystal packing of **POM-AC** does not exhibit any π-π interactions between neighboring anthracene units nor between the aromatic group and the nearest POM facet. In contrast, as shown in Figure 16, π-π interactions involving the monosubstituted aromatic rings of two adjacent benzophenone moieties lead to the formation of dimers along the z-axis in **POM-AB**. These interactions are characterized by a distance of 3.8063(1) Å between the centroids of these parallel rings [63–65].

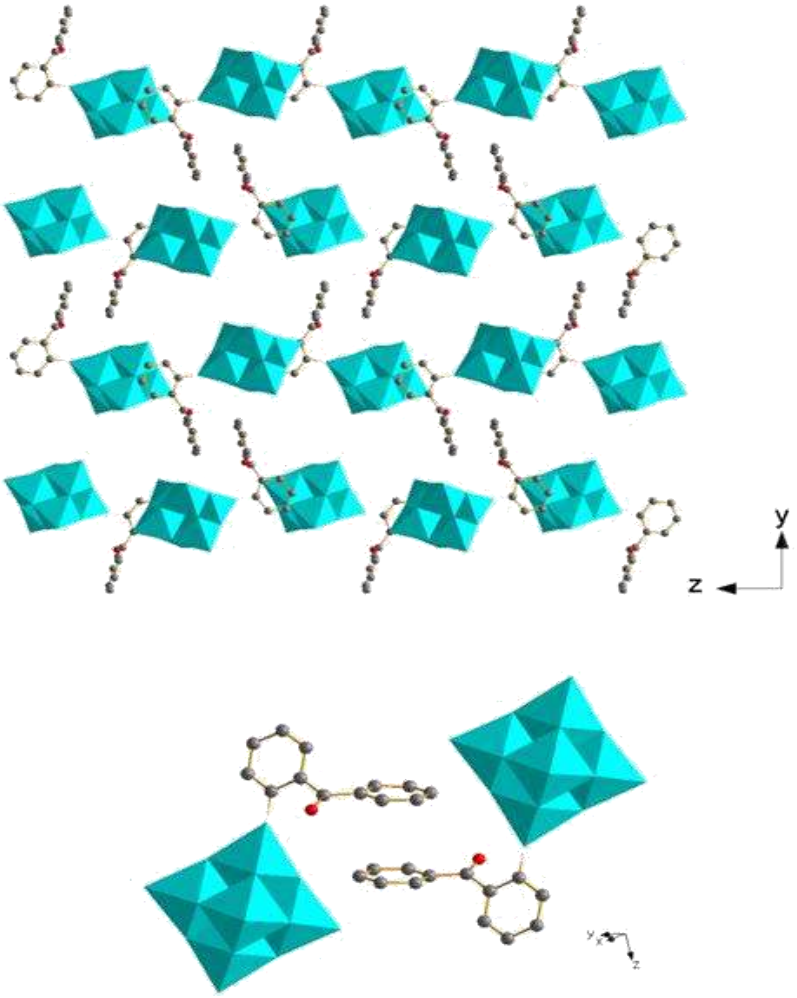

*Figure 16. Crystal packing of **POM-AB** along the z-axis (top), π-π interactions between two neighboring polyanions (bottom). TBA cations and H atoms have been omitted for clarity. Turquoise polyhedra: MoO_6 and MoO_5N, red spheres: O, blue spheres: N, grey spheres: C.*

VII. UV-Visible Spectroscopy

The electronic spectra of **POM-AB**, **POM-AC**, and **POM-AQ** with their related inorganic and organic precursors were recorded in acetonitrile at room temperature (Figures 17-19). The Lindqvist-type polyanion $(TBA)_2[Mo_6O_{19}]$ exhibits a typical absorption band positioned in the ultraviolet region at λ = 325nm (Figure 17B), which corresponds to Ligand-to-Metal charge transfer (LMCT) from the oxygen π–type highest occupied molecular orbital (HOMO) to the molybdenum π–type lowest unoccupied molecular orbital (LUMO) [50,51,66].

This band was bathochromically shifted by 24 nm (λ= 349 nm) and interestingly becomes much more intense in **POM-AB**, where the 2-aminobenzophenone segment is introduced (Figure 17). It is clear by looking, for example, at the visible wavelength (λ = 405 nm, one of

the wavelength values used in the photopolymerization process) that the molar extinction coefficients (Ɛ) for **POM-AB** ($Ɛ_{405}$= 5300 $L.mol^{-1}.cm^{-1}$) is significantly more intensified than that of the parent 2-amino -benzophenone ($Ɛ_{405}$= 1660 $L.mol^{-1}.cm^{-1}$). This observation is consistent with earlier studies on aryl imido POM derivatives, confirming the electronic interaction resulting from the covalent assembly of POM clusters and organic conjugated systems [56,65].

Notably, this is also the case after the functionalization with 2-aminoanthracene; the lowest energy electronic transition of 2-aminoanthracene at λ = 406 nm is bathochromically shifted to a broad and intense absorption band at λ = 428 nm along with a shoulder at 449 nm in **POM-AC** (Figure 18). Furthermore, the increase of the Ɛ values is strongly pronounced for **POM-AC**, with $Ɛ_{405}$ = 17230 $L.mol^{-1}.cm^{-1}$ against $Ɛ_{405}$ = 3480 $L.mol^{-1}.cm^{-1}$ for 2-aminoanthracene. This also applies to **POM-AQ** with $Ɛ_{405}$ value up to ca. 15600 $L.mol^{-1}.cm^{-1}$, much higher than the organic precursor ($Ɛ_{405}$ = 2100 $L.mol^{-1}.cm^{-1}$) (Figure 19). The bathochromic shift in early imido derivatives is related to the enhancement in the LMCT process due to the delocalization of the organic conjugated π electrons through the N-imido π bond into the Lindqvist POM [67].

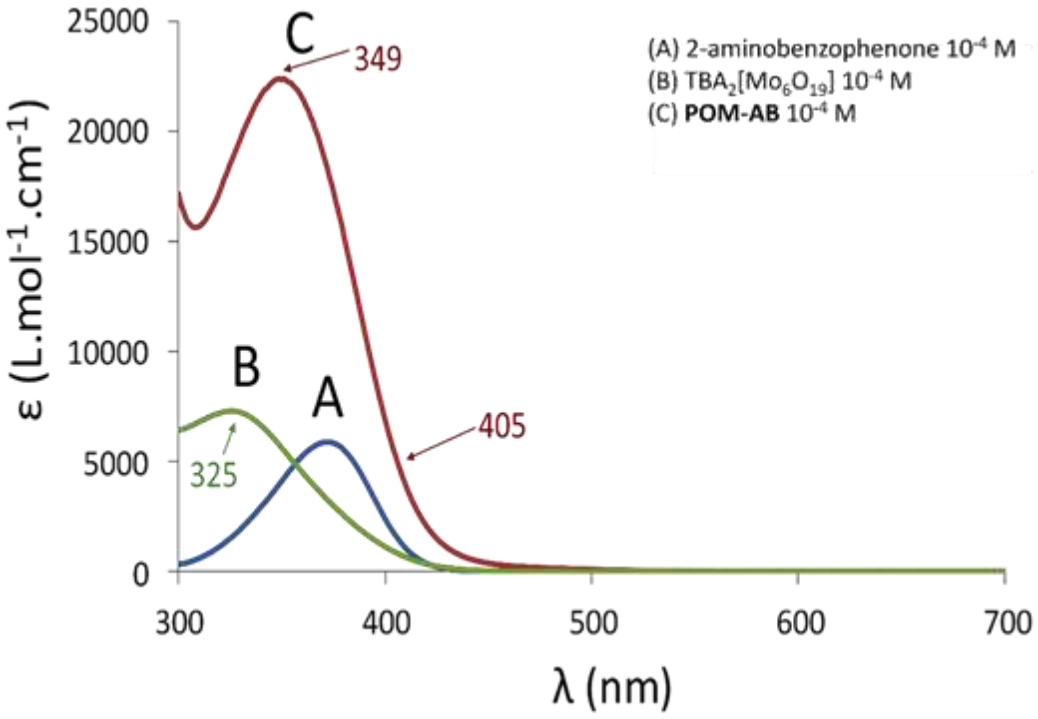

*Figure 17.UV-Visible spectra in acetonitrile of 2-aminobenzophenone (A), $(TBA)_2[Mo_6O_{19}]$ (B) and **POM-AB** (C).*

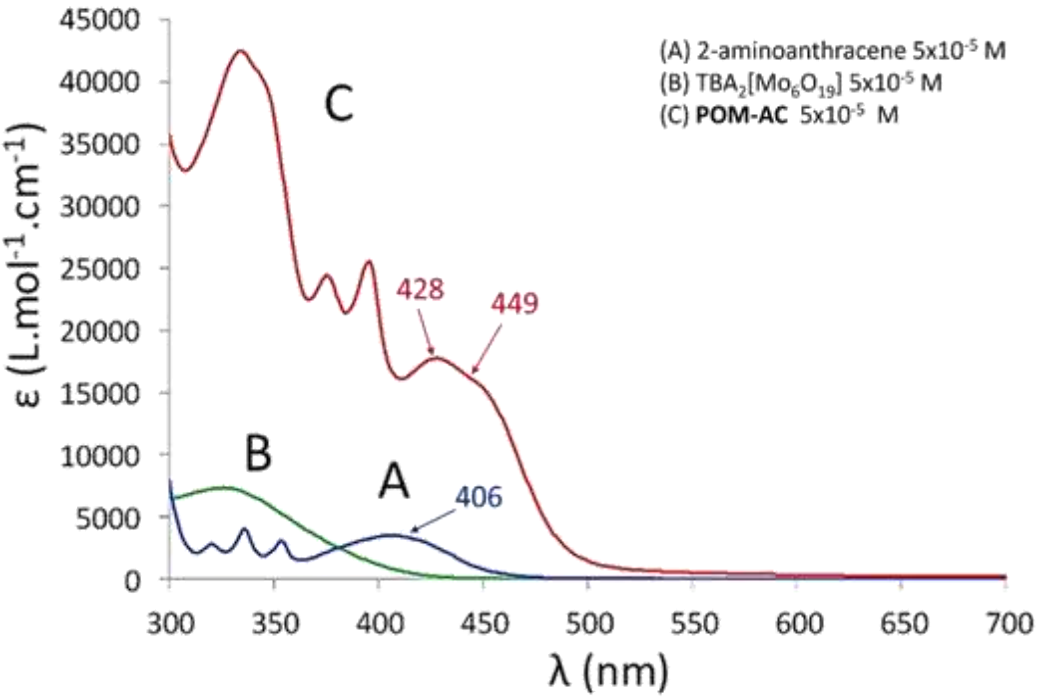

*Figure 18.UV-Visible spectra in acetonitrile of 2-aminoanthracene (A), $(TBA)_2[Mo_6O_{19}]$ (B) and **POM-AC** (C).*

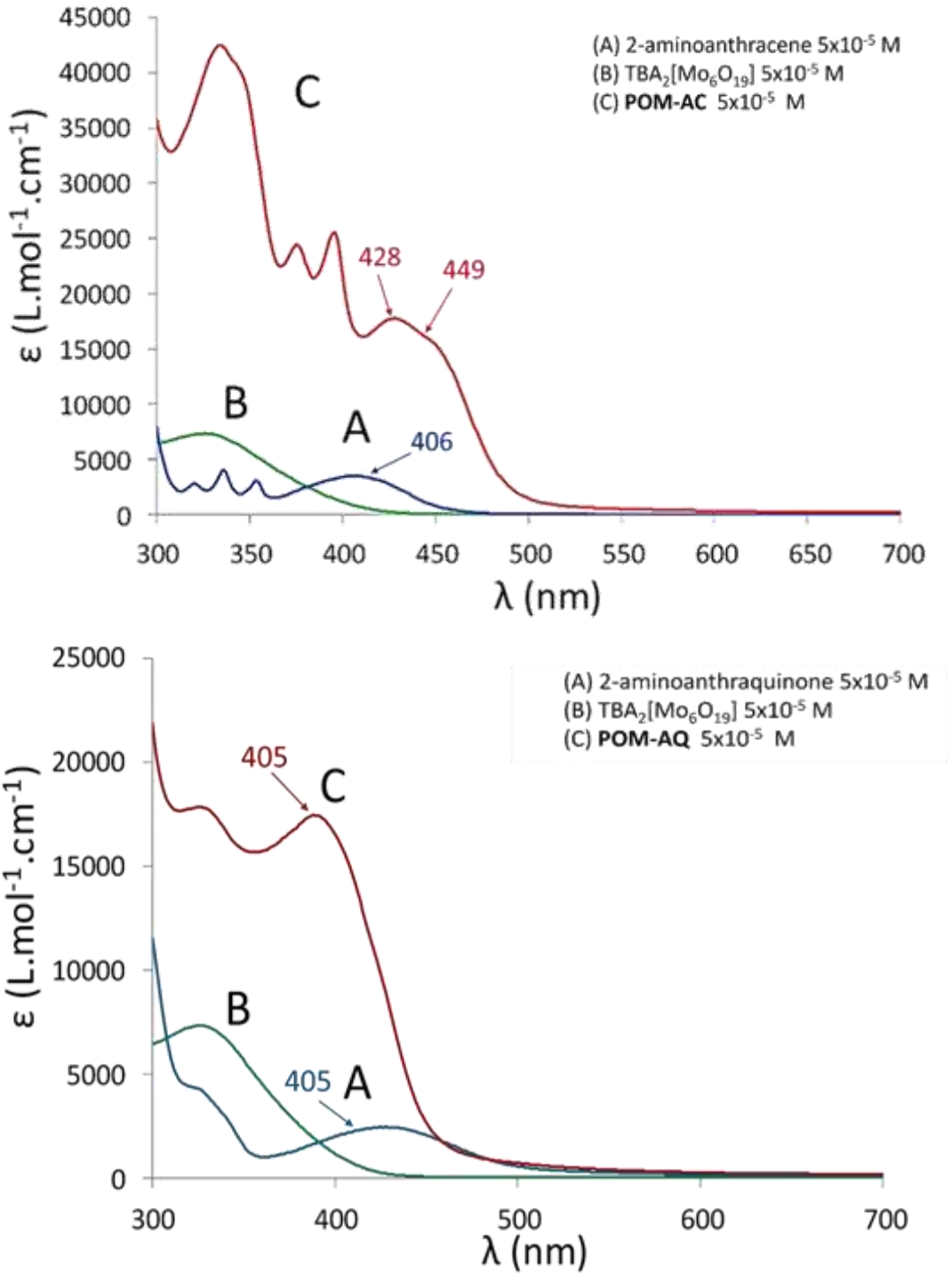

Figure 19.UV-Visible spectra in acetonitrile of 2-aminoanthraquinone (A), $(TBA)_2[Mo_6O_{19}]$ (B) and ***POM-AQ*** *(C).*

VIII. Investigation of the photochemistry of the MDEA/POM derivatives photo-initiating system.

Considering the drastic changes observed for the electronic properties of anthracene, anthraquinone and benzoquinone resulting from the coupling with Lindqvist POM, the study

of the photochemistry of the three previous hybrid POMs was performed in collaboration with Davy-Louis Versace's group in Institut de Chimie et des Matériaux Paris-Est (ICMPE) at Université Paris-Est Créteil (UPEC).

The expected red-shift of the absorption bands in **POM-AB**, **POM-AC**, and **POM-AQ** compared to both organic and inorganic precursors was indeed accompanied with remarkable molar absorption coefficient value in the visible region (above λ=400 nm). These results reinforce our strategy to examine the covalent POM-hybrids as photoinitiators in free-radical polymerization of acrylates under visible light. With this aim, anthraquinone, benzophenones, and anthracene derivatives are most efficient as type II photoinitiators (PI), which consequently requires the presence of a co-initiator as N-methyl diethanolamine (MDEA), which mediates the generation of radicals by electron donation to the PIs (Figure 20) [68].

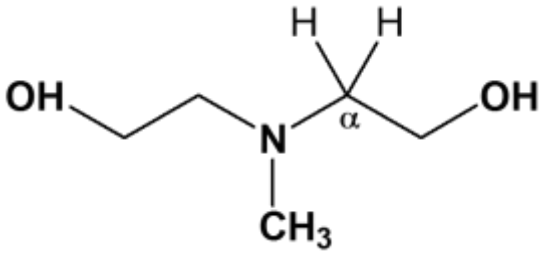

Figure 20. Structure of N-methyldiethanolamine (MDEA) co-initiator in free-radical photopolymerization (FRP) of acrylates.

Thus, the photophysical properties of photosystems made of the **POM-AC**, **POM-AB**, and **POM-AQ** complexes and N-methyldiethanolamine (MDEA) as a reducing agent have been studied.

VIII.1 Steady-State photolysis

Steady-State photolysis has been used to investigate the photochemical reactivity of the reported complexes. In other words, their tendency to produce active species provoked by visible light irradiation so they can initiate radical photopolymerization. First, the photolysis of **POM-AB**, **POM-AC,** and **POM-AQ** alone in acetonitrile shows a negligible decrease in their absorbance upon LED exposure at 405nm (Figure 21a,21c,21e), which chiefly applies to the characteristic bands (ca. 400 nm) presumably associated with the LMCT process in the three POM derivatives. This experiment underlines the good photostability of the three hybrid compounds.

Meanwhile, adding MDEA (reductive agent) to the POM hybrid causes a dramatic and fast decrease in their absorbance after 600s of LED irradiation (Figure 21b,21d,21f), which suggests an interaction between the three POM hybrids and MDEA and predicts the formation of photolysis products. Based on that, MDEA was selected later as a co-initiator with the organoimido POM derivatives in the photopolymerization experiments. This trend is

particularly pronounced for **POM-AQ** (Figure 21f), suggesting that the **POM-AQ**/MDEA system will exhibit a higher photopolymerization ability than the **POM-AB**/MDEA and **POM-AC**/MDEA.

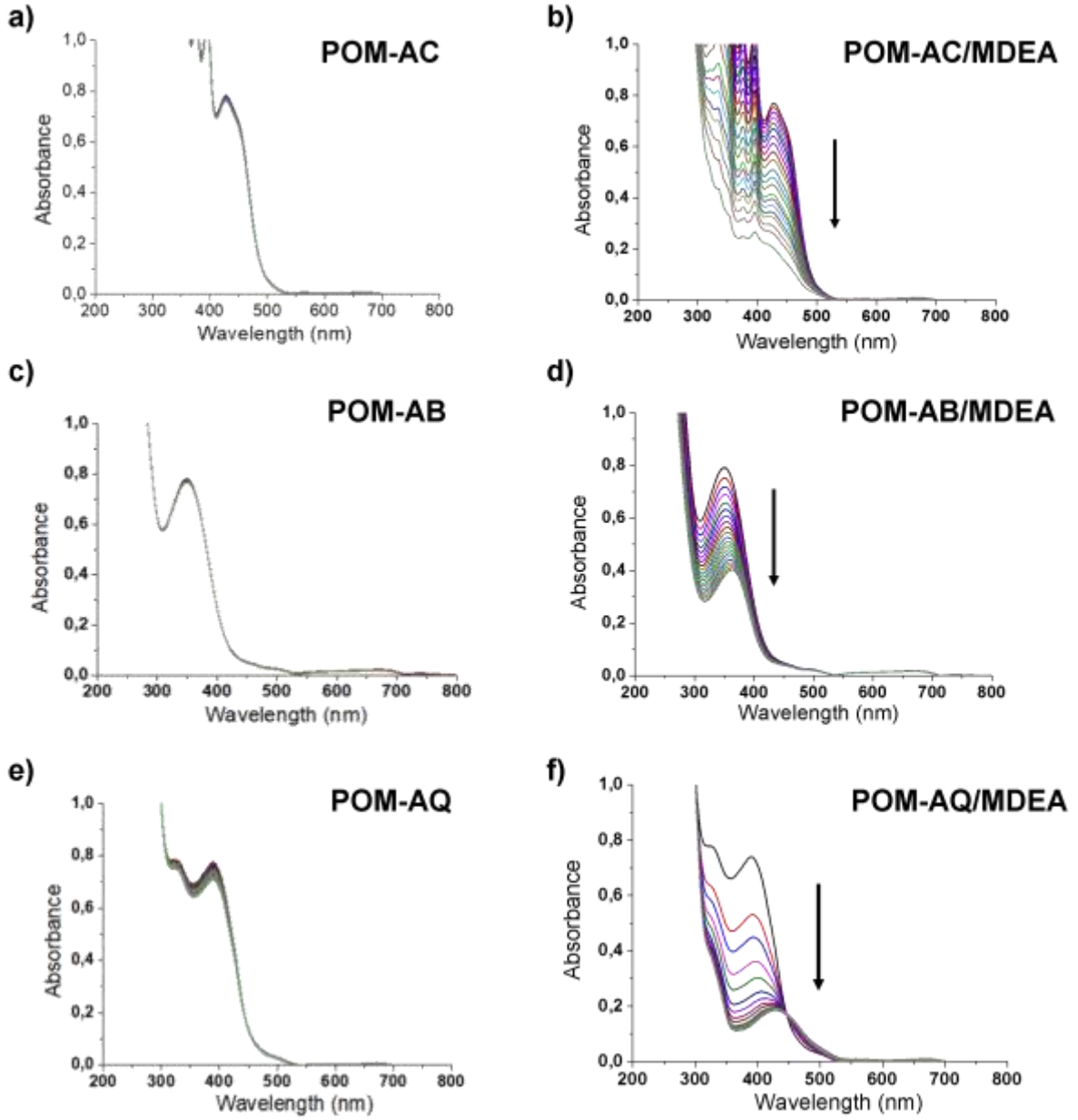

*Figure 21. Photolysis of a) **POM-AC** alone, b) **POM-AC**/MDEA, c) **POM-AB** alone, d) **POM-AB**/MDEA, e) **POM-AQ** alone, and f) **POM-AQ**/MDEA in ACN under LED at 405nm in the 0-600s. Light intensity = 25 mW.cm^{-2}. [MDEA] = 55 mM, [**POM-AC**] = 5.3 x 10^{-5} M, [**POM-AB**] = 4.0 x 10^{-5} M and [**POM-AQ**] = 4.5 x 10^{-5} M.*

VIII.2 Fluorescence experiments

Fluorescence experiments were then carried out to evaluate the possibility of interaction between the excited singlet state of POM hybrids and the co-initiator MDEA under excitation at λ = 420 nm. All the determined photophysical data are summarized in Table 5.

Regarding **POM-AQ**, a maximum of fluorescence is observed at λ= 604 nm (λ_{ex} = 420 nm), with a low fluorescence quantum yield of Φ_{fluo} = 0.013, which seems attributed from the anthraquinone entity since this value is very close to the fluorescence quantum yield of anthraquinone derivatives around 0.01 [12,69]. The gradual addition of MDEA to **POM-AQ** leads to a decrease of fluorescence (Figure 22) with a quite high Stern-Volmer constant K_{SV}^{MDEA} = 8.7 M^{-1} estimated from classical Stern-Volmer relationship (see equation S1 in the appendix) [70–72].

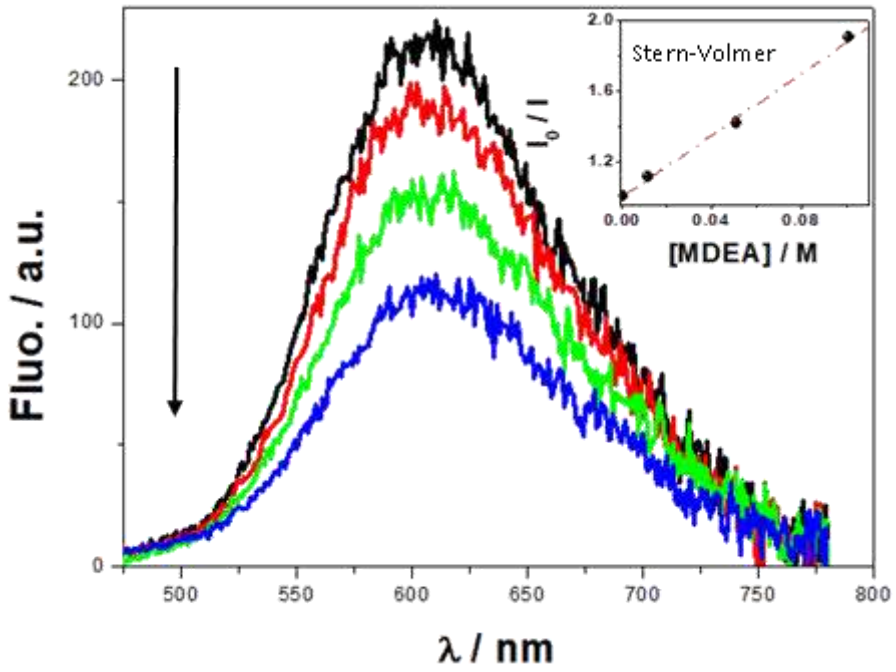

*Figure 22. Quenching of **POM-AQ** fluorescence upon gradual addition of MDEA (from black to blue curve) in acetonitrile (λ_{ex} = 420 nm). Inset: corresponding Stern-Volmer plot. Absorbance of **POM-AQ** at 425 nm = 0.05.*

Associated electron transfer yield ϕ_{eT} calculated from the equation ϕ_{eT} = (K_{SV}^{MDEA} x [MDEA]) / (1+ K_{SV}^{MDEA} x [MDEA]) afforded ϕ_{eT} = 0.812 for [MDEA] = 0.495 M, *e.g.,* for the MDEA concentration used in the kinetics of photopolymerization conditions (see below). This calculated ϕ_{eT} value is relatively high, demonstrating thus a favorable electron transfer reaction between the singlet excited state of **POM-AQ** and MDEA. This result is not surprising as Rehm-Weller equation (see equation S2 in the appendix) [73,74] which is used to determine if the electron transfer reaction from MDEA to **POM-AQ** is possible in the excited singlet state predicted favorable **POM-AQ**/MDEA interaction using the oxidation potential of MDEA (E_{ox}(MDEA) = +1.00 V/SCE), the reduction potential of **POM-AQ** (E_{red}(**POM-AQ**) =-0.38 V/SCE) estimated from cyclic voltammetry experiments done in acetonitrile discussed in the upcoming part, and the excited singlet-state energy (E_s(**POM-AQ**) = 2.48 eV, corresponding to the maximum of the fluorescence emission spectrum (Figure 22). Thus, the ΔG_S (**POM-AQ**/MDEA) Gibbs energy change value for the electron transfer reaction being indeed estimated to -1.10 eV (Table 5).

Surprisingly, no fluorescence was observed neither for **POM-AB** nor **POM-AC**, avoiding the estimation of the fluorescence quenching by MDEA. Therefore, the excited singlet-state energies of **POM-AB** and **POM-AC** have been estimated from the UV absorption band edge using Tauc method (see equations S3-S7 in the appendix) [75,76], evaluated to 2.58 eV and 2.36 eV, respectively. Interestingly, $\Delta G_{S\ (\mathbf{POM\text{-}AC}/MDEA)}$ and $\Delta G_{S\ (\mathbf{POM\text{-}AB}/MDEA)}$ are negative, demonstrating also a favorable electron transfer reaction between both POM derivatives and MDEA.

*Table 5. Photophysical properties of **POM-AC**, **POM-AB,** and **POM-AQ**.*

	$\lambda_{maxfluo}$ (nm)	Φ_{fluo}	E_S (eV)	K_{SV}^{MDEA}(M^{-1})	E_{ox} (V)	E_{Red} (V)	$\Delta G_{S\ (POM/MDEA)}$ (eV)
POM-AC	-	-	2.36*	-	1.14; 1.32	-0.57	-0.79 < 0
POM-AB	-	-	2.58*	-	1.79; 1.91	-0.58	-1 < 0
POM-AQ	604	0.013	2.48	8.7	1.40	-0.38	-1.1 < 0
MDEA	-	-	-	-	1	-	-

**Estimated from the UV absorption band edge, Φ_{fluo} = fluorescence quantum yield, E_S = excited singlet state energy, K_{SV}^{MDEA} = quenching of fluorescence by MDEA, E_{ox} = oxidation potential of the electron donor, E_{Red} = the reduction potential of the electron acceptor and $\Delta G_{S\ (POM/MDEA)}$ = Gibbs energy change value for the electron transfer reaction. E_{ox} and E_{red} values are referred to the SCE electrode.*

VIII.3 Electrochemistry

Electrochemistry tells us about the electronic properties of the polyoxometalate hybrids and expresses the effect of functionalization on the redox potential of both the polyoxometalates and the ligands. Cyclic voltammograms of **POM-AB**, **POM-AC**, and **POM-AQ** ($C=10^{-3}$ M) were recorded at room temperature in acetonitrile (Figure 23).

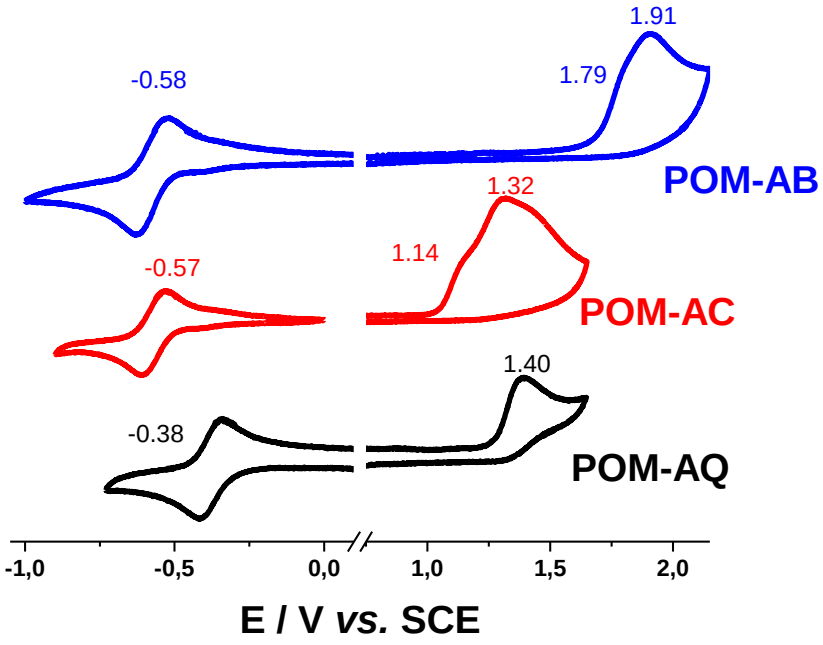

*Figure 23.Cyclic voltammograms of **POM-AB, POM-AC, and POM-AQ** ($C=10^{-3}$ M) at room temperature in acetonitrile.($[TBABF_4] = 10^{-3}$M, scan rate=0.05 $V.s^{-1}$)*

During the cathodic scan in the range -1.0 to 0V (vs. SCE), all hybrids exhibit one electron reversible reduction wave at -0.58V, -0.57V, and -0.38V (vs. SCE) for **POM-AB**, **POM-AC**, and **POM-AQ**, respectively. This is attributed to the reduction of the inorganic platform $[Mo_6O_{19}]^{2-}$, where the Mo^{VI} atom is reduced into Mo^{V}, forming the corresponding trianions. The organoimido hexamolybdate derivatives become more difficult to reduce compared to the non-coupled parent $(TBA)_2[Mo_6O_{19}]$. This observation stems from the superior donating effect of the organoimido ligand over the oxo ligand [61,77].Neverthless, **POM-AQ** is the easiest to reduce due to the electron withdrawing influence of CO groups belonging to the anthraquinone entity. This is confirmed in the fluorescence experiment results that illustrate the favorable electron transfer from the co-initiator MDEA into the **POM-AQ.**

During the anodic scan in the range 0V to 2.15V (vs. SCE), all hybrids show irreversible oxidation waves. **POM-AB** and **POM-AC** present two waves at 1.79V; 1.91V and 1.14V;1.32V, respectively, while there is one oxidation wave at 1.40V for **POM-AQ**. The oxidation potential of the organic molecules within the hybrid compounds shows great dependence on the withdrawing effect of $[Mo_6O_{19}]^{2-}$ on the π conjugation in the ligands [78]. It generally increases due to the electronic withdrawing-effect of $[Mo_6O_{19}]^{2-}$.

VIII.4 Laser Flash Photolysis

Laser flash photolysis experiments were further done on the POM derivatives and MDEA systems to explore the mechanism of the electronic transfer process between POM complexes and the co-initiator MDEA, and determine whether the singlet excited state

undergoes intersystem crossing to the triplet state. Transient absorption spectra obtained under excitation at 380 nm evidenced the presence of a large absorption band between 400 nm and 800 nm starting from 100 ns to 40 ms delay times for **POM-AQ**, **POM-AB**, and **POM-AC** (Figures 24-27).

Focusing first on the **POM-AQ** compound, we observed an absorption band at about 450 nm in the early time (Figure 24, left). This band decays rapidly in several nanoseconds and can be attributed to the singlet state absorption of the anthraquinone moiety. Then, a large absorption band between 400 and 800 nm appears in less than 100 ns until 40 ms delay times. It is generally assumed that when anthraquinone is functionalized with electron-donor groups (amine functional group), the lowest excited states show a strong charge transfer (CT) character [79]. This band mainly results from the conjugation of the free electron pair located on the p_z orbital of the nitrogen with the π electronic system of anthraquinone. In the presence of the POM moiety, the life-time associated with this CT band is evaluated to be 15±4 ms for **POM-AQ** (Figure 24, right). This long-lived CT state could be an intermediate in photoinduced electron transfer reactions between POM derivatives and MDEA.

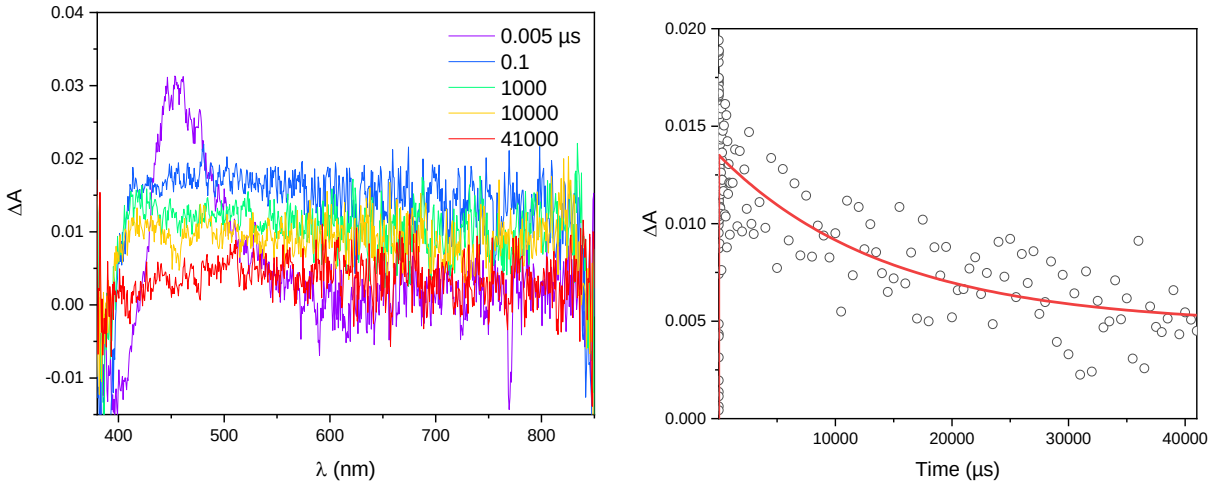

*Figure 24. Transient absorption spectra at indicated delay times (left) and the kinetic trace at 500 nm (right) of **POM-AQ** in acetonitrile ([**POM-AQ**] = 2.7 x 10^{-5} M, λ_{ex} = 380 nm).*

Similar results of long-lived CT in the millisecond time scale were obtained for **POM-AB** (CT lifetime = 21 ± 6 ms) and **POM-AC** (CT lifetime = 17 ± 5 ms). However, no singlet state at short delay times was observed in the case of **POM-AB** and **POM-AC**, which agrees with the absence of fluorescence in these compounds (Figures 25 and 26).

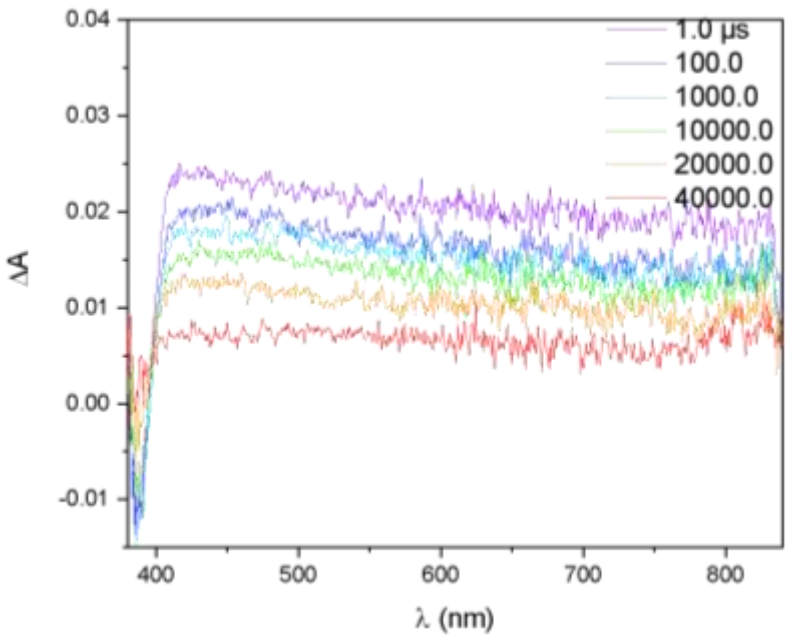

*Figure 25. Transient absorption spectra at indicated delay times of **POM-AB** in acetonitrile with λ_{ex} = 380 nm. [**POM-AB**] = 1.9 x 10^{-5} mol.L^{-1}.*

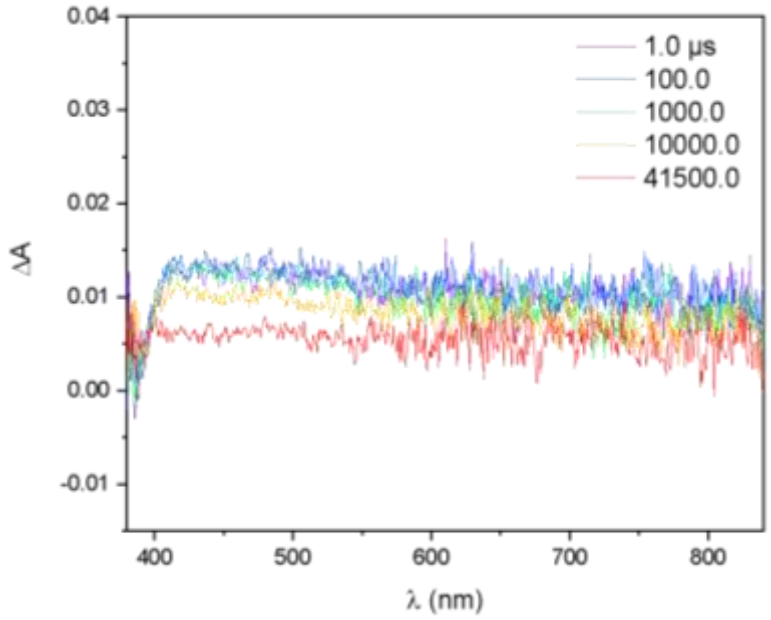

*Figure 26. Transient absorption spectra at indicated delay times of **POM-AC** in acetonitrile with, λ_{ex} = 380 nm. [**POM-AC**] = 3.1 x 10^{-5} mol.L^{-1}.*

VIII.5 EPR-ST Experiments

Additional electron paramagnetic resonance-spin trapping (EPR-ST) experiments have been done to observe radical species generated from photoinduced processes in consideration of the experimental results collected earlier, which highlights the excitation of POM

hybrids/MDEA upon irradiation, quenching potential of MDEA on the imido-functionalized hexamolybdate, and occurrence of electron transfer among the two entities.

EPR-ST technique identifies and qualifies radicals generated by photo-initiating systems under light excitation. However, electron paramagnetic resonance (EPR) alone fails to detect the free radicals due to their short lifetime, low concentrations, and high reactivity. Under these circumstances, the spin trapping (ST) technique was combined with EPR to distinguish different types of free radical species released from irradiation of photoinitiating systems. The spin trapping concept relies on using unsaturated diamagnetic molecules called spin traps, which will react with the radical products of photolysis ($R^{\bullet}$) through an addition reaction, resulting in more stable paramagnetic spin adducts [80–83].

In this work, the nitrone compound DMPO (5,5-Dimethyl-1-pyrroline *N*-oxide) (Figure 27) has been used as the spin trap in the EPR-ST technique to distinguish different types of the free radical species released from irradiation of the POM Hybrid/MDEA solutions in acetonitrile under argon using LED irradiation at 405 nm. The reaction of the radical species of photolysis ($R^{\bullet}$) with DMPO results in spin adduct nitroxide radical which is stabilized due to the delocalization of the radical along the $\pi_{N\text{-}O}$ three-electrons bond (Figure 28) [82].

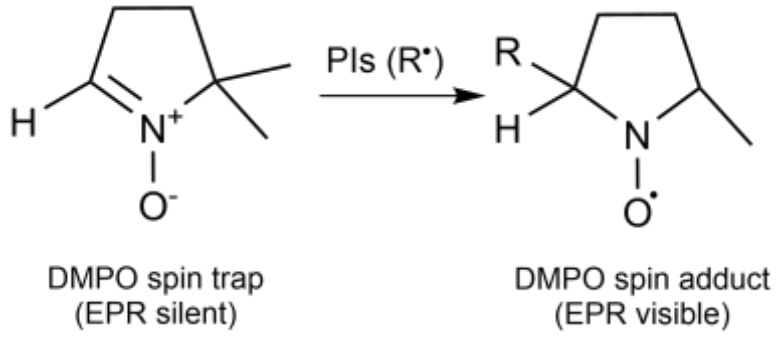

Figure 27. Principle of spin trapping with DMPO.(PIs abbreviation of photoinitiators radicals).[83]

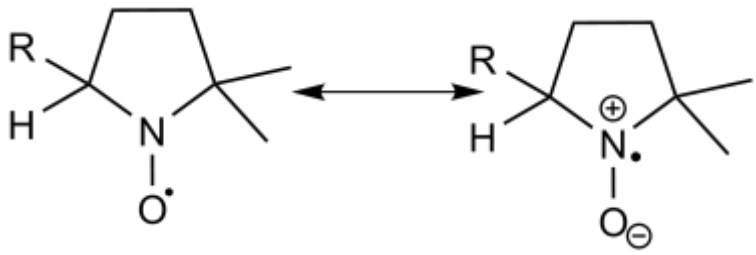

Figure 28. Equilibrium between resonance structures of nitroxide.[82]

The photoinitiation process for the generation of radicals upon irradiating the POM-hybrids (photoinitiators PIs) and MDEA co-initiator with LED at 400nm is proposed in Scheme 1. The process of electron transfer has been proven to be thermodynamically favored ($\Delta G_s<0$), where the POM-hybrids act as electron acceptors, and the MDEA acts as the electron donor

(see above the fluorescence experiments). This will result in a radical anion [POM-hybrid]$^{\bullet-}$ and a radical cation [MDEA]$^{\bullet+}$ followed by a proton transfer process through H abstraction from MDEA that will generate carbon-centered radicals as XC$^{\bullet}$–OH in case of **POM-AQ** and **POM-AB** or as XC$^{\bullet}$ in case of **POM-AC** (X: phenyl groups with the POM), along with α-aminoalkyl radical on the MDEA (Scheme 1, Figure 29) [84–88]. The carbon-centered and the α-aminoalkyl radicals will undergo addition reactions into the double bond of the DMPO spin trap, forming the nitroxide spin adducts, $^{\bullet}$DMPO-CR (aminoalkyl) and $^{\bullet}$DMPO-carbon-centered radicals (Figure 30).

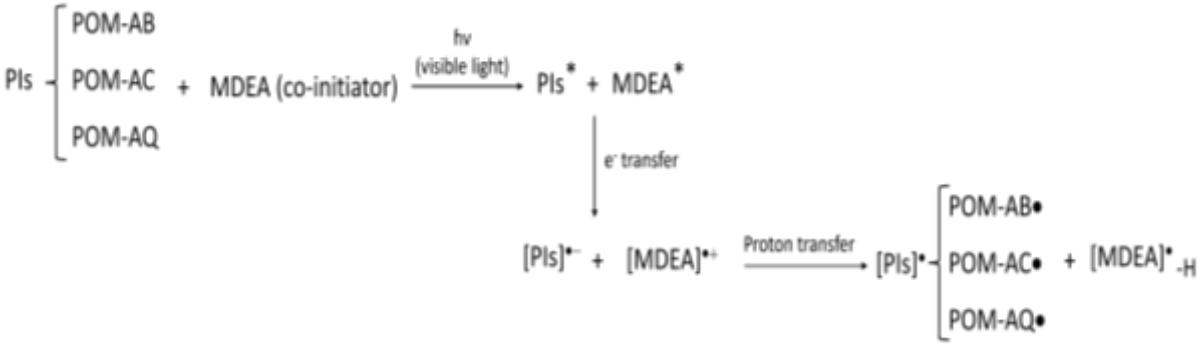

Scheme 1. Photolysis of POM-hybrids/MDEA under visible light.

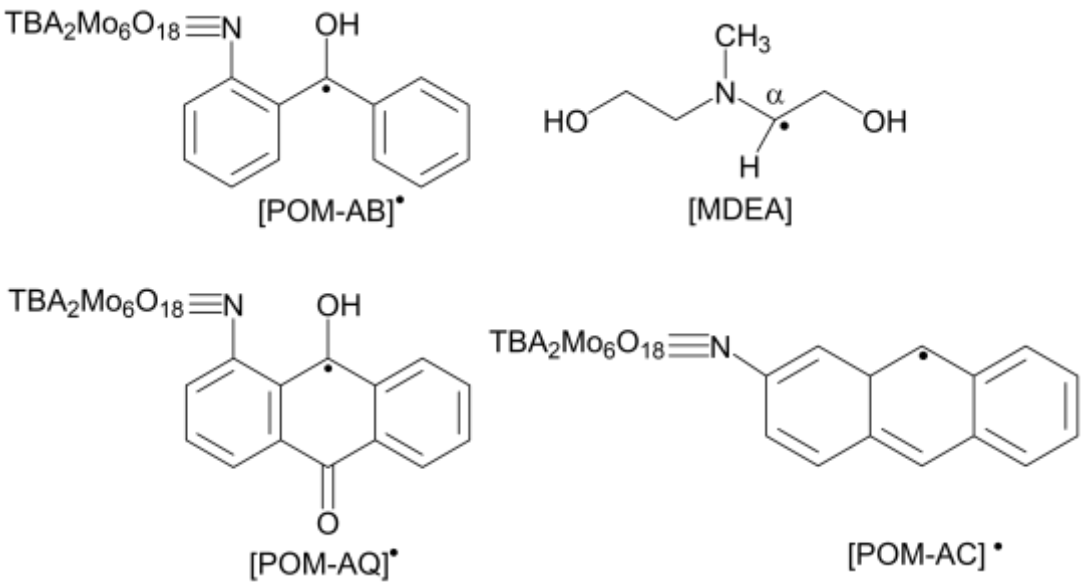

Figure 29. α-aminoalkyl radical and carbon-centered (R$^{\bullet}$) photolysis products.

The interactions between the unpaired electron of electronic spin (*S*=1/2) with the neighboring nuclei of the nuclear spin (I=1 for ^{14}N and ½ for ^{1}H) in the presence of a magnetic field applied (B_0) is known as hyperfine interaction (HF). Simultaneously, the electronic spin energy will split into (2nI + 1) levels (n is the number of neighboring equivalent nuclei) separated by values called hyperfine splitting constants ***a*,** expressed in Gauss (G) or millitesla (mT). The energy states of the electron spin are defined as :

$$E = hv = \boldsymbol{g}\mu_B B_0 M_s + \boldsymbol{a} M_s m_I$$

where ***g*** is the proportionality factor (or g-factor) derived from the equation $^{hv}/_{\beta B_0}$,and it is beneficial in the identification of the spin adduct as it is between 2.005 and 2.007 for all nitroxides, and slightly changes with different radical structures [89].

μ_B is the Bohr magneton.

Bo is the magnetic field.

M_S is the electron spin quantum number.

a is the hyperfine coupling constant.

m_I is the nuclear spin quantum number for the neighboring nucleus.

The interaction between the unpaired electron and the hydrogen nucleus (I=1/2) located two bonds (β-position) or three bonds (γ- position) far away from the nitroxide group bearing the radical causes electron spin energy level splitting into 2I + 1 =2(1/2) + 1=2 lines, separated by hyperfine coupling constant a_H^{β} and a_H^{γ}, respectively. In contrast, the interaction of unpaired electron and nitrogen (I=1) causes energy splitting into three lines separated by hyperfine coupling constant a_N.

The nitroxide nitrogen hyperfine coupling constant shows only minor variation (a_N ≈1.3 –1.6 mT), while the magnitude of hyperfine coupling constant related to the β hydrogen of the spin trap adduct (a_H^{β} ≈0.8 to 2.6 mT) depends significantly on the structure of the added substituents. The structure of the added substituent into the spin adduct influences the hyperfine constants because the bulkiness of the substituents may hinder the rotation of hydrogen nuclei spin and consequently cause a decrease in a_H^{β} value [80,82].

In the case of •DMPO-CR (aminoalkyl) radicals (Figure 30b), there are three types of hyperfine couplings: a_N, a_H^{β}, and a_H^{γ}.Notably, the interaction between the hydrogen nucleus at γ-position with the radical is negligible since it is far from the nitroxide group. Hence, the major hyperfine interaction arises majorly from the interaction of the unpaired electron with nitrogen and the hydrogen at β position belonging to the cyclic DMPO nitrone molecule. On the other hand, in the •DMPO-carbon-centered radicals (Figure 30a), there are two types of hyperfine couplings, a_N and a_H^{β} [13,90].

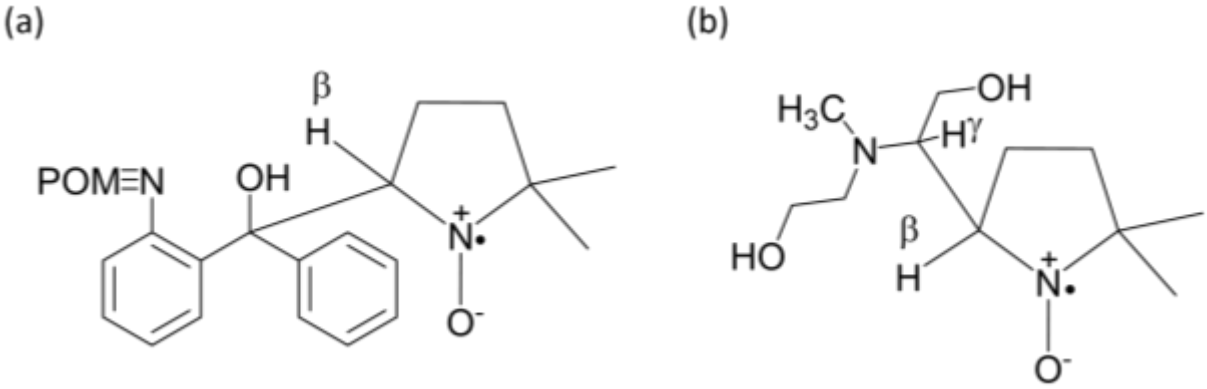

*Figure 30. Structures of **(a)** •DMPO-carbon-centered and **(b)** •DMPO-CR (aminoalkyl) radicals.*

According to previous investigations [91], the irradiation of **POM-AB**/MDEA/DMPO solutions in acetonitrile under argon using a LED@400 nm source resulted in the generation of an EPR signal (Figure 31) representing the superposition of: a dominant signal characterized by the spin-Hamiltonian parameters assigned to the DMPO-adduct with the aminoalkyl radical (a_N = 1.495±0.001 mT, a_H^{β} = 1.745±0.01 mT, a_H^{γ} = 0.136±0.01 mT, a_H^{γ} = 0.072±0.003 mT; g = 2.0057±0.0001), and other signals of DMPO-adduct with carbon-centered radical (a_N = 1.486±0.004 mT, a_H^{β} = 2.127±0.01 mT; g = 2.0058±0.0001) [92]. The a_H^{β} value in the case of DMPO–aminoalkyl substituent (a_H^{β} = 1.745±0.01 mT) is lower than that of carbon ketyl substituents (a_H^{β} = 2.127±0.01 mT), which is somehow less steric hindered due to the Mo-N triple bond linearity within the POM-hybrid compound. The intensity of both signals gradually increased upon the prolonged LED irradiation at 400 nm. The simulation best fit was calculated considering the relative concentration of •DMPO-CR (aminoalkyl) and •DMPO-carbon-centered radicals of 88 % and 12 %, respectively.

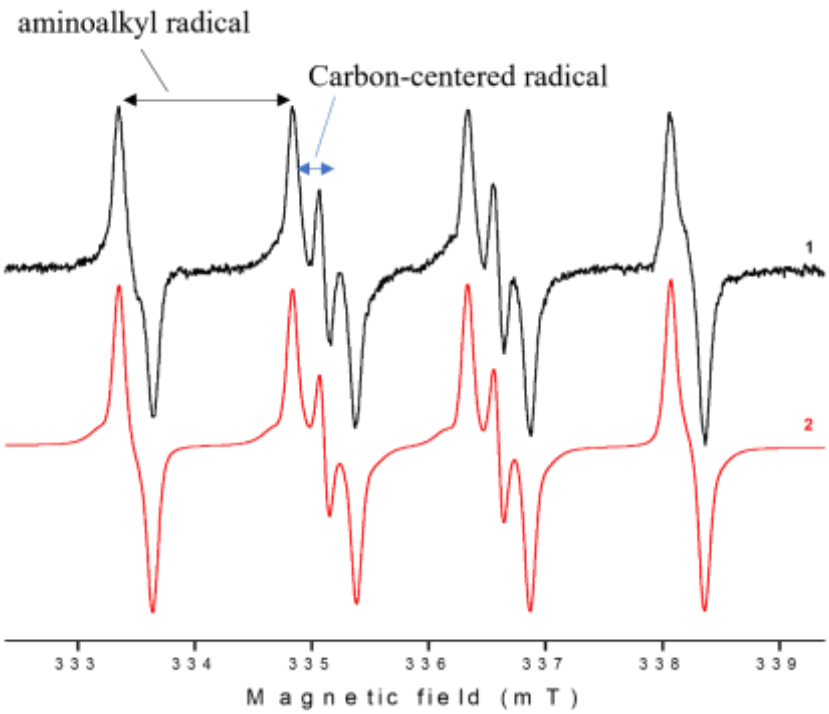

*Figure 31. The normalized experimental (1) and simulated (2) EPR spectra obtained after 900 s LED@400 nm exposure of **POM-AB**/MDEA/ACN solutions in the presence of a DMPO spin-trapping agent under argon.*

The generation of identical DMPO-adducts and gradual rise of their intensity was observed also upon LED@400 nm exposure of **POM-AC**/MDEA/DMPO (Figure 32) and **POM-AQ**/MDEA/DMPO (Figure 33) solutions in acetonitrile under argon. However, their stability in the experimental systems is very low, and the prolonged/stopped irradiation led to the rapid decline, most probably due to the high reactivity of the photoactivated system towards nitroxide moiety. The in situ generated alkyl radicals (α-aminoalkyl radical and carbon-centered radicals) from the **POM-AQ** or **POM-AC**/MDEA system in the presence of DMPO seem not stable, so they aren't just added to the cyclic nitrone DMPO but also got scavenged by the oxygen radical resulting in alkoxyamine products (Figure 34) [93].

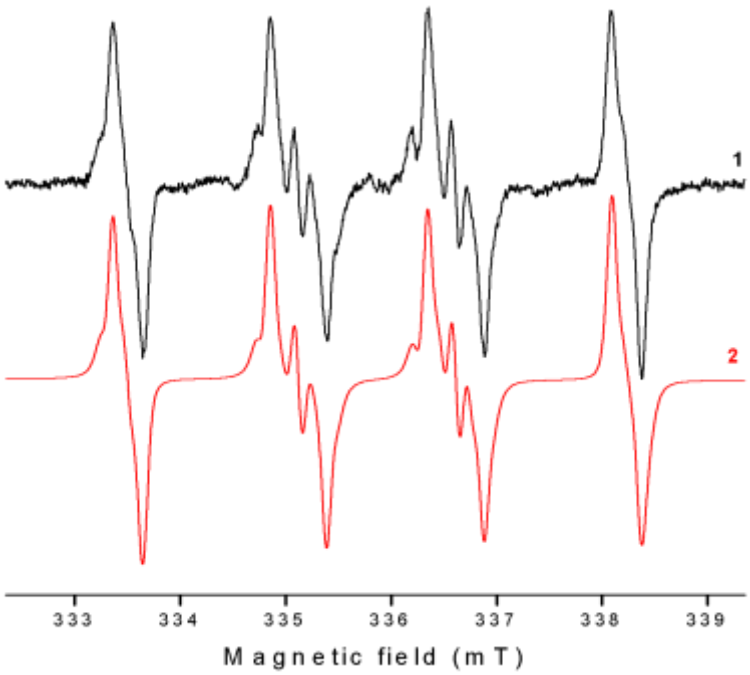

*Figure 32. The normalized experimental (1) and simulated (2) EPR spectra obtained after 900 s LED@400 nm exposure of **POM-AC**/MDEA/ACN solutions in the presence of a DMPO spin trapping agent under argon. The simulation best fit was calculated considering the relative concentration of •DMPO-CR (aminoalkyl) and •DMPO-carbon-centered radicals of 91 % and 9 %, respectively.*

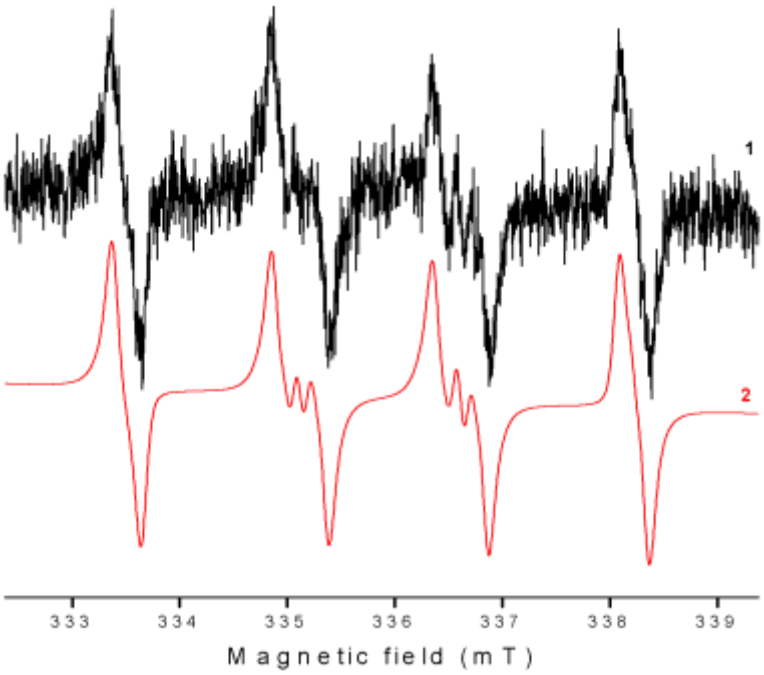

*Figure 33. The normalized experimental (1) and simulated (2) EPR spectra obtained during 225 s LED@400 nm exposure of **POM-AQ**/MDEA/ACN solutions in the presence of a DMPO spin trapping agent under argon. The simulation best fit was calculated considering the relative concentration of •DMPO-CR (aminoalkyl) and •DMPO-carbon-centered radicals of 67 % and 33 %, respectively.*

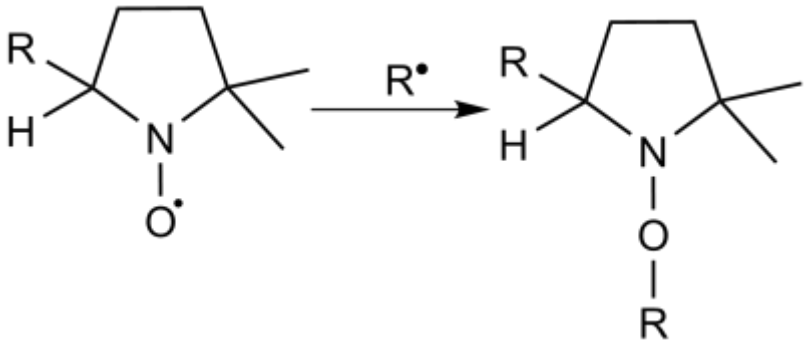

Figure 34. Scavenging of α-aminoalkyl and carbon-centered radicals by the nitroxide radical.

IX. Photopolymerization studies with POM derivatives photoinitiating systems and polymer characterization

IX.1 Free-radical photopolymerization

The use of polyoxometalates as photoinitiating systems have been scarcely studied [48–53]. To date, most of the investigations have used two- or three-component photo-initiating systems for free-radical polymerization acrylates under UV light irradiation (Hg-Xe lamp), and to the best of our knowledge, no photoinitiating systems based on POMs have been designed for initiating radical photopolymerization under irradiation with wavelengths higher than 405 nm. This may be related to the fact that the POMs considered in the previous studies do not absorb significantly in the visible range. In the following experiments, we will demonstrate the capability of imido POM derivatives to promote free-radical photopolymerization (FRP) under visible LEDs irradiation of commercial monomers, i.e., trimethylolpropane triacrylate (TMPTA) and soybean oil epoxidized acrylate (SOA).

TPMTA has three acrylate groups that polymerize rapidly in the presence of free radicals. It is widely applicable in manufacturing adhesives, packaging, and various wood, plastic, and metal coatings. Curing formulations containing TMPTA (e.g., acrylate dental fillings) induce cross-linking into the end product, providing improved mechanical properties, e.g., abrasion resistance, and high gloss potential [39]. SOA also shows excellent potential to polymerize into new materials in industrial and biomedical applications since it is renewable, biodegradable, readily available, and extensively unsaturated because it contains many acrylic groups which can polymerize with other double bonds of nearby molecules, upon exposure to UV light or Visible light. Moreover, its low viscosity renders it an outstanding, environmentally safe candidate in photocuring formulations in epoxy resin manufacturing. So, it is generally used as a plasticizer, stabilizer, reactive modifier, and diluent [40].

Photopolymerization experiments were done at room temperature under LEDs irradiation at 385, 405, 455, or 470 nm by dissolving 2 wt% and 5 wt% (with respect to the monomer weight) of POM derivatives (**POM-AC**, **POM-AB,** or **POM-AQ**) and the reductive co-initiator MDEA in

acrylate monomer (TMPTA or SOA), respectively. Infrared spectrometry was performed in parallel to monitor the decrease of the intensity of the C=C double bond characteristic band (1648-1589 cm^{-1}) in acrylate, which enables the evaluation of the %conversion of the monomer during polymerization (Figures 36-39). Table 6 summarizes the acrylate conversions of the two functional acrylate monomers in these conditions.

Upon light absorption by the photoinitiating POM-hybrids (PIs) and the co-initiator (MDEA), radicals designated as R• are generated. The radicals will be added to the acrylate monomers SOA and TMPTA (see their structures in Figure 1). Then, the acrylate chain propagates through the addition of the monomer into the radical chain. Lastly, termination occurs when the two active chain ends combine together or with the initiator radical (Figure 35).

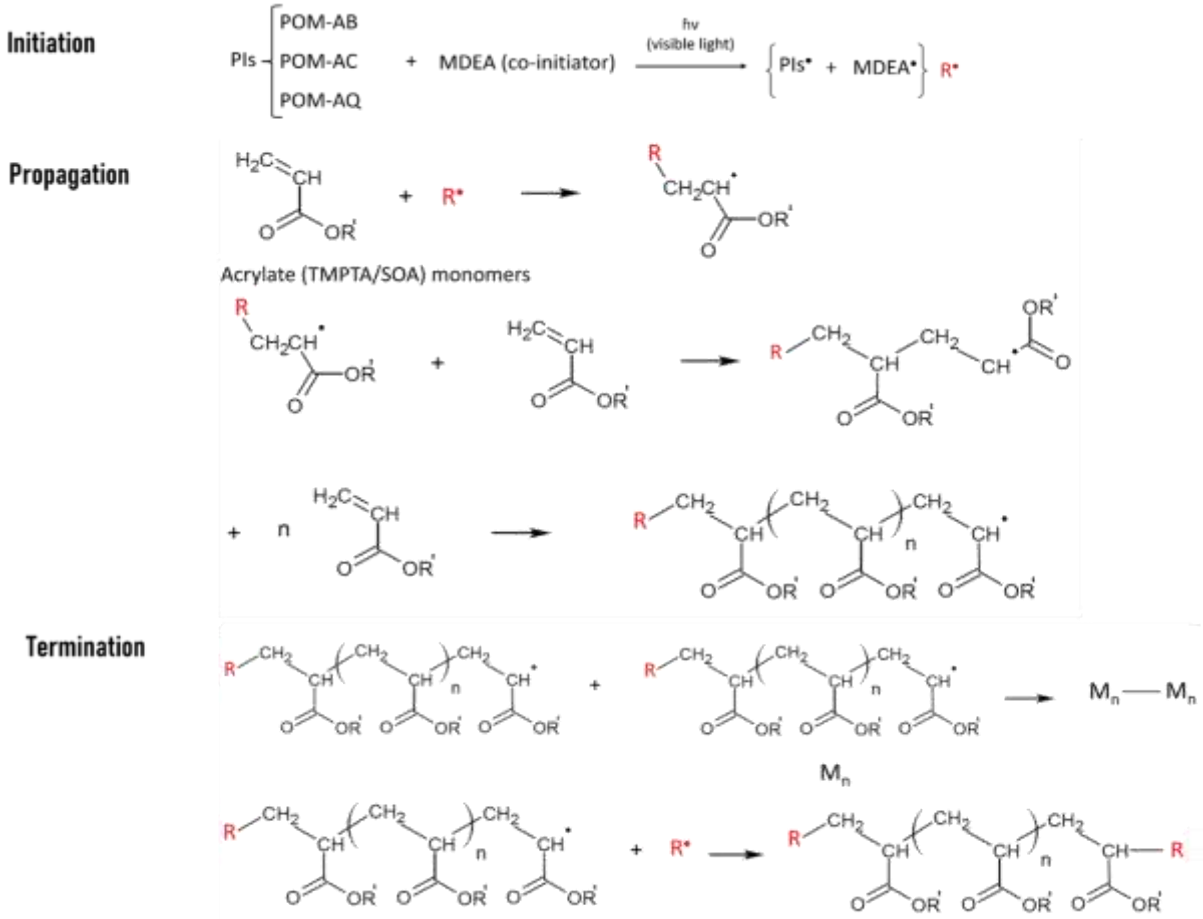

Figure 35. General mechanism of the free-radical polymerization of acrylates (TMPTA and SOA monomers) under visible light.

Conspicuously, no polymerization occurs under visible light radiation when adding each of the non-coupled precursors alone (hexamolybdate cluster or the organic entity) with the MDEA and acrylate monomers. On the other hand, POM derivatives/MDEA systems show good initiating properties, likely due to the formation of aminoalkyl and carbon-centered radical species, as demonstrated by the EPR-ST technique. The kinetics of polymerization is much

more effective in laminate (Figures 36,38) than under air (Figure 37,39) since the oxygen molecules may inhibit free-radical polymerization by several means, such as reacting with the initiators or growing chains to form stable peroxyl radical's incapable of reinitiating polymerization [94–96].

POM-AQ/MDEA photo-initiating system appears the most efficient as it records generally the highest % conversion, likely due to the highly favorable electron transfer reaction ($\Delta G_{S\ (POM\text{-}AQ/MDEA)}$ = -1.1 eV). For instance, in laminate, the use of **POM-AQ**/MDEA leads to the highest % of conversions with SOA (90% conversion) and TMPTA (50% conversion) at λ = 405 and 470nm, respectively. Overall, it is observed that the photopolymerization process occurs under LED irradiation in the visible range, with wavelength ranging from 405 to 470 nm, which, to our knowledge, is the first example of the synthesis of such composites incorporating POMs.

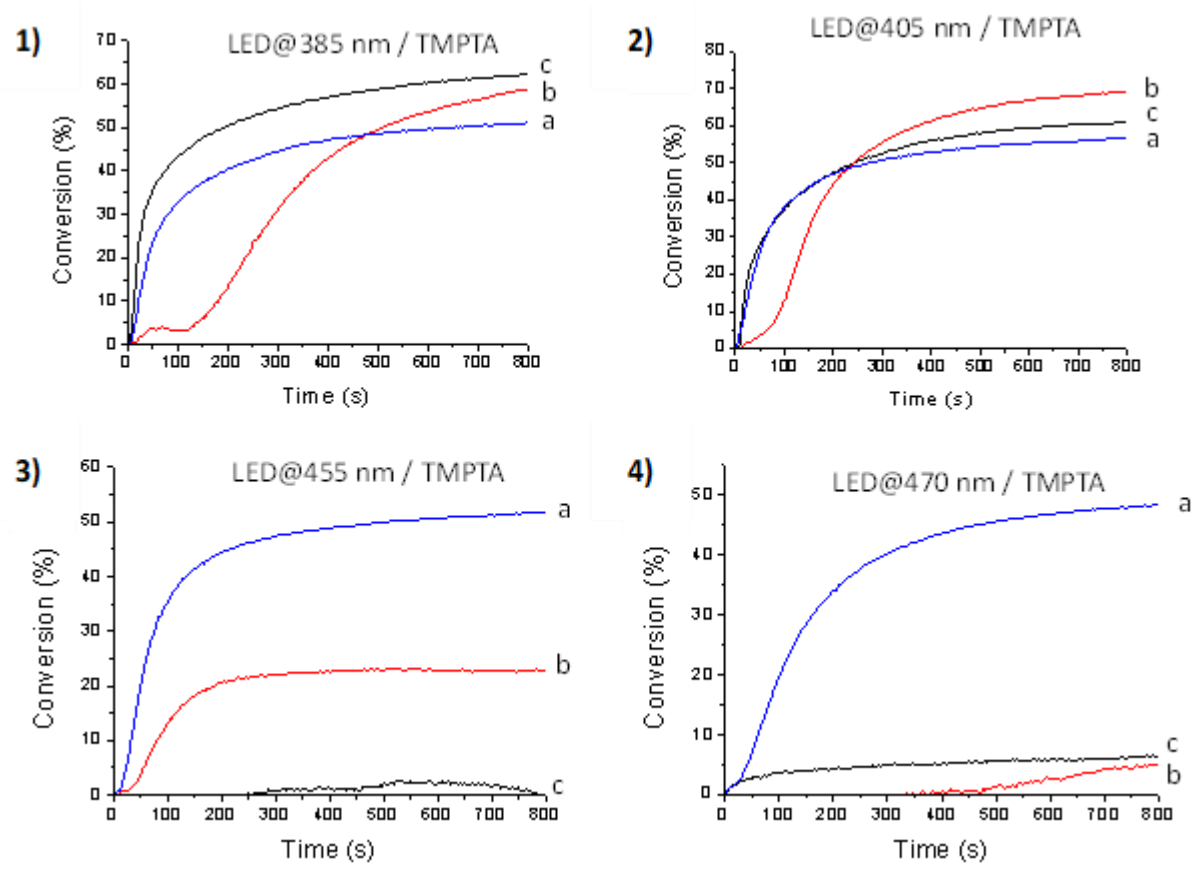

*Figure 36. Kinetic profiles were obtained by FT-IR by followeing the disappearance of the reactive acrylate groups of TMPTA in laminate in the presence of **POM-AQ**/MDEA (a), **POM-AC**/MDEA (b), and **POM-AB**/MDEA (c) upon exposure with 1) LED@385 nm, 2) LED@405nm, 3) LED@455 nm and 4) LED@470 nm. The thickness of the film = 12 µm.*

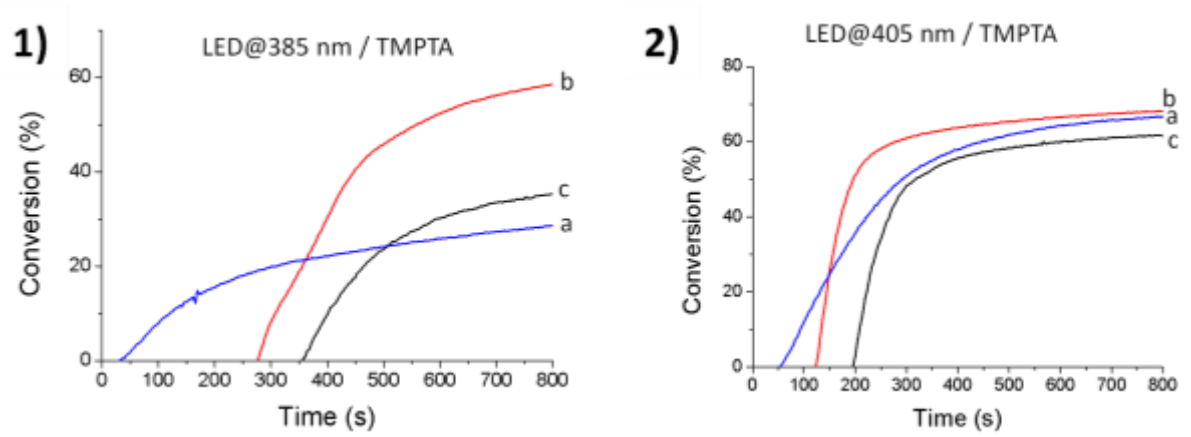

Figure 37. Kinetic profiles were obtained by FT-IR by followeing the disappearance of the reactive acrylate groups of TMPTA under air in the presence of a) ***POM-AQ****/MDEA, b)* ***POM-AC****/MDEA, and c)* ***POM-AB****/MDEA upon exposure with 1) LED@385 nm and 2) LED@405nm. The thickness of the film = 12 µm.*

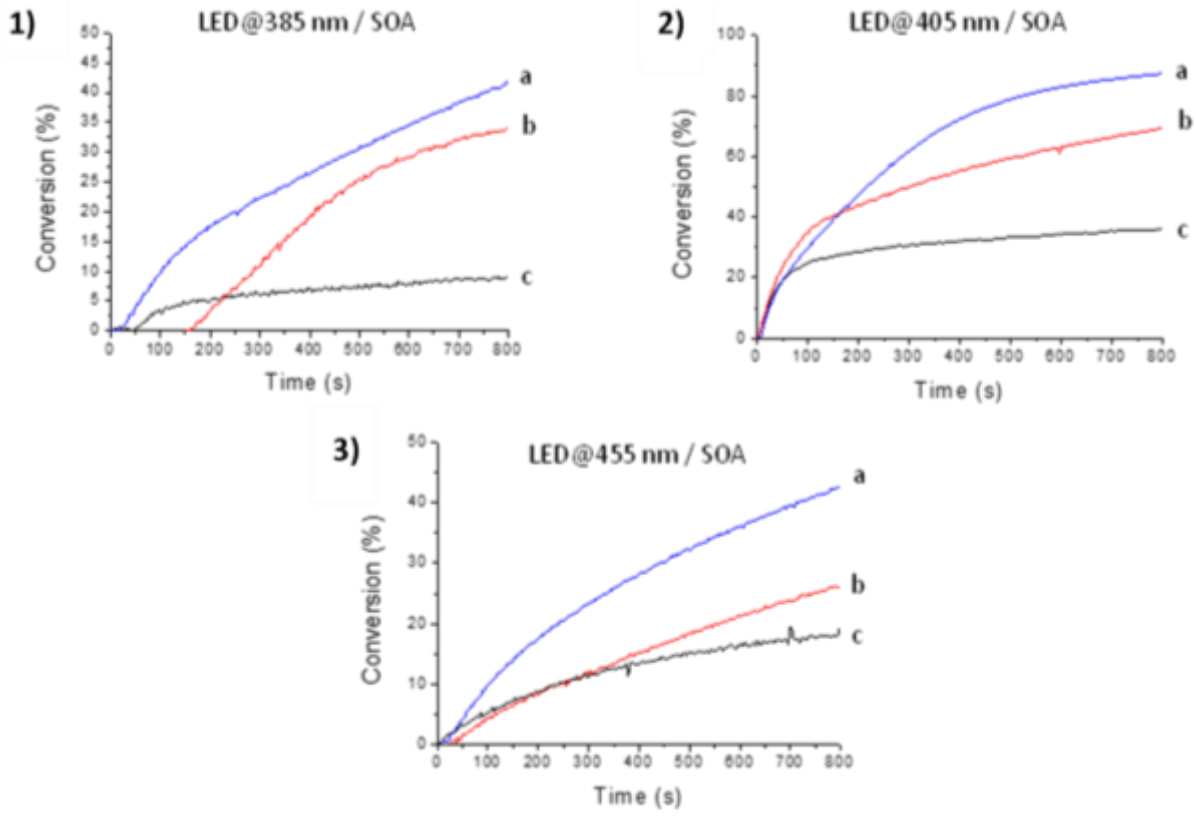

Figure 38. Kinetic profiles were obtained by FT-IR by followeing the disappearance of the reactive acrylate groups of SOA in laminate in the presence of a) ***POM-AQ****/MDEA, b)* ***POM-AC****/MDEA, and c)* ***POM-AB****/MDEA upon exposure with 1) LED@385 nm, 2) LED@405nm and 3) LED@455 nm. The thickness of the film = 12 µm.*

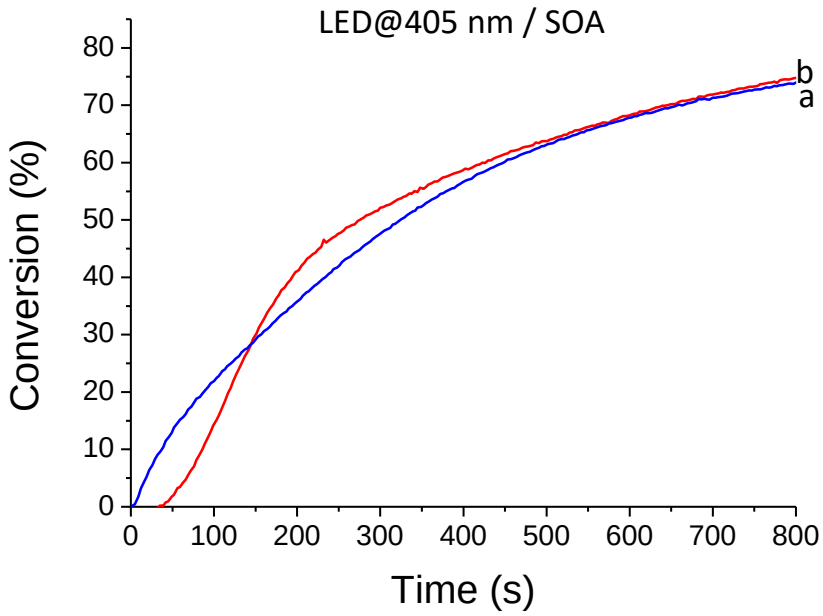

*Figure 39. Kinetic profiles of were obtained by FT-IR by followeing the disappearance of the reactive acrylate groups of SOA under air in the presence of a) **POM-AQ**/MDEA and b) **POM-AC**/MDEA upon exposure with LED@405nm. The thickness of the film = 12 µm.*

*Table 6. TMPTA and SOA final acrylate conversions (%) obtained by RT-FTIR after 800 s of irradiation (LEDs@385, 405, 455, and 470 nm) in laminate ([a]) and under air ([b]), in the presence of PIs/MDEA with PIs = **POM-AC**, **POM-AB** or **POM-AQ**.*

Photo-initiating systems	LED@385 nm	LED@405 nm	LED@455 nm	LED@470 nm
Monomer: TMPTA				
POM-AC/MDEA	58% [a], 55% [b* (280s)]	69% [a], 68% [b (130s)]	23% [a], 0% [b]	5% [a]
POM-AB/MDEA	62% [a], 35% [b* (360s)]	60% [a], 60% [b (200s)]	0% [a], 0% [b]	6% [a]
POM-AQ/MDEA	51% [a], 30% [b* (30s)]	57% [a], 66% [b* (50s)]	52% [a], 25% [b*(200s)]	50% [a]
Monomer: SOA				
POM-AC/MDEA	33% [a], 0% [b]	69% [a], 70% [b* (34s)]	26% [a], 0% [b]	-
POM-AB/MDEA	9% [a], 0% [b]	36% [a], 0% [b]	18% [a], 0% [b]	-
POM-AQ/MDEA	42% [a], 8% [b]	90% [a], 70% [b]	43% [a], 15% [b]	25% [a]

* (inhibition period in s under air)

IX.2 Materials characterization

Materials are synthesized with the best performing photo-initiating systems, i.e., **POM-AQ**/MDEA. The synthesis of rectangular **POM-AQ** derived materials (**POM-AQ**/MDEA/SOA) is performed under LED@405 nm irradiation and under air. The obtained materials adopted a rectangular shape due to the fabrication method. DSC results demonstrate that no endothermic peak is observable, meaning no further free-radical polymerization occurs

during thermal analysis in the -80°C to 200°C range. It seems that free-radical photopolymerization of SOA is complete even under air. T_g is evaluated at around 14°C (Figure 40), similar to what is described in the literature for UV-photoinduced SOA material [97].

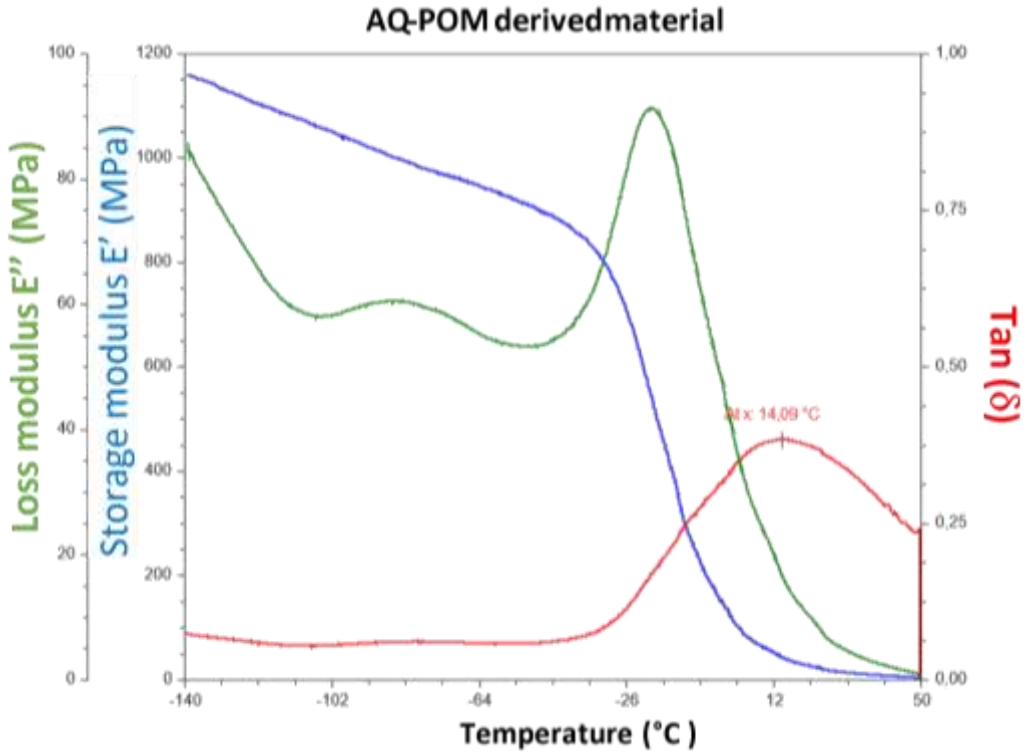

*Figure 40. Storage and loss modulus obtained by Dynamic Mechanical Analyses (DMA) between -140 and 50°C for **POM-AQ** derivatives samples. Tan (δ) in red, storage modulus (E') in blue, and loss modulus (E'') in green.*

Dynamic Mechanical Analysis were useful to characterize the viscoelastic behavior of the SOA-based polymer**.** The elasticity behavior of the polymer or its ability to store energy is given by storage modulus (E′), while the viscosity behavior or their ability to loss energy is measured by loss modulus (E''). The ratio of the loss to the storage moduli is expressed as tan (δ) and its maxima is indication of the transition glass (T_g) [98].

As seen in the DMA scan in Figure 40, the storage modulus (E') in blue, loss modulus (E'') in green, and the Tan (δ) for **POM-AQ** derivatives samples are measured between -140 and 50°C. At low temperature range -140 and -36°C,the value of the storage modulus (E') is maximum (ca. 1150) which means that the material is rigid since the polymer chains are stable. As temperature increases towards T_g at around 14°C, the polymer chains are becoming more flexible and thus the material is softer which explains the sharp decline of storage modulus (E'). At the same time, the loss modulus (E") and Tan (δ) increases until reaching maxima at T_g. Further increase of the temperature above Tg, reaching high temperature near ca. 50°C, the storage (E') and loss (E") moduli are low ,reaching a plateau that signifies that the material is rubbery(viscous).

Loading and unloading curves of the nanoindentation tests on **POM-AQ** coatings were overlapping, demonstrating an elastomeric behavior. The SOA-based polymer will expand when enough force is applied (loading). On the contrary, the material will restore its original shape gradually as applied forces decrease (unloading).

The SOA-based materials are fully elastic because they aren't deformed as they go back to their original shape, which explains how the unloading curve comes down very similarly to the loading curve and arrives at the same point at which the loading curve started. The SOA polymers are rich in cross-linking (extensive fatty acid chains), so forces applied will stretch this cross-linking, while in the unloading, the cross-links will restore their original shape. The elastic modulus of **POM-AQ**-based coatings is measured by fitting the load/displacement curve by a pure elastic indentation model and was evaluated to 96 ± 18 MPa. Surprisingly, in the same conditions, the reference coatings based on the 2,2-Dimethoxy-2-phenylacetophenone (DMPA). Surprisingly, in the same conditions, the reference coatings based on the 2,2-Dimethoxy-2-phenylacetophenone (DMPA) photo-initiating system did not lead to mechanically stable coatings for nanoindentation tests.

Considering the scratch resistance tests, the height profiles before and after scratches appear similar, confirming thus the entire recovery of the **POM-AQ**-based coatings and their noteworthy elastomeric behavior (Figure 41). It can be proposed that adding **POM-AQ** into the polymer matrix decreases the intermolecular forces into SOA films, thus improving their flexibility. Optical microscopy observation after scratches does not show any fracture, delamination, or residual imprint, demonstrating also a very good resistance to brittle fracture and adherence to the steel.

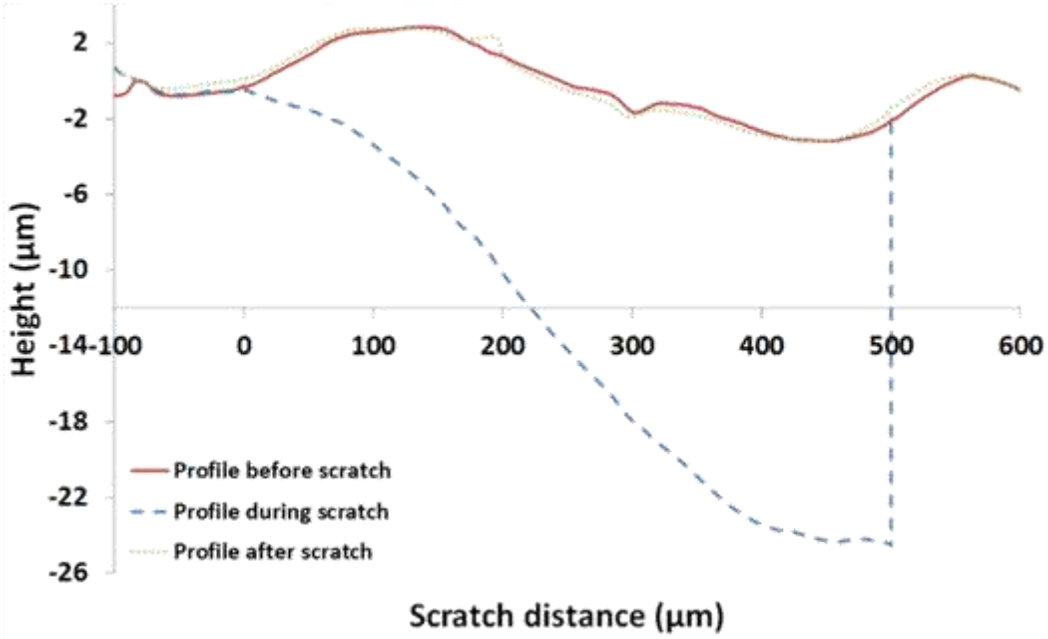

*Figure 41. Height profile before, during, and after a scratch on **POM-AQ** based coating on a steel substrate. Complete recovery of the sample after scratch confirms the elastomeric behavior and evidences a good adherence and resistance of the coating to fracture.*

X. CONCLUSION

In conclusion, we report herein a new synthetic strategy allowing shifting the photoinitiating activity of organic aromatic molecules from UV to visible light. Three imido-Lindqvist POMs obtained by reaction of amino aromatic derivatives of the anthracene, benzophenone, and anthraquinone UV photosensitizers, respectively, and the $[Mo_6O_{19}]^{2-}$ POM precursor have been fully characterized in the solid state and solution. Notably, these compounds have been obtained in one step in a very short reaction time (1 h).

Steady-State photolysis experiments evidenced a high interaction between the three reported hybrid POMs and MDEA, the reductive agent considered here for radical polymerization reactions. In addition, fluorescence studies highlight a favorable electron transfer process between the singlet excited state of **POM-AQ** and MDEA, while EPR-ST investigations allow the characterization of the MDEA-centered radical species generated from the photoinduced processes.

Very importantly, the capability of such imido POM derivatives to promote free-radical photopolymerization even under visible LED irradiation was demonstrated. After 800s, acrylate conversion yields up to 50% under 470 nm LED irradiation for the **POM-AQ**/MDEA/TMPTA photoinitiating system and 90% under 405 nm LED irradiation for the **POM-AQ**/MDEA/SOA one was indeed observed, while in such conditions no polymerization was evidenced considering 2-aminoanthraquinone as the photoinitiator.

Rectangular films prepared considering the **POM-AQ**/MDEA/SOA photosystem have been obtained, the free-radical photopolymerization of SOA being complete even when performed in the presence of air. The coatings exhibit very good flexibility, resistance to brittle fracture, and adherence to stainless steel substrate.

Overall, this work paves the way for elaborating a large range of easy-to-synthesize visible-light polymerization photoinitiators. Future work will focus on preparing related hybrids incorporating thiophene derivatives, which present very interesting photocatalytic and biological properties [99]. Also, while we report here on synthesizing POM derivatives covalently bonded to one organic fragment, imido-Lindqvist POMs incorporating up to six organic fragments can be obtained [53]. Investigation of the effect of the accumulation of organic photoinitiators around a single Lindqvist unit on the properties of the hybrid systems thus seems very appealing.

XI. Experimental Part

All chemicals and solvents for synthesis and characterizations were purchased from commercial sources except $(TBA)_2[Mo_6O_{19}]$ (TBA = tetrabutylammonium), which has been synthesized as previously described [100].

XI.1 General procedures

^{1}H NMR spectra were recorded at 298 K on a Bruker Advance 300 spectrometer operating at 300 MHz. Chemical shifts are expressed in parts per million (ppm) downfield from internal TMS. The following abbreviations were used to explain the multiplicities: s, singlet; d, doublet; t, triplet; br, broad peaks; m, multiplet or overlapping peaks.

Electrospray ionization (ESI) mass spectra were recorded on a Xevo QT of WATERS (quadrupole-time-of-flight) instrument. The temperature of the source block was set to 120 °C, and the desolvation temperature to 200 °C. A capillary voltage of 1 kV was used in the negative scan mode, and the cone voltage was set to 10 V to control the extent of fragmentation of the identified species. Mass calibration was performed using a solution of sodium formate in water: acetonitrile (2:8) from m/z = 50 to 3000. Sample solutions 50 µmol/L in acetonitrile were injected via a syringe pump directly connected to the ESI source at a 20 µL/min flow rate.

Infrared (IR) spectra were recorded on a Nicolet 30 ATR 6700 FT spectrometer. UV-vis spectra were recorded on a Perkin Elmer Lambda 750 UV/Vis/NIR spectrometer.

X-ray Diffraction. Intensity data collections were carried out with a Bruker D8 VENTURE diffractometer equipped with a PHOTON 100 CMOS bidimensional detector using a high brilliance IµS microfocus X-ray Mo Kα monochromatized radiation (λ = 0.71073 Å). The absorption corrections were based on multiple and symmetry-equivalent reflections in the data sets using the SADABS program [101] based on the method of Blessing [102]. The structures were solved by direct methods and refined by full-matrix least-squares using the SHELX-TL package [103]. The hydrogen atoms were theoretically located based on the conformation of the supporting atoms. The crystallographic data are gathered in Table 3,CCDC numbers of **POM-AB** and **POM-AC** are 2257497 and 2257498, respectively. These data can be obtained free of charge from The Cambridge Crystallographic Data Centre via www.ccdc.cam.ac.uk/data_request/cif.

UV-Visible absorption spectra were recorded using a Perkin Elmer Lambda 2 UV-Vis spectrophotometer.

Steady-State photolysis experiments. Fluorescence spectra were recorded from a FluoroMax-4 spectrofluorometer according to the previously described method [104]. The acetonitrile solutions of **POM-AQ**, **POM-AC,** and **POM-AB** were irradiated under LED@405 nm

(25 mW/cm^2) under air, with and without the presence of a reductive co-initiator MDEA to observe their photostability.

Electron Paramagnetic Resonance Spin-trapping (EPR-ST) experiments. The X-band cw-EPR spectra (modulation frequency of 100 kHz) were monitored with the EMX*plus* spectrometer (Bruker) equipped with the High Sensitivity Probe-head (Bruker) in the small quartz flat cell (Wilmad-LabGlass, WG 808-Q). The spin-trapping agent 5,5-dimethyl-1-pyrroline *N*-oxide (DMPO; Sigma-Aldrich) was distilled prior to the application and dissolved in acetonitrile (ACN; SeccoSolv® Merck). The solutions prepared by mixing stock solutions of POM-derivatives, MDEA, and DMPO in ACN were carefully saturated by argon and immediately irradiated at 295 K directly in the EPR resonator utilizing an LED@400 nm source (λ_{max} = 400 nm; Bluepoint LED, Hönle UV Technology). The EPR spectra were recorded *in situ* during/after a defined exposure. The *g*-factors were determined with an uncertainty of ± 0.0001 by exploiting a nuclear magnetic resonance teslameter (ER 036TM, Bruker) and integrated frequency counter. The experimental EPR spectra were analyzed by the WinEPR software (Bruker), and the calculations of spin-Hamiltonian parameters were performed with the EasySpin toolbox working on MatLab® platform [105]. The standard EPR spectrometer settings were as follows: microwave frequency, ~ 9.427 GHz; microwave power, ~11.10 mW or ~20.93 mW; center field, ~335.8 mT; sweep width, 8–10 mT; gain, 2.00×10^5; modulation amplitude, 0.1 mT or 0.05 mT; sweep time, 45 s; time constant, 10.24 ms; the number of scans, 5 or 10.

Cyclic voltammetry. Cyclic voltammetry scans were done according to a previously described procedure [105]. Measurements were carried out on acetonitrile solutions of POM derivatives (C = 10^{-3} M) between 0 and 2.15 V for oxidation and between 0 and -1V for reduction, with a 0.05 V. s^{-1} scan rate. The data were analyzed on GPES electrochemical software 4.9 (Utrecht, Netherlands).

Laser Flash Photolysis experiments. Nanosecond transient absorption measurements were performed using a home-built setup, which has been described previously [106]. Briefly, a Nd: YAG pumped optical parametric oscillator (OPO) laser was used for sample excitation at 380 nm with an energy of ~ 2 mJ/pulse with a repetition rate of 10 Hz. A white light continuum laser (STM-2-UV LEUKOS) at a repetition rate of 20 Hz was used as a probe. The probe beam was split into two arms, one for probing samples and the other for reference, to compensate for energy fluctuations. The probing arms were then coupled into a round-to-linear optical fiber bundle before being analyzed by a spectrograph SPEX 270M (Jobin-Yvon). The dispersed white light was detected by an intensified charge-coupled device (ICCD) detector PIMAX 4 (Princeton Instrument). Transient absorption spectra were calculated using the following formula:

$$\Delta A = \log_{10}\left(\frac{S_{ref}^{on}}{S_{ref}^{off}} \times \frac{S_{prob}^{off}}{S_{prob}^{on}}\right)$$

where S_{ref}^{on} and S_{ref}^{off} are reference spectra when the pump laser is on and off ,respectively, S_{prob}^{on} and S_{prob}^{off} are probe spectra when pump laser is on and off respectively.

Photopolymerization kinetic studies. 2 wt% (with respect to the monomer) of POM derivatives (**POM-AC**, **POM-AB,** or **POM-AQ**) were dissolved with 5 wt% (with respect to the monomer) of the reductive co-initiator MDEA in acrylate monomer (TMPTA or SOA). After stirring and sonicating the respective formulations for 5 min, photopolymerizations were performed at room temperature. 12 µm-layers of solution were put down to a BaF_2 pellet and irradiated with LED@385 nm (44 mW.cm^{-2}), LED@405 nm (25 mW.cm^{-2}), LED@455 nm (15 mW.cm^{-2}) or LED @470 nm (25 mW.cm^{-2}), under air or in laminate conditions. The Infrared spectra of the sample were continuously recorded by Real-Time Fourier Transform InfraRed Spectroscopy (RT-FTIR) with a JASCO FTIR 4700 Instrument, as previously described [107]. The photo-reactivity of the acrylate monomers was observed by following the acrylate functions absorption bands at 1636 cm^{-1}.

Nanoindentation experiments. Nanoindentation and scratch experiments were performed on steel substrate coatings at room temperature. A commercial Nano Indenter (G200 from Agilent Technologies) using a Berkovich tip (Micro Star Technologies) was used. Thirty tests were done. Samples were loaded and unloaded at a constant strain rate (0.05 s^{-1}) using a homemade method [108]. Loading was realized using the Continuous Stiffness Method (CSM) until a 1 µm depth was obtained. Unloading was performed after a hold load plateau of 60 s to achieve the viscous response. Twenty parallel scratches face a forward distant from 200 µm were performed, with a load increasing from 0 to 100 mN on a 500 µm length.

DSC measurements. DSC measurements were performed on a TA Instruments DSC25 discovery series with a refrigerated cooling system RCS90.

Dynamic Mechanical Analyses (DMA). DMA experiments were done with a TA Q800 DMA apparatus equipped with a tensile setup to characterize the thermo-mechanical behavior of the POM-derived samples according to a previous procedure [109]. Experiments were performed in a closed environment, and samples were cooled to -140 °C and heated to 50 °C with a 3 °C/min ramp rate. The applied stress frequency was 1 Hz, with a 0.1% deformation and a pre-load static force of 0.01 N.

XI.2 Synthesis of the molecular compounds

XI.2.1 Synthesis of $(TBA)_2[Mo_6O_{18}(NC_6H_4C(O)C_6H_5)]$ (POM-AB)

Under an inert atmosphere, $(TBA)_2[Mo_6O_{19}]$ (0.887 g, 0.65 mmol), 2-aminobenzophenone (0.128 g, 0.65 mmol, 1 eq) and N,N'-dicyclohexylcarbodiimide (DCC) (0.188 g, 0.91 mmol, 1.4 eq.) were suspended in 8 mL of anhydrous DMSO. The pale-yellow mixture was heated at 70°C for 1 hour, turning dark-red with time. Once the suspension cooled down to room temperature, the mixture was filtered to remove the dicyclohexylcarbodiurea. The resulting filtrate was then added into a flask containing diethyl ether (200 mL), leading to the precipitation of the crude product as an orange powder, which was recrystallized from hot acetonitrile (ca. 50°C, 10 mL). Orange crystals of POM-AB were then isolated by filtration and washed with ethanol and diethyl ether (0.709 g, 0.46 mmol, yield 71%). ^{1}H NMR (CD_3CN, 300 MHz): δ = 7.84-7.19 (m, 9H, anthracene group), 3.12 (t, 16H, TBA), 1.62 (m, 16H, TBA), 1.39 (m, 16H, TBA), 0.98 (t, 24H, TBA). FT-IR (cm^{-1}): 2958 (s), 2933 (s), 2871 (s), 1656 (s), 1598 (m), 1581 (w), 1480 (s), 1377 (m), 1330 (m), 1315 (m), 1292 (m), 1273 (m), 1166 (w), 1151 (w), 1106 (w), 1025 (w), 976 (m, ν(Mo-N)), 944 (s, ν(Mo-O_t)), 924 (sh), 879 (w), 764 (s, ν(Mo-O_b-Mo)), 588 (s). ESI/MS: $[Mo_6O_{19}]^{2-}$ *m*\z = 439.67 (exp.), *m*\z = 440.15 (calc.); $[Mo_6O_{18}(NC_6H_4$-$C(O)$-$C_6H_5)]^{2-}$ *m*\z = 529.20 (exp.), *m*\z = 529.43 (calc.); $((TBA)[Mo_6O_{18}(NC_6H_4$-$C(O)$-$C_6H_5)])^-$ *m*\z = 1302.70 (exp.), *m*\z = 1301.31 (calc.). Anal. Calcd for $Mo_6O_{19}N_3C_{45}H_{81}$ (found) %: C, 35.01 (35.16); H, 5.29 (5.17); N, 2.72 (2.75).

XI.2.2 Synthesis of $(TBA)_2[Mo_6O_{18}(NC_{14}H_9)]$ (POM-AC)

POM-AC was synthesized following the same protocol as that described for POM-AB but using 2-aminoanthracene (0.125 g, 0.65 mmol, 1 eq) instead of 2-aminobenzophenone. The reddish crude product was recrystallized from hot acetonitrile (ca. 50°C, 3 mL) and isolated by filtration as a red powder, which was washed with diethyl ether (0.349 g, 0.23 mmol, yield 35%). Crystals suitable for X-rays diffraction were obtained through diffusion of *tert*-butylmethyl ether into an acetonitrile solution. ^{1}H NMR (CD_3CN, 300 MHz): δ = 8.51 (d, 2H), 8.07 (m, 3H), 7.87 (s, 1H), 7.55 (m, 2H), 7.40 (dd, 1H), 3.12 (t, 16H, TBA), 1.61 (m, 16H, TBA), 1.36 (m, 16H, TBA), 0.98 (t, 24H, TBA). FT-IR (cm^{-1}): 2960 (s), 2932 (s), 2873 (s), 1480 (s), 1454 (s), 1377 (m), 1343 (m), 1309 (m), 1296 (m), 1239 (w), 1147 (w), 1107 (w), 1068 (w), 1029 (w), 975 (m, ν(Mo-N)), 945 (vs, ν(Mo-O_t)), 894 (s), 765 (s, ν(Mo-O_b-Mo)), 583 (s). ESI/MS: $[Mo_6O_{19}]^{2-}$ *m*\z = 439.88 (exp.), *m*\z = 440.15 (calc.); $[Mo_6O_{18}(NC_{14}H_9)]^{2-}$ *m*\z = 528.19 (exp.), *m*\z = 527.5 (calc.); $((TBA)[Mo_6O_{18}(NC_{14}H_9)])^-$ *m*\z = 1296.67 (exp.), *m*\z = 1297.0 (calc.). Anal. Calcd for $Mo_6O_{18}N_3C_{46}H_{81}$ (found) %: C, 35.90 (35.72); H, 5.30 (5.20); N, 2.70 (2.74).

XI.2.3 Synthesis of $(TBA)_2[Mo_6O_{18}(NC_{14}H_7O_2)]$ (POM-AQ)

POM-AQ was synthesized following the same protocol as that described for POM-AB but using 2-aminoanthraquinone (0.145 g, 0.65 mmol, 1 eq) instead of 2-aminobenzophenone. After filtration of the dicyclohexylcarbodiurea, the resulting filtrate was then added into a flask

containing diethyl ether (200 mL) and ethanol (50 mL), leading to the precipitation of the crude product as a brown-reddish powder. The powder was collected, washed with ethanol, and dried with ether (m = 0.856 g). It was then solubilized in a minimum of acetonitrile. After a few hours, the resulting mixture was filtrated, the solid mainly consisting of unreacted POM precursor. The filtrate was evaporated, and POM-AQ was isolated as a brown powder after trituration with diethylether (0.450 g). ^{1}H NMR (CD_3CN, 300 MHz): δ = 8.22 (m, 2.4H), 7.85 (m, 2.4H), 7.53 (dd, 0.8H), 3.16 (t, 16H, TBA), 1.65 (m, 16H, TBA), 1.40 (m, 16H, TBA), 0.98 (t, 24H, TBA). FT-IR (cm^{-1}): 2961 (s), 2933 (s), 2873 (s), 1672 (s), 1574 (s), 1464 (s), 1415 (w), 1379 (m), 1335 (s), 1315 (s), 1284 (s), 1151 (m), 1098 (w), 1063 (w), 977 (m, ν(Mo-N)), 945 (vs, ν(Mo-O_t)), 852 (w), 765 (s, ν(Mo-O_b-Mo)), 586 (s). ESI/MS: $[Mo_6O_{18}(NC_{14}H_7O_2)]^{2-}$ *m**z* = 540.17 (exp.), *m**z* = 542.48 (calc.); $(H[O_{18}Mo_6(NC_{14}H_7O_2)])^-$ *m**z* = 1085.39 (exp.), *m**z* = 1085.96 (calc.); $((TBA)[Mo_6O_{18}(NC_{14}H_7O_2)])^-$ *m**z* = 1328.67 (exp.), *m**z* = 1327.42 (calc.).

XII. References

(1) Chiulan, I.; Heggset, E. B.; Voicu, Ş. I.; Chinga-Carrasco, G. Photopolymerization of Bio-Based Polymers in a Biomedical Engineering Perspective. *Biomacromolecules* **2021**, *22* (5), 1795–1814. https://doi.org/10.1021/acs.biomac.0c01745.

(2) Zhu, J.; Zhang, Q.; Yang, T.; Liu, Y.; Liu, R. 3D Printing of Multi-Scalable Structures via High Penetration near-Infrared Photopolymerization. *Nat Commun* **2020**, *11* (1), 3462. https://doi.org/10.1038/s41467-020-17251-z.

(3) Aduba, D. C.; Margaretta, E. D.; Marnot, A. E. C.; Heifferon, K. V.; Surbey, W. R.; Chartrain, N. A.; Whittington, A. R.; Long, T. E.; Williams, C. B. Vat Photopolymerization 3D Printing of Acid-Cleavable PEG-Methacrylate Networks for Biomaterial Applications. *Materials Today Communications* **2019**, *19*, 204–211. https://doi.org/10.1016/j.mtcomm.2019.01.003.

(4) Yagci, Y.; Jockusch, S.; Turro, N. J. Photoinitiated Polymerization: Advances, Challenges, and Opportunities. *Macromolecules* **2010**, *43* (15), 6245–6260. https://doi.org/10.1021/ma1007545.

(5) Ghobril, C.; Grinstaff, M. W. The Chemistry and Engineering of Polymeric Hydrogel Adhesives for Wound Closure: A Tutorial. *Chem. Soc. Rev.* **2015**, *44* (7), 1820–1835. https://doi.org/10.1039/C4CS00332B.

(6) Velema, W. A.; Szymanski, W.; Feringa, B. L. Photopharmacology: Beyond Proof of Principle. *J. Am. Chem. Soc.* **2014**, *136* (6), 2178–2191. https://doi.org/10.1021/ja413063e.

(7) Yang, H.; Li, G.; Stansbury, J. W.; Zhu, X.; Wang, X.; Nie, J. Smart Antibacterial Surface Made by Photopolymerization. *ACS Appl. Mater. Interfaces* **2016**, *8* (41), 28047–28054. https://doi.org/10.1021/acsami.6b09343.

(8) Zhu, J.; Tang, Y.; Wang, G.; Mao, J.; Liu, Z.; Sun, T.; Wang, M.; Chen, D.; Yang, Y.; Li, J.; Deng, Y.; Yang, S. Green, Rapid, and Universal Preparation Approach of Graphene Quantum Dots under Ultraviolet Irradiation. *ACS Appl. Mater. Interfaces* **2017**, *9* (16), 14470–14477. https://doi.org/10.1021/acsami.6b11525.

(9) Yoon, B.; Ham, D.-Y.; Yarimaga, O.; An, H.; Lee, C. W.; Kim, J.-M. Inkjet Printing of Conjugated Polymer Precursors on Paper Substrates for Colorimetric Sensing and Flexible Electrothermochromic Display. *Advanced Materials* **2011**, *23* (46), 5492–5497. https://doi.org/10.1002/adma.201103471.

(10) Yasutake, M.; Andou, Y.; Hiki, S.; Nishida, H.; Endo, T. Controlled Radical Polymerization of Vaporized Vinyl Monomers on Solid Surfaces under UV Irradiation. *Macromolecular Chemistry and Physics* **2004**, *205* (4), 492–499. https://doi.org/10.1002/macp.200300089.

(11) Moore, A. R.; Kwen, H.; Beatty, A. M.; Maatta, E. A. Organoimido-Polyoxometalates as Polymer Pendants. *Chem. Commun.* **2000**, No. 18, 1793–1794. https://doi.org/10.1039/B005022I.

(12) Breloy, L.; Brezová, V.; Blacha-Grzechnik, A.; Presset, M.; Yildirim, M. S.; Yilmaz, I.; Yagci, Y.; Versace, D.-L. Visible Light Anthraquinone Functional Phthalocyanine Photoinitiator for Free-Radical and Cationic Polymerizations. *Macromolecules* **2020**, *53* (1), 112–124. https://doi.org/10.1021/acs.macromol.9b01630.

(13) Sautrot-Ba, P.; Jockusch, S.; Malval, J.-P.; Brezová, V.; Rivard, M.; Abbad-Andaloussi, S.; Blacha-Grzechnik, A.; Versace, D.-L. Quinizarin Derivatives as Photoinitiators for Free-Radical and Cationic Photopolymerizations in the Visible Spectral Range. *Macromolecules* **2020**, *53* (4), 1129–1141. https://doi.org/10.1021/acs.macromol.9b02448.

(14) Xiao, P.; Dumur, F.; Graff, B.; Fouassier, J. P.; Gigmes, D.; Lalevée, J. Cationic and Thiol–Ene Photopolymerization upon Red Lights Using Anthraquinone Derivatives as Photoinitiators. *Macromolecules* **2013**, *46* (17), 6744–6750. https://doi.org/10.1021/ma401513b.

(15) Tomane, S.; Sautrot-Ba, P.; Mazeran, P.-E.; Lalevée, J.; Graff, B.; Morlet-Savary, F.; Abbad-Andaloussi, S.; Langlois, V.; Versace, D.-L. Photoinitiating Systems Based on Anthraquinone Derivatives: Synthesis of Antifouling and Biocide Coatings. *ChemPlusChem* **2017**, *82* (10), 1298–1307. https://doi.org/10.1002/cplu.201700365.
(16) Zhang, J.; Lalevée, J.; Hill, N. S.; Launay, K.; Morlet-Savary, F.; Graff, B.; Stenzel, M. H.; Coote, M. L.; Xiao, P. Disubstituted Aminoanthraquinone-Based Multicolor Photoinitiators: Photoinitiation Mechanism and Ability of Cationic Polymerization under Blue, Green, Yellow, and Red LEDs. *Macromolecules* **2018**, *51* (20), 8165–8173. https://doi.org/10.1021/acs.macromol.8b01763.
(17) Zhu, Y.; Pi, J.; Zhang, Y.; Xu, D.; Yagci, Y.; Liu, R. A New Anthraquinone Derivative as a near UV and Visible Light Photoinitiator for Free-Radical, Thiol–Ene and Cationic Polymerizations. *Polym. Chem.* **2021**, *12* (22), 3299–3306. https://doi.org/10.1039/D1PY00347J.
(18) Xiao, P.; Dumur, F.; Graff, B.; Gigmes, D.; Fouassier, J. P.; Lalevée, J. Variations on the Benzophenone Skeleton: Novel High Performance Blue Light Sensitive Photoinitiating Systems. *Macromolecules* **2013**, *46* (19), 7661–7667. https://doi.org/10.1021/ma401766v.
(19) Zhang, J.; Zivic, N.; Dumur, F.; Xiao, P.; Graff, B.; Gigmes, D.; Fouassier, J. P.; Lalevée, J. A Benzophenone-Naphthalimide Derivative as Versatile Photoinitiator of Polymerization under near UV and Visible Lights. *Journal of Polymer Science Part A: Polymer Chemistry* **2015**, *53* (3), 445–451. https://doi.org/10.1002/pola.27451.
(20) Liu, S.; Brunel, D.; Noirbent, G.; Mau, A.; Chen, H.; Morlet-Savary, F.; Graff, B.; Gigmes, D.; Xiao, P.; Dumur, F.; Lalevée, J. New Multifunctional Benzophenone-Based Photoinitiators with High Migration Stability and Their Applications in 3D Printing. *Mater. Chem. Front.* **2021**, *5* (4), 1982–1994. https://doi.org/10.1039/D0QM00885K.
(21) Huang, T.-L.; Chen, Y.-C. Synthesis and Free Radical Photopolymerization of One-Component Type II Photoinitiator Based on Benzophenone Segment. *Journal of Photochemistry and Photobiology A: Chemistry* **2022**, *429*, 113900. https://doi.org/10.1016/j.jphotochem.2022.113900.
(22) Islam, K.; Narjinari, H.; Kumar, A. Polycyclic Aromatic Hydrocarbons Bearing Polyethynyl Bridges: Synthesis, Photophysical Properties, and Their Applications. *Asian Journal of Organic Chemistry* **2021**, *10* (7), 1544–1566. https://doi.org/10.1002/ajoc.202100134.
(23) Xue, T.; Zhao, D.; Hao, T.; Li, X.; Wang, T.; Nie, J. Synthesis, One/Two-Photon Optical and Electrochemical Properties and the Photopolymerization-Sensitizing Effect of Anthracene-Based Dyes: Influence of the Donor Groups. *New J. Chem.* **2019**, *43* (17), 6737–6745. https://doi.org/10.1039/C8NJ06520A.
(24) Xu, Y.; Noirbent, G.; Brunel, D.; Ding, Z.; Gigmes, D.; Graff, B.; Xiao, P.; Dumur, F.; Lalevée, J. Novel Ketone Derivative-Based Photoinitiating Systems for Free Radical Polymerization under Mild Conditions and 3D Printing. *Polym. Chem.* **2020**, *11* (36), 5767–5777. https://doi.org/10.1039/D0PY00990C.
(25) Miras, H. N.; Yan, J.; Long, D.-L.; Cronin, L. Engineering Polyoxometalates with Emergent Properties. *Chem. Soc. Rev.* **2012**, *41* (22), 7403–7430. https://doi.org/10.1039/C2CS35190K.
(26) Proust, A.; Matt, B.; Villanneau, R.; Guillemot, G.; Gouzerh, P.; Izzet, G. Functionalization and Post-Functionalization: A Step towards Polyoxometalate-Based Materials. *Chem. Soc. Rev.* **2012**, *41* (22), 7605–7622. https://doi.org/10.1039/C2CS35119F.
(27) Dolbecq, A.; Dumas, E.; Mayer, C. R.; Mialane, P. Hybrid Organic−Inorganic Polyoxometalate Compounds: From Structural Diversity to Applications. *Chem. Rev.* **2010**, *110* (10), 6009–6048. https://doi.org/10.1021/cr1000578.

(28) Walsh, J. J.; Bond, A. M.; Forster, R. J.; Keyes, T. E. Hybrid Polyoxometalate Materials for Photo(Electro-) Chemical Applications. *Coordination Chemistry Reviews* **2016**, *306* (P1), 217–234. https://doi.org/10.1016/j.ccr.2015.06.016.
(29) Bijelic, A.; Aureliano, M.; Rompel, A. The Antibacterial Activity of Polyoxometalates: Structures, Antibiotic Effects and Future Perspectives. *Chem. Commun.* **2018**, *54* (10), 1153–1169. https://doi.org/10.1039/C7CC07549A.
(30) Wang, S.-S.; Yang, G.-Y. Recent Advances in Polyoxometalate-Catalyzed Reactions. *Chem. Rev.* **2015**, *115* (11), 4893–4962. https://doi.org/10.1021/cr500390v.
(31) Lalevée, J.; Blanchard, N.; Tehfe, M.-A.; Fouassier, J. P. Decatungstate ($W_{10}O_{32}^{4-}$)/Silane: A New and Promising Radical Source under Soft Light Irradiation. *Macromol Rapid Commun* **2011**, *32* (11), 838–843. https://doi.org/10.1002/marc.201100099.
(32) Xiao, P.; Dumur, F.; Tehfe, M.-A.; Graff, B.; Fouassier, J. P.; Gigmes, D.; Lalevée, J. Keggin-Type Polyoxometalate ($[PMo_{12}O_{40}]^{3-}$) in Radical Initiating Systems: Application to Radical and Cationic Photopolymerization Reactions. *Macromolecular Chemistry and Physics* **2013**, *214* (15), 1749–1755. https://doi.org/10.1002/macp.201300282.
(33) Mokbel, H.; Xiao, P.; Simonnet-Jégat, C.; Dumur, F.; Gigmes, D.; Toufaily, J.; Hamieh, T.; Fouassier, J. P.; Lalevée, J. Iodonium-Polyoxometalate and Thianthrenium-Polyoxometalate as New One-Component UV Photoinitiators for Radical and Cationic Polymerization. *Journal of Polymer Science Part A: Polymer Chemistry* **2015**, *53* (8), 981–989. https://doi.org/10.1002/pola.27526.
(34) Ghali, M.; Brahmi, C.; Benltifa, M.; Dumur, F.; Duval, S.; Simonnet-Jégat, C.; Morlet-Savary, F.; Jellali, S.; Bousselmi, L.; Lalevée, J. New Hybrid Polyoxometalate/Polymer Composites for Photodegradation of Eosin Dye. *Journal of Polymer Science Part A: Polymer Chemistry* **2019**, *57* (14), 1538–1549. https://doi.org/10.1002/pola.29416.
(35) Ghali, M.; Brahmi, C.; Benltifa, M.; Vaulot, C.; Airoudj, A.; Fioux, P.; Dumur, F.; Simonnet-Jégat, C.; Morlet-Savary, F.; Jellali, S.; Bousselmi, L.; Lalevée, J. Characterization of Polyoxometalate/Polymer Photo-Composites: A Toolbox for the Photodegradation of Organic Pollutants. *Journal of Polymer Science* **2021**, *59* (2), 153–169. https://doi.org/10.1002/pol.20200568.
(36) Brahmi, C.; Benltifa, M.; Ghali, M.; Dumur, F.; Simonnet-Jégat, C.; Valérie, M.; Morlet-Savary, F.; Bousselmi, L.; Lalevée, J. Performance Improvement of the Photocatalytic Process for the Degradation of Pharmaceutical Compounds Using New POM/Polymer Photocatalysts. *Journal of Environmental Chemical Engineering* **2021**, *9* (5), 106015. https://doi.org/10.1016/j.jece.2021.106015.
(37) Wei, Y.; Xu, B.; Barnes, C. L.; Peng, Z. An Efficient and Convenient Reaction Protocol to Organoimido Derivatives of Polyoxometalates. *J. Am. Chem. Soc.* **2001**, *123* (17), 4083–4084. https://doi.org/10.1021/ja004033q.
(38) Zhu, Y.; Xiao, Z.; Ge, N.; Wang, N.; Wei, Y.; Wang, Y. Naphthyl Amines as Novel Organoimido Ligands for Design of POM-Based Organic−Inorganic Hybrids: Synthesis, Structural Characterization, and Supramolecular Assembly of $(Bu_4N)_2[Mo_6O_{18}N(Naph\text{-}1)]$. *Crystal Growth & Design* **2006**, *6* (7), 1620–1625. https://doi.org/10.1021/cg0600694.
(39) Kirkland, D.; Fowler, P. A Review of the Genotoxicity of Trimethylolpropane Triacrylate (TMPTA). *Mutation Research/Genetic Toxicology and Environmental Mutagenesis* **2018**, *828*, 36–45. https://doi.org/10.1016/j.mrgentox.2018.02.006.
(40) Mauck, S. C.; Wang, S.; Ding, W.; Rohde, B. J.; Fortune, C. K.; Yang, G.; Ahn, S.-K.; Robertson, M. L. Biorenewable Tough Blends of Polylactide and Acrylated Epoxidized Soybean Oil Compatibilized

by a Polylactide Star Polymer. *Macromolecules* **2016**, *49* (5), 1605–1615. https://doi.org/10.1021/acs.macromol.5b02613.

(41) Mohs, T. R.; Du, Y.; Plashko, B.; Maatta, E. A. Homogeneous Modeling of Ammoxidation Chemistry: Nitrile Formation Using a Soluble Analogue of MoO_3. *Chemical Communications* **1997**, *0* (18), 1707–1708. https://doi.org/10.1039/A703790B.

(42) Zhang, J.; Xiao, F.; Hao, J.; Wei, Y. The Chemistry of Organoimido Derivatives of Polyoxometalates. *Dalton Trans.* **2012**, *41* (13), 3599–3615. https://doi.org/10.1039/C2DT11948J.

(43) Lv, C.; Hu, J.; Zhou, H.; Li, Z.; Khan, R. N. N.; Wei, Y. Theoretical Investigation of the Mechanism of Primary Amines Reacting with Hexamolybdate: An Insight into the Organoimido Functionalization and Related Reactions of Polyoxometalates. *Chemistry – A European Journal* **2012**, *18* (28), 8681–8691. https://doi.org/10.1002/chem.201103470.

(44) Al-Yasari, A.; Steerteghem, N. V.; Moll, H. E.; Clays, K.; Fielden, J. Donor–Acceptor Organo-Imido Polyoxometalates: High Transparency, High Activity Redox-Active NLO Chromophores. *Dalton Trans.* **2016**, *45* (7), 2818–2822. https://doi.org/10.1039/C6DT00115G.

(45) Al-Yasari, A.; Van Steerteghem, N.; Kearns, H.; El Moll, H.; Faulds, K.; Wright, J. A.; Brunschwig, B. S.; Clays, K.; Fielden, J. Organoimido-Polyoxometalate Nonlinear Optical Chromophores: A Structural, Spectroscopic, and Computational Study. *Inorg. Chem.* **2017**, *56* (17), 10181–10194. https://doi.org/10.1021/acs.inorgchem.7b00708.

(46) Al-Yasari, A.; Spence, P.; Moll, H. E.; Steerteghem, N. V.; Horton, P. N.; Brunschwig, B. S.; Clays, K.; Fielden, J. Fine-Tuning Polyoxometalate Non-Linear Optical Chromophores: A Molecular Electronic "Goldilocks" Effect. *Dalton Trans.* **2018**, *47* (31), 10415–10419. https://doi.org/10.1039/C8DT01491D.

(47) Al-Yasari, A.; Moll, H. E.; Purdy, R.; Vincent, K. B.; Spence, P.; Malval, J.-P.; Fielden, J. Optical, Third Order Non-Linear Optical and Electrochemical Properties of Dipolar, Centrosymmetric and C2v Organoimido Polyoxometalate Derivatives. *Phys. Chem. Chem. Phys.* **2021**, *23* (20), 11807–11817. https://doi.org/10.1039/D0CP06610A.

(48) Breibeck, J.; Gumerova, N. I.; Rompel, A. Oxo-Replaced Polyoxometalates: There Is More than Oxygen. *ACS Org. Inorg. Au* **2022**. https://doi.org/10.1021/acsorginorgau.2c00014.

(49) Gumerova, N. I.; Rompel, A. Synthesis, Structures and Applications of Electron-Rich Polyoxometalates. *Nat Rev Chem* **2018**, *2* (2), 1–20. https://doi.org/10.1038/s41570-018-0112.

(50) Poblet, J. M.; López, X.; Bo, C. Ab Initio and DFT Modelling of Complex Materials: Towards the Understanding of Electronic and Magnetic Properties of Polyoxometalates. *Chem. Soc. Rev.* **2003**, *32* (5), 297–308. https://doi.org/10.1039/B109928K.

(51) Bridgeman, A. J.; Cavigliasso, G. Structure and Bonding in $[M_6O_{19}]^{n-}$ Isopolyanions. *Inorg. Chem.* **2002**, *41* (7), 1761–1770. https://doi.org/10.1021/ic011086f.

(52) Wei, Y.; Lu, M.; Cheung, C. F.; Barnes, C. L.; Peng, Z. Functionalization of $[MoW_5O_{19}]^{2-}$ with Aromatic Amines: Synthesis of the First Arylimido Derivatives of Mixed-Metal Polyoxometalates. *Inorg. Chem.* **2001**, *40* (22), 5489–5490. https://doi.org/10.1021/ic0155683.

(53) Huang, Y.; Zhang, J.; Hao, J.; Wei, Y. A General and Highly Regioselective Synthesis Approach to Multi-Functionalized Organoimido Derivatives of Polyoxometalates. *Sci Rep* **2016**, *6* (1), 24759. https://doi.org/10.1038/srep24759.

(54) Lv, C.; Khan, R. N. N.; Zhang, J.; Hu, J.; Hao, J.; Wei, Y. Bifunctionalization of Polyoxometalates with Two Different Organoimido Ligands. *Chemistry – A European Journal* **2013**, *19* (4), 1174–1178. https://doi.org/10.1002/chem.201203204.

(55) Jangir, R.; Rajendran, A.; Murugavel, R. New Sterically Encumbered Arylimido Hexamolybdates for Organic Oxidation Reactions. *New Journal of Chemistry* **2015**, *40*. https://doi.org/10.1039/C5NJ02330K.

(56) Hao, J.; Ruhlmann, L.; Zhu, Y.; Li, Q.; Wei, Y. Naphthylimido-Substituted Hexamolybdate: Preparation, Crystal Structures, Solvent Effects, and Optical Properties of Three Polymorphs. *Inorg. Chem.* **2007**, *46* (12), 4960–4967. https://doi.org/10.1021/ic070064b.

(57) Du, Y.; Rheingold, A. L.; Maatta, E. A. A Polyoxometalate Incorporating an Organoimido Ligand: Preparation and Structure of $[Mo_5O_{18}(MoNC_6H_4CH_3)]^{2-}$. *J. Am. Chem. Soc.* **1992**, *114* (1), 345–346. https://doi.org/10.1021/ja00027a046.

(58) Roesner, R. A.; McGrath, S. C.; Brockman, J. T.; Moll, J. D.; West, D. X.; Swearingen, J. K.; Castineiras, A. Mono- and Di-Functional Aromatic Amines with p-Alkoxy Substituents as Novel Arylimido Ligands for the Hexamolybdate Ion. *Inorganica Chimica Acta* **2003**, *342*, 37–47. https://doi.org/10.1016/S0020-1693(02)01075-7.

(59) Cao, J.; Wang, Q.; Liu, C.; An, S. Gas-Phase Chemistry of Arylimido-Functionalized Hexamolybdates $[Mo_6O_{19}]_{2-}$. *J. Am. Soc. Mass Spectrom.* **2018**, *29* (6), 1331–1334. https://doi.org/10.1007/s13361-018-1948-4.

(60) Morrison, D. L.; Wigley, D. E. Multiple Imido Complexes of Molybdenum: Synthesis and Reactivity of the D0 $Mo(:NR)_3$ Functional Group. *Inorg. Chem.* **1995**, *34* (10), 2610–2616. https://doi.org/10.1021/ic00114a019.

(61) Rino A. Michelin. Metal-Ligand Multiple Bonds.: W.A. Nugent and J.M. Mayer, Wiley Interscience, New York, 1988, Xi + 334 Pp., £33.15. *Inorganica Chimica Acta* **1989**, *163* (2), 112,123-125. https://doi.org/10.1016/S0020-1693(00)83459-3.

(62) Xiao, F.; Misdrahi, M. F.; Zhang, J.; Yin, P.; Hao, J.; Lv, C.; Xiao, Z.; Liu, T.; Wei, Y. Buildup of Amphiphilic Molecular Bola from Organic–Inorganic Hybrid Polyoxometalates and Their Vesicle-Like Supramolecular Assembly. *Chemistry – A European Journal* **2011**, *17* (43), 12006–12009. https://doi.org/10.1002/chem.201101966.

(63) Xu, L.; Lu, M.; Xu, B.; Wei, Y.; Peng, Z.; Powell, D. R. Towards Main-Chain-Polyoxometalate-Containing Hybrid Polymers: A Highly Efficient Approach to Bifunctionalized Organoimido Derivatives of Hexamolybdates. *Angewandte Chemie International Edition* **2002**, *41* (21), 4129–4132. https://doi.org/10.1002/1521-3773(20021104)41:21<4129::AID-ANIE4129>3.0.CO;2-R.

(64) Wu, P.; Li, Q.; Ge, N.; Wei, Y.; Wang, Y.; Wang, P.; Guo, H. An Easy Route to Monofunctionalized Organoimido Derivatives of the Lindqvist Hexamolybdate. *European Journal of Inorganic Chemistry* **2004**, *2004* (14), 2819–2822. https://doi.org/10.1002/ejic.200400168.

(65) Xia, Y.; Wu, P.; Wei, Y.; Wang, Y.; Guo, H. Synthesis, Crystal Structure, and Optical Properties of a Polyoxometalate-Based Inorganic−Organic Hybrid Solid, $(n\text{-}Bu_4N)_2[Mo_6O_{17}(\equiv NAr)_2]$ (Ar = o-$CH_3OC_6H_4$). *Crystal Growth & Design* **2006**, *6* (1), 253–257. https://doi.org/10.1021/cg0503797.

(66) Hermosilla-Ibáñez, P.; Wrighton-Araneda, K.; Cañón-Mancisidor, W.; Gutiérrez-Cutiño, M.; Paredes-García, V.; Venegas-Yazigi, D. Substitution Effect on the Charge Transfer Processes in Organo-Imido Lindqvist-Polyoxomolybdate. *Molecules* **2018**, *24* (1), E44. https://doi.org/10.3390/molecules24010044.

(67) Strong, J. B.; Yap, G. P. A.; Ostrander, R.; Liable-Sands, L. M.; Rheingold, A. L.; Thouvenot, R.; Gouzerh, P.; Maatta, E. A. A New Class of Functionalized Polyoxometalates: Synthetic, Structural, Spectroscopic, and Electrochemical Studies of Organoimido Derivatives of $[Mo_6O_{19}]^{2-}$. *J. Am. Chem. Soc.* **2000**, *122* (4), 639–649. https://doi.org/10.1021/ja9927974.

(68) Green, W. Arthur. Industrial Photoinitiators: A Technical Guide. by W. Arthur Green. *ChemPhysChem* **2011**, *12* (7), 1389–1389. https://doi.org/10.1002/cphc.201000542.
(69) Navas Diaz. Absorption and Emission Spectroscopy and Photochemistry of 1,10-Anthraquinone Derivatives: A Review. *Journal of Photochemistry and Photobiology A: Chemistry* **1990**, *53* (2), 141–167. https://doi.org/10.1016/1010-6030(90)87120-Z.
(70) J.-P. Fouassier. Photoinitiation, Photopolymerization and Photocuring. J.-P. Fouassier. Hanser Publishers, Munich, 1995. ISBN 3-446-17069-3. *Polymer International* **1996**, *40* (4), 315–315. https://doi.org/10.1002/(SICI)1097-0126(199608)40:4<315::AID-PI566>3.0.CO;2-T.
(71) Marcus, R. A.; Sutin, N. Electron Transfers in Chemistry and Biology. *Biochimica et Biophysica Acta (BBA) - Reviews on Bioenergetics* **1985**, *811* (3), 265–322. https://doi.org/10.1016/0304-4173(85)90014-X.
(72) Verhoeven, J. W. Glossary of terms used in photochemistry (IUPAC Recommendations 1996). *Pure and Applied Chemistry* **1996**, *68* (12), 2223–2286. https://doi.org/10.1351/pac199668122223.
(73) Toma, H. E.; Creutz, Carol. Pentacyanoferrate(II) Complexes: Evaluation of Their Formal Potentials and Mechanism of Their Quenching of Tris(2,2'-Bipyridine)Ruthenium(II) Luminescence. *Inorg. Chem.* **1977**, *16* (3), 545–550. https://doi.org/10.1021/ic50169a008.
(74) Rehm, D.; Weller, A. Kinetics of Fluorescence Quenching by Electron and H-Atom Transfer. *Israel Journal of Chemistry* **1970**, *8* (2), 259–271. https://doi.org/10.1002/ijch.197000029.
(75) Davis, E. A.; Mott, N. F. Conduction in Non-Crystalline Systems V. Conductivity, Optical Absorption and Photoconductivity in Amorphous Semiconductors. *The Philosophical Magazine: A Journal of Theoretical Experimental and Applied Physics* **1970**, *22* (179), 0903–0922. https://doi.org/10.1080/14786437008221061.
(76) Abdelghany, A. M.; Abdelrazek, E. M.; Badr, S. I.; Morsi, M. A. Effect of Gamma-Irradiation on (PEO/PVP)/Au Nanocomposite: Materials for Electrochemical and Optical Applications. *Materials & Design* **2016**, *C* (97), 532–543. https://doi.org/10.1016/j.matdes.2016.02.082.
(77) Hogarth, G.; Konidaris, P. C.; Saunders, G. C. Electrochemistry of Dimolybdenum Complexes Containing Oxo, Imido, and Sulphido Moieties. A Measure of Their Relative π-Donor Abilities? *Journal of Organometallic Chemistry* **1991**, *406* (1), 153–157. https://doi.org/10.1016/0022-328X(91)83182-4.
(78) Er, S.; Suh, C.; Marshak, M. P.; Aspuru-Guzik, A. Computational Design of Molecules for an All-Quinone Redox Flow Battery. *Chem. Sci.* **2015**, *6* (2), 885–893. https://doi.org/10.1039/C4SC03030C.
(79) Dahiya, P.; Kumbhakar, M.; Maity, D. K.; Mukherjee, T.; Mittal, J. P.; Tripathi, A. B. R.; Chattopadhyay, N.; Pal, H. Photophysical Properties of 2-Amino-9,10-Anthraquinone: Evidence for Structural Changes in the Molecule with Solvent Polarity. *Photochem Photobiol Sci* **2005**, *4* (1), 100–105. https://doi.org/10.1039/b411547c.
(80) Buettner, G. R. Spin Trapping: ESR Parameters of Spin Adducts 1474 1528V. *Free Radical Biology and Medicine* **1987**, *3* (4), 259–303. https://doi.org/10.1016/S0891-5849(87)80033-3.
(81) Janzen, E. G. Spin Trapping. *Acc. Chem. Res.* **1971**, *4* (1), 31–40. https://doi.org/10.1021/ar50037a005.
(82) Janzen, E. G.; Stronks, H. J.; Dubose, C. M.; Poyer, J. L.; McCay, P. B. Chemistry and Biology of Spin-Trapping Radicals Associated with Halocarbon Metabolism in Vitro and in Vivo. *Environ Health Perspect* **1985**, *64*, 151–170.
(83) Peyrot, F.; Lajnef, S.; Versace, D.-L. Electron Paramagnetic Resonance Spin Trapping (EPR–ST) Technique in Photopolymerization Processes. *Catalysts* **2022**, *12* (7), 772. https://doi.org/10.3390/catal12070772.

(84) Sandner, M. R.; Osborn, C. L.; Trecker, D. J. Benzophenone/Triethylamine-Photoinitiated Polymerization of Methyl Acrylate. *Journal of Polymer Science Part A-1: Polymer Chemistry* **1972**, *10* (11), 3173–3181. https://doi.org/10.1002/pol.1972.170101105.

(85) Viswanathan, K.; Hoyle, C.; Jönsson, E.; Nason, C.; Lindgren, K. Effect of Amine Structure on Photoreduction of Hydrogen Abstraction Initiators. *Macromolecules* **2002**, *35*. https://doi.org/10.1021/ma0120308.

(86) Sautrot-Ba, P.; Contreras, A.; Andaloussi, S. A.; Coradin, T.; Hélary, C.; Razza, N.; Sangermano, M.; Mazeran, P.-E.; Malval, J.-P.; Versace, D.-L. Eosin-Mediated Synthesis of Polymer Coatings Combining Photodynamic Inactivation and Antimicrobial Properties. *J. Mater. Chem. B* **2017**, *5* (36), 7572–7582. https://doi.org/10.1039/C7TB01358B.

(87) Zhang, J.; Lalevée, J.; Hill, N. S.; Kiehl, J.; Zhu, D.; Cox, N.; Langley, J.; Stenzel, M. H.; Coote, M. L.; Xiao, P. Substituent Effects on Photoinitiation Ability of Monoaminoanthraquinone-Based Photoinitiating Systems for Free Radical Photopolymerization under LEDs. *Macromolecular Rapid Communications* **2020**, *41* (18), 2000166. https://doi.org/10.1002/marc.202000166.

(88) Breloy, L.; Brezová, V.; Malval, J.-P.; Anda, A. R. de; Bourgon, J.; Kurogi, T.; Mindiola, D. J.; Versace, D.-L. Well-Defined Titanium Complex for Free-Radical and Cationic Photopolymerizations under Visible Light and Photoinduction of Ti-Based Nanoparticles. *Macromolecules* **2019**. https://doi.org/10.1021/acs.macromol.8b02719.

(89) Roessler, M. M.; Salvadori, E. Principles and Applications of EPR Spectroscopy in the Chemical Sciences. *Chem. Soc. Rev.* **2018**, *47* (8), 2534–2553. https://doi.org/10.1039/C6CS00565A.

(90) Breloy, L.; Losantos, R.; Sampedro, D.; Marazzi, M.; Malval, J.-P.; Heo, Y.; Akimoto, J.; Ito, Y.; Brezová, V.; Versace, D.-L. Allyl Amino-Thioxanthone Derivatives as Highly Efficient Visible Light H-Donors and Co-Polymerizable Photoinitiators. *Polym. Chem.* **2020**, *11* (26), 4297–4312. https://doi.org/10.1039/D0PY00551G.

(91) Boulmier, A.; Haouas, M.; Tomane, S.; Michely, L.; Dolbecq, A.; Vallée, A.; Brezová, V.; Versace, D.-L.; Mialane, P.; Oms, O. Photoactive Polyoxometalate/DASA Covalent Hybrids for Photopolymerization in the Visible Range. *Chemistry – A European Journal* **2019**, *25* (63), 14349–14357. https://doi.org/10.1002/chem.201902573.

(92) Barker, P.; Beckwith, A. L. J.; Cherry, W. R.; Huie, R. Characterization of Spin Adducts Obtained with Hydrophobic Nitrone Spin Traps. *J. Chem. Soc., Perkin Trans. 2* **1985**, No. 8, 1147–1150. https://doi.org/10.1039/P29850001147.

(93) Nicolas, J.; Guillaneuf, Y.; Lefay, C.; Bertin, D.; Gigmes, D.; Charleux, B. Nitroxide-Mediated Polymerization. *Progress in Polymer Science* **2013**, *38* (1), 63–235. https://doi.org/10.1016/j.progpolymsci.2012.06.002.

(94) O'Brien, A. K.; Bowman, C. N. Impact of Oxygen on Photopolymerization Kinetics and Polymer Structure. *Macromolecules* **2006**, *39* (7), 2501–2506. https://doi.org/10.1021/ma051863l.

(95) Stansbury, J. W. Independent Control of Singlet Oxygen and Radical Generation via Irradiation of a Two-Color Photosensitive Molecule. **2019**. https://doi.org/10.1021/acs.macromol.9b00424.

(96) Ligon, S.; Husár, B.; Wutzel, H.; Holman, R.; Liska, R. Strategies to Reduce Oxygen Inhibition in Photoinduced Polymerization. *Chemical Reviews* **2013**, *114*, 557–589. https://doi.org/10.1021/cr3005197.

(97) Li, Y. T.; Yang, L. T.; Zhang, H.; Tang, Z. J. Synthesis and Properties of a Novel Bio-Based Polymer from Modified Soybean Oil. *IOP Conf. Ser.: Mater. Sci. Eng.* **2017**, *170* (1), 012010. https://doi.org/10.1088/1757-899X/170/1/012010.

(98) Menard, K. P.; Menard, N. R. Dynamic Mechanical Analysis in the Analysis of Polymers and Rubbers. In *Encyclopedia of Polymer Science and Technology*; John Wiley & Sons, Ltd, 2015; pp 1–33. https://doi.org/10.1002/0471440264.pst102.pub2.
(99) Vallan, L.; Istif, E.; Gómez, I. J.; Alegret, N.; Mantione, D. Thiophene-Based Trimers and Their Bioapplications: An Overview. *Polymers* **2021**, *13* (12), 1977. https://doi.org/10.3390/polym13121977.
(100) Klemperer, W. Inorganic Syntheses, Volume 27. In *Cheminform*; 2007; Vol. 22, pp 71–85. https://doi.org/10.1002/9780470132586.ch14.
(101) G. M. SADABS, S. *, Program for Scaling and Correction of Area Detector Data, University of Göttingen, Germany, 1997.*
(102) Blessing, R. H. An Empirical Correction for Absorption Anisotropy. *Acta Crystallogr A* **1995**, *51 (Pt 1)*, 33–38. https://doi.org/10.1107/s0108767394005726.
(103) Sheldrick G. M., . SHELX-TL. *Software Package for the Crystal Structure Determination, Siemens Analytical X-ray Instrument Division, Madison, WI USA, 1994.*
(104) Breloy, L.; Brezová, V.; Richeter, S.; Clément, S.; Malval, J.-P.; Andaloussi, S. A.; Versace, D.-L. Bio-Based Porphyrins Pyropheophorbide a and Its Zn-Complex as Visible-Light Photosensitizers for Free-Radical Photopolymerization. *Polym. Chem.* **2022**, *13* (12), 1658–1671. https://doi.org/10.1039/D1PY01714D.
(105) Stoll, S.; Schweiger, A. EasySpin, a Comprehensive Software Package for Spectral Simulation and Analysis in EPR. *J Magn Reson* **2006**, *178* (1), 42–55. https://doi.org/10.1016/j.jmr.2005.08.013.
(106) S, M. M.; Mh, H.-T.; Vt, P.; A, Q.; T, P.; C, L.; T, C.; W, L.; A, A. Time-Resolved Interception of Multiple-Charge Accumulation in a Sensitizer-Acceptor Dyad. *Angewandte Chemie (International ed. in English)* **2017**, *56* (50). https://doi.org/10.1002/anie.201706564.
(107) Sautrot-Ba, P.; Brezová, V.; Malval, J.-P.; Chiappone, A.; Breloy, L.; Abbad-Andaloussi, S.; Versace, D.-L. Purpurin Derivatives as Visible-Light Photosensitizers for 3D Printing and Valuable Biological Applications. *Polym. Chem.* **2021**, *12* (17), 2627–2642. https://doi.org/10.1039/D1PY00126D.
(108) Mazeran, P.-E.; Beyaoui, M.; Bigerelle, M.; Guigon, M. Determination of Mechanical Properties by Nanoindentation in the Case of Viscous Materials. *International Journal of Materials Research* **2012**, *103* (6), 715–722. https://doi.org/10.3139/146.110687.
(109) Haider, T.; Shyshov, O.; Suraeva, O.; Lieberwirth, I.; von Delius, M.; Wurm, F. R. Long-Chain Polyorthoesters as Degradable Polyethylene Mimics. *Macromolecules* **2019**, *52* (6), 2411–2420. https://doi.org/10.1021/acs.macromol.9b0018.

Chapter Four

Chapter 4: Playing with the chaotropic effect to improve the encapsulation of decaborate clusters within cyclodextrins.

I. Introduction

Cyclodextrins (CDs) are water-soluble natural macrocyclic oligosaccharides comprised of 6, 7, and 8 D-glucopyranose units linked by α-(1,4) bonds and named α-, β- and γ-CD, respectively (Figure 1). CDs are attractive for the design of drug delivery systems because of their robustness, non-toxicity, and ability to host in their hydrophobic cavity a wide variety of organic or inorganic guest species in aqueous media [1–6].

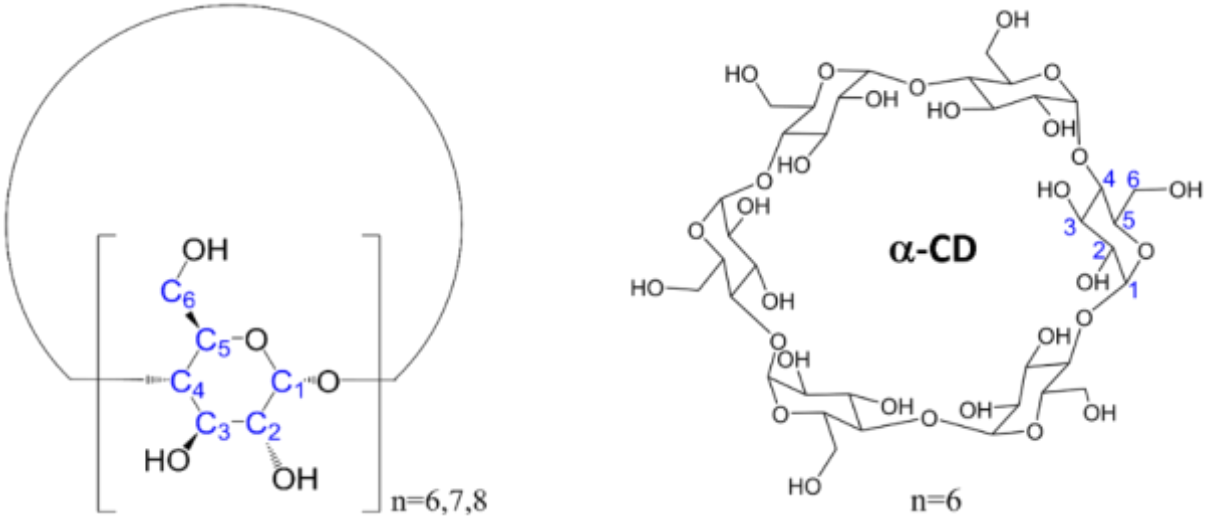

Figure 1. ***(a)*** *General structure of CDs composed of α-D-glucopyranose,* ***(b)*** *Structure of α-CD.*

On the other hand, boron-based clusters show relatively low toxicity besides high thermal and chemical stability. Hence, they are excellent for designing therapeutic and diagnostic drug systems delivered selectively to cancerous cells through binding to specific receptors (antibodies, proteins, etc.) [7]. For example, icosahedral carbon-containing boron cages named carboranes are well-known reagents for constructing HIV enzyme inhibitors and designing drug systems useful for boron neutron capture therapy [8–10]; however, they are extremely hydrophobic. Therefore, complexing them within cyclodextrins' hydrophobic cavity enhances their aqueous solubility and bioavailability [11,12]. Such as the inclusion complex of carborane carboxylate derivative {*closo*-1,2-$C_2B_{10}H_{11}CH_2COOH$} and β-CD (Figures 2a,c), which reaches binding constant in the range of 10^3-10^4 M^{-1} [13], close to standard affinities reported with well-known complexes between CD and organic adamantane derivatives (e.g., 1-adamantanecarboxylic acid) (Figure 2b) [14,15].

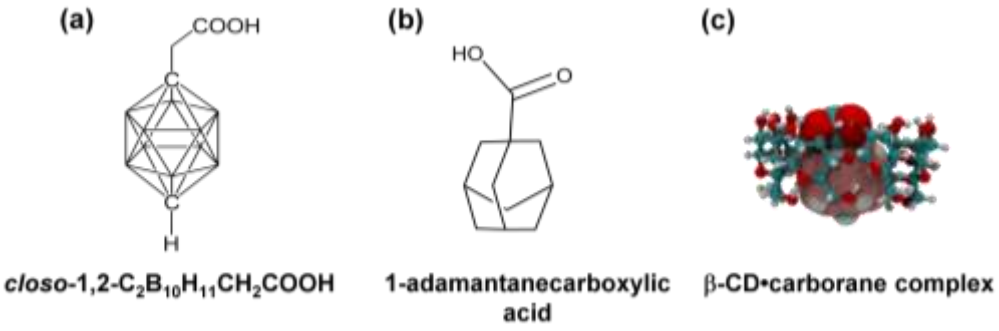

*Figure 2. Chemical structures of **(a)** carborane carboxylate derivative {closo-1,2-$C_2B_{10}H_{11}CH_2COOH$}, **(b)** admantanecarboxylic acid, and **(c)** DFT-optimized structure of CD•carborane carboxylate complex.*[13]

The main driving forces for the formation of inclusion complexes between these guests or any other hydrophobic organic guest molecules and the hydrophobic cavity of CD are i) size fit between the solute and the cavity of cyclodextrin, ii) the hydrophobic effect described as the destruction of the ordered water shell surrounding the weakly solvated solutes (hydrophobe) which would fit into the hydrophobic cavity replacing the high energy water molecules inside. This effect invariably presents a positive (favorable) entropy change as a thermodynamic fingerprint [16–18].

In contrast, bulky anionic compounds such as polyoxometalates (Keggin and Dawson POMs), metallic clusters of type M_6X_n, the *closo*-dodecaborate anion $[B_{12}H_{12}]^{2-}$ (Figure 3a) and their derivatives, metal bis(dodecaborate) $[\{M(C_2B_9H_{11})\}_2]^-$ (M = Metal) (Figure 3b), and *closo-closo*-$[B_{21}H_{18}]^-$ (Figure 3c) are highly soluble molecules and form very stable inclusion complexes with cyclodextrins. Binding affinities were found to be extremely high, exceeding those measured with carboranes or other neutral hydrophobic organic guest molecules [2,4,19–22].

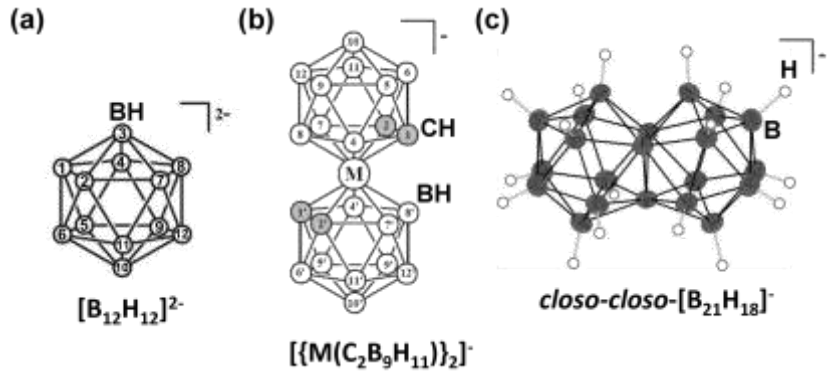

*Figure 3. Chemical structures of **(a)** dodecaborate $[B_{12}H_{12}]^{2-}$, **(b)** metal bis(dodecaborate) $[\{M(C_2B_9H_{11})\}_2]^-$ (M=Metal), and **(c)** closo-closo-$[B_{21}H_{18}]^-$ anions.*

Nau, Gabel, Assaf, and coworkers evidenced in their work that the boron-based clusters mentioned above have a chaotropic effect, different than the classical hydrophobic interactions, which justifies their unexpected complexing with cyclodextrin with high

measured values of binding affinities [18]. Although solutes in the chaotropic and hydrophobic effect are considered weakly solvated, they still behave differently than the hydrophobic effect in terms of the structure of the hydration shell around them.

In the classical CD inclusion complexes, the hydrophobic guest molecules aggregate spontaneously in the aqueous medium and become surrounded by the ordered structured hydration shell. Hence, the desolvation of the guest molecule and their association with CD will destroy the hydration shell around and increase the disorder of the bulk water molecules; therefore, the formation of the inclusion complex is entropically driven. Meanwhile, chaotropic molecules have less structured hydration shell around them. Consequently, their complexation with cyclodextrin will replace the frustrated high-energy water molecules inside the macrocyclic hydrophobic pocket. At the same time, the bulk regains its intermolecular hydrogen bonding, so water molecules become ordered. This process is classically driven by a dominant negative enthalpic term.

The Chaotropic effect increases with polarizability, thus directly proportional to the molecule's volume charge density. These factors play an important role in stabilizing inclusion complexes with cyclodextrins by enhancing the host-guest dispersion interactions [18].

Nau et al. nicely explained that *closo*-dodecaborate derivatives have a superchaotropic effect exceeding that of the classical small anionic chaotropes (ClO_4^- < SCN^- < PF_6^- << $B_{12}H_{12}^{2-}$) since they are large molecules with a delocalized doubly negative charge which means they have low charge density thus higher chaotropic effect. Furthermore, they have confirmed that increasing the volume of the B_{12} cage through halogenation with Br^-, Cl^-, and I^- while all still having (-2) charge generally resulted in strong affinity constants with cyclodextrins but highest with $[B_{12}Br_{12}]^{2-}$ and γ-CD due to ideal size matching [23].

Accordingly, they continued their investigations with larger boron clusters having lower charge (-1): the metallocarboranes {3,3`-Co[1,2-$C_2B_9H_{11}]^2$}$^-$ (Figure 3b), and the macro-icosahedral borane anion {*closo-closo*-$[B_{21}H_{18}]^-$} (Figure 3c). Their lower charge density means an enhanced chaotropic effect, thus showing binding affinities with CDs twice higher than those of the halogenated B_{12} cluster [22,24]. On the contrary, *the closo*-decahydrodecaborate cluster $[B_{10}H_{10}]^{2-}$ is slightly chaotropic. It has the same (-2) charge but with a smaller volume, which means higher electron density. In this sense, the best binding affinity recorded by Manal Diab during her PhD work (2014-2017) was with the $[B_{10}H_{10}]^{2-}$@β-CD inclusion complex with a binding constant K= 40 M^{-1}, two orders of magnitude lower than the parent compound $[B_{12}H_{12}]^{2-}$ [25].

Following on from previous studies, and in order to highlight the parameters that will enable encapsulation processes strong enough to be considered for biological application, we set out to increase the chaotropic character of $[B_{10}H_{10}]^{2-}$ by playing with its volume and charge. Herein, we will study the encapsulation of $[B_{10}H_9NCCH_3]^-$ and $[B_{20}H_{18}]^{2-}$ anions within α-, β- and γ-CD in two different parts.

II. Encapsulation of $[B_{10}H_9NCCH_3]^-$ within cyclodextrins

We selected $[B_{10}H_9NCCH_3]^-$ which is a bit bigger than $[B_{10}H_{10}]^{2-}$ and less charged (Figure 4). Moreover, adding a substituent on the B_{10} cluster should also contribute to breaking the symmetry around the cluster and avoiding the organization of water solvates, a key point for the chaotropic effect. The encapsulation process must be favored for such a cluster compared to $[B_{10}H_{10}]^{2-}$. Herein, the encapsulation of $[B_{10}H_9NCCH_3]^-$ within α-, β- and γ-CD will systematically be studied by ESI-MS, ^{1}H NMR, and ITC.

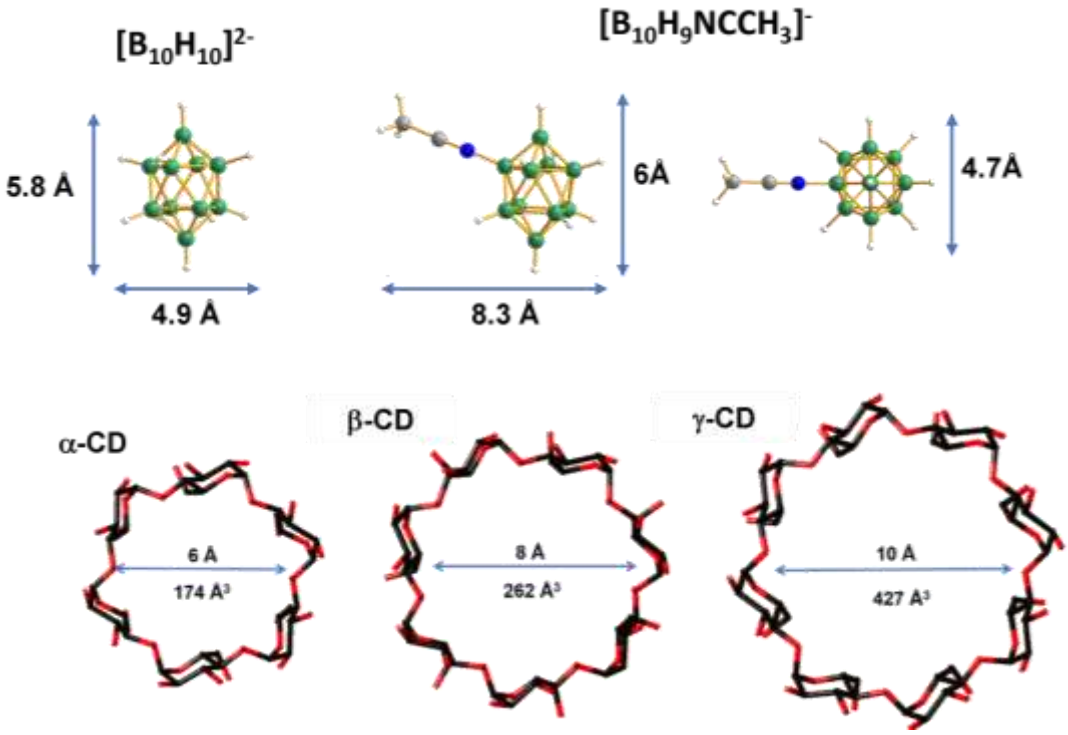

Figure 4. Molecular structures of the clusters ***$[B_{10}H_{10}]^{2-}$*** *and* ***$[B_{10}H_9NCCH_3]^-$*** *with α-, β-, and γ-cyclodextrins highlighting host and guest sizes. (Legends: B in blue; H in white; C in grey)*

II.1 Synthesis of $(Et_3NH)[B_{10}H_9NCCH_3]$

The triethylammonium 2-(acetonitrilium) closo-decaborate anion $(Et_3NH)[B_{10}H_9NCCH_3]$ was isolated as colorless crystals according to the literature procedure (see details in experimental section) [26]. As seen in Figure 5, the trifluoroacetic acid protonates the parent [*closo*-$B_{10}H_{10}]^{2-}$ anion to give [*closo*-$B_{10}H_{11}]^-$, then the exo-polyhedral hydride at the equatorial position (noted as B2) was replaced by nucleophilic substitution with nitrilium group (-NCR, R = CH_3) where the solvent plays the role of the ligand (L = -$NCCH_3$). The FT-IR spectrum (Figure S1 in the appendix), ESI-MS (Figure 10), and NMR spectra perfectly agree with the expected compound (Figures 6-9).

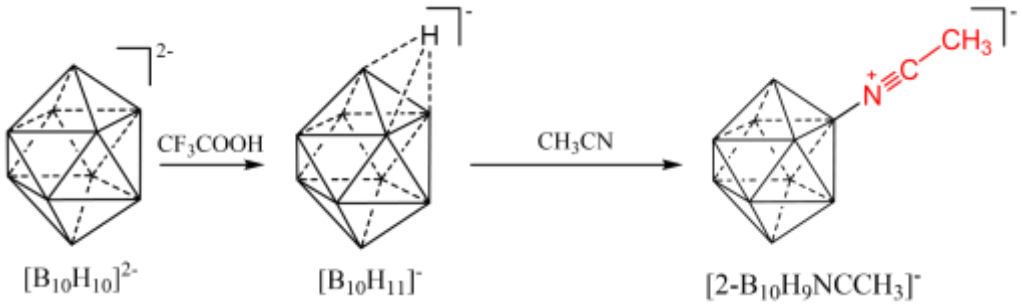

Figure 5. Synthesis of acetonitrile derivatives of decaborate.

II.2 NMR studies of $(Et_3NH)[B_{10}H_9NCCH_3]$

The $^{11}B\{^1H\}$ and $^1H\{^{11}B\}$ NMR spectra of $(Et_3NH)[2\text{-}B_{10}H_9NCCH_3]$ and the parent compound $(Et_3NH)_2[B_{10}H_{10}]$ given in Figures 6-9 are in agreement with the literature [26,27]. The $^{11}B\{^1H\}$ spectrum of $(Et_3NH)_2[B_{10}H_{10}]$ (Figure 6) shows two singlets of the intensities 2:8 at -0.93 and -28.92 ppm corresponding to the apical (B_{ap}) and equatorial (B_{eq}) boron atoms, respectively, in agreement with the D_{4d} symmetry of $[B_{10}H_{10}]^{2-}$ cluster.

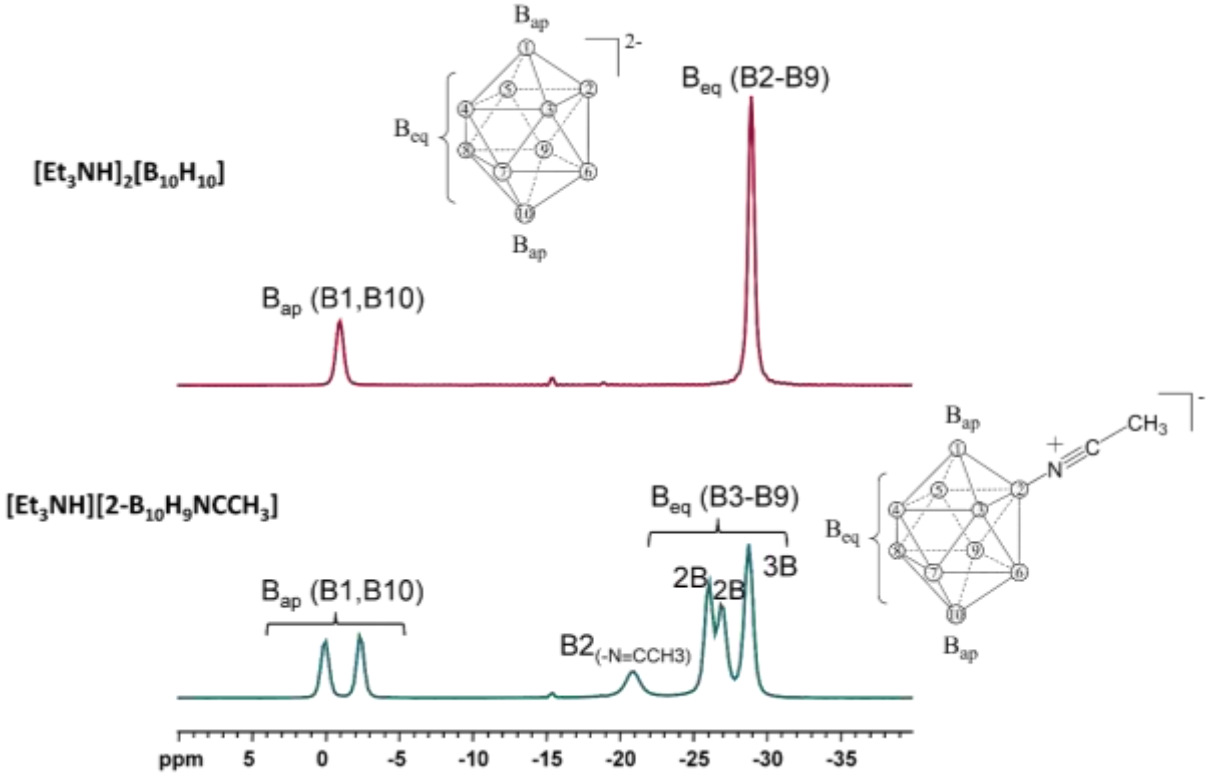

*Figure 6. $^{11}B\{^1H\}$ NMR spectra (400 MHz) of **$(Et_3NH)[B_{10}H_9NCCH_3]$** and **$(Et_3NH)_2[B_{10}H_{10}]$** in CD_3CN.*

On the other hand, there is clearly a significant change in the chemical shifts as seen in the $^{11}B\{^1H\}$ spectrum of $(Et_3NH)[2\text{-}B_{10}H_9NCCH_3]$ (Figure 6) due to the loss of D_{4d} symmetry upon the functionalization of the B_{10} cage with $-NCCH_3$ group. The signal of the apical boron atoms (B_{ap}) at positions (B1,B10) at -0.93 ppm splits into two signals at +0.10 and -2.3 ppm, while

the signals of the equatorial boron atoms (B_{eq}) at positions B(3-9) split into four signals of the following chemical shifts and intensities: -20.9 (1B), -26.1 (2B), -26.8 (2B), -28.7 (unresolved 2B + 1B).

The ^{11}B NMR spectra without decoupling from ^{1}H nuclei of the $(Et_3NH)[2\text{-}B_{10}H_9NCCH_3]$ derivative (Figure 7) compared to the ^{11}B NMR spectra with decoupling reveals that all signals have split into doublets except for the signal at -20.9 ppm. This confirms that the hydrogen atom at the B_{10} cage is monosubstituted at the equatorial position. The FT-IR experiment (Figure S1 in the appendix) is in agreement with the reaction of $(Et_3NH)_2[B_{10}H_{10}]$ with CH_3CN showing a broad absorption band of stretching vibrations ν(C≡N) at 2467 cm^{-1} overlapping with ν(B–H) at 2510 cm^{-1} [26,27].

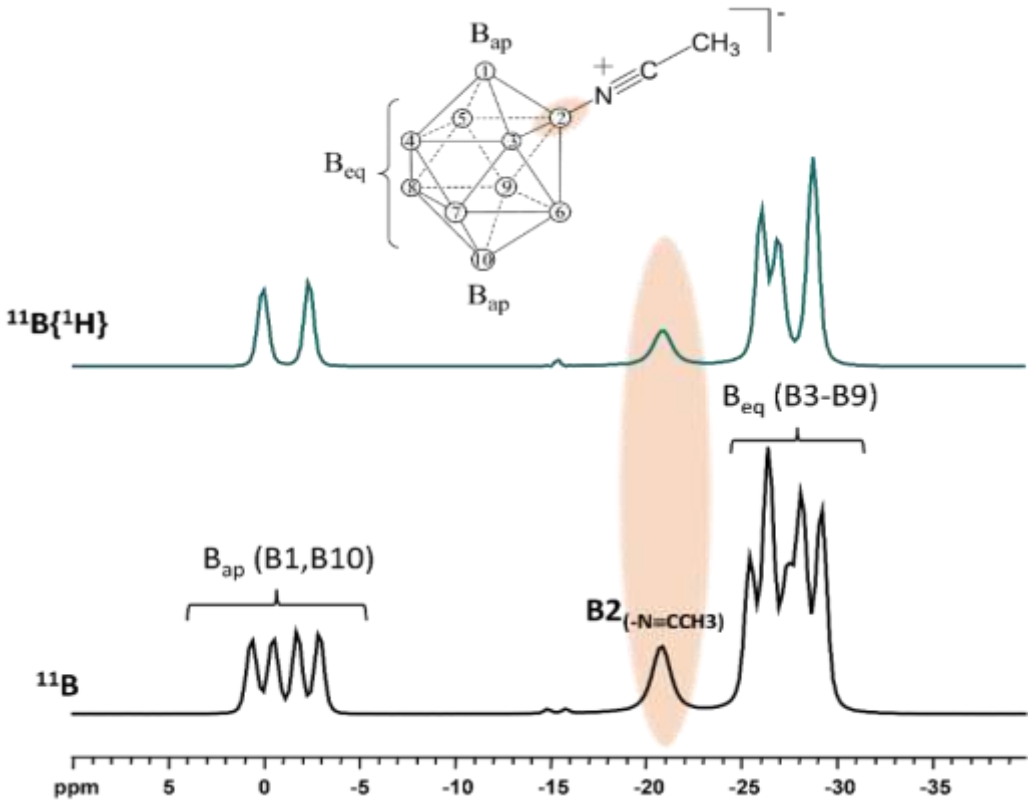

Figure 7. ^{11}B and $^{11}B\{^{1}H\}$ NMR spectra (400 MHz) of ***$(Et_3NH)[B_{10}H_9NCCH_3]$*** *in CD_3CN.*

In this context, ^{1}H and ^{11}B NMR spectra recorded in CD_3CN require decoupling from ^{11}B and ^{1}H nuclei, respectively, not only to facilitate the assignments of all signals but also to ensure no unreacted compounds remain. In particular, the ^{1}H spectra without decoupling from ^{11}B of $(Et_3NH)[2\text{-}B_{10}H_9NCCH_3]$ (Figure 8) leads to broad multiplets of the BH_{eq} and BH_{ap} protons in the ranges -0.4-1 and 3.2-4 ppm, respectively, which makes it difficult to assign chemical shifts confidently.

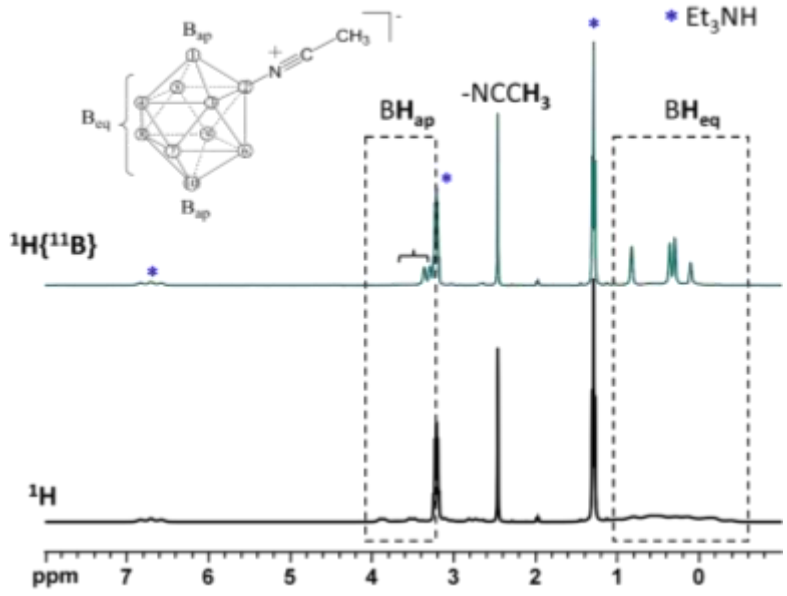

Figure 8. ^{1}H and $^{1}H\{^{11}B\}$ NMR spectra (400 MHz) of ***(Et₃NH)[B₁₀H₉NCCH₃]*** *in CD_3CN.*

Comparison between $^{1}H\{^{11}B\}$ of $(Et_3NH)[2\text{-}B_{10}H_9NCCH_3]$ and $(Et_3NH)_2[B_{10}H_{10}]$ (Figure 9) reveals a loss of symmetry in the $[B_{10}H_{10}]^{2-}$ cage upon grafting of $-NCCH_3$. The broad signal of B**H$_{eq}$** (-0.05 ppm, 8H) in the parent $[B_{10}H_{10}]^{2-}$ splits into four signals in the range 0.10-0.80 ppm. At the same time, the signal of B**H$_{ap}$** (3.18 ppm, 2H), which is masked behind counter cation signal at 3.18 ppm, also splits into two signals, at 3.29 and 3.36 ppm, present near the signal of the methyl group ($B_{10}H_9$-NCC**H$_3$**) at 2.46 ppm.

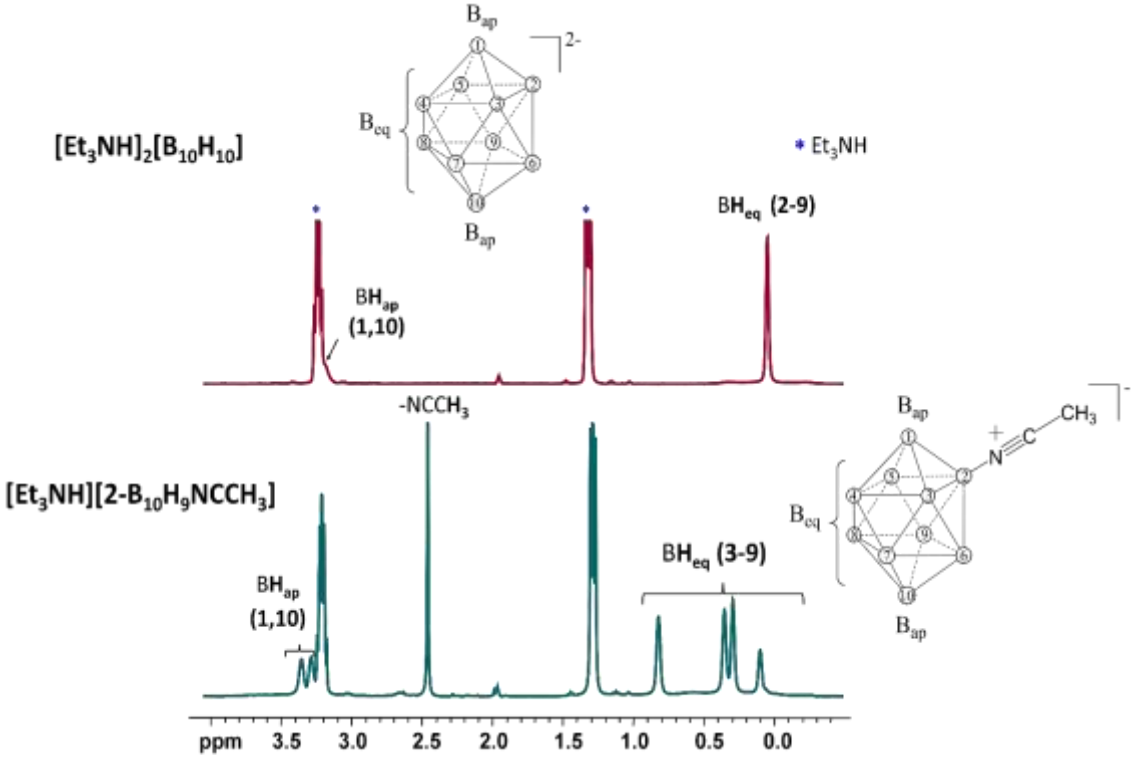

Figure 9. $^{1}H\{^{11}B\}$ NMR spectra (400 MHz) of ***(Et₃NH)[B₁₀H₉NCCH₃]*** *and* ***(Et₃NH)₂[B₁₀H₁₀]*** *in CD_3CN.*

II.3 Interaction between cyclodextrins and $(Et_3NH)[B_{10}H_9NCCH_3]$ in D_2O

II.3.1 ESI-MS studies of $[B_{10}H_9NCCH_3]^-$/CD in D_2O

Following previous work concerning $[B_{10}H_{10}]^{2-}$ encapsulation within CD [25], we decided to analyze 10^{-5} M aqueous mixtures of $(Et_3NH)[B_{10}H_9NCCH_3]$ and α-,β-, or γ-CD with a 1:1 ratio. The ESI-MS spectra are given in Figure 10. All spectra show the same peak at *m/z* 176.19, which can be assigned to the monoanionic species $\{B_{10}H_9NCCH_3(H_2O)\}^-$. The free CD appears as a monoanionic species $\{(CD)-H\}^-$ at *m/z* 971.31 (α-CD), 1134.37 (β-CD), and 1296.43 (γ-CD).

The formation of 1:1 adducts as dianionic species, $\{(B_{10}H_9NCCH_3)(CD)(H_2O)-H\}^{2-}$, is confirmed by the peaks at *m/z* 547.25, 655.28 and 736.30 for α-, β- and γ-CD, respectively. The relatively low-intensity peaks of free α-CD and its 1:1 adduct compared to those of β-CD and γ-CD suggest the lower boron cluster affinity for the α-CD and probably a less efficient encapsulation.

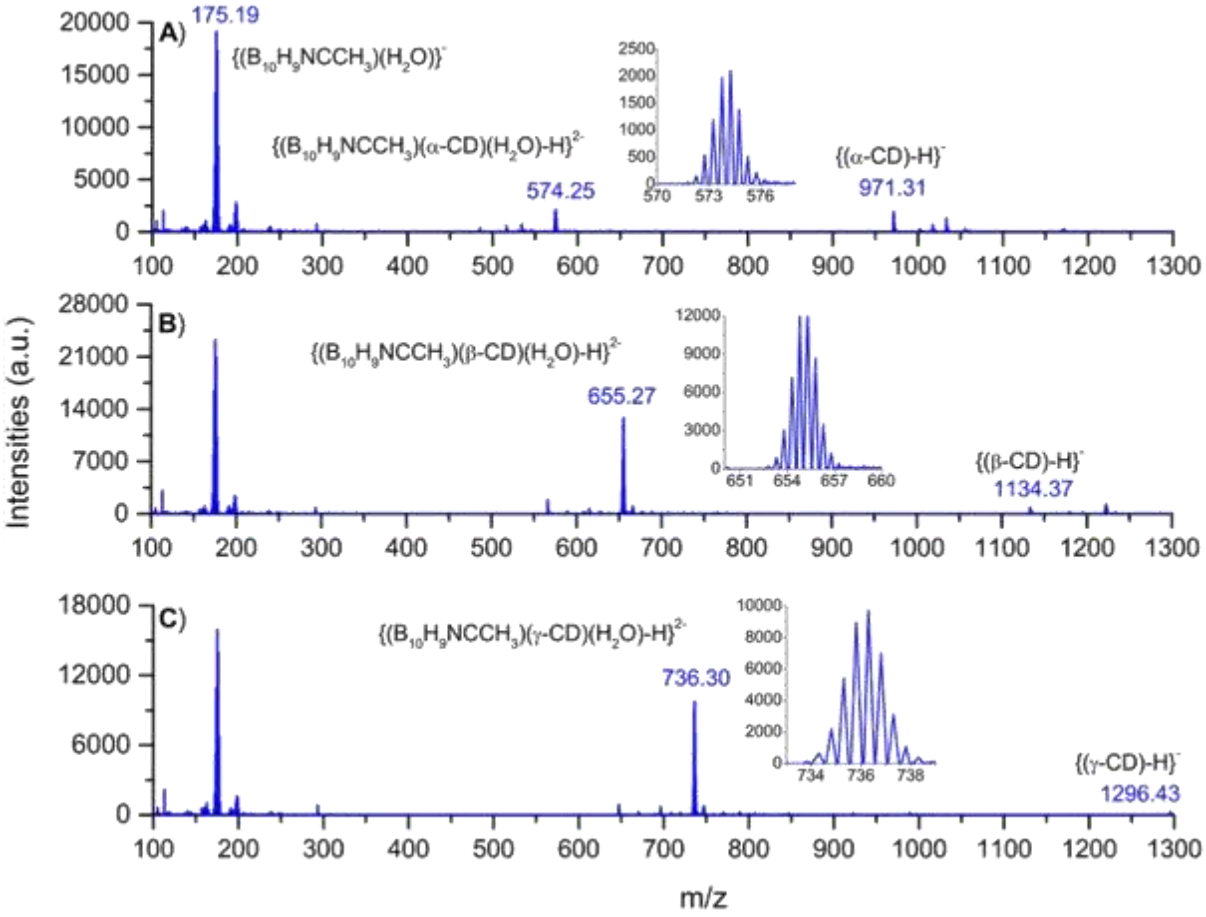

Figure 10. ESI-MS spectra of the aqueous mixtures in 1:1 ratio of ***$(Et_3NH)[B_{10}H_9NCCH_3]$*** *($10^{-5}$ M) and* ***(a)*** *α-CD,* ***(b)*** *β-CD, and* ***(c)*** *γ-CD.*

II.3.2 NMR studies of $[B_{10}H_9NCCH_3]^-$/CD in D_2O

The encapsulation process of the $[B_{10}H_{10}]^{2-}$ cluster was previously studied by using it as an ammonium salt [25]. In the present case, the triethylammonium salt of $[B_{10}H_9NCCH_3]^-$ was used. To verify that the countercation cannot play a significant role in the encapsulation process, a titration of β-CD by Et_3NHCl was first realized. By adding up to 8 equivalents of Et_3NHCl per CD, no significant change in the NMR spectrum of the CD was seen (see Figure S2 in the appendix). This counter-cation plays no competitive role in CD complexation, and the observed effects are solely due to the interaction of the boron cluster with the host.

The encapsulation of $(Et_3NH)[B_{10}H_9NCCH_3]$ cluster within the cavity of α-, β- or γ-CD has been monitored by ^1H NMR titration in D_2O of fixed concentration CD solutions (3 mM) with variable concentrations of $[B_{10}H_9NCCH_3]^-$.Two mother solutions of the concentrations C_1 = 6 mM and $C_2 = 8C_1$ = 48 mM were prepared in D_2O for CD and $(Et_3NH)[B_{10}H_9NCCH_3]$ compounds, respectively. Then, 500 µL of CD solution was mixed with various volumes (µL) of B_{10} compound of the concentrations C_2 = (0, 0.25, 0.5, 1, 2, 4, and 8) C_1. Finally, D_2O was added to get a total volume of 1 ml.

II.3.3 Interaction between α-CD and $(Et_3NH)[B_{10}H_9NCCH_3]$ in D_2O

The ^1H NMR spectra of various **$[B_{10}H_9NCCH_3]^-$/α-CD** mixtures are given in Figure 11. The variations of the chemical shifts of α-CD protons in various $[B_{10}H_9NCCH_3]^-$/α-CD mixtures are given in Table S1 in the appendix. As reported in our previous studies [25], the boron cluster encapsulation into CDs can induce slight shifts variation of the internal protons corresponding to the primary (H5 and H6) and/or secondary (H3) CDs faces (Scheme 1).

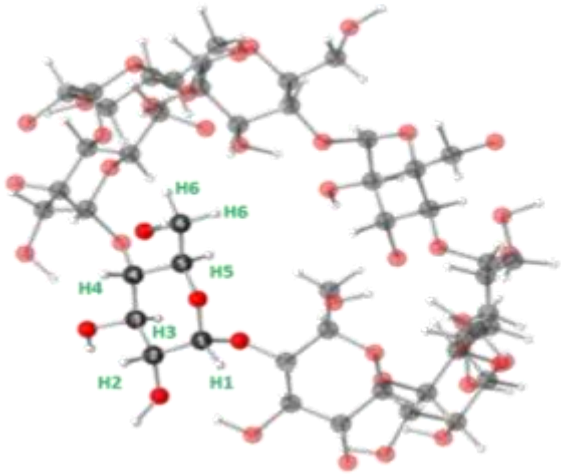

*Scheme 1. Numbering of protons within **α-cyclodextrin**.*

Thus, in the case of α-CD (Figure 11), increasing the **$[B_{10}H_9NCCH_3]^-$/α-CD** ratio induces no major changes in the NMR spectra except for a slight shift of **H3** protons with a maximum variation of only **+0.058 ppm** (see Table S1 in the appendix). This demonstrates weak

interactions of the α-CD with the cluster, and an encapsulation process within the cyclodextrin cavity is unlikely.

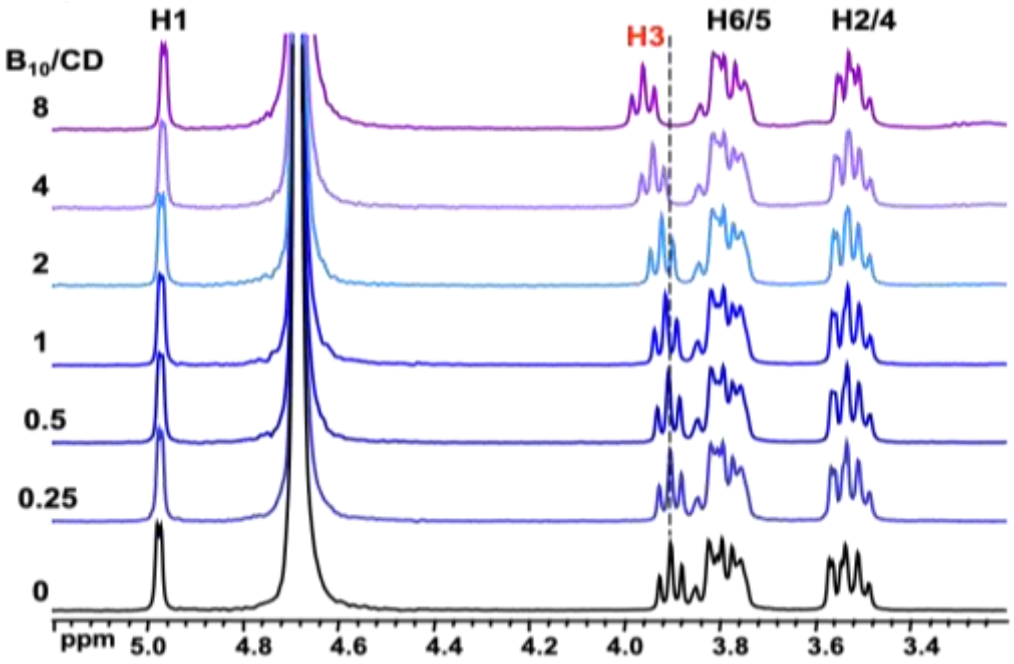

*Figure 11. ^{1}H NMR spectra in D_2O for different ratios of **$B_{10}H_9NCCH_3$/α-CD** from the titration of 3 mM aqueous α-CD solution with $(Et_3NH)[B_{10}H_9NCCH_3]$.*

Job's plot represents the product of the molar fraction in CD (x_{CD}) and chemical shift variation of **H3** ($\Delta\delta = \delta_{obs} - \delta_{H3}$; where δ_{obs} is the chemical shift of H3 upon addition of B_{10} compound while δ_{H3} is the chemical shift of H_3 in free CD) versus x_{CD} under boron cluster titration. The variation of the chemical shift of H3 for α-CD with $[B_{10}H_9NCCH_3]^-$ in D_2O is very small; hence, the Job's plot (Figure 12) does not permit us to see a clear maximum on the curve. It suggests a very weak interaction of the boron cluster with α-CD on its outer surface in a random fashion, and the observed variation in the chemical shift of H3 does not reflect the formation of a two-component adduct.

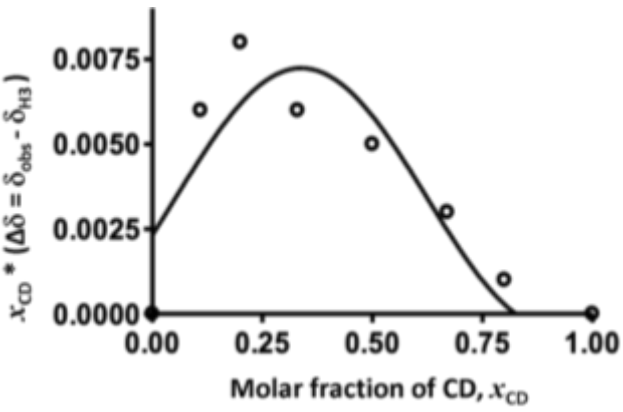

*Figure 12. Job's plot for **$[B_{10}H_9NCCH_3]^-$ with α-CD** in D_2O.*

II.3.4 Interaction between β-CD and $(Et_3NH)[B_{10}H_9NCCH_3]$ in D_2O

In contrast to α-CD, titration of β-CD with $[B_{10}H_9NCCH_3]^-$ cluster leads to a stronger shift of **H5**-CD protons with maximum variation up to **+0.157** ppm (Figure 13). The variations of the chemical shifts of β-CD protons in various **$[B_{10}H_9NCCH_3]^-$/β-CD** mixtures are given in Table S2 in the appendix. This behaviour suggests stronger interactions of the boron cluster with β-CD and the encapsulation of the cluster within the cavity of this CD.

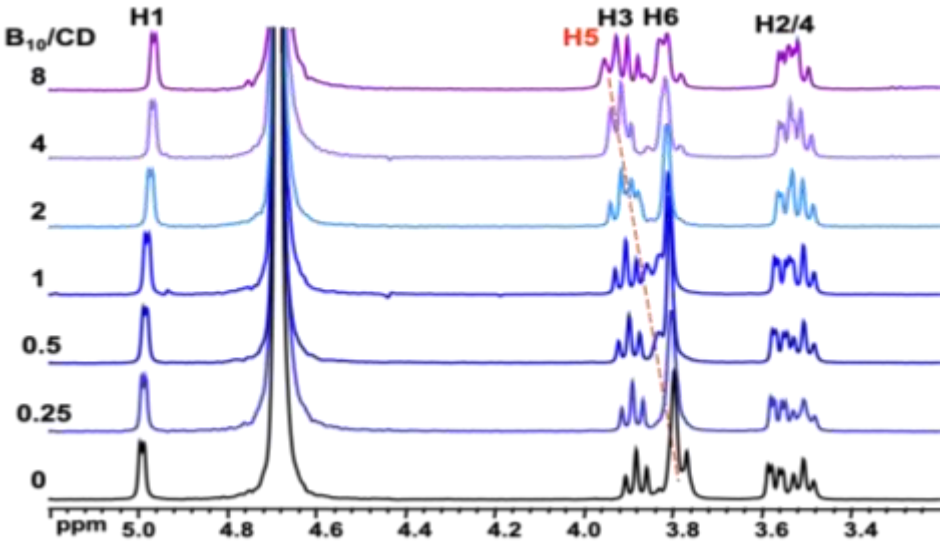

*Figure 13. ^1H NMR spectra in D_2O for different ratios of **$B_{10}H_9NCCH_3$/β-CD** from the titration of 3 mM aqueous β-CD solution with $(Et_3NH)[B_{10}H_9NCCH_3]$.*

In the case of β-CD, Job's plot represents the product of the molar fraction in CD (x_{CD}) and chemical shift variation of **H5** ($\Delta\delta = \delta_{obs} - \delta_{H5}$) versus x_{CD} under boron cluster titration (Figure 14). The variation of the chemical shift of H5 for β-CD with $[B_{10}H_9NCCH_3]^-$ in D_2O permits us to see a clear maximum on the curve at x_{CD} about 0.5, consistent with the formation of 1:1 adducts, $\{(B_{10}H_9NCCH_3)(\beta\text{-CD})\}^-$.

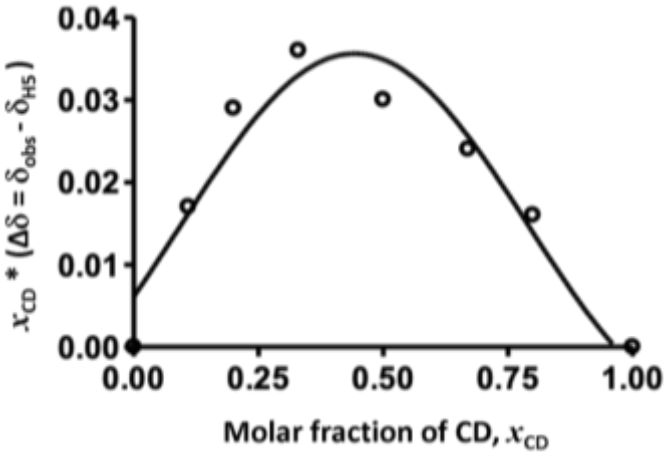

*Figure 14. Job's plot for **$[B_{10}H_9NCCH_3]^-$** with **β-CD** in D_2O.*

II.3.5 Interaction between γ-CD and $(Et_3NH)[B_{10}H_9NCCH_3]$ in D_2O

As in the case of β-CD, the titration of γ-CD with $[B_{10}H_9NCCH_3]^-$ cluster (Figure 15) leads to a strong shift of **H5**-CD protons with maximum variation up to **+0.182** ppm. The variation of the chemical shifts of γ-CD protons in various **$[B_{10}H_9NCCH_3]^-$/γ-CD** mixtures are given in Table S3 in the appendix. This behaviour suggests stronger interactions of the boron cluster with γ-CD and the encapsulation of the cluster within the cavity of this CD.

Job's plot in Figure 16 focused on the variation of the chemical shift of **H5** for γ-CD with $[B_{10}H_9NCCH_3]^-$ in D_2O, permits us to see a clear maximum on the curve at x_{CD} about 0.5, consistent with the formation of 1:1 adducts, $\{(B_{10}H_9NCCH_3)(\gamma\text{-CD})\}^-$.

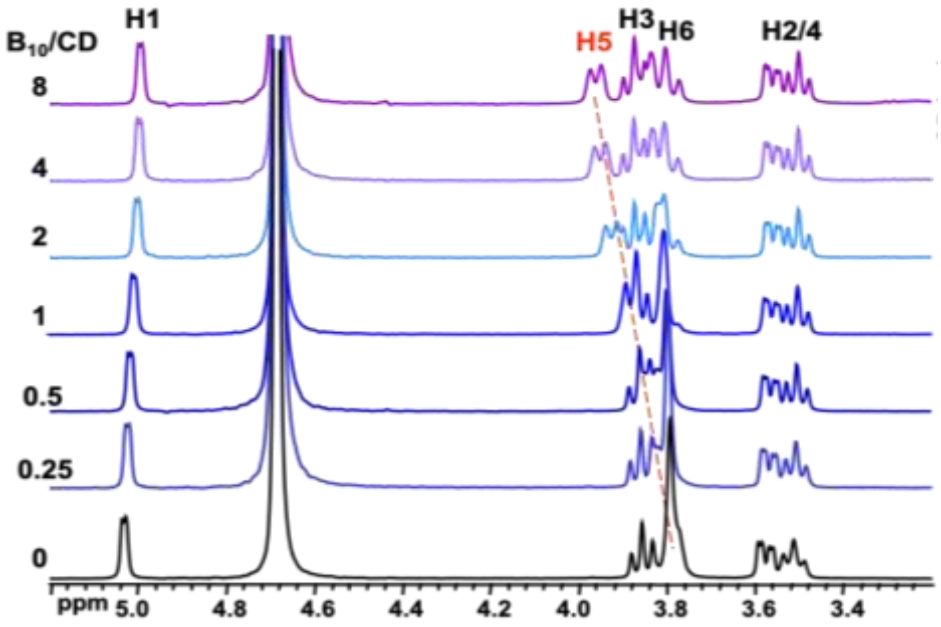

Figure 15. ^1H NMR spectra in D_2O for different ratios of **$B_{10}H_9NCCH_3$/γ-CD** from the titration of 3 *mM aqueous δ-CD solution with* $(Et_3NH)[B_{10}H_9NCCH_3]$.

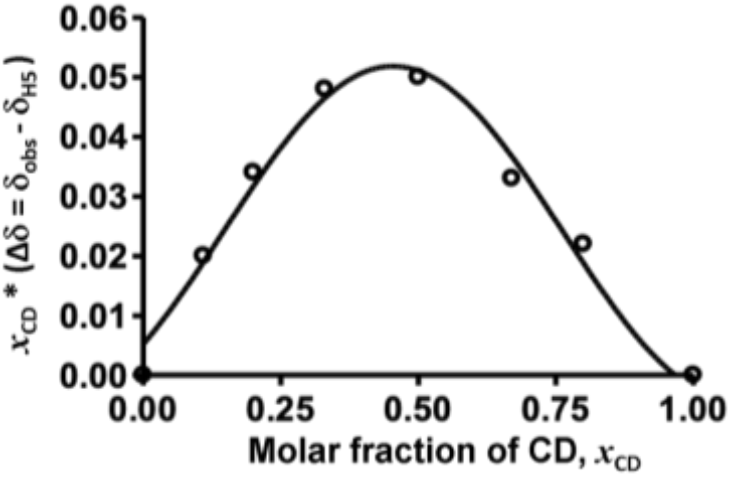

Figure 16. Job's plot for ***$[B_{10}H_9NCCH_3]^-$*** *with* ***γ-CD*** *in* D_2O.

II.3.6 Determination of association constants by nonlinear least-squares method

Finally, the association constants of boron cluster to CDs have been determined from the NMR titration applying a mathematical approach [28]. As the NMR spectra indicate a fast chemical exchange regime, the observed chemical shift variations of H3 or H5 protons (δ_{obs}) of CD should correspond to a linear combination of the chemical shifts of the free CD and the 1:1 adducts (equation 1), noted δ_0 and $\delta_{1:1}$ respectively. The x_0 and $x_{1:1}$ are the CD molar fractions in the free state, and 1:1 adducts correspondingly.

$$\delta_{obs} = x_0\delta_0 + x_{1:1}\delta_{1:1} \qquad (\textbf{eq. } \textit{1})$$

Considering a 1:1 adduct, the association constant K is given by equation 2, using the CD molar fractions x_0 and $x_{1:1}$ and expressed as a function of the initial concentration of CD (C^0) and the molar ratio R = [$B_{10}H_9NCCH_3$]/[CD].

$$K = \frac{x_{1:1}}{x_0\left(R - \left(\frac{1 - x_0 + x_{1:1}}{2}\right)\right)C^0} \qquad (\textbf{eq. 2})$$

Combining equations 1 and 2 and considering that $x_0 + x_{1:1} = 1$, one can deduce the expression of the observed chemical shift as a function of binding constant K (equation 3).

$$\delta_{obs} = \delta_0\left[\frac{KC^0 - KC^0R - 1 + \sqrt{(KC^0R - KC^0 + 1)^2 + 4KC^0}}{2KC^0}\right] + \delta_{1:1}\left[\frac{KC^0 - KC^0R + 1 - \sqrt{(KC^0R - KC^0 + 1)^2 + 4KC^0}}{2KC^0}\right] \quad \textit{(eq. 3)}$$

Modeling the experimental data leads to the binding constants gathered in Table 1. The best fits of the variation of the experimental chemical shift δ_{obs} as a function of the ratio R = B_{10}/CD according to the equation 3 using these K values are shown in Figure 17. The simulated variation of δ_{obs} matches well the experimental data.

Table 1. Formation constant K (M^{-1}) of the 1:1 adduct complexes formed between $[B_{10}H_9NCCH_3]^-$ and native cyclodextrins (α-, β-, and γ-CD), obtained from ^1H chemical shifts at 298 K (equation 3), in comparison with formation constants from previous data obtained with $[B_{10}H_{10}]^{2-}$ [25].

B_{10} Compound	**CD**	**K (M^{-1})**
$[B_{10}H_9NCCH_3]^-$	α-CD	34.1 ± 0.8
	β-CD	300 ± 20
	γ-CD	720 ± 40
$[B_{10}H_{10}]^{2-}$ [25]	α-CD	35 ± 10
	β-CD	110 ± 70
	γ-CD	60 ± 20

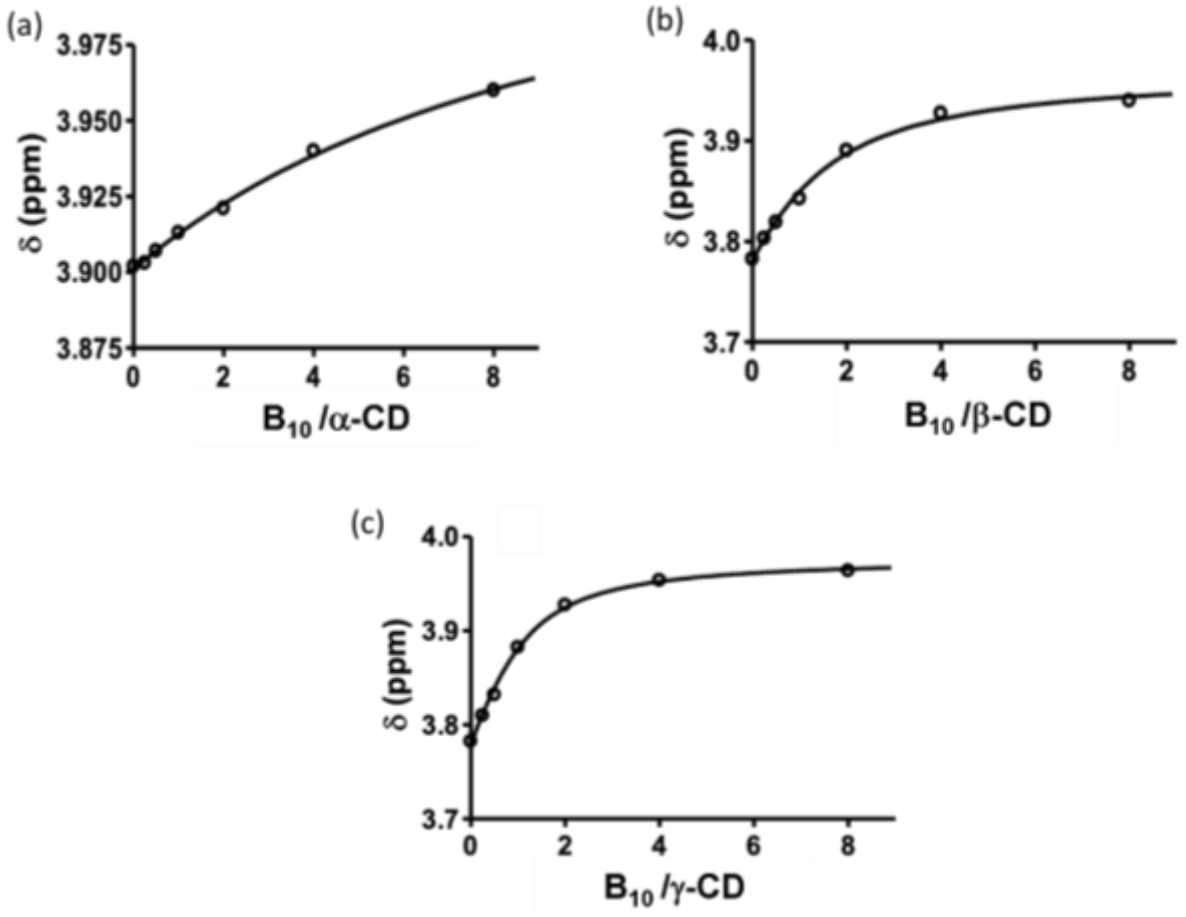

Figure 17. The variations of the observed chemical shift of ***(a)*** *α-CD-H3,* ***(b)*** *β-CD-H5, and* ***(c)*** *γ-CD-H5 internal protons versus* ***[B10H9NCCH3]-*** *content.*

The association constants found by NMR first evidence that *K* values increase in the following order α-CD < β-CD < γ-CD, suggesting again the low affinity of the boron cluster to the α-CD and an optimal affinity with the γ-CD. Previously, the optimal affinity of $[B_{10}H_{10}]^{2-}$ was found for β-CD, while the cavity of γ-CD was too large to accommodate this cluster [25]. In the present case, the volume of the cluster $[B_{10}H_9NCCH_3]^-$ is a little higher, and logically the γ-CD is better adapted. Secondly, these data, in agreement with ITC results (vide infra), show that the affinity constants are improved for host-guest systems with β- and γ-CD by replacing $[B_{10}H_{10}]^{2-}$ with $[B_{10}H_9NCCH_3]^-$. As expected, the affinity constant for γ-CD appears 12 times higher with $[B_{10}H_9NCCH_3]^-$ due to the chaotropic effect. Finally, for both clusters, the affinity for α-CD appears very weak as the size of the host cavity also plays a crucial role.

II.3.7 Association constants and thermodynamic data by ITC

Even if association constants of labile host-guest complexes in aqueous solution can be determined from NMR titrations, isothermal calorimetric titration (ITC) measurements usually lead to more reliable data. In a previous study, it was shown that the encapsulation of $[B_{10}H_{10}]^{2-}$ was characterized by weak interactions between the host and the guest [25]. In such

a case, dedicated protocols have been employed for ITC measurements, *i.e.*, release, annihilated release, and reverse titration experiments, to increase ITC characterization accuracy [25]. In the case of $[B_{10}H_9NCCH_3]^-$, the affinity constant appears one order of magnitude higher. Therefore, the $(Et_3NH)[B_{10}H_9NCCH_3]$@CD systems were studied by titration (injection of 5 mM CD solution on a 0.5 mM $(Et_3NH)[B_{10}H_9NCCH_3]$ solution) and release (injection of 5 mM CD and 5 mM $(Et_3NH)[B_{10}H_9NCCH_3]$ solution on water solution) protocols and thermodynamic parameters were determined by global nonlinear regression analysis of these experiments [29]. The corresponding ITC thermograms and isotherms are given in Figures 18 and 19, while the thermodynamic parameters are gathered in Table 2.

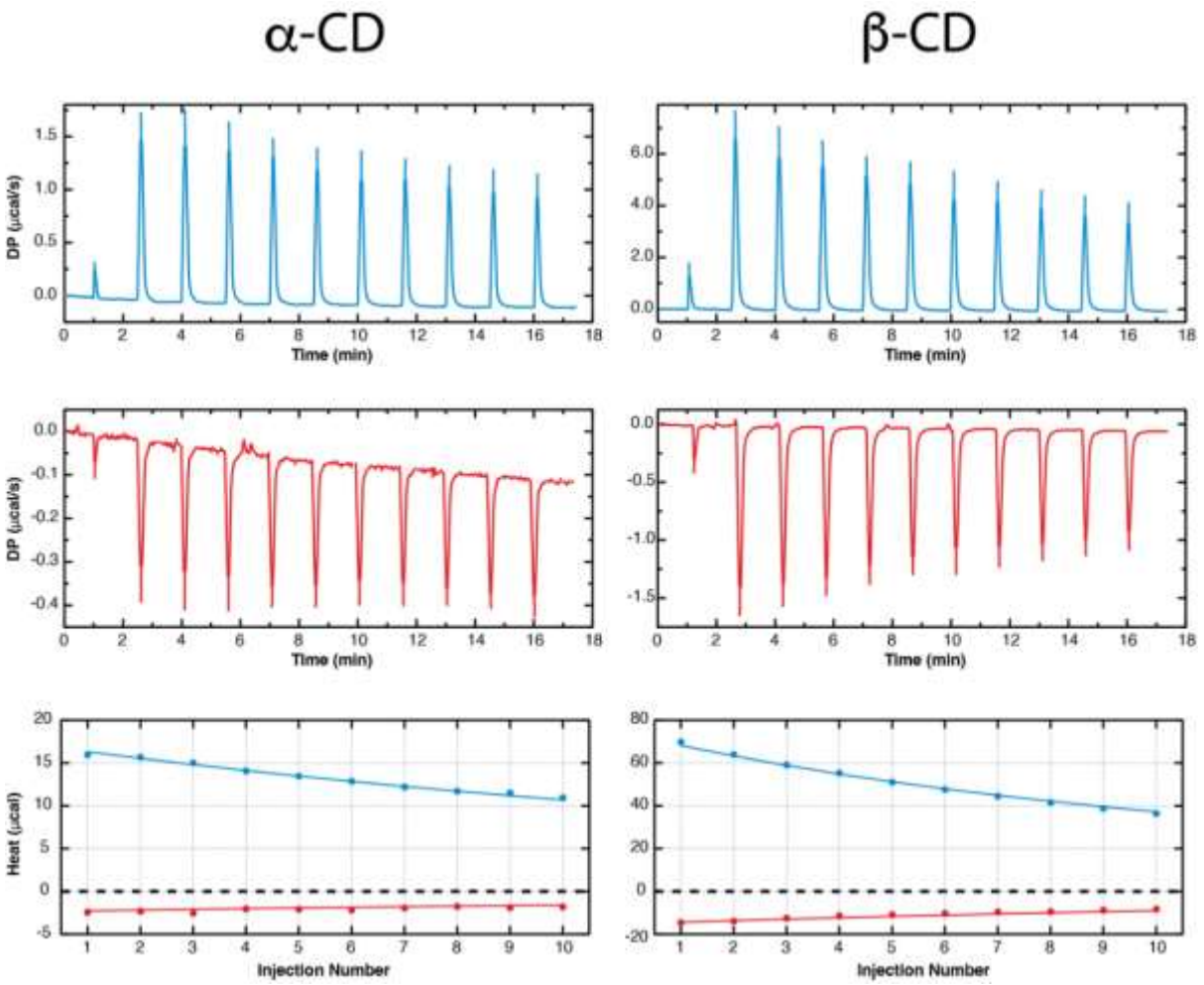

Figure 18. ITC thermograms were obtained respectively for the titration and release experiments at 298 K (upper part) and global analysis of experimental isotherms (lower part) for the systems ***$[B_{10}H_9NCCH_3]^-$/CD (α- and β-forms)****. Dots and lines correspond to experimental and theoretical heats, respectively.*

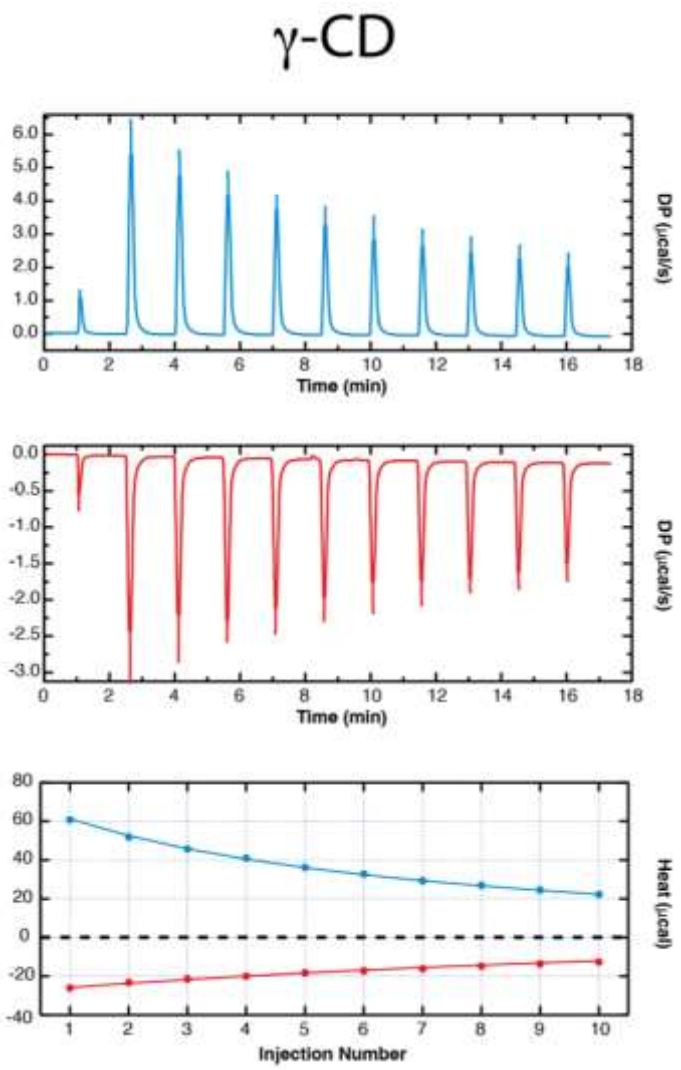

Figure 19. ITC thermograms were obtained respectively for the titration and release experiments at 298 K (upper part) and global analysis of experimental isotherms (lower part) for the systems ***[$B_{10}H_9NCCH_3$]$^-$/γ-CD****. Dots and lines correspond to experimental and theoretical heats, respectively.*

Table 2. Binding constants, enthalpy, entropy, and Gibbs energy of 1:1 adduct complexes formation between $(Et_3NH)[B_{10}H_9NCCH_3]$ or $(NH_4)_2[B_{10}H_{10}]$ [25] and native cyclodextrins (α-, β- and γ-CD), obtained from ITC data, at 298 K.

		K (M^{-1})	ΔH ($kJ.mol^{-1}$)	TΔS ($kJ.mol^{-1}$)	ΔG ($kJ.mol^{-1}$)
$(Et_3NH)[B_{10}H_9NCCH_3]$	α-CD	45 ± 11	-25.2 ± 4.1	-15.8 ± 4.7	-9.4 ± 0.6
	β-CD	149 ± 4	-51.2 ± 0.5	-39.2 ± 0.6	-12.4 ± 0.1
	γ-CD	577 ± 8	-29.1 ± 0.1	-13.4 ± 0.2	-15.7 ± 0.1
$(NH_4)_2[B_{10}H_{10}]$ [25]	α-CD	4 ± 3	-25 ± 16	-21 ± 16	-2.9 ± 1.6
	β-CD	40 ± 4	-34.7 ± 0.8	-25.5 ± 1.2	-9.2 ± 0.5
	γ-CD	19 ± 5	-39.7 ± 2.0	-32.2 ± 2.8	-7.5 ± 0.9

All experimental data agree with a 1:1 stoichiometric model. As expected from a qualitative evaluation of the ITC isotherms, the inclusion of $[B_{10}H_9NCCH_3]^-$ in α-, β-, and γ-CD was characterized by an important compensation between a strong enthalpic stabilization and a slightly lower entropic destabilization, leading to significant affinities: 45, 149 and 577 M^{-1} for α-, β- and γ-CD, respectively, in agreement with NMR studies.

From a thermodynamic point of view, the negative enthalpy values found in all cases demonstrate that the process of encapsulation of the $[B_{10}H_9NCCH_3]^-$ cluster is enthalpically driven, while the negative entropy variations indicate that the inclusion process of the monoanionic $[B_{10}H_9NCCH_3]^-$ within cyclodextrins is associated to a chaotropic effect, in agreement with the previous study on $[B_{10}H_{10}]^{2-}$ [25] and the work of Nau and coworkers [19–21] for dodecaborate derivatives $[B_{12}X_{12}]^{2-}$. This solvent effect can be explained by the migration of the borate cluster from the bulk aqueous medium into the pockets of CD, allowing the recovery of the water structure distorted by the chaotropes.

The strength of the chaotropic behavior is notably related to the volume charge density of the anion. A lower chaotropic effect is expected when the volume charge density increases. The volume charge density decreases from $[B_{10}H_{10}]^{2-}$ to $[B_{10}H_9NCCH_3]^-$. Thus, the chaotropic character of the latter is increased, resulting in an increase in the entropy change associated with the recovery of the water structure upon inclusion in CDs.

Additionally, as commonly observed for cyclodextrins, the increasing enthalpic contribution is counterbalanced by an increasing entropy penalty called enthalpy-entropy compensation. Figure 20 gives the ΔH *vs* TΔS plot associated with the 1:1 complexes of $[B_{10}H_9NCCH_3]^-$ with

CDs (red dots) in comparison to previous thermodynamic data reported for $[B_{10}H_{10}]^{2-}$ [25] and dodecaborate derivatives [21]. The thermodynamic parameters determined for adducts obtained with $[B_{10}H_9NCCH_3]^-$ showed a stronger enthalpy-entropy compensation contrast, which is the typical signature of the chaotropic effect in the complexation of CDs [21].

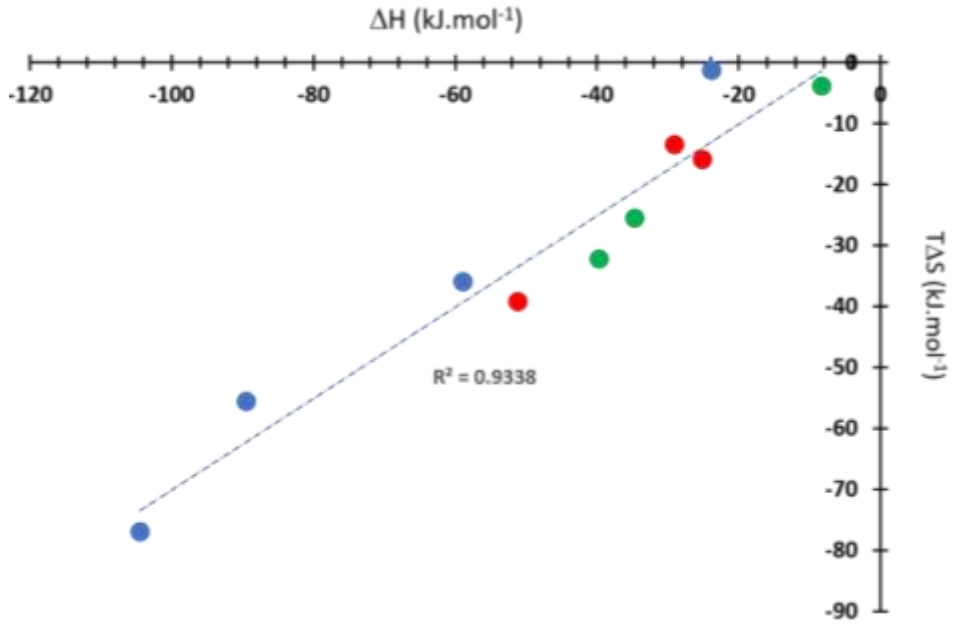

Figure 20. Enthalpy-entropy compensation plot for 1:1 complexes formed between α-, β-, and γ-CD with ***$[B_{10}H_{10}]^{2-}$*** *(green dots),* ***$[B_{10}H_9NCCH_3]^-$*** *(red dots) and* ***$[B_{12}X_{12}]^{2-}$*** *derivatives (blue dots).*[21]

In summary, this work reports the host-guest processes involving the anionic cluster $[B_{10}H_9NCCH_3]^-$ with α-, β- and γ-cyclodextrins through solution studies using ESI-MS, NMR, and ITC, demonstrating the formation of 1:1 inclusion complexes between $[B_{10}H_9NCCH_3]^-$ and β- and γ-CDs, while weaker interactions are evidenced with the α-CD.

III. Encapsulation of the cluster $[B_{20}H_{18}]^{2-}$

The octadecahydro-eicosaborate dianion $[trans\text{-}B_{20}H_{18}]^{2-}$ corresponds to the dimeric derivative of $[B_{10}H_{10}]^{2-}$. This cluster was chosen because its volume is twice that of $[B_{10}H_{10}]^{2-}$ while retaining the same charge (-2). Its charge density is therefore lower, which would enhance its chaotropic effect. The encapsulation of $[trans\text{-}B_{20}H_{18}]^{2-}$ within α-, β-, and γ-CD will be studied by NMR and ITC.

The macropolyhedral trans-octadecahydro-eicisaborate anion $[trans\text{-}B_{20}H_{18}]^{2-}$ was first discovered in 1962 by the Kaczmarczyk's group through oxidation of the closo-decahydrodecaborate anion $[B_{10}H_{10}]^{2-}$ by ferric anion Fe^{3+} in refluxing aqueous medium [30]. Structurally, it consists of two parallel $[B_{10}H_9]^-$ cages, resulting from losing a hydride atom from each $[B_{10}H_{10}]^{2-}$ anion. The two B_{10} units are connected through two pairs of 3c-2e (three centers-two electrons) B-B-B bridges involving two adjacent equatorial (eq) and apical (ap) boron atoms from each B_{10} unit sharing two electrons, as seen in Figure 21 [31].

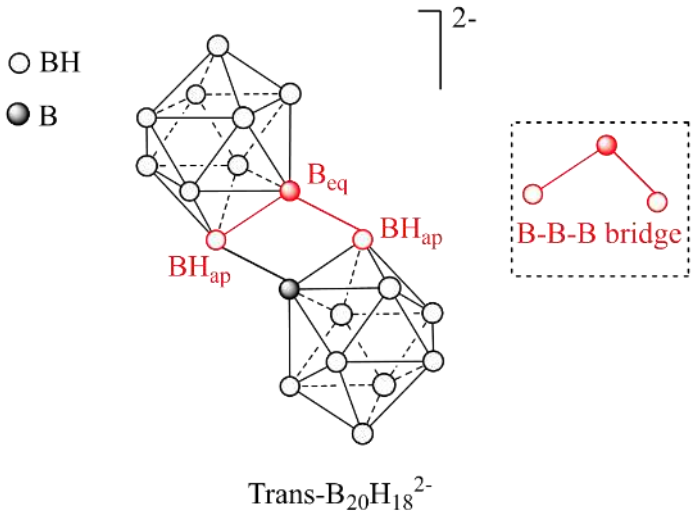

Figure 21.Structure of the trans isomer of ***$[B_{20}H_{18}]^{2-}$***.

B_{20} derivatives such as $Na_3[B_{20}H_{17}NH_3]$ and $Na_4[B_{20}H_{17}NH_3]$ have been proven to be effective in Boron neutron capture therapy (BNCT). They allow the biodistribution of boron content selectively into murine tumors in vivo through encapsulation inside synthetic spherical vesicles called liposomes having a hydrophilic cavity and outer lipophilic membrane analogous to the natural phospholipid bilayer membrane [32,33]. We therefore decided to investigate the encapsulation of the B_{20} cluster in CD cavities, which would pave the way for the development of novel B_{20} systems effective in tumor therapy. The lithium salt of $[trans\text{-}B_{20}H_{18}]^{2-}$ is of particular interest as it is water-soluble with a potentially high chaotropic effect.

III.1 Synthesis of $Li_2[trans\text{-}B_{20}H_{18}]$

First, we synthesized the triethyl ammonium salt of $[B_{20}H_{18}]^{2-}$ based on the literature [34] by refluxing $(Et_3NH)_2[trans\text{-}B_{10}H_{10}]$ with excess of $FeCl_3$ in distilled water. In cold water, $(Et_3NH)[trans\text{-}B_{20}H_{18}]$ was formed as an insoluble pale-yellow solid, which was purified through recrystallization from boiling water and isolated in a high yield (74%).

Since $(Et_3NH)[trans\text{-}B_{20}H_{18}]$ isn't soluble in an aqueous medium, we performed a cationic exchange of Et_3NH^+ with Li^+ cation through a column packed with Li^+ resin in H_2O/CH_3CN (50/50) mixture as the eluent. $Li_2B_{20}H_{18}$ was isolated as a yellow powder with 97% yield (see experimental section for detailed synthesis procedures). FT-IR (Figure S4 in the appendix) and NMR spectra perfectly agree with the expected compound (Figures 22-23,25-26).

III.2 NMR studies of Et_3NH^+ and Li^+ salts of $[B_{20}H_{18}]^{2-}$

The identification of the $[trans\text{-}B_{20}H_{18}]^{2-}$ was based for so long on primitive ^1H and ^{11}B NMR studies done early in the 1960s [30,35,36]. However, we have carried out advanced structural NMR studies using correlation experiments, e.g., 2D ($^{11}B\{^1H\}$ - $^{11}B\{^1H\}$) COSY and 2D ($^{11}B\{^1H\}$ - $^1H\{^{11}B\}$) HETCOR. These 2D NMR studies have proved very useful in differentiating the structures of position isomers, as recently demonstrated by Avdeeva and coworkers [37].

The $^{11}B\{^1H\}$ NMR spectrum of [trans-$B_{20}H_{18}]^{2-}$ in CD_3CN (Figure 22) has characteristic seven singlets as following: 29.88 ($2B_{ap}$), 15.32 ($2B_{eq}$), -7.49 ($2BH_{eq}$), -12.9 ($4BH_{eq}$),-16.52 ($4BH_{eq}$), -19.96 ($4BH_{eq}$), and-26.18 ppm ($2BH_{ap}$). In comparison with the non-decoupled ^{11}B NMR spectrum, all peaks become doublets due to the coupling with H atoms except for the singlet at 15.32 ppm, which means it correlates with the two equatorial boron atoms that have lost their hydrogen atoms during oxidative dimerization.

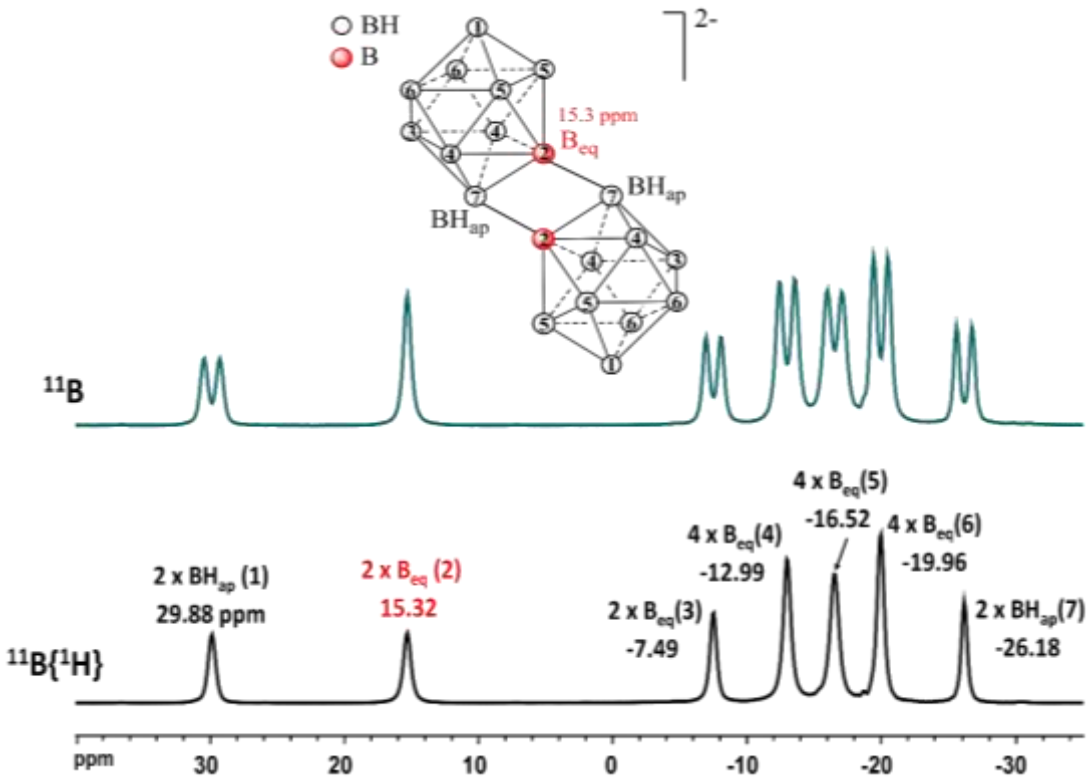

Figure 22. $^{11}B\{^1H\}$ and ^{11}B NMR spectra (400 MHz) of ***[trans-$B_{20}H_{18}]^{2-}$*** *in CD_3CN.*

The 2D ($^{11}B\{^1H\}$ - $^{11}B\{^1H\}$) COSY NMR spectrum of $[B_{20}H_{18}]^{2-}$ (Figure 23) has allowed us to figure out its geometry as "*trans*" configuration as designated in Figure 24, through the correlations between boron chemical shifts, as seen in Table 3, in agreement with ^{11}B NMR.

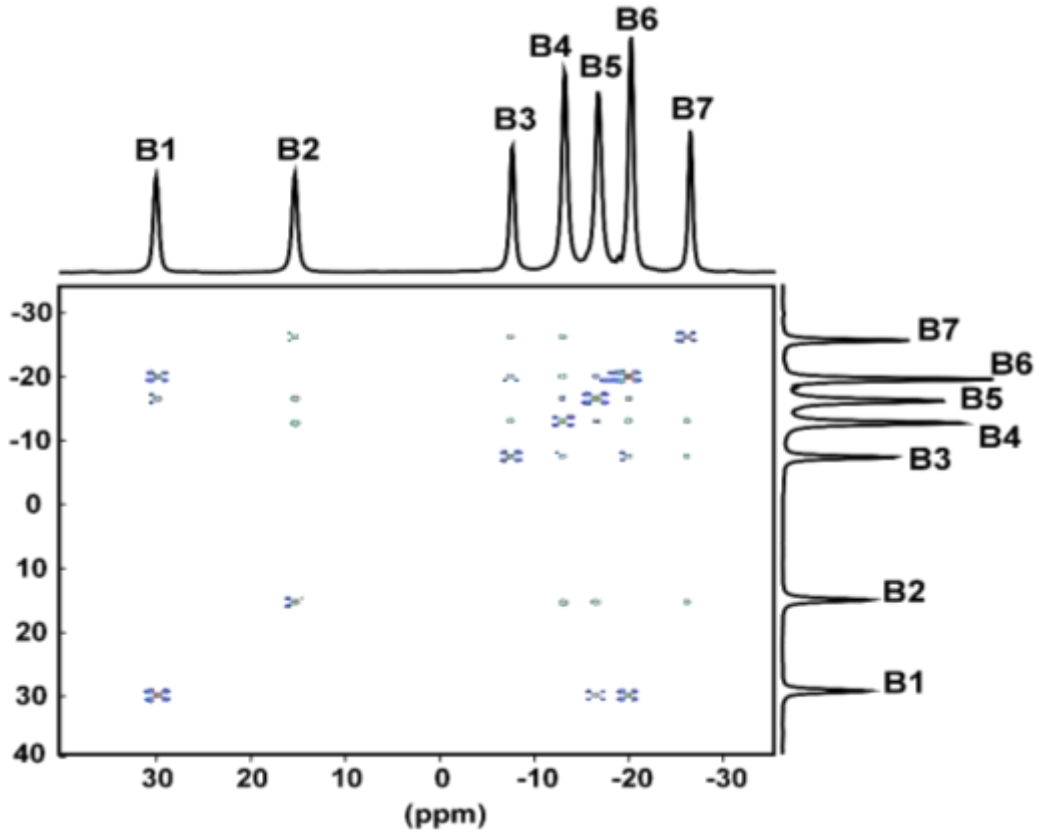

Figure 23. 2D ^{11}B-^{11}B COSY NMR spectrum (400 MHz) of ***[trans-$B_{20}H_{18}$]$^{2-}$*** *in CD_3CN.*

Table 3. The correlations between boron chemical shifts from 2D ^{11}B-^{11}B COSY NMR spectrum of ***[$B_{20}H_{18}$]$^{2-}$****.*

	B1	B2	B3	B4	B5	B6	B7
B1					x	x	
B2				x	x		x
B3				x		x	x
B4		x	x		x	x	x
B5	x	x		x		x	
B6	x		x	x	x		
B7		x	x	x			

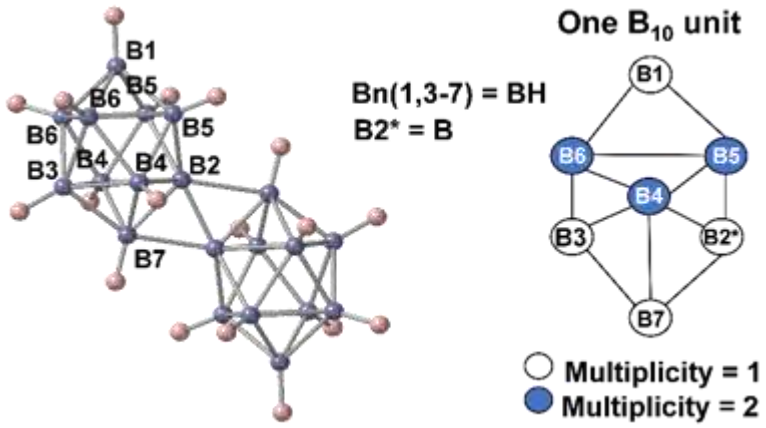

Figure 24. The trans configuration of ***$[B_{20}H_{18}]^{2-}$*** *proposed from the 2D ^{11}B-^{11}B COSY NMR spectrum (400 MHz) in CD_3CN. (Legends: B in blue; H in pink)*

The comparison between $^{1}H\{^{11}B\}$ of $[B_{10}H_{10}]^{2-}$ with the macropolyhedral cluster $[B_{20}H_{18}]^{2-}$ (Figure 25) reveals the appearance of six new peaks upon dimerization of the B_{10} cluster. The signal of BH_{eq} (1.05 ppm, 8H) in the parent $[B_{10}H_{10}]^{2-}$ splits into four signals in the range 0.7-1.9 ppm. At the same time, the signal of BH_{ap} (3.18 ppm, 2H), masked behind the counter cation signal at 3.18 ppm, also splits into two signals at ca. 2.73 and 5.40 ppm. Clearly, the disappearance of Et_3NH^+ signals in the $^{1}H\{^{11}B\}$ spectrum of $Li_2[B_{20}H_{18}]$ confirms the cationic exchange. This also makes it possible to visualize the H4 signal, which is superimposed with the counter-cation signal at 1.26 ppm in the organic salt.

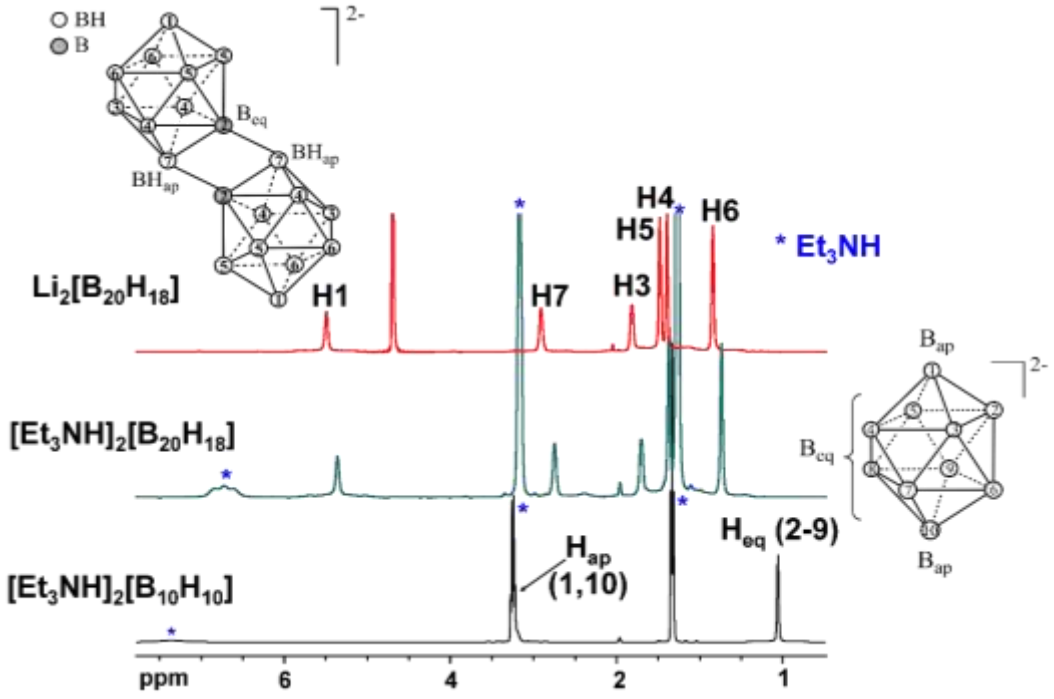

Figure 25. $^{1}H\{^{11}B\}$ NMR spectra (400 MHz) of ***$(Et_3NH)_2[B_{10}H_{10}]$****,* ***$(Et_3NH)_2[B_{20}H_{18}]$****, and* ***$Li_2[B_{20}H_{18}]$*** *in CD_3CN.*

The 2D ($^{11}B\{^1H\}$ - $^1H\{^{11}B\}$) HETCOR NMR spectrum of $[B_{20}H_{18}]^{2-}$ (Figure 26) shows the correlations between boron and proton chemical shifts involved in the direct B-H bond. This experiment makes it possible to assign the six types of protons in the "*trans*" configuration, with the help of $^{11}B\{1H\}$, $^1H\{^{11}B\}$, and 2D ^{11}B-^{11}B COSY NMR spectra.

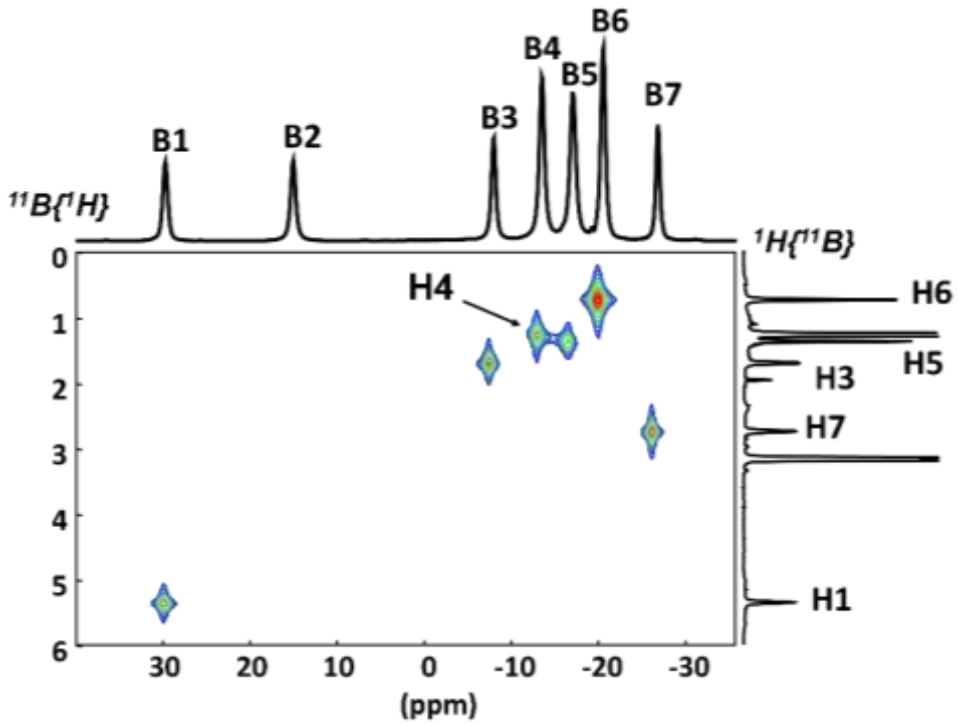

Figure 26. 2D ($^{11}B\{^1H\}$ - $^1H\{^{11}B\}$) HETCOR NMR spectrum (400 MHz) of ***$(Et_3NH)_2[B_{20}H_{18}]$*** *in CD_3CN. Note the signal H4 in the 1D ^1H NMR spectrum (shown in the indirect dimension) is overlapping with the signal of $(Et_3NH)^+$, and becomes visible in the 2D map.*

III.3 Interaction between cyclodextrins and $Li_2[B_{20}H_{18}]$ in D_2O

III.3.1 NMR studies of the interaction between cyclodextrins and $Li_2[B_{20}H_{18}]$ in D_2O

As in the case of $(Et_3NH)[B_{10}H_9NCCH_3]$ and CD, the interaction of $Li_2[B_{20}H_{18}]$ within α-, β- and γ-CD will systematically be studied by NMR and ITC. The $^1H\{^{11}B\}$ and $^{11}B\{^1H\}$ NMR titrations are done in two different manners.

The first method consists of preparing two mother solutions in D_2O of the concentrations C_1 = 6 mM and C_2= 8C_1 = 48 mM for CD and $Li_2[B_{20}H_{18}]$ compounds, respectively. Then, 500 µL of CD solution was mixed with various volumes (µL) of B_{10} compound of the concentrations C_2 = (0, 0.25, 0.5, 1, 2, 4, 8, and 16) C_1. Finally, D_2O was added to get a total volume of 1 ml. This method allows to better visualize the effect of increasing the amount of B_{20} species on CD signals during the complexation process. In contrast, the second method involves a constant amount of $Li_2[B_{20}H_{18}]$ while that of CD was varied to better see the effect of increasing the amount of CD on the B_{20} NMR resonances (^1H and ^{11}B).

III.3.1.1 Interaction between α-CD and Li2[B20H18] in D2O

The $^{1}H\{^{11}B\}$ and $^{11}B\{^{1}H\}$ NMR spectra of various **{α-CD (3 mM) + $[B_{20}H_{18}]^{2-}$}** solutions are given in Figure 27 and S5, respectively. As seen in Figure 27, increasing $[B_{20}H_{18}]^{2-}$/α-CD ratio induces no major changes in the NMR spectra except for a slight downfield shift of the **H3** signal of α-CD with a maximum variation of only **+0.097 ppm** compared to free α-CD. The variations of the chemical shifts of α-CD protons in various $[B_{20}H_{18}]^{2-}$/α-CD mixtures are given in Table S4 in the appendix. On the boron side, no shifts are detected either for B**H** signals or boron (B) signals in comparison with $^{1}H\{^{11}B\}$ and $^{11}B\{^{1}H\}$ spectra of free $[B_{20}H_{18}]^{2-}$ in Figure 27 and S5, respectively. This demonstrates weak interactions of the α-CD with the cluster.

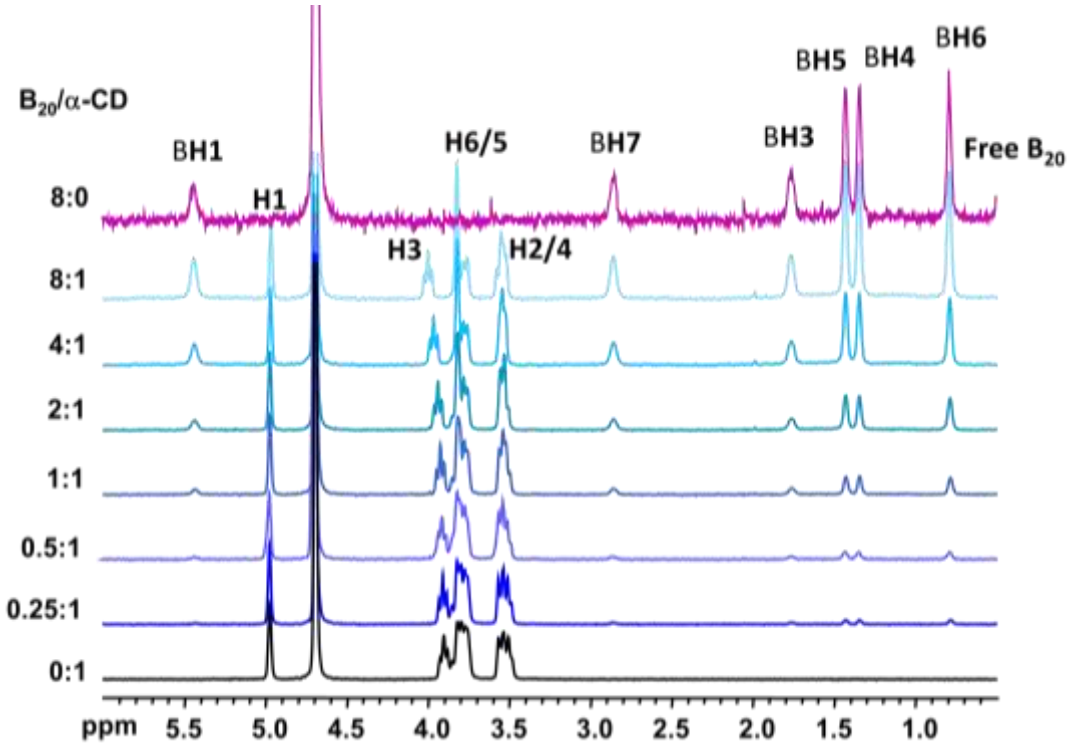

*Figure 27. $^{1}H\{^{11}B\}$ NMR spectra in D_2O for different ratios of **$B_{20}H_{18}$/α-CD** from the titration of 3 mM aqueous α-CD solution with $Li_2[B_{20}H_{18}]$.*

Job's plot represents the product of the molar fraction in α-CD ($x_{\alpha\text{-CD}}$) and the chemical shift variation of H3 ($\Delta\delta = \delta_{obs} - \delta_{H3}$) versus $x_{\alpha\text{-CD}}$ under boron cluster titration (Figure 28). The variation of the chemical shift of **H3** for α-CD with $[B_{20}H_{18}]^{2-}$ in D_2O permits us to see a clear maximum on the curve at $x_{\alpha\text{-CD}}$ about 0.5, consistent with the formation of 1:1 adduct, $\{(B_{20}H_{18})(\alpha\text{-CD})\}^{2-}$. This adduct does not necessarily represent an inclusion complex, as the effect on the host NMR signals is too weak.

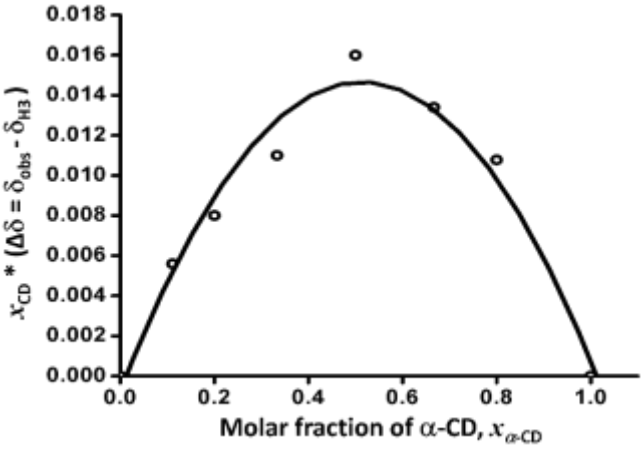

Figure 28. Job's plot for ***$[B_{20}H_{18}]^{2-}$*** *with* ***α-CD*** *in D_2O.*

To get insight of the effects on the boron side, inverse titration was carried out. The $^{1}H\{^{11}B\}$ and $^{11}B\{^{1}H\}$ NMR spectra of various **{$[B_{20}H_{18}]^{2-}$ (3 mM) + α-CD}** solutions are given in Figures S6 (in the appendix), 29, and 30. Increasing the amount of α-CD added while keeping $[B_{20}H_{18}]^{2-}$ concentration constant induces a slight upfield shifts of the B**H1** and B**H6** protons with a maximum variation of only **-0.05 ppm** relative to the free B_{20} anion, while no significant shift was observed with the other BH protons (Figure 29). At the same time, the $^{11}B\{^{1}H\}$ NMR spectra show a broadening of all B_{20} signals (Figure 30). Such a broadening should be an indication of some inter-species interaction between the boron cluster and the CD, restricting the molecular tumbling of the anionic species. The variations of the chemical shifts of (B**H**) protons and boron atoms (B1-B7) are collected in Tables S5 and S6 in the appendix, respectively.

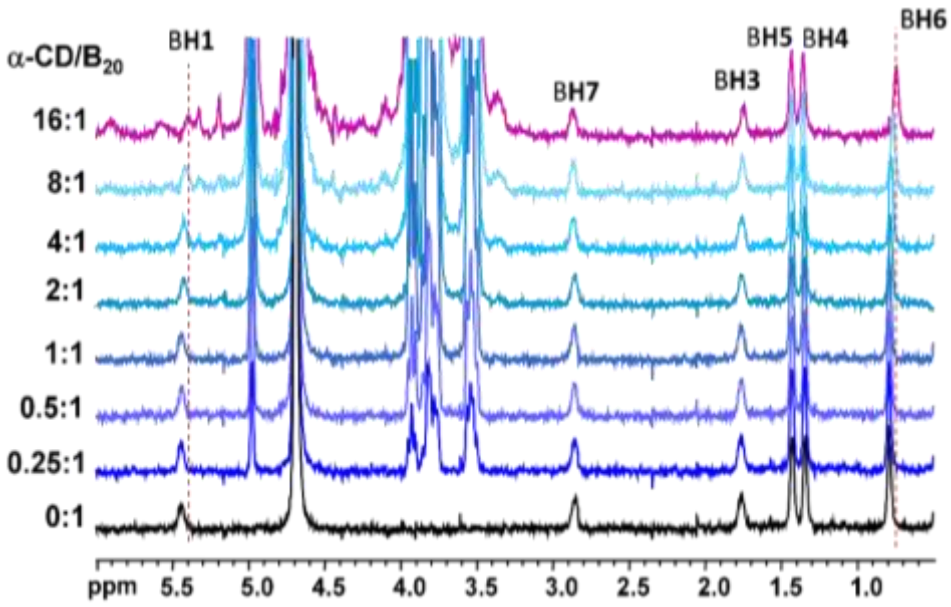

Figure 29. $^{1}H\{^{11}B\}$ NMR spectra in D_2O for different ratios of ***α-CD/$B_{20}H_{18}$*** *from the titration of 3 mM aqueous $Li_2[B_{20}H_{18}]$ with α-CD solution, focusing on B**H** protons.*

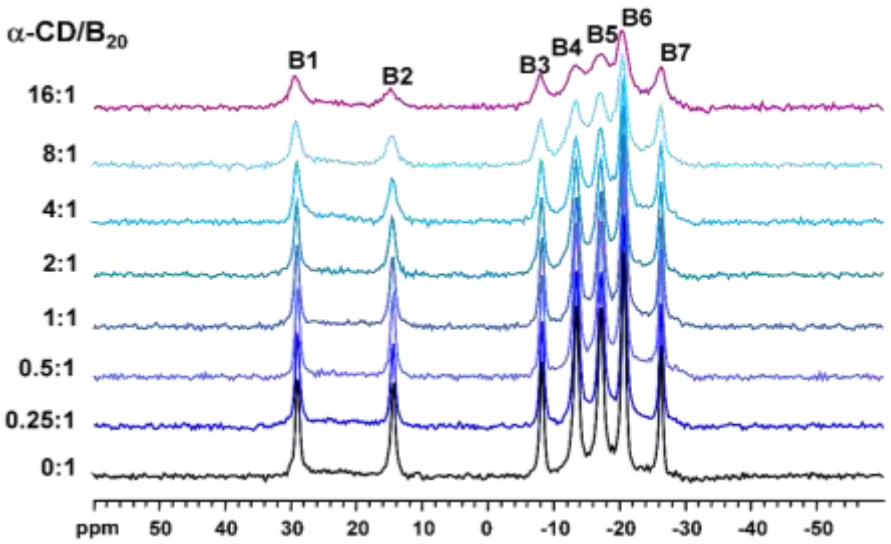

*Figure 30. $^{11}B\{^1H\}$ NMR spectra in D_2O for different ratios of **α-CD/$B_{20}H_{18}$** from the titration of 3 mM aqueous $Li_2[B_{20}H_{18}]$ with α-CD solution.*

III.3.1.2 Interaction between β-CD and $Li_2[B_{20}H_{18}]$ in D_2O

The $^1H\{^{11}B\}$ and $^{11}B\{^1H\}$ NMR spectra of various **{β-CD (C = 3mM) + $[B_{20}H_{18}]^{2-}$}** solutions are given in Figures 31, S7, and S8. Increasing $[B_{20}H_{18}]^{2-}$/β-CD ratio provokes a split of the two **H6** protons signal beside strong downfield shifts of the **H3** and **H5** peaks of the CD, up to **+0.224** and **+0.427 ppm**, respectively (Figure 31), while the other protons are much less affected, compared to free β-CD. The variations of the chemical shifts of β-CD protons are given in Table S7 in the appendix.

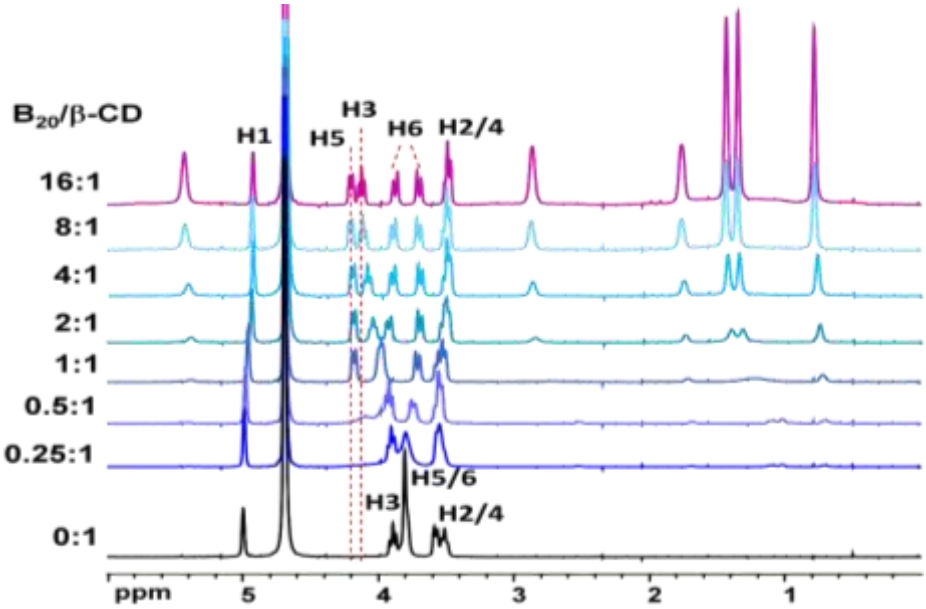

*Figure 31. $^1H\{^{11}B\}$ NMR spectra in D_2O for different ratios of **$B_{20}H_{18}$/β-CD** from the titration of 3 mM aqueous β-CD solution with $Li_2[B_{20}H_{18}]$.*

Concomitantly, in comparison with the spectra of free B_{20} anion, the B**H4**, B**H5**, and B**H7**, located far from the apices, are strongly downfield shifted by **+0.33, +0.40**, and **+0.36 ppm**, respectively (Figure S7 in the appendix). On the boron side, all boron signals show prominent broadening (Figure S8 in the appendix). This suggests deep inclusion of $[B_{20}H_{18}]^{2-}$ within the cavity of β-CD. The variations of the chemical shifts of (B**H**) protons and boron atoms(B1-B7) for various $B_{20}H_{18}$/β-CD mixtures are collected in Tables S8 and S9 in the appendix, respectively.

Job's plot represents the product of the molar fraction in β-CD ($x_{\beta\text{-CD}}$) and chemical shift variation of H5 ($\Delta\delta = \delta_{obs} - \delta_{H5}$) versus $x_{\beta\text{-CD}}$ under boron cluster titration (Figure 32). The variation of the chemical shift of **H5** for β-CD with $[B_{20}H_{18}]^{2-}$ in D_2O permits us to see a clear maximum on the curve at $x_{\beta\text{-CD}}$ about 0.5, consistent with the formation of 1:1 adduct, $\{(B_{20}H_{18})(\beta\text{-CD})\}^{2-}$.

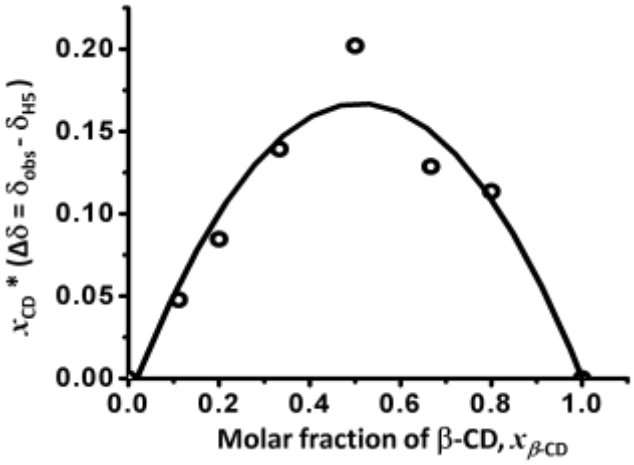

Figure 32. Job's plot for ***$[B_{20}H_{18}]^{2-}$*** *with* ***β-CD*** *in D_2O.*

The $^1H\{^{11}B\}$ and $^{11}B\{^1H\}$ NMR spectra of various **$\{[B_{20}H_{18}]^{2-}$ (C = 3mM) + β-CD}** solutions are given in Figures S9, 33, and 34. Increasing the amount of β-CD while keeping the concentration of B_{20} constant has the same effect on β-CD chemical shifts as the previous experiments of {β-CD (C = 3 mM) + $[B_{20}H_{18}]^{2-}$}, such as the chemical shifts of **H3** and **H5** are respectively shifted by **-0.194** and **-0.419 ppm**, while other protons are much less affected. Also, the two peaks (dd) of the **H6** protons overlap into a broad, intense signal (Figure S9). The variations of the chemical shifts of β-CD protons are given in Table S10 in the appendix.

In comparison with the spectra of free B_{20} anion, the B**H** groups have an important upfield shift of B**H4**, B**H5**, and B**H7** by **-0.32**, **-0.34**, and **-0.35 ppm**, respectively (Figure 33). Concerning Boron signals, $^{11}B\{^1H\}$ NMR spectra show strong broadening of all B_{20} signals (Figure 34), which is clearly much more pronounced than the previous broadening observed with α-CD. We can then confirm here the efficient inclusion between β-CD and $[B_{20}H_{18}]^{2-}$. The variations of the chemical (B**H**) protons and boron atoms (B1-B7) in various β-CD/$[B_{20}H_{18}]^{2-}$ mixtures are given in Tables S11 and S12 in the appendix.

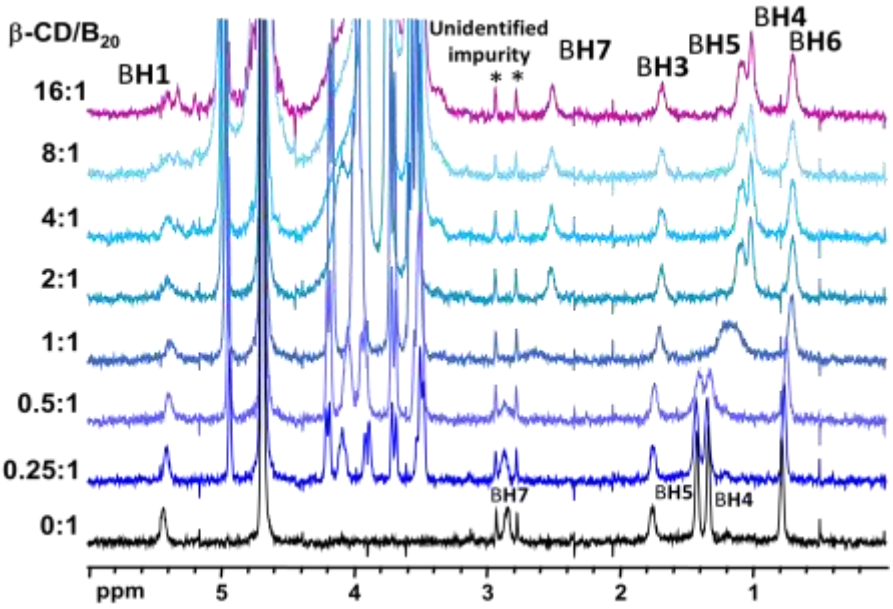

Figure 33. $^{1}H\{^{11}B\}$ NMR spectra in D_2O for different ratios of ***β-CD/$B_{20}H_{18}$*** *from the titration of 3 mM aqueous $Li_2[B_{20}H_{18}]$ with β-CD solution, focusing on B**H** protons.*

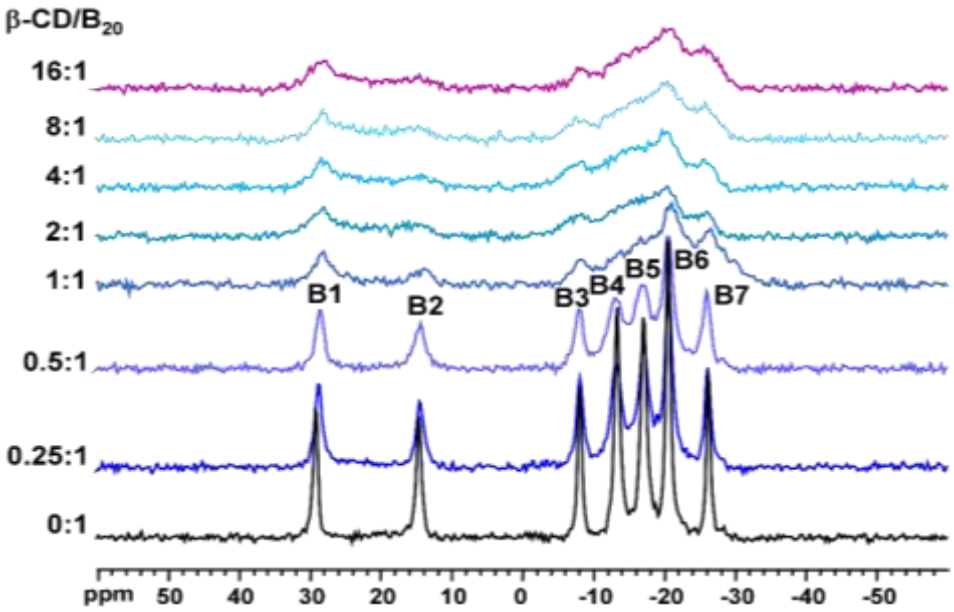

Figure 34. $^{11}B\{^{1}H\}$ NMR spectra in D_2O for different ratios of ***β-CD/$B_{20}H_{18}$*** *from the titration of 3 mM aqueous $Li_2[B_{20}H_{18}]$ with β-CD solution.*

III.3.1.3 Interaction between γ-CD and $Li_2[B_{20}H_{18}]$ in D_2O

The $^{1}H\{^{11}B\}$ and $^{11}B\{^{1}H\}$ NMR spectra of various **{γ-CD (3 mM) + $[B_{20}H_{18}]^{2-}$}** solutions are given in Figures 35, S10 and S11. Increasing $[B_{20}H_{18}]^{2-}$/γ-CD ratio provokes a split of the two **H6** protons signal beside strong downfield shifts of the **H3** and **H5** peaks of the CD, up to **+0.071** and **+0.145** ppm, respectively, while the other protons are much less affected (Figure 35).

These variations are bigger than those observed with α-CD (maximum +0.1 ppm, Figure 27), but smaller than those observed with β-CD (maximum + 0.4 ppm, Figure 31). The variations of the chemical shifts of γ-CD protons in various $[B_{20}H_{18}]^{2-}$/γ-CD mixtures are given in Table S13 in the appendix.

At the same time, in comparison with the spectra of free B_{20} anion, all B**H** groups signals have shown slight downfield shift variations of ca. +0.1 ppm (Figure S10 in the appendix), which is also smaller than those observed with β-CD (maximum +0.4 ppm, Figure S7 in the appendix).On the other hand, the signals of the Boron atoms **B1**, **B3** and **B7** show major chemical shift variations of **+1.03**, **+0.5**, and **-0.6** ppm; respectively, , as seen in Figure S11 in the appendix. The variations of the chemical shifts of (B**H**) protons and boron atoms(B1-B7) for various $B_{20}H_{18}$/γ-CD mixtures are collected in Tables S14 and S15 in the appendix, respectively.

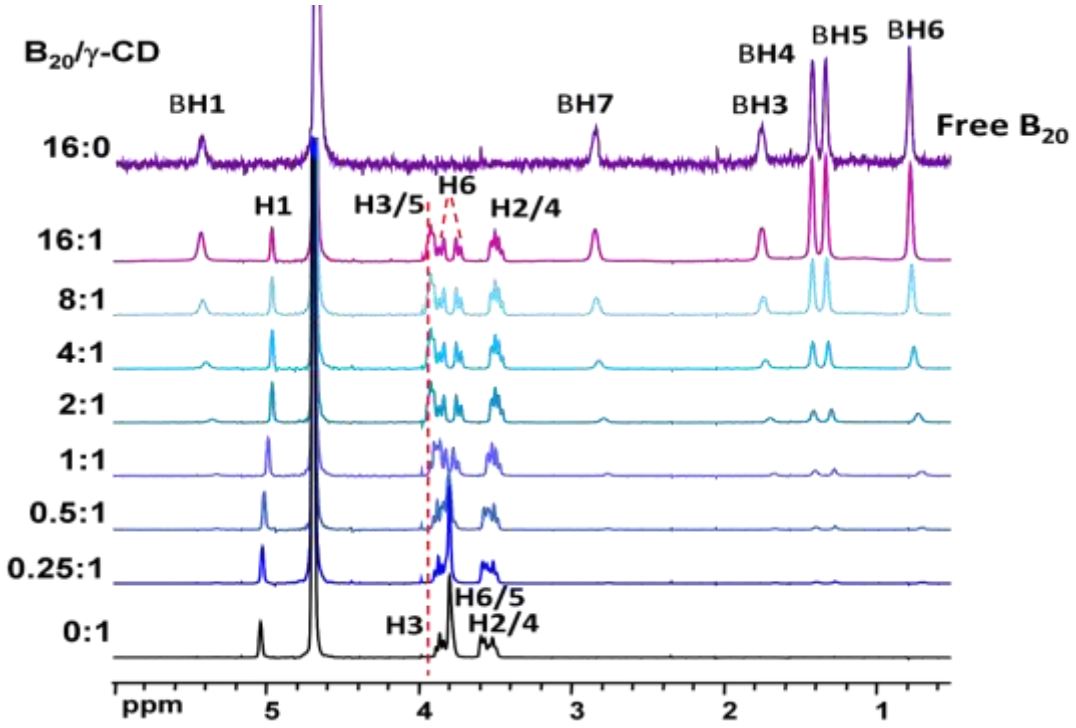

*Figure 35. $^{1}H\{^{11}B\}$ NMR spectra in D_2O for different ratios of **$B_{20}H_{18}$/γ-CD** from the titration of 3 mM aqueous γ-CD solution with $Li_2[B_{20}H_{18}]$.*

Job's plot in Figure 36 focused on the variation of the chemical shift of **H5** for γ-CD with $[B_{20}H_{18}]^{2-}$ in D_2O, permits us to see a clear maximum on the curve at x_{CD} about 0.5, consistent with the formation of 1:1 adduct, $\{(B_{20}H_{18})(\gamma\text{-CD})\}^{2-}$.

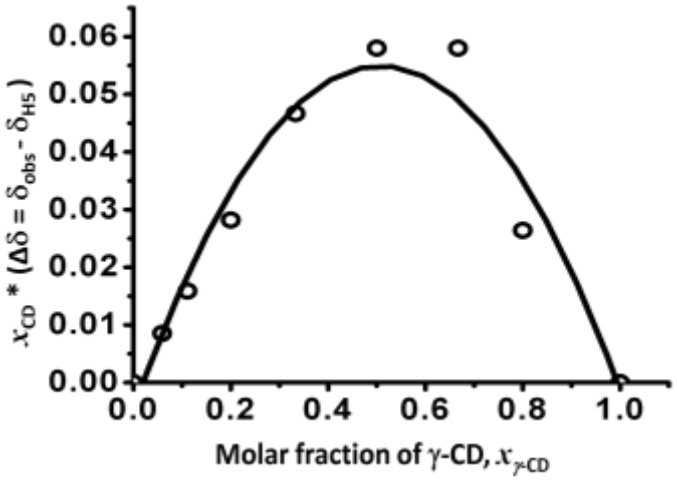

Figure 36. Job's plot for ***$[B_{20}H_{18}]^{2-}$*** *with* ***γ-CD*** *in D_2O.*

The $^{1}H\{^{11}B\}$ and $^{11}B\{^{1}H\}$ NMR spectra of **{$[B_{20}H_{18}]^{2-}$ (C = 3 mM) + γ-CD}** are given in Figures S12, 37, and 38. Increasing the amount of γ-CD provokes upfield shifts of the **H3** and **H5** protons by **-0.065** and **-0.139**, respectively, while other protons are much less affected. Also, the two peaks (dd) of the **H6** proton overlap into a broad, intense signal (Figure S12). The variations of the chemical shifts of γ-CD protons are given in Table S16 in the appendix.

The BH groups have an important upfield shift majorly of the B**H3**, and B**H7** groups by **-0.17** ppm (Figure 37). These variations are between those observed for α-CD (maximum variation of -0.05 ppm, Figure 29) and β-CD (maximum variation of -0.35 ppm, Figure 33). Concerning Boron signals, the B1 and B7 groups are mostly affected since they are shifted by **-1.43** and **+0.6** ppm, respectively (Figure 38). These strong variations may indicate efficient inclusion between γ-CD and $[B_{20}H_{18}]^{2-}$ but most probably different from the one observed with β-CD since the ^{11}B line broadening is also different and less extensive than that resulting with β-CD (Figure 34).The variations of the chemical shifts (B**H**) protons and boron atoms (B1-B7) in various γ-CD/$[B_{20}H_{18}]^{2-}$ mixtures are given in Tables S17 and S18 in the appendix, respectively.

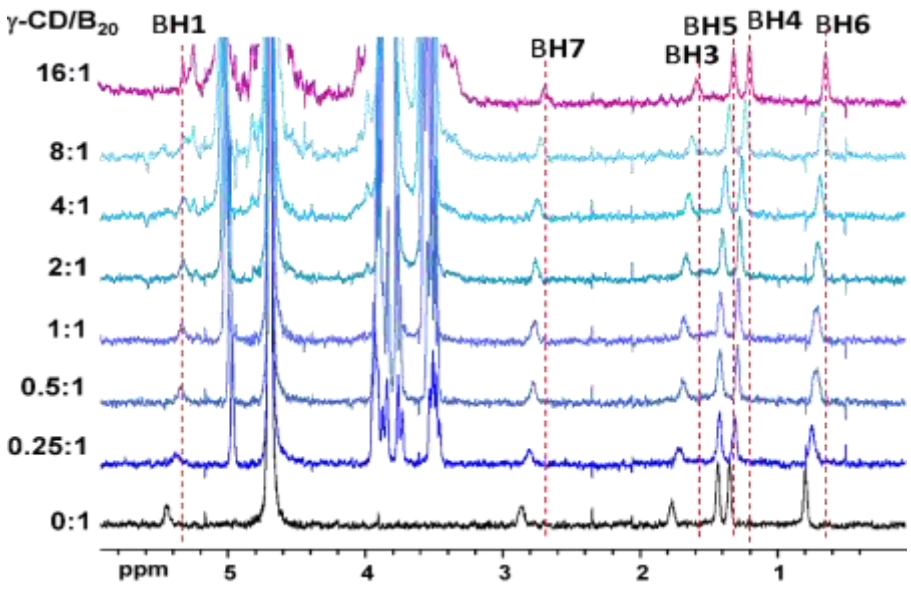

Figure 37. $^{1}H\{^{11}B\}$ NMR spectra in D_2O for different ratios of ***γ-CD/$B_{20}H_{18}$*** *from the titration of 3 mM aqueous $Li_2[B_{20}H_{18}]$ with γ-CD solution, focusing on B**H** protons.*

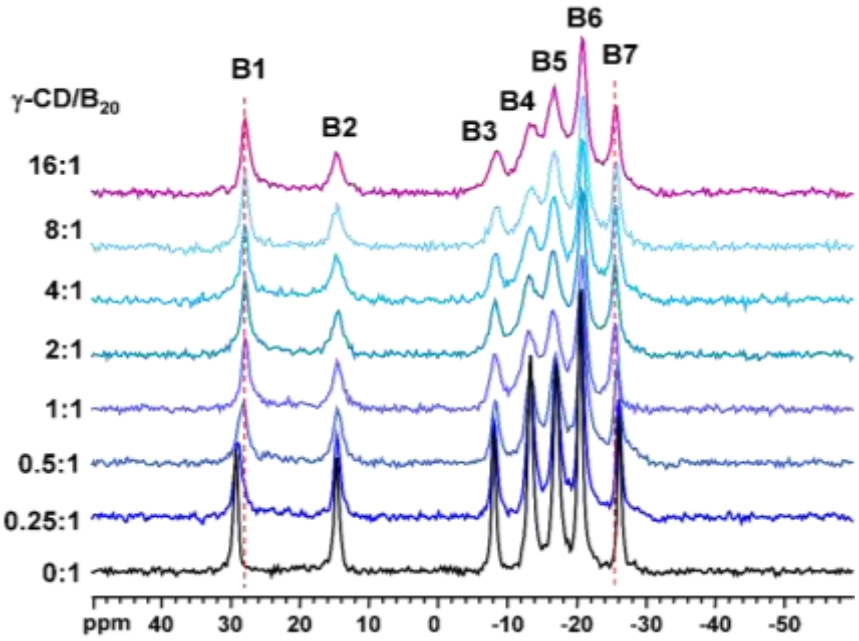

Figure 38. $^{11}B\{^{1}H\}$ NMR spectra in D_2O for different ratios of ***γ-CD/$B_{20}H_{18}$*** *from the titration of 3 mM aqueous $Li_2[B_{20}H_{18}]$ with γ-CD solution.*

III.3.2 Determination of association constants by nonlinear least-squares method

NMR titration experiments with fixing the initial concentration of CD (C^0) and varying the molar ratio R = $[B_{20}H_{18}]^{2-}$/[CD] allows us to estimate the association constants between CDs and $[B_{20}H_{18}]^{2-}$ by the nonlinear least-squares method using equation 3 as applied previously to $[B_{10}H_9NCCH_3]^-$ (see section II.3.6). The chemical shifts of the free CD and the 1:1 adducts,

noted δ_0 and $\delta_{1:1}$, respectively, are used as input constants. Modeling the experimental data leads to the binding constants gathered in Table 4. The best fits of the variation of the experimental chemical shift δ_{obs} as a function of the ratio *R* = B_{20}/CD according to the equation 3 using these *K* values are shown in Figure 39. The simulated variation of δ_{obs} of H3 protons for α-CD and H5 for β- and γ-CDs matches well the experimental data.

Table 4. Formation constant K (M^{-1}) of the 1:1 adduct complexes formed between $[B_{20}H_{18}]^{2-}$ and native cyclodextrins (α-, β-, and γ-CD), obtained from ^1H chemical shifts at 298 K (equation 3) in comparison with $[B_{10}H_9NCCH_3]^-$.

B Compound	CD	K (M^{-1})
$Li_2[B_{20}H_{18}]$	α-CD	37 ± 0.4
	β-CD	100000 ± 40000
	γ-CD	4000 ± 2000
$(Et_3NH)[B_{10}H_9NCCH_3]$	α-CD	45 ± 11
	β-CD	149 ± 4
	γ-CD	577 ± 8

The association constants found by NMR for binding of $[B_{20}H_{18}]^{2-}$ cluster were 37 M^{-1} with α-CD, ca. 100000 M^{-1} with β-CD and 4000 M^{-1} with γ-CD. Hence, as expected, the affinity constants have enhanced greatly with large CDs compared to $[B_{10}H_{10}]^{2-}$ and $[B_{10}H_9NCCH_3]^-$ clusters since $[B_{20}H_{18}]^{2-}$ has lower charge density which would enhance its chaotropic effect. However, with the smallest α-CD the affinity constant remained weak as for the case of $[B_{10}H_9NCCH_3]^-$, because this cavitant molecule is too small to encapsulate the boron cluster. The optimal affinity was found with the β-CD, probably because it matches well the size of the cluster.

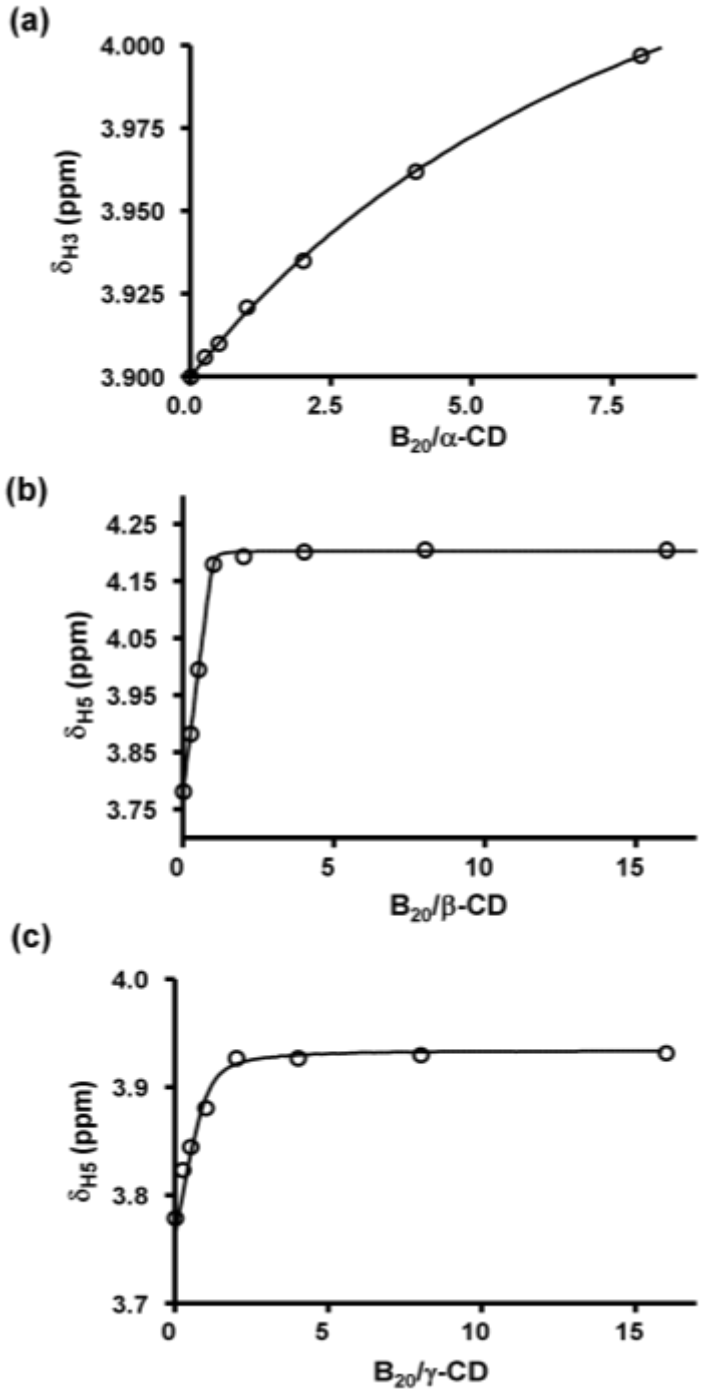

Figure 39. The variations of the observed chemical shift of ***(a)*** *α-CD-H3,* ***(b)*** *β-CD-H5, and* ***(c)*** *γ-CD-H5 internal protons versus* $[B_{20}H_{18}]^{2-}$ *content.*

III.3.3 Association constants and thermodynamic data by ITC

Isothermal calorimetric titration (ITC) was also used to determine the binding affinities, , the enthalpy (ΔH) and the entropy (ΔS) of the reactions of systems $[B_{20}H_{18}]^{2-}$/α-,β-, and γ-CD solutions. The corresponding ITC parameters are given in Table 5.

As expected, the inclusion of $[B_{20}H_{18}]^{2-}$ in α-, β-, and γ-CD was characterized by a strong enthalpic stabilization. Thus, the process of encapsulation of the $[B_{20}H_{18}]^{2-}$ cluster is enthalpically driven, leading to a dramatic increase in binding affinities, particularly with β- and γ-CD, probably due to adequate size match fit.

On the other hand, entropy variations are negative for α- and β-CD, indicating that the inclusion process of the $[B_{20}H_{18}]^{2-}$ cluster within cyclodextrins is associated to a chaotropic effect [18]. This is due to the recovery of the solvation water structure when the chaotropes migrate into CD pockets distorting its solvation shell, which represent an energy-intensive process. The binding constants obtained by ITC showed increasing values with increasing CD size. While the orders of magnitude recorded for 1:1 complexes of $[B_{20}H_{18}]^{2-}$ with α- or β-CD, are in agreement with the values obtained from NMR titrations, different result is observed with the largest γ-CD. ITC revealed not only a very strong association with this CD, but also a higher stoichiometry, i.e., $1CD:2B_{20}$ clusters. This latter observation could explain the discrepancies between the NMR and ITC data, as NMR analysis is based on the simple 1:1 binding mode. Hence, to obtain more information, ESI-MS measurements are in progress to investigate the stoichiometry of B_{20}@γ-CD complexes, while DFT calculations in collaboration with Dr. Xavier Lopez in Spain are also underway. Finally, new ITC measurements using the competitive titrations method are needed to clarify these data.

Table 5. Binding constants, enthalpy, entropy, and Gibbs energy of adduct complexes formation between ***$Li_2[B_{20}H_{18}]$*** *and native cyclodextrins (****α-, β-*** *and* ***γ-CD****), obtained from ITC data, at 298 K.*

		K	ΔH (kJ.mol^{-1})	TΔS (kJ.mol^{-1})	ΔG (kJ.mol^{-1})
	α-CD	35 ± 7 M^{-1}	-43.5 ± 6.4	-34.7 ± 6.9	-8.8 ± 0.5
$Li_2[B_{20}H_{18}]$	**β-CD**	137414 ± 3570 M^{-1}	-60.3 ± 0.3	-31 ± 0.3	-29.3 ± 0.1
	γ-CD	$3.33x10^{10} \pm 0.795x10^{10}$ M^{-2}	-54.0 ± 0.4	6 ± 1	-60 ± 0.6

III.4 Effect of CD interaction with $[B_{20}H_{18}]^{2-}$ cluster on its proton-deuterium exchange process

The proton-deuterium (H/D) exchange process has already been reported for various polyhedral boranes such as carborane ($CB_{11}H_{12}$, CB_9H_{10}), $[B_{12}H_{12}]^{2-}$, and $[B_{10}H_{10}]^{2-}$ anions in deuterated solvents. Regarding $[B_{10}H_{10}]^{2-}$, the precursor of our compound of interest $[B_{20}H_{18}]^{2-}$, several papers have focused on understanding the mechanism, rate, and regioselectivity of the proton-deuterium (H/D) exchange process to get more insight into dihydrogen contact between B-H….HX (N, O) [38–40].

To our knowledge, no reports have been recorded by now for H/D exchanges with $[B_{20}H_{18}]^{2-}$. Therefore, we decided to study the behavior of the latter in D_2O solution over a period of time by $^1H\{^{11}B\}$,$^{11}B\{^1H\}$, and ^{11}B NMR experiments.

III.4.1 Proton-Deuterium exchange in $[B_{20}H_{18}]^{2-}$

III.4.1.1 NMR studies

The $^1H\{^{11}B\}$ NMR spectrum of freshly prepared $[B_{20}H_{18}]^{2-}$ solution in D_2O has been repeated in two different periods: twenty days and five months later (Figure 40).

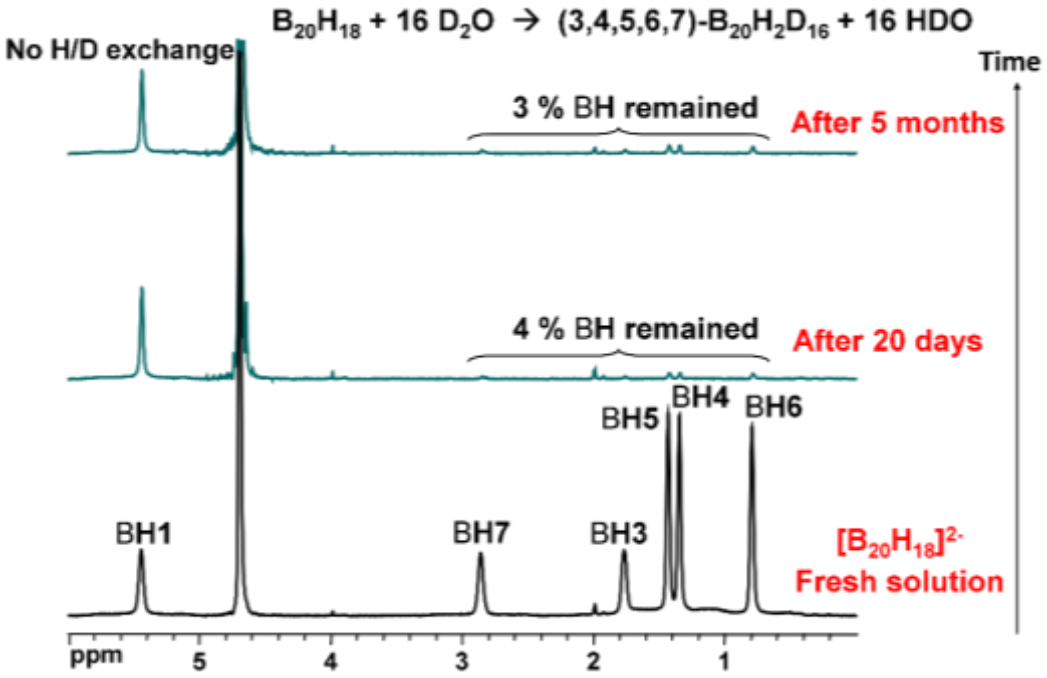

*Figure 40. $^1H\{^{11}B\}$ NMR spectra of **$Li_2[B_{20}H_{18}]$** in D_2O solution, in freshly prepared solution, after twenty days and after five months.*

Comparison between the three spectra reveals an important decrease in the intensities or almost disappearance of B**H** protons by 96 and 97 % after 20 days and five months, respectively. Remarkably, no change in the B**H1** protons has been detected over time. This suggests that the BH protons at the position (3-7) are exchanged with deuterium except for the B**H1** protons, as seen in Figure 41.

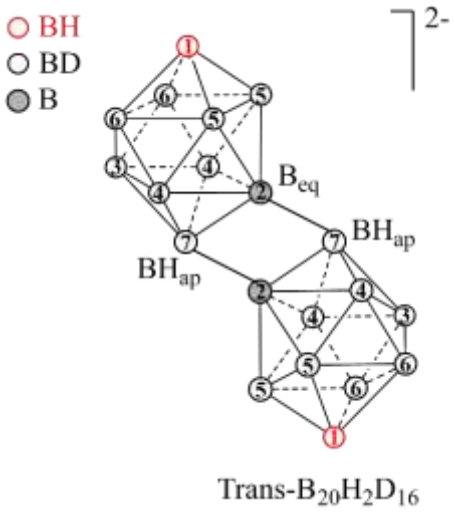

Figure 41. Structure of ***[3,4,5,6,7-$B_{20}H_2D_{16}$]$^{2-}$***.

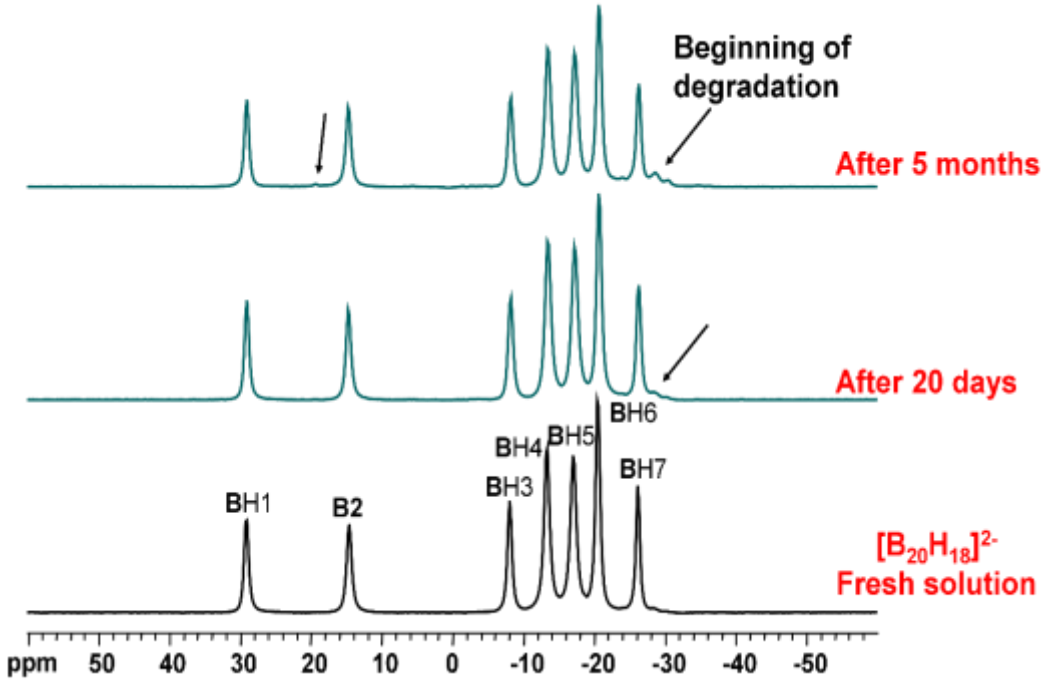

Figure 42. ^{11}B NMR spectra of ***$Li_2[B_{20}H_{18}]$*** *in D_2O solution, in freshly prepared solution, after twenty days and after five months.*

On the boron side, $^{11}B\{^1H\}$ NMR spectra recorded over time (Figure 42) reveal the appearance of a few new peaks near 21 ppm and the range between -29 and -31 ppm, which evidence the beginning of degradation of $[B_{20}H_{18}]^{2-}$. Noteworthy, H/D exchange can't be detected from $^{11}B\{^1H\}$ NMR alone since all peaks appear as singlets. Interestingly, boron atoms in **B**-D and **B**-H groups could be easily distinguished through comparison between ^{11}B NMR (^{11}B nuclei coupled with ^1H nuclei) and NMR $^{11}B\{^1H\}$ (^{11}B nuclei decoupled from ^1H nuclei).

As seen in Figure 43, there is a splitting of BH singlets in the $^{11}B\{^1H\}$ NMR spectrum of $[B_{20}H_{18}]^{2-}$ fresh solution into doublets in the ^{11}B due to the presence of J_{BH} coupling, which means no H/D exchange in $[B_{20}H_{18}]^{2-}$ fresh solution, in agreement with $^1H\{^{11}B\}$ NMR (Figure 40). However, there was no splitting of **B**H signals after twenty days, regardless of the experiment's proton coupling condition, except for the signal of the Boron atom in position (1). This is because J_{BH} is equal to zero due to the replacement of B**H** protons at the positions (3,4,5,6,7) with deuterium nuclei (Figure 40).

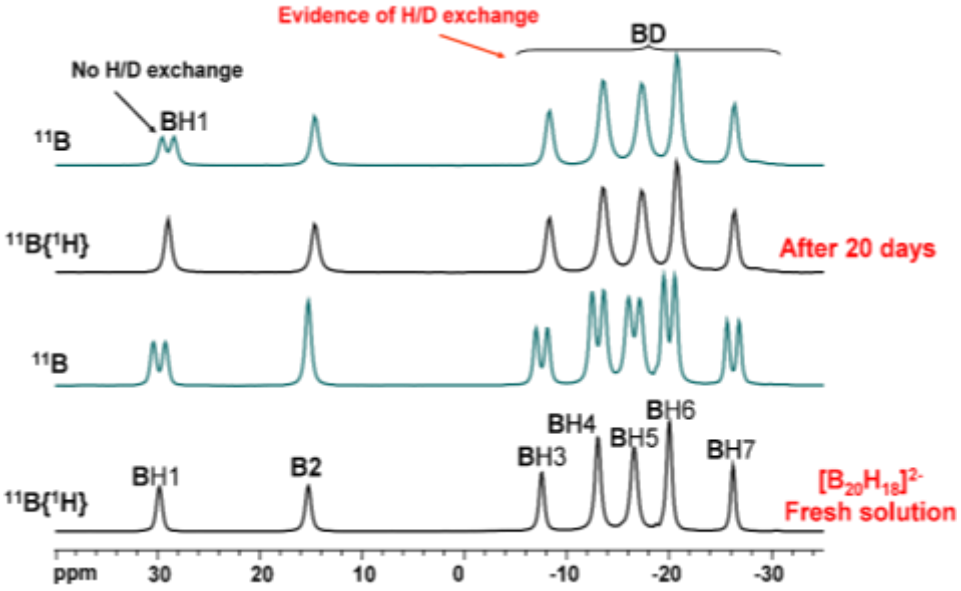

*Figure 43. ^{11}B and $^{11}B\{^1H\}$ NMR spectra of **$Li_2[B_{20}H_{18}]$** solution in D_2O, recorded just after preparation, and after twenty days.*

We can conclude from ^1H and ^{11}B NMR studies that $[B_{20}H_{18}]^{2-}$ compound is stable in fresh D_2O solution. Over time, however, it undergoes slow H/D exchange accompanied by degradation, as shown by ^{11}B NMR spectra (Figure 42). Thus, we had to protect the B_{20} cluster from H/D exchange and degradation in the D_2O solution so its quality doesn't decline with time and can be used as long as possible.

III.4.2 Proton-Deuterium exchange in solutions of $[B_{20}H_{18}]^{2-}$ with CD

On the other hand, cyclodextrin interactions with guest molecules are well known to improve the guest's physiochemical properties, protecting them from degradation, oxidation, or deterioration. Accordingly, the complexation of $[B_{20}H_{18}]^{2-}$ with cyclodextrin could protect the boron cluster from H/D exchange and, consequently, from degradation through time. Therefore, we repeated the $^1H\{^{11}B\}$ and $^{11}B\{^1H\}$ NMR experiments for solutions of $[B_{20}H_{18}]^{2-}$ with α, β and γ-CD after four months to see the effect of cyclodextrin in the H/D exchange and the stability of $[B_{20}H_{18}]^{2-}$. It should be noted that $\{^{11}B\}$ and $^{11}B\{^1H\}$ NMR experiments for freshly prepared solutions of $[B_{20}H_{18}]^{2-}$ with α-, β- and γ-CD are already mentioned in previous section.

III.4.2.1 Proton-deuterium exchange in solutions of $[B_{20}H_{18}]^{2-}$ with α-CD

Mixing just a small amount of $[B_{20}H_{18}]^{2-}$ (0.25 eq) with α-CD didn't prevent the H/D exchange that happens over time in the B**H** (3-7) groups of $[B_{20}H_{18}]^{2-}$ in the D_2O solution. As seen in the $^{1}H\{^{11}B\}$ NMR spectra recorded after four months for $[B_{20}H_{18}]^{2-}$/α-CD mixture of the ratio 0.25 (Figure 44), there is complete H/D exchange as in the case of $[B_{20}H_{18}]^{2-}$ being alone in solution (Figure 40). Furthermore, the $^{11}B\{^{1}H\}$ NMR spectrum shows new strong peaks at -30.1 and 19 ppm, compared to $[B_{20}H_{18}]^{2-}$ fresh solution, which refers to degradation products (Figure 45).

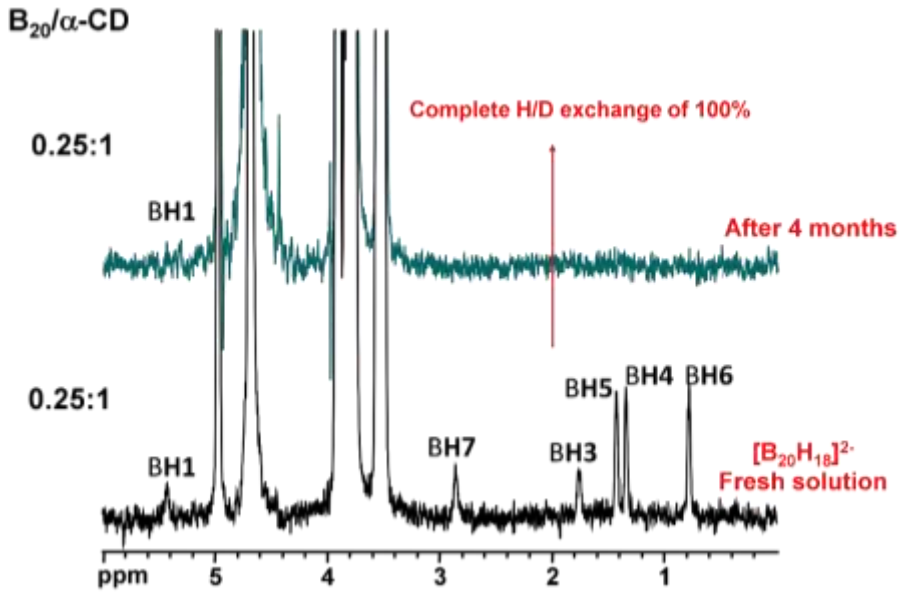

*Figure 44. $^{1}H\{^{11}B\}$ NMR spectra of **$Li_2[B_{20}H_{18}]$/α-CD (3 mM)** solution of the ratio 0.25 in D_2O solution, in the freshly prepared solution and after four months.*

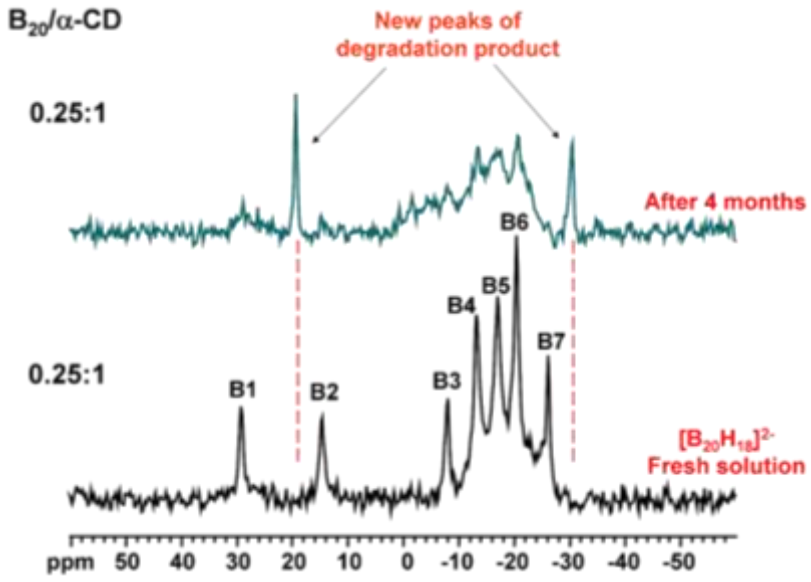

*Figure 45. $^{11}B\{^{1}H\}$ NMR spectra of **$Li_2[B_{20}H_{18}]$/α-CD (3 mM)** solution of the ratio 0.25 in D_2O solution, in freshly prepared solution and after four months.*

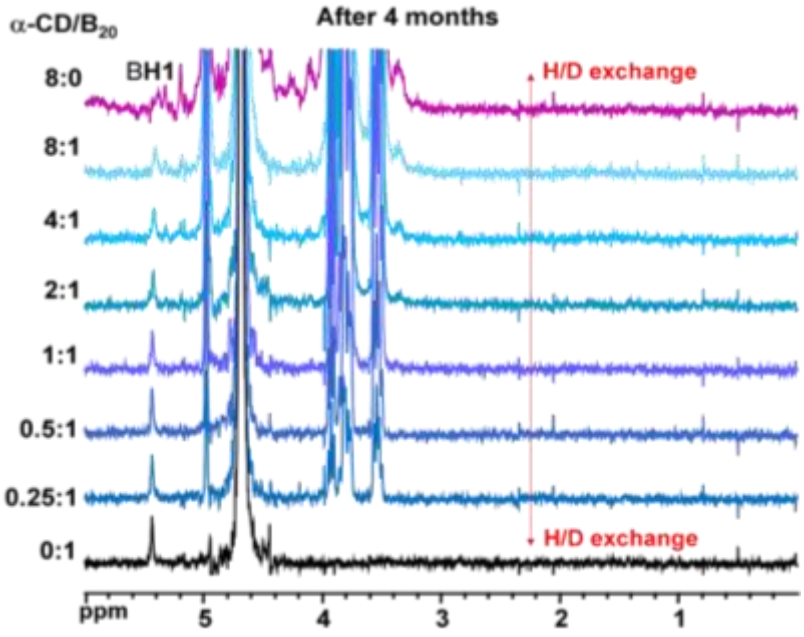

*Figure 46. $^{1}H\{^{11}B\}$ NMR spectra in D_2O for different ratios of **α-CD/$B_{20}H_{18}$** from the titration of 3 mM aqueous $Li_2[B_{20}H_{18}]$ with α-CD solution.*

Notably, there is still complete H/D exchange and degradation of $[B_{20}H_{18}]^{2-}$ despite increasing the amount of α-CD added to $[B_{20}H_{18}]^{2-}$ of fixed concentration, as revealed in the $^{1}H\{^{11}B\}$ and $^{11}B\{^{1}H\}$ NMR spectra of various α-CD/$[B_{20}H_{18}]^{2-}$ ratios measured after four months, respectively (Figures 46 and 47).

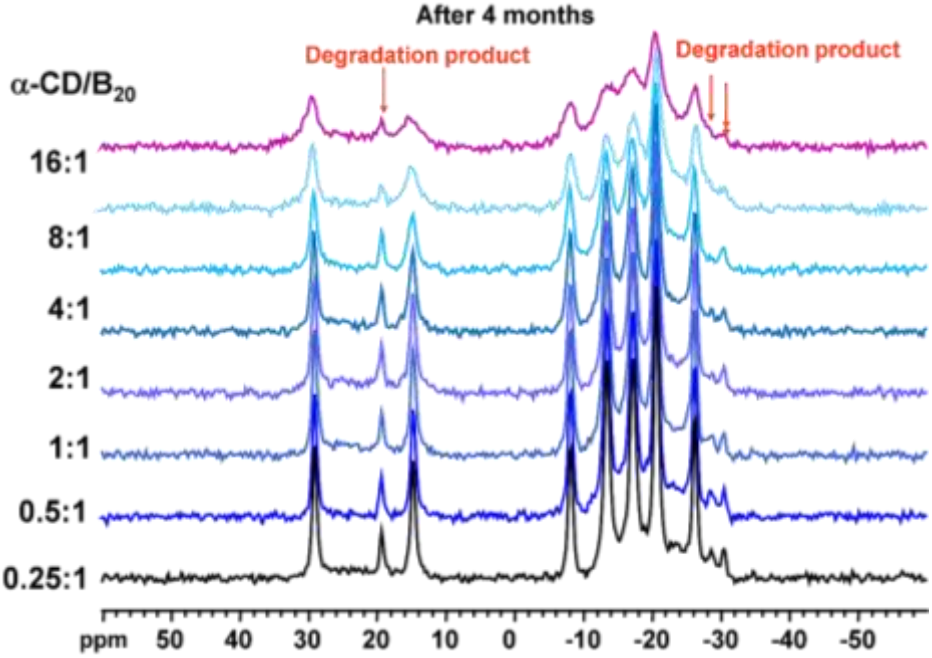

*Figure 47. $^{11}B\{^{1}H\}$ NMR spectra in D_2O for different ratios of **α-CD/$B_{20}H_{18}$** from the titration of 3 mM aqueous $Li_2[B_{20}H_{18}]$ with α-CD solution.*

III.4.2.2 Proton-deuterium exchange in solutions of $[B_{20}H_{18}]^{2-}$ with β-CD

In contrast to the ineffectiveness of α-CD on protecting the $[B_{20}H_{18}]^{2-}$ from degradation in D_2O with time, mixing 0.5 eq of $[B_{20}H_{18}]^{2-}$ with β-CD shows in the $^{1}H\{^{11}B\}$ spectra that 70% of the B**H** (3-7) protons are retained after four months compared to that of $[B_{20}H_{18}]^{2-}$ alone in solution (Figure 48), at the same time, minor new signals are detected in the $^{11}B\{^{1}H\}$ spectrum of $[B_{20}H_{18}]^{2-}$/β-CD solution of the ratio 0.5, so only slight degradation has happened with time (Figure 49).

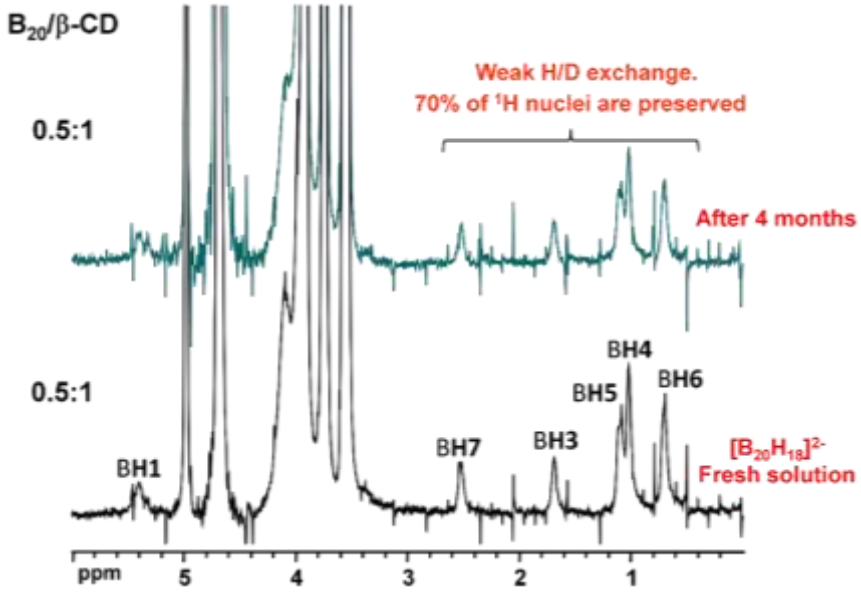

*Figure 48. $^{1}H\{^{11}B\}$ NMR spectra of **$Li_2[B_{20}H_{18}]$/β-CD (3 mM)** solution of the ratio 0.5 in D_2O solution, freshly prepared solution, and after four months.*

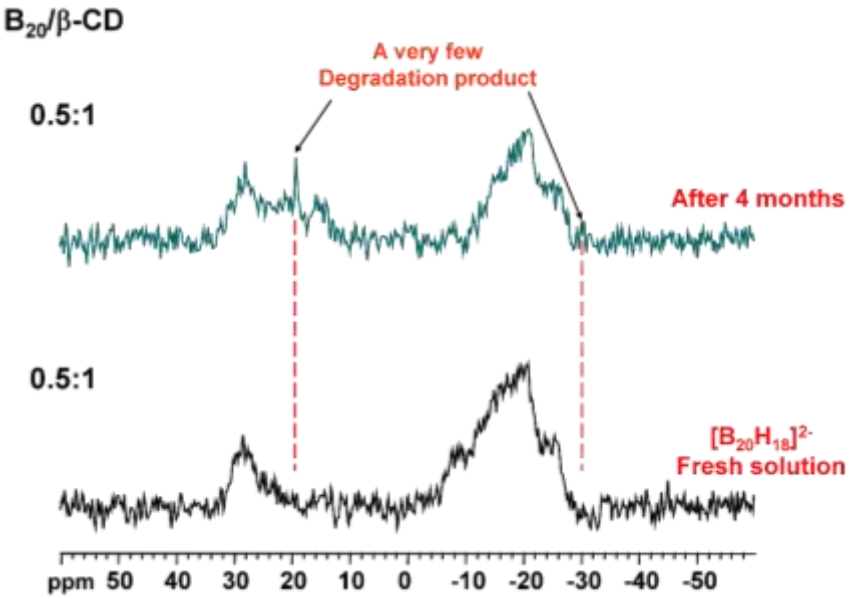

*Figure 49. $^{11}B\{^{1}H\}$ NMR spectra of **$Li_2[B_{20}H_{18}]$/β-CD (3 mM)** solution of the ratio 0.5 in D_2O solution, in freshly prepared solution and after four months.*

Fixing the concentration of $[B_{20}H_{18}]^{2-}$ while increasing the amount of β-CD shows that after four months, complete H/D exchange occurs for $[B_{20}H_{18}]^{2-}$ up to the ratio 1:1 for the β-CD/$[B_{20}H_{18}]^{2-}$mixture (Figure 50). Nevertheless, excess of β-CD sustains 90-100% of the B**H** (3-7) protons in the B_{20} cluster. Whereas the $^{11}B\{^1H\}$ spectrum reveals that degradation of the cluster takes place for β-CD/$[B_{20}H_{18}]^{2-}$ < 2 (Figure 51). Clearly, β-CD provides better protection to $[B_{20}H_{18}]^{2-}$ from H/D exchange and degradation than α-CD.

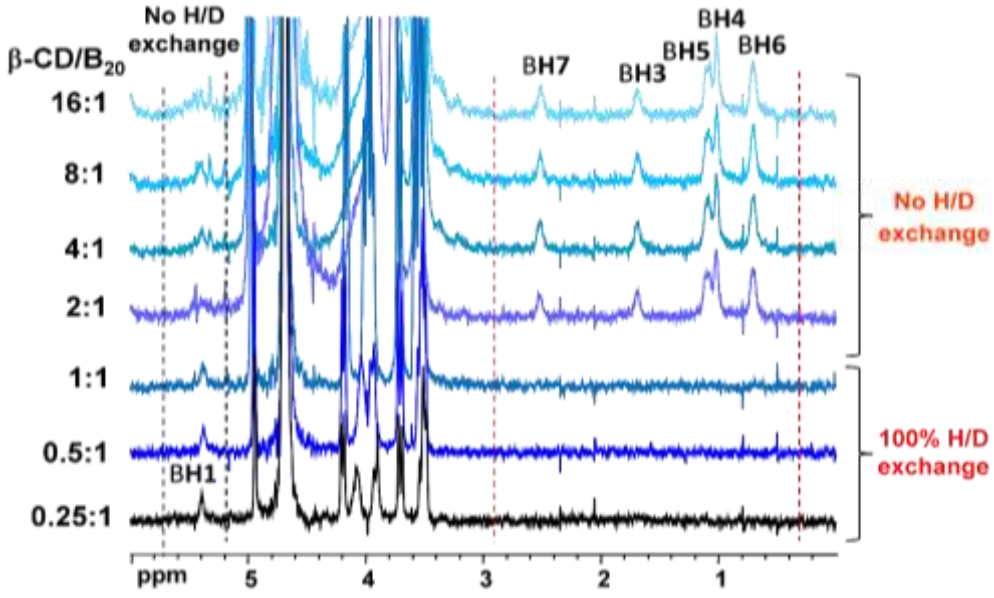

*Figure 50. $^1H\{^{11}B\}$ NMR spectra in D_2O for different ratios of **β-CD/$B_{20}H_{18}$** from the titration of 3 mM aqueous $Li_2[B_{20}H_{18}]$ with β-CD solution.*

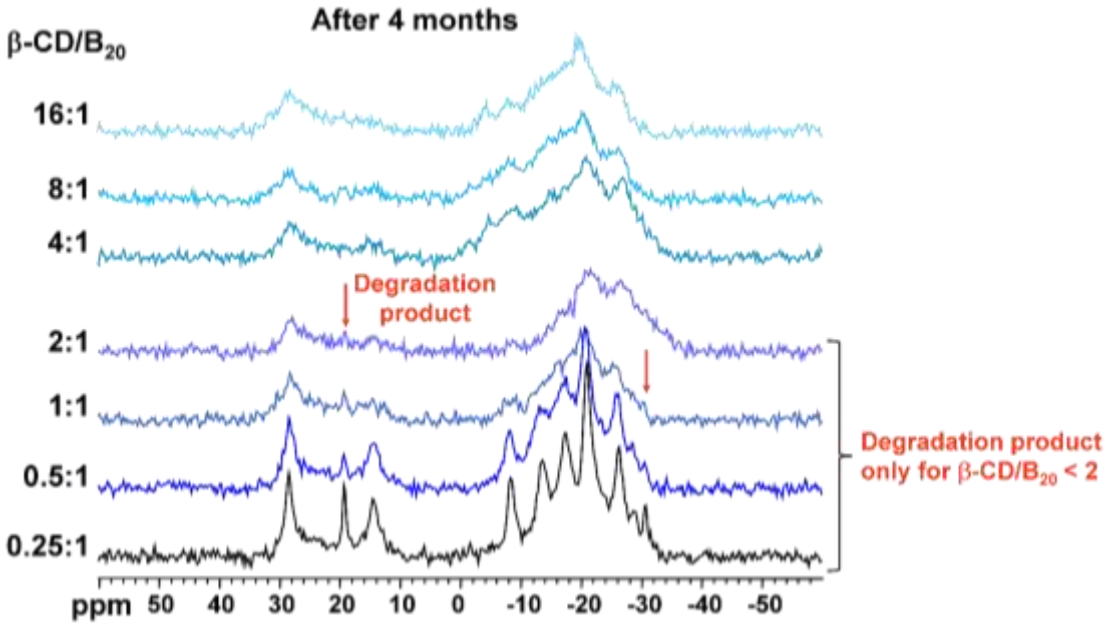

*Figure 51. $^{11}B\{^1H\}$ NMR spectra in D_2O for different ratios of **β-CD/$B_{20}H_{18}$** from the titration of 3 mM aqueous $Li_2[B_{20}H_{18}]$ with β-CD solution.*

III.4.2.3 Proton-deuterium exchange in solutions of $[B_{20}H_{18}]^{2-}$ with γ-CD

The same studying pattern has been done with γ-CD and $[B_{20}H_{18}]^{2-}$ mixture in D_2O. Mixing equivalent amounts of γ-CD and $[B_{20}H_{18}]^{2-}$ results in a partial H/D exchange of 45% in $[B_{20}H_{18}]^{2-}$ after four months (Figure 52), which is less effective in protecting the boron cluster than in the case β-CD (%H/D = 30%) (Figure 48). Subsequently, reasonable degradation is spotted through the appearance of a new peak at 18.2 ppm in the $^{11}B\{^1H\}$ spectrum of and $[B_{20}H_{18}]^{2-}$ /γ-CD mixture (Figure 53).

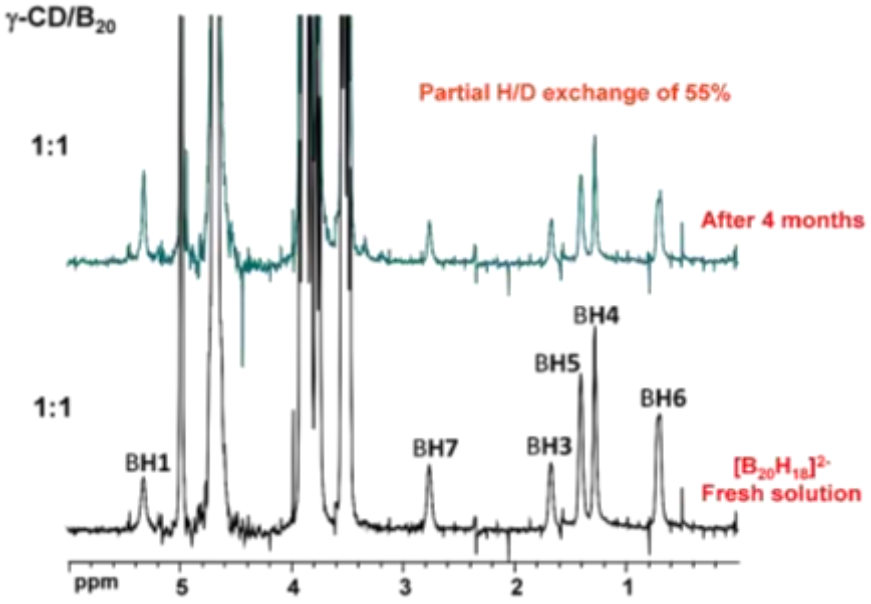

*Figure 52. $^1H\{^{11}B\}$ NMR spectra of **$Li_2[B_{20}H_{18}]^{2-}$/γ-CD (3 mM)** solution of the ratio 1 in D_2O solution, in freshly prepared solution and after four months.*

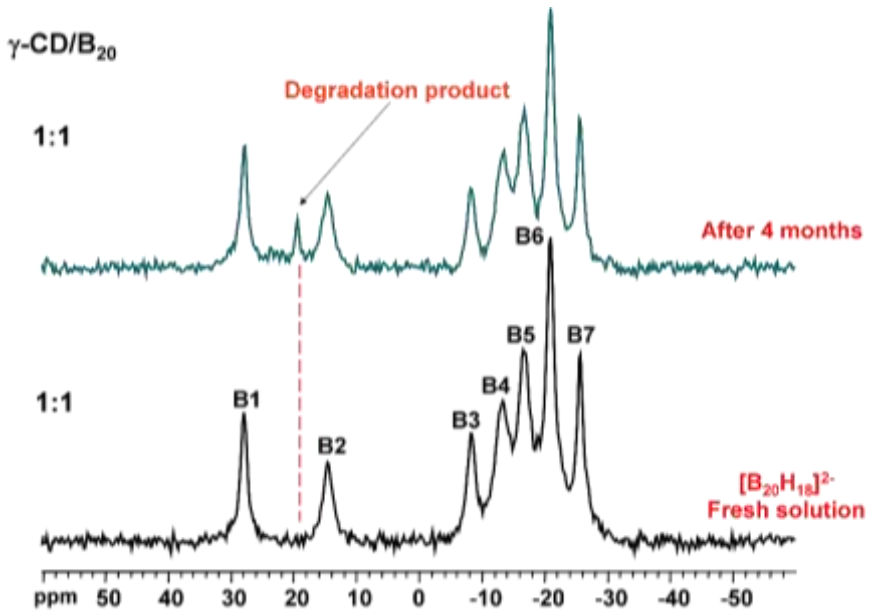

*Figure 53. $^{11}B\{^1H\}$ NMR spectra of **$Li_2[B_{20}H_{18}]^{2-}$/γ-CD (3 mM)** solution of the ratio 1 in D_2O solution, in freshly prepared solution and after four months.*

Fixing the concentration of $[B_{20}H_{18}]^{2-}$ while increasing the amount of γ-CD shows that after four months (Figure 54), complete H/D exchange occurs for $[B_{20}H_{18}]^{2-}$ up to the ratio 0.5 for the γ-CD/$[B_{20}H_{18}]^{2-}$mixture. Excess of γ-CD sustains 55-65% of the B**H** (3-7) protons in the B_{20} cluster. Concomitantly, the $^{11}B\{^1H\}$ spectrum reveals two types of new peaks related to degradation products at -30.1 and 19 ppm (Figure 55). Notably, maximum degradation occurs at the ratio γ-CD/$[B_{20}H_{18}]^{2-}$ =0.25, then decreases significantly as the ratio γ-CD amount increases.

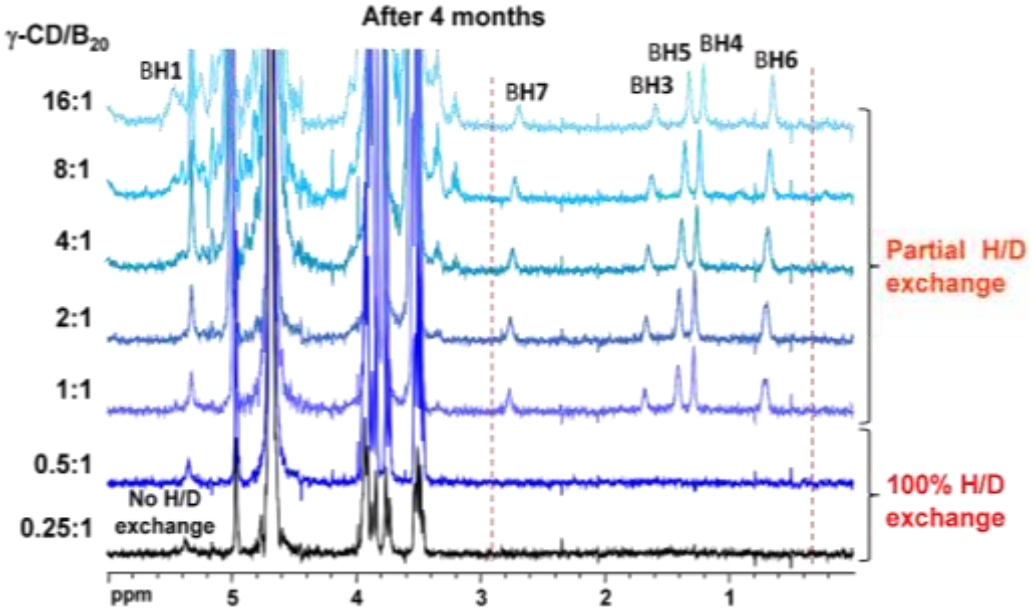

Figure 54. $^1H\{^{11}B\}$ NMR spectra in D_2O for different ratios of ***γ-CD/$B_{20}H_{18}$*** *from the titration of 3 mM aqueous $Li_2[B_{20}H_{18}]$ with γ-CD solution.*

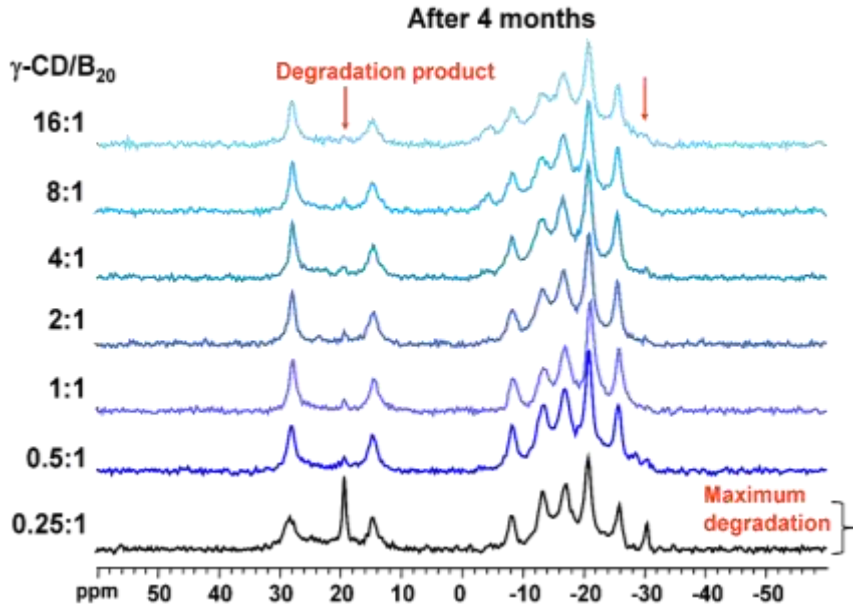

Figure 55. $^{11}B\{^1H\}$ NMR spectra in D_2O for different ratios of ***γ-CD/$B_{20}H_{18}$*** *from the titration of 3 mM aqueous $Li_2[B_{20}H_{18}]$ with γ-CD solution.*

IV. Conclusion

As a conclusion of this chapter, we reported the host-guest process involving the anionic clusters $[B_{10}H_9NCCH_3]^-$ and $[B_{20}H_{18}]^{2-}$ with α-, β- and γ-cyclodextrins.

Solution studies performed by ESI-MS, NMR, and ITC with $[B_{10}H_9NCCH_3]^-$ and the three CDs evidenced the formation of 1:1 inclusion complexes between $[B_{10}H_9NCCH_3]^-$ and β- and γ-CDs for which the association constants were determined by NMR and ITC, while weaker interactions are evidenced with α-CD. As expected, both techniques evidence a drastic enhancement of the encapsulation process of $[B_{10}H_9NCCH_3]^-$ compared to $[B_{10}H_{10}]^{2-}$, while the most stable host-guest system is obtained with γ-CD.

The ITC studies evidenced the chaotropic character of the cluster $[B_{10}H_9NCCH_3]^-$. The stability increases compared to previous studies with $[B_{10}H_{10}]^{2-}$, perfectly matches with a higher chaotropic effect expected when the charge density decreases. The less charged and more voluminous $[B_{10}H_9NCCH_3]^-$ induces a change in its solvation properties that favors adsorption onto hydrophobic cavities such as the macrocyclic CDs. Despite that, this effect of solvent alone on the encapsulation process of $[B_{10}H_9NCCH_3]^-$ could not be sufficient, and the size-matching effect between host and guest may also play an important role.

Nevertheless, this process remains moderate. In fact, even if the global charge is 1-, locally, the charge of "$B_{10}H_9$" moiety globally remains 2- while a 1+ charge is localized on the nitrogen atom of the grafted acetonitrile molecule. A stronger effect would probably be observed if the charge's delocalization occurs on the entire molecule. This work is now in progress.

On the other hand, solution studies performed by NMR and ITC with $[B_{20}H_{18}]^{2-}$ and the three CDs allowed demonstrating the formation of weak inclusion complexes with α-CD, while stronger with β-, and γ-CDs for which the association constants were determined by NMR and ITC. As expected, both techniques evidence a drastic enhancement of the encapsulation process compared to $[B_{10}H_{10}]^{2-}$ and $[B_{10}H_9NCCH_3]^-$. ITC experiments agree with this dramatic increase and affinity constants appears exceptional and comparable to those found by Nau and coworkers on B_{12} derivatives [23]. However, the model to adjust the ITC titrations seems to indicate and unexpected stoichiometry of two clusters to one γ-CDs. Such an adduct has not been evidenced by NMR. ESI-MS measurements are in progress to evidence (or not) such a species, while DFT calculation in collaboration with Dr Xavier Lopez in Spain is in progress. Finally, new ITC measurements using competitive titrations method are needed to clarify these data.

In the last part of the chapter, we studied H/D exchange process with $[B_{20}H_{18}]^{2-}$, which is to our knowledge, has never been discussed in the literature. $^1H\{^{11}B\}$ and $^{11}B\{^1H\}$ NMR studies of $[B_{20}H_{18}]^{2-}$ anion in D_2O reveal the presence of degradation and selective deuterium-proton exchange processes with the protons at equatorial positions over a period of time. Interestingly, after four months, the same NMR studies for various $[B_{20}H_{18}]^{2-}$/CD solutions in

D_2O signify the efficiency of B_{20}@CD complexes in protecting the anion from degradation and H/D exchange. Particularly, β-CD has been shown to prevent efficiently both decomposition and H/D exchange, while γ-CD reduces significantly H/D exchange but to a lesser extent decomposition. In the contrast, α-CD cannot protect the B_{20} against neither decomposition nor H/D exchange. Notably, no studies discuss the stability of boron compounds over such a long period (4-5 months). However, in this work, we succeeded in (1) investigating the encapsulation of new boron compounds ($B_{10}H_9NCCH_3^-$ and $B_{20}H_{18}^{2-}$) that have never been tested with CD, (2) maximizing their binding affinity, and (3) protecting them from degradation for a long time. These three outcomes would open the way for developing new boron derivatives presenting candidates for drug designing.

V. Experimental Part

V.1 General methods

Fourier Transform Infrared (FT-IR) spectra were recorded on a 6700 FT-IR Nicolet spectrophotometer, using the diamond ATR technique. ATR correction was applied.

Electrospray Ionization Mass Spectrometry (ESI-MS) spectra were collected using a Q-TOF instrument supplied by WATERS. Samples were solubilized in water at a concentration of 10^{-4} M and were introduced into the spectrometer via an ACQUITY UPLC WATERS system while a Leucine Enkephalin solution was co-injected via a micro pump as an internal standard.

Nuclear magnetic resonance (NMR) solution spectra were recorded at 25 °C in D_2O. ^{1}H and ^{11}B NMR were measured with a Bruker Avance 400 MHz spectrometer equipped with a 5 mm BBI probe head and operated at a magnetic field strength of 9.4 T. Quartz NMR tubes are used to avoid background signals from standard glass tubes in case of ^{11}B. Typically, ^{1}H spectra were recorded with one pulse sequence at a 30° flip angle (pulse duration 2.4 µs), using 1 s recycle delay, 1.6 s acquisition time, and 80 number of scans. In the case of samples containing boron, ^{11}B decoupling was systematically applied during the acquisition of ^{1}H spectra. The ^{11}B spectra were recorded with Hahn echo sequence (echo delay 117 µs) under proton decoupling condition, using 0.1 s recycle delay, 21 ms acquisition time, and 1024 number of scans. Chemical shifts are reported relative to 1% Me_4Si in $CDCl_3$ for ^{1}H and 15% $BF_3.Et_2O$ in $CDCl_3$ for ^{11}B using external standards [41].

Isothermal titration calorimetry ITC. Formation constants and inclusion enthalpies of host-guest systems $[B_{10}H_9NCCH_3]^-$@CD were simultaneously determined for each system by the use of an isothermal calorimeter (ITC200, MicroCal Inc.) at 298 K. Degassed water solutions were used in both cell (202.8 µL) and syringe (40 µL).

Each $(Et_3NH)[B_{10}H_9NCCH_3]$ system was studied by titration (injection of 5 mM CD solution on a 0.5 mM $(Et_3NH)[B_{10}H_9NCCH_3]$ solution) and release (injection of 5 mM CD and 5 mM $(Et_3NH)[B_{10}H_9NCCH_3]$ solution on water solution) protocols. Experiments involved one initial aliquot of 0.5 µL followed by ten aliquots of 3.5 µL of the syringe solution, delivered over 7 s for each injection. The time interval between two consecutive injections and agitation speed was set to 90 s and 1000 rpm, respectively.

The resulting heat flow was recorded as a function of time. The heat of dilution was eliminated from each titration by subtracting the raw signal obtained for the corresponding blank titrations. The peak area following each addition was obtained by integrating the resulting signal and expressed as the heat effect per injection. Thermodynamic parameters were determined by global nonlinear regression analysis of the titration and release isotherms using a dedicated homemade program [29].

V.2 Syntheses and isolation of products

All reagents were purchased from commercial sources and used without further purification. All synthetic reactions were performed under an argon atmosphere using a vacuum line and Schlenk-techniques. All solvents were dried and distilled unless stated otherwise because of the sensitivity of the boron precursor used. $(Et_3NH)_2[B_{10}H_{10}]$ is provided by katchem company.

V.2.1 Synthesis of $(Et_3NH)[B_{10}H_9NCCH_3]$

The synthesis of $(Et_3NH)[B_{10}H_9NCCH_3]$ was performed according to literature procedure [26]. $(Et_3NH)_2[B_{10}H_{10}]$ (0.2 g, 0.62 mmol) was dissolved in 10 ml of distilled CH_3CN. Next, 1 ml of CF_3COOH was added while stirring at room temperature under an inert atmosphere. The solution was warmed to 60°C for 30 min, then cooled at room temperature. Afterwards, it was cooled by liquid nitrogen. The volume of the solution was reduced by half under reduced pressure and cooled at -10°C for 24 hours. A white precipitate (0.15 g, 0.57 mmol, 93% yield) was collected by filtration. The product was characterized by ESI-MS, FT-IR, and NMR. **FT-IR/cm^{-1}** (ATR Diamond) (see Figure S1 in the appendix): 3075 (s), 2510 (s, BH), 2467 (s, CN), 1476 (m), 1461 (m), 1451 (m), 1404 (m), 1389 (m), 1364 (m), 1299 (w), 1156 (m), 1072 (w), 1033 (w), 1001 (s), 936 (w), 881 (w), 835 (m), 813 (w), 777 (w). **^{1}H{^{11}B} NMR** (δ ppm, CD_3CN): 0.10 (1H), 0.30 (2H), 0.36 (2H), 0.80 (2H), 2.46 (3H, Me), 3.29 (1H), 3.36 (1H), 1.29 (9H, Et_3NH^+), 3.21 (6H, Et_3NH^+), 6.70 (3H, Et_3NH^+); **^{11}B{^{1}H} NMR** (δ ppm, CD_3CN): 3.36 (1B), -2.3 (1B), -20.9 (1B), -26.1 (2B), -26.8 (2B), -28.7 (3B). **ESI-MS** (CH_3CN) *m/z* found 176.19 (calculated for $\{[B_{10}H_9NCCH_3](H_2O)\}^-$ *m/z* 176.25).

V.2.2 Synthesis of $(Et_3NH)_2[B_{20}H_{18}]$

The synthesis of $(Et_3NH)_2[B_{20}H_{18}]$ was performed according to literature procedure [34]. $(Et_3NH)_2[B_{10}H_{10}]$ (3 g, 9.3 mmol) was refluxed in 30 ml H_2O at 85°C. A solution of $FeCl_3.6H_2O$ (7.5 g, 27.7 mmol) was added dropwise while stirring under an inert atmosphere. Then, the mixture was kept refluxing for three hours at 80°C. After cooling the solution at room temperature, a yellow solid was collected by filtration and recrystallized from boiling water, yielding $(Et_3NH)_2[B_{20}H_{18}]$ (1.5 g, 3.42 mmol, 74% yield). The product was characterized by FT-IR and NMR. **FT-IR/cm^{-1}** (ATR Diamond) (see Figure S3 in the appendix): 3151 (s), 2520 (s, BH), 1457 (m), 1398 (m), 1361 (m), 1276 (w), 1187 (w), 1159 (m), 1030 (m), 993 (w), 958 (w), 877 (m), 826 (w), 793 (w), 675 (w). **^{1}H{^{11}B} NMR** (δ ppm, CD_3CN): 0.73 (4B**H$_{eq}$**), 1.26 (4B**H$_{eq}$**, overlapped with Et_3NH^+:-HN^+CH_2C**H$_3$** peak), 1.37 (4B**H$_{eq}$**), 1.70 (2B**H$_{eq}$**), 2.74 (2B**H$_{ap}$**), 3.16 (18H,Et_3NH^+ :-HN^+C**H$_2$**CH_3), 5.36 (2B**H$_{ap}$**), 6.72 (2H,Et_3NH^+:-**H**$N^+CH_2CH_3$) ; **^{11}B{^{1}H} NMR** (δ ppm, CD_3CN) : 29.88 (2B, d; B_{ap}), 15.32 (2B, s; B_{eq}), -7.49 (2B, d; B_{eq}), -12.99 (4B, d; B_{eq}), -16.52 (4B, d; B_{eq}), -19.96 (4B, d; B_{eq}), -26.18(2B, d; B_{ap}).

V.2.3 Synthesis of $Li_2[B_{20}H_{18}]$

$(Et_3NH)_2[B_{20}H_{18}]$ (0.2 g, 0.45 mmol) was dissolved in 12 ml of acetonitrile-water solution of the proportions (50:50), then it was passed through a column packed with Li^+ resin. Approximately 50 ml of the mobile phase (CH_3CN-H_2O) was collected. The organic phase was evaporated in a rotatory evaporator. A brown residue (0.11 g, 0.44 mmol, 97% yield) was obtained after the aqueous phase was evaporated in vacuum. The product was characterized by FT-IR and NMR. **FT-IR/cm^{-1}** (ATR Diamond) (see Figure S4 in the appendix): 3570 (br), 3517 (br), 2538 (s, BH), 2494 (s, BH), 1629 (m), 1610 (m), 959 (w), 873 (m), 821 (w), 751 (w), 699 (w). **^{1}H{^{11}B} NMR** (δ ppm, CD_3CN): 0.79 (4B**H$_{eq}$**), 1.34 (4B**H$_{eq}$**), 1.43 (4B**H$_{eq}$**), 1.76 (2B**H$_{eq}$**), 2.86 (2B**H$_{ap}$**), 5.44 (2B**H$_{ap}$**); **^{11}B{^{1}H} NMR** (δ ppm, CD_3CN) : 29.23 (2B, d; B_{ap}), 14.63 (2B, s; B_{eq}), -8.04 (2B, d; B_{eq}), -13.32 (4B, d; B_{eq}), -17.07 (4B, d; B_{eq}), -20.52 (4B, d; B_{eq}), -26.29(2B, d; B_{ap}).

VI. References

(1) Abramov, P. A.; Ivanov, A. A.; Shestopalov, M. A.; Moussawi, M. A.; Cadot, E.; Floquet, S.; Haouas, M.; Sokolov, M. N. Supramolecular Adduct of γ-Cyclodextrin and $[\{Re_6Q_8\}(H_2O)_6]^{2+}$ (Q=S, Se). *J Clust Sci* **2018**, *29* (1), 9–13. https://doi.org/10.1007/s10876-017-1312-z.

(2) Ivanov, A. A.; Falaise, C.; Landy, D.; Haouas, M.; Mironov, Y. V.; Shestopalov, M. A.; Cadot, E. Tuning the Chaotropic Effect as an Assembly Motif through One-Electron Transfer in a Rhenium Cluster. *Chem. Commun.* **2019**, *55* (67), 9951–9954. https://doi.org/10.1039/C9CC05136H.

(3) Moussawi, M. A.; Leclerc-Laronze, N.; Floquet, S.; Abramov, P. A.; Sokolov, M. N.; Cordier, S.; Ponchel, A.; Monflier, E.; Bricout, H.; Landy, D.; Haouas, M.; Marrot, J.; Cadot, E. Polyoxometalate, Cationic Cluster, and γ-Cyclodextrin: From Primary Interactions to Supramolecular Hybrid Materials. *J Am Chem Soc* **2017**, *139* (36), 12793–12803. https://doi.org/10.1021/jacs.7b07317.

(4) Khlifi, S.; Marrot, J.; Haouas, M.; Shepard, W. E.; Falaise, C.; Cadot, E. Chaotropic Effect as an Assembly Motif to Construct Supramolecular Cyclodextrin–Polyoxometalate-Based Frameworks. *J. Am. Chem. Soc.* **2022**, *144* (10), 4469–4477. https://doi.org/10.1021/jacs.1c12049.

(5) Ivanov, A. A.; Falaise, C.; Abramov, P. A.; Shestopalov, M. A.; Kirakci, K.; Lang, K.; Moussawi, M. A.; Sokolov, M. N.; Naumov, N. G.; Floquet, S.; Landy, D.; Haouas, M.; Brylev, K. A.; Mironov, Y. V.; Molard, Y.; Cordier, S.; Cadot, E. Host–Guest Binding Hierarchy within Redox- and Luminescence-Responsive Supramolecular Self-Assembly Based on Chalcogenide Clusters and γ-Cyclodextrin. *Chemistry – A European Journal* **2018**, *24* (51), 13467–13478. https://doi.org/10.1002/chem.201802102.

(6) Izzet, G.; Ménand, M.; Matt, B.; Renaudineau, S.; Chamoreau, L.-M.; Sollogoub, M.; Proust, A. Cyclodextrin-Induced Auto-Healing of Hybrid Polyoxometalates. *Angew Chem Int Ed Engl* **2012**, *51* (2), 487–490. https://doi.org/10.1002/anie.201106727.

(7) Sivaev, I.; Bregadze, V. ChemInform Abstract: Polyhedral Boranes for Medical Applications: Current Status and Perspectives. *European Journal of Inorganic Chemistry* **2009**, *2009*, 1433–1450. https://doi.org/10.1002/ejic.200900003.

(8) Řezáčová, P.; Pokorná, J.; Brynda, J.; Kožíšek, M.; Cígler, P.; Lepšík, M.; Fanfrlík, J.; Řezáč, J.; Grantz Šašková, K.; Sieglová, I.; Plešek, J.; Šícha, V.; Grüner, B.; Oberwinkler, H.; Sedláček', J.; Kräusslich, H.-G.; Hobza, P.; Král, V.; Konvalinka, J. Design of HIV Protease Inhibitors Based on Inorganic Polyhedral Metallacarboranes. *J. Med. Chem.* **2009**, *52* (22), 7132–7141. https://doi.org/10.1021/jm9011388.

(9) Valliant, J. F.; Guenther, K. J.; King, A. S.; Morel, P.; Schaffer, P.; Sogbein, O. O.; Stephenson, K. A. The Medicinal Chemistry of Carboranes. *Coordination Chemistry Reviews* **2002**, *232* (1), 173–230. https://doi.org/10.1016/S0010-8545(02)00087-5.

(10) Gao, S.; Zhu, Y.; Hosmane, N. Nanostructured Boron Compounds for Boron Neutron Capture Therapy (BNCT) in Cancer Treatment. In *Boron-Based Compounds*; John Wiley & Sons, Ltd, **2018**; pp 371–388. https://doi.org/10.1002/9781119275602.ch3.4.

(11) Neirynck, P.; Schimer, J.; Jonkheijm, P.; Milroy, L.-G.; Cigler, P.; Brunsveld, L. Carborane–β-Cyclodextrin Complexes as a Supramolecular Connector for Bioactive Surfaces. *J. Mater. Chem. B* **2014**, *3* (4), 539–545. https://doi.org/10.1039/C4TB01489H.

(12) Xiong, H.; Li, Y.; Ye, H.; Huang, G.; Zhou, D.; Huang, Y. Self-Healing Supramolecular Hydrogels through Host–Guest Interaction between Cyclodextrin and Carborane. *J. Mater. Chem. B* **2020**, *8* (45), 10309–10313. https://doi.org/10.1039/D0TB01886D.

(13) Nekvinda, J.; Grüner, B.; Gabel, D.; Nau, W. M.; Assaf, K. I. Host–Guest Chemistry of Carboranes: Synthesis of Carboxylate Derivatives and Their Binding to Cyclodextrins. *Chemistry – A European Journal* **2018**, *24* (49), 12970–12975. https://doi.org/10.1002/chem.201802134.
(14) Weickenmeier, M.; Wenz, G. Cyclodextrin Sidechain Polyesters — Synthesis and Inclusion of Adamantan Derivatives. *Macromolecular Rapid Communications* **1996**, *17* (10), 731–736. https://doi.org/10.1002/marc.1996.030171008.
(15) Voskuhl, J.; Waller, M.; Bandaru, S.; Tkachenko, B. A.; Fregonese, C.; Wibbeling, B.; Schreiner, P. R.; Ravoo, B. J. Nanodiamonds in Sugar Rings: An Experimental and Theoretical Investigation of Cyclodextrin–Nanodiamond Inclusion Complexes. *Org. Biomol. Chem.* **2012**, *10* (23), 4524–4530. https://doi.org/10.1039/C2OB06915F.
(16) Del Valle, E. M. M. Cyclodextrins and Their Uses: A Review. *Process Biochemistry* **2004**, *39* (9), 1033–1046. https://doi.org/10.1016/S0032-9592(03)00258-9.
(17) Szejtli, J. Introduction and General Overview of Cyclodextrin Chemistry. *Chem Rev* **1998**, *98* (5), 1743–1754. https://doi.org/10.1021/cr970022c.
(18) Assaf, K. I.; Nau, W. M. The Chaotropic Effect as an Assembly Motif in Chemistry. *Angewandte Chemie International Edition* **2018**, *57* (43), 13968–13981. https://doi.org/10.1002/anie.201804597.
(19) Assaf, K.; Suckova, O.; Al Danaf, N.; von Glasenapp, V.; Gabel, D.; Nau, W. Dodecaborate-Functionalized Anchor Dyes for Cyclodextrin-Based Indicator Displacement Applications. *ORGANIC LETTERS* **2016**, *18* (5), 932–935. https://doi.org/10.1021/acs.orglett.5b03611.
(20) Zhang, J.; Gabel, D.; Assaf, K.; Nau, W. A Fluorescein-Substituted Perbrominated Dodecaborate Cluster as an Anchor Dye for Large Macrocyclic Hosts and Its Application in Indicator Displacement Assays. *ORGANIC LETTERS* **2022**, *24* (50), 9184–9188. https://doi.org/10.1021/acs.orglett.2c03615.
(21) Assaf, K. I.; Ural, M. S.; Pan, F.; Georgiev, T.; Simova, S.; Rissanen, K.; Gabel, D.; Nau, W. M. Water Structure Recovery in Chaotropic Anion Recognition: High-Affinity Binding of Dodecaborate Clusters to γ-Cyclodextrin. *Angewandte Chemie International Edition* **2015**, *54* (23), 6852–6856. https://doi.org/10.1002/anie.201412485.
(22) Assaf, K. I.; Begaj, B.; Frank, A.; Nilam, M.; Mougharbel, A. S.; Kortz, U.; Nekvinda, J.; Grüner, B.; Gabel, D.; Nau, W. M. High-Affinity Binding of Metallacarborane Cobalt Bis(Dicarbollide) Anions to Cyclodextrins and Application to Membrane Translocation. *J. Org. Chem.* **2019**, *84* (18), 11790–11798. https://doi.org/10.1021/acs.joc.9b01688.
(23) Assaf, K. I.; Ural, M. S.; Pan, F.; Georgiev, T.; Simova, S.; Rissanen, K.; Gabel, D.; Nau, W. M. Water Structure Recovery in Chaotropic Anion Recognition: High-Affinity Binding of Dodecaborate Clusters to γ-Cyclodextrin. *Angewandte Chemie International Edition* **2015**, *54* (23), 6852–6856. https://doi.org/10.1002/anie.201412485.
(24) Assaf, K. I.; Holub, J.; Bernhardt, E.; Oliva-Enrich, J. M.; Fernández Pérez, M. I.; Canle, M.; Santaballa, J. A.; Fanfrlík, J.; Hnyk, D.; Nau, W. M. Face-Fusion of Icosahedral Boron Hydride Increases Affinity to γ-Cyclodextrin: Closo,Closo-$[B_{21}H_{18}]^-$ as an Anion with Very Low Free Energy of Dehydration. *ChemPhysChem* **2020**, *21* (10), 971–976. https://doi.org/10.1002/cphc.201901225.
(25) Diab, M.; Floquet, S.; Haouas, M.; Abramov, P. A.; López, X.; Landy, D.; Damond, A.; Falaise, C.; Guérineau, V.; Touboul, D.; Naoufal, D.; Cadot, E. Encapsulation of Chaotropic Closo-Decahydrodecaborate Clusters Within Cyclodextrins: Synthesis, Solution Studies, and DFT Calculations. *European Journal of Inorganic Chemistry* **2019**, *2019* (29), 3373–3382. https://doi.org/10.1002/ejic.201900602.

(26) Dou, D.; Mavunkal, I. J.; Bauer, J. A. K.; Knobler, C. B.; Hawthorne, M. F.; Shore, S. G. Synthesis and Structure of Triethylammonium 2-(Acetonitrile)Nonahydro-Closo-Decaborate(1-). *Inorg. Chem.* **1994**, *33* (26), 6432–6434. https://doi.org/10.1021/ic00104a069

(27) Zhdanov, A. P.; Lisovsky, M. V.; Goeva, L. V.; Razgonyaeva, G. A.; Polyakova, I. N.; Zhizhin, K. Yu.; Kuznetsov, N. T. Nucleophilic Addition of Alcohols to the C-N Multiple Bonds of the Nitrilium Substituent in the Anion $[2\text{-}B_{10}H_9(N{\equiv}CMe)]^-$. *Russ Chem Bull* **2009**, *58* (8), 1694–1700. https://doi.org/10.1007/s11172-009-0234-9.

(28) Yao, S.; Falaise, C.; Leclerc, N.; Roch-Marchal, C.; Haouas, M.; Cadot, E. Improvement of the Hydrolytic Stability of the Keggin Molybdo- and Tungsto-Phosphate Anions by Cyclodextrins. *Inorg. Chem.* **2022**, *61* (9), 4193–4203. https://doi.org/10.1021/acs.inorgchem.2c00095.

(29) Bertaut, E.; Landy, D. Improving ITC Studies of Cyclodextrin Inclusion Compounds by Global Analysis of Conventional and Non-Conventional Experiments. *Beilstein J. Org. Chem.* **2014**, *10* (1), 2630–2641. https://doi.org/10.3762/bjoc.10.275.

(30) Kaczmarczyk, A.; Dobrott, R. D.; Lipscomb, W. N. REACTIONS OF $B_{10}H_{10}^{-2}$ ION. *Proc Natl Acad Sci U S A* **1962**, *48* (5), 729–733.

(31) Hawthorne, M. F.; Shelly, K.; Li, F. The Versatile Chemistry of the $[B_{20}H_{18}]^{2-}$ Ions: Novel Reactions and Structural Motifs. *Chem. Commun.* **2002**, No. 6, 547–554. https://doi.org/10.1039/b110076a.

(32) Feakes, D. A.; Shelly, K.; Hawthorne, M. F. Selective Boron Delivery to Murine Tumors by Lipophilic Species Incorporated in the Membranes of Unilamellar Liposomes. *Proc Natl Acad Sci U S A* **1995**, *92* (5), 1367–1370. https://doi.org/10.1073/pnas.92.5.1367.

(33) Hawthorne, M. F. The Role of Chemistry in the Development of Boron Neutron Capture Therapy of Cancer. *Angewandte Chemie International Edition in English* **1993**, *32* (7), 950–984. https://doi.org/10.1002/anie.199309501.

(34) Hawthorne, M. F.; Pilling, R. L.; Stokely, P. F. The Preparation and Rearrangement of the Three Isomeric $B_{20}H_{18}^{-4}$ Ions. *J. Am. Chem. Soc.* **1965**, *87* (9), 1893–1899. https://doi.org/10.1021/ja01087a011.

(35) Pilling, R. L.; Hawthorne, M. Frederick.; Pier, E. A. The Boron-11 Nuclear Magnetic Resonance Spectrum of $B_{20}H_{18}^{-2}$ at 60 Mc./Sec. *J. Am. Chem. Soc.* **1964**, *86* (17), 3568–3569. https://doi.org/10.1021/ja01071a039.

(36) Chamberland, B. L.; Muetterties, E. L. Chemistry of Boranes. XVIII. Oxidation of $B_{10}H_{10}^{-2}$ and Its Derivatives. *Inorg. Chem.* **1964**, *3* (10), 1450–1456. https://doi.org/10.1021/ic50020a025.

(37) Avdeeva, V. V.; Privalov, V. I.; Kubasov, A. S.; Nikiforova, S. E.; Malinina, E. A.; Kuznetsov, N. T. 2D COSY 11B NMR Spectroscopy in the Interpretation of the Structures of Iso and Trans Isomers of the Macropolyhedral Boron Cluster $[B_{20}H_{18}]^{2-}$. *Inorganica Chimica Acta* **2023**, *555*, 121564. https://doi.org/10.1016/j.ica.2023.121564.

(38) Muetterties, E. L.; Balthis, J. H.; Chia, Y. T.; Knoth, W. H.; Miller, H. C. Chemistry of Boranes. VIII. Salts and Acids of B10H10-2 and B1212-2. *Inorg. Chem.* **1964**, *3* (3), 444–451. https://doi.org/10.1021/ic50013a030.

(39) Sivaev, I. B.; Bragin, V. I.; Prikaznov, A. V.; Petrovskii, P. V.; Bregadze, V. I.; Filippov, O. A.; Teplinskaya, T. A.; Titov, A. A.; Shubina, E. S. Study of Proton-Deuterium Exchange in Ten-Vertex Boron Hydrides. *Collect. Czech. Chem. Commun.* **2007**, *72* (12), 1725–1739. https://doi.org/10.1135/cccc20071725.

(40) Sivaev, I. B.; Petrovskii, P. V.; Filin, A. M.; Shubina, E. S.; Bregadze, V. I. Regioselective Hydrogen-Deuterium Exchange in the $[B_{10}H_{10}]^{2-}$ Anion. Syntheses of $[1,10\text{-}B_{10}H_8D_2]^{2-}$ and

[2,3,4,5,6,7,8,9-$B_{10}H_2D_8$]$^{2-}$. *Russian Chemical Bulletin* **2001**, *50* (6), 1115–1116. https://doi.org/10.1023/A:1011306410852.
(41) Harris, R. K.; Becker, E. D.; Cabral de Menezes, S. M.; Goodfellow, R.; Granger, P. NMR Nomenclature: Nuclear Spin Properties and Conventions for Chemical Shifts: IUPAC Recommendations 2001. *Solid State Nuclear Magnetic Resonance* **2002**, *22* (4), 458–483. https://doi.org/10.1006/snmr.2002.0063.

General Conclusion

General Conclusion

The initial goal of this work was the development of new POM-borate hybrids and optimizing their properties, especially towards biological applications. We started by isolating and characterizing the mono-adduct of the Keggin POM SiW_{10} and the decaborate derivative [2-$B_{10}H_9CO]^-$, namely $[(SiW_{10}O_{36})(B_{10}H_9CONHC_3H_6Si)(NH_2C_3H_6Si)O]^{6-}$, using the protocol established by Manal Diab. However, we performed an additional unusual technique, ^1H-^{15}N HMQC NMR, which helped us visualize the free amine group involved in the H-H interaction with the decaborate cluster, as evidenced in previous DFT calculations. To synthesize the target multifunctional compound, we reacted the nucleophilic free amine group of the SiW_{10}-monoB_{10} derivative with different organic ligands containing electrophilic groups. ^1H and ^{11}B NMR reveal no reactions with **pyridine-4-carboxaldehyde and 4-chloromethyl benzonitrile,** probably because of the stability of the SiW_{10}-monoB_{10} compound due to the intramolecular hydrogen bonding formed between the free amine group and hydrides of the B_{10} cluster. Hence, we chose another ligand **3-(Iodomethyl)pyridine** with a strong leaving group. ^1H and ^{11}B NMR reveal that the syntheses were very sensitive to many parameters, such as the ratio of the reactants and the quantity of the base. The adducts were possibly formed but not stable in time . We assume that intermolecular interactions between reactants are more favored than covalent coupling in the organic medium and discussion with other groups working on similar topics seems in agreement with that. This point would deserve a full study in organic medium but this is not the purpose of the PhD work. Hence, in the following parts, we focused on investigating POM and borate chemistries, each on its own.

In the next part, we aimed to shift the activity of organic photoinitiators from UV to Visible light via covalent grafting to polyoxometalates. We succeeded in synthesizing new organoimido POM hybrids through covalent coupling of anthracene, benzophenone, and anthraquinone-based UV photosensitizers with the $[Mo_6O_{19}]^{2-}$ POM precursor, denoted as **POM-AC**, **POM-AB**, and **POM-AQ**, respectively. These derivatives were characterized in the solid state by FT-IR, elemental analysis, and X-ray diffraction and characterized in CD_3CN solution by ^1H NMR, ESI-MS, and UV-visible spectroscopy and electrochemistry. ^1H NMR spectra confirm the formation of POM-hybrids in agreement with FT-IR, ESI-MS, and X-ray diffraction. UV-Visible spectra evidence strong electronic interactions between the hexamolybdate core and the organic part through the Mo-N triple bond, leading to a strong red shift of the absorption bands along with higher Ɛ values compared to the organic precursors. To our knowledge, the potential of such functionalized POMs to act as photoactive species in the visible range has never been explored. Therefore, photophysical properties of photosystems made of the **POM-AC**, **POM-AB**, and **POM-AQ** complexes, respectively, and N-methyldiethanolamine (MDEA) as reducing agent have been studied, and the relevance of these hybrids as PIs for acrylate monomer photopolymerization under visible-light LED irradiation has also been investigated. Steady-state photolysis experiments suggested a photoinduced electron transfer reaction between the three POMs and MDEA,

acting as a reducing agent. The fluorescence studies evidenced a favorable electron transfer process between the singlet excited state of **POM-AQ** and MDEA. In addition, EPR-ST investigations allowed us to distinguish different types of free radical species released from irradiation of the POM Hybrid/MDEA systems. Consequently, we demonstrated the capability of imido POM derivatives to promote free-radical photopolymerization (FRP) under visible LEDs irradiation with wavelengths ranging from 405 to 470 nm of commercial monomers, i.e., trimethylolpropane triacrylate (TMPTA) and soyabean oil epoxidized acrylate (SOA), which to our knowledge is a first example for the synthesis of such composites incorporating POMs. Characterization of the polymer materials synthesized with the best performing photoinitiating systems, i.e., **POM-AQ**/MDEA, has been investigated. Coatings prepared using the **POM-AQ**/MDEA/soybean oil epoxidized acrylate photosystem exhibit excellent mechanical properties, with very good flexibility, resistance to brittle fracture, and adherence to the steel. Finally, POM-AQ was shown to have a remarkable capacity to generate singlet oxygen species under visible light irradiation.

In the last part, we aimed to prepare novel CD/borate complexes strong enough to envision biological applications. We reported 1:1 inclusion complexes between $[B_{10}H_9NCCH_3]^-$ and β- and γ-CDs while weaker interactions are evidenced with α-CD studies through ESI-MS, NMR, and ITC studies of $[B_{10}H_9NCCH_3]^-$ and the three CDs . The binding affinities of the two domains determined by NMR and ITC seems drastically enhanced compared that of $[B_{10}H_{10}]^{2-}$ with CDs. ITC studies evidenced the chaotropic character of the cluster $[B_{10}H_9NCCH_3]^-$ which was expected to increase with the decrease of the charge. The less charged and more voluminous $[B_{10}H_9NCCH_3]^-$ induces a change in its solvation properties that favors adsorption onto hydrophobic cavities such as the macrocyclic CDs. Despite that, this effect of solvent alone on the encapsulation process of $[B_{10}H_9NCCH_3]^-$ could not be sufficient, and the size-matching effect between host and guest may also play an important role. Thus, most stable host-guest system is obtained with γ-CD due to the well match-size fit.

Solution studies performed by NMR and ITC with $[B_{20}H_{18}]^{2-}$ and the three CDs also allowed demonstrating the formation of weak inclusion complexes with α-CD, while stronger with β-, and γ-CDs. The association constants found by NMR for binding of $[B_{20}H_{18}]^{2-}$ cluster were enhanced greatly with large CDs compared to $[B_{10}H_{10}]^{2-}$ and $[B_{10}H_9NCCH_3]^-$ clusters since $[B_{20}H_{18}]^{2-}$ has lower charge density which would enhance its chaotropic effect. However, with the smallest α-CD the affinity constant remained weak as for the case of $[B_{10}H_9NCCH_3]^-$, because this cavitand molecule is too small to encapsulate the boron cluster. The optimal affinity was found with the β-CD, probably because it matches well the size of the cluster.

On the other hand, entropy variations are negative for α- and β-CD, indicating that the inclusion process of the $[B_{20}H_{18}]^{2-}$ cluster within cyclodextrins is associated to a chaotropic effect. The binding constants obtained by ITC showed increasing values with increasing CD size. While the orders of magnitude recorded for 1:1 complexes of $[B_{20}H_{18}]^{2-}$ with α- or β-CD, are in agreement with the values obtained from NMR titrations, different result is observed

with the largest γ-CD. ITC revealed not only a very strong association with this CD, but also a higher stoichiometry, i.e., 1CD : 2 B_{20} clusters. This latter observation could explain the discrepancies between the NMR and ITC data, as NMR analysis is based on the simple 1:1 binding mode. Hence, to obtain more information, ESI-MS measurements are in progress to investigate the stoichiometry of B_{20}@γ-CD complexes, while DFT calculations in collaboration with Dr. Xavier Lopez in Spain are also underway. Finally, new ITC measurements using the competitive titrations method are needed to clarify these data.

Furthermore, we investigated the stability of $[B_{20}H_{18}]^{2-}$ in aqueous solutions for the first time. $^{1}H\{^{11}B\}$ and $^{11}B\{^{1}H\}$ NMR studies of $[B_{20}H_{18}]^{2-}$ anion in D_2O revealed selective deuterium-proton exchange processes with the protons at equatorial positions, in addition to formation of degradation products over a period of time. Same NMR studies recorded in D_2O for $B_{20}H_{18}^{2-}$ in the presence of CD showed that encapsulating B_{20} cluster in CD complexes decrease H/D exchange and protects the anion from degradation and H/D exchange. Particularly, β-CD has been shown to prevent efficiently both decomposition and H/D exchange, while γ-CD reduces significantly H/D exchange but to a lesser extent decomposition.In the contrast, α-CD cannot protect the B_{20} against neither decomposition nor H/D exchange. These results would open the way for designing new compounds with interesting biological properties desirable as drugs in the medical field.

Appendices

Appendix of Chapter 2

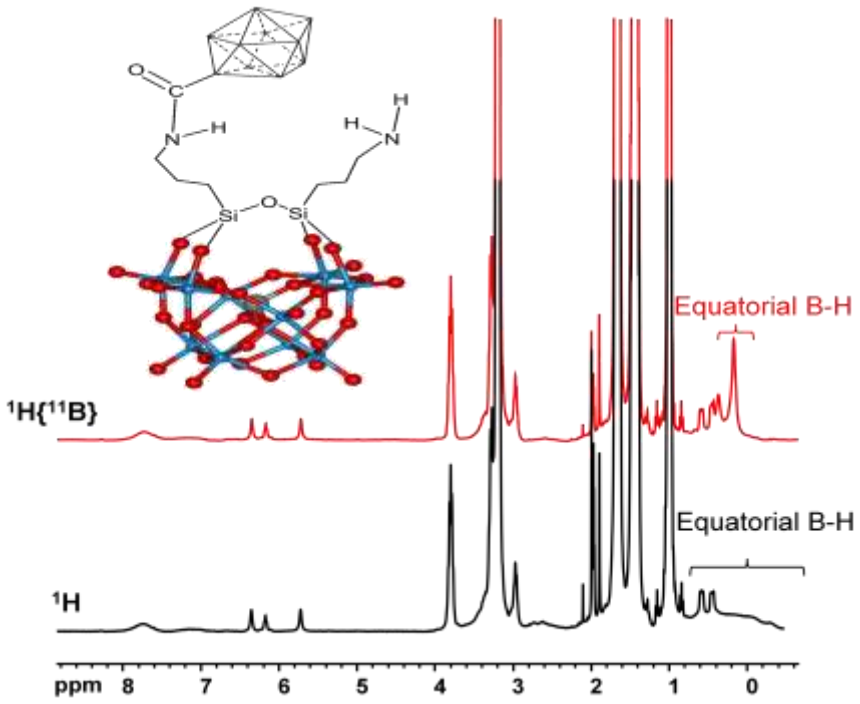

Figure S1. ^1H and $^1H\{^{11}B\}$ NMR spectra of ***SiW_{10}monoB$_{10}$*** *in CD_3CN at 400MHz.*

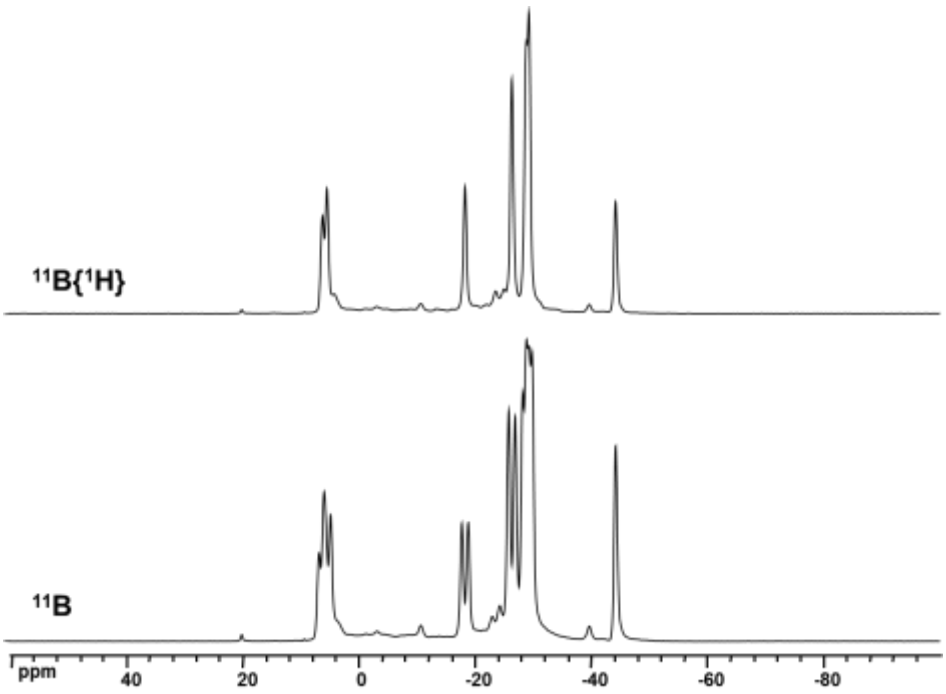

Figure S2.^{11}B and ^{11}B $\{^1H\}$ NMR spectra of ***$TBAB_{10}H_9CO$*** *in CD_3CN at 400MHz.*

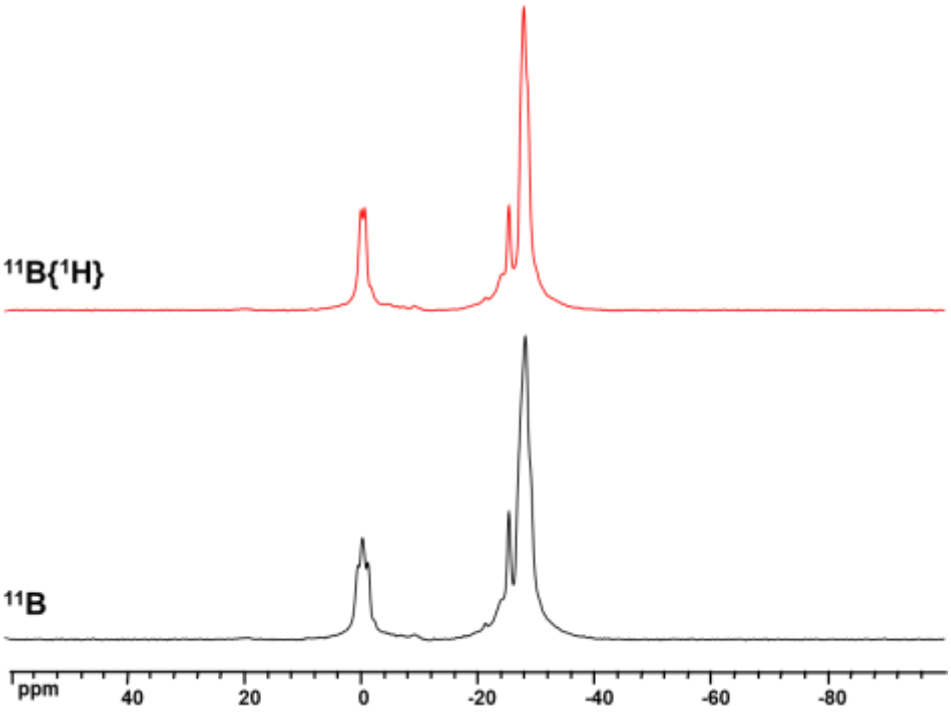

*Figure S3.^{11}B and $^{11}B\{^1H\}$ NMR spectra of **SiW_{10}-$monoB_{10}$** in CH_3CN at 400MHz.*

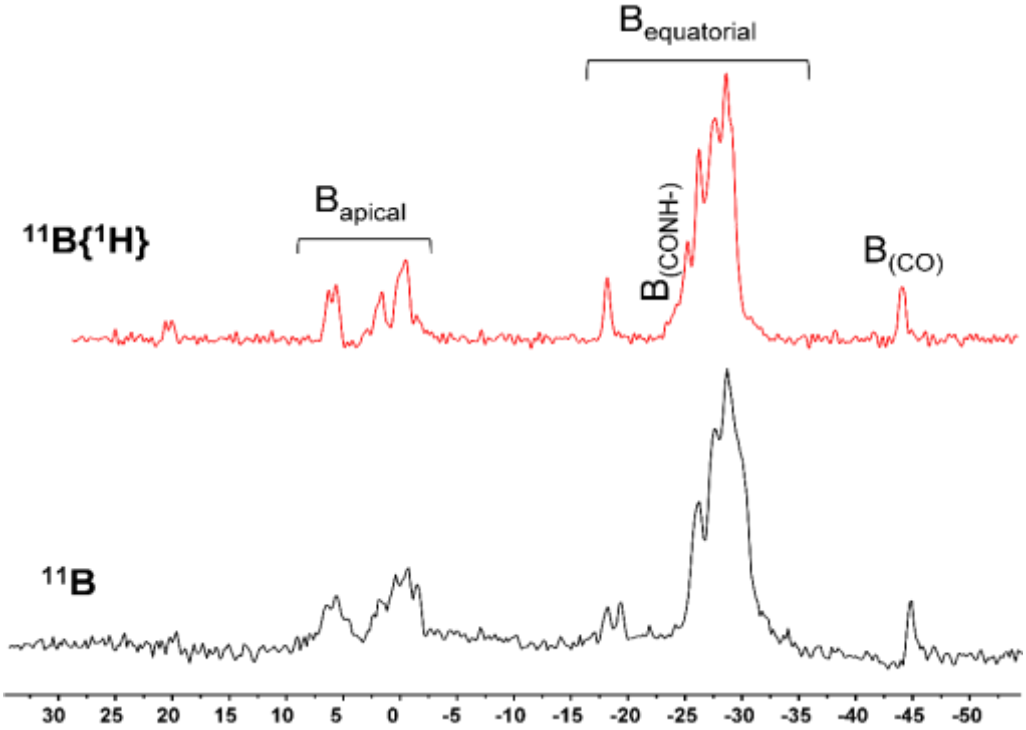

*Figure S4.^{11}B and $^{11}B\{^1H\}$ NMR spectra of **SiW_{10}-$monoB_{10}$/C_6H_6NI.HI (1/1)** in CD_3CN at 400MHz.*

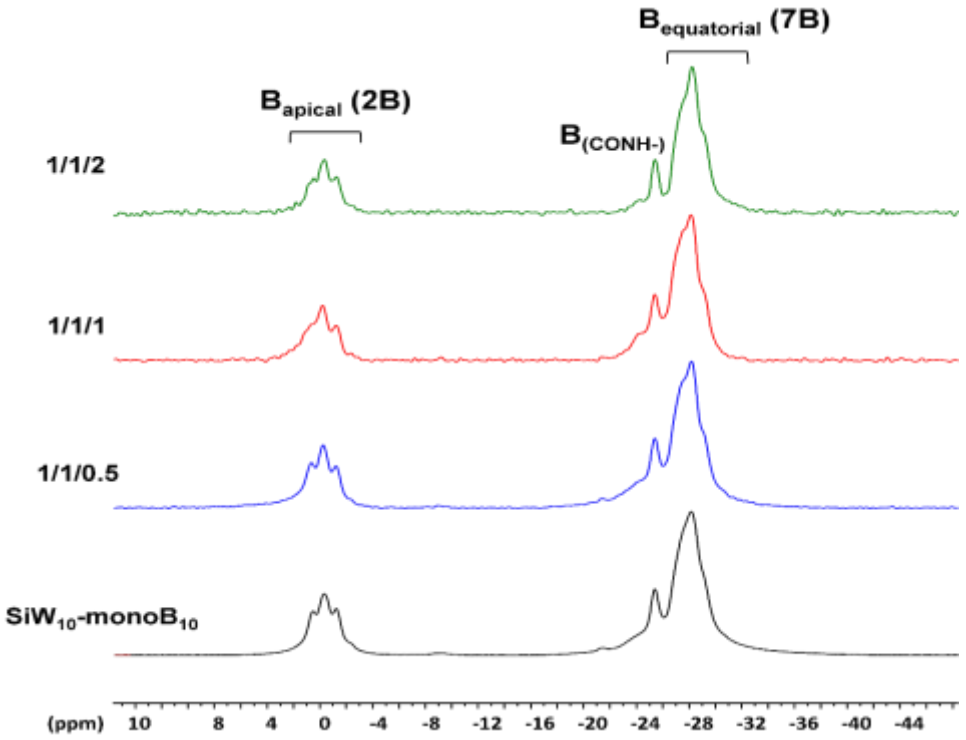

*Figure S5. ^{11}B NMR spectra of **SiW_{10}-monoB$_{10}$** and **SiW_{10}-monoB$_{10}$/C_6H_6NI.HI/DIPEA** mixtures in CH_3CN at 400MHz.*

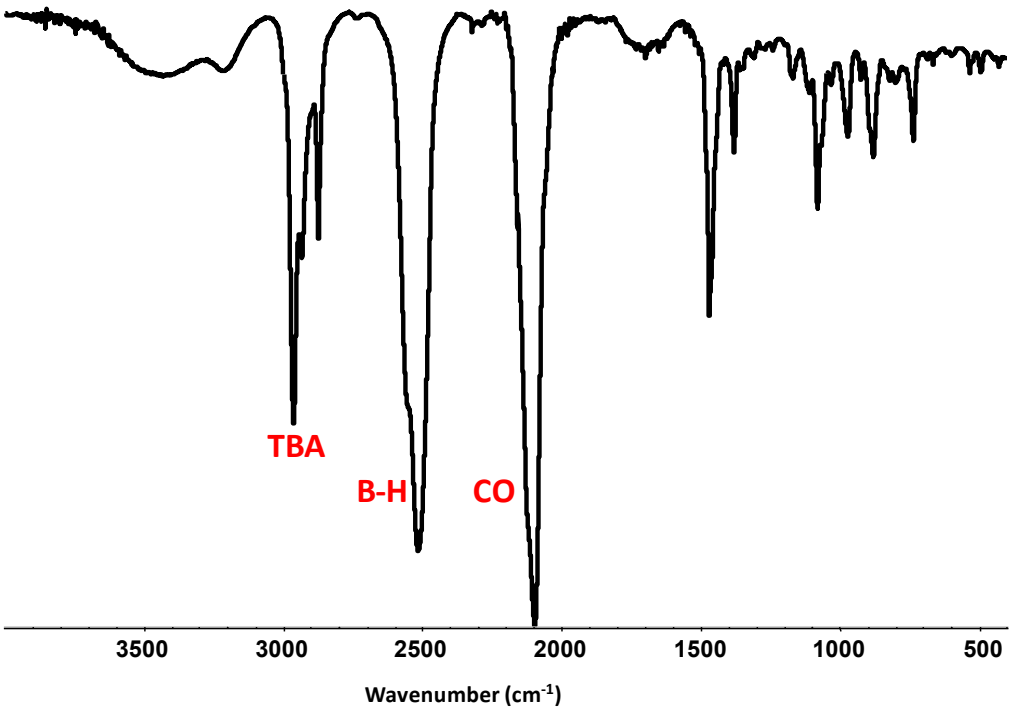

*Figure S6. The infrared spectrum of **TBAB$_{10}$H$_9$CO**.*

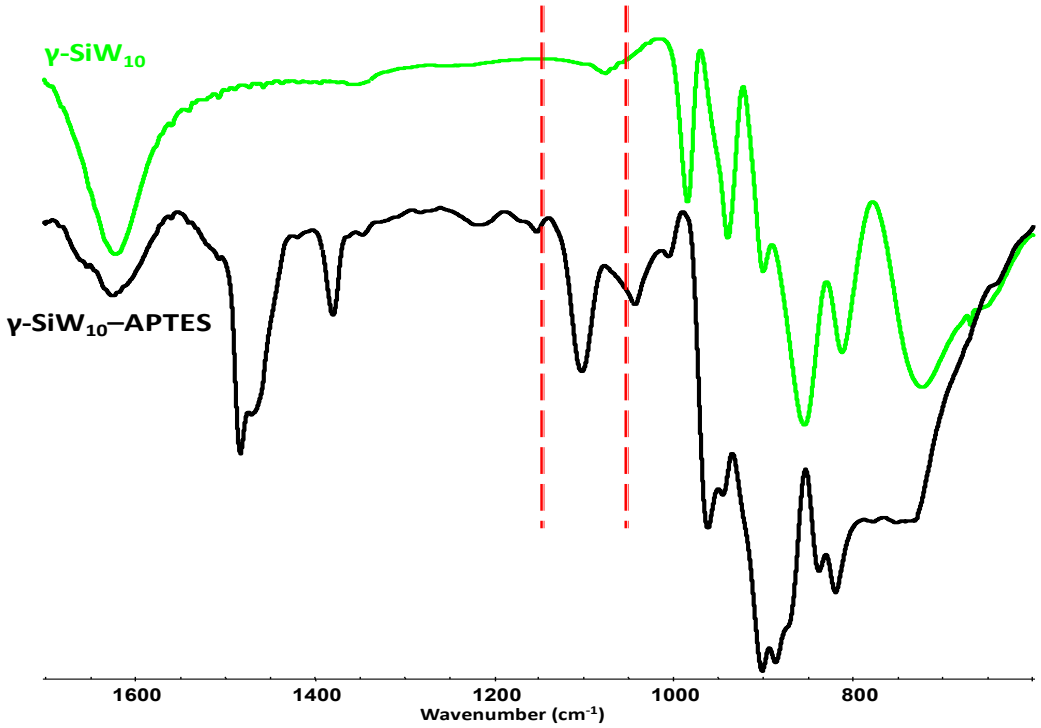

Figure S7. Infrared spectra for ***γ-SiW₁₀*** *(green) and* ***γ-SiW₁₀-APTES*** *(black). Dashed lines represent a guide for the eye to highlight the appearance of a band at 1100 cm^{-1} for Si-O-Si.*

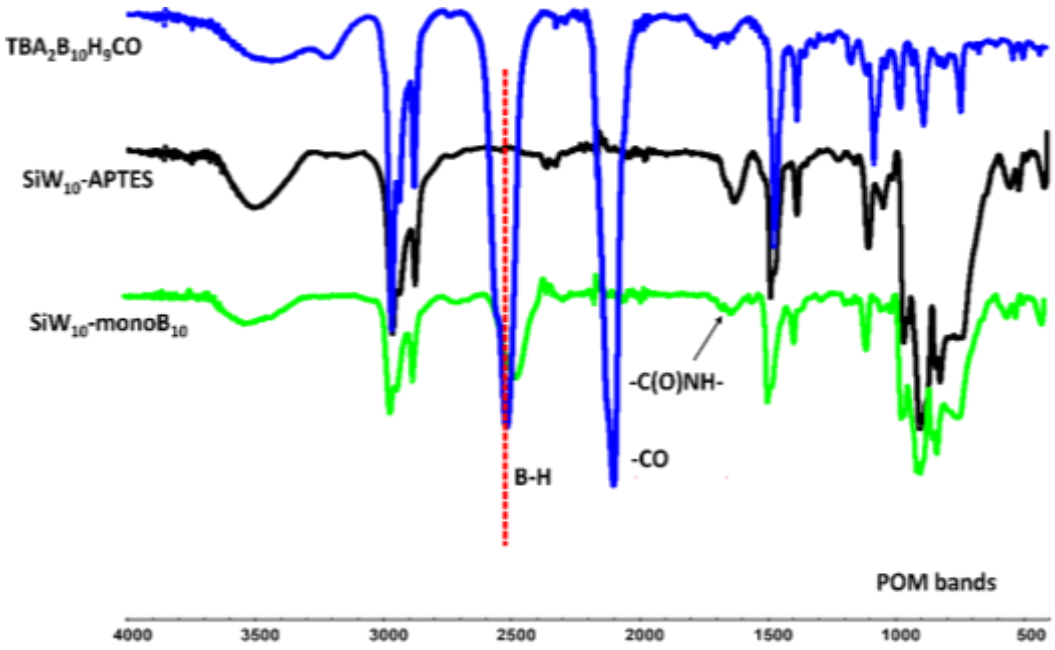

Figure S8. IR spectra comparing ***TBA[B₁₀H₉CO]****,* ***SiW₁₀-APTES****, and* ***SiW₁₀-monoB₁₀****.*

Appendix of Chapter 3

Equation S1: Stern-Volmer relationship [1–3]

$$\frac{I_0}{I} = 1 + K_{sv}[MDEA] \qquad \boldsymbol{eq.S1}$$

Where I and I_0 stand for the fluorescence intensity of the POM hybrid with and without a quencher (here is MDEA), respectively, and K_{sv} is the fluorescence quenching constant.

Equation S2: Rehm-Weller equation [4,5]

$$\Delta G = E_{ox} - E_{red} + E_s + C \qquad \boldsymbol{eq.S2}$$

Where E_{ox}, E_{red}, E_S, and C are the oxidation potential of the electron donor, the reduction potential of the electron acceptor, the excited singlet state energy and the Coulombic term, respectively. C is usually neglected as experiments are done in polar solvents.

Equations S3-S7:

E_s=2.48 eV was estimated using Tauc's relationship (eq.S3) as proposed by Davis and Mott [6].

$$(\alpha h\nu)^{\gamma} = K(h\nu - E_g) \qquad \boldsymbol{eq.S3}$$

α : absorption coefficient

h : Planck's constant

ν : photons frequency

K : proportionality constant

E_g or E_s: band gap energy

γ : nature of electronic transition (γ=2 direct allowed transition, γ=1/2 indirect allowed transition)

Hence, the basic procedure for Tauc analysis is to acquire the optical absorbance data of the sample that spans a range of transition energies from below the bandgap transition to above. Plotting $(\alpha h\nu)^{\gamma}$ versus $(h\nu - E_g)$ is a matter of testing γ=2 or 1/2 to compare which provides the better fit and thus identifies the adequate transition type, which brings the necessity to evaluate the absorption coefficient α from the absorbance values A in the UV-Vis spectra of the POM-hybrids, according to the Beer-Lambert Law (eq. S4a).

$$\frac{I}{I_0} = e^{-\alpha l} \qquad \boldsymbol{eq.S4a}$$

$$log\ \frac{I}{I_0} = log\ e^{-\boldsymbol{\alpha} l} = -\boldsymbol{\alpha} l\ log(e) = -\boldsymbol{\alpha} l(0.4343) \qquad \boldsymbol{eq.S4b}$$

$$log\ \frac{I_0}{I} = \boldsymbol{A}\ (\text{Absorbance}) \qquad \boldsymbol{eq.S4c}$$

$$log\ \frac{I}{I_0} = \boldsymbol{\alpha} l(0.4343) \qquad \boldsymbol{eq.S4d}$$

$$\boldsymbol{A} = \boldsymbol{\alpha} l(0.4343) \quad l = 1\ cm$$

$$\boldsymbol{\alpha} = 2.302\ \boldsymbol{A}\ \ (cm^{-1})$$

I_0: Intensity of the incident light

I: Intensity of the transmitted light

l : Thickness of the cuvette

Then the absorption coefficient α can be calculated from the absorbance values *A*.

Now to estimate the E_s from band, plot $\boldsymbol{(\alpha h\nu)^{\gamma}}$ versus $\boldsymbol{E = h\nu}$.

$$E{=}h\nu\ (Joules) \qquad \boldsymbol{eq.S5}$$

$$E = \frac{hc}{\lambda} = \frac{6.625 \times 10^{-34}(Js) \times 2.998 \times 10^{8}(m/s)}{\lambda(m)} \qquad \boldsymbol{eq.S6}$$

$$E = \frac{1.986 \times 10^{-25}(eV\ m)}{\lambda(m) \times 1.602 \times 10^{-19}}$$

$$E = \frac{1240 \times 10^{-9}\ (eV\ M)}{\lambda(m)}$$

$$E = \frac{1240}{\lambda(nm)}\ \ (eV) \qquad \boldsymbol{eq.S7}$$

The band gap (Eg) was determined as the intersection point between the energy axis and the line extrapolated from the linear portion of the absorption edge in Tauc's plot [6,7].

References

(1) J.-P. Fouassier. Photoinitiation, Photopolymerization and Photocuring. J.-P. Fouassier. Hanser Publishers, Munich, 1995. ISBN 3-446-17069-3. *Polymer International* **1996**, *40* (4), 315–315. https://doi.org/10.1002/(SICI)1097-0126(199608)40:4<315::AID-PI566>3.0.CO;2-T.

(2) Marcus, R. A.; Sutin, N. Electron Transfers in Chemistry and Biology. *Biochimica et Biophysica Acta (BBA) - Reviews on Bioenergetics* **1985**, *811* (3), 265–322. https://doi.org/10.1016/0304-4173(85)90014-X.

(3) Verhoeven, J. W. Glossary of terms used in photochemistry (IUPAC Recommendations 1996). *Pure and Applied Chemistry* **1996**, *68* (12), 2223–2286. https://doi.org/10.1351/pac199668122223.

(4) Toma, H. E.; Creutz, Carol. Pentacyanoferrate(II) Complexes: Evaluation of Their Formal Potentials and Mechanism of Their Quenching of Tris(2,2'-Bipyridine)Ruthenium(II) Luminescence. *Inorg. Chem.* **1977**, *16* (3), 545–550. https://doi.org/10.1021/ic50169a008.

(5) Rehm, D.; Weller, A. Kinetics of Fluorescence Quenching by Electron and H-Atom Transfer. *Israel Journal of Chemistry* **1970**, *8* (2), 259–271. https://doi.org/10.1002/ijch.197000029.

(6) Davis, E. A.; Mott, N. F. Conduction in Non-Crystalline Systems V. Conductivity, Optical Absorption and Photoconductivity in Amorphous Semiconductors. *The Philosophical Magazine: A Journal of Theoretical Experimental and Applied Physics* **1970**, *22* (179), 0903–0922. https://doi.org/10.1080/14786437008221061.

(7) Abdelghany, A. M.; Abdelrazek, E. M.; Badr, S. I.; Morsi, M. A. Effect of Gamma-Irradiation on (PEO/PVP)/Au Nanocomposite: Materials for Electrochemical and Optical Applications. *Materials & Design* **2016**, *C* (97), 532–543. https://doi.org/10.1016/j.matdes.2016.02.082.

Appendix of Chapter 4

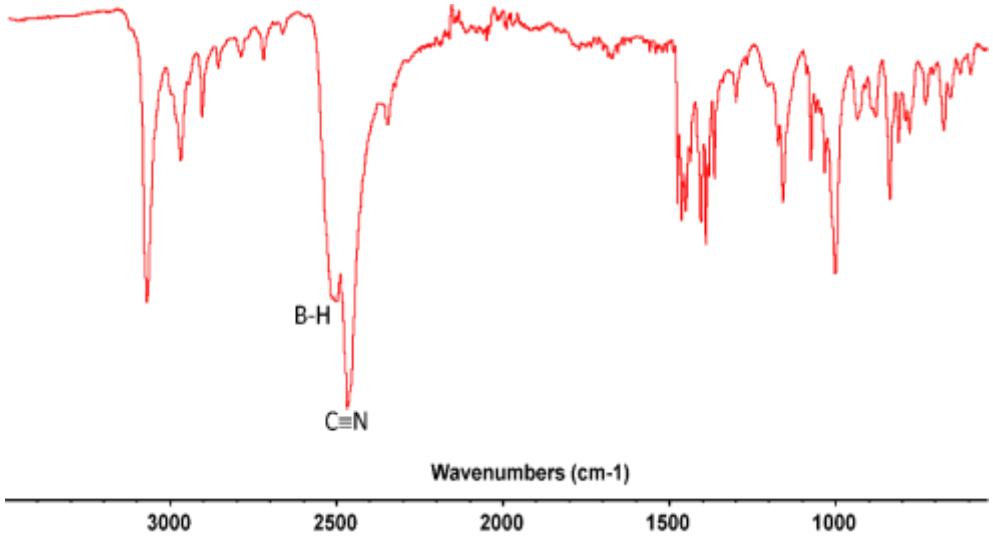

Figure S1.The infrared spectrum of ***(Et₃NH)[B₁₀H₉NCCH₃]****.*

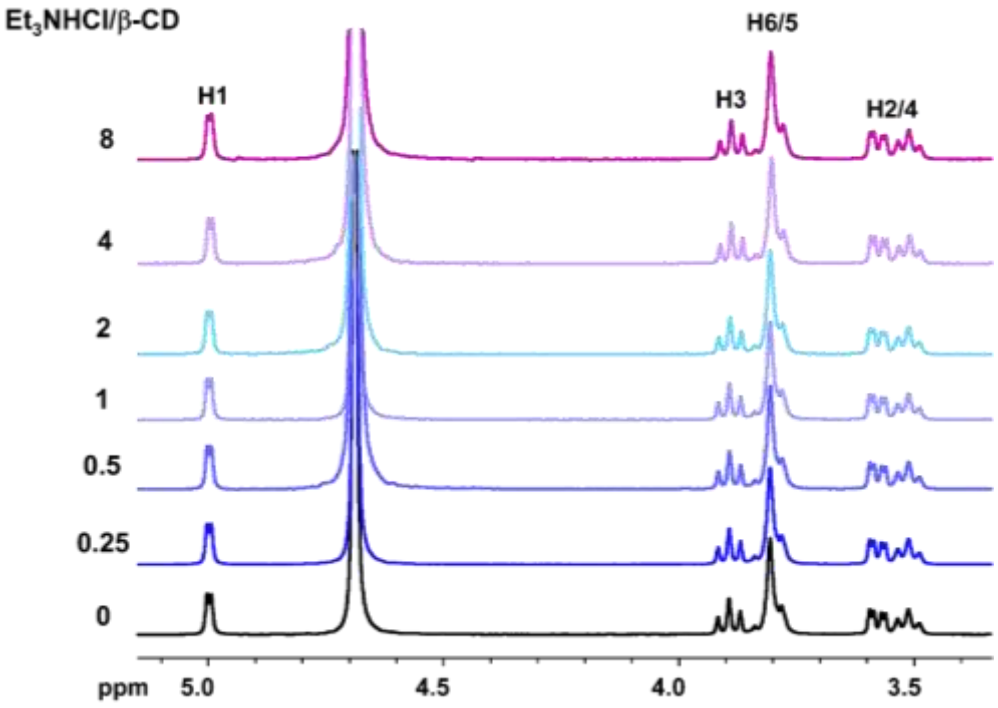

Figure S2. $^{1}H\{^{11}B\}$ *NMR spectra in* D_2O *for different ratios of* ***Et₃NHCl/β-CD*** *from the titration of 3 mM aqueous β-CD solution with* ***Et₃NHCl****.*

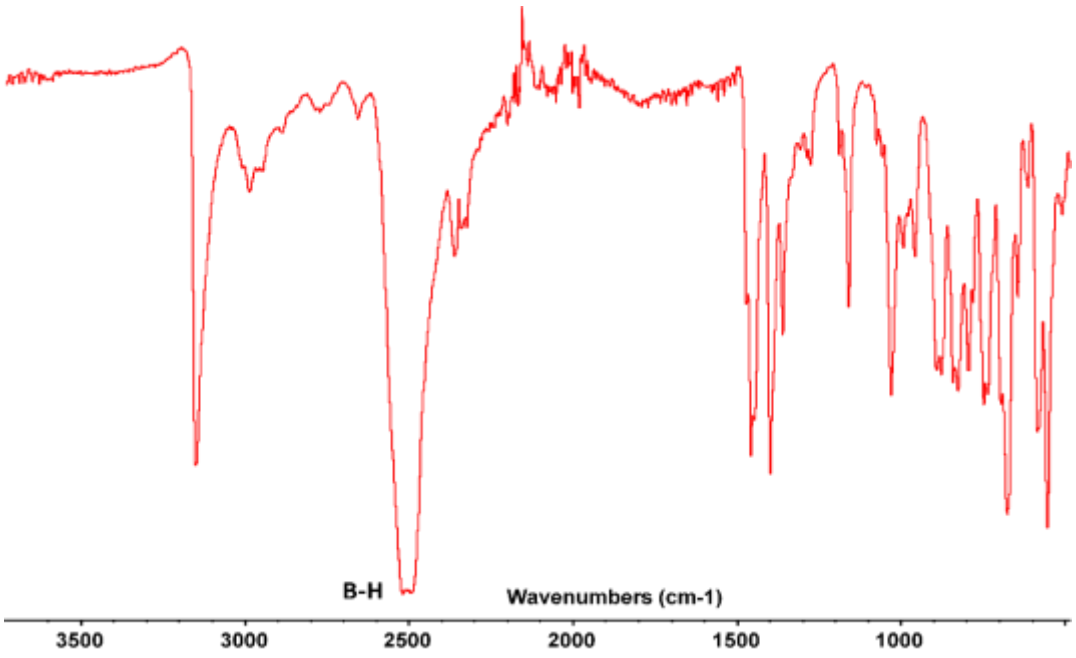

Figure S3. The infrared spectrum of ***$(Et_3NH)_2[B_{20}H_{18}]$***.

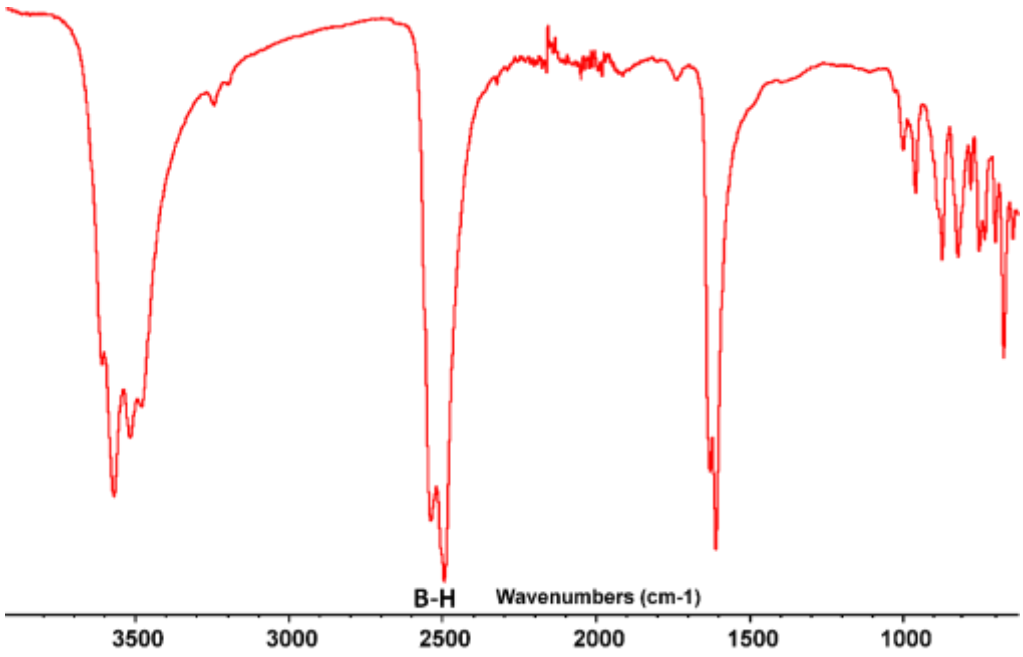

Figure S4. The infrared spectrum of **$Li_2[B_{20}H_{18}]$**.

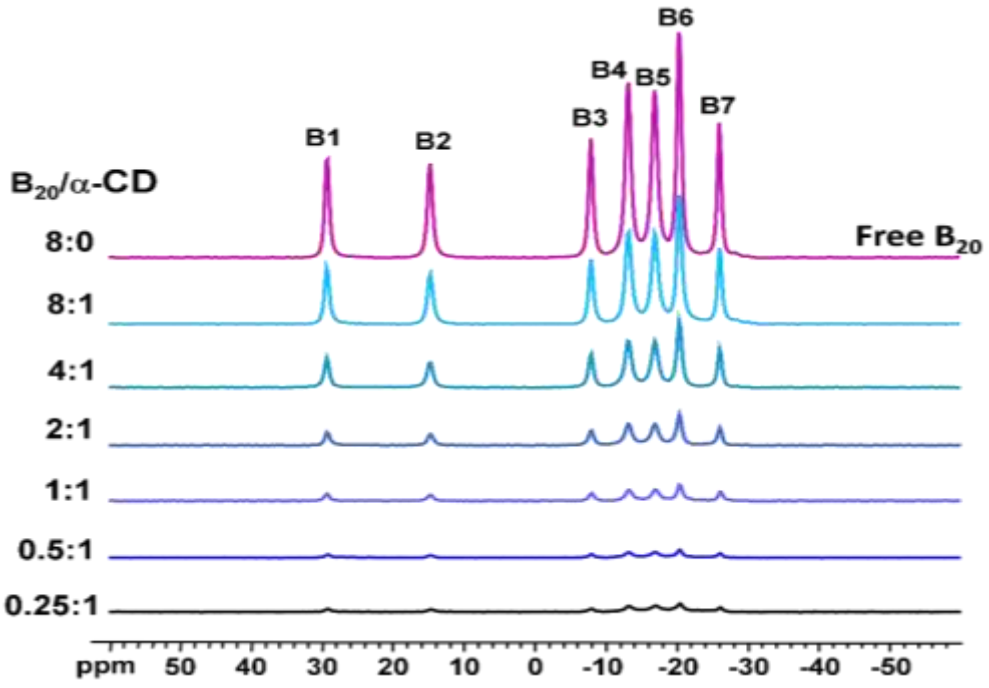

Figure S5. $^{11}B\{^{1}H\}$ NMR spectra in D_2O for different ratios of ***$B_{20}H_{18}$/α-CD*** *from the titration of 3 mM aqueous α-CD solution with $Li_2[B_{20}H_{18}]$.*

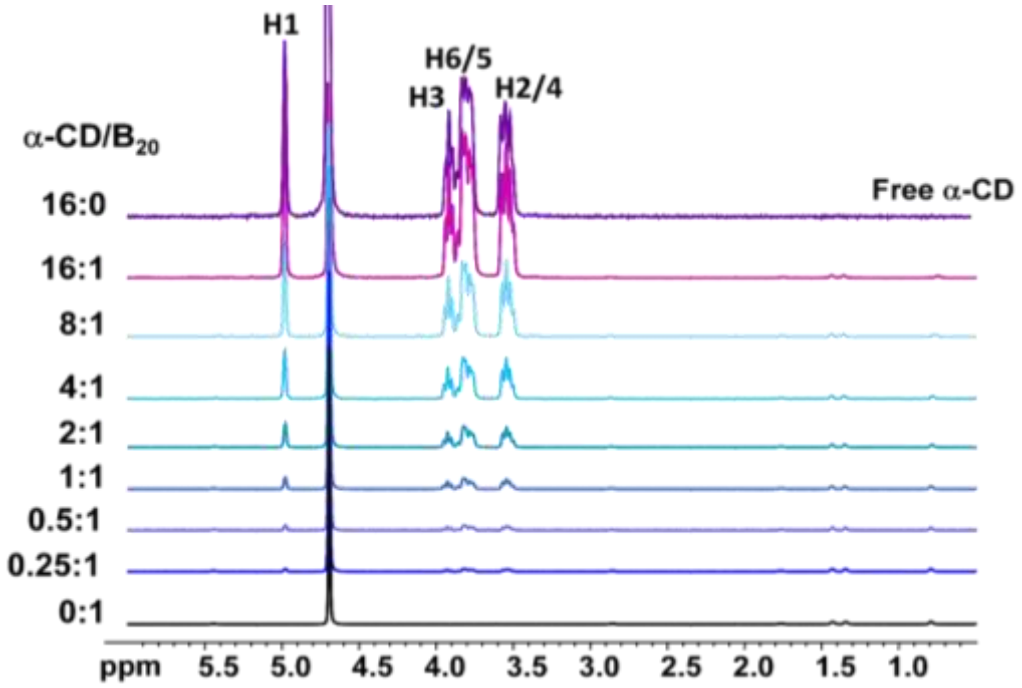

Figure S6. $^{1}H\{^{11}B\}$ NMR spectra in D_2O for different ratios of ***α-CD/$B_{20}H_{18}$*** *from the titration of 3 mM aqueous $Li_2[B_{20}H_{18}]$ with α-CD solution.*

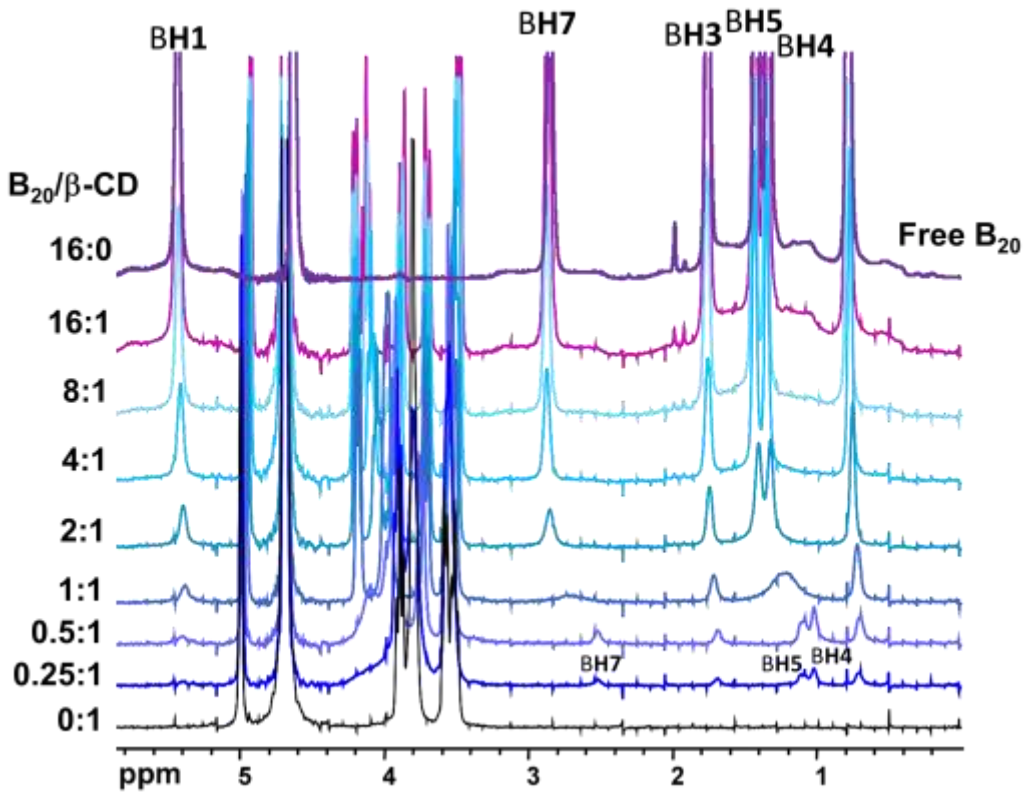

Figure S7. $^{1}H\{^{11}B\}$ NMR spectra in D_2O for different ratios of ***$B_{20}H_{18}$/β-CD*** *from the titration of 3 mM aqueous β-CD solution with $Li_2[B_{20}H_{18}]$, focusing on B**H** protons.*

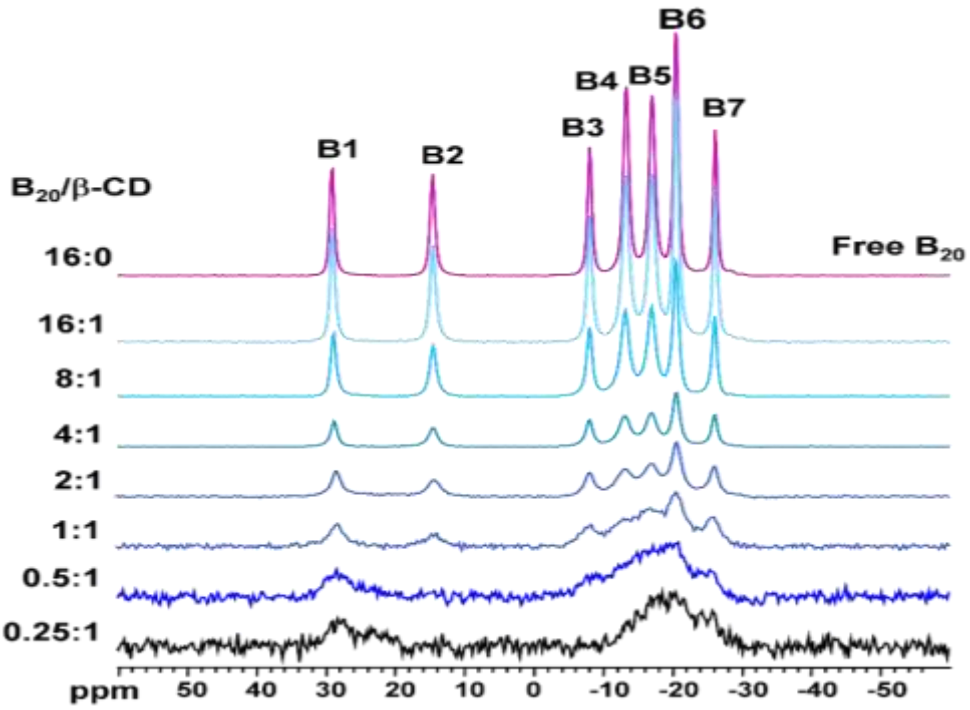

Figure S8. $^{11}B\{^{1}H\}$ NMR spectra in D_2O for different ratios of ***$B_{20}H_{18}$/β-CD*** *from the titration of 3 mM aqueous β-CD solution with $Li_2[B_{20}H_{18}]$.*

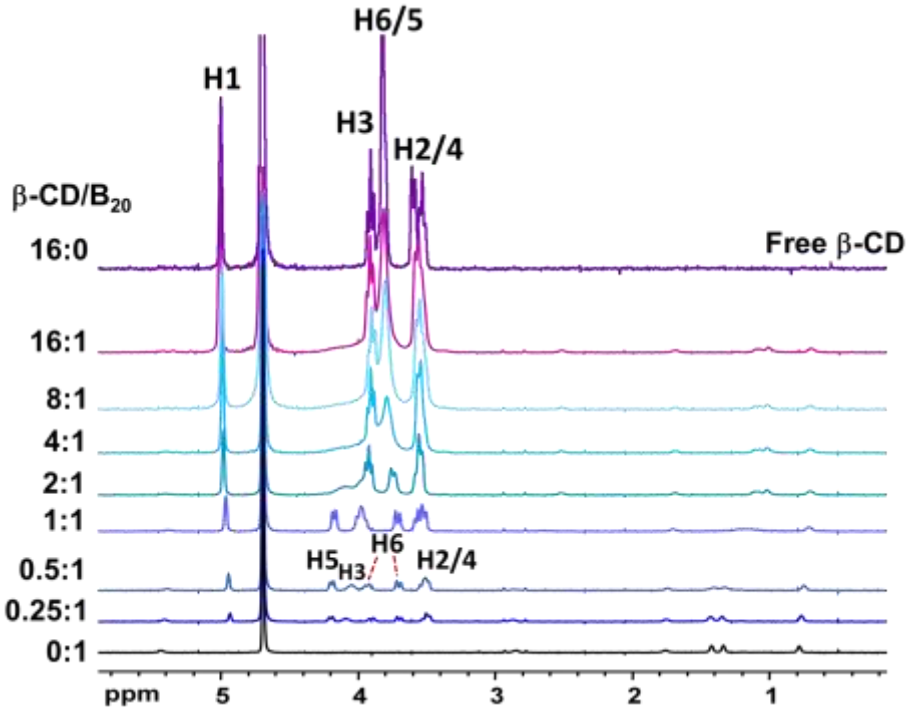

*Figure S9. $^{1}H\{^{11}B\}$ NMR spectra in D_2O for different ratios of **β-CD/$B_{20}H_{18}$** from the titration of 3 mM aqueous $Li_2[B_{20}H_{18}]$ with β-CD solution.*

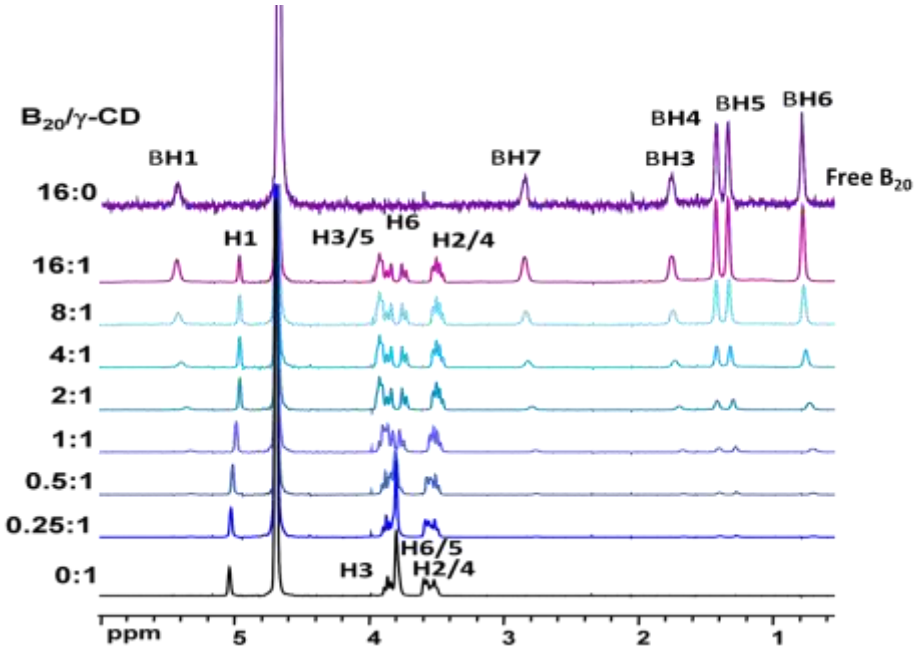

*Figure S10. $^{1}H\{^{11}B\}$ NMR spectra in D_2O for different ratios of **$B_{20}H_{18}$/γ-CD** from the titration of 3 mM aqueous $Li_2[B_{20}H_{18}]$ with γ-CD solution, focusing on B**H** protons.*

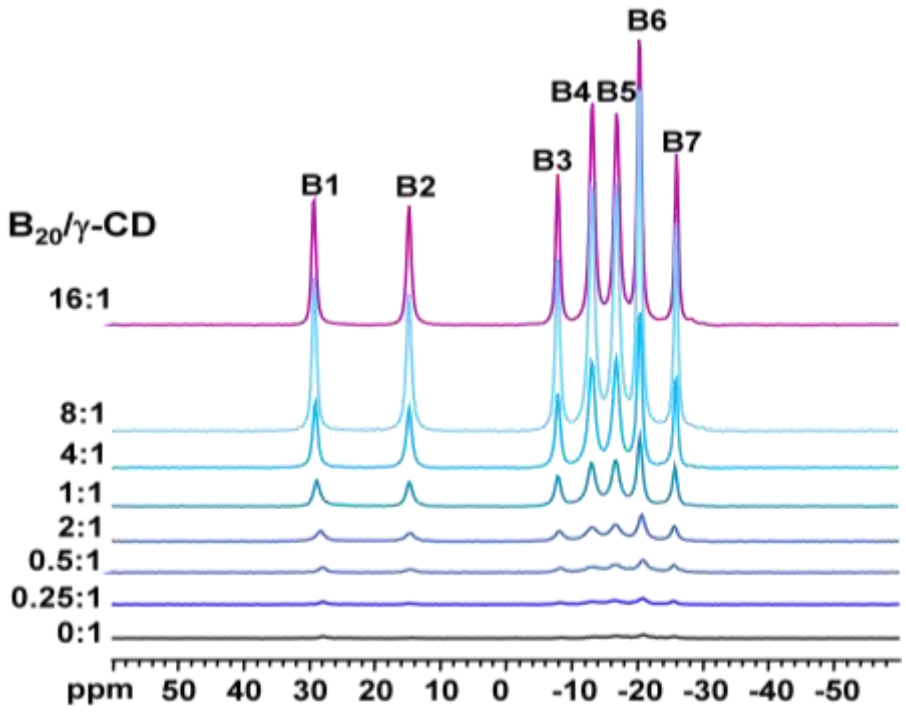

Figure S11. $^{11}B\{^{1}H\}$ NMR spectra in D_2O for different ratios of ***$B_{20}H_{18}$/γ-CD*** *from the titration of 3 mM aqueous γ-CD solution with $Li_2[B_{20}H_{18}]$.*

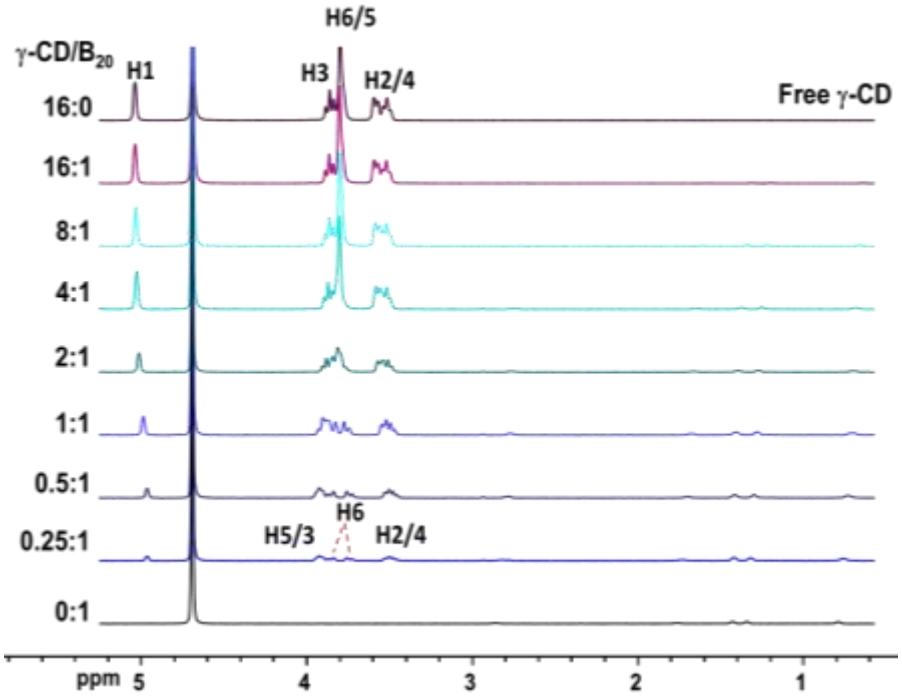

Figure S12. $^{1}H\{^{11}B\}$ NMR spectra in D_2O for different ratios of ***γ-CD/$B_{20}H_{18}$*** *from the titration of 3 mM aqueous $Li_2[B_{20}H_{18}]$ with γ-CD solution.*

*Table S1. $^1H\{^{11}B\}$ NMR data of α-CD protons in D_2O for different ratios of **$B_{10}H_9NCCH_3$/α-CD** from the titration of 3 mM aqueous α-CD solution with $B_{10}H_9NCCH_3^-$.*

$B_{10}H_9NCCH_3$: α-CD	H1	H2	H3	H4	H5	H6
8 : 1	4.967	3.541	3.961	3.509	3.803	3.778
4 : 1	4.969	3.546	3.940	3.506	3.803	3.780
2 : 1	4.971	3.546	3.922	3.509	3.805	3.780
1 : 1	4.972	3.550	3.914	3.507	3.805	3.782
$\frac{1}{2}$: 1	4.973	3.550	3.908	3.508	3.805	3.782
$\frac{1}{4}$: 1	4.974	3.550	3.904	3.510	3.805	3.782
0 : 1	4.977	3.554	3.903	3.511	3.807	3.783
$\delta_{obs} - \delta_{H(\alpha\text{-CD})}$	-0.001	-0.013	**+0.058**	-0.002	-0.004	-0.005

*Table S2. $^1H\{^{11}B\}$ NMR data for β-CD protons in D_2O for different ratios of **$B_{10}H_9NCCH_3$/β-CD** from the titration of 3 mM aqueous β-CD solution with $B_{10}H_9NCCH_3^-$.*

$B_{10}H_9NCCH_3$: β-CD	H1	H2	H3	H4	H5	H6
8 : 1	4.965	3.548	3.926	3.519	3.942	3.821
4 : 1	4.967	3.545	3.916	3.512	3.929	3.817
2 : 1	4.973	3.548	3.916	3.508	3.884	3.814
1 : 1	4.979	3.555	3.906	3.506	3.847	3.811
$\frac{1}{2}$: 1	4.985	3.560	3.898	3.506	3.823	3.807
$\frac{1}{4}$: 1	4.987	3.564	3.890	3.506	3.803	3.804
0 : 1	4.991	3.570	3.882	3.506	3.785	3.784
$\delta_{obs} - \delta_{H(\beta\text{-CD})}$	-0.026	-0.022	+0.044	+0.013	**+0.157**	+0.037

*Table S3. $^{1}H\{^{11}B\}$ NMR data for γ-CD in D_2O for different ratios of **$B_{10}H_9NCCH_3$/γ-CD** from the titration of 3 mM aqueous γ-CD solution with $B_{10}H_9NCCH_3^-$.*

$B_{10}H_9NCCH_3$: γ-CD	H1	H2	H3	H4	H5	H6
8 : 1	4.998	3.564	3.877	3.504	3.965	3.807
4 : 1	5.000	3.563	3.877	3.504	3.954	3.808
2 : 1	5.004	3.561	3.875	3.503	3.928	3.809
1 : 1	5.012	3.564	3.871	3.505	3.884	3.809
$\frac{1}{2}$: 1	5.020	3.566	3.863	3.506	3.832	3.809
$\frac{1}{4}$: 1	5.025	3.569	3.860	3.508	3.814	3.804
0 : 1	5.033	3.575	3.857	3.512	3.783	3.799
$\delta_{obs} - \delta_{H(\gamma\text{-CD})}$	-0.04	-0.011	+0.02	-0.008	**+0.182**	+0.008

*Table S4. $^{1}H\{^{11}B\}$ NMR data for α-CD in D_2O for different ratios of **$B_{20}H_{18}$/α-CD** from the titration of 3 mM aqueous α-CD solution with $B_{20}H_{18}^{2-}$.*

$B_{20}H_{18}^{2-}$: α-CD	H1	H2	H3	H4	H5	H6
8 : 1	4.965	3.545	3.996	3.527	3.820	3.823
4 : 1	4.968	3.540	3.962	3.525	3.815	3.816
2 : 1	4.971	3.540	3.935	3.524	3.812	3.814
1 : 1	4.971	3.549	3.921	3.495	3.805	3.809
$\frac{1}{2}$: 1	4.973	3.549	3.911	3.510	3.808	3.807
$\frac{1}{4}$: 1	4.974	3.551	3.906	3.506	3.807	3.807
0 : 1	4.972	3.548	3.899	3.502	3.804	3.804
$\delta_{obs} - \delta_{H(\text{Free }\alpha\text{-CD})}$	-0.007	-0.003	**+0.097**	+0.025	+0.016	+0.019

*Table S5. $^{1}H\{^{11}B\}$ NMR data of B**H** protons in D_2O for different ratios of **α-CD/$B_{20}H_{18}$** from the titration of 3 mM aqueous $B_{20}H_{18}^{2-}$ solution with α-CD.*

α-CD : $B_{20}H_{18}^{2-}$	BH1	BH3	BH4	BH5	BH6	BH7
16:1	5.39	1.75	1.36	1.43	0.74	2.88
8 : 1	5.41	1.75	1.35	1.43	0.76	2.87
4 : 1	5.42	1.75	1.35	1.43	0.78	2.86
2 : 1	5.43	1.77	1.35	1.43	0.78	2.86
1 : 1	5.44	1.76	1.35	1.43	0.79	2.86
$\frac{1}{2}$: 1	5.43	1.77	1.34	1.43	0.79	2.86
$\frac{1}{4}$: 1	5.44	1.77	1.34	1.43	0.79	2.85
0 : 1 (Free B_{20})	5.44	1.76	1.34	1.43	0.79	2.86
$\delta_{obs} - \delta_{H(Free\ B20)}$	**-0.05**	-0.01	+0.02	0.00	**-0.05**	+0.02

*Table S6. $^{11}B\{^{1}H\}$ NMR data for **Boron atoms** in D_2O for different ratios of **α-CD/$B_{20}H_{18}$** from the titration of 3 mM aqueous $B_{20}H_{18}^{2-}$ solution with α-CD.*

α-CD : $B_{20}H_{18}^{2-}$	B1	B2	B3	B4	B5	B6	B7
16:1	29.43	15.13	-7.84	-13.12	-16.93	-20.32	-26.19
8 : 1	29.24	15.20	-7.77	-13.18	-16.77	-20.26	-26.13
4 : 1	29.27	14.92	-7.84	-13.14	-16.94	-20.32	-26.18
2 : 1	29.30	14.83	-7.90	-13.20	-16.93	-20.36	-26.13
1 : 1	29.45	14.71	-8.00	-13.31	-17.05	-20.48	-26.18
$\frac{1}{2}$: 1	29.49	14.70	-8.05	-13.31	-17.07	-20.51	-26.19
$\frac{1}{4}$: 1	29.65	14.72	-8.02	-13.28	-17.05	-20.49	-26.17
0 : 1 (Free B_{20})	29.23	14.63	-8.04	-13.32	-17.07	-20.52	-26.19
$\delta_{obs} - \delta_{B(Free\ B20)}$	+0.2	+0.5	+0.2	+0.2	+0.2	+0.14	0.00

*Table S7. $^{1}H\{^{11}B\}$ NMR data for β-C in D_2O for different ratios of **$B_{20}H_{18}$/β-CD** from the titration of 3 mM aqueous β-CD solution with $B_{20}H_{18}^{2-}$.*

$B_{20}H_{18}$: β-CD	H1	H2	H3	H4	H5	H6
8 : 1	4.932	3.500	4.117	3.500	4.205	3.797
4 : 1	4.936	3.508	4.093	3.508	4.201	3.804
2 : 1	4.964	3.510	4.052	3.510	4.196	3.821
1 : 1	4.962	3.547	3.983	3.529	4.182	3.712
$\frac{1}{2}$: 1	4.981	3.558	3.922	3.558	3.971	3.743
$\frac{1}{4}$: 1	4.989	3.564	3.906	3.564	3.920	3.800
0 : 1	4.996	3.576	3.893	3.511	3.778	3.807
$\delta_{obs} - \delta_{H(Free\ \beta\text{-}CD)}$	-0.064	-0.076	**+0.224**	-0.011	**+0.427**	-0.01

*Table S8. $^{1}H\{^{11}B\}$ NMR data of B**H** protons in D_2O for different ratios of **$B_{20}H_{18}$/β-CD** from the titration of 3 mM aqueous β-CD solution with $B_{20}H_{18}^{2-}$.*

$B_{20}H_{18}$: β-CD	BH1	BH3	BH4	BH5	BH6	BH7
0 : 8 (Free B_{20})	5.44	1.76	1.34	1.43	0.79	2.86
8 : 1	5.43	1.76	1.35	1.44	0.78	2.87
4 : 1	5.41	1.76	1.35	1.43	0.77	2.87
2 : 1	5.40	1.75	1.32	1.40	0.75	2.85
1 : 1	5.38	1.72	1.29	1.22	0.72	2.74
$\frac{1}{2}$: 1	5.40	1.69	1.08	1.02	0.70	2.54
$\frac{1}{4}$: 1	5.37	1.68	1.01	1.03	0.69	2.50
$\delta_{H(Free\ B20)} - \delta_{obs}$	0.07	0.08	**+0.33**	**+0.4**	0.1	**+0.36**

*Table S9. $^{11}B\{^1H\}$ NMR data for **Boron atoms** in D_2O for different ratios of **$B_{20}H_{18}$/β-CD** from the titration of 3 mM aqueous β-CD solution with $B_{20}H_{18}^{2-}$.*

$B_{20}H_{18}$: β-CD	B1	B2	B3	B4	B5	B6	B7
16 : 0 (Free B_{20})	29.23	14.63	-8.04	-13.32	-17.07	-20.52	-26.19
16:1	28.97	14.58	-7.99	-13.15	-16.97	-20.48	-26.06
8 : 1	28.81	14.54	-7.99	-13.09	-16.95	-20.50	-26.02
4 : 1	28.60	14.44	-7.84	-13.16	-17.00	-20.51	-26.00
2 : 1	28.40	14.10	-8.19	-12.80	-16.70	-20.50	-25.85
1 : 1	br	br	br	br	br	br	br
$\frac{1}{2}$: 1	br	br	br	br	br	br	br
$\frac{1}{4}$: 1	br	br	br	br	br	br	br
$\delta_{B(Free\ B20)} - \delta_{obs}$	**+0.83**	+0.53	+0.15	-0.52	-0.37	-0.02	**-0.35**

*Table S10. $^1H\{^{11}B\}$ NMR data for β-CD in D_2O for different ratios of **β-CD/$B_{20}H_{18}$** from the titration of 3 mM aqueous $B_{20}H_{18}^{2-}$ solution with β-CD.*

β-CD : $B_{20}H_{18}$	H1	H2	H3	H4	H5	H6
16 : 0 (Free β-CD)	4.996	3.576	3.893	3.511	3.778	3.807
16:1	4.986	3.548	3.898	3.548	3.798	3.798
8 : 1	4.988	3.549	3.899	3.549	3.800	3.800
4 : 1	4.985	3.542	3.906	3.560	3.789	3.789
2 : 1	4.978	3.556	3.920	3.556	3.804	3.742
1 : 1	4.962	3.552	3.976	3.532	4.174	3.708
$\frac{1}{2}$: 1	4.942	3.701	4.047	3.507	4.195	3.933
$\frac{1}{4}$: 1	4.931	3.698	4.087	3.504	4.197	3.902
$\delta_{H(Free\ β\text{-}CD)} - \delta_{obs}$	0.065	-0.122	**-0.194**	0.007	**-0.419**	-0.095

*Table S11. $^{1}H\{^{11}B\}$ NMR data of B**H** protons in D_2O for different ratios of **β-CD/$B_{20}H_{18}$** from the titration of 3 mM aqueous $B_{20}H_{18}^{2-}$ solution with β-CD.*

β-CD : $B_{20}H_{18}$	BH1	BH3	BH4	BH5	BH6	BH7
16 : 1	5.40	1.69	1.02	1.09	0.70	2.51
8 : 1	5.39	1.69	1.01	1.08	0.70	2.51
4 : 1	5.40	1.68	1.02	1.08	0.70	2.52
2 : 1	5.40	1.69	1.02	1.08	0.70	2.52
1 : 1	5.38	1.71	1.21	1.21	0.70	2.64
$\frac{1}{2}$: 1	5.39	1.74	1.33	1.40	0.75	2.87
$\frac{1}{4}$: 1	5.41	1.75	1.34	1.43	0.77	2.87
0 : 1 (Free B_{20})	5.44	1.76	1.34	1.43	0.79	2.86
$\delta_{obs} - \delta_{H(Free\ B20)}$	-0.04	-0.07	**-0.32**	**-0.34**	-0.09	**-0.35**

*Table S12. $^{11}B\{^{1}H\}$ NMR data for **Boron atoms** in D_2O for different ratios of **β-CD/$B_{20}H_{18}$** from the titration of 3 mM aqueous $B_{20}H_{18}^{2-}$ solution with β-CD.*

β-CD : $B_{20}H_{18}$	B1	B2	B3	B4	B5	B6	B7
16:1	28.10	br	br	br	br	br	br
8 : 1	28.40	br	-7.40	br	br	-20. 30	-25.20
4 : 1	28.7	br	-8.40	br	br	-20.30	-25.50
2 : 1	28.40	14.70	-8.20	br	br	-20.20	-26.00
1 : 1	28.40	14.1	-7.6	-13.9	-15.7	-20.17	-26.00
$\frac{1}{2}$: 1	28.53	14.39	-7.86	-13.03	-16.70	-20.45	-25.91
$\frac{1}{4}$: 1	28.81	14.57	-8.01	-13.40	-16.94	-20.51	-26.03
0 : 1	29.23	14.63	-8.04	-13.32	-17.07	-20.52	-26.19
$\delta_{obs} - \delta_{B(Free\ B20)}$	**-1.13**	0.07	+0.64	-0.58	**+1.37**	+0.22	+0.99

*Table S13. $^{1}H\{^{11}B\}$ NMR data for γ-C in D_2O for different ratios of **$B_{20}H_{18}$/γ-CD** from the titration of 3 mM aqueous γ-CD solution with $B_{20}H_{18}^{2-}$.*

$B_{20}H_{18}$: γ-CD	H1	H2	H3	H4	H5	H6
16 : 1	4.971	3.513	3.932	3.487	3.932	3.802
8 : 1	4.968	3.509	3.930	3.484	3.930	3.801
4 : 1	4.966	3.506	3.928	3.482	3.928	3.802
2 : 1	4.964	3.506	3.927	3.481	3.927	3.800
1 : 1	4.989	3.509	3.921	3.497	3.881	3.777
$\frac{1}{2}$: 1	5.014	3.541	3.880	3.510	3.845	3.805
$\frac{1}{4}$: 1	5.024	3.544	3.827	3.513	3.824	3.800
0 : 1	5.034	3.551	3.861	3.515	3.787	3.796
$\delta_{obs} - \delta_{H(Free\ \gamma\text{-}CD)}$	-0.06	-0.038	**+0.071**	-0.028	**+0.145**	+0.006

*Table S14. $^{1}H\{^{11}B\}$ NMR data for γ-C in D_2O for different ratios of **$B_{20}H_{18}$/γ-CD** from the titration of 3 mM aqueous γ-CD solution with $B_{20}H_{18}^{2-}$.*

$B_{20}H_{18}$: γ-CD	BH1	BH3	BH4	BH5	BH6	BH7
0 : 8 (Free B_{20})	5.44	1.76	1.34	1.43	0.79	2.86
16:1	5.46	1.76	1.34	1.43	0.79	2.86
8 : 1	5.42	1.75	1.34	1.43	0.78	2.84
4 : 1	5.40	1.73	1.32	1.43	0.76	2.82
2 : 1	5.36	1.70	1.30	1.42	0.73	2.79
1 : 1	5.33	1.68	1.29	1.4	0.70	2.77
$\frac{1}{2}$: 1	5.32	1.66	1.28	1.34	0.70	2.76
$\frac{1}{4}$: 1	5.32	1.66	1.27	1.39	0.69	2.76
$\delta_{H(Free\ B20)} - \delta_{obs}$	+0.12	+0.1	+0.07	+0.04	+0.1	+0.1

*Table S15. $^{11}B\{^1H\}$ NMR data for **Boron atoms** in D_2O for different ratios of **$B_{20}H_{18}$/γ-CD** from the titration of 3 mM aqueous γ-CD solution with $B_{20}H_{18}^{2-}$.*

$B_{20}H_{18}$: β-CD	B1	B2	B3	B4	B5	B6	B7
16 : 0 (Free B_{20})	29.23	14.63	-8.04	-13.32	-17.07	-20.52	-26.19
16:1	29.10	14.64	-8.01	-13.32	-16.96	-20.47	-26.05
8 : 1	28.95	14.63	-8.04	-13.23	-16.93	-20.51	-26.01
4 : 1	28.74	14.61	-8.09	-13.22	-16.89	-20.57	-25.92
2 : 1	28.12	14.52	-8.18	-13.13	-16.74	-20.72	-25.70
1 : 1	27.93	14.52	-8.27	-13.25	-16.47	-20.83	-25.58
$\frac{1}{2}$: 1	28.20	14.51	-8.29	-13.29	-16.72	-20.85	-25.47
$\frac{1}{4}$: 1	28.20	14.43	-8.54	-13.52	-16.97	-20.89	-25.59
$\delta_{B(Free\ B20)} - \delta_{obs}$	**+1.03**	+0.2	+0.5	+0.2	-0.1	+0.37	-0.6

*Table S16. $^1H\{^{11}B\}$ NMR data for γ-CD in D_2O for different ratios of **γ-CD/$B_{20}H_{18}$** from the titration of 3 mM aqueous $B_{20}H_{18}^{2-}$ solution with γ-CD.*

γ-CD : $B_{20}H_{18}$	H1	H2	H3	H4	H5	H6
16 : 0 (Free CD)	5.034	3.551	3.861	3.515	3.787	3.796
16 : 1	5.039	3.558	3.867	3.523	3.787	3.804
8 : 1	5.037	3.555	3.867	3.521	3.784	3.804
4 : 1	5.09	3.548	3.867	3.517	3.784	3.799
2 : 1	5.023	3.544	3.875	3.515	3.842	3.803
1 : 1	5.011	3.533	3.891	3.508	3.904	3.804
$\frac{1}{2}$: 1	4.983	3.518	3.913	3.492	3.930	3.802
$\frac{1}{4}$: 1	4.964	3.517	3.926	3.480	3.926	3.798
$\delta_{H(Free\ \gamma\text{-}CD)} - \delta_{obs}$	0.07	0.034	**-0.065**	0.035	**-0.139**	-0.002

*Table S17. $^{1}H\{^{11}B\}$ NMR data of B**H** protons in D_2O for different ratios of **γ-CD/$B_{20}H_{18}$** from the titration of 3 mM aqueous $B_{20}H_{18}^{2-}$ solution with γ-CD.*

γ-CD : $B_{20}H_{18}$	BH1	BH3	BH4	BH5	BH6	BH7
16 : 1	5.32	1.59	1.21	1.32	0.65	2.69
8 : 1	5.39	1.69	1.01	1.08	0.70	2.51
4 : 1	5.40	1.64	1.25	1.37	0.68	2.74
2 : 1	5.32	1.66	1.27	1.40	0.70	2.76
1 : 1	5.33	1.67	1.28	1.41	0.70	2.76
$\frac{1}{2}$: 1	5.33	1.69	1.29	1.41	0.71	2.78
$\frac{1}{4}$: 1	5.38	1.72	1.31	1.42	0.74	2.80
0 : 1 (Free B_{20})	5.44	1.76	1.34	1.43	0.79	2.86
$\delta_{obs} - \delta_{H(Free\ B20)}$	-0.12	**-0.17**	-0.13	-0.11	-0.14	**-0.17**

*Table S18. $^{11}B\{^{1}H\}$ NMR data for **Boron atoms** in D_2O for different ratios of **γ-CD/$B_{20}H_{18}$** from the titration of 3 mM aqueous $B_{20}H_{18}^{2-}$ solution with γ-CD.*

γ-CD : $B_{20}H_{18}$	B1	B2	B3	B4	B5	B6	B7
16:1	27.80	14.63	-8.27	-13.32	-16.73	-20.93	-25.59
8 : 1	27.80	14.63	-8.27	-13.23	-16.66	-20. 93	-25.46
4 : 1	27.86	14.63	-8.41	-13.16	-16.58	-20.84	-25.59
2 : 1	27.80	14.63	-8.25	-13.09	-16.63	-20.83	-25.56
1 : 1	27.80	14.63	-8.31	-13.12	-16.84	-20.82	-25.55
$\frac{1}{2}$: 1	27.80	14.63	-8.13	-13.09	-16.83	-20.83	-25.48
$\frac{1}{4}$: 1	28.57	14.63	-8.07	-13.25	-16.86	-20.60	-25.83
0 : 1	29.23	14.63	-8.04	-13.32	-17.07	-20.52	-26.19
$\delta_{obs} - \delta_{B(Free\ B20)}$	**-1.43**	0.00	-0.23	0.00	+0.34	-0.41	**+0.6**